机电学院公布 2015 年度代表性论文

机电学院经过认真审议，综合考虑论文学术水平、期刊水平和影响力，从本学院 2015 年发表的 156 篇 SCI 检索论文中遴选出 13 篇代表性论文，现予以公布。

（以第一作者姓氏拼音顺序排名）

1. 常洪龙，王沙沙，苑伟政等
   Chang H, Gong X, Wang S, et al. On Improving the Performance of a Triaxis Vortex Convective Gyroscope Through Suspended Silicon Thermistors[J]. IEEESensors Journal, 2015, 15(2): 946-955.

2. 邓超，蒋建军，刘发，方良超，王俊彪，李德佳，吴建军
   Deng C, Jiang J, Liu F, et al. Influence of carbon nanotubes coatings onto carbon fiber by oxidative treatments combined with electrophoretic deposition on interfacial properties of carbon fiber composite[J]. Applied Surface Science, 2015, 357: 1274-1280.

3. 兑红炎，司书宾等
   Dui H, Si S, Zuo M J, et al. Semi-Markov process-based integrated importance measure for multi-state systems[J]. IEEE Transactions on Reliability, 2015, 64(2): 754-765.

4. 高欢欢，朱继宏，张卫红，周莹
   Gao H H, Zhu J H, Zhang W H, et al. An improved adaptive constraint aggregation for integrated layout and topology optimization[J]. Computer Methods in Applied Mechanics and Engineering, 2015, 289: 387-408.

5. 侯永锋，张定华，吴宝海，罗明
   Hou Y, Zhang D, Wu B, et al. Milling Force Modeling of Worn Tool and Tool Flank Wear Recognition in End Milling[J]. IEEE/ASME Transactions on Mechatronics, 2015, 20(3): 1024-1035.

6. 黄瑞，张树生等
   Huang R, Zhang S, Xu C, et al. A flexible and effective NC machining process reuse approach for similar subparts[J]. Computer-Aided Design, 2015, 62: 64-77.

7. 李天成等
   Li T, Bolic M, Djuric P M. Resampling methods for particle filtering: classification, implementation, and strategies[J]. IEEE Signal Processing Magazine, 2015, 32(3): 70-86.

8. 齐乐华，钟宋义，罗俊，左寒松等
   Qi L, Zhong S, Luo J, et al. Quantitative characterization and influence of parameters on surface topography in metal micro-droplet deposition manufacture[J]. International Journal of Machine Tools and Manufacture, 2015, 88: 206-213.

9. 宋丹龙，李原，张开富，程晖，吴涛
Song D, Li Y, Zhang K, et al. Stress distribution modeling for interference-fit area of each individual layer around composite laminates joint[J]. Composites Part B: Engineering, 2015, 78: 469-479.

10. 万敏等
Wan M, Kilic Z M, Altintas Y. Mechanics and dynamics of multifunctional tools[J]. Journal of Manufacturing Science and Engineering, 2015, 137(1): 011019.

11. 汪焰恩等
Wang Y, Li X, Li C, et al. Binder droplet impact mechanism on a hydroxyapatite microsphere surface in 3D printing of bone scaffolds[J]. Journal of Materials Science, 2015, 50(14): 5014-5023.

12. 杨昀，张卫红，马颖超，万敏
Yang Y, Zhang W H, Ma Y C, et al. Generalized method for the analysis of bending, torsional and axial receptances of tool–holder–spindle assembly[J]. International Journal of Machine Tools and Manufacture, 2015, 99: 48-67.

13. 张映锋;杜微;王军强;孙树栋等
Zhang Y, Zhang G, Du W, et al. An optimization method for shopfloor material handling based on real-time and multi-source manufacturing data[J]. International Journal of Production Economics, 2015, 165: 282-292.

On Improving the Performance of a Triaxis Vortex Convective Gyroscope Through Suspended Silicon Thermistors

Honglong Chang, *Member, IEEE*, Xianghui Gong, Shasha Wang, Pingwei Zhou, and Weizheng Yuan

***Abstract*— This paper reports on a triaxis vortex convective gyroscope, in which a suspended arch-shaped silicon thermistor is proposed to improve performance by reducing the thermal-induced stress and heat dissipation to the substrate. The arch structure of the thermistor reduced the thermal-induced stress up to 88.7% compared with the clamped–clamped structure of the thermistor in our previous study. The suspended state reduced the heat dissipation to the substrate up to 32%. The experimental test results indicated that the sensitivities of the sensor for the *x*-axis, *y*-axis, and *z*-axis gyroscope were 0.642, 0.528, and 0.241 mV/°/s, respectively. The sensitivity improvement reached 49.65%, 56.21%, and 51.57% for each axis. The measured nonlinearity for the *x*-axis, *y*-axis, and *z*-axis gyroscope were 2.1%, 3.8%, and 4.5% in the range of ±100 °/s, respectively. An improvement in the linearity of 23.53%, 36.67%, and 6.25% was obtained.**

***Index Terms*— Gyroscope, thermistors, thermal-induced stress, heat conduction losses, MEMS.**

I. Introduction

MICROMACHINED gyroscopes are primarily vibratory gyroscopes, which have attracted significant attention over the past 20 years [1], [2]. Vibratory gyroscopes have the advantages of small size and mass production. However, the presence of the proof mass and moving parts in the vibratory gyroscope give rise to inherent problems, such as low shock resistance, structural fatigue, and vibration noise [2], [3], etc.

The replacement of the solid proof mass with fluid particles has created a relatively new field in MEMS research known as fluidic inertial sensing, which avoids moving parts and the associated problems [4]. Zhu et al. reported a MEMS fluidic gyroscope based on natural convection that can sense the Z-axis angular rate and X/Y-axis acceleration [5]. The limitations of the sensor are its dependence on the earth's gravity field and its low sensitivity. High sensitivities can be achieved by forced-convection MEMS gyroscopes, which use various piezoelectric micro-pumps to facilitate the fluidic motion. The increased fluid velocity can enlarge the Coriolis effect and thus improve the sensitivities. A variety of forced-convection gyroscopes has been reported. Zhou *et al.* [6] reported the design and fabrication of a single-axis forced-convection gyroscope. Dau et al. reported a dual-axis forced-convection gyroscope [7] and a 5-DOF forced-convection sensor consisting of a 3-axis gyroscope and a 2-axis accelerometer [8]. A common feature among these forced-convection gyroscopes is that they use a linear jet flow that the piezoelectric micro-pumps created. In our previous study, a six degree-of-freedom (6-DOF) vortex inertial sensor prototype consisting of a 3-axis gyroscope and a 3-axis accelerometer was proposed [9], [10]. The sensor used a vortex gas flow instead of a traditional linear gas flow to sense the angular rate and linear acceleration.

For gas gyroscopes [5]–[10], detection is based on the thermoresistive effect of thermistors. Thus, it is obvious that the sensor performance is heavily dependent on the thermistor. The thermistor used in our previous study [9], [10] was fixed at both ends and not suspended. This type of clamped-clamped thermistor will cause a large thermal stress when the working temperature changes. Furthermore, more heat will dissipate into the substrate because the thermistors are not suspended [11]. The thermal stress and heat loss will significantly deteriorate the performance of the sensor.

To reduce the thermal-induced stress and heat dissipations, a suspended arch-shaped thermistor was proposed in our previous study [12] to improve the performance of the gyroscope. Consequently, the sensitivity of the gyroscope with the new thermistors was improved by approximately 50%, which is a significant improvement. However, in the previous study, we only provided a rough estimation on the contribution made by the thermistors. The reasons for the improvement in performance were not analyzed quantitatively. In this study, a numerical model is built to explain the specific sensitivity improvement benefited from the thermistors. The reduction in the heat conduction losses and the thermal stress in the new thermistors were modeled and their contributions to the performance improvement were calculated.

This report is organized as follows: in Section II, the working principle of the tri-axis vortex gyroscope, the deduction of the sensitivity formulas of the gyroscope and the

Manuscript received August 18, 2014; accepted September 11, 2014. Date of publication September 17, 2014; date of current version November 25, 2014. This work was supported in part by the National Science Foundation of China under Grant 61273052, in part by the Fundamental Research Funds for the Central Universities under Grant 3102014JC02010505, and in part by the 111 Project under Grant B13044. This is an expanded paper from the IEEE SENSORS 2013 Conference. The associate editor coordinating the review of this paper and approving it for publication was Dr. M. R. Yuce.

The authors are with the Key Laboratory of Micro and Nano Systems for Aerospace, Ministry of Education, Northwestern Polytechnical University, Xi'an 710072, China (e-mail: changhl@nwpu.edu.cn; npugongxh@163.com; 18292809670@163.com; zhoupingwei1356@yeah.net; yuanwz@nwpu.edu.cn).

Color versions of one or more of the figures in this paper are available online at http://ieeexplore.ieee.org.

Digital Object Identifier 10.1109/JSEN.2014.2358700

1530-437X © 2014 IEEE. Personal use is permitted, but republication/redistribution requires IEEE permission.
See http://www.ieee.org/publications_standards/publications/rights/index.html for more information.

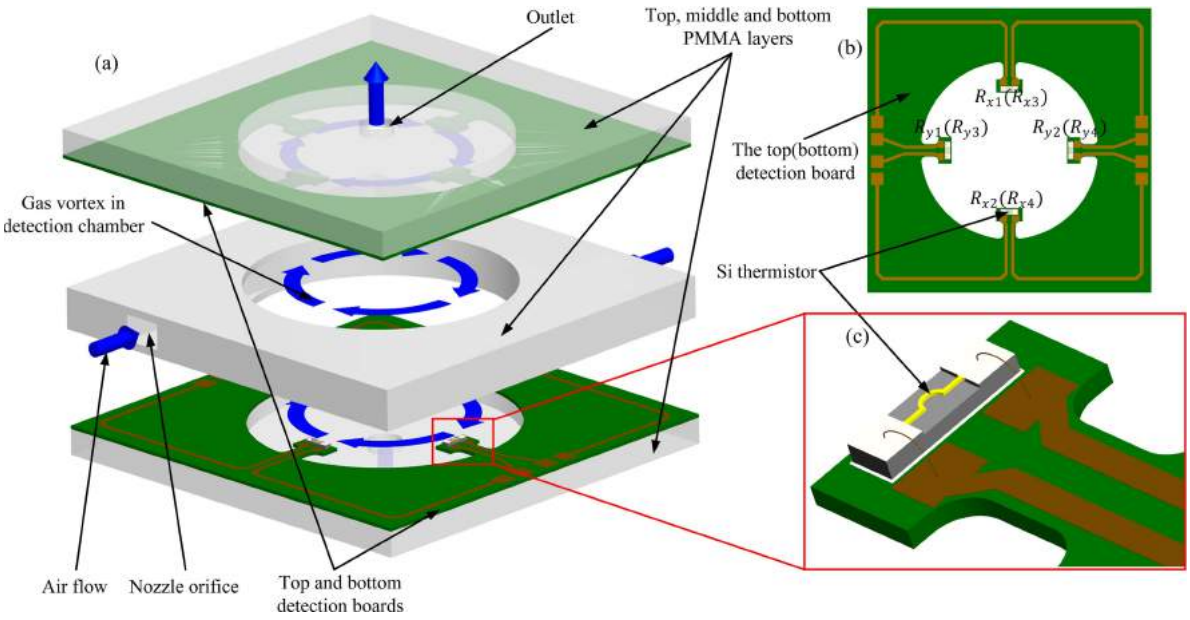

Fig. 1. Configuration of the tri-axis gyroscope: (a) general view of the gyroscope; (b) structure of the top (bottom) detection board with four thermistors bonded on it; and (c) structure of the thermistor.

multi-axis decoupling principle of the gyroscope are introduced. In Section III, the modeling process of the thermal stresses and the heat losses for the two types of thermistor are presented. In Section IV, the arrangement of the thermistors inside the vortex sensor is discussed. In Section V, the experimental testing and verification results of the gyroscope's performance are presented. Finally, conclusions are presented in Section VI.

II. Working Principle

The configuration of the vortex sensor is schematically depicted in Fig. 1. The sensor is composed of a cylindrical detection chamber, two nozzle orifices, two outlets, one bottom detection board and one top detection board. In Fig. 1, eight thermistors, shown in yellow, are distributed onto two detection boards. During operation, the gas flow, shown in blue, generated by an external air pump is injected into the detection chamber in opposite directions through two nozzles to form a vortex, and the exhausted gas is emitted through two outlets. To illustrate the velocity gradient of the vortex flow in the case of the inertial input, the gas flow in Fig. 1(a) is intentionally drawn in three layers. In the case of an angular rate, the vortex will be deflected due to the Coriolis effect. The velocity gradient of the vortex will cause a temperature-induced variation in the thermistor resistance because of the convective heat transfer and the thermo-resistive effect [13], [14]. The relationship between the change in the thermistor's resistance and the input angular rate is the underlying operating principle of the vortex inertial sensor.

A. Z-Axis Gyroscope

The operating principle of the Z-axis gyroscope is conceptually illustrated in Fig. 2. As an angular rate $\vec{\omega}_z$ is applied about the Z-axis, as indicated in Fig. 2(a), the gas vortex will deflect along the radial direction under the Coriolis effect. The gas deflection along the radial direction, which is directly proportional to the magnitude of the applied angular rate about the Z-axis [10], [13], causes the same flow velocity change at the location of the thermistors R_{x1}, R_{x2}, R_{y1} and R_{y2}. Thus, the temperature of the thermistors changes, and con-

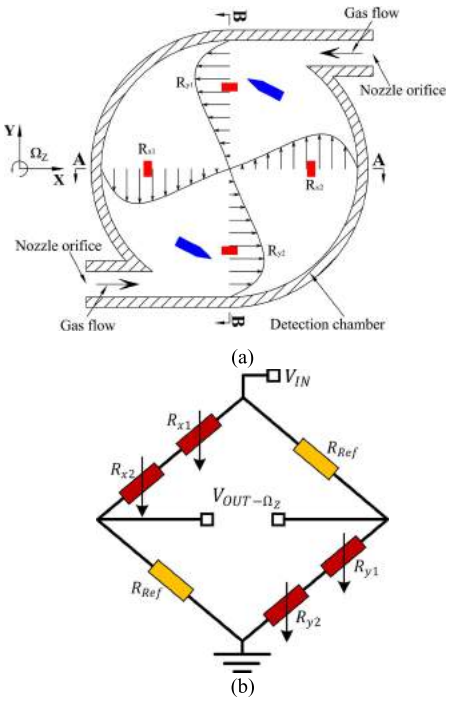

Fig. 2. Working principle for Z-axis angular rate detection. (a) Top view of the vortex deflection induced by angular rate ω_z. The blue arrows indicate the deflecting direction of the gas vortex. (b) Circuit diagram of the Wheatstone bridge to measure the Z-axis angular rate.

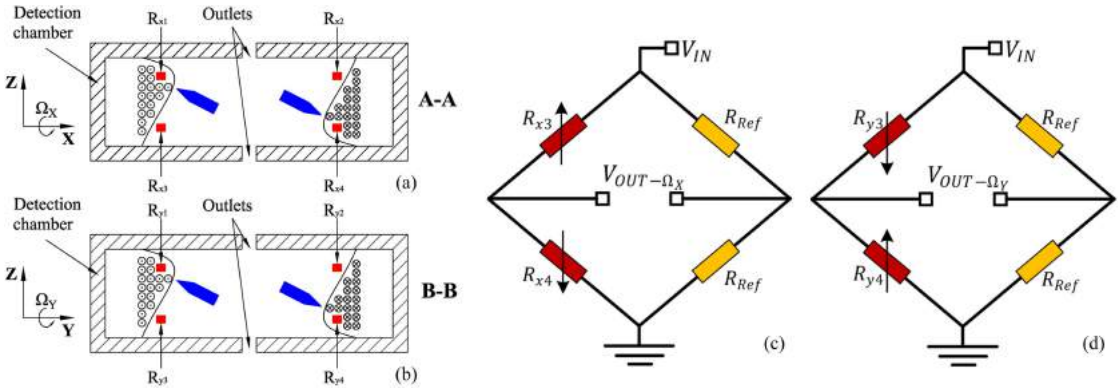

Fig. 3. Working principle for X/Y-axis-angular rate detection. (a) Front view of the vortex deflection induced by ω_x. (b) Side view of the vortex deflection induced by ω_y. The blue arrows indicate the deflecting direction of the gas vortex; $\odot$ and $\otimes$ indicate the directions of the gas flow that are perpendicular to the surface of the paper outwardly and inwardly, respectively. (c) Circuit diagram of the Wheatstone bridge to measure the X-axis angular rate. (d) Circuit diagram of the Wheatstone bridge to the measure Y-axis angular rate.

sequently, their resistances change by the same amount due to the thermoresistive effect. According to [10] and [13], the change in resistance has a linear relation with the applied angular rate, the deduction of which is omitted in this study. Interested readers can refer to our prior study [10] for a relatively comprehensive study of the related deduction.

As shown in Fig. 2(b), a Wheatstone half-bridge denoted by the Ω_Z-bridge is used to measure the resistance change in the thermistors. The induced voltage $V_{out\omega_z}$ under the Z-axis angular rate can be measured as the output of the gyroscope as follows:

$$V_{out\omega_z} = \frac{1}{4}\left(\frac{\Delta R_{x1}+\Delta R_{x2}}{R_{x1}+R_{x2}} + \frac{\Delta R_{y1}+\Delta R_{y2}}{R_{y1}+R_{y2}}\right) V_{in} \quad (1)$$

where V_{in} is the input voltage.

B. X/Y-Axis Gyroscope

Fig. 3 presents the operating principle of the X/Y-axis gyroscope. When an angular rate ω_x around the X-axis is applied, the vortex deflects due to the Coriolis effect around the Y-axis. The applied X-axis angular rate induces opposite changes in the resistance between two opposing thermistors along the X-axis direction, i.e., thermistors R_{y3} and R_{y4}. The change in resistance can be measured using the Wheatstone bridge denoted by the Ω_X-bridge, as indicated in Fig. 3(c). The output voltage $V_{out\omega_x}$ of the Ωx-bridge can be expressed as follows:

$$V_{out\omega_x} = \frac{1}{4}\left(\frac{\Delta R_{x3}}{R_{x3}} - \frac{\Delta R_{x4}}{R_{x4}}\right) V_{in} \quad (2)$$

Similarly, the Ω_Y-bridge can be used to measure the applied Y-axis angular rate, as indicated in Figs. 3(b) and (d). The output voltage $V_{out\omega_y}$ of the Ω_Y-bridge can be expressed as follows:

$$V_{out\omega_y} = \frac{1}{4}\left(\frac{\Delta R_{y3}}{R_{y3}} - \frac{\Delta R_{y4}}{R_{y4}}\right) V_{in}. \quad (3)$$

C. Decoupling Principle

In the tri-axis detection approach, the relationship between one axis' angular rate input and the corresponding output must be independent of the other axes. In this section, the decoupling principles of the tri-axis vortex gyroscope are analyzed in detail. Based on the working principle of the gyroscope, the resistance changes in the eight thermistors under different angular rate inputs are summarized in Table I.

TABLE I
CHANGE IN RESISTANCE IN THERMISTORS UNDER APPLIED ANGULAR RATE

	Ω_X-bridge		Ω_Y-bridge		Ω_Z-bridge			
	R_{x3}	R_{x4}	R_{y3}	R_{y4}	R_{x1}	R_{x2}	R_{y1}	R_{y2}
ω_x	+	−	0	0	−	+	0	0
ω_y	0	0	+	−	0	0	−	+
ω_z	−	−	−	−	−	−	−	−

Note: (+) and (-) signs indicate an increase or decrease, respectively. (0) means unchanged.

In the presence of the Z-axis angular rate, from Fig. 3 and Table I, the resistance changes in the two thermistors of the Ω_X-bridge (Ω_Y-bridge) are the same. Based on (2) and (3), the Ω_X-bridge and Ω_Y-bridge are still in balance, and the output voltages of the Ω_X-bridge and Ω_Y-bridge are zero. In brief, the two bridges have no response to the applied Z-axis angular rate. Therefore, the output voltage signal of the bridges that detect the X/Y-axis angular rate is not affected by the applied Z-axis angular rate.

In the presence of the X-axis angular rate, from Figs. 3(b) and (d) and Table I, the thermistors of the Ω_Y-bridge will not change. From Fig. 2 and Table I, thermistors R_{x1} and R_{x2} of the Ω_Z-bridge undergo an opposite change while thermistors R_{y1} and R_{y2} do not change. Based on (3) and (1), the Ω_Y-bridge and Ω_Z-bridge are still in balance and the output voltages of the Ω_Y-bridge and Ω_Z-bridge are zero, i.e., the two bridges have no response to the applied X-axis angular rate. Thus, the output voltage signal of the bridges that detect the Y-axis angular rate and the Z-axis angular rate is not affected by the applied X-axis angular rate.

Similarly, we can conclude that the applied Y-axis angular rate has no effect on the output voltage signal for the Ω_Z-bridge and the Ω_X-bridge.

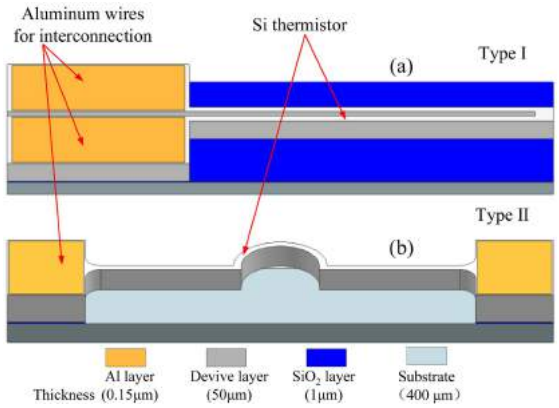

Fig. 4. Schematic view of two types of p-type Si thermistor.

III. Modeling the Contributions From the Thermistors

A suspended arch-shaped silicon thermistor, as schematically depicted in Fig. 4(b), is designed to reduce the thermal-induced stress and heat losses to improve the performance of the sensor compared to the clamped-clamped thermistor (Fig. 4(a)). Here, a numerical model of the new thermistors is introduced, and its contribution to the improvement in performance is analyzed.

A. Thermal Stress Analysis

Because sensor detection is based on the thermoresistive effect of the thermistor, thermal-induced stress will occur as the temperature of a thermistor increases or decreases. Because the type I thermistor is fixed at both ends, the thermistor is hardly able to release its thermal-induced stress by free deformation when its temperature changes. Consequently, a large thermal stress occurs within the thermistor.

The thermal stress in a silicon thermistor will change the resistance of the thermistor due to the piezoresistive effect. Accordingly, the total change in the resistance in a long thin thermistor as its temperature changes by ΔT can be expressed as follows:

$$\left(\frac{\Delta R}{R}\right) = \left(\frac{\Delta R}{R}\right)_p + \left(\frac{\Delta R}{R}\right)_t = -\pi_l \sigma_l + \alpha \Delta T \qquad (4)$$

where subscripts p and t correspond to the piezoresistive effect and thermoresistive effect, respectively; and π_l and σ_l are the longitudinal piezoresistive coefficient and longitudinal stress. The longitudinal stress σ_l can be defined as $\sigma_l = \beta E \Delta T$, where β and E are the thermal expansion coefficient and Young's modulus of the thermistor material.

Both the clamped-clamped thermistor and the suspended thermistor are fabricated to align along the <100> crystal direction in the (100) silicon plane. Because π_l has positive values for the p-type silicon in the <100> crystal orientation and the coefficient TCR α of the p-type silicon thermistor also has a positive value, the piezoresistive effect reduces the sensitivity of the sensor.

The suspended arch structure of the proposed thermistor (Fig. 4(b)) releases thermal stress by allowing the thermistor to expand freely when the temperature increases. The commercial simulation software COMSOL Multiphysics was used to investigate the thermal-stress distribution on the thermistors (Fig. 5). Numerical simulations were used to perform a coupled field analysis of the electric-thermal-structure. A constant current (1.06 mA), convective coefficients (27.8 $W/(m^2 \cdot K)$) and mechanical boundary conditions were applied on the 3-D model. The working temperature of the thermistors at the angular rate free state is 60 °C. The results indicate that the average thermal stress of the thermistor with the clamped-clamped structure increases to 15.9 MPa when the thermistor is heated from a room temperature of 25 °C, whereas that of the new structure was 1.8 MPa (0.051 MPa/°C), i.e., 88.7% of the thermal-induced stress was reduced.

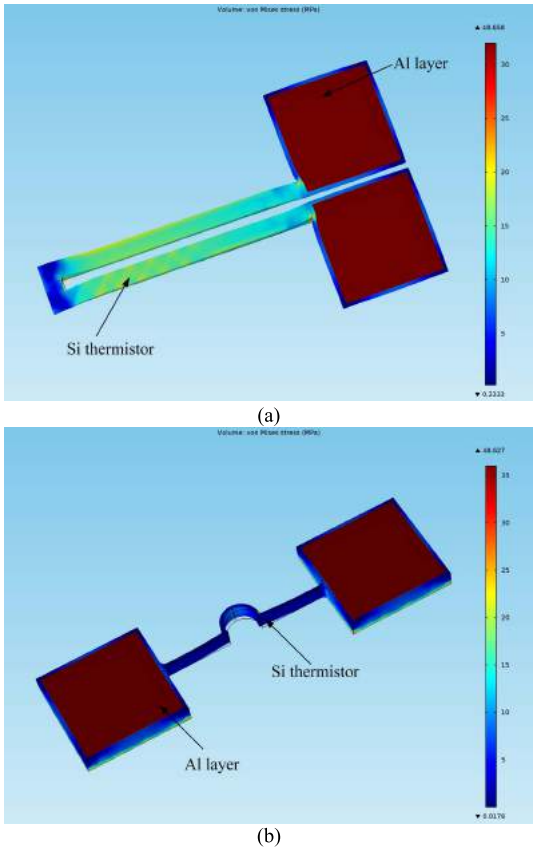

Fig. 5. Thermal stress distribution on thermistor (MPa): (a) type I and (b) type II.

According to [15], the sensitivity of the fluidic gyroscope can be written as follows:

$$S_{gyro} = \frac{1}{2}\frac{V_{in}}{\omega} \cdot \alpha \cdot \Delta T = \frac{1}{2}\frac{V_{in}}{\omega}\left(\frac{\Delta R}{R}\right) \qquad (5)$$

where S_{gyro} is the sensitivity; V_{in} is the supply voltage; and ΔR is the difference in the thermistor resistance due to the application of the angular rate ω.

Based on (4) and (5), the sensitivities of the type I thermistor and the type II thermistor can be calculated using (6) and (7),

respectively, as follows:

$$S_{\mathrm{I}} = \frac{1}{2}\frac{V_{in}}{\omega}\left[\alpha\Delta T - \pi_l\left(\beta E \Delta T\right)\right] \tag{6}$$

$$S_{\mathrm{II}} = \frac{1}{2}\frac{V_{in}}{\omega}\left[\alpha\Delta T - \pi_l\left(11.3\% \cdot \beta E \Delta T\right)\right] \tag{7}$$

The sensitivity improvement of the gyroscope using the type II thermistor can be calculated as follows:

$$\delta_s = \frac{S_{\mathrm{II}} - S_{\mathrm{I}}}{S_{\mathrm{I}}} \tag{8}$$

When the thermistor is heated to 60 °C, i.e. standard working condition of the gyroscope, with a doping concentration of $10^{17}/\mathrm{cm}^3$, we have $\pi_l = 9.2 \times 10^{-10}/\mathrm{Pa}$, $E = 1.9 \times 10^{11}$ Pa, and $\beta = 2.33 \times 10^{-6}/°\mathrm{C}$ [16]. By substituting (6) and (7) into (8), it is determined that the sensitivity of the gyroscope with an arch-shaped thermistor can be improved by 9.28%. It should be noted that the parameter TCR of the two types of thermistors are set to the same value ($4.3 \times 10^{-3}/°\mathrm{C}$) here to compare the sensitivities. Furthermore, we calculated that the decrease in the sensitivity of the clamped-clamped thermistor due to the piezoresistive effect is 9.5% while that of the arch-shaped thermistor is calculated to be only 1.07%.

B. Heat Loss Analysis

When the gyroscope is in operation, an electric current through the thermistor produces the Joule heat denoted by Q_E. A portion of the Joule heat, which is denoted by Q_{cond}, is transferred to the gas flow through forced convection. Meanwhile, the other portion of the Joule heat, which is denoted by Q_{conv}, is dissipated into the substrate through heat conduction. Without considering the heat storage, thermal radiation and natural convection, the heat balance equation for the thermistor under electrical Joule heating can be expressed as follows:

$$Q_E = Q_{cond} + Q_{conv} \tag{9}$$

The basic principle of reduction in the heat losses into the substrate using a suspended structure is depicted in Fig. 6.

The COMSOL Multiphysics software was used to investigate the heat conduction losses into the substrate for the two types of thermistors. The Electric Currents and Heat Transfer in Solids modules were used to perform the coupled field analysis. As presented in Fig. 7, the conductive heat flux of the two types of thermistors was obtained. The simulation results illustrate that the type II thermistor can reduce 32% of heat losses into the substrate compared with the type I thermistor under the same power consumption (Fig. 8). Thus, a considerable reduction in the heat conduction dissipation into the substrate can be achieved using the suspended arch-shaped thermistor.

Here, the thermal efficiency of the thermistor η_{te} can be defined as follows:

$$\eta_{te} = \frac{Q_{conv}}{Q_E} = 1 - \frac{Q_{cond}}{Q_E} \tag{10}$$

Based on (6) and Fig. 8, it is determined that the efficiency of the previously designed type I thermistor is 60.7% while

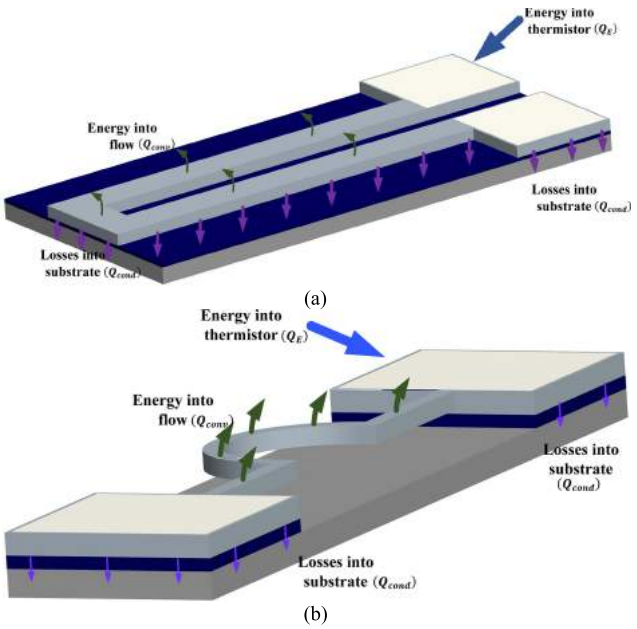

Fig. 6. (a) Energy equilibrium of thermistor type I and (b) thermistor type II. The size of the arrows corresponds to the amount of energy transferred.

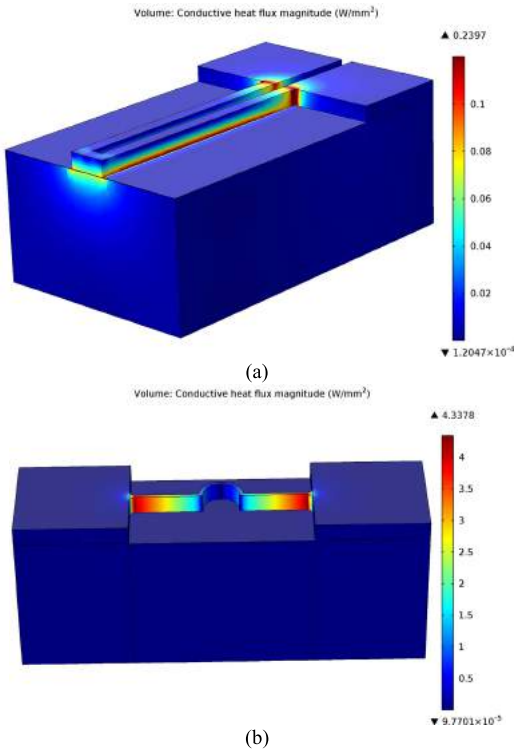

Fig. 7. (a) Conductive heat flux of thermistor type I and (b) thermistor II.

that of the proposed type II thermistor is up to 73.4%. Therefore, the thermal efficiency of the sensor can be improved by 12.7% using the type II thermistor.

As the heat losses into the substrate are reduced, more power is available to heat up the thermistor, which reaches a higher temperature. A larger difference in the thermistor temperature compared to the airflow temperature will yield

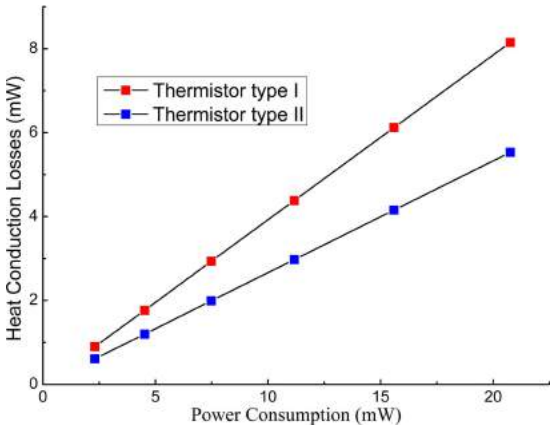

Fig. 8. Conduction losses into the substrate between the two types of thermistors under different power consumption.

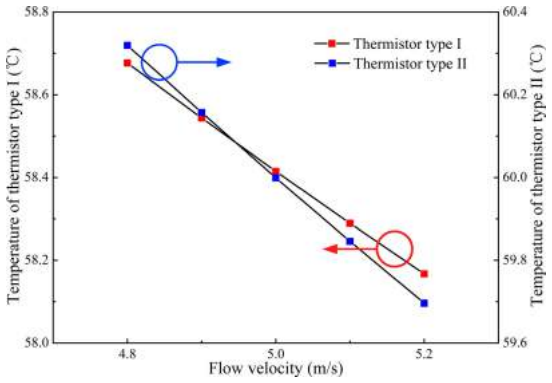

Fig. 9. Relations between the flow velocity at the location of thermistors and the thermistor temperatures. It should be noted that the TCR and the supply voltage of the two types of thermistors are set to the same value.

a higher sensitivity of the sensor.

Based on (5), the sensitivity of the gyroscope can be written as follows:

$$S_{gyro} = \frac{1}{2}\frac{\alpha \Delta T}{\omega} V_{in} \tag{11}$$

where S_{gyro} is the sensitivity; and ΔT is the difference of the mean temperatures of the thermistors due to the application of the angular rate ω.

According to [10] and [13], the flow velocity change ΔV_{vortex} at the location of the thermistors has a linear relation with the applied angular rate ω, as shown in the equation as follows:

$$\Delta V_{vortex} = k \cdot \omega \tag{12}$$

where k is a constant of the scaling factor.

By combining (11) and (12), we can obtain the expression as follows:

$$S_{gyro} = \left(\frac{k\alpha}{2} V_{in}\right) \cdot \frac{\Delta T}{\Delta V_{vortex}} \tag{13}$$

Here, the sensitivities of the sensors are compared in the form of the performance factor, which is the ratio between the temperature change in the thermistor (ΔT) and the velocity change (ΔV_{vortex}). Fig. 9 provides the simulation results of the relations between the flow velocity at the location of the thermistors and the thermistor temperature. The slope represents the sensitivity. The simulation results indicate that the type II thermistor can improve the sensitivity by 22.31% over type I, which is due to the reduction in the heat dissipation into the substrate.

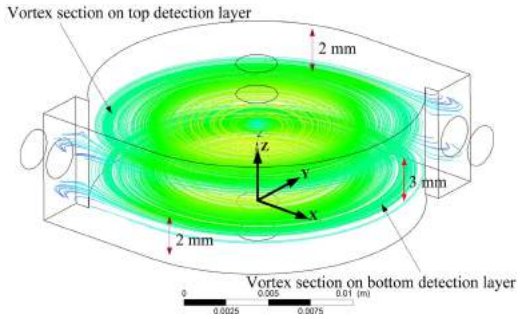

Fig. 10. Flow pattern on bottom and top detection layers.

C. Explanation of the Sensitivity Improvement

As analyzed above, the thermal stress and heat dissipation of the thermistor have a significant impact on the sensitivity of the gyroscope. Equation (13) indicates that the TCR of the thermistor can also affect the sensitivity of the gyroscope.

When considering these three factors, the sensitivities of the gyroscope using the type I and type II thermistors can be respectively written as follows:

$$S_{\mathrm{I}} = \left(\frac{k}{2} V_{in}\right) \cdot \alpha_{\mathrm{I}} \cdot \left(\frac{\Delta T}{\Delta V_{vortex}}\right)_{\mathrm{I}} \cdot (1 - 9.5\%) \tag{14}$$

$$S_{\mathrm{II}} = \left(\frac{k}{2} V_{in}\right) \cdot \alpha_{\mathrm{II}} \cdot \left(\frac{\Delta T}{\Delta V_{vortex}}\right)_{\mathrm{II}} \cdot (1 - 1.07\%) \tag{15}$$

where the two types of thermistors have an identical voltage value V_{in}; α_{I} and α_{II} are the TCRs of thermistor type I and type II, the values of which are 4300 ppm/°C and 4738 ppm/°C, respectively.

By substituting (14) and (15) into (8), it is calculated that the gyroscope using the suspended arch-shaped thermistor has its sensitivity improved by 47.32% compared with that of the clamped-clamped thermistor. The results agree well with the experimental test results shown in the previous study [12], where the sensitivity was improved by approximately 50%.

IV. Implementation of the Vortex Sensor

A. Arrangement of Thermistors

For the vortex gyroscope, it is of vital importance to arrange the thermistors into a proper position in the fluid field. A numerical simulation was performed using ANSYS-CFX to determine where the thermistors should be exactly placed. As presented in Fig. 10, the coordinate system was established by regarding the bottom center of the chamber as the origin. The X-axis and Y-axis were set to be parallel to and perpendicular to the nozzle orifice, respectively. Based on the previous study [10], the z = 2 mm and z = 5 mm planes were selected as the positions for the detection layers, which

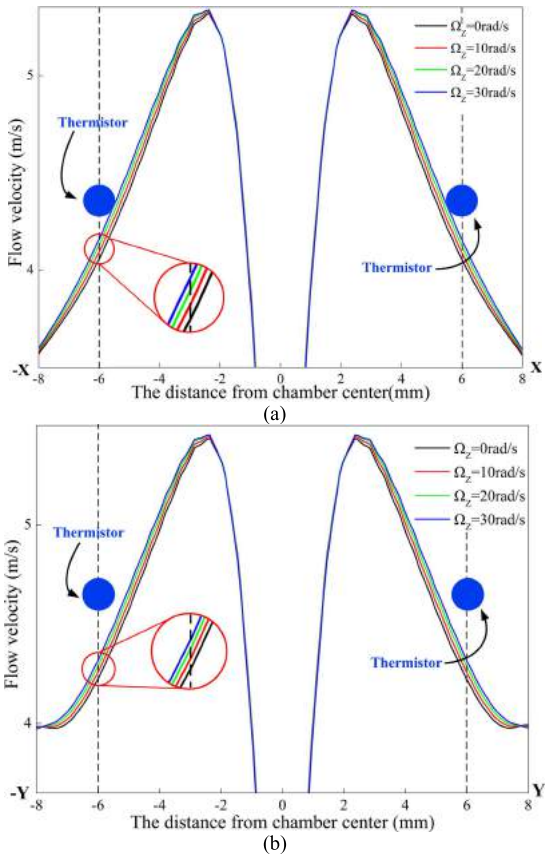

Fig. 11. Flow simulation results achieved by ANSYS-CFX. The velocity curves of the vortex along the X-axis (a) and along the Y-axis (b) on the plane of z = 2 mm at different applied Z-axis angular rates.

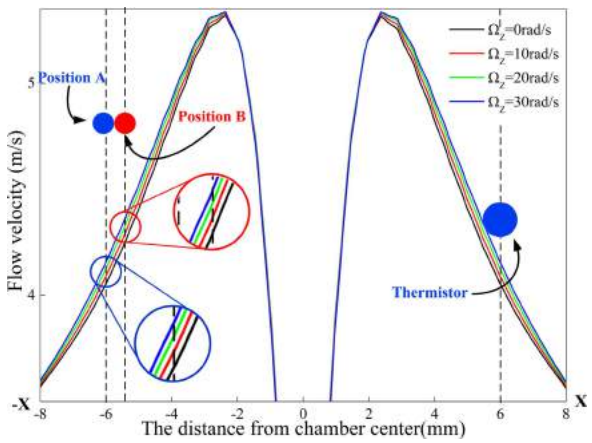

Fig. 12. Velocity curves of the vortex along the X-axis on the z=2 mm plane at different applied Z-axis angular rates. Position A denotes the accurate position where thermistors should be placed and Position B denotes the misaligned position.

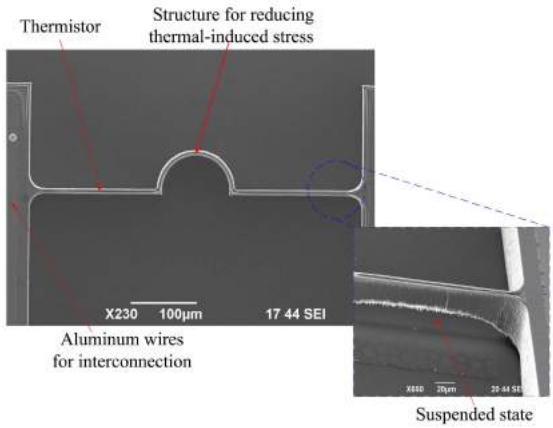

Fig. 13. SEM graphs of the type II thermistor.

could achieve a high sensitivity of the X-axis gyroscope and the Y-axis gyroscope as well as avoid the wall effect.

For the detection layers, e.g., the top detection layer at z = 2 mm, the flow velocity distributions along the X-axis and Y-axis under different applied angular rates are provided in Figs. 11(a) and 11(b), respectively. Because the orientation of the nozzle orifice is parallel to the X-axis, the velocity of vortex along the Y-axis is larger than that along the X-axis. However, the optimal linear range for the velocity changes of both are the same, which are (2.5 mm−7 mm) and (−2.5 mm−7 mm). In this study, the locations (x, y) = (±6 mm, 0) were selected as the positions of the X-axis thermistors. Similarly, the locations (x, y) = (0, ±6 mm) were selected as the positions of the Y-axis thermistors.

When the thermistors are placed at (±6 mm, 0) and (0, ±6 mm), a small misalignment of the thermistors has minimal effect on the performance of the gyroscope. As indicated in Fig. 12, position A denotes the accurate position where thermistors should be placed while position B is the misaligned position. In the presence of the Z-axis angular rate, we can evidently observe from the figure that the velocity change in position A is almost identical to that in position B, i.e., the small misalignment of thermistors has minimal effect on the velocity change induced by the angular rate. Therefore, the effect that the misalignment of the thermistors caused by manual assembly has on the performance of the gyroscope is extremely small and can be neglected here.

B. Assembly of the Vortex Sensor

The proposed arch-shaped thermistor was fabricated by the silicon-on-insulator (SOI) process using the notching effect in the DRIE process [12]. The SEM graphs of the type II thermistor are presented in Fig. 13.

Eight fabricated thermistors are glued onto two PCB detection boards. The thermistors are aligned with the white marks in a rectangle shape to ensure the position with high accuracy. The anchors of the thermistors are connected to the anchors on the PCB board through gold wires. Then, the two PCB detection boards are assembled to the detection chamber. Currently, the detection chamber is fabricated from polymethylmethacrylate (PMMA). The gas flow generated by an external air pump $\Phi \times H$ = 120 mm × 80 mm (Taiwan Honlite) is injected into the detection chamber in opposite directions through two nozzles to form a vortex and exits through two outlets. The external air pump is controlled by an electronic circuit to regulate the velocity of the gas flow.

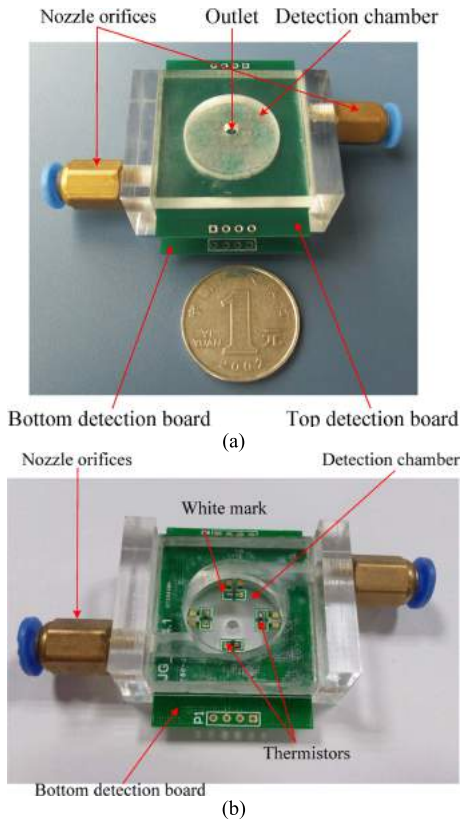

Fig. 14. (a) Assembled structure of the vortex sensor with double detection layers. (b) Cutaway view of the vortex sensor with single detection board to which the thermistor is bonded.

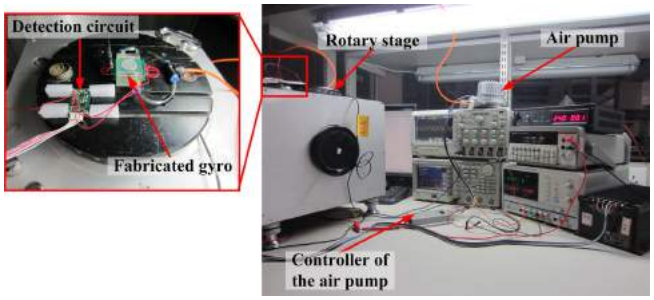

Fig. 15. Experimental setup for testing the gyroscope.

An image of the gas gyroscope is provided in Fig. 14(a). The cutaway view of the vortex sensor in Fig. 14(b) reveals that the thermistors are placed in the detection chamber based on the design.

V. Experimental Verification and Discussions

The velocity of the gas flow injected through the nozzle orifice by the external air pump was measured to be approximately 5 m/s. The resistance and TCR of the thermistor were measured to be 15.8 kΩ and 4738 ppm/°C, respectively.

Fig. 15 presents the experimental setup for testing the gyroscope. It primarily consists of the detection circuit board on a rotation table, an external air pump with its controller, a 24 V power supply and a 2 V control voltage supply for the air pump, a function generator, and an oscilloscope. In testing

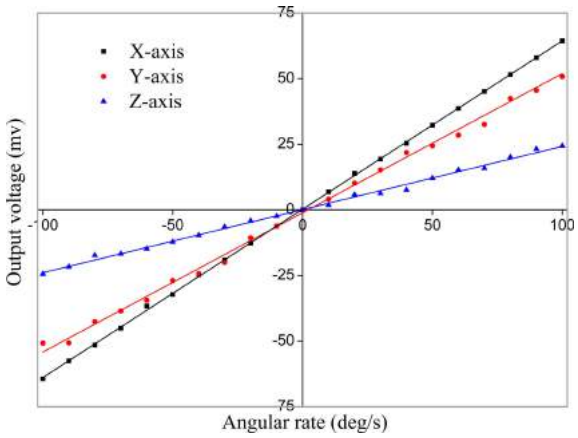

Fig. 16. Output voltage of the vortex gyroscope versus the applied angular rates.

the vortex gyroscope, the airflow pipes and wires were long enough to allow the rotation table to make three revolutions without entanglement.

As indicated in Fig. 16, the measured sensitivities of the sensor for the X-axis, Y-axis and Z-axis gyroscope were 0.642 mV/°/s, 0.528 mV/°/s and 0.241 mV/°/s, respectively. The sensitivity improvement reached 49.65%, 56.21% and 51.57% for each axis compared to our previous study [10]. The nonlinearities for the X-axis, Y-axis and Z-axis gyroscope were 2.1%, 3.8% and 4.5% in the range of ±100 °/s, respectively. An improvement in the linearity of 23.53%, 36.67% and 6.25% was obtained.

To obtain the resolution of the sensor, the noise floor of the sensor should be initially determined. For the thermistors, there are primarily two typical noise sources: Johnson noise and $1/f$ noise. Johnson noise is the electronic noise generated by the thermal agitation of the charge carriers in any electrical conductor and can be expressed as follows [13]:

$$V_{Jn(rms)} = \sqrt{4K_B TRB} \tag{16}$$

where K_B is the Boltzmann's constant, 1.38×10^{-23} J/K; T is the absolute temperature; R is the resistance of the thermistor; B is the measurement bandwidth; T is 60 °C, R is 15.8 KΩ; and B is 50 Hz; Thus, $V_{Jn} = 0.1205$ μV for one thermistor.

Fluctuations known as 1/f noise are observed in any electrical conductor; the associated voltage has been empirically determined as follows [17]:

$$V^2_{1/f(rms)} = \frac{\alpha_H V^2_{in}}{N} ln(\frac{f_{max}}{f_{min}}) \tag{17}$$

where α_H is the Hooge parameter, which has been determined to depend on the quality of a material and generally ranges from 10^{-7} to 10^{-4} [18]. For homogeneous p-type silicon with an impurity concentration of 10^{17}/cm^3, α_H has been reported to be approximately 10^{-4} [19]. V_{in} is the bias voltage across a thermistor; in this case, the value is equal to 15 V. N is the total number of carriers, which is proportional to the volume of the thermistor; in this case, $N = 2.86 \times 10^{10}$ atoms. The bandwidth frequency limits are $f_{max} = 50$ Hz and $f_{min} = 1$ Hz; thus, $V_{1/f(rms)} = 1.75$ μV for one thermistor.

For the gyroscopes, there are 2, 2 and 4 thermistors used to detect the angular rates about the X-axis, Y-axis and Z-axis, respectively. Therefore, by combining the noise level and the sensitivity, the resolutions of the X, Y and Z gyroscope are theoretically calculated to be 0.04°/s, 0.05°/s and 0.2°/s, respectively.

VI. Discussions and Conclusion

A tri-axis gas gyroscope has been developed based on thermal convective and thermoresistive effects. The numerical simulation and experimental results proved that the proposed suspended arch structure of thermistors is beneficial in improving the performance of the vortex inertial sensor. Based on the established theoretical model, the gyroscope using the suspended arch-shaped thermistor has its sensitivity improved by 47.32% compared with that of the clamped-clamped thermistor. The results agree well with the experimental test results shown in the previous study, where the sensitivity was improved by approximately 50%.

The theoretical resolution of the vortex gyroscope has been theoretically calculated. However, in actual measurement, it is difficult to obtain the resolution due to the instability of vortex flow. A further study on experimentally measuring the resolution will be performed in the future.

References

[1] N. Yazdi, F. Ayazi, and K. Najafi, "Micromachined inertial sensors," *Proc. IEEE*, vol. 86, no. 8, pp. 1640–1659, Aug. 1998.

[2] K. Liu *et al.*, "The development of micro-gyroscope technology," *J. Micromech. Microeng.*, vol. 19, no. 11, pp. 113001-1–113001-29, Nov. 2009.

[3] S. Nasiri. (Jun. 2012). *A Critical Review of MEMS Gyroscopes Technology and Commercialization Status*. [Online]. Available: http://invensense.com/mems/gyro/documents/whitepapers/MEMSGyroComp.pdf

[4] J. Bahari, R. Feng, and A. M. Leung, "Robust MEMS gyroscope based on thermal principles," *J. Microelectromech. Syst.*, vol. 23, no. 1, pp. 100–116, Feb. 2014.

[5] R. Zhu, Y. Su, and H. Ding, "A MEMS hybrid inertial sensor based on convection heat transfer," in *13th Int. Conf. Solid-State Sensors, Actuat., Microsyst. (TRANSDUCERS) Dig. Tech. Papers*, Jun. 2005, pp. 113–116.

[6] J. Zhou, G. Yan, Y. Zhu, Z. Xiao, and J. Fan, "Design and fabrication of a microfluid angular rate sensor," in *Proc. 18th IEEE Int. Conf. MEMS*, Jan./Feb. 2005, pp. 363–366.

[7] T. Shiozawa, V. T. Dau, D. V. Dao, H. Kumagai, and S. Sugiyama, "A dual axis thermal convective silicon gyroscope," in *Proc. Int. Symp. Micro-Nanomechatron. Human Sci., 4th Symp. Micro-Nanomechatron. Inf.-Based Soc.*, Oct./Nov. 2004, pp. 277–282.

[8] V. T. Dau, T. Otake, T. X. Dinh, and S. Sugiyama, "Design and fabrication of convective inertial sensor consisting of 3DOF gyroscope and 2DOF accelerometer," in *Proc. 15th IEEE Int. Conf. Solid-State Sensors, Actuat., Microsyst.*, Jun. 2009, pp. 1170–1173.

[9] Z. Xie, H. Chang, Y. Yang, X. Li, P. Zhou, and W. Yuan, "Design and fabrication of a vortex inertial sensor consisting of 3-DOF gyroscope and 3-DOF accelerometer," in *Proc. 25th IEEE Int. Conf. MEMS*, Jan./Feb. 2012, pp. 551–554.

[10] H. Chang, P. Zhou, Z. Xie, X. Gong, Y. Yang, and W. Yuan, "Theoretical modeling for a six-DOF vortex inertial sensor and experimental verification," *J. Microelectromech. Syst.*, vol. 22, no. 5, pp. 1100–1108, Oct. 2013.

[11] U. Buder, A. Berns, R. Petz, W. Nitsche, and E. Obermeier, "AeroMEMS wall hot-wire anemometer on polyimide substrate featuring top side or bottom side bondpads," *IEEE Sensors J.*, vol. 7, no. 8, pp. 1095–1101, Aug. 2007.

[12] H. Chang, P. Zhou, X. Gong, J. Xie, and W. Yuan, "Development of a tri-axis vortex convective gyroscope with suspended silicon thermistors," in *Proc. 12th IEEE Int. Conf. Sensors*, Nov. 2013, pp. 457–460.

[13] D. V. Dao, V. T. Dau, T. Shiozawa, and S. Sugiyama, "Development of a dual-axis convective gyroscope with low thermal-induced stress sensing element," *J. Microelectromech. Syst.*, vol. 16, no. 4, pp. 950–958, Aug. 2007.

[14] J. Chen and C. Liu, "Development and characterization of surface micromachined, out-of-plane hot-wire anemometer," *J. Microelectromech. Syst.*, vol. 12, no. 6, pp. 979–988, Dec. 2003.

[15] V. T. Dau, D. V. Dao, T. Shiozawa, H. Kumagai, and S. Sugiyama, "Development of a dual-axis thermal convective gas gyroscope," *J. Micromech. Microeng.*, vol. 16, no. 7, pp. 1301–1306, May 2006.

[16] T. Toriyama and S. Sugiyama, "Analysis of piezoresistance in p-type silicon for mechanical sensors," *J. Microelectromech. Syst.*, vol. 11, no. 5, pp. 598–604, Oct. 2002.

[17] F. N. Hooge, "$1/f$ noise is no surface effect," *Phys. Lett. A*, vol. 29, no. 3, pp. 139–140, Apr. 1969.

[18] F. N. Hooge and L. K. J. Vandamme, "Lattice scattering causes $1/f$ noise," *Phys. Lett. A*, vol. 66, no. 4, pp. 315–316, 1978.

[19] F. N. Hooge, "$1/f$ noise sources," *IEEE Trans. Electron Devices*, vol. 41, no. 11, pp. 1926–1935, Nov. 1994.

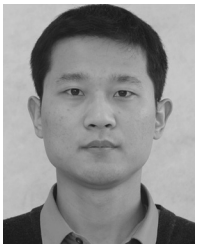

Honglong Chang (M'04) received the B.S., M.S., and Ph.D. degrees in mechanical engineering from Northwestern Polytechnical University (NPU), Xi'an, China, in 1999, 2002, and 2005, respectively. He is currently a Professor with the Micro and Nano Electromechanical Systems Laboratory, NPU, where he is also the Chair of the Department of Microsystem Engineering. From 2011 to 2012, he was a Visiting Associate (Faculty) with the Micromachining Laboratory, California Institute of Technology, Pasadena, CA, USA. His research interests include microfluidics, microelectromechanical systems (MEMS) design tools, and MEMS inertial sensors. He has authored over 24 international journal papers and over 20 international conference papers in the MEMS field.

Xianghui Gong received the B.S. degree from the Shandong University of Science and Technology, Qingdao, China, in 2012. He is currently pursuing the M.S. degree at the Micro and Nano Electromechanical Systems Laboratory, Northwestern Polytechnical University, Xi'an, China. His current research interests include microelectromechanical systems inertial sensors.

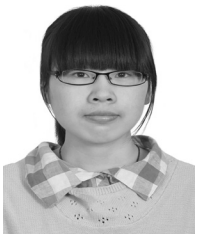

Shasha Wang received the B.S. degree from Beijing Forestry University, Beijing, China, in 2013. She is currently pursuing the M.S. degree at the Micro and Nano Electromechanical Systems Laboratory, Northwestern Polytechnical University, Xi'an, China. Her current research interests include microelectromechanical systems inertial sensors and circuit control.

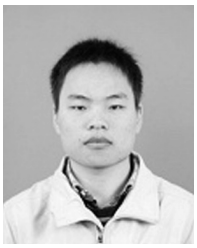

Pingwei Zhou received the B.S. degree in mechanical engineering from Northwestern Polytechnical University (NPU), Xi'an, China, in 2011. He is currently pursuing the M.S. degree at the Micro and Nano Electromechanical Systems Laboratory, NPU. His current research interests include microelectromechanical systems inertial sensors and flexible sensors.

Weizheng Yuan is currently a Professor with the Micro and Nano Electromechanical Systems Laboratory, Northwestern Polytechnical University, Xi'an, China, where he is also the Dean of the School of Mechanical Engineering. His research interests include microfluidics and microelectromechanical systems applications.

Applied Surface Science 357 (2015) 1274–1280

Contents lists available at ScienceDirect

Applied Surface Science

journal homepage: www.elsevier.com/locate/apsusc

Influence of carbon nanotubes coatings onto carbon fiber by oxidative treatments combined with electrophoretic deposition on interfacial properties of carbon fiber composite

Chao Deng, Jianjun Jiang*, Fa Liu, Liangchao Fang, Junbiao Wang, Dejia Li, Jianjun Wu

Shaanxi Engineering Research Center for Digital Manufacturing Technology, Northwestern Polytechnical University, Xi'an 710072, PR China

ARTICLE INFO

Article history:
Received 14 July 2015
Received in revised form
20 September 2015
Accepted 21 September 2015
Available online 25 September 2015

Keywords:
Carbon fibers
Carbon nanotubes
Electrophoretic deposition
Interfacial property

ABSTRACT

To improve the interfacial performance of carbon fiber (CF) and epoxy resin, carbon nanotubes (CNTs) coatings were utilized to achieve this purpose through coating onto CF by the treatment with hydrogen peroxide and concentrated nitric acid combined with electrophoretic deposition (EPD) process. The influence of electrophoretically deposited CNTs coatings on the surface properties of CFs were investigated by Fourier transform infrared spectrometer, atomic force microscopy, scanning electron microscopy and dynamic contact angle analysis. The results indicated that the deposition of carbon nanotubes introduced some polar groups to carbon fiber surfaces, enhanced surface roughness and changed surface morphologies of carbon fibers. Surface wettability of carbon fibers may be significantly improved by increasing surface free energy of the fibers due to the deposition of CNTs. The thickness and density of the coatings increases with the introduction of pretreatment of the CF during the EPD process. Short beam shear test was performed to examine the effect of carbon fiber functionalization on mechanical properties of the carbon fiber/epoxy resin composites. The interfacial adhesion of CNTs/CF reinforced epoxy composites showed obvious enhancement of interlaminar shear strength by 60.2% and scanning electron microscope photographs showed that the failure mode of composites was changed after the carbon fibers were coated with CNTs.

© 2015 Elsevier B.V. All rights reserved.

1. Introduction

Carbon fiber (CF) was developed into an important high strength; high modulus reinforcement material used in the fabrication of high performance composites. Due to the exceptionally high specific strength, high modulus, low density, and reasonable cost, CF reinforced composites are one of the most attractive materials for their wide application in aeronautical and aerospace applications, automobile, and many military applications. However, the untreated CF has large surface inertia and small active specific surface area, which affects the carbon fiber composite material's excellent performance into full play [1–3]. As a result, extensive researches have been devoted to the surface treatment of CF in order to improve interfacial properties of CF reinforced composites, such as sizing process [4], plasma treatment [5] and preparation of carbon nanotubes (CNTs)/CF hybrid fiber [6]. Among these methods, introducing CNTs on the surface of CF improves interfacial adhesion, because CNTs on carbon fiber surface can increase surface area and create interfacial mechanical interlocking between the hybrid fiber and matrix [7], as the ideal nanofillers, CNTs in composites have been increasingly adopted to give an insight into researches on hybrid composites [8–10].

Recently, many grafting methods have been proposed such as chemical vapor deposition (CVD) [11–13], chemical grafting [14–16] and electrophoretic deposition (EPD) [17–20]. All methods reported successful attachment of CNTs on the fiber surface. However, CVD method needed high temperature and predeposited catalysts [13], too many chemical treatments and long processing time employed for chemical grafting method makes it less environmentally friendly, taken together with the difficulties in processing large panels and the practical application.

Due to process simplicity, uniformity of the deposited films and good control of the deposited thickness, EPD is known to be one of the most promising manipulation techniques to produce large-scale reinforcement of nano-particles in composite applications, which was proposed to avoid these problems and has been successfully applied to prepare CNTs/CF hybrid fiber [21–27]. Successful EPD depends on the functionalization of the CNTs, in the previous

* Corresponding author.
E-mail address: jianjun@nwpu.edu.cn (J. Jiang).

http://dx.doi.org/10.1016/j.apsusc.2015.09.178
0169-4332/© 2015 Elsevier B.V. All rights reserved.

study [28]; acid treatment produces a higher extent of oxidation and larger fraction of highly oxidized functional groups compared to the other treatment like ozone treatment, which is beneficial to deposition of CNTs films. Recently, Thostenson et al. [17] deposited polyethyleneimine-functionalized CNTs onto the surface of carbon fiber fabric that was then used to manufacture composites. Results indicated an increase in interlaminar shear strength (ILSS) and fracture energy due to the relatively high levels of MWCNTs that occupied the resin-rich interlaminar regions.

Most studies reported improved properties of composites. However, the carboxylic acid-functionalized CNTs were sparsely and nonuniform deposited on the surface of CF and the effect of oxidative treatments of CF on the quality and quantity of deposited CNTs has rarely been studied. For solving this problem, we explored a method to prepare carbon nanotube/carbon fiber hybrid fiber by oxidative treatments combined with electrophoretic deposition. In this study, we focused on the influence of electrophoretically deposited carboxylic acid-functionalized CNTs on the interface of carbon fiber reinforced composite, special emphasis is put on the carbon fibers surface which was modified by the two-step treatment with hydrogen peroxide and concentrated nitric acid combined with EPD. Surface roughness and surface morphologies of the fibers were examined using atomic force microscopy (AFM) and scanning electron microscopy (SEM), changes in surface chemistry were studied using Fourier transform infrared spectrometer (FTIR), surface free energy and contact angle of the fibers were characterized by dynamic contact angle analysis (DCAA), respectively, the mechanical properties of composites were evaluated by ILSS.

2. Experimental

2.1. Materials and processing

PAN-based CF tow (T700, 12K and diameter about 7 μm) was purchased from Toray Industries, Japan. CNTs (95% purity, diameter about 10–20 nm, length 10–30 μm) were purchased from Nanjing Xianfeng. Port. Co., Ltd. The unidirectional CF layers were comprised of PAN-based 12K carbon fibers that have areal density of 300 g/cm^2, as provided by the vendor. The epoxy was diglycidyl ether of bisphenol A (E-51), which were obtained from Yueyang Chemical Reagent Co., Ltd. of China. The curing agent was 3,3′-diethyl-4,4′-diaminodiphenylmethane (H-256), which were supplied by Shanghai Jingchun Chemical Reagent Co., Ltd. of China.

The CF tow was refluxed in acetone at 80 °C for 72 h and washed with deionized water repeatedly, the resulting CF tow was dried under vacuum at 80 °C for 3 h to remove sizing agent (labeling as CF-desized). Then, the CF tow was stirred for 2 h in hydrogen peroxide (300 mL) under 108 °C. Immersed into nitric acid (300 mL) at 115 °C for 2 h and washed with deionized water repeatedly and then dried under vacuum at 80 °C for 3 h (labeling as CF-oxidized).

The as-received CNTs were refluxed in a 1:3 volume ratio of HNO_3 and H_2SO_4 solution at 60 °C for 4 h to introduce carboxylic acid groups. The mixture was vacuum-filtered washed with deionized water repeatedly and dried under vacuum at 80 °C for 3 h. The acid-treated CNTs were dispersed for 3 h in deionized water by ultrasonic to obtain dispersions of 0.05 g/L.

2.2. Preparation of CNTs coatings

A schematic of the EPD deposition setup is shown in Fig. 1. For the EPD of CNTs onto the CF, the CF tow was used as the deposition electrode, and two 50 × 20 cm^2 stainless steel plates were positioned opposite to carbon fibers as the counter electrode. CNTs concentration was 0.05 g/L. The EPD process was carried out at constant voltages of 20 V for 20 min, with electrode distance of 2 cm,

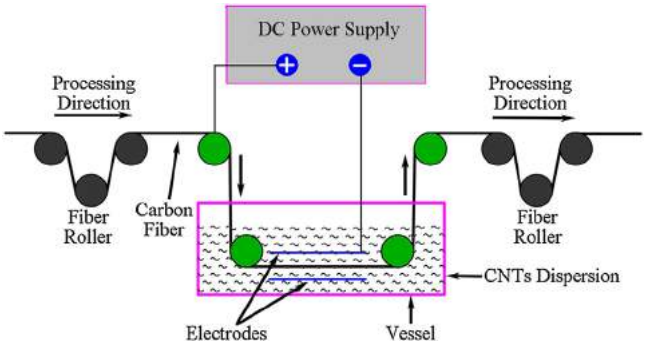

Fig. 1. Schematic for continuous EPD process of CNTs onto carbon fiber.

after the EPD process, CF tow with the length of 50 cm was coated and the CF tow was wound up on a roll. Once the EPD process was completed, the resulting CF was dried in an oven at 100 °C for 2 h.

2.3. Coating characterizations

Surface morphologies of the CF were characterized using scanning electron microscope at 10 kV (JOEL, JCM-6000) with gold painting. To investigate fracture mechanisms of CF-reinforced EP composite, surface morphologies of the fractured composite were still observed. Fiber samples were cut with scissors to expose a transverse cross-section for SEM observation and the thickness of the coating was measured. An electronic balance with an accuracy of 0.1 mg was used to measure the weight gain of the samples.

Surface roughness and surface morphologies of CF were characterized by atomic force microscopy (Park, XE-100). All AFM images of CF using the tapping mode obtained with the scan area of 4 mm × 4 mm. Surface roughness of the fibers was calculated from Eqs. (1) and (2) by the instrument software. At least 20 valid data were applied for each specimen.

$$R_q = \sqrt{\frac{1}{N^2}\sum_{i=1}^{N}\sum_{j=1}^{N}(z_{ij} - z_{av})^2} \quad (1)$$

$$R_a = \frac{1}{N}\sum_{i=1}^{N}\sum_{j=1}^{N}|z_{ij} - z_{cp}| \quad (2)$$

Fig. 2. Photograph illustrating the infiltration of the carbon nanotube/carbon fiber preforms with vacuum-assisted resin transfer molding (VARTM).

where R_q is root mean square (RMS) roughness, R_a is arithmetic mean roughness, N is the number of data points in the image, i and j are pixel locations on the AFM image, z_{ij} is the height value at i and j locations, z_{av} is the average height value within the given area, and z_{cp} the height value from the center plane [32].

Fourier transform infrared spectra (FTIR) were conducted on Nicolet 20DXB 60,000 spectrophotometer in the range of 500–4000 cm^{-1} to evaluate the chemical structures using a KBr pellet.

Dynamic contact angle tests were measured using a dynamic contact angle meter (DCAT21, Data-physics Instruments, Germany). Deionized water ($\gamma^d = 21.8\,m\,Nm^{-1}$, $\gamma^p = 51.0\,m\,Nm^{-1}$, $\gamma = 72.8\,m\,Nm^{-1}$) and glycol ($\gamma^d = 29.3\,m\,Nm^{-1}$, $\gamma^p = 19\,m\,Nm^{-1}$, $\gamma = 48.3\,m\,Nm^{-1}$) were used as test liquids, the surface free energy, and its dispersive and polar components can be derived as the following equations:

$$\gamma_1(1+\cos\theta) = \frac{4\gamma_1^d \cdot \gamma_s^d}{\gamma_1^d + \gamma_s^d} + \frac{4\gamma_1^p \cdot \gamma_s^p}{\gamma_1^p + \gamma_s^p} \quad (3)$$

$$\gamma_{Total} = \gamma_s^d + \gamma_s^p \quad (4)$$

where θ is the dynamic contact angle, γ_1, γ_1^d and γ_1^p is surface tension of the testing liquid, its dispersive and polar component, each measurement was performed at least ten times.

2.4. Composite specimen preparation and characterization

Carbon fiber layers were used as the base material to synthesize the hybrid composites. The pretreatment of the carbon fiber layer was carried out following a similar process as for CF tow, to remove the sizing, the layers were soaked in acetone for 24 h and washed with deionized water repeatedly and then dried under vacuum at 80 °C for 3 h. Then, the layers were stirred for 2 h in hydrogen peroxide (300 mL) under 108 °C. Immersed into nitric acid (300 mL) at 115 °C for 2 h and washed with deionized water repeatedly and then dried under vacuum at 80 °C for 3 h. EPD treatment of carbon fiber layer was carried out following a similar process as for CF tow, carbon fiber layer of $50 \times 20\,cm^2$ with opposing stainless steel plates electrodes placed was used as the deposition electrode, the EPD process was carried out at constant voltages of 20 V for 20 min. Once the EPD process was completed, the resulting CF layer was dried in an oven at 100 °C for 2 h.

Four flat panels of $15 \times 10\,cm^2$ were manufactured to study the mechanical properties of the composites, the first laminate was made with desized CF as a standard laminate, the second laminate was made with preforms containing oxidized CF, the third and fourth laminate were made with preforms comprised of CNTs/CF-desized and CNTs/CF-oxidized hybrid fiber. The preforms of all laminate were comprised of 11 layers of CNTs coated or uncoated carbon fiber layers, which took about 40 h to prepare

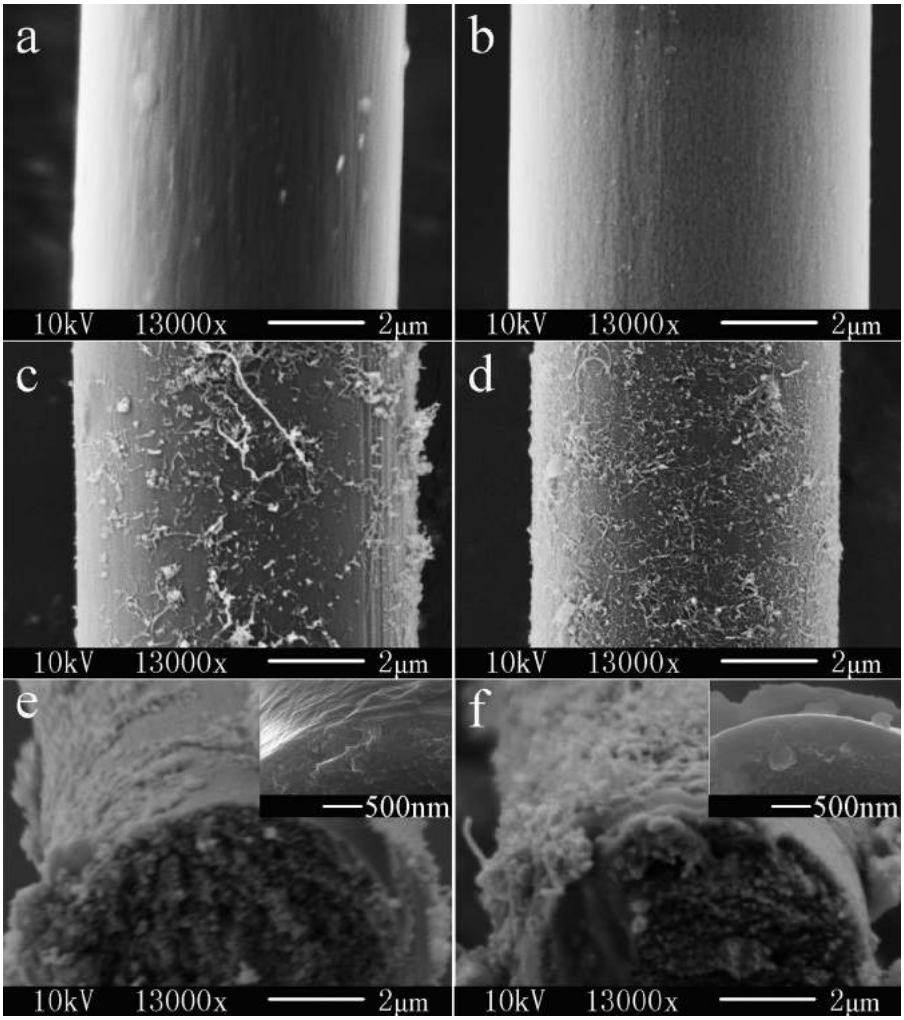

Fig. 3. SEM images of surface morphologies of (a) desized CF; (b) oxidized CF; (c) CNTs/CF-desized hybrid fiber; (d) CNTs/CF-oxidized hybrid fiber and cross-section of (e) CNTs/CF-desized hybrid fiber; (f) CNTs/CF-oxidized hybrid fiber.

enough material for the preparation of the laminates. The preforms were infiltrated with epoxy using vacuum-assisted resin transfer molding (VARTM) with the epoxy resin and curing agent at a ratio of 100/33 parts by weight. In the VARTM process (Fig. 2), the epoxy resin is infused into the carbon fibers under vacuum. After the infiltration of epoxy, the composites were cured for 12 h at 80 °C. Interfacial property of CF/EP composite was evaluated by ILSS. The ILSS of the CF/EP composites were measured by short beam shear tests according to ASTM D 2344. The tests were performed on a universal testing machine with a constant cross head rate of 2 mm/min and a span to thickness ratio of 5. The tests were carried out at 20 °C and 50% relative humidity. Specimen dimensions were $25 \times 6 \times 2\ mm^3$, The ILSS was calculated as the following equation:

$$\tau = \frac{3P_b}{4b \cdot h} \quad (5)$$

where τ is the ILSS, P_b is the maximum load, b and h are the width and the thickness of the specimen. All of the ILSS results were taken as the average value of more than five successful measurements.

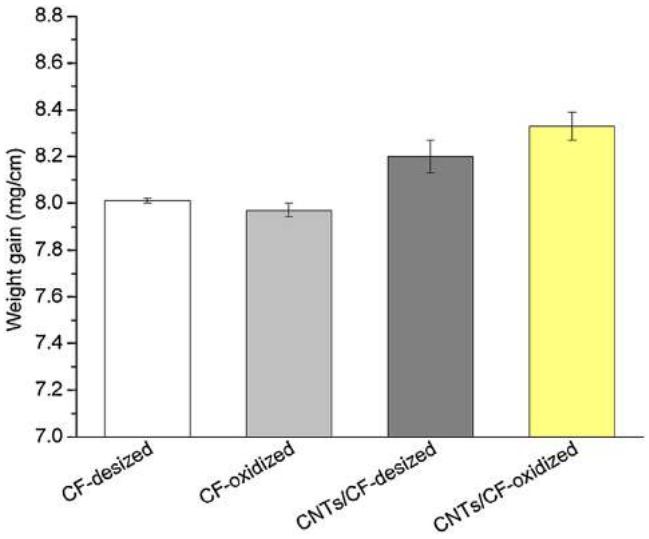

Fig. 4. Effect of the CNTs coatings on weight gain.

3. Results and discussion

3.1. Morphology study and surface roughness

Surface morphologies and cross-sectional morphologies of CF at different stages are illustrated in Fig. 3. Initially, it was found that the desized CF had a smooth surface (Fig. 3(a)), after oxidative treatment, the oxidation do not apparently destroy the surface morphology (Fig. 3(b)), the similar phenomenon was reported in Refs [29,30], oxidative treatment of CF only remove the little residual polymer sizing or a thin layer of the weakly bonded materials at apparent surface of carbon fiber, which did not affect the CF strength. As shown in Fig. 3(c) and (d), CNTs were deposited on the surface of CF, which indicated that EPD was an effective method to prepare CNTs/CF hybrid fiber, and that is effective to improve the

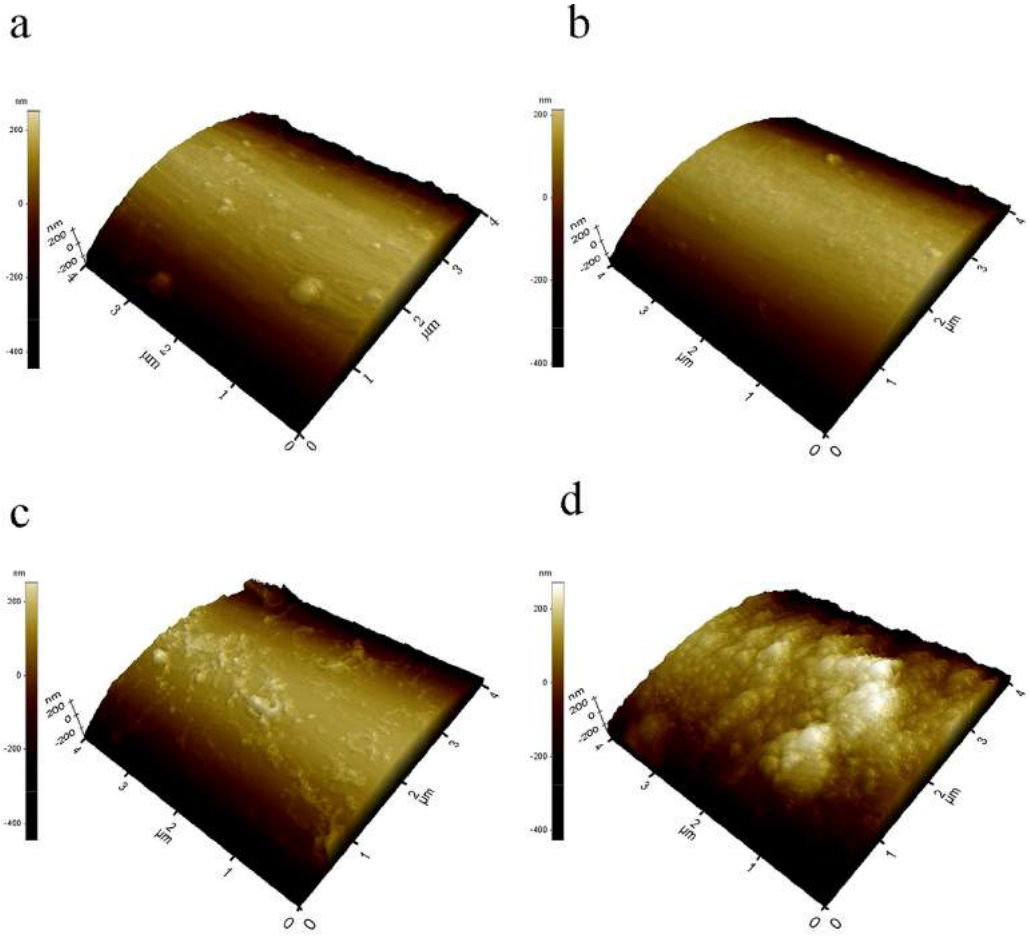

Fig. 5. AFM images of (a) desized CF; (b) oxidized CF; (c) CNTs/CF-desized hybrid fiber; (d) CNTs/CF-oxidized hybrid fiber.

Table 1
Arithmetic mean roughness R_a, and RMS roughness R_q of carbon fiber.

	R_a (nm)	R_a (nm)
Desized CF	111.3 (10.4)	135.4 (5.4)
Oxidized CF	113.1 (9.5)	136.6 (4.1)
CNTs/CF-desized hybrid fiber	138.5 (11.6)	159.2 (13.3)
CNTs/CF-oxidized hybrid fiber	141.9 (10.7)	188.6 (9.2)

interfacial property. Another observation that can be seen from the SEM images of CNTs/CF hybrid fiber is uniform and dense nanotubes network due to pretreatment of the CF, the CNTs were sparsely deposited on the surface of CF and did not form a uniform and dense network without pretreatment of the CF (Fig. 3(c)), whereas the CNTs formed a thin internetwork wraps up the whole surface of carbon fibers with pretreatment of the CF (Fig. 3(d)). Fig. 3(e) and (f) are representative of the cross-sectional morphologies of CNTs/CF hybrid fiber. The average thickness (measured by SEM scale bar) of the CNTs coating on desized CF and oxidized CF is around 100 nm and 300 nm, respectively. Fig. 4 illustrates the quantitative weight of the CF and CNTs/CF hybrid fiber. The density of the CNTs coatings was calculated as the surface weight gain in the CNTs/CF hybrid fiber, it shows that the density of the coatings in the CNTs/CF-desized hybrid fiber is two times as high as in CNTs/CF-oxidized hybrid fiber. The result means the quality and quantity of deposited CNTs were increased and improved by the introduction of pretreatment of the CF during the EPD process.

In order to have better understanding of the surfaces, AFM studies have also been carried out. In Fig. 5 a comparison of AFM images of the untreated and EPD treated carbon fiber is shown. It can be found that the surfaces of CF and CF-oxidized seem to be neat and smooth (Fig. 5(a) and (b)). In the case of CNTs/CF hybrid fiber, after CNTs deposited on the CF, the surfaces showed small spots (Fig. 5(c)) and large area of protuberances (Fig. 5(d)).

Surface roughness of carbon fiber was analyzed by AFM with the instrument software. The surface roughness R_a and R_q of carbon fibers and the standard deviations of the roughness are shown in Table 1. For the desized carbon fiber, R_a and R_q were 111.3 nm and 135.4 nm, respectively. After CNTs deposited on the oxidized CF, R_a of carbon fibers increased to 141.9 nm, and R_q of the carbon fiber went up to 188.6 nm. The results indicate that CNTs deposition enhanced the surface roughness of CF and the surface morphologies of CF became more complicated, which is beneficial to enhance mechanical interlocking between the fiber and matrix and improve the wettability and interfacial adhesion between carbon fibers and matrix.

3.2. Surface functional group

The FTIR was used to determine the functionalization during EPD process, as shown in Fig. 6. For the desized CF, three peaks located at 3468 cm^{-1}, 2925 cm^{-1}, 1644 cm^{-1}, and 1384 cm^{-1} in the IR spectrum are observed (Fig. 6(a)), which are allocated to ν(O—H), ν(C—H), ν(C=C), and ν(C—C). After oxidization by hydrogen peroxide and concentrated nitric acid, ν(C=O) at 1725 cm^{-1}, and ν(C—O) at 1250 cm^{-1} are visible (Fig. 6(b)), these imply that the carboxyl groups and hydroxyl are formed due to the oxidation of surface carbon atoms by acid. After depositing CNTs on the desized CF, the characteristic peak of ν(C=O) at 1725 cm^{-1} are visible in comparison with that of desized CF (Fig. 6(a) and (c)), which demonstrates successfully depositing of CNTs onto the CF, when depositing CNTs on the oxidized CF (Fig. 6(d)), the broader peaks of ν(C=C) at 1644 cm^{-1} and ν(C=O) at 1725 cm^{-1} indicate that the introduction of pretreatment of the CF during the EPD process increased the amount of carbon nanotubes coatings.

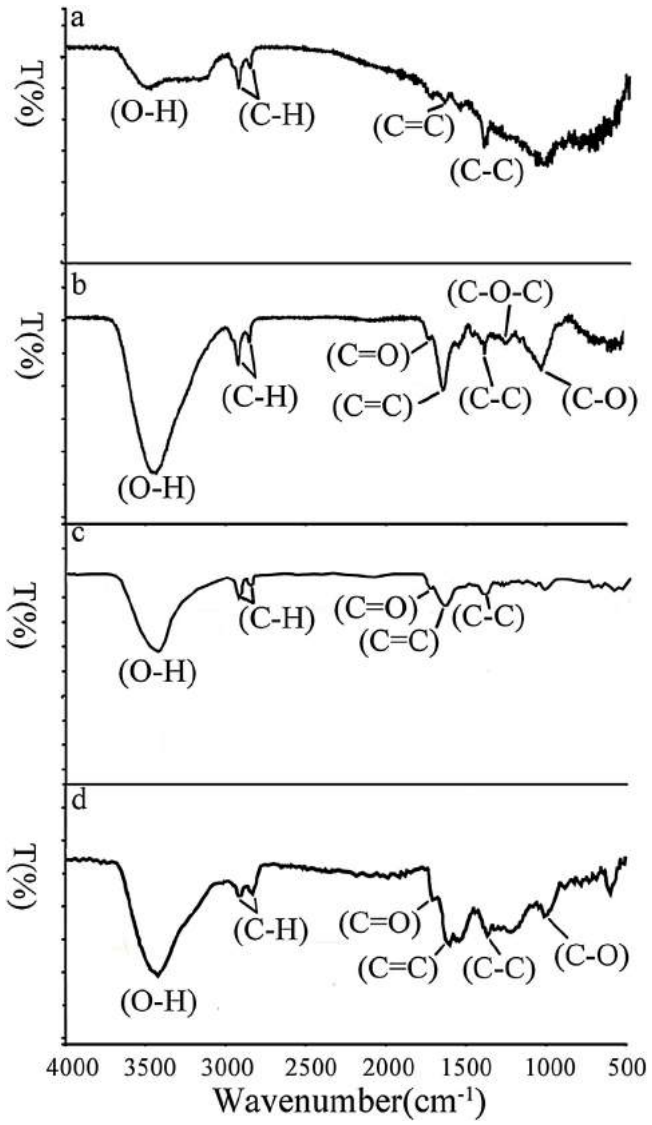

Fig. 6. FTIR spectra of (a) desized CF; (b) oxidized CF; (c) CNTs/CF-desized hybrid fiber; (d) CNTs/CF-oxidized hybrid fiber.

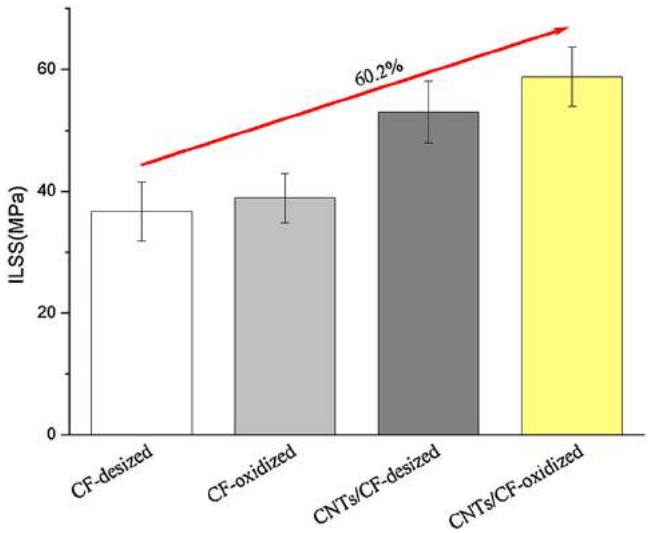

Fig. 7. ILSS of the composites reinforced by the desized CF, oxidized CF, CNTs/CF-desized hybrid fiber and CNTs/CF-oxidized hybrid fiber.

Table 2
Contact angles and surface free energy.

	θ_{water} (°)	θ_{glycol} (°)	γ^d (mJ/m^2)	γ^p (mJ/m^2)	γ (mJ/m^2)
Desized CF	76.07 (2.5)	62.56 (2.1)	9.54	23.18	32.72
Oxidized CF	72.20 (1.6)	58.89 (0.8)	10.02	25.28	35.30
CNTs/CF-desized hybrid fiber	56.78 (1.1)	47.43 (1.3)	10.58	35.9	46.48
CNTs/CF-oxidized hybrid fiber	50.14 (0.8)	42.65 (2.1)	11.48	40.43	51.38

3.3. Surface wettability

The effects of deposition of CNTs on surface wettability of CF were characterized by DCAA. The surface free energy of various CF derived from contact angle is presented in Table 2. The contact angles of water, the dispersive component of surface free energy, the polar component of surface free energy, and the total surface free energy on the desized CF was 76.07°, 9.54, 23.18 and 32.72 mN/m, In Addition, after depositing CNTs on the oxidized CF, the contact angles of water on CF reduced to 50.14°, the dispersive component of surface energy and the polar component of surface energy increased 11.48 and 40.43 mN/m, whereas the total surface free energy increased to 51.38 mN/m, this comes from two resources: the increasing surface area and polar groups due to the deposition of CNTs, which has a strong effect on the wettability of CF. Respectively, it can be also found that the free energy increased from 46.68 mN/m for CNTs/CF-desized hybrid fiber to 51.38 mN/m for CNTs/CF-oxidized hybrid fiber by 9.1%, the improvement of surface free energy can be attributed to the increase of surface polarization caused by the pretreatment of the CF, which is beneficial to the deposition of CNTs on carbon fiber surface. Increasing in the wettability of carbon fiber is beneficial to the spreadability of epoxy resin and provides intimate molecular contact between fibers and epoxy resin, thus improves interfacial adhesion.

3.4. Interlaminar shear strength

The interfacial adhesion between CF and EP resin was evaluated by ILSS. The effects of CNTs deposited treatment on ILSS and the error bars of standard deviation were given in Fig. 7. It is found that the carbon fiber with CNTs deposited have strong effects on its composite interfacial adhesion properties. After oxidization, the IFSS of composites has a slight increase (from 36.7 to 38.9 MPa) in comparison with that of desized CF, after CNTs deposited, the ILSS further increased to 58.81 MPa with an increment of about 60.2%. These results suggest that depositing CNTs on the fiber surface significantly improved the interfacial adhesion of the CF/EP composites by increasing surface roughness, which provides intimate molecular contact and stronger interfacial mechanical interlocking between the hybrid fiber and matrix. In addition, the oxygen-based functional groups of the CNTs are beneficial to enhance the interfacial adhesion by establish the hydrogen bonding with many sites in the epoxy resin during curing process and finally lead to the improvement of the interlaminar shear strength. In particular, ILSS for CNTs/CF-oxidized/EP hybrid composite is 58.81 MPa which is higher than that of CNTs/CF-desized/EP hybrid composite with the value of 53.03 MPa, we can see that the depositing density plays a critical role in determining the ILSS of composites.

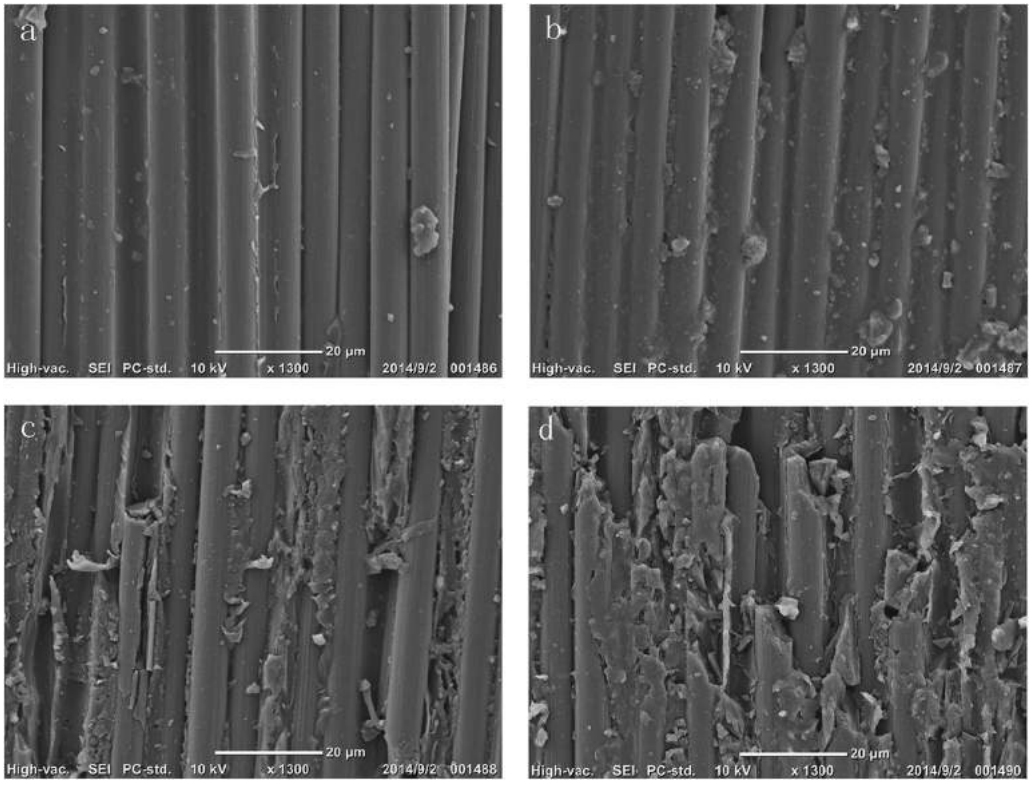

Fig. 8. Fractured SEM images of CF reinforced composite (a) desized CF; (b) oxidized CF; (c) CNTs/CF-desized hybrid fiber; (d) CNTs/CF-oxidized hybrid fiber.

3.5. Composite fracture mechanism analysis

The SEM images of fractured surface of CF-reinforced EP composites, which provides direct evidence of the interfacial property enhancement, are shown in Fig. 8. It is obvious that in Fig. 8(a) and (b), the fiber surfaces were smooth with little resin remains onto the carbon fiber, indicating the debond location was the interface between CF and EP resin. However, the fracture surface of the composites with CNTs deposition show completely different, with resin adhered to the fiber surfaces (Fig. 8(b) and (c)), the debond location shifted from the interface to matrix. The improvement in the interfacial adhesion could be attributed to the new interface layer formed by depositing CNTs on the fiber surface. After depositing CNTs, the primary failure of CF-reinforced EP composites changes from interface failure to matrix fracture. The results showed that the primary failure mode of the untreated CF-reinforced composite was interface failure; while the primary failure mode of the CNTs coated CF-reinforced composite was matrix fracture. Previous studies on the adhesion strength of carbon fibers to epoxy resin suggest that the interfacial shear strength increases by shifting the fracture surface away from the carbon fiber surface [31], the improvement in the interfacial adhesion could be attributed to the new interface layer formed by depositing CNTs on the fiber surface.

4. Conclusions

In the present study, CNTs were successfully coated onto carbon fiber surfaces via oxidative treatments combined with electrophoretic deposition, which avoids complex chemical reactions and long processing duration, thereby provides great potential for industrial applications. SEM and AFM analysis showed that the deposition of CNTs enhanced the surface roughness and changed the surface morphologies of carbon fiber. DCAA results indicated that the deposition of CNTs significantly improved surface free energy of carbon fiber by increasing surface area and polar groups. The introduction of CNTs in the CF reinforced composite results in an enhancement of ILSS by 60.2% compared to desized CF reinforced epoxy composite. Fractured SEM images of CF reinforced composite suggested that the primary failure mode of carbon fiber/epoxy composites changed from interface failure to matrix fracture after the carbon fibers were treated. It was also proved that CNTs coated onto carbon fibers by EPD gave a negative effect to the mechanical properties of composites.

References

[1] S. Chand, Review carbon fibers for composites, J. Mater. Sci. 35 (2000) 1303–1313.
[2] J.D. Schaefer, A.J. Rodriguez, M.E. Guzman, C.-S. Lim, B. Minaie, Effects of electrophoretically deposited carbon nanofibers on the interface of single carbon fiber embedded in epoxy matrix, Carbon 49 (2011) 2750–2759.
[3] M.A. Montes-Moran, R.J. Young, Raman spectroscopy study of HM carbon fibres: effect of plasma treatment on the interfacial properties of single fibre/epoxy composites – Part I: fibre characterization, Carbon 40 (2002) 845–855.
[4] J. Liu, H. Ge, J. Chen, D. Wang, H. Liu, The preparation of emulsion type sizing agent for carbon fiber and the properties of carbon fiber/vinyl ester resin composites, J. Appl. Polym. Sci. 124 (2012) 864–872.
[5] J.F. Xie, D.W. Xin, H.Y. Cao, C.T. Wang, Y. Zhao, L. Yao, F. Ji, Y.P. Qiu, Improving carbon fiber adhesion to polyimide with atmospheric pressure plasma treatment, Surf. Coat. Technol. 206 (2011) 191–201.
[6] J.R. Alejandro, E.G. Mauricio, C.S. Lim, B. Minaie, Mechanical properties of carbon nanofiber/fiber-reinforced hierarchical polymer composites. Manufactured with multiscale-reinforcement fabrics, Carbon 49 (2011) 937–948.
[7] J.D. Schaefer, A.J. Rodriguez, M.E. Guzman, C.S. Lim, B. Minaie, Effects of electrophoretically deposited carbon nanofibers on the interface of single carbon fiber embedded in epoxy matrix, Carbon 49 (2011) 2750–2759.
[8] J.L. Thomason, L. Yang, Temperature dependence of the interfacial shear strength in glass–fibre polypropylene composites, Compos. Sci. Technol. 71 (2011) 1600–1605.
[9] J.L. Thomason, Micromechanical parameters from macromechanical measurements on glass reinforced polyamide 6, 6, Compos. Sci. Technol. 61 (2001) 2007–2016.
[10] L. Mei, X. He, Y. Li, R. Wang, C. Wang, Q. Peng, Grafting carbon nanotubes onto carbon fiber by use of dendrimers, Mater. Lett. 64 (2010) 2505–2508.
[11] V.P. Veedu, A. Cao, X. Li, K. Ma, C. Soldano, S. Kar, P.M. Ajayan, M.N. Ghasemi-Nejhad, Multifunctional composites using reinforced laminae with carbon-nanotube forests, Nat. Mater. 5 (2006) 457–462.
[12] F. An, C.X. Lu, J.H. Guo, S.Q. He, H.B. Lu, Y. Yang, Preparation of vertically aligned carbon nanotube arrays grown onto carbon fiber fabric and evaluating its wettability on effect of composite, Appl. Surf. Sci. 258 (2011) 1069–1076.
[13] S. Rahmanian, A.R. Suraya, R. Zahari, E.S. Zainudin, Synthesis of vertically aligned carbon nanotubes on carbon fiber, Appl. Surf. Sci. 271 (2013) 424–428.
[14] W.H. Liu, S. Zhang, L.F. Hao, F. Yang, W.C. Jiao, X.Q. Li, R.G. Wang, Fabrication of carbon nanotubes/carbon fiber hybrid fiber in industrial scale by sizing process, Appl. Surf. Sci. 284 (2013) 914–920.
[15] Q.Y. Peng, X.D. He, Y.B. Li, C. Wang, R.G. Wang, P.A. Hu, Y.D. Yan, T. Sritharan, Chemically and uniformly grafting carbon nanotubes onto carbon fibers by poly(amidoamine) for enhancing interfacial strength in carbon fiber composites, J. Mater. Chem. 22 (2012) 5928–5931.
[16] F. Zhao, Y.D. Huang, Preparation and properties of polyhedral oligomeric silsesquioxane and carbon nanotube grafted carbon fiber hierarchical reinforcing structure, J. Mater. Chem. 21 (2011) 2867–2870.
[17] Q. An, A.N. Rider, E.T. Thostenson, Electrophoretic deposition of carbon nanotubes onto carbon-fiber fabric for production of carbon/epoxy composites with improved mechanical properties, Carbon 50 (2012) 4130–4143.
[18] J.H. Guo, C.X. Lu, Continuous preparation of multiscale reinforcement by electrophoretic deposition of carbon nanotubes onto carbon fiber tows, Carbon 50 (2012) 3101–3103.
[19] C. Wang, J. Ma, W. Cheng, Formation of polyetheretherketone polymer coating by electrophoretic deposition method, Surf. Coat. Technol. 173 (2003) 271–275.
[20] J.H. Guo, C.X. Lu, F. An, S. He, Preparation and characterization of carbon nanotubes/carbon fiber hybrid material by ultrasonically assisted electrophoretic deposition, Mater. Lett. 66 (2012) 382–384.
[21] A. Chavez-Valdez, A.R. Boccaccini, Innovations in electrophoretic deposition: alternating current and pulsed direct current methods, Electrochim. Acta 65 (2012) 70–89.
[22] L. Besra, M. Liu, A review on fundamentals and applications of electrophoretic deposition (EPD), Prog. Mater. Sci. 52 (2007) 1–61.
[23] Q. Wang, Q. Wang, M.S. Li, S. Szunerits, R. Boukherroub, Preparation of reduced graphene oxide-Cu nanoparticle composites through electrophoretic deposition: application for nonenzymatic glucose sensing, RSC Adv. 5 (2015) 15861–15869.
[24] P. Subramanian, A. Lesniewski, I. Kaminska, A. Vlandas, A. Vasilescu, J. Niedziolka-Jonsson, E. Pichonat, H. Happy, R. Boukherroub, S. Szunerits, Lysozyme detection on aptamer functionalized graphene-coated SPR interfaces, Biosens. Bioelectron. 50 (2013) 239–243.
[25] S. Zhang, W.B. Liu, L.F. Hao, W.C. Jiao, F. Yang, R.G. Wang, Preparation of carbon nanotube/carbon fiber hybrid fiber by combining electrophoretic deposition and sizing process for enhancing interfacial strength in carbon fiber composites, Compos. Sci. Technol. 88 (2013) 120–125.
[26] E. Bekyarova, E.T. Thostenson, A. Yu, H. Kim, J. Gao, J. Tang, H.T. Hahn, T.-W. Chou, M.E. Itkis, R.C. Haddon, Multiscale carbon nanotube-carbon fiber reinforcement for advanced epoxy composites, Langmuir 23 (2007) 3970–3974.
[27] Q. Song, K.Z. Li, H.J. Li, Q.G. Fu, Increasing the tensile property of unidirectional carbon/carbon composites by grafting carbon nanotubes onto carbon fibers by electrophoretic deposition, J. Mater. Sci. Technol. 29 (2013) 711–714.
[28] K.A. Wepasnick, B.A. Smith, K.E. Schrote, H.K. Wilson, S.R. Diegelmann, D.H. Fairbrother, Surface and structural characterization of multi-walled carbon nanotubes following different oxidative treatments, Carbon 49 (2011) 24–36.
[29] H.B. Xu, X.Q. Zhang, D. Liu, Y. Chun, X.Y. Fan, A high efficient method for introducing reactive amines onto carbon fiber surfaces using hexachlorocyclophosphazene as a new coupling agent, Appl. Surf. Sci. 320 (2014) 43–51.
[30] F. Vautard, P. Fioux, L. Vidal, J. Schultz, M. Nardin, B. Defoort, Influence of an oxidation of the carbon fiber surface on the adhesion strength in carbon fiber-acrylate composites cured by electron beam, Int. J. Adhes. 34 (2012) 93–106.
[31] A.N. Rider, Q. An, N. Brack, E.T. Thostenson, Polymer nanocomposite-fiber model interphases: influence of processing and interface chemistry on mechanical performance, Chem. Eng. J. 269 (2015) 121–134.
[32] C.S. Zhang, P. Chen, B.L. Sun, C. Lu, X.Y. Zhang, D. Liu, Influence of oxygen plasma treatment on interfacial properties of poly(p-phenylene benzobisoxazole) fiber-reinforced poly(phthalazinone ether sulfone ketone) composite, J. Appl. Polym. Sci. 113 (2009) 71–77.

Semi-Markov Process-Based Integrated Importance Measure for Multi-State Systems

Hongyan Dui, Shubin Si, *Member, IEEE*, Ming J. Zuo, *Senior Member, IEEE*, and Shudong Sun, *Member, IEEE*

***Abstract*—Importance measures in reliability engineering are used to identify weak components of a system and signify the roles of components in contributing to proper functioning of the system. Recently, an integrated importance measure (IIM) has been proposed to evaluate how the transition of component states affects the system performance based on the probability distributions and transition rates of component states. In the system operation phase, the bathtub curve presents the change of the transition rate of component states with time, which can be described by three different Weibull distributions. The behavior of a system under such distributions can be modeled by the semi-Markov process. So, based on the reported IIM equations of component states, this paper studies how the transition of component states affects system performance under the semi-Markov process. This measure can provide useful information for preventive actions (such as monitoring enhancement, construction improvement, etc.), and provide support to improve system performance. Finally, a simple numerical example is presented to illustrate the utilization of the proposed method.**

***Index Terms*—Component state, importance measure, multi-state system, semi-Markov processes.**

Abbreviation:

IIM	Integrated importance measure

Notations:

n	number of components in the system
i	index of component $i, i = 1, 2, \ldots, n$
$x_i(t)$	state of component i at time $t, x_i(t) = 0, 1, 2, \ldots, M_i$; when taking no account of $t, x_i(t) = x_i$
$X(t)$	$(x_1(t), x_2(t), \ldots, x_n(t))$, state vector of all the components at time t; when taking no account of $t, X(t) = X$
$\Phi(X(t))$	system structure function with domain $\{0, 1, \ldots, M_i\}^n$ at time t, and range $\{0, 1, \ldots, M\}, \Phi(X(t)) = \Phi(x_1(t), x_2(t), \ldots, x_n(t))$
$(\cdot_i, X(t))$	$(x_1(t), \ldots, x_{i-1}(t), \cdot, x_{i+1}(t), \ldots, x_n(t))$
$\Phi(m_i, X(t))$	$\Phi(x_1(t), \ldots, x_{i-1}(t), m_i, x_{i+1}(t), \ldots, x_n(t))$
$P^i_{lm}(t)$	$\Pr(x_i(t) = m \mid x_i(0) = l)$
$P^i_m(t)$	$\Pr(x_i(t) = m)$
P^i_m	the probability that component i is in state m
b^i_{ml}	the transition rate of component i from state m to state $l, l, m \in \{0, 1, \ldots, M_i\}$
a_j	the performance level corresponding to state j of the system
$\rho^i_m(t)$	$\Pr\{x_i(t) < m\}$
$\hat{Q}^i_{lm}(s)$	Laplace transform of $q^i_{lm}(t)$
$\hat{Q}'^i_{lm}(s)$	$d\hat{Q}^i_{lm}(s)/ds$
$U(t)$	$U(t) = \sum_{l=0}^{M} a_l \Pr(\Phi(X(t)) = l)$, the expected value of the performance level of the system at time t

Manuscript received September 02, 2013; revised July 02, 2014, October 20, 2014, and November 17, 2014; accepted November 21, 2014. Date of publication April 06, 2015; date of current version June 01, 2015. This work was supported in part by the National Natural Science Foundation of China (No. 71271170 and 51375078), Program for New Century Excellent Talents in University (No. NCET-13-0475), the Natural Sciences and Engineering Research Council of Canada (NSERC), Strategic Research Grant of the City University of Hong Kong (No. 7004087), Specialized Research Fund for Young Teachers program of Zhengzhou University (No. F0000492), and the Aeronautical Science Foundation of China (No. 2014ZG53080). Associate Editor: O. Gaudoin. (*Corresponding author: Shubin Si.*)

H. Dui is with the School of Management Engineering, Zhengzhou University, Zhengzhou 450001, China (e-mail: duihongyan@zzu.edu.cn).

S. Si and S. Sun are with the Department of Industrial Engineering, School of Mechanical Engineering, Northwestern Polytechnical University, Xi'an 710072, China (e-mail: sisb@nwpu.edu.cn; sdsun@nwpu.edu.cn).

M. J. Zuo is with the School of Mechanical, Electronic, and Industrial Engineering, University of Electronic Science and Technology of China, Chengdu 611731, China, and also with Department of Mechanical Engineering, Faculty of Engineering, University of Alberta, Edmonton, AB T6G 2G8, Canada (e-mail: ming.zuo@ualberta.ca).

Digital Object Identifier 10.1109/TR.2015.2413031

I. Introduction

A. Background

IMPORTANCE MEASURES are used to evaluate the contribution of individual components to system reliability or performance. According to the information on the importance of components of a system, system designers and managers can trace the technical bottlenecks of a system. This tracing provides guidelines for effective actions of system reliability or performance improvement.

Birnbaum [1] originally defined component importance measures for binary coherent systems in 1969. In a binary system, each component of the system may experience only two possible states, either working or failed. However, since the mid-1970s, the focus has shifted to multi-state systems which may experience more than two states [2]. For example, many multi-state systems appear in communication networks, production, manufacturing, power generation, computer systems, sensor networks, logic circuits, transportation of oil and gas, and others [3], [4]. El-Neweihi *et al.* [5] analyzed the theoretical relationships between multi-state system reliability behavior and multi-state component performance. Griffith [6] proposed an importance measure which represents a change

0018-9529 © 2015 IEEE. Personal use is permitted, but republication/redistribution requires IEEE permission.
See http://www.ieee.org/publications_standards/publications/rights/index.html for more information.

in system performance when a component deteriorates from state m to state $m-1$. Wu and Chan [7] defined the utility importance of the state of a component in a multi-state system to overcome some drawbacks of the Griffith importance measure, and studied the relationship between the new utility importance and the Griffith importance. Levitin and Xing [8], and Levitin *et al.* [9] evaluated the performance distribution of complex multi-state systems. Levitin *et al.* [10] considered some commonly used importance measures in multi-state systems. Zio and Podofillini [11] estimated some frequently used importance measures of the components at a given performance level. Natvig *et al.* [12]–[15] analyzed the multistate systems reliability, and considered the dynamic and stationary measures of importance of a component in a multistate system. Kuo and Zhu [16]–[18] summarized the concepts of importance measures in reliability and their application in broad areas.

Various approaches have also been proposed to estimate the reliabilities and importance measures of multi-state systems. Generally, these reported methods can be divided into four different approaches: the Monte-Carlo simulation technique, the extension of the Boolean models to the multi-valued case, the stochastic process (mainly Markov and semi-Markov) approach, and the universal generating function approach [19]. Natvig [15] provided a descriptive account of various types of multistate systems, and probabilistic modeling of the monitoring and maintenance of multistate systems. Levitin and Lisnianski [20] used the universal generating function to analyze the importance measures for multi-state systems. Zio *et al.* [21] discussed the Monte-Carlo estimation of importance measures under restrictions on the performance levels of its multi-state components. Ramirez-Marquez and Coit [22] described a Monte-Carlo simulation methodology for estimating the reliability of a multi-state system. The stochastic process methods are widely used for the reliability analysis of multi-state systems. Markov and semi-Markov processes are two examples of stochastic processes. Compared with the Markov process, the semi-Markov process provided a much more general model for probabilistic systems. The discrete and continuous-time Markov processes are special cases of the semi-Markov process. Chryssaphinou *et al.* [23] analyzed multi-state reliability systems under the semi-Markov hypothesis. Most papers on importance measures utilizing stochastic processes focused on the Markov process. If all failure and repair times of components follow an exponential distribution, then the Markov process can be used to analyze reliability and importance measures. Chadjiconstantinidis and Koutras [24] exploited the advantages of the Markov chain approach to investigate the behavior of reliability importance measures for a wide class of Markov chain systems. Do Van *et al.* [25], [26] used the perturbation method to estimate an importance factor, called the multi-directional sensitivity measure, in the framework of Markov systems, and developed an importance measure based on directional derivatives in the context of Markov reliability models.

B. Motivation

One of the properties of Markov processes is that the sojourn time (holding time) in any state follows an exponential distribution with a parameter depending on that state. However, in practice, such as the component reliability assessment, if the lifecycle and repair-time distributions are not exponential distributions, then the process is far from the Markov process, and will reduce the accuracy of the simulation results. The semi-Markov process does not require the exponential distribution assumption on the sojourn time. For example, the bathtub curve is an example of changing failure rate with time, which can be described by three different Weibull distributions. The behavior of a system under such distributions can be modeled by the semi-Markov process. So, studying how the transition between component states affects the system performance based on the semi-Markov process can provide useful information for preventive maintenance actions, and provide the support to improve system performance and extend service life.

For the integrated importance measure (IIM) reported in Si *et al.* [27], the authors considered the expected number of component failures in unit time, and how the transition of component states affects the system performance. Si *et al.* [28] used the multi-state system Bayesian network to represent the multi-state system under uncertainty, and proposed the IIM to describe the effects of component failures on the state distribution of the multi-state system. Si *et al.* [27], [29] further explained the physical meaning of this IIM, explored the characteristics of IIM in typical systems for the deterioration process and the maintenance process, and discussed the properties of IIM in the Markov process. Si *et al.* [30] extended the IIM from the component state to the component to describe which component is the most important to keep in some state and above for improving the performance of the system. In the system operation phase, according to the bathtub curve, the transition rate of component states changing with time can be described by the Weibull distribution or the Gamma distribution. The behavior of a system under such distributions can be modeled by the semi-Markov process. The integrated importance measure reported in [27], [29] is extended from the Markov assumption in [27] to the semi-Markov assumption in this paper. The semi-Markov assumption allows a non-exponential sojourn time distribution in each state. Thus, the extended integrated importance measure under the new semi-Markov assumption is applicable for more practical situations where the sojourn time distribution in each state usually follows non-exponential distributions. Thus, based on the above IIM concept, studying the IIM under the semi-Markov process can help evaluate the effect of component state on the system performance as a function of time, and provide information for the improvement of system performance and the extension of service life.

The semi-Markov process provides a much more general model for systems than the Markov process. For the Markov process, it can be thought of as memoryless, and is a stochastic process in which the probability distribution of the current state is conditionally independent of the path of past states. However, the transition rates to other states may change over the duration of a state. For example, the lifetime of an electronic component may follow an exponential distribution. But for the fatigue failure, the vacuum tube failure, and the bearing failure of the mechanical and electrical products, the lifetime distributions of the products may follow the Weibull distribution, and the

inter-arrival times between subsequent states would no longer be exponentially distributed. For such mechanical and electrical products, the semi-Markov process can describe the reliability indexes, and IIM can be used to evaluate the effect of the state transitions of the mechanical and electrical products on the system performance.

In this paper, we study the IIM under the semi-Markov process, and discuss some characteristics of IIM corresponding to the semi-Markov process. The IIM of the semi-Markov process indicates which state of a component is most worthy to keep to improve system performance. This approach can evaluate the effect of component state on the performance during different time periods of the system, and provide information to improve system performance and extend service life.

The rest of the paper is structured as follows. The generalized version of the IIM under the semi-Markov process is analyzed in Section II. Section III discusses some key characteristics of the IIM of component states in typical system structures under the semi-Markov process. A simple example is presented to illustrate the generalized IIM in Section IV. Section V concludes this paper, and points out future research directions.

Assumptions:

1) The multi-state system is monotone and coherent [30].
2) The state space of component i is $\{0, 1, 2, \ldots, M_i\}$, and the state space of the system is $\{0, 1, 2, \ldots, M\}$, where 0 represents the complete failure state, and M_i (or M) is the perfect functioning state of component i (or the system). The states are ordered from 0 to M_i (or M). The states $\{1, 2, \ldots, M_i(or M) - 1\}$ denote some degradation of component i (or system), but not complete failure.
3) All components are statistically independent.
4) As a component is used, it may make transitions from better states to worse states. Maintenance actions may be used to improve the state of a component.

II. The IIM Under the Semi-Markov Model

The Griffith importance was proposed to evaluate the importance of state m of component i in multi-state systems as follows [6].

$$\begin{aligned} I_m^G(i) &= \sum_{j=1}^{M} (a_j - a_{j-1}) \big[\Pr(\Phi(m_i, X) \geq j) \\ &\quad - \Pr(\Phi((m-1)_i, X) \geq j) \big] \\ &= \sum_{j=1}^{M} a_j \big[\Pr(\Phi(m_i, X) = j) \\ &\quad - \Pr(\Phi((m-1)_i, X) = j) \big], \end{aligned} \tag{1}$$

where $0 = a_0 < a_1 < \cdots < a_M$, $\Phi(m_i, X) = \Phi(x_1, \ldots, x_{i-1}, m_i, x_{i+1}, \ldots, x_n)$, and $I_m^G(i)$ is interpreted as the change of system performance when a component deteriorates from state m to state $m-1$.

The IIM of the deterioration process is defined as [27]

$$\begin{aligned} IIM_m^i &= P_m^i \cdot b_{m0}^i \sum_{j=1}^{M} a_j \\ &\quad \times \left[\Pr\left(\Phi(m_i, X) = j\right) - \Pr\left(\Phi(0_i, X) = j\right) \right], \end{aligned} \tag{2}$$

where P_m^i is the probability that component i is in state m.

The IIM_m^i represents the expected loss of system performance when component i deteriorates from state m to state 0 in unit time. When we consider the maintenance process, the IIM can be represented as [29]

$$\begin{aligned} IIM_{l,q}^i &= P_l^i \cdot b_{lq}^i \sum_{j=1}^{M} a_j \\ &\quad \times \left[\Pr\left(\Phi(l_i, X) = j\right) - \Pr\left(\Phi(q_i, X) = j\right) \right], \end{aligned} \tag{3}$$

where $q > l$. The $IIM_{l,q}^i$ represents the change of the system performance when component i improves from state l to state q.

For repairable systems, there is a need to consider both the effects of deterioration and the effects of maintenance. Thus, it is important to obtain a generalized IIM which takes into consideration both the deterioration process and the maintenance process.

The generalized version of IIM considering both the deterioration and the maintenance processes for the Markov process is given at time t as

$$\begin{aligned} IIM_{m,l}^i &= P_m^i \cdot b_{ml}^i \sum_{j=1}^{M} a_j \\ &\quad \times \left[\Pr\left(\Phi(m_i, X) = j\right) - \Pr\left(\Phi(l_i, X) = j\right) \right], \end{aligned} \tag{4}$$

where $l \neq m$; if $m < l$, then $m \in \{0, 1, \ldots, M_i - 1\}$; and if $m > l$, then $m \in \{1, \ldots, M_i\}$.

We can interpret $IIM_{m,l}^i$ as the change of the system's performance when component i transfers from state m to state l, which is either due to an improvement or deterioration of component i.

One of the properties of the Markov processes is that the sojourn time (holding time) in any state follows an exponential distribution with a parameter depending on that state. The semi-Markov processes are generalizations of the Markov processes in that the distribution of the sojourn time in any state can, in principle, be arbitrary [31]. Furthermore, in the semi-Markov process, the finite dimensional distributions of the sample paths of the process are modeled directly in terms of arbitrary distributions of sojourn times for each state, and conditional distributions of a jump to another future state, given the present state.

Our earlier work [27], [29] is for the homogeneous case, and the memoryless assumption; thus, we can get rid of the sojourn time dependency in the transition rates from expressions like (4). In this paper, we are presenting the study for the more general case that the memoryless assumption is being relaxed here in semi-Markov processes. In such a case, we define the importance measure considering two time scales, age (t), and sojourn time (y), as in expressions like (12). The following is the analysis.

Let $F_{m,l}^j(y)$ denote the distribution function of the sojourn time y in state m, given that the next state is l for component j. To define the semi-Markov process which represents the

changes of the component states, the corresponding kernel matrix $Q^j(t)(Q^j_{ml}(t) = \int_0^t \prod_{k=0,k\neq l}^{M_j}[1-F^j_{m,k}(\tau)]dF^j_{m,l}(\tau);\, m,l \in \{0,1,\ldots,M_j\})$ can be written as [31]

$$Q^j(t) = \begin{vmatrix} Q^j_{00}(t) & Q^j_{01}(t) & \cdots & Q^j_{0M_j}(t) \\ Q^j_{10}(t) & Q^j_{11}(t) & \cdots & Q^j_{1M_j}(t) \\ \cdots & \cdots & \ddots & \cdots \\ Q^j_{M_j0}(t) & Q^j_{M_j1}(t) & \cdots & Q^j_{M_jM_j}(t) \end{vmatrix},$$

where [32]–[34]

$$G^j_{ml} = \lim_{t\to\infty} Q^j_{ml}(t), \tag{5}$$

$$Q^j_{ml}(t) = G^j_{ml}F^j_{m,l}(t). \tag{6}$$

The distribution function of the sojourn time in state m is [32]

$$H^j_m(t) = \sum_{l=0}^{M_j} Q^j_{ml}(t). \tag{7}$$

The probability of the component state can be represented as [31]

$$P^j_{ml}(t) = \delta_{ml}[1 - \sum_{s=0}^{M_j} Q^j_{ms}(t)] + \sum_{s=0}^{M_j}\int_0^t q^j_{ms}(\tau)P^j_{sl}(t-\tau)d\tau,$$
$$q^j_{ms}(\tau) = \frac{dQ^j_{ms}(\tau)}{d\tau}, \delta_{ml} = \begin{cases} 1 & m=l \\ 0 & m\neq l \end{cases}, m,l \in \{0,1,\ldots,M_j\}. \tag{8}$$

In general, the initial state distribution of each component is assumed to be given. We can solve the renewal equation (8) by applying a Laplace transform and an inverse Laplace transform. We assume that, at time 0, every component j is in its best state (M_j). Hence, the state probability $P^j_m(t)$ of component j is represented as

$$P^j_m(t) = P^j_{M_jm}(t), m \in \{0,1,\ldots,M_j\}. \tag{9}$$

When $t\to\infty$, the steady state probability that component j stays in state l can be obtained as [33]

$$\lim_{t\to\infty} P^j_{ml}(t) = \frac{\pi^j_l w^j(l)}{\sum_{s=0}^{M_j}\pi^j_s w^j(s)}, \tag{10}$$

where π^j_l, and $w^j(l)$, for $l \in \{0,1,\ldots,M_j\}$, denote the stationary probability, and the expected sojourn time in state l for component j, respectively.

In the semi-Markov processes, the transition rate is related to the sojourn time y as [34]

$$b^j_{ml}(y) = \frac{G^j_{ml}\cdot f^j_{m,l}(y)}{(1-H^j_m(y))}, \tag{11}$$

where $f^j_{m,l}(y) = dF^j_{m,l}(y)/dy$.

Then, using the state probabilities $P^j_m(t)$, $m \in \{0,1,\ldots,M_j\}$ given in (9), and the transition rate $b^j_{ml}(y)$ given in (11), we can measure the importance of any component state for the semi-Markov process considering the two time scales of age (t) and sojourn time (y) as

$$IIM^i_{m,l}(t,y) = P^i_m(t)\cdot b^i_{ml}(y)\sum_{j=1}^{M} a_j \times [\Pr(\Phi(m_i(t),X(t)) = j) - \Pr(\Phi(l_i(t),X(t)) = j)]. \tag{12}$$

In practice, any change in design or operation usually leads to changes in groups of transition rates of multi-state components. Therefore, in the operation and optimization phases, managers are interested in specific groups of transition rates among component states. In order to evaluate the overall effect of component states on system performance based on the groups of transition rates, for the deterioration process, we can get $IIM^i_{\mathrm{dp}}(t) = \sum_{m=1}^{M_i}\sum_{l=0}^{m-1} IIM^i_{m,l}(t)$; and for the maintenance process, we can get $IIM^i_{\mathrm{mp}}(t) = \sum_{m=0}^{M_i-1}\sum_{l=m+1}^{M_i} IIM^i_{m,l}(t)$. Based on these two results, we can find out which component is able to provide the largest improvement in system performance.

III. Characteristics of the IIM for a Typical System Under the Semi-Markov Model

We now provide the form of the IIM of component states for series and parallel system structures under the semi-Markov model. The structure function of a series system is $\Phi(X(t)) = \min_{1\le i\le n}\{x_i(t)\}$, and that of a parallel system is $\Phi(X(t)) = \min_{1\le i\le n}\{x_i(t)\}$.

In this section, we discuss the relationships between $IIM^i_{m,l}(t,y)$ and $IIM^j_{m,l}(t,y)$ in these two typical system structures. Based on (12),

$$IIM^i_{m,l}(t,y) - IIM^j_{m,l}(t,y) = P^i_m(t)\cdot b^i_{ml}(y)\sum_{k=1}^{M} a_k \times [\Pr(\Phi(m_i(t),X(t)) = k) - \Pr(\Phi(l_i(t),X(t)) = k)] - P^j_m(t)\cdot b^j_{ml}(y)\sum_{k=1}^{M} a_k[\Pr(\Phi(m_j(t),X(t)) = k) - \Pr(\Phi(l_j(t),X(t)) = k)].$$

According to [27], we can get the IIM of component i in the series system under the semi-Markov model as shown in the first equation at the bottom of the next page, and the IIM of component i in the parallel system under the semi-Markov model as shown in the second equation at the bottom of the next page.

Next, we provide four propositions on the IIM of the adjacent states m and $m+1$, or m and $m-1$, of the components. Discussions and interpretations of these propositions will be provided right after Proposition 4.

Proposition 1: For the same state m of components i and j in the series system, we have two conditions as follows.

1) $P^i_m(t)\cdot b^i_{m(m-1)}(y)/(1-\rho^i_m(t)) \ge P^j_m(t)\cdot b^j_{m(m-1)}(y)/(1-\rho^j_m(t))$ iff $\left|IIM^i_{m,(m-1)}(t,y)\right| \ge \left|IIM^j_{m,(m-1)}(t,y)\right|$, where $m \in \{1,\ldots,\min(M_i,M_j)\}$. When $M_i < M_j$, $b^i_{M_iM_i-1}(y) \ge P^j_{M_i}(t)\cdot b^j_{M_i(M_i-1)}(y)/(1-\rho^j_{M_i}(t))$ iff $\left|IIM^i_{M_i,(M_i-1)}(t,y)\right| \ge \left|IIM_{M_i,(M_i-1)}(t,y)\right|$. When $M_i = M_j$, $b_{M_i(M_i-1)}(y) \ge$

$b^j_{M_j(M_j-1)}(y)$ iff $\left|IIM^i_{M_i,(M_i-1)}(t,y)\right| \geq \left|IIM^j_{M_j,(M_j-1)}(t,y)\right|$.

2) $P^i_m(t) \cdot b^i_{m(m+1)}(y)/(1-\rho^i_{m+1}(t)) \geq P^j_m(t) \cdot b^j_{m(m+1)}(y)/(1-\rho^j_{m+1}(t))$ iff $\left|IIM^i_{m,(m+1)}(t,y)\right| \geq \left|IIM^j_{m,(m+1)}(t,y)\right|$, where $m \in \{0,1,\ldots,\min(M_i,M_j)-1\}$.

Proof: See the Appendix.

Proposition 2: For the same state m of components i and j in the series system, we have

1) $b^i_{m(m-1)}(y)\pi^i_m \sum_{s=0}^{M_i}\hat{Q}'^i_{ms}(0) \Big/ \sum_{k=m}^{M_i}\left(\pi^i_k \sum_{s=0}^{M_i}\hat{Q}'^i_{ks}(0)\right) \geq b^j_{m(m-1)}(y)\pi^j_m \sum_{s=0}^{M_j}\hat{Q}'^j_{ms}(0) \Big/ \sum_{k=m}^{M_j}\left(\pi^j_k \sum_{s=0}^{M_j}\hat{Q}'^j_{ks}(0)\right)$ iff $\left|IIM^i_{m,(m-1)}(t,y)\right| \geq \left|IIM^j_{m,(m-1)}(t,y)\right|$ at the steady state, where $m \in \{1,\ldots,\min(M_i,M_j)\}$; and

2) $b^i_{m(m+1)}(y)\pi^i_m \sum_{s=0}^{M_i}\hat{Q}'^i_{ms}(0) \Big/ \sum_{k=m+1}^{M_i}\left(\pi^i_k \sum_{s=0}^{M_i}\hat{Q}'^i_{ks}(0)\right) \geq b^j_{m(m+1)}(y)\pi^j_m \sum_{s=0}^{M_j}\hat{Q}'^j_{ms}(0) \Big/ \sum_{k=m+1}^{M_j}\left(\pi^j_k \sum_{s=0}^{M_j}\hat{Q}'^j_{ks}(0)\right)$ iff $\left|IIM^i_{m,(m+1)}(t)\right| \geq \left|IIM^j_{m,(m+1)}(t)\right|$ at the steady state, where $m \in \{0,1,\ldots,\min(M_i,M_j)-1\}$.

Proof: See the Appendix.

According to Proposition 1 and Proposition 2, for a series system, under semi-Markov processes, when considering the effects of adjacent states' deterioration or improvement of a component on system performance, the most important component can be identified at any time t, and at the steady state from the point of view of the IIM, respectively. If two components are in the same state, then the component with the larger IIM should be maintained first in the operation of a series system to get the larger improvement in system performance.

Proposition 3: For the same state m of components i and j in the parallel system, we have two results as follows.

1) $P^i_m(t) \cdot b^i_{m(m-1)}(y)/\rho^i_m(t) \geq P^j_m(t) \cdot b^j_{m(m-1)}(y)/\rho^j_m(t)$ iff $\left|IIM^i_{m,(m-1)}(t,y)\right| \geq \left|IIM^j_{m,(m-1)}(t,y)\right|$, where $m \in \{1,\ldots,\min(M_i,M_j)\}$. When $M_i < M_j$, $(1/\rho^i_{M_i}(t)-1)b^i_{M_i(M_i-1)}(y) \geq P^j_{M_i}(t) \cdot b^j_{M_i(M_i-1)}(y)/\rho^j_{M_i}(t)$ iff $\left|IIM^i_{M,(M-1)}(t,y)\right| \geq \left|IIM^j_{M,(M-1)}(t,y)\right|$. When $M_i = M_j$, $(1/\rho^i_{M_i}(t)-1)b^i_{M_i(M_i-1)}(y) \geq (1/\rho^j_{M_j}(t)-1)b^j_{M_j(M_j-1)}(y)$ iff $\left|IIM^i_{M_i,(M_i-1)}(t,y)\right| \geq \left|IIM^j_{M_j,(M_j-1)}(t,y)\right|$.

2) $P^i_m(t) \cdot b^i_{m(m-1)}(y)/\rho^i_{m+1}(t) \geq P^j_m(t) \geq b^j_{m(m+1)}(y)/\rho^j_{m+1}(t)$ iff $\left|IIM^i_{m,(m+1)}(t,y)\right| \geq \left|IIM^j_{m,(m+1)}(t,y)\right|$, where $m \in \{0,1,\ldots,\min(M_i,M_j)-1\}$.

Proof: See the Appendix.

Proposition 4: For the same state m of components i and j in the parallel system, we have

1) $b^i_{m(m-1)}(y)\pi^i_m \sum_{s=0}^{M_i}\hat{Q}'^i_{ms}(0) \Big/ \sum_{k=0}^{m-1}(\pi^i_k \sum_{s=0}^{M_i}\hat{Q}'^i_{ks}(0)) \geq b^j_{m(m-1)}(y)\pi^j_m \sum_{s=0}^{M_j}\hat{Q}'^j_{ms}(0) \Big/ \sum_{k=0}^{m-1}(\pi^j_k \sum_{s=0}^{M_j}\hat{Q}'^j_{ks}(0))$ iff $\left|IIM^i_{m,(m-1)}(t,y)\right| \geq \left|IIM^j_{m,(m-1)}(t,y)\right|$ at steady state, where $m \in \{1,\ldots,\min(M_i,M_j)\}$; and

2) $b^i_{m(m+1)}(y)\pi^i_m \sum_{s=0}^{M_i}\hat{Q}'^i_{ms}(0) \Big/ \sum_{k=0}^{m}(\pi^i_k \sum_{s=0}^{M_i}\hat{Q}'^i_{ks}(0)) \geq b^j_{m(m+1)}(y)\pi^i_m \sum_{s=0}^{M_j}\hat{Q}'^j_{ms}(0) \Big/ \sum_{k=0}^{m}(\pi^j_k \sum_{s=0}^{M_j}\hat{Q}'^j_{ks}(0))$ iff $\left|IIM^i_{m,(m+1)}(t,y)\right| \geq \left|IIM^j_{m,(m+1)}(t,y)\right|$ at steady state, where $m \in \{0,1,\ldots,\min(M_i,M_j)-1\}$.

Proof: See the Appendix.

According to Proposition 3 and Proposition 4, for a parallel system, under semi-Markov processes, if the left hand side is

$$IIM^i_{m,l}(t,y) = \begin{cases} P^i_m(t)\cdot b^i_{ml}(y)\sum_{r=l+1}^{m}(a_r-a_{r-1})\prod_{k=1,k\neq i}^{n}(1-\rho^k_r(t)), & m>l \\ -P^i_m(t)\cdot b^i_{ml}(y)\sum_{r=m+1}^{l}(a_r-a_{r-1})\prod_{k=1,k\neq i}^{n}(1-\rho^k_r(t)), & m<l \end{cases}$$

$$IIM^i_{m,l}(t,y) = \begin{cases} P^i_m(t)\cdot b^i_{ml}(y)\sum_{r=l+1}^{m}(a_r-a_{r-1})\prod_{k=1,k\neq i}^{n}\rho^k_r(t), & m>l \\ -P^i_m(t)\cdot b^i_{ml}(y)\sum_{r=m+1}^{l}(a_r-a_{r-1})\prod_{k=1,k\neq i}^{n}\rho^k_r(t), & m<l \end{cases}$$

larger than the right hand side in 1) and 2), then the result is the same as in the series system. The IIM is a generalization of Birnbaum importance, and concerns not only the probability distributions and transition rates of the corresponding component states, but also the change in the system performance caused by the transitions of the component states. According to these propositions, we can get the order of the IIM of components. Then proper actions can be applied to the weakest component to get the largest improvement in system performance.

If the series system and the parallel system are composed of the same type of components, then we can get the following two Corollaries.

Corollary 1: For the same state m of components i and j, we have the following.

1) Under the condition of $P_m^i(t) \cdot b_{m(m-1)}^i(y) \geq P_m^j(t) \cdot b_{m(m-1)}^j(y)$, if $\left|IIM_{m,(m-1)}^i(t,y)\right| \geq \left|IIM_{m,(m-1)}^j(t,y)\right|$ in the series system, then $\left|IIM_{m,(m-1)}^i(t,y)\right| \leq \left|IIM_{m,(m-1)}^j(t,y)\right|$ in the parallel system; under the same condition, if $\left|IIM_{m,(m-1)}^i(t,y)\right| \geq \left|IIM_{m,(m-1)}^j(t,y)\right|$ in the parallel system, then $\left|IIM_{m,(m-1)}^i(t,y)\right| \leq \left|IIM_{m,(m-1)}^j(t,y)\right|$ in the series system.
2) Under the condition of $P_m^i(t) \cdot b_{m(m+1)}^i(y) \leq P_m^j(t) \cdot b_{m(m-1)}^j(y)$, if $\left|IIM_{m,(m+1)}^i(t,y)\right| \geq \left|IIM_{m,(m+1)}^j(t,y)\right|$ in the series system, then $\left|IIM_{m,(m+1)}^i(t,y)\right| \leq \left|IIM_{m,(m+1)}^j(t,y)\right|$ in the parallel system; under the same condition, if $\left|IIM_{m,(m+1)}^i(t,y)\right| \geq \left|IIM_{m,(m+1)}^j(t,y)\right|$ in the parallel system, then $\left|IIM_{m,(m+1)}^i(t,y)\right| \leq \left|IIM_{m,(m+1)}^j(t,y)\right|$ in the series system.

Proof: See the Appendix.

Corollary 2: For the same state m of components i and j, we have the following.

1) Under the condition of $b_{m(m-1)}^j(y)\pi_m^i \sum_{s=0}^{M_i} \hat{Q}'^{ij}_{ms}(0) \Big/ \sum_{k=0}^{M_i}\left(\pi_k^j \sum_{s=0}^{M_j} \hat{Q}'^{ij}_{ks}(0)\right) \leq b_{m(m-1)}^j(y)\pi_m^j \sum_{s=0}^{M_j} \hat{Q}'^{ij}_{ms}(0) \Big/ \sum_{k=0}^{M_j}\left(\pi_k^j \sum_{s=0}^{M_j} \hat{Q}'^{ij}_{ks}(0)\right)$, if $\left|IIM_{m,(m-1)}^i(t,y)\right| \geq \left|IIM_{m,(m-1)}^j(t,y)\right|$ at the steady state in the series system, then $\left|IIM_{m,(m-1)}^i(t,y)\right| \leq \left|IIM_{m,(m-1)}^j(t,y)\right|$ at the steady state in the parallel system; under the same condition, if $\left|IIM_{m,(m-1)}^i(t,y)\right| \geq \left|IIM_{m,(m-1)}^j(t,y)\right|$ at the steady state in the parallel system, then $\left|IIM_{m,(m-1)}^i(t,y)\right| \leq \left|IIM_{m,(m-1)}^j(t,y)\right|$ at the steady state in the series system.
2) Under the condition of $b_{m(m+1)}^i(y)\pi_m^i \sum_{s=0}^{M_j} \hat{Q}'^{ii}_{ms}(0) \Big/ \sum_{k=0}^{M_i}\left(\pi_k^i \sum_{s=0}^{M_i} \hat{Q}'^{ii}_{ks}(0)\right) \leq b_{m(m+1)}^j(y)\pi_m^j \sum_{s=0}^{M_j} \hat{Q}'^{ij}_{ms}(0) \Big/ \sum_{k=0}^{M_j}\left(\pi_k^j \sum_{s=0}^{M_j} \hat{Q}'^{ij}_{ks}(0)\right)$, if $\left|IIM_{m,(m+1)}^i(t)\right| \geq \left|IIM_{m,(m+1)}^j(t)\right|$ at the steady state in the series system, then $\left|IIM_{m,(m+1)}^i(t)\right| \leq \left|IIM_{m,(m+1)}^j(t)\right|$ at the steady state for in the parallel system. Under the same condition, if $\left|IIM_{m,(m+1)}^i(t)\right| \geq \left|IIM_{m,(m+1)}^j(t)\right|$ at the steady state in the parallel system, then $\left|IIM_{m,(m+1)}^i(t)\right| \leq \left|IIM_{m,(m+1)}^j(t)\right|$ at the steady state in the series system.

Proof: See the Appendix.

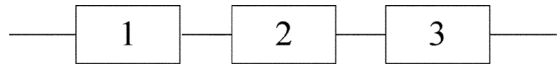

Fig. 1. A series system.

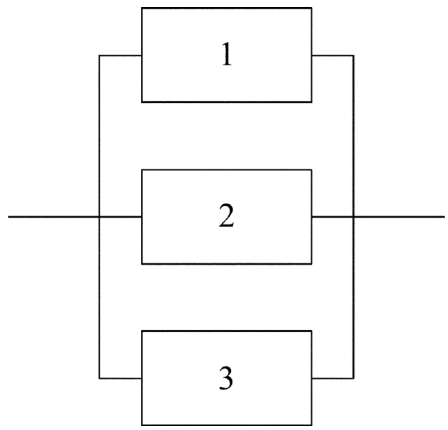

Fig. 2. A parallel system.

According to Corollary 1 and Corollary 2, under the condition that the series system and the parallel system are composed of the same type of components, if we have identified the most important component in the series (parallel) system, then we have also found the most important component in the parallel (series) system. Corollary 1 and Corollary 2 provide the convenience to identify the most important component for engineers in the series and the parallel systems consisting of the same type of components, which can be used in the design phase of the system structures to get the maximal system reliability.

In the following, we give an example to demonstrate the application of Corollary 1 only. The application of Corollary 2 is similar. A series system consisting of three components is given as in Fig. 1.

The three same type of components may be used to construct the parallel system as in Fig. 2.

In Figs. 1 and 2, we assume that all components have three states. We assume that at time $t = 0$, $P_2^1(0) = P_2^2(0) = P_2^3(0) = 1$; and at time $t = 3$, $(P_0^1(3), P_1^1(3), P_2^1(3)) = (0.2, 0.5, 0.3)$, $(P_0^2(3), P_1^2(3), P_2^2(3)) = (0.4, 0.3, 0.3), (P_0^3(3), P_1^3(3), P_2^3(3)) = (0.25, 0.5, 0.25)$.

TABLE I
VALUES OF $b^i_{ml}(1)$

	$b^i_{01}(1)$	$b^i_{12}(1)$	$b^i_{10}(1)$	$b^i_{21}(1)$
Component 1	0.5	2	1.5	0.6
Component 2	0.8	1.5	2	0.5
Component 3	0.4	1.8	1	0.4

TABLE II
VALUES OF λ^i_{ml} AND n^i_{ml}

i	$\lambda^i_{01}(n^i_{01})$	$\lambda^i_{10}(n^i_{10})$	$\lambda^i_{11}(n^i_{11})$	$\lambda^i_{02}(n^i_{02})$	$\lambda^i_{20}(n^i_{20})$	$\lambda^i_{12}(n^i_{12})$	$\lambda^i_{21}(n^i_{21})$	$\lambda^i_{22}(n^i_{22})$
1	2 (5)	3 (1)	2 (2)					
2	1 (2)	1 (5)	0.3(0.5)	0.2(0.2)	0.1(0.1)	1.5 (3)	2 (4)	0.2(0.6)
3	2.5 (5)	3.5 (1)	0.1(0.1)					
4	3 (2)	3 (3)	1(1)	1 (4)	2 (1)	4 (2)	5 (1)	0.8(0.6)

The transition rates to adjacent states for all components have also been given, when $y = 1$, in Table I.

We assume that $(a_0, a_1, a_2) = (0,300,1000)$, in which states 0, 1, and 2 correspond to the complete failure state, the medium state, and the perfectly working state, respectively. According to Corollary 1, we have $P^1_1(3)\cdot b^1_{10}(1) = 0.75 > P^2_1(3)\cdot b^2_{10}(1) = 0.6$, and $\left|IIM^1_{1,0}(3,1)\right| = 101.25 < \left|IIM^2_{1,0}(3,1)\right| = 108$ for Components 1 and 2 in Fig. 1. We calculate $\left|IIM^1_{1,0}(3,1)\right| = 22.5 > \left|IIM^2_{1,0}(3,1)\right| = 18$ in Fig. 2. The result is consistent with Corollary 1. Similarly, for components 1, and 3, we have $P^1_0(3)\cdot b^1_{01} = 0.1 = P^3_0(3)\cdot b^3_{01}(1)$, $\left|IIM^1_{0,1}(3,1)\right| = 13.5 < \left|IIM^3_{0,1}(3,1)\right| = 14.4$, and $P^1_1(3)\cdot b^1_{12} = 1 > P^3_1(3)\cdot b^3_{12}(1) = 0.9$, $\left|IIM^1_{1,2}(3,1)\right| = 52.5 < \left|IIM^3_{1,2}(3,1)\right| = 56.7$ in Fig. 1. We calculate $\left|IIM^1_{0,1}(3,1)\right| = 3 > \left|IIM^3_{0,1}(3,1)\right| = 2.4$, and $\left|IIM^1_{1,2}(3,1)\right| = 367.5 > \left|IIM^3_{1,2}(3,1)\right| = 308.7$ in Fig. 2. So Component 1 has the biggest importance in Fig. 2. This shows that, in the design phase of the system structure, Component 1 should be improved first to get the maximal system reliability.

IV. NUMERICAL EXAMPLE OF IIM FOR THE SEMI-MARKOV MODEL

In this section, we illustrate how the importance measures of component states are measured under the semi-Markov process, and how to identify which component state is the most important in a mixed parallel series system.

The reliability block diagram of a mixed parallel series system is given in Fig. 3 which consists of four components.

We assume that the distribution functions of the waiting times given the present and the next states follow the Gamma distribution; that is, $F^i_{m,l}(y) = \Gamma(n^i_{ml}, \lambda^i_{ml}, y)$. Obviously the exponential distribution is a special case of the Gamma distribution when the parameter $n^i_{ml} = 1$. Components 1 and 3 have two possible states $\{0,1\}$, while Components 2 and 4 have three possible states $\{0,1,2\}$. The system structure function is $\Phi(X(t)) = \min\{\max\{\min\{x_1(t), x_3(t)\}, x_2(t)\}, x_4(t)\}\}$.

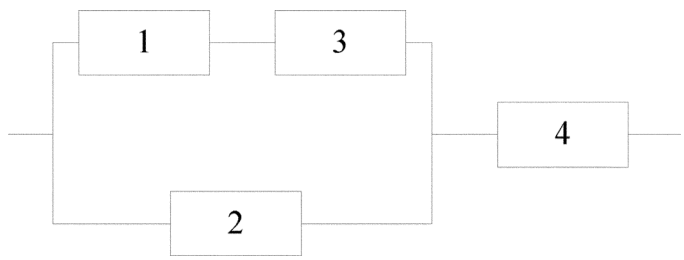

Fig. 3. A series-parallel system.

The values of the shape parameters n^i_{ml} and the scale parameters λ^i_{ml} of the Gamma distributions are given in Table II.

According to the system structure function, this system has 3 states. We suppose that $(a_0, a_1, a_2) = (0,400,1200)$. We can get the IIM of component states at an arbitrary time point. Based on (12), we give the IIM when Component 2 deteriorates from State 1 to State 0 as

$$IIM^2_{1,0}(t,y) = P^2_1(t)b^2_{10}(y)\sum_{j=1}^{2} a_j \left(\Pr(\mathbf{\Phi}(1_2, X(t)) = j) - \Pr(\mathbf{\Phi}(0_2, X(t)) = j)\right).$$

$\Pr(\mathbf{\Phi}(1_2, X(t)) = 1) = 1 - P^4_0(t)$, $\Pr(\mathbf{\Phi}(0_2, X(t)) = 1) = P^1_1(t)P^3_1(t)(1 - P^4_0(t))$, so we have

$$\begin{aligned}&\Pr(\mathbf{\Phi}(1_2, X(t)) = 1) - \Pr(\mathbf{\Phi}(0_2, X(t)) = 1)\\ &= 1 - P^1_1(t)P^3_1(t) - P^4_0(t) + P^1_1(t)P^3_1(t)P^4_0(t).\end{aligned}$$

$\Pr(\mathbf{\Phi}(1_2, X(t)) = 2) = 0, \Pr(\mathbf{\Phi}(0_2, X(t)) = 2) = 0$, so we have

$$\begin{aligned}&\sum_{j=1}^{2} a_j \left(\Pr\left(\mathbf{\Phi}(1_2, X(t)) = j\right) - \Pr\left(\mathbf{\Phi}(0_2, X(t)) = j\right)\right)\\ &= a_1 \cdot \left(1 - P^1_1(t)P^3_1(t) - P^4_0(t) + P^1_1(t)P^3_1(t)P^4_0(t)\right).\end{aligned}$$

TABLE III
VALUES OF $IIM^i_{m,l}(t,y) m > l$

	t=1	t=5	t=7	t=10	t=12	t=15	t=∞
$IIM^1_{1,0}(t,y)$	11.66968	30.62319	30.76512	30.76332	30.76294	30.76289	30.76289
$IIM^2_{1,0}(t,y)$	116.3496	97.24827	97.21694	97.23214	97.23267	97.23274	97.23274
$IIM^2_{2,1}(t,y)$	313.1987	160.3399	159.1077	159.0893	159.0922	159.0925	159.0925
$IIM^3_{1,0}(t,y)$	25.31903	66.44139	66.74933	66.74540	66.74458	66.74450	66.74450
$IIM^4_{1,0}(t,y)$	209.4933	136.9955	136.5239	136.5212	136.5225	136.5227	136.5227
$IIM^4_{2,0}(t,y)$	50.87687	29.45852	29.29364	29.29163	29.29204	29.29208	29.29208
$IIM^4_{2,1}(t,y)$	546.2778	279.6631	277.5139	277.4819	277.4869	277.4875	277.4875

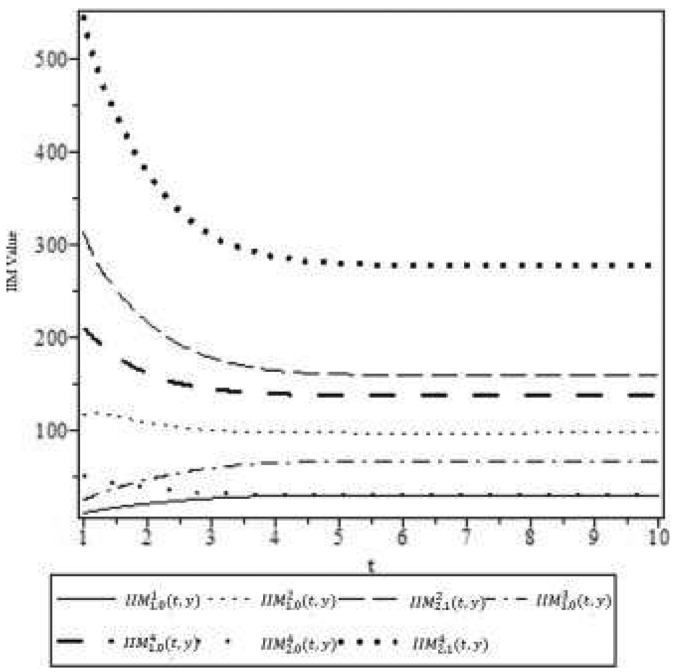

Fig. 4. Behavior of $IIM^i_{m,l}(t,y), i = 1,2,3,4$, and $m > l$.

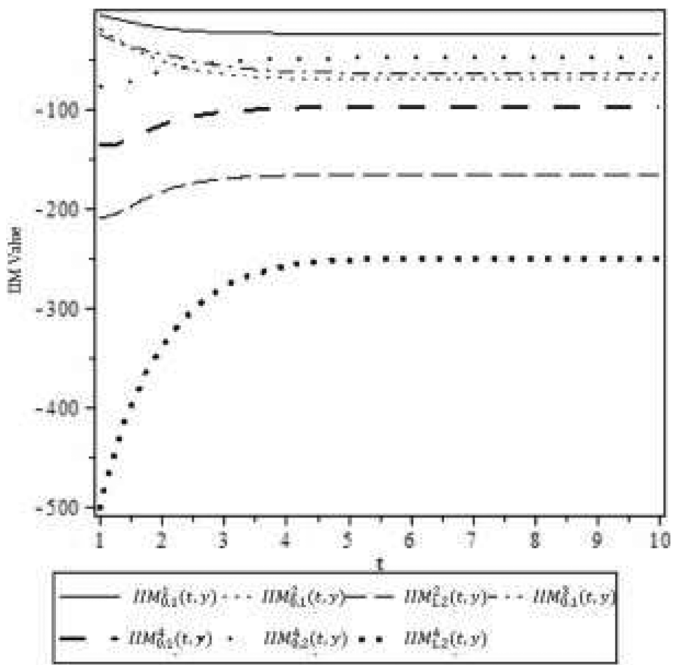

Fig. 5. Behavior of $IIM^i_{m,l}(t,y), i = 1,2,3,4$, and $m < l$.

Then $IIM^2_{1,0}(t,y) = P^2_1(t) \cdot b^2_{10}(y) \cdot a_1 \cdot \left(1 - P^1_1(t)P^3_1(t) - P^4_0(t) + P^1_1(t)P^3_1(t)P^4_0(t)\right)$, where $b^2_{10}(y) = (2+18y)/(3+9y)$ is based on (11).

Let's assume that the current sojourn time of component i at state m is $y = 1$. Based on the given data, (8), and (10), the value of $IIM^2_{1,0}(t,y)$ as well as the IIM of other component states can be calculated. The values when $t = 1$, $t = 5$, $t = 7$, $t = 10$, $t = 12$, $t = 15$, $t \to \infty$ are listed in Table III.

Figs. 4 and 5 display the behaviors of the IIM of component states over time. The current sojourn time y is 1, so the time axis starts from 1. We can compare the importance values among the states of the same component or different components. For example, for component i, $|IIM^i_{m_1,l}(t,y)| > |IIM^i_{m_2,l}(t,y)|$ indicates that state m_1 is more important than state m_2 based on state l at time t, and $|IIM^i_{m,l}(t,y)| > |IIM^i_{m,l}(t,y)|$ indicates that state m of component i is more important than that of component j based on state l at time t. For the same state of a component, values of the IIM from this state to different states are different. For instance, $IIM^4_{2,1}(t,y) > IIM^4_{2,0}(t,y)$ in Fig. 4. In general, $IIM^i_{m,l}(t,y) + IIM^i_{l,m}(t,y) \neq 0, m > l$, such as $IIM^2_{1,0}(10,y) = 97.23214$, and $IIM^2_{0,1}(10,y) = -70.00696$ in Fig. 5, because the transition rate $b^i_{ml}(y)$ and $b^i_{lm}(y)$ may be distinct, and the state probabilities $P^i_m(t)$ and $P^i_l(t)$ are different.

Figs. 4 and 5 show that $IIM^4_{2,1}(t,y) > IIM^2_{2,1}(t,y)$, and $IIM^4_{1,2}(t,y) < IM^2_{1,2}(t,y)$, respectively. However, this situation may not always hold for all states of the components. For instance, $IIM^3_{1,0}(t,y)$ intersects with $IIM^4_{2,0}(t,y)$ in Fig. 4, and $IIM^4_{0,2}(t,y)$ intersects with $IIM^2_{0,1}(t,y)$ and $IIM^3_{0,1}(t,y)$ in Fig. 5. Furthermore, it is possible that the most important component state will change over time. In Figs. 4 and 5, when $t > 5$,

TABLE IV
IIM AND GRIFFITH IMPORTANCE OF COMPONENT 1, $m > l$

	t=1	t=5	t=7	t=10
IIM	11.66968	30.62319	30.76512	30.76332
Griffith importance	15.36791	92.38923	92.79636	92.98629

TABLE V
IIM OF ALL COMPONENTS FOR THE MAINTENANCE PROCESS AT STEADY STATE

	$IIM^{I}_{0,1}(t,y)$	Order of $IIM^{I}_{0,1}(t,y)$	$IIM^{I}_{1,2}(t,y)$	Order of $IIM^{I}_{1,2}(t,y)$
Component 1	-23.73138	4		
Component 2	-70.00756	2	-165.7213	2
Component 3	-63.56618	3		
Component 4	-98.18876	1	-249.3922	1

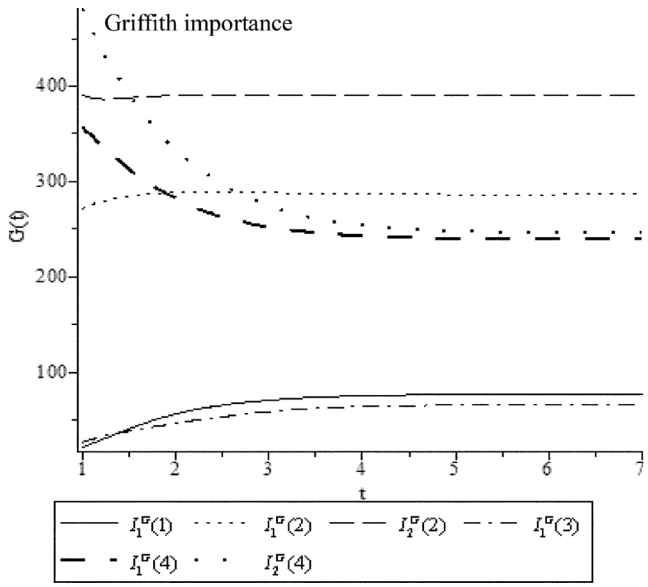

Fig. 6. Behavior of Griffith importance.

the values of the IIM of all components nearly stabilize, as is determined by the property of the Gamma distribution, and shows that the semi-Markov process has reached the steady state.

Fig. 6 shows the change of the Griffith importance which can be interpreted as the change of the system performance when a component deteriorates from state m to state $m-1$. Next, we compare the differences between the IIM and the Griffith importance for Component 1.

At time 5, the IIM of Component 1 in Fig. 4 is smaller than the Griffith importance of Component 1 in Fig. 6, as in Table IV. The reason for the difference in these two numbers at time 5 is that the IIM is related to the probability of State 1, and the transition rate from State 1 to State 0 of Component 1; but the Griffith importance is not. With the increase of system life, the probability of State 1 of Component 1 becomes smaller. In real life, the state transition of Component 1 is stochastic. The Griffith importance only considers the effect of Component 1 on system performance when the transition from State 1 to State 0 occurs. But the Griffith importance does not include the transition probabilities. For example, Component 1 for sure has failed when time goes to infinity. Thus, the Griffith importance is incomplete because it does not consider the transition probabilities.

The transition of component states is stochastic. The Griffith importance is concerned with the effect of the component on system performance at the moment after the state transition of the component has occurred, and is not concerned with the probability of this transition of the component state. The IIM takes care of the average effect of the component on the system performance when considering the transition rates of component states and the probability of a component in a certain state with time. The Griffith importance does not consider the joint effect of the probability distributions, transition rate of component state, and the system performance; and the Griffith importance is for the degradation process only.

For the maintenance process, Table V shows the IIM of all components for the maintenance process at the steady state condition. Suppose all components are in State 0 at a specific time. According to Table V, the engineer should improve Component 4 from State 0 to State 1 first to get the largest improvement in system performance. According to the order of the component IIM, after the state of Component 4 is improved from State 0 to State 1, Component 2 should be improved from State 0 to State 1. When Components 2 and 4 are in State 1, Component 4 should be improved from State 1 to State 2 to get the largest improvement in the system performance. This effect is the reason that we state that the proposed IIM can be used for selective maintenance decision making when the current states of components are known [35].

In summary, the IIM considers the changes (both degradation and improvement) of all component states. The IIM is useful for both the design of systems and for selective maintenance optimization of multi-state systems. Thus, designers and maintenance managers both can take advantage of the information provided by the IIM.

V. CONCLUSIONS

This paper extends the IIM to the semi-Markov processes, and presents several propositions of the IIM for semi-Markov processes in the typical series and parallel structures. Some of these propositions give the condition that one component state is more important than another. The results are useful for designers and maintenance managers to identify which compo-

nent state generates more improvement considering transition rates and state probabilities. However, the component states of all systems that this paper studies are statistically independent from each other. The analysis of the IIM of the system when the components are statistically dependent is outside the scope of this paper, and it is one of our future research directions.

APPENDIX

Proof of Proposition 1:

Proof: 1) Similarly to Si *et al.* [23], we can get the IIM of component i in the series system under the semi-Markov model as shown in the equation at the bottom of the page. Immediately, we have

$$\begin{aligned} IIM^i_{m,m-1}(t,y) &= P^i_m(t)\cdot b^i_{m(m-1)}(y)\cdot(a_m-a_{m-1}) \\ &\quad\times\prod_{k=1,k\neq i}^{n}(1-\rho^k_m(t)), \\ IIM^i_{m,m+1}(t,y) &= -P^i_m(t)\cdot b^i_{m(m+1)}(y)\cdot(a_{m+1}-a_m) \\ &\quad\times\prod_{k=1,k\neq i}^{n}(1-\rho^k_{m+1}(t)). \end{aligned}$$

The behavior of component i can be defined by a semi-Markov process; then $P^k_l(t) > 0 (t > 0, l \in \{0,1,\ldots,M_k\})$, that is $0 < p^k_l(t) < 1$. Then,

$$\begin{aligned} &|IIM^i_{m,m-1}(t,y)| \geq |IIM^j_{m,m-1}(t,y)| \\ &\Leftrightarrow \left|P^i_m(t)\cdot b^i_{m(m-1)}(y)\cdot(a_m-a_{m-1})\prod_{k=1,k\neq i}^{n}(1-\rho^k_m(t))\right| \\ &\geq \left|P^j_m(t)\cdot b^j_{m(m-1)}(y)\cdot(a_m-a_{m-1})\prod_{k=1,k\neq j}^{n}(1-\rho^k_m(t))\right| \\ &\Leftrightarrow \left|\frac{P^i_m(t)\cdot b^i_{m(m-1)}(y)\cdot(a_m-a_{m-1})\prod_{k=1}^{n}(1-\rho^k_m(t))}{(1-\rho^i_m(t))}\right| \\ &\geq \left|\frac{P^j_m(t)\cdot b^j_{m(m-1)}(y)\cdot(a_m-a_{m-1})\prod_{k=1}^{n}(1-\rho^k_m(t))}{(1-\rho^j_m(t))}\right| \\ &\Leftrightarrow \frac{P^i_m(t)\cdot b^i_{m(m-1)}(y)}{(1-\rho^i_m(t))} \geq \frac{P^j_m(t)\cdot b^j_{m(m-1)}(y)}{(1-\rho^j_m(t))}. \end{aligned}$$

When $M_i < M_j$, and $m = M_i$, $P^i_{M_i}(t)\cdot b^i_{M_i(M_i-1)}(y)/(1-\rho^i_{M_i}(t)) = P^i_{M_i}(t)\cdot b^i_{M_i(M_i-1)}(y)/P^i_{M_i}(t) = b^i_{M_i(M_i-1)}(y)$. Then $|IIM^i_{M_i(M_i-1)}(t,y)| \geq |IIM^j_{M_i(M_i-1)}(t,y)| \Leftrightarrow b^i_{M_i(M_i-1)}(y) \geq P^j_{M_i}(t)\cdot b^j_{M_i(M_i-1)}(y)/(1-\rho^j_{M_i}(t))$. When $M_i = M_j$, we get $|IIM^i_{M_i(M_i-1)}(t,y)| \geq |IIM^j_{M_i(M_i-1)}(t,y)| \Leftrightarrow b^i_{M_i(M_i-1)}(y) \geq b^j_{M_j(M_j-1)}(y)$.

2) This case is similar to that of part 1). □

Proof of Proposition 2:

Proof: 1) According to the proof of Proposition 1, we have shown that

$$\begin{aligned} &\frac{|IIM^i_{m,m-1}(t,y)| \geq |IIM^j_{m,m-1}(t,y)| \Leftrightarrow P^i_m(t)\cdot b^i_{m(m-1)}(y)}{(1-\rho^i_m(t))} \\ &\geq \frac{P^j_m(t)\cdot b^j_{m(m-1)}(y)}{(1-\rho^j_m(t))}. \end{aligned}$$

Based on (9) and (10), when $t \to \infty$, $P^i_m(t)\cdot b^i_{m(m-1)}(y)/(1-\rho^i_m(t)) = b^i_{m(m-1)}(y)\pi^i_m w^i(m) \Big/ \sum_{k=m}^{M_i}(\pi^i_k w^i(k))$.

We have $w^i(m) = \int_0^\infty [1-\sum_{s=0}^{M_i} Q^i_{ms}(t)]dt = -\sum_{s=0}^{M_i}\hat{Q}'^i_{ms}(0)$, where $\hat{Q}'^i_{ms}(s)$ is obtained by a Laplace transform of the function $\hat{Q}^i_{ms}(t)$. So $P^i_m(t)\cdot b^i_{m(m-1)}(y)/(1-\rho^i_m(t)) = b^i_{m(m-1)}(y)\pi^i_m \sum_{s=0}^{M_i}\hat{Q}'^i_{ms}(0) \Big/ \sum_{k=m}^{M_i}\left(\pi^i_k \sum_{s=0}^{M_i}\hat{Q}'^i_{ks}(0)\right)$.

Then

$$\begin{aligned} &|IIM^i_{m,m-1}(t,y)| \geq |IIM^j_{m,m-1}(t,y)| \\ &\Leftrightarrow \frac{b^i_{m(m-1)}(y)\pi^i_m \sum_{s=0}^{M_i}\hat{Q}'^i_{ms}(0)}{\sum_{k=m}^{M_i}\left(\pi^i_k \sum_{s=0}^{M_i}\hat{Q}'^i_{ks}(0)\right)} \\ &\geq \frac{b^i_{m(m-1)}(y)\pi^j_m \sum_{s=0}^{M_j}\hat{Q}'^j_{ms}(0)}{\sum_{k=m}^{M_j}\left(\pi^j_k \sum_{s=0}^{M_j}\hat{Q}'^j_{ks}(0)\right)}, \end{aligned}$$

where $m \in \{1,\ldots,\min(M_i,M_j)\}$.

2) This case is similar to that of part 1). □

Proof of Proposition 3:

Proof: This proof follows similar to Proposition 1.

Proof of Proposition 4:

Proof: This proof follows similar to Proposition 2.

Proof of Corollary 1:

Proof: Based on Proposition 1 and Proposition 3,

$$IIM^i_{m,l}(t,y) = \begin{cases} P^i_m(t)\cdot b^i_{ml}(y)\sum_{j=l+1}^{m}(a_j-a_{j-1})\prod_{k=1,k\neq i}^{n}(1-\rho^k_j(t)), & m > l \\ -P^i_m(t)\cdot b^i_{ml}(y)\sum_{j=m+1}^{l}(a_j-a_{j-1})\prod_{k=1,k\neq i}^{n}(1-\rho^k_j(t)), & m < l \end{cases}$$

1) for the same state m of components i and j in a series system, when $m \in \{1, \ldots, \min(M_i, M_j)\}$, we can get

$$\frac{|IIM^i_{m,m-1}(t,y)| \geq |IIM^j_{m,m-1}(t,y)| \Leftrightarrow P^i_m(t) \cdot b^i_{m(m-1)}(y)}{(1-\rho^i_m(t))}$$
$$\geq \frac{P^j_m(t) \cdot b^j_{m(m-1)}(y)}{(1-\rho^j_m(t))}$$
$$\Leftrightarrow P^i_m(t) \cdot b^i_{m(m-1)}(y) - P^i_m(t) \cdot b^i_{m(m-1)}(y) \cdot \rho^j_m(t)$$
$$\geq \rho^j_m(t) \geq P^j_m(t) \cdot b^j_{m(m-1)}(y) - P^j_m(t) \cdot b^j_{m(m-1)}(y).\rho^i_m(t)$$
$$\Leftrightarrow P^j_m(t) \cdot b^j_{m(m-1)}(y).\rho^i_m(t) \geq P^i_m(t) \cdot b^i_{m(m-1)}(y) \cdot \rho^j_m(t)$$
$$+ (P^j_m(t) \cdot b^j_{m(m-1)}(y) - P^i_m(t) \cdot b^i_{m(m-1)}(y)).$$

If $P^j_m(t) \cdot b^j_{m(m-1)}(y) - P^i_m(t) \cdot b^i_{m(m-1)}(y) \geq 0$, then

$$P^j_m(t) \cdot b^j_{m(m-1)}(y).\rho^i_m(t) \geq P^i_m(t) \cdot b^i_{m(m-1)}(y) \cdot \rho^j_m(t)$$
$$\Leftrightarrow \frac{b^j_{m(m-1)}(y)}{\rho^j_m(t)} \geq \frac{P^i_m(t) \cdot b^i_{m(m-1)}(y)}{\rho^i_m(t)}.$$

Thus, for state m of the two same type of components i and j in a parallel system, we get $|IIM^j_{m,m-1}(t)| \geq |IIM^i_{m,m-1}(t)|$.

Conversely, for state m of the two same type of components i and j in a series system, we get $|IIM^j_{m,m-1}(t)| \geq |IIM^i_{m,m-1}(t)|$.

2) This case is similar to part 1). □

Proof of Corollary 2:

Proof: 1) From Proposition 2 and Proposition 4, for the same state m of components i and j in a series system, when $m \in \{1, \ldots, \min(M_i, M_j)\}$, we have

$$|IIM^i_{m,m-1}(t)| \geq |IIM^j_{m,m-1}(t)|$$
$$\Leftrightarrow \frac{b^i_{m(m-1)}(y)\pi^i_m \sum_{s=0}^{M_i} \hat{Q}'^i_{ms}(0)}{\sum_{k=m}^{M_i} \left(\pi^i_k \sum_{s=0}^{M_i} \hat{Q}'^i_{ks}(0)\right)}$$
$$\geq \frac{b^j_{m(m-1)}(y)\pi^j_m \sum_{s=0}^{M_j} \hat{Q}'^j_{ms}(0)}{\sum_{k=m}^{M_j} \left(\pi^j_k \sum_{s=0}^{M_j} \hat{Q}'^j_{ks}(0)\right)}$$
$$\Leftrightarrow \pi^i_m \sum_{s=0}^{M_i} \hat{Q}'^i_{ms}(0) \cdot b^i_{m(m-1)}(y) \cdot \sum_{k=m}^{M_j} \left(\pi^j_k \sum_{s=0}^{M_j} \hat{Q}'^j_{ks}(0)\right)$$
$$\geq \pi^j_m \sum_{s=0}^{M_j} \hat{Q}'^j_{ms}(0) b^j_{m(m-1)}(y) \sum_{k=m}^{M_i} \left(\pi^i_k \sum_{s=0}^{M_i} \hat{Q}'^i_{ks}(0)\right)$$
$$\Leftrightarrow \pi^i_m \sum_{s=0}^{M_i} \hat{Q}'^i_{ms}(0) \cdot b^i_{m(m-1)}(y) \cdot \left(\sum_{k=0}^{M_j} \left(\pi^j_k \sum_{s=0}^{M_j} \hat{Q}'^j_{ks}(0)\right)\right.$$
$$\left. - \sum_{k=0}^{m-1} \left(\pi^j_k \sum_{s=0}^{M_j} \hat{Q}'^j_{ks}(0)\right)\right) \geq$$
$$\pi^j_m \sum_{s=0}^{M_j} \hat{Q}'^j_{ms}(0) \cdot b^j_{m(m-1)}(y) \cdot \left(\sum_{k=0}^{M_i} \left(\pi^i_k \sum_{s=0}^{M_i} \hat{Q}'^i_{ks}(0)\right)\right.$$
$$\left. - \sum_{k=0}^{m-1} \left(\pi^i_k \sum_{s=0}^{M_i} \hat{Q}'^i_{ks}(0)\right)\right)$$
$$\Leftrightarrow \pi^j_m \sum_{s=0}^{M_j} \hat{Q}'^j_{ms}(0) \cdot b^j_{m(m-1)}(y) \cdot \sum_{k=0}^{m-1} \left(\pi^i_k \sum_{s=0}^{M_i} \hat{Q}'^i_{ks}(0)\right)$$
$$\geq \pi^i_m \sum_{s=0}^{M_i} \hat{Q}'^i_{ms}(0) \cdot b^i_{m(m-1)}(y) \cdot \sum_{k=0}^{m-1} \left(\pi^j_k \sum_{s=0}^{M_j} \hat{Q}'^j_{ks}(0)\right) +$$
$$\pi^j_m \sum_{s=0}^{M_j} \hat{Q}'^j_{ms}(0) \cdot b^j_{m(m-1)}(y) \cdot \sum_{k=0}^{M_i} \left(\pi^i_k \sum_{s=0}^{M_i} \hat{Q}'^i_{ks}(0)\right)$$
$$- \pi^i_m \sum_{s=0}^{M_i} \hat{Q}'^i_{ms}(0) \cdot b^i_{m(m-1)}(y) \cdot \sum_{k=0}^{M_j} \left(\pi^j_k \sum_{s=0}^{M_j} \hat{Q}'^j_{ks}(0)\right).$$

If $\pi^j_m \sum_{s=0}^{M_j} \hat{Q}'^j_{ms}(0) \cdot b^j_{m(m-1)}(y) \cdot \sum_{k=0}^{M_i} \left(\pi^i_k \sum_{s=0}^{M_i} \hat{Q}'^i_{ks}(0)\right) \geq \pi^i_m \sum_{s=0}^{M_i} \hat{Q}'^i_{ms}(0) \cdot b^i_{m(m-1)}(y) \cdot \sum_{k=0}^{M_j} \left(\pi^j_k \sum_{s=0}^{M_j} \hat{Q}'^j_{ks}(0)\right)$, then

$$\pi^j_m \sum_{s=0}^{M_j} \hat{Q}'^j_{ms}(0) \cdot b^j_{m(m-1)}(y) \cdot \sum_{k=0}^{m-1} \left(\pi^i_k \sum_{s=0}^{M_i} \hat{Q}'^i_{ks}(0)\right)$$
$$\geq \pi^i_m \sum_{s=0}^{M_i} \hat{Q}'^i_{ms}(0) \cdot b^i_{m(m-1)}(y) \cdot \sum_{k=0}^{m-1} \left(\pi^j_k \sum_{s=0}^{M_j} \hat{Q}'^j_{ks}(0)\right)$$
$$\Leftrightarrow \frac{\pi^j_m \sum_{s=0}^{M_j} \hat{Q}'^j_{ms}(0)}{\sum_{k=0}^{m-1} \left(\pi^j_k \sum_{s=0}^{M_j} \hat{Q}'^j_{ks}(0)\right)} b^j_{m(m-1)}(y)$$
$$\geq \frac{\pi^i_m \sum_{s=0}^{M_i} \hat{Q}'^i_{ms}(0)}{\sum_{k=0}^{m-1} \left(\pi^i_k \sum_{s=0}^{M_i} \hat{Q}'^i_{ks}(0)\right)} b^i_{m(m-1)}(y).$$

Thus, for state m of the two same type of components i and j in a parallel system, we can get $|IIM^j_{m,m-1}(t)| \geq |IIM^i_{m,m-1}(t)|$.

Conversely, for state m of the two same type of components i and j in a series system, we get $|IIM^j_{m,m-1}(t)| \geq |IIM^i_{m,m-1}(t)|$.

2) This case is similar to part 1). □

ACKNOWLEDGMENT

Comments from the reviewers and the Editor are very much appreciated.

REFERENCES

[1] Z. W. Birnbaum, "On the importance of different components in a multi-component system," in *Multivariate Analysis II*. New York, NY, USA: Academic Press, 1969, pp. 581–592.

[2] M. J. Zuo and M. Liang, "Reliability of multistate consecutively-connected systems," *Rel. Eng. Syst. Saf.*, vol. 44, no. 2, pp. 173–176, 1994.

[3] A. Lisnianski and G. Levitin, *Multi-State System Reliability: Assessment, Optimization and Applications*. New York, NY, USA: World Scientific, 2003.

[4] G. Levitin, *The Universal Generating Function in Reliability Analysis and Optimization*. London, U.K.: Springer-Verlag, 2005.

[5] E. El-Neweihi, F. Proschan, and J. Sethuraman, "Multistate coherent systems," *J. Appl. Probab.*, vol. 15, no. 4, pp. 675–688, 1978.

[6] W. S. Griffith, "Multi-state reliability models," *J. Appl. Probab.*, vol. 17, no. 3, pp. 735–744, 1980.

[7] S. Wu and L. Chan, "Performance utility-analysis of multi-state systems," *IEEE Trans. Rel.*, vol. 52, no. 1, pp. 14–21, 2003.

[8] G. Levitin and L. Xing, "Reliability and performance of multi-state systems with propagated failures having selective effect," *Rel. Eng. Syst. Saf.*, vol. 95, no. 6, pp. 655–661, 2010.

[9] G. Levitin, L. Xing, H. Ben-Haim, and Y. Dai, "Multi-state systems with selective propagated failures and imperfect individual and group protections," *Rel. Eng. Syst. Saf.*, vol. 96, no. 12, pp. 1657–1666, 2011.
[10] G. Levitin, L. Podofillini, and E. Zio, "Generalized importance measures for multi-state elements based on performance level restrictions," *Rel. Eng. Syst. Saf.*, vol. 82, no. 3, pp. 287–298, 2003.
[11] E. Zio and L. Podofillini, "Monte-Carlo simulation analysis of the effects on different system performance levels on the importance on multi-state components," *Rel. Eng. Syst. Saf.*, vol. 82, no. 1, pp. 63–73, 2003.
[12] B. Natvig and J. Gåsemyr, "New results on the Barlow-Proschan and Natvig measures of component importance in nonrepairable and repairable systems," *Methodol. Comput. Appl. Probab.*, vol. 11, no. 4, pp. 603–620, 2009.
[13] B. Natvig, K. A. Eide, J. Gåsemyr, A. B. Huseby, and S. L. Isaksen, "Simulation based analysis and an application to an offshore oil and gas production system of the Natvig measures of component importance in repairable systems," *Rel. Eng. Syst. Saf.*, vol. 94, no. 10, pp. 1629–1638, 2009.
[14] B. Natvig, A. B. Huseby, and M. O. Reistadbakk, "Measures of component importance in repairable multistate systems—a numerical study," *Rel. Eng. Syst. Saf.*, vol. 96, no. 12, pp. 1680–1690, 2011.
[15] B. Natvig, *Multistate Systems Reliability Theory with Applications*. London, U.K.: Wiley, 2011.
[16] W. Kuo and X. Zhu, *Importance Measures in Reliability, Risk, and Optimization: Principles and Applications*. London, U.K.: Wiley, 2012.
[17] W. Kuo and X. Zhu, "Some recent advances on importance measures in reliability," *IEEE Trans. Rel.*, vol. 61, no. 2, pp. 344–360, 2012.
[18] W. Kuo and X. Zhu, "Relations and generalizations of importance measures in reliability," *IEEE Trans. Rel.*, vol. 61, no. 3, pp. 659–674, 2012.
[19] G. Levitin, "A universal generating function approach for the analysis of multi-state systems with dependent elements," *Rel. Eng. Syst. Saf.*, vol. 84, no. 3, pp. 285–292, 2004.
[20] G. Levitin and A. Lisnianski, "Importance and sensitivity analysis of multi-state systems using the universal generating function," *Rel. Eng. Syst. Saf.*, vol. 65, no. 3, pp. 271–282, 1999.
[21] E. Zio, L. Podofillini, and G. Levitin, "Estimation of the importance measures of multi-state elements by Monte Carlo simulation," *Rel. Eng. Syst. Saf.*, vol. 86, no. 3, pp. 191–204, 2004.
[22] J. E. Ramirez-Marquez and D. W. Coit, "A Monte-Carlo simulation approach for approximating multi-state two-terminal reliability," *Rel. Eng. Syst. Saf.*, vol. 87, no. 2, pp. 253–264, 2005.
[23] O. Chryssaphinou, N. Limnios, and S. Malefaki, "Multi-state reliability systems under discrete time semi-Markovian hypothesis," *IEEE Trans. Rel.*, vol. 60, no. 1, pp. 80–87, 2011.
[24] S. Chadjiconstantinidis and M. V. Koutras, "Measures of component importance for Markov chain imbeddable reliability structures," *Naval Res. Logist.*, vol. 46, no. 6, pp. 613–639, 1999.
[25] P. Do Van, A. Barros, and C. Berenguer, "Reliability importance analysis of Markovian systems at steady state using perturbation analysis," *Rel. Eng. Syst. Saf.*, vol. 93, no. 11, pp. 1605–1615, 2008.
[26] P. Do Van, A. Barros, and C. Berenguer, "From differential to difference importance measures for markov reliability models," *Eur. J. Oper. Res.*, vol. 204, no. 3, pp. 513–521, 2010.
[27] S. Si, H. Dui, X. Zhao, S. Zhang, and S. Sun, "Integrated importance measure of component states based on loss of system performance," *IEEE Trans. Rel.*, vol. 61, no. 1, pp. 192–202, 2012.
[28] S. Si, Z. Cai, S. Sun, and S. Zhang, "Integrated importance measures of multi-state systems under uncertainty," *Comput. Ind. Eng.*, vol. 59, no. 4, pp. 921–928, 2010.
[29] S. Si, H. Dui, Z. Cai, and S. Sun, "The integrated importance measure of multi-state coherent systems for maintenance processes," *IEEE Trans. Rel.*, vol. 61, no. 2, pp. 266–273, 2012.
[30] S. Si, G. Levitin, H. Dui, and S. Sun, "Component state-based integrated importance measure for multi-state systems," *Rel. Eng. Syst. Saf.*, vol. 116, pp. 75–83, 2013.
[31] C. Huber and O. Pons, "Independent competing risks versus a general semi-Markov model," *Far East J. Theoret. Statist.*, vol. 16, no. 1, pp. 87–104, 2005.
[32] A. Lisnianski, "Extended block diagram method for a multi-state system reliability assessment," *Rel. Eng. Syst. Saf.*, vol. 92, no. 12, pp. 1601–1607, 2007.
[33] G. D'Amico, J. Janssen, and R. Manca, "Homogeneous semi-markov reliability models for credit risk management," *Decisions Econ. Finance*, vol. 28, no. 2, pp. 79–93, 2005.
[34] N. Limnios and G. Oprisan, *Semi-Markov Processes and Reliability*. Boston, MA, USA: Birkhauser Boston, 2001.
[35] M. Pandey, M. J. Zuo, R. Moghaddas, and M. K. Tiwari, "Selective maintenance for binary systems under imperfect repair," *Rel. Eng. Syst. Saf.*, vol. 113, pp. 42–51, 2013.

Hongyan Dui received his PhD (2013) from the School of Mechanical Engineering, Northwestern Polytechnical University, China.

He is currently a lecturer in the School of Management Engineering, Zhengzhou University, Henan, China. His research interests include importance analysis, and system reliability.

Shubin Si received his PhD (2006) from the School of Mechanical Engineering, Northwestern Polytechnical University, China.

He is a professor at the Department of Industrial Engineering, School of Mechanical Engineering, Northwestern Polytechnical University, China. His research interests include system modeling, and importance measures.

Ming J. Zuo received the Master of Science degree in 1986, and the Ph.D. degree in 1989, both in Industrial Engineering from Iowa State University, Ames, IA, USA.

He is affiliated with the University of Electronic Science and Technology of China, and the Department of Mechanical Engineering at the University of Alberta, Canada. His research interests include system reliability analysis, maintenance planning and optimization, signal processing, and fault diagnosis.

Dr. Zuo is a Department Editor of *IIE Transactions*. He is an Associate Editor of the IEEE TRANSACTIONS ON RELIABILITY. He is a senior member of IEEE, and a Fellow of IIE.

Shudong Sun received his PhD (1989) from the School of Mechanical Engineering, Nanjing University of Aeronautical and Astronautical, China.

He is a professor of the Department of Industrial Engineering, School of Mechanical Engineering, Northwestern Polytechnical University, China. His research interests include production planning, maintenance management, and robotics.

Available online at www.sciencedirect.com
ScienceDirect
Comput. Methods Appl. Mech. Engrg. 289 (2015) 387–408
Computer methods in applied mechanics and engineering
www.elsevier.com/locate/cma

An improved adaptive constraint aggregation for integrated layout and topology optimization

Gao Huan-Huan, Zhu Ji-Hong*, Zhang Wei-Hong, Zhou Ying

Engineering Simulation & Aerospace Computing (ESAC), Northwestern Polytechnical University, Xi'an, Shaanxi 710072, China

Received 7 August 2014; received in revised form 14 February 2015; accepted 17 February 2015
Available online 24 February 2015

Highlights

- We present an improved adaptive constraint aggregation approach based on the KS function.
- Steffensen iteration is used to obtain better aggregation parameters.
- The improved approach is applied with the finite circle method to avoid the components' overlap in integrated layout and topology optimization design.
- Multi-point constraints (MPC) are applied to establish the interconnections between movable components and supporting structures.
- The improved approach can handle the constraint aggregation and the integrated optimization well.

Abstract

The purpose of this paper is to present a Kreisselmeier–Steinhauser (KS) function based adaptive constraint aggregation approach. It is implemented within the integrated layout and topology optimization of multi-component structure systems to avoid using large numbers of non-overlapping constraints defined by means of the previously proposed finite circle method (FCM). An improved adaptive approach is then put forward to obtain proper aggregation parameters for the KS function based constraint aggregation, contributing to less numerical difficulties while meeting the same aggregation precision compared with the existing adaptive approach. Furthermore, the complex step derivative approximation is utilized to yield better sensitivities for the aggregated constraint functions with high nonlinearity. Moreover, during the integrated layout and topology optimization, multi-point constraints (MPC) are applied to establish the interconnections between movable components and supporting structures, which can use fixed finite element meshes and analytical sensitivities. Finally, some numerical examples are tested to demonstrate the validity and effectiveness of the proposed formulation.

© 2015 Elsevier B.V. All rights reserved.

Keywords: Multi-component systems; Topology optimization; Constraint aggregation; KS function; Multi-point constraints; Complex step derivative approximation

* Corresponding author.
E-mail address: jh.zhu@nwpu.edu.cn (J.-H. Zhu).

http://dx.doi.org/10.1016/j.cma.2015.02.022
0045-7825/© 2015 Elsevier B.V. All rights reserved.

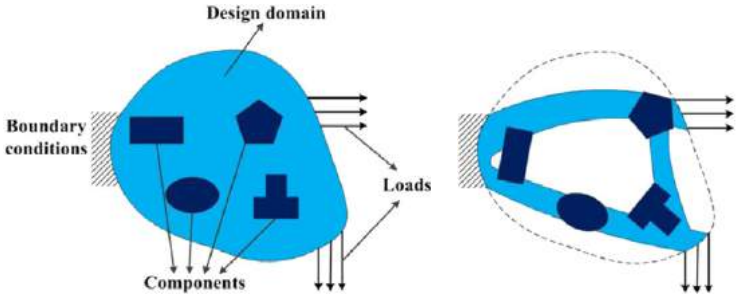

(a) Problem definition. (b) Optimized design.

Fig. 1. Illustration of integrated layout and topology optimization of multi-component systems.

1. Introduction

Topology optimization has been recognized as an effective approach to figure out the structure layout during the conceptual design phase since the homogenization based method was firstly proposed [1]. Different schemes including pseudo-density based methods, evolutionary methods and level-set methods were successively established [2–5]. Up until now, the idea of topology optimization has received much success in both theoretical study and practical applications [6–11], where optimization designs of multi-component structure systems were among the most challenging efforts. For example, in the early works [12], separated structural parts were considered as numbers of components designated as different design domains. A simultaneous design approach was developed to optimize the structural patterns of several components and locations of interconnections using density based topology optimization method. Similar implementations were also noted in some other previous works [13,14].

Another case of multi-component structure system commonly exists in the design of aeronautics and astronautics systems, where many functional components are assembled in some finite domains with supporting structures. Take a multi-satellite structure system design for example. The satellites' locations and the corresponding supporting structures are the critical determinants of structural mechanical performances. The idea was to carry out the topology optimization with movable solid or void components to obtain proper layout of components and structures simultaneously, which was mentioned as the integrated layout and topology optimization [15,16] as illustrated in Fig. 1.

During the optimization procedure, it is essentially important to avoid the geometry overlapping of different components, or components and design domain boundaries. Varieties of component shapes and design domain boundaries will lead to high nonlinearity and even discontinuity of the non-overlapping constraint functions. To solve this problem, different CAD modeling techniques such as octrees [17,18], sphere trees [19] and S-bounds based trees [20] have been proposed to detect the object collisions. These techniques approximated the components with various levels of small cubes or spheres and refined the model partition iteratively. However, they were confined to detect rather than evaluate the overlap. As a result, more necessary information could not be provided to find the searching directions and verify the attainment of optimum.

Later, the finite circle method (FCM) [21,22] and level-set based non-overlapping constraints [23,24] were therefore proposed to obtain the sensitivities of the collision. In FCM, contours of the components were approximately described using enormous numbers of circles. Feasible designs could be attained by controlling the distances between the circles. This method could provide effective sensitivity information to avoid the overlap in any case and had a rather simple analytical expression. In the level-set based method, the overlapping area of two components was calculated by the integral operation and constrained to zero, guaranteeing the two components would not overlap.

FCM proved effective in integrated layout and topology optimization but suffered from the tremendous numbers of constraints and considerable computing time due to the circles used for geometry approximation. As a result, it was necessary to use different constraint aggregation strategies, e.g. P-norm function and KS function, which have been popularly used for stress constraint problems [25–28] to improve the optimization efficiency. An essential issue of applying these functions was how to choose proper aggregation parameters. Constant aggregation parameters may not meet the demand for good aggregation performance in different iterations. Therefore, an adaptive approach was made to obtain proper aggregation parameters [29,30]. In these works, the first derivative of KS function w.r.t. the aggregation parameter was used as the aggregation performance index. By setting a lesser threshold for the first derivative, the

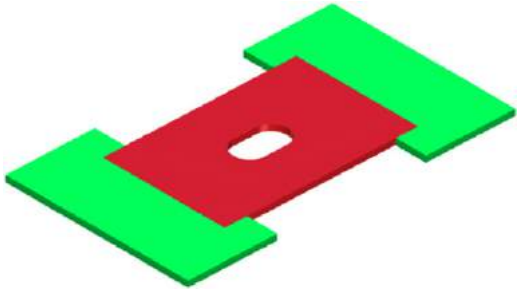

Fig. 2. Illustration of the embedded component.

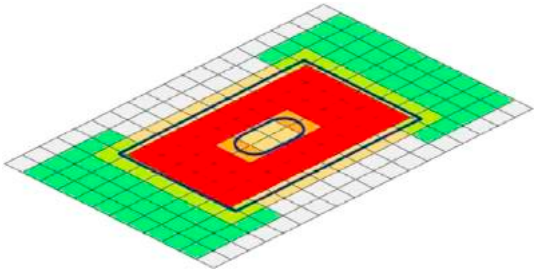

Fig. 3. Component's geometric and material description.

aggregation parameter was adaptively estimated for current design points according to an assumed linear relationship between KS function's first derivative and its aggregation parameter in logarithmic scale. This adaptive approach established a valid practical standard for choosing the aggregation parameter, and showed a certain degree of flexibility in the optimization process.

Note that the above adaptive approach was based on an assumed estimation and thus may introduce methodological errors during calculation of the aggregation parameter. In this paper, an improved adaptive approach is presented to eliminate these methodological errors, ameliorating the optimization process of the integrated layout and topology optimization for the purposes of both constraint aggregation and computational time savings. The aggregation parameter was determined by utilizing Steffensen iteration method alternatively with two prescribed thresholds of KS function's first derivative, which showed a fast convergence and high efficiency. Furthermore, due to the high nonlinearity and complexity of the aggregated constraint function, the calculation of analytical sensitivities will become extremely complicated both in expression of formulation and in programming. Meanwhile, the finite difference scheme usually leads to inaccurate output. As a result, we choose to use complex step derivative approximation [31,32] to enhance the precision.

Another key issue in integrated layout and topology optimization is the description of the interface between the components and supporting structures. Presently, most of the pioneering efforts used components which were embedded in the design domain, as shown in Fig. 2. To describe the geometries and material properties of the moving components during optimization, different finite element modeling methods have been proposed. For example, exponential functions, level-set functions and R-functions were introduced to describe the components' geometries [15,23,24,33,34]. Material properties of the elements on the interface were then approximated with stiffness interpolation schemes displayed in Fig. 3(b) or X-FEM. Those interpolation schemes used fixed mesh and analytical sensitivities, and usually lead to high optimization efficiency. Alternatively, precise material distributions of the components and detailed finite element meshes were also used as a different strategy [16,35–38]. Layout design of components was treated as the extension of packing optimization problems. Techniques of embedded meshing and density point illustrated in Fig. 4(a) and (b) respectively were adopted to update the pseudo-density variables and implement the components' movements.

In this paper, we consider another situation where components are assembled onto the surfaces of a structure by rivets or bolts with designated positions in advance [39] as illustrated in Fig. 5(a) and (b), where multi-point constraints (MPC) are used to simulate the point connections. Series of displacement constraint equations are introduced to

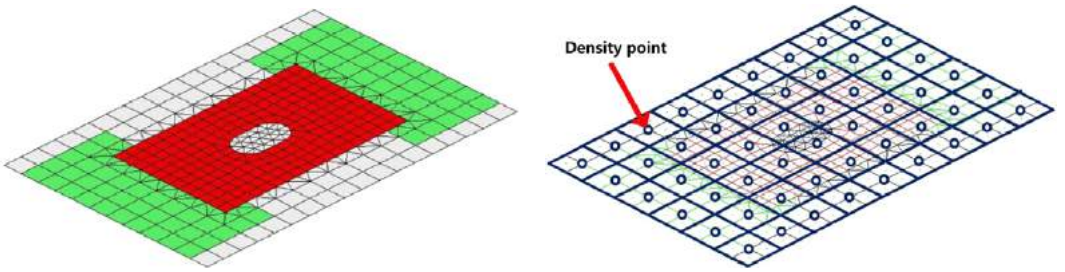

(a) Embedded meshing. (b) Definition of density points.

Fig. 4. Techniques of embedded meshing and density point.

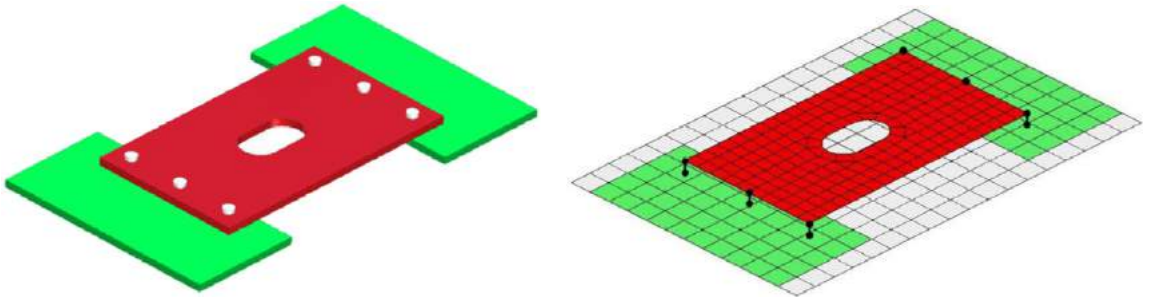

(a) Components assembled onto the structure. (b) Finite element model with MPC.

Fig. 5. Illustration of practical connections and MPC.

maintain the displacement consistence of both components and supporting structures at the connection positions. Thus fixed mesh and analytical sensitivities can be also used without any interpolation scheme during the implementation of integrated design.

As a consequence, the contributions of this paper are to propose the improved adaptive aggregation approach and to use the MPC based modeling scheme in the integrated layout and topology optimization. To test the effect of the new design methods, two different structure system design problems will be optimized considering both external mechanical loads and design dependent self-weight.

2. Basic formulations of integrated optimization

2.1. KS function based non-overlapping constraint aggregation

In numbers of preceding works, FCM was effectively used to avoid components overlapping. As illustrated in Fig. 6, a series of circles were used to describe the contours of components and the design domain roughly. The overlapping can thus be analytically evaluated by distances of these circles according to their center coordinates and radii.

$$g_m = \left(r_{c1}^{(i)} + r_{c2}^{(j)}\right)^2 - \left[\left(x_{c1}^{(i)} - x_{c2}^{(j)}\right)^2 + \left(y_{c1}^{(i)} - y_{c2}^{(j)}\right)^2\right] \le 0, \quad c1 \ne c2 \tag{1}$$

where $r_{c1}^{(i)}$, $x_{c1}^{(i)}$ and $y_{c1}^{(i)}$ denote the radius and center coordinate of the ith circle for component $c1$. Similar definitions are used for $r_{c2}^{(j)}$, $x_{c2}^{(j)}$ and $y_{c2}^{(j)}$. g_m stands for the mth constraint function.

FCM holds the advantages of simple explicit expression which can be easily differentiated to yield sensitivities for gradient-based optimizations. Moreover, FCM can be easily extended to deal with 3D overlapping problems by using spheres instead of circles.

In fact, precise description of components' geometries needs more circles which will lead to large numbers of overlapping constraints and costly computing time when the packing optimization problem is solved iteratively. It is

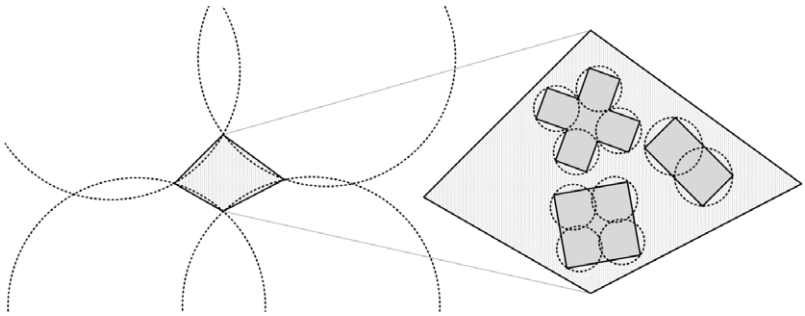

Fig. 6. Overlapping constraints defined by FCM.

therefore crucial to use fewer circles [22] on the one hand while maintaining the approximation precision. Some constraint aggregation approaches such as KS function, etc. are applicable. The standard form of KS function is expressed as

$$KS(\mu) = \frac{1}{\mu} \ln \sum_{m=1}^{N_g} \exp(\mu g_m) \tag{2}$$

where N_g stands for the number of constraints. μ is the aggregation parameter. Generally, the constraints should be normalized into the same scale, which will be much helpful for the constraint aggregation, especially when the constraints are in different magnitudes.

Normally, an equivalent form is used to avoid some numerical difficulties.

$$KS(\mu) = g_{\max} + \frac{1}{\mu} \ln \sum_{m=1}^{N_g} \exp[\mu (g_m - g_{m\max})] \tag{3}$$

where $g_{\max}$ stands for the maximum value of all the constraints. We also have

$$\begin{aligned} &g_{\max} < KS(\mu) < g_{\max} + \frac{1}{\mu} \ln(N_g) \\ &\lim_{\mu \to +\infty} KS(\mu) = g_{\max}. \end{aligned} \tag{4}$$

A two-variable testing example with six constraints will show how the feasible region changes when the aggregation parameter varies. The six constraints form one single non-convex feasible region as shown in Fig. 7.

$$\begin{aligned} g_1 &= 1 - x_1 \le 0 \\ g_2 &= x_1 - 5 \le 0 \\ g_3 &= 2 - x_2 \le 0 \\ g_4 &= x_2 - 4 \le 0 \\ g_5 &= 0.25 - \left[(x_1 - 3)^2 + (x_2 - 2.3)^2\right] \le 0 \\ g_6 &= 0.25 - \left[(x_1 - 3)^2 + (x_2 - 3.7)^2\right] \le 0. \end{aligned} \tag{5}$$

Those six constraints are then aggregated by the KS function using different aggregation parameters. The approximated feasible region will be split into two separate ones with small aggregation parameters, which are not satisfying due to a great loss of the real feasible designs. When the aggregation parameter increases, the two separated feasible regions merge into one as expected. Obviously, choosing larger values for aggregation parameters has the advantages for a precise description of the feasible region.

However, a too large value of the aggregation parameter will lead to an ill-conditioned Hessian matrix of KS function and results in optimization instability when the current design point locates very close to, or right at the points

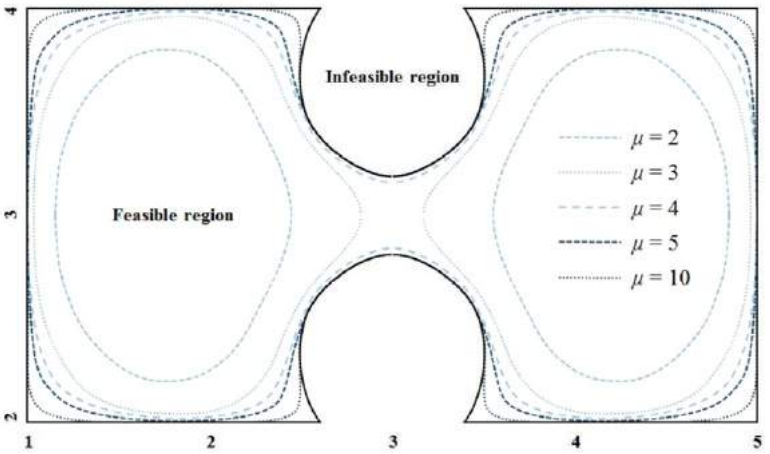

Fig. 7. Illustration of KS function based constraint aggregation.

where multiple constraints are active. Practically, μ should be properly defined considering both the precision and stability of optimization.

In the existing adaptive aggregation method [29,30], $|\mathrm{d}KS/\mathrm{d}\mu|$ is chosen as the criterion to determine the proper aggregation parameters adaptively during each iteration.

$$\left|\frac{\mathrm{d}KS}{\mathrm{d}\mu}\right| \leq \varepsilon \tag{6}$$

ε is a prescribed small positive value. By assuming a linear relationship between $|\mathrm{d}KS/\mathrm{d}\mu|$ and μ in logarithmic scale, the derivative of $|\mathrm{d}KS/\mathrm{d}\mu|$ w.r.t. μ was then obtained with a finite difference scheme. The desired value of $\mu = \mu_d$ satisfying Eq. (6) was thus directly obtained by

$$\frac{\log\left|\frac{\mathrm{d}KS}{\mathrm{d}\mu}\Big|_{\mu=\mu_1}\right| - \log\left|\frac{\mathrm{d}KS}{\mathrm{d}\mu}\Big|_{\mu=\mu_0}\right|}{\log\mu_1 - \log\mu_0} = \frac{\log\left|\frac{\mathrm{d}KS}{\mathrm{d}\mu}\Big|_{\mu=\mu_d}\right| - \log\left|\frac{\mathrm{d}KS}{\mathrm{d}\mu}\Big|_{\mu=\mu_0}\right|}{\log\mu_d - \log\mu_0} \tag{7}$$

where μ_0 is set to an initial value of 50, and $\mu_1 = \mu_0 + 10^{-3}$. Note that when $\mu = \mu_d$, $|\mathrm{d}KS/\mathrm{d}\mu|$ is equal to ε.
Here we firstly need to explain the conditions in which Eq. (7) holds. By considering the standard form of the KS function, we have its first derivative

$$\frac{\mathrm{d}KS}{\mathrm{d}\mu} = \frac{\sum_{m=1}^{Ng}(g_m - KS)\exp(\mu g_m)}{\mu\sum_{m=1}^{Ng}\exp(\mu g_m)}. \tag{8}$$

In most cases, the linear relationship between $|\mathrm{d}KS/\mathrm{d}\mu|$ and μ in logarithmic scale cannot be attained. But in some special situations, e.g., when all the constraints' values are equal at current design point, i.e.

$$g_1 = g_2 = \cdots = g_{N_g} = g_{\max}. \tag{9}$$

The aggregation absolute error can be written as

$$KS - g_{\max} = \frac{1}{\mu}\ln N_g. \tag{10}$$

Substituting Eq. (10) into Eq. (8), we have

$$\frac{\mathrm{d}KS}{\mathrm{d}\mu} = -\frac{\ln N_g}{\mu^2}. \tag{11}$$

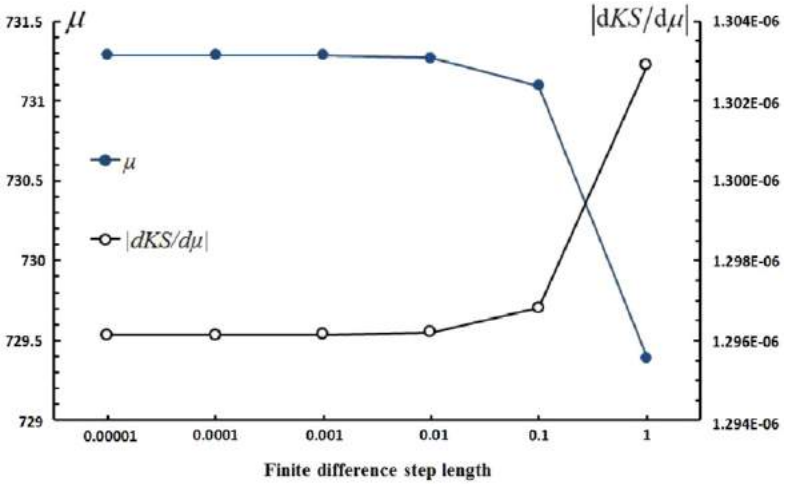

Fig. 8. Aggregation parameters and $|\mathrm{d}KS/\mathrm{d}\mu|$ w.r.t. different step lengths.

Therefore, the linear relationship between $|\mathrm{d}KS/\mathrm{d}\mu|$ and μ in logarithmic scale can be obtained.

$$\log\left|\frac{\mathrm{d}KS}{\mathrm{d}\mu}\right| = \log(\ln N_g) - 2\log\mu. \tag{12}$$

As the linear assumption only exists in few particular cases, thus the adaptive approach may fail in obtaining proper aggregation parameters. Here another simple case with three constraints $(g_1, g_2, g_3) = (-0.07, -0.04, -0.04)$ is tested, where ε is 10^{-6}.

Then the existing adaptive approach proposed is applied to obtain the aggregation parameters and calculate $|\mathrm{d}KS/\mathrm{d}\mu|$ w.r.t. different finite difference step lengths as shown in Fig. 8. It is found that all the values of $|\mathrm{d}KS/\mathrm{d}\mu|$ are larger than the prescribed ε, which indicates the procedure failed to obtain the expected aggregation parameters. Moreover, this situation cannot be enhanced by changing the finite difference step lengths.

To solve the problem, here we improve the adaptive approach based on the Steffensen iteration. Firstly we have

$$\frac{\mathrm{d}^2KS}{\mathrm{d}\mu^2} = \frac{2a(a\ln a - \mu b) + \mu^2(ac - b^2)}{\mu^3 a^2} \tag{13}$$

where

$$\begin{aligned} a &= \sum_{m=1}^{N_g} \exp(\mu g_m); \\ b &= \sum_{m=1}^{N_g} g_m \exp(\mu g_m); \\ c &= \sum_{m=1}^{N_g} g_m^2 \exp(\mu g_m). \end{aligned} \tag{14}$$

It is easy to obtain

$$\begin{aligned} &a > 0; \\ &a\ln a - \mu b = a\mu KS - \mu b = \mu \sum_{m=1}^{N_g} (KS - g_m)\exp(\mu g_m) > 0; \\ &ac - b^2 = \frac{1}{2}\sum_{m=1}^{N_g}\sum_{n=1}^{N_g}(g_m - g_n)^2 \exp(\mu g_m + \mu g_n) \geq 0, \quad m \neq n. \end{aligned} \tag{15}$$

Consequently, we can prove

$$\frac{\mathrm{d}^2 KS}{\mathrm{d}\mu^2} > 0 \tag{16}$$

and

$$\lim_{\mu \to +\infty} \frac{\mathrm{d}KS}{\mathrm{d}\mu} = 0^{-}. \tag{17}$$

Such that by giving a small positive value ε, there is one and only one positive μ_ε satisfying the following equation

$$|\mathrm{d}KS/\mathrm{d}\mu_\varepsilon| = \varepsilon. \tag{18}$$

So we propose using an iterative adaptive approach to search the aggregation parameter by introducing both upper and lower bounds for $|\mathrm{d}KS/\mathrm{d}\mu|$.

$$\upsilon\varepsilon \le |\mathrm{d}KS/\mathrm{d}\mu| \le \varepsilon, \quad 0 \le \upsilon \le 1. \tag{19}$$

Here we use the equivalent form of KS function

$$\frac{\mathrm{d}KS}{\mathrm{d}\mu} = -\frac{1}{\mu}\left(KS - g_{m\max}\right) + \frac{\sum_{m=1}^{Ng}\left(g_m - g_{m\max}\right)\exp\left[\mu\left(g_m - g_{m\max}\right)\right]}{\mu\sum_{m=1}^{Ng}\exp\left[\mu\left(g_m - g_{m\max}\right)\right]}. \tag{20}$$

Then we assume

$$f = \frac{\sum_{m=1}^{Ng}\mu\left(g_m - g_{m\max}\right)\exp\left[\mu\left(g_m - g_{m\max}\right)\right]}{\sum_{m=1}^{Ng}\exp\left[\mu\left(g_m - g_{m\max}\right)\right]} \tag{21}$$

which leads to

$$\frac{\mathrm{d}KS}{\mathrm{d}\mu} = -\frac{1}{\mu}\left(KS - g_{m\max}\right) + \frac{f}{\mu^2}. \tag{22}$$

We use the Steffensen iteration to obtain the root of the following equation

$$-\frac{1}{\mu}\left(KS - g_{m\max}\right) + \frac{f}{\mu^2} = -\varepsilon. \tag{23}$$

The stable point formula chosen for Steffensen iteration can be reorganized as

$$\mu = \sqrt{\frac{\mu}{\varepsilon}\left(KS - g_{m\max}\right) - \frac{f}{\varepsilon}}. \tag{24}$$

Then the final formula of Steffensen iteration can be expressed as

$$\begin{aligned} \varphi\left(\mu_k\right) &= \sqrt{\frac{\mu_k}{\varepsilon}\left(KS_k - g_{m\max}\right) - \frac{f_k}{\varepsilon}} \\ \mu_{k+1} &= \mu_k - \frac{\left[\varphi\left(\mu_k\right) - \mu_k\right]^2}{\varphi\left[\varphi\left(\mu_k\right)\right] - 2\varphi\left(\mu_k\right) + \mu_k} \end{aligned} \tag{25}$$

where μ_k is initially set to be 50, a common value chosen in many previous works. Then $\mathrm{d}KS/\mathrm{d}\mu$ is iteratively calculated and evaluated until Eq. (19) is satisfied. Since Steffensen iteration has proved at least quadratically convergent, the proper value of μ can be obtained efficiently.

Table 1
The constraints' values in four problems.

Problem 1	$(g_1, g_2) = (1.1, 1)$
Problem 2	$(g_1, g_2, g_3, \ldots, g_{10}) = (1.1, 1, 1, \ldots, 1)$
Problem 3	$(g_1, g_2, g_3, \ldots, g_{100}) = (1.1, 1, 1, \ldots, 1)$
Problem 4	$(g_1, g_2, g_3) = (-0.07, -0.04, -0.04)$

Table 2
Constraint aggregation performance with two different approaches.

		Existing adaptive approach	Improved adaptive approach
Problem 1	μ	78.6160	74.1455
	$KS(\mu)$	$1.1 + 4.8996 \times 10^{-6}$	$1.1 + 8.1225 \times 10^{-6}$
	$\lvert dKS/d\mu \rvert$	5.5219×10^{-7}	0.9215×10^{-6}
Problem 2	μ	115.0933	92.9900
	$KS(\mu)$	$1.1 + 7.8476 \times 10^{-7}$	$1.1 + 8.8537 \times 10^{-6}$
	$\lvert dKS/d\mu \rvert$	8.5291×10^{-8}	0.9802×10^{-6}
Problem 3	μ	241.5204	115.0478
	$KS(\mu)$	$1.1 + 1.3292 \times 10^{-11}$	$1.1 + 8.6712 \times 10^{-6}$
	$\lvert dKS/d\mu \rvert$	1.3842×10^{-12}	0.9421×10^{-6}
Problem 4	μ	731.2847	851.4261
	$KS(\mu)$	$-0.04 + 9.4785 \times 10^{-4}$	$-0.04 + 8.1410 \times 10^{-4}$
	$\lvert dKS/d\mu \rvert$	1.2961×10^{-6}	0.9562×10^{-6}

Consider four problems with different constraints listed in Table 1. Values of ε and υ are set as 10^{-6} and 0.9, respectively.

Then we calculate the aggregation parameters with existing adaptive approach and the improved adaptive approach, respectively. The final aggregation parameters are given in Table 2, together with the *KS* function values and their derivative values.

As shown in Table 2, in the first three problems, the improved approach obtains better aggregation parameters with much smaller values than the existing approach, especially when the number of constraints increases. Moreover in Problem 4, the improved approach can handle the case when the existing adaptive approach fails.

2.2. Formulation of MPC

In the integrated layout and topology optimization, structural material distribution and components' layout are designed simultaneously. To simulate the connections between components and structures, MPC is used here as shown in Fig. 9. For example, $\mathbf{P}_1$ is one of the connecting nodes of the components, which is projected to point $\mathbf{P}_1^*$ inside the structural element e_1. Then we enable the following MPC equation

$$\mathbf{u}_{\mathbf{P}1} = \mathbf{u}_{\mathbf{P}1}^* = \mathbf{N}_{e1}\left(\mathbf{P}_1^*\right) \cdot \mathbf{u}_{e1} \tag{26}$$

or

$$\mathbf{u}_{\mathbf{P}1} - \mathbf{N}_{e1}\left(\mathbf{P}_1^*\right) \cdot \mathbf{u}_{e1} = \mathbf{0} \tag{27}$$

where $\mathbf{u}_{\mathbf{P}1}$ and $\mathbf{u}_{\mathbf{P}1}^*$ denote the displacement vectors of node $\mathbf{P}_1$ and point $\mathbf{P}_1^*$, respectively. $\mathbf{u}_{e1}$ and $\mathbf{N}_{e1}\left(\mathbf{P}_1^*\right)$ are displacement vectors of the element e_1 and the shape function coefficient matrix at the point $\mathbf{P}_1^*$, respectively.

When several connecting nodes are involved, these MPC equations can be regarded as a linear combination of nodal displacements as

$$\mathbf{H}\mathbf{u} = \mathbf{0}. \tag{28}$$

$\mathbf{H}$ is the coefficient matrix determined by shape functions of structural elements and coordinates of connecting nodes. $\mathbf{u}$ denotes the global displacement vector of the integrated structure system with components.

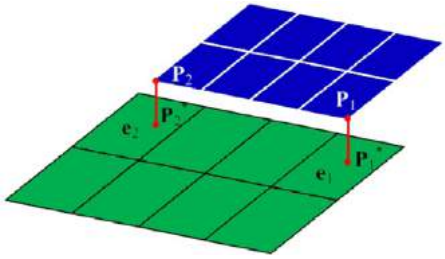

Fig. 9. The definition of MPC connections.

Considering the displacement constraints in Eq. (28), the revised form of the overall potential energy of the global system under loads can be expressed as

$$\Pi(\mathbf{u}, \boldsymbol{\lambda}) = \frac{1}{2}\mathbf{u}^T\mathbf{K}\mathbf{u} - \mathbf{F}^T\mathbf{u} + \boldsymbol{\lambda}^T\mathbf{H}\mathbf{u} \tag{29}$$

where $\mathbf{K}$ is the global stiffness matrix. $\mathbf{F}$ is the nodal load vector which consists of the design independent external loads $\mathbf{f}$ and design dependent inertial loads $\mathbf{G}$. $\boldsymbol{\lambda}$ is the Lagrange multiplier vector.

Then we have the stationary conditions

$$\begin{cases} \mathbf{K}\mathbf{u} + \mathbf{H}^T\boldsymbol{\lambda} = \mathbf{F} \\ \mathbf{H}\mathbf{u} = \mathbf{0}. \end{cases} \tag{30}$$

Vectors $\mathbf{u}$ and $\boldsymbol{\lambda}$ can be obtained by resolving the above equations. More explanations of solving MPC equations can be noted in some existing works [40,41].

2.3. Formulation of the optimization model

The design objective of the optimization is to minimize the global elastic strain energy of the structure system with a prescribed material volume fraction. The design variables are the pseudo-densities describing the material distribution and the geometry variables indicating the components' locations and orientations. The aggregated non-overlapping constraint is imposed to avoid the components' overlapping and keep all the components inside the design domain. The optimization problem can be mathematically elaborated as:

$$\begin{aligned} &\text{Find :} && \eta_i,\ i = 1, 2, \ldots, N_d; \\ &&& (\xi_{jx}, \xi_{jy}, \xi_{j\theta}),\ j = 1, 2, \ldots, N_c \\ &\min : && C = \frac{1}{2}\mathbf{u}^T\mathbf{K}\mathbf{u} \\ &\text{subject to :} && \text{Eq. (4)} \\ &&& V \le V_U \\ &&& KS(\mu) = g_{m\max} + \frac{1}{\mu}\ln\left(\sum_{m=1}^{Ng} e^{\mu(g_m - g_{m\max})}\right) \le 0 \end{aligned} \tag{31}$$

where N_d and N_c are the numbers of the pseudo-density variables and the components, respectively. η_i denotes the ith pseudo-density. ξ_{jx}, ξ_{jy} and $\xi_{j\theta}$ are the geometry design variables i.e. the location and orientation related to the jth component, which is the case for 2D layout design. C is the strain energy of the structure system and $\mathbf{K}$ is the global stiffness matrix. V is the material volume fraction of the design domain with an upper limit of V_U.

Here we use a polynomial material interpolation [36] to establish the relationship between the pseudo-density and its related elastic modulus.

$$E(i) = \left[(1-\alpha)\,\eta_i^p + \alpha\eta_i\right] E_0(i) \tag{32}$$

where $E(i)$ stands for the corresponding elastic modulus of one element. $E_0(i)$ represents the elastic modulus of a solid element. p is the penalty factor and α is polynomial coefficient, which are set to be 4 and $1/16$ in this study.

3. Sensitivity analysis

In this section, sensitivities of the objective function with respect to both pseudo-densities and geometry variables are analytically achieved. Sensitivities of the aggregated non-overlapping constraint are derived by the complex step derivative approximation method.

3.1. Sensitivity analysis of strain energy

Firstly, we focus on the sensitivity analysis w.r.t. pseudo-density design variables. Considering the static equation, the differentiation w.r.t. the pseudo-density variable η_i can be written as

$$\frac{\partial \mathbf{K}}{\partial \eta_i}\mathbf{u} + \mathbf{K}\frac{\partial \mathbf{u}}{\partial \eta_i} = \frac{\partial(\mathbf{F} - \mathbf{H}^T\boldsymbol{\lambda})}{\partial \eta_i}. \tag{33}$$

Assuming $\mathbf{F} = \mathbf{f} + \mathbf{G}$, where $\mathbf{f}$ and $\mathbf{G}$ stand for design independent external loads and design dependent inertial loads, respectively. With $\partial \mathbf{f}/\partial \eta_i = \mathbf{0}$, the following equation holds

$$\frac{\partial(\mathbf{F} - \mathbf{H}^T\boldsymbol{\lambda})}{\partial \eta_i} = \frac{\partial(\mathbf{G} - \mathbf{H}^T\boldsymbol{\lambda})}{\partial \eta_i}. \tag{34}$$

Then we have the derivative of the strain energy

$$\frac{\partial C}{\partial \eta_i} = \mathbf{u}^T\mathbf{K}\frac{\partial \mathbf{u}}{\partial \eta_i} + \frac{1}{2}\mathbf{u}^T\frac{\partial \mathbf{K}}{\partial \eta_i}\mathbf{u}. \tag{35}$$

As $\partial \mathbf{H}^T/\partial \eta_i = \mathbf{0}$, we obtain

$$\frac{\partial C}{\partial \eta_i} = \mathbf{u}^T\frac{\partial \mathbf{G}}{\partial \eta_i} - \mathbf{u}^T\mathbf{H}^T\frac{\partial \boldsymbol{\lambda}}{\partial \eta_i} - \frac{1}{2}\mathbf{u}^T\frac{\partial \mathbf{K}}{\partial \eta_i}\mathbf{u}. \tag{36}$$

As $\mathbf{u}^T\mathbf{H}^T = \mathbf{0}$, the above equation can be simplified as

$$\frac{\partial C}{\partial \eta_i} = \mathbf{u}^T\frac{\partial \mathbf{G}}{\partial \eta_i} - \frac{1}{2}\mathbf{u}^T\frac{\partial \mathbf{K}}{\partial \eta_i}\mathbf{u} \tag{37}$$

where the derivatives of the stiffness matrix and the inertial loads vector can be easily obtained according to the material interpolation model. In the first test in Section 4, the inertial loads are ignored, so $\partial \mathbf{G}/\partial \eta_i = 0$.

Then we concentrate on the sensitivity analyses w.r.t. one of the geometry design variables, e.g. ξ_j. The differentiation of the static equation can be written as

$$\frac{\partial \mathbf{K}}{\partial \xi_j}\mathbf{u} + \mathbf{K}\frac{\partial \mathbf{u}}{\partial \xi_j} = -\frac{\partial\left(\mathbf{H}^T\boldsymbol{\lambda}\right)}{\partial \xi_j}. \tag{38}$$

Note that the inertial load vector is not influenced by the components movement. Then the derivative of the strain energy is similarly written as

$$\frac{\partial C}{\partial \xi_j} = -\mathbf{u}^T\frac{\partial \mathbf{H}^T}{\partial \xi_j}\boldsymbol{\lambda} - \frac{1}{2}\mathbf{u}^T\frac{\partial \mathbf{K}}{\partial \xi_j}\mathbf{u}. \tag{39}$$

Suppose ξ_j is a translational variable, the stiffness matrix of the components will remain unchanged after a translational motion. So we obtain

$$\frac{\partial C}{\partial \xi_j} = -\mathbf{u}^T\frac{\partial \mathbf{H}^T}{\partial \xi_j}\boldsymbol{\lambda}. \tag{40}$$

If ξ_j is a rotational design variable, the stiffness matrix of the jth component after its rotation can be expressed as

$$\mathbf{K}_j = \mathbf{A}_j^T\mathbf{K}_j^*\mathbf{A}_j \tag{41}$$

where $\mathbf{K}_j^*$ is the initial stiffness matrix of the jth component and $\mathbf{A}_j$ is the corresponding rotational transformation matrix. Suppose $\mathbf{u}_j$ is the displacement vector of the jth component, then

$$\mathbf{u}^T \frac{\partial \mathbf{K}}{\partial \xi_j}\mathbf{u} = \mathbf{u}_j^T \frac{\partial \mathbf{K}_j}{\partial \xi_j}\mathbf{u}_j = \mathbf{u}_j^T \left(\mathbf{A}_j^T \mathbf{K}_j^* \frac{\partial \mathbf{A}_j}{\partial \xi_j} + \frac{\partial \mathbf{A}_j^T}{\partial \xi_j} \mathbf{K}_j^* \mathbf{A}_j \right) \mathbf{u}_j. \tag{42}$$

The derivative of the rotational transformation matrix can be easily calculated according to the coordinate transformation matrix, so we have

$$\frac{\partial C}{\partial \xi_j} = -\mathbf{u}^T \frac{\partial \mathbf{H}^T}{\partial \xi_j}\boldsymbol{\lambda} - \mathbf{u}_j^T \mathbf{A}_j^T \mathbf{K}_j^* \frac{\partial \mathbf{A}_j}{\partial \xi_j}\mathbf{u}_j. \tag{43}$$

Note that $\mathbf{H}$ consists of the shape function coefficient matrices of the corresponding elements, which depend upon the connection positions and the geometrical variables which describe the components' locations and orientations.

3.2. Sensitivity analysis for aggregated non-overlapping constraint

As substantial amount of non-overlapping constraints has been aggregated into one with high nonlinearity, precise sensitivity analyses become an important issue. The finite difference and the analytical scheme are two usual methods to achieve design sensitivities.

The finite difference scheme is easy to implement but leads to inaccurate sensitivities. It has been proved that each design variable in different iterations needs adaptive step lengths to ensure a stable sensitivity output. Typically, tiny finite difference step lengths will not improve the precision as expected due to the numerical calculation errors.

On the contrary, the analytical method holds the advantage of accuracy. However, compared with the finite difference scheme, the analytical method for the aggregated non-overlapping constraint needs more operations due to the tedious formulations and derivations.

As a result, we use the complex step derivative approximation [42,31,32] here. Consider an analytical complex function with complex variables. It can be expanded by using a Taylor series at the current design point

$$f(x+ih) = f(x) + ihf'(x) - h^2 \frac{f''(x)}{2!} - ih^3 \frac{f'''(x)}{3!} + \cdots. \tag{44}$$

Then only the imaginary parts are extracted

$$f'(x) = \frac{\mathrm{Im}[f(x+ih)]}{h} + h^2 \frac{f'''(x)}{3!} + \cdots. \tag{45}$$

Ignoring the high-order items, we obtain an approximation form by using a small size of h

$$f'(x) \approx \frac{\mathrm{Im}[f(x+ih)]}{h}. \tag{46}$$

This formulation ensures more accurate sensitivity output than standard finite difference method. On the one hand, it is based on an $O(h^2)$ approximation of $f'(x)$. On the other hand, subtraction operations leading to cancellation errors are avoided in the complex formulation.

The complex step derivative approximation used in our problem is expressed as

$$\frac{\partial KS(\xi_j)}{\partial \xi_j} \approx \frac{\mathrm{Im}[KS(\xi_j + ih)]}{h} \tag{47}$$

where $\mathrm{Im}\left[KS(\xi_j + ih)\right]$ denotes the imaginary output after a small imaginary perturbation ih is brought into the KS function. In this paper, $h = 10^{-12}$.

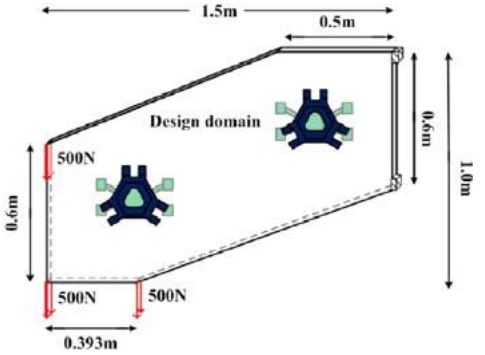

Fig. 10. Optimization problem with four components.

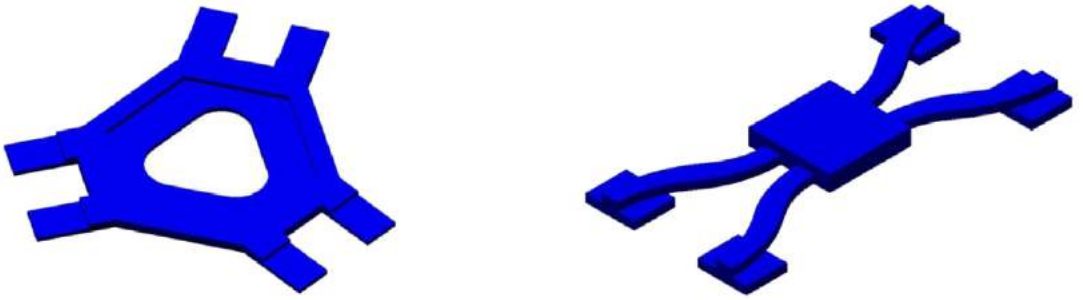

(a) The 3D models of two sets of components.

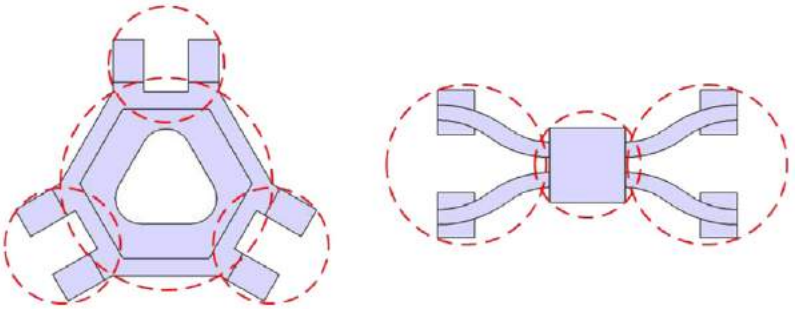

(b) Circle approximation by FCM.

Fig. 11. Detailed illustrations of the components.

4. Numerical examples

4.1. A hexagonal plate with four components

As illustrated in Fig. 10, the hexagonal plate with a thickness of 0.036 m is discretized into three layers of total 18 000 solid hexahedron elements. External loads are applied at three different positions. Each position has 4 nodes and the 500 N downward force has been applied to each single node. The design domain is described with six large circles by FCM. The material properties of the plate are: the Young's modulus $E_S = 7.0 \times 10^{10}$ Pa, and Poisson's ratio $\nu_S = 0.3$.

The first two identical six-foot components are approximately described by four circles. Their material properties are: the elastic modulus $E_{c1} = 1.1 \times 10^{11}$ Pa and Poisson's ratio $\nu_{c1} = 0.3$. The material properties of the second group of two four-foot components described by three circles are: the elastic modulus $E_{c2} = 2.0 \times 10^{11}$ Pa and Poisson's ratio $\nu_{c2} = 0.3$. Detailed configurations of the components are illustrated in Fig. 11 and all the four components are connected onto the supporting structure surface through the nodes in their foot areas.

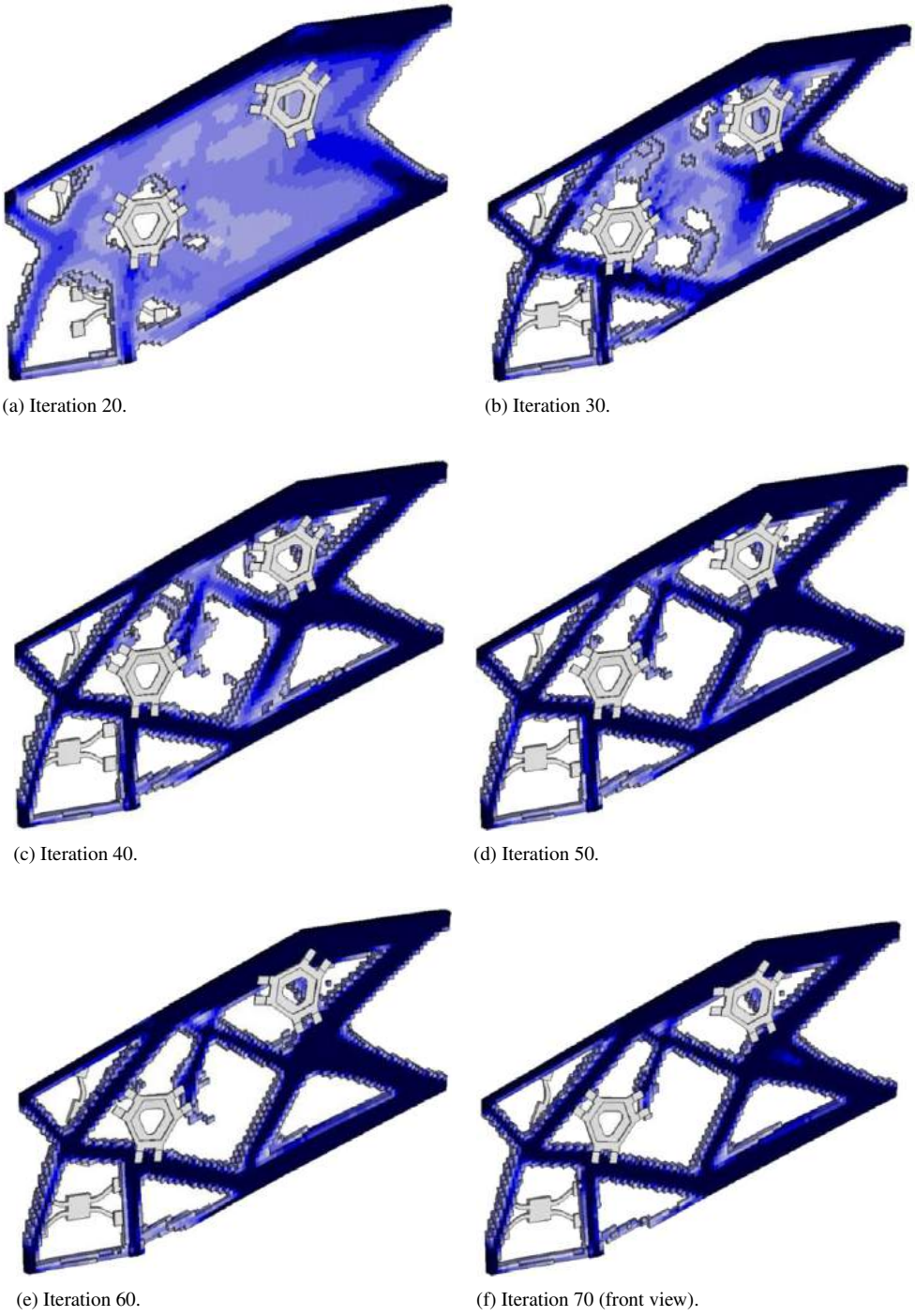

(a) Iteration 20.

(b) Iteration 30.

(c) Iteration 40.

(d) Iteration 50.

(e) Iteration 60.

(f) Iteration 70 (front view).

Fig. 12. Design iterations of structural topology and components' layout.

There are total 109 non-overlapping constraints aggregated by the KS function in this problem. The upper bound of material volume fraction is 0.4. The algorithm GCMMA [43] within the general purpose optimization platform Boss-Quattro [44] is used to solve the problem.

As shown in Fig. 12(a)–(g), clear structural topologies are obtained and all the four components find their proper locations to reinforce the structure locally. The optimization converges after 70 iterations with the global strain energy

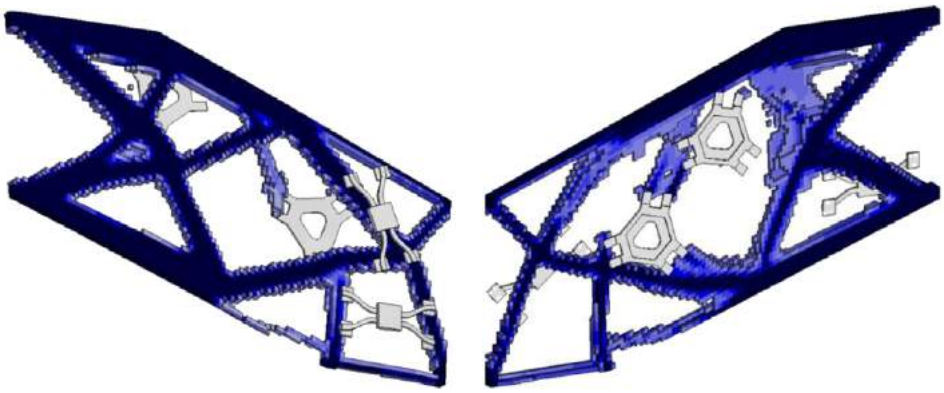

(g) Iteration 70 (back view).

(h) Final design obtained by the existing adaptive constraint aggregation approach.

Fig. 12. (*continued*)

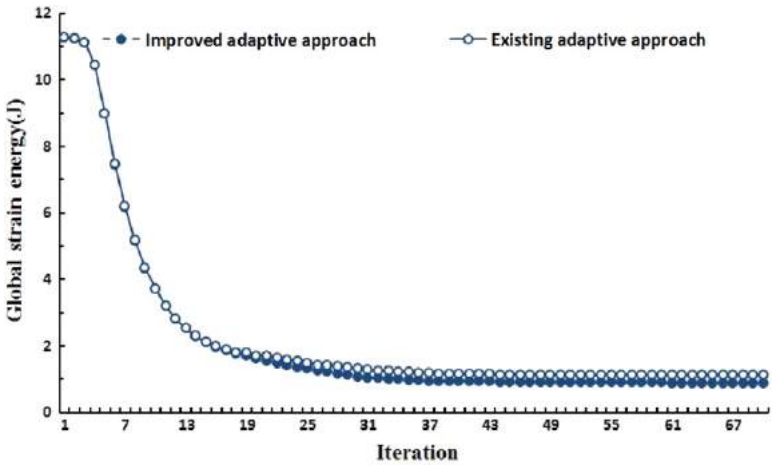

Fig. 13. Iteration history of the global strain energy.

decreasing smoothly from initial 11.267 to final 0.877 J as plotted in Fig. 13. In the optimized design, it is found that the two four-foot components are relatively ineffective in carrying loads, which finally behave as the adhering and reinforcing components. In contrast, the six-foot components are much stiffer and they are thus located on the key load carrying path.

For the purpose of comparison, this problem is then solved with the existing adaptive constraint aggregation approach. The final structural topology shows that the optimization does not converge after 70 iterations, as shown in Fig. 12(h). Its final global strain energy is also higher than that obtained by the improved approach in Fig. 13. Later, the final design is found infeasible due to the overlapping between one component and the design domain boundary. The aggregated constraints of the improved adaptive approach and the existing adaptive approach are shown in Fig. 14.

The aggregation parameters and their derivatives in both adaptive approaches are also calculated in different iterations as shown in Figs. 15 and 16. It is found in Fig. 15 that the aggregation parameters obtained by the improved adaptive approach show a convergent history, while those calculated by the existing approach keep divergent during the whole optimization. It can be seen in Fig. 16 that the improved adaptive approach has a better control of the derivatives of aggregated constraints, compared with the existing adaptive approach.

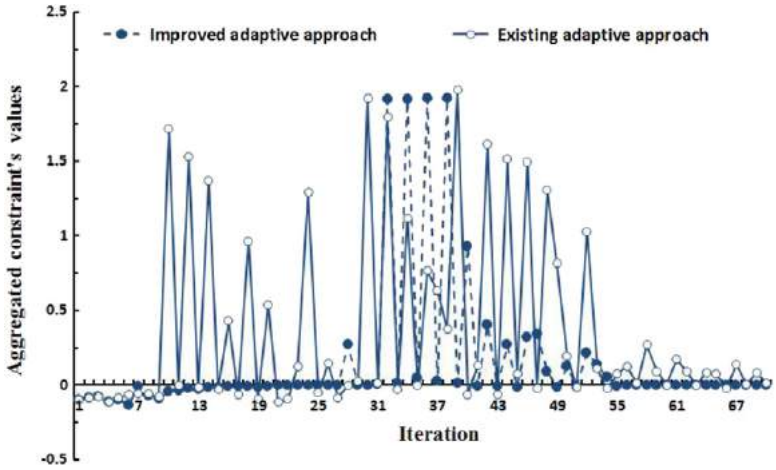

Fig. 14. Iteration history of aggregated constraint's values.

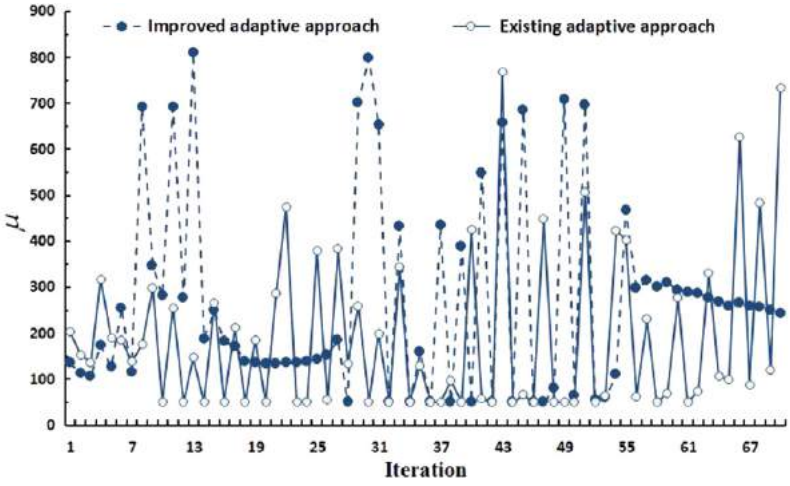

Fig. 15. Iteration history of aggregation parameters obtained by both approaches.

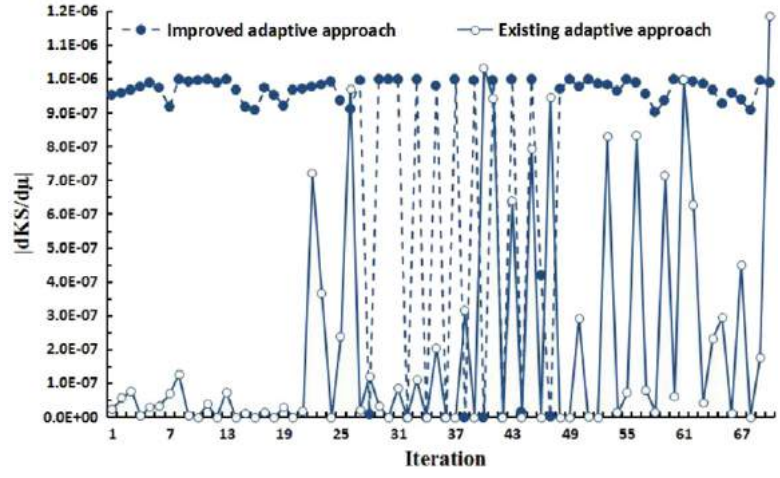

Fig. 16. Comparison of $|\mathrm{d}KS/\mathrm{d}\mu|$ calculated by both approaches.

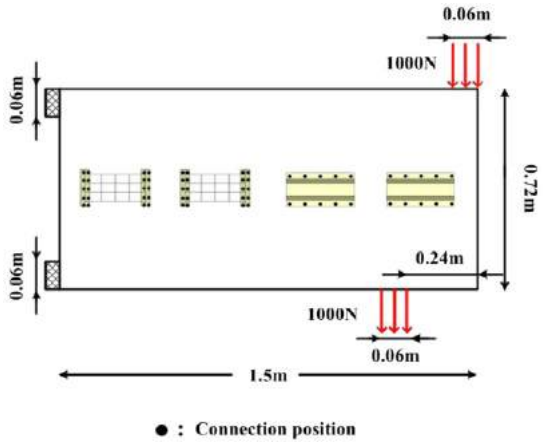

Fig. 17. Optimization problem with four components.

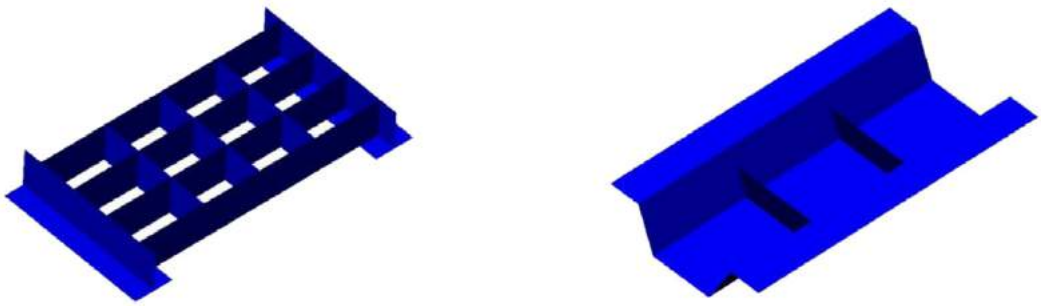

(a) The 3D model of the two different components.

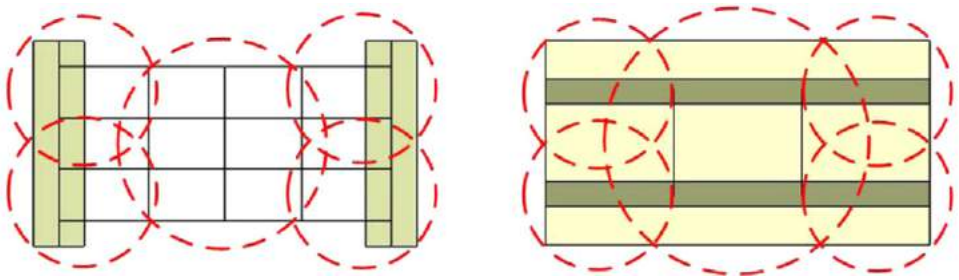

(b) Circle approximation by FCM.

Fig. 18. Detailed illustrations of the components.

4.2. A rectangle beam with four components

In the second test, a 1.5 m × 0.72 m rectangle cantilever with a thickness of 0.02 m is assigned as the topology design domain and discretized into 10 800 shell elements. The boundary conditions and static loads are applied on the cantilever as illustrated in Fig. 17. Self-weight is taken into consideration with an acceleration of 10 m/s^2 applied on the global structure system. External loads are applied at two different positions. Each position has 7 nodes and the downward 1000 N force is applied on each single node. The material properties are: the elastic modulus $E_S = 7.0 \times 10^{10}$ Pa, the density $\rho_S = 2700$ kg/m^3, Poisson's ratio $\nu_S = 0.3$.

Four components are bonded onto the front surface of the cantilever. The first two components are the same in configurations and material properties: the elastic modulus $E_{c1} = 2.0 \times 10^{11}$ Pa, the density $\rho_{c1} = 7800$ kg/m^3, and Poisson's ratio $\nu_{c1} = 0.3$. The material properties of the next two components are: the elastic modulus $E_{c2} = 1.1 \times 10^{11}$ Pa,

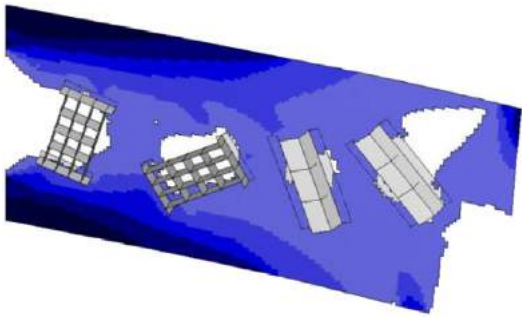

(a) Iteration 10.

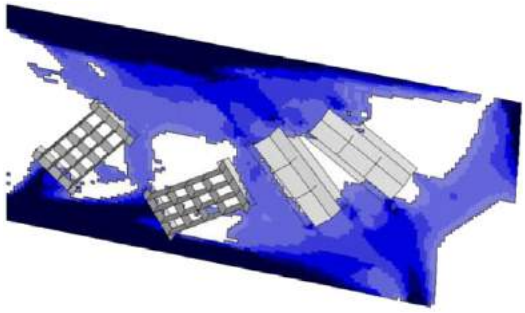

(b) Iteration 20.

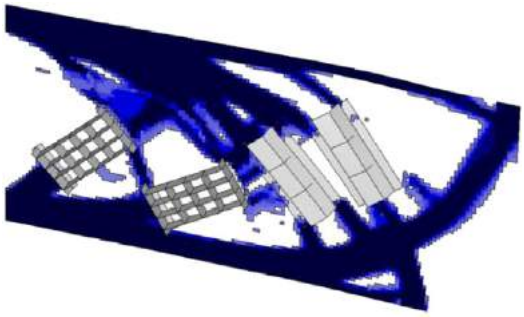

(c) Iteration 30.

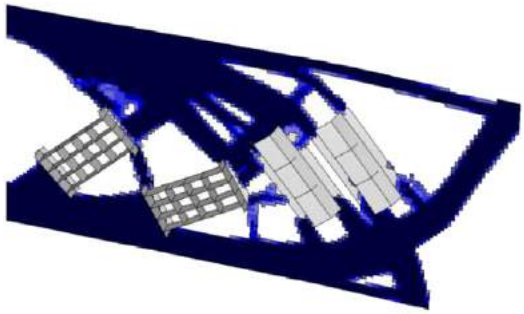

(d) Iteration 40.

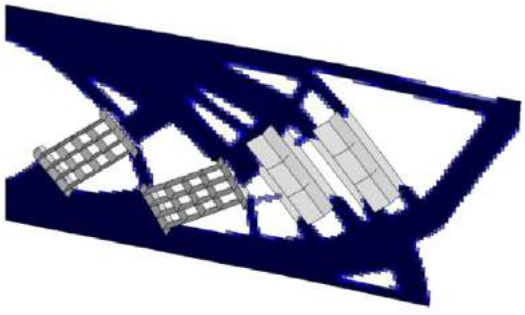

(e) Iteration 50.

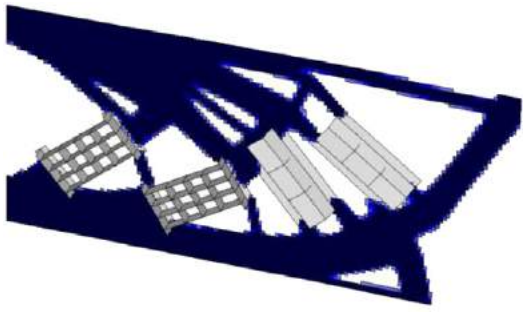

(f) Iteration 60.

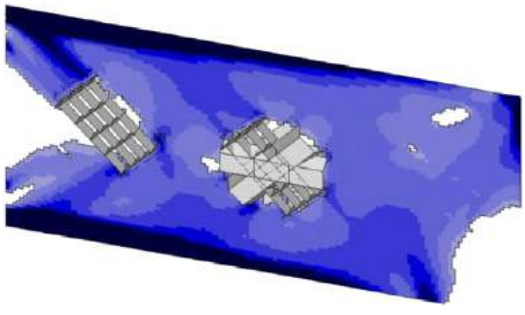

(g) Final design obtained by the existing adaptive constraint aggregation approach.

Fig. 19. Design iterations of structural topology and components' layout.

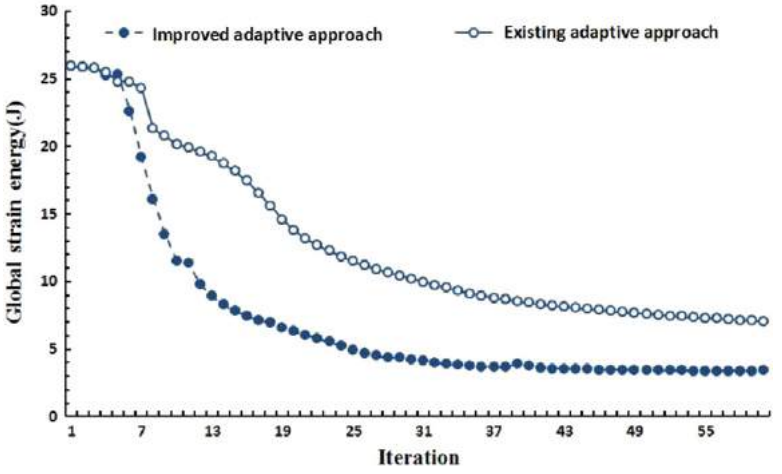

Fig. 20. Iteration history of the global strain energy.

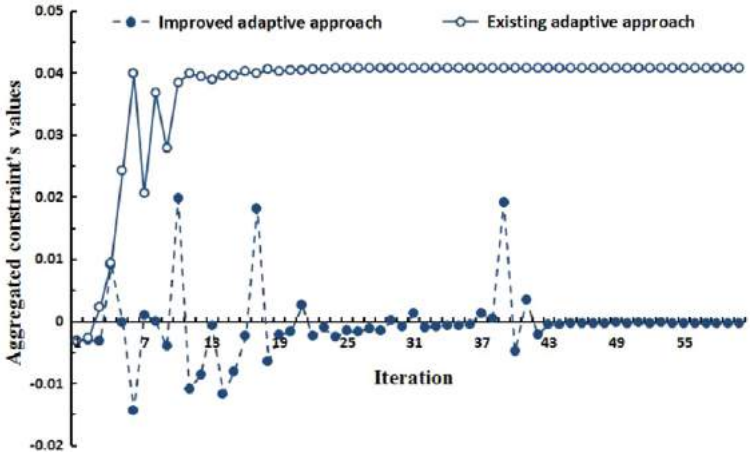

Fig. 21. Iteration history of aggregated constraint's values.

the density $\rho_{c2} = 4500\ \mathrm{kg/m^3}$, and Poisson's ratio $\nu_{c2} = 0.3$. Each component is approximated with five circles as shown in Fig. 18.

The number of non-overlapping constraints reaches 230 and they are aggregated using the two adaptive approaches, respectively. The upper bound of volume fraction constraint is set to be 0.5.

After optimization, the evolution history of the structure and components by the improved adaptive approach is shown in Fig. 19(a)–(f). In the final design, all the four components occupy prominent positions and work positively to bear the loads. The global strain energy decreases from 25.268 to 3.431 J steadily as shown in Fig. 20. The history of the aggregated constraint displayed in Fig. 21 also indicates the optimization is converged into a feasible region. As a comparison, the existing adaptive approach is also tested for this problem with its final design shown in Fig. 19(g). It is noted that a serious overlapping occurs in the final design and the optimization converges into an infeasible region. Furthermore, its final strain energy is also much higher than that obtained by the improved approach, as shown in Fig. 20.

Meanwhile, comparisons of the aggregation parameters calculated by both two approaches are carried out and plotted in Fig. 22, together with their derivatives in Fig. 23. The same conclusion can be drawn as in the previous test that the improved adaptive approach can always have a better control of the constraint aggregation behaviors.

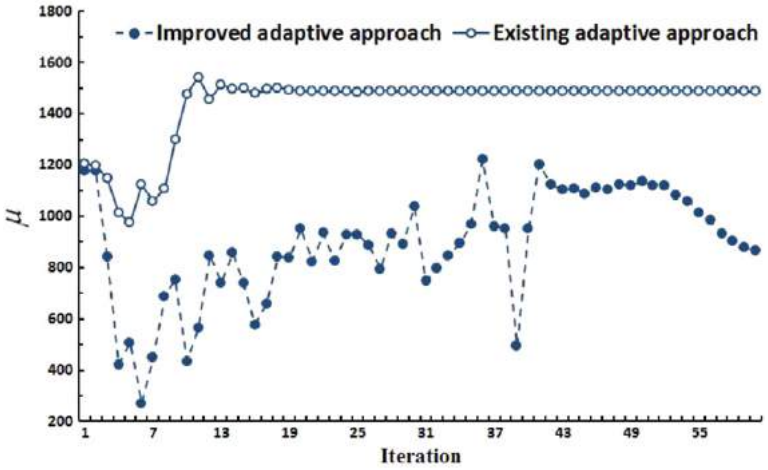

Fig. 22. Iteration history of aggregation parameters obtained by both approaches.

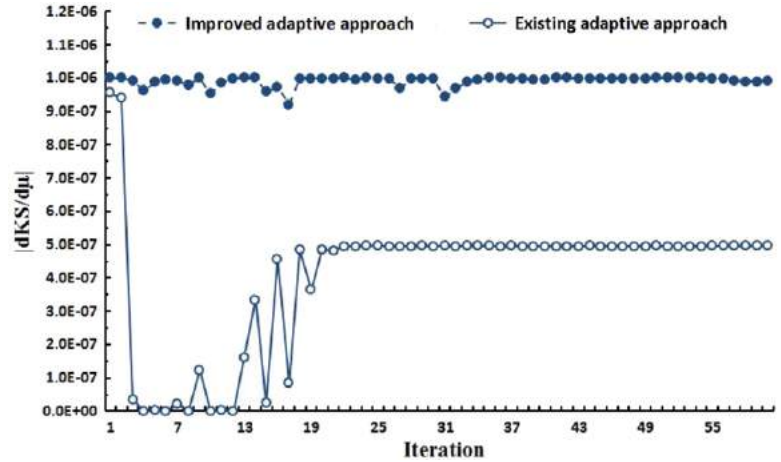

Fig. 23. Comparison of $|\mathrm{d}KS/\mathrm{d}\mu|$ calculated by both approaches.

5. Conclusion

In this paper, an improved adaptive KS function based constraint aggregation approach is proposed to deal with the large number of non-overlapping constraints implemented in the integrated layout and topology optimization design. Two thresholds are set to control the range and Steffensen iteration is used to obtain proper values of aggregation parameters, which help guaranteeing aggregation accuracy and avoiding numerical instabilities. Taking advantage of the complex step derivative approximation approach, sensitivities of the aggregated constraints are obtained with high accuracy.

Two numerical examples in which components are bonded to the supporting structures with MPC are implemented to test the validity of the proposed approaches. The optimized results have shown that the components and the structures are joined as integrities to carry the loads together. Meanwhile, the improved constraint aggregation approach performs well in handling large-scale multi-constraint problems by reducing the amount of constraints. Compared with the existing adaptive constraint aggregation approach, the improved adaptive approach can help obtain better and feasible designs. Furthermore, the effect of this approach may be potentially validated by problems with even larger numbers of constraints, such as the topology optimization problems with stress constraints.

Acknowledgments

This work is supported by National Natural Science Foundation of China (11432011, 51275424 and 11172236), 111 Project (B07050), Science and Technology Research and development projects in Shaanxi Province (2014KJXX-37), and the Fundamental Research Funds for the Central Universities (3102014JC02020505).

References

[1] M.P. Bendsøe, N. Kikuchi, Generating optimal topologies in structural design using a homogenization method, Comput. Methods Appl. Mech. Engrg. 71 (1988) 197–224.
[2] M.P. Bendsøe, O. Sigmund, Topology Optimization: Theory, Method and Application, second ed., Springer Verlag, 2003.
[3] M. Stolpe, K. Svanberg, An alternative interpolation scheme for minimum compliance topology optimization, Struct. Multidiscip. Optim. 22 (2001) 116–124.
[4] Y.M. Xie, G.P. Steven, A simple evolutionary procedure for structural optimization, Comput. Struct. 49 (1993) 885–896.
[5] M.Y. Wang, X.M. Wang, D.M. Guo, A level set method for structural topology optimization, Comput. Methods Appl. Mech. Engrg. 192 (2003) 227–246.
[6] G. Allaire, F. Jouve, H. Maillot, Topology optimization for minimum stress design with the homogenization method, Struct. Multidiscip. Optim. 28 (2004) 87–98.
[7] X. Guo, G.D. Cheng, Recent development in structural design and optimization, Acta Mech. Sin. 26 (6) (2010) 807–823.
[8] W.S. Lee, S.K. Youn, Topology optimization of rubber isolators considering static and dynamic behaviours, Struct. Multidiscip. Optim. 27 (4) (2004) 284–294.
[9] K. Maute, M. Allen, Conceptual design of aeroelastic structures by topology optimization, Struct. Multidiscip. Optim. 27 (2004) 27–42.
[10] B. Niu, J. Yan, G.D. Cheng, Optimum structure with homogeneous optimum cellular material for maximum fundamental frequency, Struct. Multidiscip. Optim. 39 (2009) 115–132.
[11] A. Remouchamps, M. Bruyneel, C. Fleury, S. Grihon, Application of a bi-level scheme including topology optimization to the design of an aircraft pylon, Struct. Multidiscip. Optim. 44 (6) (2011) 739–750.
[12] H. Chickermane, H.C. Gea, Design of multi-component structural systems for optimal layout topology and joint locations, Eng. Comput. 13 (1997) 235–243.
[13] Q. Li, G.P. Steven, Y.M. Xie, Evolutionary structural optimization for connection topology design of multi-component systems, Eng. Comput. 18 (2001) 460–479.
[14] Z.D. Ma, N. Kikuchi, C. Pierre, B. Raju, Multidomain topology optimization for structural and material designs, J. Appl. Mech. 73 (2006) 565–573.
[15] Z.Y. Qian, G.K. Ananthasuresh, Optimal embedding of rigid objects in the topology design of structures, Mech. Based Des. Struct. Mach. 32 (2004) 165–193.
[16] J.H. Zhu, W.H. Zhang, Coupled design of components layout and supporting structures using shape and topology optimization, in: Proceedings of the Fourth China–Japan–Korea Joint Symposium on Optimization of Structural and Mechanical Systems, Kunming, China, November 6–9, 2006.
[17] D. Meagher, Geometric modeling using octree encoding, Comput. Graph. Image Process. 19 (1982) 129–147.
[18] H. Samet, Spatial Data Structures: Quadtree, Octree and Other Hierarchical Methods, Addison Wesley, 1989.
[19] A. Moore, The circle tree—a hierarchical structure for efficient storage, access and multi-scale representation of spatial data, in: SIRC 2002 Dunedin, New Zealand 2002.
[20] S. Cameron, Approximation hierarchies and s-bounds, in: Proceedings Symposium on Solid modeling Foundations and CAD/CAM Applications, 1991, pp. 129–137.
[21] W.H. Zhang, J.H. Zhu, A new finite-circle family method for optimal multi-component packing design, in: WCCM VII, Los Angeles 2006.
[22] J.H. Zhu, W.H. Zhang, L. Xia, Q. Zhang, D.H. Bassir, Optimal packing configuration design with finite-circle method, J. Intell. Rob. Syst. 67 (2012) 185–199.
[23] P. Shan, Optimal embedding objects in the topology design of structure (Master thesis), Dalian University of Technology, 2008.
[24] Z. Kang, Y.Q. Wang, Integrated topology optimization with embedded movable holes based on combined description by material density and level sets, Comput. Methods Appl. Mech. Engrg. 255 (2013) 1–13.
[25] R.J. Yang, C.J. Chen, Stress-based topology optimization, Struct. Optim. 12 (2–3) (1996) 98–105.
[26] P. Duysinx, O. Sigmund, New developments in handling stress constraints in optimal material distribution, in: Proc of the 7th AIAA/USAF/NASAISSMO Symp on Multidisciplinary Analysis and Optimization, Vol. 1, 1998, pp. 1501–1509.
[27] C. Le, J. Norato, T. Bruns, C. Ha, D. Tortorelli, Stress-based topology optimization for continua, Struct. Multidiscip. Optim. 41 (4) (2010) 605–620.
[28] G.Y. Qiu, X.S. Li, A note on the derivation of global stress constraints, Struct. Multidiscip. Optim. 40 (1–6) (2010) 625–628.
[29] M.K. Nicholas Poon, R.R.A. Joaquim Martins, On structural optimization using constraint aggregation, in: 6th World Congress on Structural and Multidisciplinary Optimization, Rio de Janeiro, Brazil, 2005.
[30] M.K. Nicholas Poon, R.R.A. Joaquim Martins, An adaptive approach to constraint aggregation using adjoint sensitivity analysis, Struct. Multidiscip. Optim. 34 (1) (2007) 61–73.
[31] M.K. Nicholas Poon, R.R.A. Joaquim Martins, The complex-step derivative approximation, ACM Trans. Math. Software (TOMS) 29 (3) (2003) 245–262.
[32] K.L. Lai, J.L. Crassidis, Extensions of the first and second complex-step derivative approximations, J. Comput. Appl. Math. 219 (1) (2008) 276–293.

[33] L. Xia, J.H. Zhu, W.H. Zhang, An implicit model for the integrated optimization of component layout and structure topology, Comput. Methods Appl. Mech. Engrg. 257 (2013) 87–102.
[34] J. Zhang, W.H. Zhang, J.H. Zhu, Integrated layout design of multi-component systems using XFEM and analytical sensitivity analysis, Comput. Methods Appl. Mech. Engrg. 245–246 (2012) 75–89.
[35] J.H. Zhu, W.H. Zhang, P. Beckers, Y.Z. Chen, Z.Z. Guo, Simultaneous design of components layout and supporting structures using coupled shape and topology optimization, Struct. Multidiscip. Optim. 36 (1) (2008) 29–41.
[36] J.H. Zhu, W.H. Zhang, P. Beckers, Integrated layout design of multi-component system, Internat. J. Numer. Methods Engrg. 78 (2009) 631–651.
[37] J.H. Zhu, W.H. Zhang, Integrated layout design of supports and structures, Comput. Methods Appl. Mech. Engrg. 199 (9–12) (2010) 557–569.
[38] L. Xia, J.H. Zhu, W.H. Zhang, A superelement formulation for the efficient layout design of complex multi-component system, Struct. Multidiscip. Optim. 45 (2012) 643–655.
[39] J.H. Zhu, H.H. Gao, W.H. Zhang, Y. Zhou, A multi-point constraints based integrated layout and topology optimization design of multi-component systems, Struct. Multidiscip. Optim. (2014) http://dx.doi.org/10.1007/s00158-014-1134-7.
[40] M. Ainsworth, Essential boundary conditions and multi-point constraints in finite element analysis, Comput. Methods Appl. Mech. Engrg. 190 (2001) 6323–6339.
[41] K.H. Yoon, S.P. Heo, K.N. Song, Y.H. Jung, Dynamic impact analysis of the grid structure using multi-point constraint (MPC) equation under the lateral impact load, Comput. & Structures 82 (23–26) (2004) 2221–2228.
[42] W. Squire, G. Trapp, Using complex variables to estimate derivatives of real functions, SIAM Rev. 40 (1) (1998) 110–112.
[43] K. Svanberg, On a globally convergent version of MMA, in: 7th World Congress on Structural and Multidisciplinary Optimization, COEX Seoul, Korea, 2007.
[44] Y. Radovcic, A. Remouchamps, BOSS QUATTRO: an open system for parametric design, Struct. Multidiscip. Optim. 23 (2) (2002) 140–152.

Milling Force Modeling of Worn Tool and Tool Flank Wear Recognition in End Milling

Yongfeng Hou, Dinghua Zhang, Baohai Wu, and Ming Luo

***Abstract*—The wear state of a cutting tool is an important factor which affects machining quality. Therefore, monitoring tool wear is extremely essential to ensure workpiece quality and improve tool life. This paper models the milling forces of a worn tool and proposes a recognition method of milling tool wear state based on the influence relationships between the milling force features and tool wear. In the milling force model, the friction effect force and the shearing force are treated separately, and the friction stress distribution on tool flank is described. Then the force model is calibrated and verified through experiments. In the tool wear recognition method, the relationship between the milling force feature vector and tool wear is investigated. On this basis, the tool flank wear recognition method is proposed. A tool wear experiment is performed using superalloy material. In the experiment, the recognition results are expressed in confidence intervals which can represent the recognized tool wear more effectively and accurately. Finally, the scheme of tool flank wear online monitoring is proposed.**

***Index Terms*—Friction effect force, milling force feature vector, milling force modeling, model calibration, tool wear recognition.**

I. Introduction

In the machining process, tool wear state is an important factor affecting the workpiece quality. The tool will be worn gradually in the cutting process. The tool is ultimately becomes blunt, and cannot be used normally. More and more difficult-to-cut materials are used in the aviation industry, particularly aero-engine, owing to the high performance requirements and complex structure. These materials have the excellent comprehensive performance of resisting high temperature and resisting corrosion, but have poor machinability. In their cutting process, the tool wears fast, and the usable life is short. Thus, the demand for tool wear state recognition is particularly urgent in the machining of difficult-to-cut materials.

In the automated and intelligent machining process, the condition information, particularly tool wear state, is required. If the tool wear state is recognized accurately, the intelligent monitoring system can make a decision, according to tool wear state, to adjust the using strategies of the tool and the process parameters, and to give a warning of any changes in the tool or change the tool automatically. The quality, efficiency, and usability of the tool are improved maximally, the unnecessary losses are reduced or avoided, and the production costs are significantly reduced.

The tool changes from sharp to blunt gradually in the cutting process, and the change of tool wear state will cause the changes of cutting force signals directly. Thus, the cutting force signals contain plenty of information about tool wear state. Since the cutting force signals have the advantages of fast response, high sensitivity, real-time collection, and fully reflecting the tool wear state, the recognition of tool conditions through cutting force signals has been widely studied.

In recent years, a lot of research for machining tool wear had been carried out in which Li *et al.* [1] studied the tool wears of different tools and process parameters through experiments. Chen and Li [2] analyzed the tool wears of different processing time in nickel-base alloy milling, and fitted the tool wear widths linearly, then proposed an observing model of tool wear based on experiments. Said *et al.* [3] developed a milling force model of worn ball end tool, considering the tool wear and geometry of chips. Other researchers adopted the shape spectrum and machine vision to obtain the contour information of worn tool for assessing tool wear and predicting tool life. The tool wear state was tracked and assessed through pattern recognition, and then the remaining useful tool life was calculated [4], [5]. The machining process must be interrupted in this class of methods, the tool moved to specified location, and the shape patterns were collected by cutting on a standard test-piece or the visual information was captured by photographing, and the monitoring and evaluating on-line of tool wear could not be achieved. In the study about the laws of tool wear, the statistical analysis methods based on tool wear experiments were widely used. Ghani *et al.* [6] proposed a recognition approach of tool wear based on the statistics and regression analysis of cutting force signals for turning process. Choi *et al.* [7] used wavelet analysis and linear regression to estimate the cutting forces and tool wears in ramp milling. Wang *et al.* [8] obtained cutting forces in two directions and their feature through milling experiments, and then established a cointegration relationship between the tool wear and the cutting force feature. On this basis, a tool wear recognition approach based on cointegration theory was proposed. Oraby and Hayhurst [9] analyzed the variation of the cutting forces ratio with the tool wear through experiments in turning process, and assessed the turning tool wear using this variation law. The artificial intelligent recognitions had been researched for the tool wear. Kaya *et al.* [10] extracted the statistical features from triaxial cutting forces, triaxial accelerations, torque

Manuscript received March 31, 2014; revised August 2, 2014; accepted October 6, 2014. Date of publication November 24, 2014; date of current version May 18, 2015. Recommended by Guest Editor S. Melkote. This work was supported in part by the National Basic Research Program of China under Grant 2013CB035802 and the National Natural Science Foundation of China under Grant 51305354.

The authors are with the Key Laboratory of Contemporary Design and Integrated Manufacturing Technology, Ministry of Education, Northwestern Polytechnical University, Xi'an 710072, China (e-mail: houyf061094@126.com; dhzhang@nwpu.edu.cn; wubaohai@nwpu.edu.cn; luoming@nwpu.edu.cn).

Color versions of one or more of the figures in this paper are available online at http://ieeexplore.ieee.org.

Digital Object Identifier 10.1109/TMECH.2014.2363166

1083-4435 © 2014 IEEE. Personal use is permitted, but republication/redistribution requires IEEE permission.
See http://www.ieee.org/publications_standards/publications/rights/index.html for more information.

and acoustic emission signals to train the binary decision tree of support vector machine (SVM), and then predicted the milling tool state using the trained SVM. Uros *et al.* [11] used the neuro-fuzzy to predict the milling tool flank wear through the cutting force signals in end milling. The applications of artificial intelligent detection and recognition in other fields were also studied [12]–[14]. This class of research was based on a large number of experiments, and the laws of tool condition recognition were statistical from experimental data. Thus, there was no support of the cutting force and wear model. Other researchers studied the influences of tool wear on cutting forces from the perspective of cutting force model, and recognized tool wear using the influence relations. Wherein, Choudhury and Rath [15] proposed an evaluating approach of milling tool flank wear based on the relationship between average tangential cutting force coefficients and tool wear. Cui [16] discussed the influences of process parameters, tool parameters, and tool wear on tangential cutting force coefficients in his dissertation. And a recognition approach of milling tool wear was proposed, based on the relationship between tangential cutting force coefficients and tool wear. This approach needed to solve the cutting force coefficients through actual cutting forces, and then the tool wear was recognized through the solved tangential cutting force coefficients. The complex calculations caused that the recognition speed was low, and the result was not precise enough. Shao *et al.* [17] established a cutting power model in face milling, which included the cutting conditions and the tool flank wear, and then proposed a tool wear monitoring approach based on this power model. However, the random errors of instantaneous cutting force, the deviation of cutting force phase, and the difficulty of solving cutting force coefficients in real time caused that the direct recognitions of tool wear through instantaneous cutting forces were not reliable. For this problem, some researchers had analyzed the variations of cutting forces with the increasing of tool wear. On this basis, the indicating variables were defined to characterize tool wear, and then the tool wear state was recognized through the relationships between the indicating variables and tool wear. Wherein, Kuljanic and Sortino [18] defined two indicating variables through cutting forces, which were the normalized cutting force indicator (NCF) and the torque-force distance indicator (TFD), and validated the effectiveness in a single tooth cutting. Sarhan *et al.* [19] analyzed the influence of tool wear on the cutting forces in frequency domain through computer simulation. The cutting force components in frequency domain were adopted as feature variables to propose a tool wear monitoring approach. Bhattacharyya *et al.* [20] studied the relationships between the average signal energy and the signal mean square error and tool wear, and then proposed an evaluating approach of tool wear. Lee and Tarng [21] used discrete wavelet transform to decompose the spindle current, and extracted the features of tool failure. The milling tool state was monitored using the failure features.

However, there are three major shortcomings in these existent studies. 1) The tool condition recognitions are aimed at the general cutting processes, and the applicability to the milling of difficult-to-cut materials in aero-engine is not enough. 2) The statistical and artificial intelligent methods are widely used, and there is a lack of tool wear model in the recognitions. 3) A single indicating variable of tool wear state is adopted, thus the recognition results are impacted largely by uncertain interferences. The robustness is weak in practical applications.

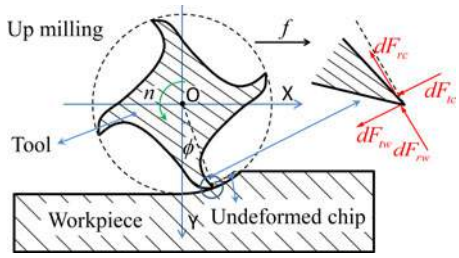

Fig. 1. Force analysis on a section.

For these problems, this paper takes the milling process of superalloy as the study object, and proposes a wear recognition method of flat end milling tool based on the features of milling force vector. In this method, the milling forces are modeled including tool wear first. Then, the calibration experiment is designed, and the shearing force coefficients and various friction and press forces on unit flank length are calibrated. On this basis, several force features related to tool wear are defined and combined into the feature vector. And then, the relationship between the feature vector and tool wear is analyzed. Finally, the relationship is adopted to recognize tool wears. In the verification experiment, the same wear states are recognized repeatedly, and the recognition results are expressed in confidence intervals.

II. Milling Force Modeling of Worn Tool

In milling process, the shearing force caused by shearing effect on the rake face and the friction force and press force caused by flank wear on the tool flank make up the milling force. The friction force and press force caused by flank wear will be collectively called friction effect force in this paper. The shearing force is related to undeformed chip thickness, and the tool flank wear is not explicitly considered. The friction effect force is engendered by the friction and press of tool flank and machining surface. Therefore, the friction effect force is related to tool flank wear, and unrelated to undeformed chip thickness. Force analysis on an infinitesimal piece of tool is shown in Fig. 1. In the figure, dF_{rc} is radial infinitesimal force, dF_{tc} is tangential infinitesimal force. They are caused by shearing effect, and act on tool rake face. dF_{rw} and dF_{tw} are radial press force and tangential friction force respectively. They are caused by friction effect on tool flank wear.

A. Shearing Force Model

The tool is divided into infinitesimal pieces along axis direction. The shearing force on the infinitesimal piece can be expressed as

$$\begin{cases} dF_{j,\mathrm{tc}}(\phi_j(z)) = K_{\mathrm{tc}} h(\phi_j(z)) dz \\ dF_{j,\mathrm{rc}}(\phi_j(z)) = K_{\mathrm{rc}} h(\phi_j(z)) dz \\ dF_{j,\mathrm{ac}}(\phi_j(z)) = K_{\mathrm{ac}} h(\phi_j(z)) dz \end{cases} \tag{1}$$

wherein $dF_{j,\mathrm{tc}}(\phi_j(z))$, $dF_{j,\mathrm{rc}}(\phi_j(z))$, and $dF_{j,\mathrm{ac}}(\phi_j(z))$ are tangential, radial, and axial infinitesimal shearing forces respectively. K_{tc}, K_{rc}, and K_{ac} are tangential, radial, and axial shearing force coefficients, respectively. $\phi_j(z)$ is tooth rotation angle of the infinitesimal piece in the height of z. $h(\phi_j(z))$ is undeformed chip thickness. $h(\phi_j(z))$ can be expanded as

$$h(\phi_j(z)) = f\sin(\phi_j(z)) \tag{2}$$

wherein f is feed rate per tooth.

The infinitesimal forces are converted into O-XYZ coordinate system, and the result is

$$\begin{cases} dF_{j,\mathrm{xc}}(\phi_j(z)) = -dF_{j,\mathrm{tc}}\cos(\phi_j(z)) - dF_{j,\mathrm{rc}}\sin(\phi_j(z)) \\ dF_{j,\mathrm{yc}}(\phi_j(z)) = +dF_{j,\mathrm{tc}}\sin(\phi_j(z)) - dF_{j,\mathrm{rc}}cos(\phi_j(z)) \\ dF_{j,\mathrm{zc}}(\phi_j(z)) = +dF_{j,\mathrm{ac}}. \end{cases} \tag{3}$$

B. Friction Effect Force Model

Tool flank wear has no influence on axial milling force according to the theory of Teitenberg [22], therefore the friction effect force is modeled only in *XY* plane. The infinitesimal friction and press forces can be expressed as

$$\begin{cases} dF_{\mathrm{tw}} = F_{\mathrm{tw}}(VB)dz \\ dF_{\mathrm{rw}} = F_{\mathrm{rw}}(VB)dz \end{cases} \tag{4}$$

wherein dF_{tw} and dF_{rw} are tangential friction force and radial press force, respectively. $F_{\mathrm{tw}}(VB)$ and $F_{\mathrm{rw}}(VB)$ are friction force and press force on unit flank length, respectively; they are all related to tool flank wear.

The infinitesimal friction and press forces are converted into O-XYZ coordinate system, and the result is

$$\begin{cases} dF_{j,\mathrm{xw}}(\phi_j(z)) = -dF_{\mathrm{tw}}\cos(\phi_j(z)) - dF_{\mathrm{rw}}\sin(\phi_j(z)) \\ dF_{j,\mathrm{yw}}(\phi_j(z)) = +dF_{\mathrm{tc}}\sin(\phi_j(z)) - dF_{\mathrm{rw}}\cos(\phi_j(z)). \end{cases} \tag{5}$$

C. Stress Distribution on Tool Flank

The friction force and press force on unit flank length can be expressed as

$$\begin{cases} F_{\mathrm{tw}}(VB) = \displaystyle\int_0^{VB} \tau(x)dx \\ F_{\mathrm{rw}}(VB) = \displaystyle\int_0^{VB} \sigma(x)dx \end{cases} \tag{6}$$

wherein $\tau(x)$and $\sigma(x)$ are the stresses tangential and normal to tool flank, x is the distance to tool edge, and VB is milling tool flank wear width.

The contact area of worn flank and workpiece is divided into plastic flow region and elastic contact region, according to the studies of Lapsley and Waldorf [23], [24], as shown in Fig. 2. The studies about the contact of worn flank and workpiece are based on material flow and slip-line field.

The tangential and normal stresses are all constant values τ_0 and σ_0 in plastic flow region, and distributed in accordance with quadratic form in the elastic contact region [25]–[28]. The distribution of stresses is shown in Fig. 3.

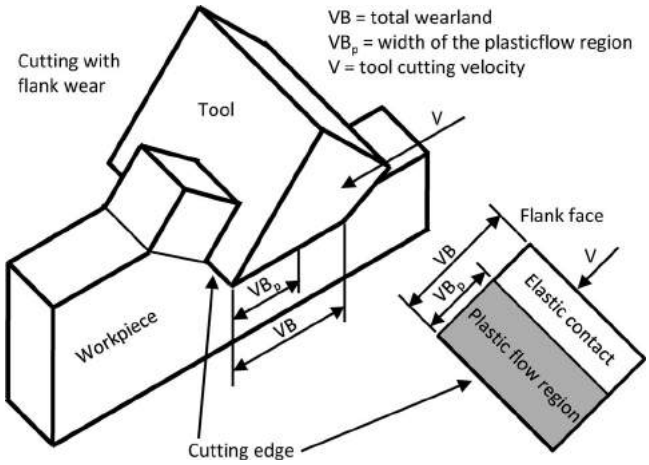

Fig. 2. Plastic flow region and elastic contact region.

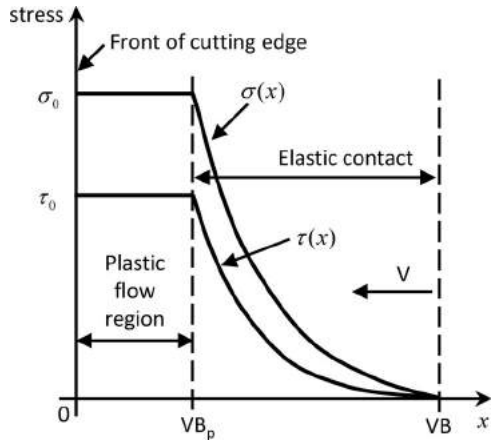

Fig. 3. Distribution of stresses on worn tool flank.

When $0 < x < VB_P$, in plastic flow region, the stress distribution is

$$\begin{cases} \tau(x) = \tau_0 \\ \sigma(x) = \sigma_0 \end{cases}. \tag{7}$$

When $VB_P < x < VB$, in elastic contact region, the stress distribution is

$$\begin{cases} \tau(x) = \tau_0 \cdot \left(\dfrac{VB - x}{VB - VB_P}\right)^2 \\ \sigma(x) = \sigma_0 \cdot \left(\dfrac{VB - x}{VB - VB_P}\right)^2. \end{cases} \tag{8}$$

Here VB_P is the boundary of plastic flow region and elastic contact region. When tool wear reaches a certain amount, the width of elastic contact region is maintained constant and the width of the plastic flow region increases along with the increasing of tool flank wear, according to the study of Smithey [29]. The expressions are:

when $VB < VB^*$,

$$VB_P = 0 \tag{9}$$

when $VB \geq VB^*$,

$$VB_P = VB - VB^* \tag{10}$$

wherein VB^* is the constant width of elastic contact region.

The friction and press forces on unit flank length are obtained through substituting (7), (10) into (6) and integrating.

when $VB < VB^*$,

$$\begin{cases} F_{\mathrm{tw}}(VB) = \dfrac{\tau_0}{3} \cdot VB \\ F_{\mathrm{rw}}(VB) = \dfrac{\sigma_0}{3} \cdot VB, \end{cases} \tag{11}$$

when $VB \geq VB^*$,

$$\begin{cases} F_{\mathrm{tw}}(VB) = \tau_0 \cdot \left(VB - \dfrac{2}{3} VB^* \right) \\ F_{\mathrm{rw}}(VB) = \sigma_0 \cdot \left(VB - \dfrac{2}{3} VB^* \right). \end{cases} \tag{12}$$

D. Resultant Force of Worn Tool

The resultant force on tool is the sum of shearing force and friction effect force, and it can be expressed as

$$\overrightarrow{F} = \overrightarrow{F_c} + \overrightarrow{F_w}. \tag{13}$$

The infinitesimal forces on infinitesimal tool pieces are integrated in the axial depth of milling, and then the shearing forces and the friction effect forces on each tooth can be calculated in O-XYZ coordinate system, the calculations are same as the study of Altintas [30]:

$$\begin{cases} F_{j,\mathrm{xc}}(\phi_j) = \dfrac{f}{4k_\beta} \times \\ \quad \{-K_{\mathrm{tc}} \cos 2\phi_j(z) + K_{\mathrm{rc}} [2\phi_j(z) - \sin 2\phi_j(z)]\}_{z_{j,1}(\phi_j)}^{z_{j,2}(\phi_j)} \\ F_{j,\mathrm{yc}}(\phi_j) = -\dfrac{f}{4k_\beta} \times \\ \quad \{K_{\mathrm{tc}} [2\phi_j(z) - \sin 2\phi_j(z)] + K_{\mathrm{rc}} \cos 2\phi_j(z)\}_{z_{j,1}(\phi_j)}^{z_{j,2}(\phi_j)} \\ F_{j,\mathrm{zc}}(\phi_j) = \dfrac{f}{k_\beta} \times [K_{\mathrm{ac}} \cos \phi_j(z)]_{z_{j,1}(\phi_j)}^{z_{j,2}(\phi_j)} \end{cases} \tag{14}$$

$$\begin{cases} F_{j,\mathrm{xw}}(\phi_j) = \dfrac{1}{k_\beta} \times \\ \quad \{F_{\mathrm{tw}}(VB) \sin \phi_j(z) - F_{\mathrm{rw}}(VB) \cos \phi_j(z)\}_{z_{j,1}(\phi_j)}^{z_{j,2}(\phi_j)} \\ F_{j,\mathrm{yw}}(\phi_j) = \dfrac{1}{k_\beta} \times \\ \quad \{F_{\mathrm{tw}}(VB) \cos \phi_j(z) + F_{\mathrm{rw}}(VB) \sin \phi_j(z)\}_{z_{j,1}(\phi_j)}^{z_{j,2}(\phi_j)} \end{cases} \tag{15}$$

wherein $k_\beta = \tan \beta / R$, β is helix angle of milling tool, R is radius of milling tool, $z_{j,1}(\phi_j)$ and $z_{j,2}(\phi_j)$ are the engagement limits of tool and workpiece.

When the cutting depth in the axial direction is not very large, i.e., a single tooth can be completely immersed into the workpiece material, the engagement limits of a tooth and workpiece can be expressed in three segments [30].

When $\phi_j \in [\theta_{j,1}, \theta_{j,1} + k_\beta \cdot a_p]$, cutting in to full tooth immersion:

$$\begin{cases} z_{j,1}(\phi_j) = 0 \\ z_{j,2}(\phi_j) = (\phi_j - \theta_{j,1}) / k_\beta. \end{cases}$$

When $\phi_j \in (\theta_{j,1} + k_\beta \cdot a_p, \theta_{j,2}]$, full tooth immersion:

$$\begin{cases} z_{j,1}(\phi_j) = 0 \\ z_{j,2}(\phi_j) = a_p. \end{cases}$$

When $\phi_j \in (\theta_{j,2}, \theta_{j,2} + k_\beta \cdot a_p]$, full immersion to complete cutting out:

$$\begin{cases} z_{j,1}(\phi_j) = (\phi_j - \theta_{j,2}) / k_\beta \\ z_{j,2}(\phi_j) = a_p \end{cases}$$

wherein $\theta_{j,1}$ is tooth entrance angle, $\theta_{j,2}$ is tooth exit angle, and a_p is axial cutting depth.

The resultant forces on each tooth can be expressed as

$$\begin{cases} F_{j,x}(\phi_j) = F_{j,\mathrm{xc}}(\phi_j) + F_{j,\mathrm{xw}}(\phi_j) \\ F_{j,y}(\phi_j) = F_{j,\mathrm{yc}}(\phi_j) + F_{j,\mathrm{yw}}(\phi_j) \\ F_{j,z}(\phi_j) = F_{j,\mathrm{zc}}(\phi_j). \end{cases} \tag{16}$$

III. Model Calibration and Validation

According to the aforementioned model, there is no friction effect force when the tool is not worn. Therefore, the shearing force coefficients can be calibrated through the average milling force when tool is fresh. The rubbing forces caused by other factors except tool flank wear are comparatively tiny, thus they are included in the shearing forces when calibrating the force model. In the same cutting condition but with different tool flank wears, the various friction and press forces on unit flank length can be calibrated through the differences between average milling forces with various flank wear and without flank wear. And then the stress distributions are obtained through (12) and (8).

A. Calculation of Average Milling Force on Single Tooth

Tool flank wear does not influence the axial milling force [19], therefore the average milling forces in *X* and *Y* directions are calculated in the range of immersion angle. The calculations are same as the study of Altintas [30]:

$$\begin{cases} \overline{F_{j,x}} = \overline{F_{j,\mathrm{xc}}} + \overline{F_{j,\mathrm{xw}}} \\ \overline{F_{j,y}} = \overline{F_{j,\mathrm{yc}}} + \overline{F_{j,\mathrm{yw}}} \end{cases}. \tag{17}$$

The average shearing forces per engagement angle are

$$\begin{cases} \overline{F_{j,\mathrm{xc}}} = \dfrac{1}{\theta_{j,2} - \theta_{j,1} + k_\beta \cdot a_p} \displaystyle\int_{\theta_{j,1}}^{\theta_{j,2} + k_\beta \cdot a_p} F_{j,\mathrm{xc}}(\phi_j) \cdot d\phi_j \\ \overline{F_{j,\mathrm{yc}}} = \dfrac{1}{\theta_{j,2} - \theta_{j,1} + k_\beta \cdot a_p} \displaystyle\int_{\theta_{j,1}}^{\theta_{j,2} + k_\beta \cdot a_p} F_{j,\mathrm{yc}}(\phi_j) \cdot d\phi_j. \end{cases}$$

TABLE I
EQUIPMENT AND MATERIAL OF EXPERIMENT

Item	Content
Machine tool	YHVT850Z four-axis CNC machine tool
Milling tool	Four teeth flat end milling tool, diameter 8 mm, helix angle 35°
Material	GH4169
Force measurement	Kistler 9255B piezoelectric dynamometer
Tool measurement	Reading microscope

The calculation results are

$$\begin{cases} \overline{F_{j,\mathrm{xc}}} = \dfrac{a_p \cdot f}{4 \cdot (\theta_{j,2} - \theta_{j,1} + k_\beta \cdot a_p)} \times \\ \quad [K_{\mathrm{tc}} \cdot \cos(2\phi_j) + K_{\mathrm{rc}} \cdot (\sin(2\phi_j) - 2\phi_j)]|_{\theta_{j,1}}^{\theta_{j,2}} \\ \overline{F_{j,\mathrm{yc}}} = \dfrac{a_p \cdot f}{4 \cdot (\theta_{j,2} - \theta_{j,1} + k_\beta \cdot a_p)} \times \\ \quad [K_{\mathrm{tc}} \cdot (2\phi_j - \sin(2\phi_j)) + K_{\mathrm{rc}} \cdot \cos(2\phi_j)]|_{\theta_{j,1}}^{\theta_{j,2}} . \end{cases} \tag{18}$$

The average friction effect forces per engagement angle are

$$\begin{cases} \overline{F_{j,\mathrm{xw}}} = \dfrac{1}{\theta_{j,2} - \theta_{j,1} + k_\beta \cdot a_p} \displaystyle\int_{\theta_{j,1}}^{\theta_{j,2} + k_\beta \cdot a_p} F_{j,\mathrm{xw}}(\phi_j) \cdot d\phi_j \\ \overline{F_{j,\mathrm{yw}}} = \dfrac{1}{\theta_{j,2} - \theta_{j,1} + k_\beta \cdot a_p} \displaystyle\int_{\theta_{j,1}}^{\theta_{j,2} + k_\beta \cdot a_p} F_{j,\mathrm{yw}}(\phi_j) \cdot d\phi_j . \end{cases}$$

The calculation results are

$$\begin{cases} \overline{F_{j,\mathrm{xw}}} = \dfrac{a_p}{\theta_{j,2} - \theta_{j,1} + k_\beta \cdot a_p} \times \\ \quad [-F_{\mathrm{tw}}(VB) \cdot \sin(\phi_j) + F_{\mathrm{rw}}(VB) \cdot \cos(\phi_j)]|_{\theta_{j,1}}^{\theta_{j,2}} \\ \overline{F_{j,\mathrm{yw}}} = \dfrac{a_p}{\theta_{j,2} - \theta_{j,1} + k_\beta \cdot a_p} \times \\ \quad [-F_{\mathrm{tw}}(VB) \cdot \cos(\phi_j) - F_{\mathrm{rw}}(VB) \cdot \sin(\phi_j)]|_{\theta_{j,1}}^{\theta_{j,2}} . \end{cases} \tag{19}$$

B. Calibration Experiment

The milling forces in *X* and *Y* directions are measured through milling tests, when the tool is without flank wear and with a series of flank wear. The experiment equipment are listed in Table I. These average milling forces with different flank wear are substituted into the aforesaid equations, the shearing force coefficients, a series of friction and press forces on unit flank length will be obtained by solving these equations, and then the stress distributions are obtained.

GH4169 alloy not only has high tensile strength, yield strength, endurance strength, and ductility, but also excellent performance of antifatigue, antioxidation, antiradiation, and anticorrosion. Because of the excellent comprehensive performance, it has become a key material in aerospace, nuclear energy and petrochemical, and the application in aero-engine is most typical.

The tool flank wear land can be seen through the reading microscope, the tool edge and the boundary of wear land are measured through adjusting the cross hairs of the microscope. The distance of the tool edge and the boundary of wear land is tool flank wear width.

Four milling tests are proposed according to the need of calibrating the milling force model. In the first test fresh tool is used, in the other three tests the tools with different flank wear are used, and the flank wear widths are 0.1, 0.2, and 0.3 mm, respectively. The conditions of the four tests are listed in Table II.

TABLE II
PROCESS PARAMETERS OF EXPERIMENT

No.	a_p (mm)	a_e (mm)	f (mm/Z)	V_c (m/min)	VB (mm)
1	0.5	1	0.04	60	0
2	0.5	1	0.04	60	0.1
3	0.5	1	0.04	60	0.2
4	0.5	1	0.04	60	0.3

Note: a_p is the axial cutting depth, a_e is the radial cutting depth.

TABLE III
AVERAGE MILLING FORCES IN DIFFERENT FLANK WEAR

No.	1		2		3		4	
	$\overline{F_x}$ (N)	$\overline{F_y}$ (N)	$\overline{F_x}$ (N)	$\overline{F_y}$ (N)	$\overline{F_x}$ (N)	$\overline{F_y}$ (N)	$\overline{F_x}$ (N)	$\overline{F_y}$ (N)
1	43.44	19.46	51.76	29.41	71.79	37.86	90.72	49.62
2	-	-	51.56	28.56	75.11	41.63	95.76	57.63
3	-	-	53.83	29.58	74.04	39.57	96.63	59.44
4	-	-	51.56	27.01	76.30	39.18	93.17	54.45
5	-	-	49.28	23.82	74.62	40.48	96.69	66.35

The test using fresh tool is used to calibrate the shearing force coefficients, so only one test result is adopted in the first test. In the other three tests, five test results are adopted respectively, the results are used to calculate the corresponding friction and press forces on unit flank length, and then the stress distributions are obtained through these friction and press forces on unit flank length.

C. Experiment Results and Data Processing

In these tests, the milling is always in single tooth engagement state, and there is no superimposition of multiple teeth milling forces. Therefore, the average milling forces could be obtained through calculating a single waveform of the forces.

The average milling forces of the four tests are listed in Table III.

The shearing force coefficients are obtained through substituting the average forces of the first test into (18) and solving the equations. The five average milling forces of the test 2, 3, and 4 subtract the average milling forces of the test 1 respectively, and then the corresponding average friction effect forces are obtained. The friction and press forces on unit flank length in different flank wear are calculated through substituting the average friction effect forces into (19) respectively. In (18) and (19), the axial cutting depth a_p is 0.5 mm, the feed rate per tooth f is 0.04 mm/Z, and $k_\beta = \tan\beta/R$ is 0.1751 mm^{-1}. The entrance and exit angles are calculated through the milling tool and cutting parameters, the entrance angle $\theta_{j,1}$ is 0, and the exit

TABLE IV
SHEARING FORCE COEFFICIENTS/FRICTION AND PRESS FORCES ON UNIT FLANK LENGTH

	0		0.1		0.2		0.3	
VB (mm)	K_{tc} (MPa)	K_{rc} (MPa)	$F_{\mathrm{tw}}(VB)$ (N/mm)	$F_{\mathrm{rw}}(VB)$ (N/mm)	$F_{\mathrm{tw}}(VB)$ (N/mm)	$F_{\mathrm{rw}}(VB)$ (N/mm)	$F_{\mathrm{tw}}(VB)$ (N/mm)	$F_{\mathrm{rw}}(VB)$ (N/mm)
1	4871.22	6127.56	9.78	28.07	45.85	62.42	76.91	102.95
2	-	-	10.03	26.09	49.92	73.19	81.23	124.22
3	-	-	14.07	30.12	49.30	67.91	81.62	128.80
4	-	-	11.29	22.76	54.46	68.90	78.25	115.30
5	-	-	8.99	14.08	49.80	70.33	76.16	143.67

angle $\theta_{j,2}$ is 0.7227. The shearing force coefficients, friction and press forces on unit flank length in different flank wear are listed in Table IV.

The relationship of friction and press forces on unit flank length and flank wear width is piecewise linear according to (11) and (12). First, the friction and press forces on unit flank length of flank wear width 0.1, 0.2, and 0.3 mm are fitted according to (12), the τ_0, σ_0, and VB^* are solved, and then (11) is calculated through the solved VB^*. Finally, if the tool wear data used for fitting meet $VB \geq VB^*$ is validated, if meet, the result is valid, if not, need to fit the friction and press forces on unit flank length of flank wear width 0.2 and 0.3 mm again according to (12).

The two lines of friction and press force on unit flank length have the same intercept on VB-axis, according to (12). Therefore, the two lines cannot be fitted separately, the total residual error of the two lines should be considered comprehensively, and the principle of least square is adopted to fit the two lines, to ensure that the two fitted lines have the same intercept on VB-axis. The total residual error is

$$\begin{aligned} E = & \left[\boldsymbol{F}_{\mathrm{tw}T} - \tau_0 \cdot \left(\boldsymbol{V}B_T - \frac{2}{3}VB^* \cdot \boldsymbol{e}\right)\right]^T \\ & \cdot \left[\boldsymbol{F}_{\mathrm{tw}T} - \tau_0 \cdot \left(\boldsymbol{V}B_T - \frac{2}{3}VB^* \cdot \boldsymbol{e}\right)\right] \\ & + \left[\boldsymbol{F}_{\mathrm{rw}T} - \sigma_0 \cdot \left(\boldsymbol{V}B_T - \frac{2}{3}VB^* \cdot \boldsymbol{e}\right)\right]^T \\ & \cdot \left[\boldsymbol{F}_{\mathrm{rw}T} - \sigma_0 \cdot \left(\boldsymbol{V}B_T - \frac{2}{3}VB^* \cdot \boldsymbol{e}\right)\right]. \end{aligned} \tag{20}$$

wherein E is the total residual error of fitting. $\boldsymbol{V}B_T$ is the tool wear vectors, and is a column vector composed by the tool flank wear widths of the 15 test data. $\boldsymbol{F}_{\mathrm{tw}T}$ and $\boldsymbol{F}_{\mathrm{rw}T}$ are the calculated friction and press force column vectors, respectively, and are calculated through the 15 tested average milling force data. $\boldsymbol{e} = \left[1 \cdots 1\right]^T$, $\boldsymbol{e}$ has 15 elements, and all the elements are 1. τ_0, σ_0, and VB^* are the parameters to be solved.

The two fitted lines should make the total residual error to meet the minimum, according to the principle of least square. The tool wear model shows that the minimum of the total residual error exists, and the total residual error is meeting the minimum when all the partial derivatives are zero respectively, that the following equations must be satisfied:

$$\begin{cases} \dfrac{\partial E}{\partial \tau_0} = 2\left[\dfrac{2}{3}VB^* \cdot \boldsymbol{e} - \boldsymbol{V}\mathbf{B}_T\right]^T \cdot \\ \qquad \left[\boldsymbol{F}_{\mathrm{tw}T} - \tau_0 \cdot \left(\boldsymbol{V}\mathbf{B}_T - \dfrac{2}{3}VB^* \cdot \boldsymbol{e}\right)\right] = 0 \\ \dfrac{\partial E}{\partial \sigma_0} = 2\left[\dfrac{2}{3}VB^* \cdot \boldsymbol{e} - \boldsymbol{V}\mathbf{B}_T\right]^T \cdot \\ \qquad \left[\boldsymbol{F}_{\mathrm{rw}T} - \sigma_0 \cdot \left(\boldsymbol{V}\mathbf{B}_T - \dfrac{2}{3}VB^* \cdot \boldsymbol{e}\right)\right] = 0 \\ \dfrac{\partial E}{\partial VB^*} = \dfrac{4}{3}\tau_0 \cdot \boldsymbol{e}^T \cdot \left[\boldsymbol{F}_{\mathrm{tw}T} - \tau_0 \cdot \left(\boldsymbol{V}\mathbf{B}_T - \dfrac{2}{3}VB^* \cdot \boldsymbol{e}\right)\right] \\ \qquad + \dfrac{4}{3}\sigma_0 \cdot \boldsymbol{e}^T \cdot \left[\boldsymbol{F}_{\mathrm{rw}T} - \sigma_0 \cdot \left(\boldsymbol{V}\mathbf{B}_T - \dfrac{2}{3}VB^* \cdot \boldsymbol{e}\right)\right] = 0 \end{cases} \tag{21}$$

wherein the specific values of $\mathbf{F}_{\mathrm{tw}T}$ and $\mathbf{F}_{\mathrm{rw}T}$ are provided in Table IV, and they are substituted into (21) respectively, two solutions are obtained through solving the equations, they are

$$\begin{cases} \tau_{0,1} = 329.0843 \\ \sigma_{0,1} = 501.0119 \\ VB_1^* = 0.0857 \end{cases} \quad \begin{cases} \tau_{0,2} = 10.9346 \\ \sigma_{0,2} = -7.1823 \\ VB_2^* = 0.3700. \end{cases}$$

The second solution does not accord with the physical meaning of the wear model, thus the second solution is discarded, and the first solution is selected, the result is proposed by (22)

$$\begin{cases} \tau_0 = 329.0843 \\ \sigma_0 = 501.0119 \\ VB^* = 0.0857. \end{cases} \tag{22}$$

The result in (22) is substituted into (11) and (12), to calculate the relationships of friction and press force on unit flank length and tool flank wear width, the results arewhen $VB < 0.0857$,

$$\begin{cases} F_{\mathrm{tw}}(VB) = 109.6948 \times VB \\ F_{\mathrm{rw}}(VB) = 167.0040 \times VB \end{cases} \tag{23}$$

when $VB \geq 0.0857$,

$$\begin{cases} F_{\mathrm{tw}}(VB) = 329.0843 \times (VB - 0.0572) \\ F_{\mathrm{rw}}(VB) = 501.0119 \times (VB - 0.0572). \end{cases} \tag{24}$$

The results show that the boundary of occurring plastic flow is 0.0857 mm, the tool flank wear widths used in the fitting are

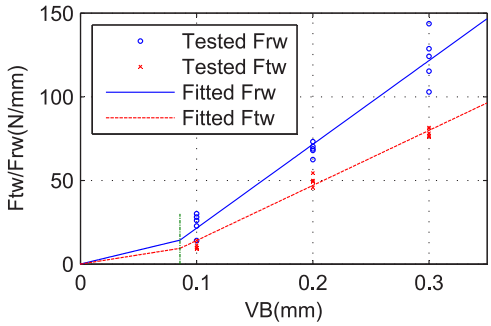

Fig. 4. Fitting results of F_{tw} and F_{rw}.

all greater than the boundary, therefore the results are valid. The fitting results are shown in Fig. 4.

In the figure it can be seen that, the friction and press forces on unit flank length are increased with the increasing of tool flank wear. The short green vertical line in the figure is the boundary of occurring plastic flow, $VB^* = 0.0857$. When $VB < 0.0857$, only elastic contact occurs, and plastic flow does not occur on the tool flank. When $VB \geq 0.0857$, the elastic contact and plastic flow occur simultaneously on the tool flank. The piecewise linear relationships occur transition at the boundary.

D. Milling Force Model Validation

The milling forces of the tool flank wear width 0.1, 0.2, and 0.3 mm are calculated through corresponding shearing force coefficients and (24). And then the calculated results and the measured data are compared, the results are shown in Fig. 5.

In the figures it can be seen that, the calculated milling forces are accurate, and the wave profiles of calculated and measured milling forces are close. However, at the cutting in part of tool flank wear width 0.1 0.2 mm, and at whole the immersed angle of tool flank wear width 0.3 mm, the measured milling forces are more fluctuant. The fluctuations are related to the cutting in and the tool wear state. But, the factors of the fluctuations are complex, such fluctuations do not be predicted in this model.

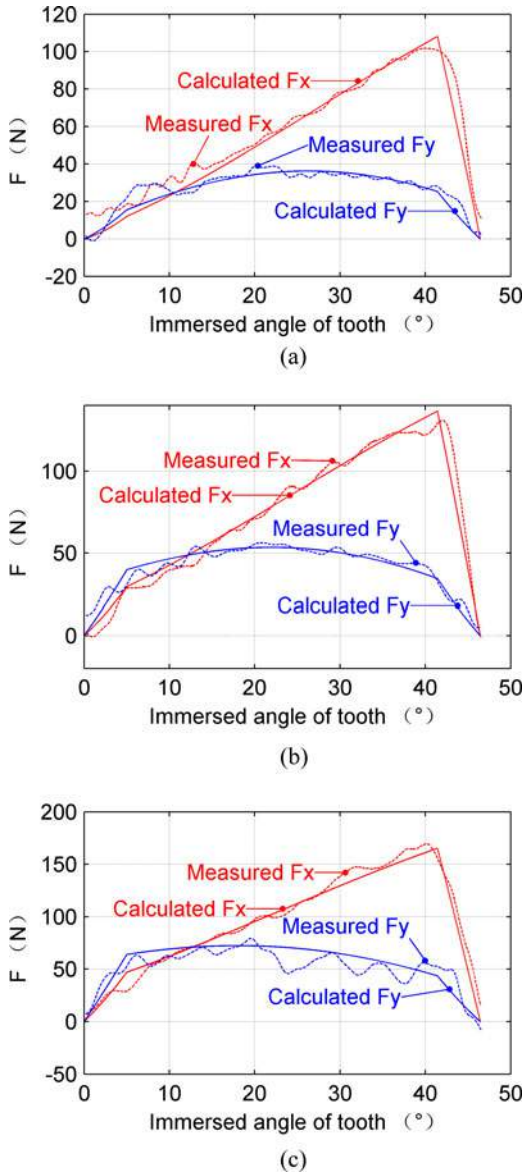

Fig. 5. Comparisons of calculated and measured milling force. (a) $VB = 0.1$ mm. (b) $VB = 0.2$ mm. (c) $VB = 0.3$ mm.

IV. Milling Tool Wear Recognition

A. Feature Vector of Milling Forces

The milling forces of various tool wear are calculated according to the aforementioned milling force model. Various features of the milling force vector are calculated, and constitute the feature vector of milling force. The relationship of feature vector and tool flank wear width is investigated, and the relationship is used to recognize the milling tool flank wear through monitoring the forces in actual milling process. The simulated milling forces of various tool wears are shown in Fig. 6.

In the first two figures, the curves represent the milling forces of different tool flank wear widths, the corresponding tool wear widths from small to large are the values from 0 to 0.35 mm, the spacing is 0.01 mm, and the total number is 36. In the last figure, the level direction is F_x, and the vertical direction is F_y, the curves represent the corresponding milling force vectors to the aforementioned two figures. The milling forces increase from zero with the increasing of tooth immersed angle, and decrease back to zero finally. In the stage from start of cutting in to full tooth immersion, the forces in *Y*-direction increase faster and the force vectors rise approximately linearly. In the stage of full tooth immersion, the forces in *X*-direction increase unceasingly and the forces in *Y*-direction vary smaller, the force vectors show curves. In the stage from full immersion to complete cutting out, the forces in *X* and *Y* directions decrease rapidly, and the force vectors back to zero approximately linearly. When the tool flank wear is growing, the whole patterns of milling forces are similar; the amplitudes are becoming larger and larger; in the frequency domain, the signal of base frequency will become larger and larger. These evolutions are corroborated by the experiment results in Fig. 5.

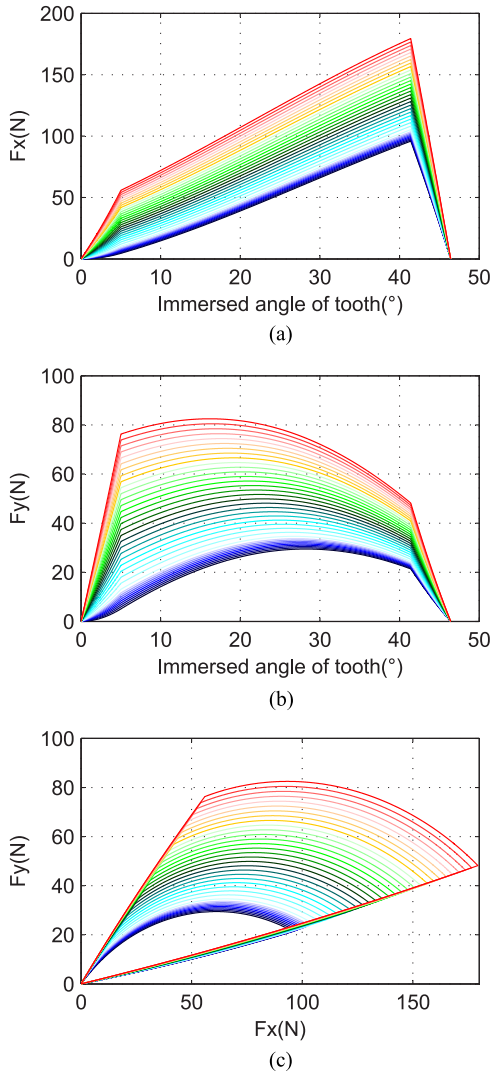

Fig. 6. Simulated milling forces of various tool wears. (a) Milling forces in *X*-direction. (b) Milling forces in *Y*-direction. (c) Milling force vectors.

According to the simulated milling forces, the relationships of the following features and tool wear are investigated.

1) SDRF: the standard deviation of resultant force vector in *XY* plane (N);
2) SDDRF: the standard deviation of the derivative of resultant force vector in *XY* plane (N/s);
3) ALOW: the area of resultant force vector in *XY* plane under the spectrum in the low frequency range (from once to fourfold tooth-passing frequency);
4) RSF2-1: the ratio of spectral force at twice and once the tooth-passing frequency;
5) RSF3-2: the ratio of spectral force at thrice and twice the tooth-passing frequency.

These milling force features of various tool wear are calculated according to the simulated forces respectively, and graphs of these features are drawn in Fig. 7.

In Fig. 7 it can be seen that, each of the milling force features varies obviously, when the tool wear width increasing. The force

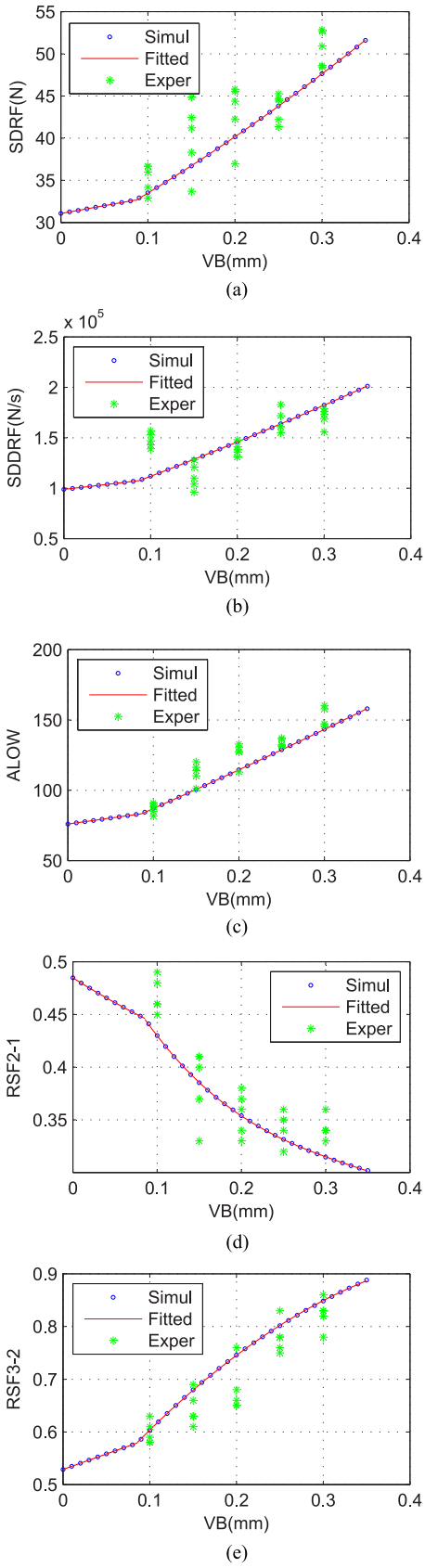

Fig. 7. Milling force features. (a) Fitting curve of SDRF. (b) Fitting curve of SDDRF. (c) Fitting curve of ALOW. (d) Fitting curve of RSF2-1. (e) Fitting curve of RSF3-2.

feature RSF2-1 decreases with the increasing of tool wear, the other force features all increase, and the turning point occurs obviously at the boundary of $VB^* = 0.0857$.

Each of the milling force features is fitted piecewise, according to the calculated data of features, and the fitted result is a mapping relationship of tool flank wear and milling force features, the results are

$$\text{SDRF: } p_1(VB) = \begin{cases} 18.5900 \cdot VB + 31.0700 \\ 38.8800 \cdot VB^2 + 55.1200 \cdot VB + 27.5900 \end{cases}$$

$$\text{SDDRF: } p_2(VB) = \begin{cases} 10^4 \cdot (3.9360 \cdot VB^2 + 9.6680 \cdot VB + 9.8840) \\ 10^5 \cdot (1.1640 \cdot VB^2 + 3.0600 \cdot VB + 8.0020) \end{cases}$$

$$\text{ALOW: } p_3(VB) = \begin{cases} 85.1836 \cdot VB + 75.9679 \\ 59.1485 \cdot VB^2 + 257.8232 \cdot VB + 60.6242 \end{cases}$$

$$\text{RSF2} - 1\text{: } p_4(VB) = \begin{cases} 0.6148 \cdot VB^2 - 0.5029 \cdot VB + 0.4847 \\ -4.3428 \cdot VB^3 + 4.4697 \cdot VB^2 \\ y - 1.7976 \cdot VB + 0.5691 \end{cases}$$

$$\text{RSF3} - 2\text{: } p_5(VB) = \begin{cases} 0.5865 \cdot VB + 0.5289 \\ -1.9047 \cdot VB^2 + 1.9905 \cdot VB + 0.4235. \end{cases}$$

The fitted features are combined into the feature vector of milling force vector, the expression of the feature vector is

$$\boldsymbol{P}(VB) = \begin{bmatrix} p_1(VB) \\ \vdots \\ p_5(VB) \end{bmatrix}. \tag{25}$$

B. Milling Tool Flank Wear State Recognition

The components of the milling force feature vector i.e., the force features are sensitive to the tool flank wear width, and have been fitted in the polynomial form of tool flank wear width. Therefore, the tool flank wear state can be recognized through the feature vector $\boldsymbol{P}(VB)$ of the actual milling force vector. The recognition process of tool flank wear is to calculate the tool flank wear VB_t, to make the weighted distance of the feature vector $\boldsymbol{P}(VB_t)$ and the actual feature vector $\boldsymbol{P}_t$ monitored in actual machining reach the minimum.

The weighted distance of the corresponding feature vector $\boldsymbol{P}(VB)$ of arbitrary tool wear VB and the actual feature vector $\boldsymbol{P}_t$ monitored in actual machining can be expressed as

$$D = \sqrt{(\boldsymbol{P}(VB) - \boldsymbol{P}_t)^T \times \boldsymbol{W} \times (\boldsymbol{P}(VB) - \boldsymbol{P}_t)}. \tag{26}$$

wherein D is the weighted distance. $\boldsymbol{W}$ is the weight matrix of the components in force feature vector. In $\boldsymbol{W}$, the elements on main diagonal are weight coefficient, they are expressed as vector $\boldsymbol{w}$, and the other elements are 0. The elements of $\boldsymbol{w}$ are inversely proportional to the square of the range of the corresponding component in force feature vector. The ranges of the components in force feature vector are obtained from the fitted results of the force features, they are

$$[20.52 \;\; 1.024 \times 10^5 \;\; 82.04 \;\; 0.1829 \;\; 0.3594].$$

The square of them are

$$[421.2 \;\; 1.048 \times 10^{10} \;\; 6730 \;\; 0.03346 \;\; 0.1292 \;].$$

The reciprocal of them are

$$[2.374 \times 10^{-3} \;\; 9.546 \times 10^{-11} \;\; 1.486 \times 10^{-4} \;\; 29.88 \;\; 7.740].$$

$\boldsymbol{w}$ is the unitization of them, and $\boldsymbol{w}$ is

$$\boldsymbol{w} = [6.3105 \times 10^{-5} \;\; 2.5371 \times 10^{-12} \;\; 3.9490 \times 10^{-6} \;\; 0.7942 \;\; 0.2057].$$

Calculating the actual tool flank wear VB_t is to solve the VB when the weighted distance D is reaching the minimum. According to mathematical method, when $\frac{dD}{dVB} = 0$, D reaches the minimum. Therefore, the VB_t can be obtained through solving (27), and then the tool flank wear width is recognized:

$$\frac{dD}{dVB} = \frac{1}{D} \times (\boldsymbol{P}(VB) - \boldsymbol{P}_t)^T \times \boldsymbol{W} \times \frac{d\boldsymbol{P}(VB)}{dVB} = 0. \tag{27}$$

wherein $\frac{d\boldsymbol{P}(VB)}{dVB}$ is the derivative vector of the components of $\boldsymbol{P}(VB)$ to VB.

TABLE V
PROCESS PARAMETERS OF TOOL WEAR RECOGNITION EXPERIMENT

a_p (mm)	a_e (mm)	f (mm/Z)	V_c (m/min)
0.5	1	0.04	60

TABLE VI
AVERAGE MILLING FORCE FEATURES

VB_{real} (mm)	SDRF (N)	SDDRF (10^5 N/s)	ALOW (N/s)	RSF2-1	RSF3-2
0.1	35.28	1.48	87.21	0.47	0.60
0.15	40.12	1.12	112.44	0.38	0.64
0.2	43.00	1.39	126.21	0.36	0.68
0.25	43.62	1.66	133.82	0.34	0.78
0.3	50.70	1.71	151.61	0.34	0.82

V. VERIFICATION EXPERIMENTS OF TOOL WEAR RECOGNITION

The experiments are performed on YHVT850Z four-axis CNC machine tool. The equipment and material are same as Table I. Up milling is used in the experiments. The process parameters are same as the calibration experiment, and shown in Table V.

In the experiment, the tool flank wear widths are measured in a fixed cutting length interval, the milling forces are

TABLE VII
STATISTICAL ANALYSIS OF RECOGNITION RESULTS

VB_{real} (mm)	Average VB_{calc} (mm)	Absolute error (mm)	Relative error	Standard deviation (mm)	95% confidence interval (mm)	Interval width (mm)
0.1	0.1013	0.0013	1.30%	0.0066	0.0931–0.1095	0.0164
0.15	0.1519	0.0019	1.27%	0.0043	0.1466–0.1572	0.0106
0.2	0.2011	0.0011	0.55%	0.0082	0.1910–0.2112	0.0202
0.25	0.2495	0.0005	0.20%	0.0118	0.2349–0.2641	0.0292
0.3	0.3019	0.0019	0.63%	0.0112	0.2880–0.3158	0.0278

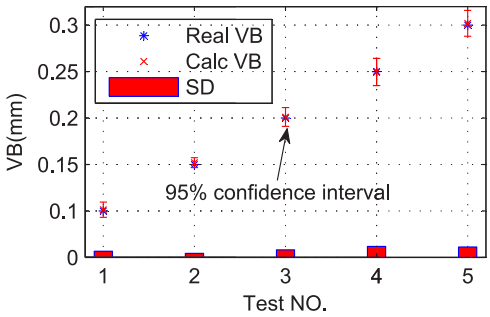

Fig. 8. Comparison of recognition results and actual tool flank wears.

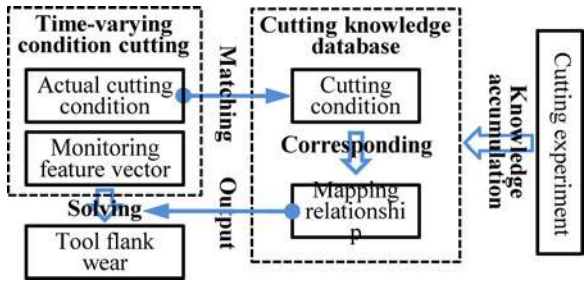

Fig. 9. Tool flank wear online recognition in time-varying cutting condition.

monitored, when tool flank wear width is 0.1, 0.15, 0.2, 0.25, and 0.3 mm. Five milling force waveforms are extracted randomly from each monitored milling forces. The feature vectors of these milling force waveforms are calculated, and substituted into (27), and then the recognized tool wear widths VB_{calcu} are obtained through solving (27). The force features from experiment are drawn in Fig. 7. The average force feature vectors are listed in Table VI.

In the recognition, the recognized results of same actual tool wear have some differences, and it is difficult to give an accurate recognition result. Therefore, the average of five recognitions and confidence interval are adopted to indicate the recognition result. The averages, standard deviations, and 95% confidence intervals of the different recognized results are calculated, and they are listed in Table VII.

In the tables, VB_{real} is the real tool flank wear width from measurement, and VB_{calc} indicates the calculated tool flank wear width.

The comparison of the confidence intervals of recognized tool wears and the actual tool wears are shown in Fig. 8. In the figure, SD is the standard deviation.

It can be seen from the results, the errors of the average recognitions are small, and the variations of the errors are small. The minimum absolute error is 0.0005 mm, the maximum absolute error is 0.0019 mm, the minimum relative error is 0.20%, and the maximum relative error is 1.30%. The relative error of recognition is relatively greater, when the actual tool flank wear width is 0.1 mm. The main reason is that the actual tool flank wear width is small, so that the relative error is amplified in the calculation. The minimum standard deviation of five recognitions is 0.0043 mm, and the maximum standard deviation is 0.0118 mm. The 95% confidence intervals of the tool wear recognitions are calculated, and all the confidence intervals contain the corresponding actual tool flank wear width. Therefore, using of the confidence interval to represent the recognized tool wear can describe the actual tool flank wear more accurately.

The aforementioned analysis shows that, the milling tool flank wear can be recognized accurately and efficiently through the relationship between milling force vector and tool flank wear.

VI. APPLICATION ON MONITORING ONLINE

The aforementioned recognition method applies to only the certain cutting condition. In a time-varying cutting condition, this recognition method needs the support of a cutting knowledge database. In a series of cutting conditions, the force model coefficients are calibrated through cutting experiments, and the mapping relationships of tool flank wear and the feature vector of milling force are fitted, and then the mapping relationships are stored into the cutting knowledge database. The cutting condition contains workpiece material, milling tool information, cutting type, and cutting parameters.

In the time-varying cutting condition, the tool flank wear online recognition contains three steps: 1) Matching the actual cutting condition and the cutting condition in cutting knowledge database. 2) Obtaining the mapping relationship of tool flank wear and feature vector corresponding to the actual cutting condition from the cutting knowledge database. 3) Solving the tool flank wear according to the monitored feature vector of milling force, through the obtained mapping relationship. The recognition process is shown in Fig. 9.

The tool flank wear online recognition is achieved, the automated and intelligent machining process can make decision according to the tool wear state, to adjust the using strategies of tool and the process parameters, or to give an alarm of changing tool or change tool automatically.

VII. Conclusion

The following conclusions can be drawn.

1) In the simulations of milling force features, the turning points occurred in force features with the increasing of tool flank wear. The turning points were caused by the occurring of plastic flow region, according to the friction effect force model.
2) The milling force model of worn tool could predict milling forces with a series of tool flank wear effectively. However, there were still some errors. The high-frequency fluctuations could not be predicted in this force model. The vibration of tool was the main reason of the high-frequency fluctuations. The force errors in the first five degrees of immersion were mainly caused by the chips attaching to workpiece, and they were not considered in this force model. The errors would bring some uncertain influences on tool flank wear recognition.
3) In Fig. 7 the force features from experiment had biggish errors comparing with the simulated force features, however the recognitions using the feature vector comprising multiple milling force features achieved a high accuracy. The feature vector reduced the influence of uncertain factors in a single force feature, and the recognition accuracy was improved effectively. Therefore, using the milling force feature vector to recognize tool wear state had a higher stability, robustness and recognition accuracy.
4) It could be seen that, the averages of five recognitions had the obviously small errors, and the variations of the errors were small. The 95% confidence intervals of tool wear recognitions were narrow, the interval ranges were all less than 0.03 mm, and the actual tool flank wears were all included in the corresponding confidence interval of recognitions. Therefore, using the confidence interval to represent the recognition result was more accurate and reliable.
5) The establishment of the cutting knowledge database needs a large number of cutting experiments to obtain the model coefficients and the mapping relationships. This will be a study focus of the proposed method. Other recognition approaches of flaking and fracturing can also be developed, and combined with this approach to form a perfect solution of tool condition monitoring, which provides a technical support for the highly automated and intelligent machining process.

References

[1] H. Z. Li, H. Zeng, and X. Q. Chen, "An experimental study of tool wear and cutting force variation in the end milling of Inconel 718 with coated carbide inserts," *J. Mater. Process. Tech.*, vol. 180, no. 1–3, pp. 296–304, Dec. 2006.

[2] X. Q. Chen and H. Z. Li, "Development of a tool wear observer model for online tool condition monitoring and control in machining nickel-based alloys," *Int. J. Adv. Manuf. Tech.*, vol. 45, no. 7–8, pp. 786–800, Dec. 2009.

[3] M. B. Said, K. Saï, and W. B. Saï, "An investigation of cutting forces in machining with worn ball-end mill," *J. Mater. Process. Tech.*, vol. 209, no. 7, pp. 3198–3217, Apr. 2009.

[4] C. Zhang, X. H. Liu, J. W. Fang, and L. S. Zhou, "A new tool wear estimation method based on shape mapping in the milling process," *Int. J. Adv. Manuf. Tech.*, vol. 53, no. 1–4, pp. 121–130, Mar. 2011.

[5] C. Zhang and J. L. Zhang, "On-line tool wear measurement for ball-end milling cutter based on machine vision," *Comput. Ind.*, vol. 64, no. 6, pp. 708–719, Aug. 2013.

[6] J. A. Ghani, M. Rizal, M. Z. Nuawi, C. H. C. Haron, and R. Ramli, "Statistical analysis for detection cutting tool wear based on regression model," in *Proc. Int. MultiConf. Eng. Comput. Scientists*, Hong Kong, China, 2010, pp. 1784–1788.

[7] Y. Choi, R. Narayanaswami, and A. Chandra, "Tool wear monitoring in ramp cuts in end milling using the wavelet transform," *Int. J. Adv. Manuf. Tech.*, vol. 23, no. 5–6, pp. 419–428, Mar. 2004.

[8] G. F. Wang, C. Liu, Y. H. Cui, and X. L. Feng. (2013, Jul.). Tool wear monitoring based on cointegration modeling of multisensory information. *Int. J. Comput. Integr. Manuf.* [Online]. *27(5)*, pp. 1–9. Available: http://www.tandfonline.com/doi/abs/10.1080/0951192X.2013.814162

[9] S. E. Oraby and D. R. Hayhurst, "Tool life determination based on the measurement of wear and tool force ratio variation," *Int. J. Mach. Tool. Manuf.*, vol. 44, no. 12–13, pp. 1261–1269, Oct. 2004.

[10] B. Kaya, C. Oysu, H. M. Ertunc, and H. Ocak, "A support vector machine-based online tool condition monitoring for milling using sensor fusion and a genetic algorithm," *Proc. Institution Mech. Eng. Part B: J. Eng. Manuf.*, vol. 226, no. 11, pp. 1808–1818, Nov. 2012.

[11] Z. Uros, C. Franc, and K. Edi, "Adaptive network based inference system for estimation of flank wear in end-milling," *J. Mater. Process. Tech.*, vol. 209, no. 3, pp. 1504–1511, Feb. 2009.

[12] E. T. Esfahani, S. Wang, and V. Sundararajan, "Multisensor wireless system for eccentricity and bearing fault detection in induction motors," *IEEE/ASME Trans. Mechatronics*, vol. 19, no. 3, pp. 818–826, Jun. 2014.

[13] R. G. Montague, C. Bingham, and K. Atallah, "Magnetic gear pole-slip prevention using explicit model predictive control," *IEEE/ASME Trans. Mechatronics*, vol. 18, no. 5, pp. 1535–1543, Oct. 2013.

[14] H. Purwins, B. Barak, A. Nagi, R. Engel, U. Hockele, A. Kyek, S. Cherla, B. Lenz, G. Pfeifer, and K. Weinzierl, "Regression methods for virtual metrology of layer thickness in chemical vapor deposition," *IEEE/ASME Trans. Mechatronics*, vol. 19, no. 1, pp. 1–8, Feb. 2014.

[15] S. K. Choudhury and S. Rath, "In-process tool wear estimation in milling using cutting force model," *J. Mater. Process. Tech.*, vol. 99, no. 1–3, pp. 113–119, Mar. 2000.

[16] Y. J. Cui, "Tool wear monitoring for milling by tracking cutting force model coefficients," M.S. thesis, Dept. Mech. Eng., Univ. of New Hampshire, Durham, USA, 2008.

[17] H. Shao, H. L. Wang, and X. M. Zhao, "A cutting power model for tool wear monitoring in milling," *Int. J. Mach. Tool. Manuf.*, vol. 44, no. 14, pp. 1503–1509, Nov. 2004.

[18] E. Kuljanic and M. Sortino, "TWEM, a method based on cutting forces—monitoring tool wear in face milling," *Int. J. Mach. Tool. Manuf.*, vol. 45, no. 1, pp. 29–34, Jan. 2005.

[19] A. Sarhan, R. Sayed, A. A. Nassr, and R. M. El-Zahry, "Interrelationships between cutting force variation and tool wear in end-milling," *J. Mater. Process. Tech.*, vol. 109, no. 3, pp. 229–235, Feb. 2001.

[20] P. Bhattacharyya, D. Sengupta, and S. Mukhopadhyay, "Cutting force-based real-time estimation of tool wear in face milling using a combination of signal processing techniques," *Mech. Syst. Signal Process.*, vol. 21, no. 6, pp. 2665–2683, Aug. 2007.

[21] B. Y. Lee and Y. S. Tarng, "Application of the discrete wavelet transform to the monitoring of tool failure in end milling using the spindle motor current," *Int. J. Adv. Manuf. Tech.*, vol. 15, no. 4, pp. 238–243, Apr. 1999.

[22] T. M. Teitenberg, A. E. Bayoumi, and G. Yuscesan, "Tool wear modeling through an analytic mechanistic model of milling processes," *Wear*, vol. 154, no. 2, pp. 287–304, May 1992.

[23] J. T. Lapsley, R. C. Grassi, and E. G. Thomsen, "Correlation of plastic deformation during metal cutting with tensile properties of the work material," *Trans. Amer. Soc. Mech. Eng.*, vol. 72, pp. 979–986, 1950.

[24] D. J. Waldorf, "Shearing, ploughing, and wear in orthogonal machining," Ph.D. dissertation, Dept. Mech. Sci. Eng., Univ. of Illinois at Urbana-Champaign, Champaign, US, 1996.

[25] E. Usui, T. Shirakashi, and T. Kitagawa, "Analytical prediction of cutting tool wear," *Wear*, vol. 100, no. 1–3, pp. 129–151, Dec. 1984.

[26] S. G. Kapoor, R. E. DeVor, R. Zhu, R. Gajjela, G. Parakkal, and D. Smithey, "Development of mechanistic models for the prediction of machining performance: Model-building methodology," *Mach. Sci. Technol.*, vol. 2, no. 2, pp. 215–238, 1998.
[27] A. Ber and M. Y. Friedman, "On the mechanism of flank wear in carbide tools," *Ann. CIRP*, vol. 15, pp. 211–216, 1967.
[28] D. J. Waldorf, S. G. Kapoor, and R. E. DeVor, "Worn tool forces based on ploughing stresses," *Trans. North Amer. Manuf. Res. Inst. Soc. Manuf. Eng.*, vol. 27, pp. 165–170, Jan. 1999.
[29] D. W. Smithey, S. G. Kapoor, and R. E. DeVor, "A new mechanistic model for predicting worn tool cutting forces," *Mach. Sci. Technol.*, vol. 5, no. 1, pp. 23–42, 2001.
[30] Y. Altintas, "Mechanics of metal cutting," in *Manufacturing Automation: Metal Cutting Mechanics, Machine Tool Vibrations, and CNC Design*, 1st ed., New York, NY, USA: Cambridge University Press, 2000, pp. 4–62.

Yongfeng Hou was born in 1986. He received the B.S. degree in advanced manufacturing engineering from Northwestern Polytechnical University, Xi'an, China, in 2010. He is currently working toward the doctoral degree in advanced manufacturing engineering at Northwestern Polytechnical University, Xi'an, China.

His research interests include CAD/CAM, fault detection and diagnosis in manufacturing, intelligent process automation, mechatronics in manufacturing processes, and smart machining.

Dinghua Zhang was born in 1958. He received the B.S., M.S., and Ph.D. degrees in advanced manufacturing engineering from Northwestern Polytechnical University, Xi'an, China, in 1981, 1984, and 1989, respectively.

He was with Cornell University, Ithaca, NY and Rochester University, Rochester, NY as a Visiting Scholar in 1996–1999. He is currently the Director of the Key Laboratory of Contemporary Design and Integrated Manufacturing Technology, Ministry of Education, Northwestern Polytechnical University, Xi'an, China. His research interests include smart NC machining, mold design and manufacturing, digital manufacturing system, and digital testing.

Prof. Zhang is a member of ASME, Chinese Mechanical Engineering Society, and Chinese Aerospace Society. He has received the following awards: 1) Development and Application of Precision Five-Axis NC Machining Technology for Turbine Blisk of Aero-Engine, Second Prize of National Scientific and Technological Progress, 2006; 2) Development and Application of a CAD/CAM System for Turbo-machinery, Third Prize of National Scientific and Technological Progress, 1992; 3) NPU—an Interactive Computer Graphics NC programming System, First Prize of Shaanxi Scientific and Technological Progress, 1991; 4) Precision Casting Mold CAD/CAM system for Hollow Turbine-Blade of Aero-engine, First Prize of Scientific and Technological Progress (Aero-Industrial Ministry, P. R. China), 1999; 5) Accurate and Efficient Calibration Method for a Selenium Flat-panel Detector-based Volume Tomographic Angiography Imaging System, SPIE Medical Imaging'99 Honorable mention Award.

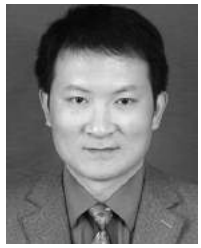

Baohai Wu was born in 1975. He received the B.S., M.S., and Ph.D. degrees from Xian Jiaotong University, Xi'an, China, in 1997, 2000, and 2005, respectively.

He is currently an Associate Professor of advanced manufacturing engineering at the key Laboratory of Contemporary Design and Integrated Manufacturing Technology, Ministry of Education, Northwestern Polytechnical University, Xi'an, China. His research interests include multiaxis NC machining, CAD/CAM, and smart machining technology.

Ming Luo was born in 1983. He received the B.S., M.S., and Ph.D. degrees in advanced manufacturing engineering from Northwestern Polytechnical University, Xi'an, China, in 2005, 2008, and 2012, respectively.

He is currently a Junior Research Scientist at the key Laboratory of Contemporary Design and Integrated Manufacturing Technology, Ministry of Education, Northwestern Polytechnical University, Xi'an, China. His research interests include multiaxis NC machining, smart machining, CAD/CAM, machining process simulation, and machining dynamics.

Computer-Aided Design 62 (2015) 64–77

Contents lists available at ScienceDirect

Computer-Aided Design

journal homepage: www.elsevier.com/locate/cad

A flexible and effective NC machining process reuse approach for similar subparts

Rui Huang *, Shusheng Zhang, Changhong Xu, Ximao Zhang, Congcong Zhang

The Key Laboratory of Contemporary Designing and Integrated Manufacturing Technology, Ministry of Education, Northwestern Polytechnical University, Xi'an, 710072, China

HIGHLIGHTS

- A feature-based parameter-driven model to guide NC process reuse is established.
- The NC process parameter-driven characteristic of similar feature is revealed.
- An NC process reusability assessment approach of similar pocket/subpart is proposed.
- We extend feature-based NC process reuse to a greater granularity of subpart.

ARTICLE INFO

Article history:
Received 8 January 2014
Accepted 27 October 2014

Keywords:
Feature-based machining
Reusability assessment
Inheritance mechanism
NC machining process reuse

ABSTRACT

NC machining process reuse is widely accepted as an effective strategy for engineers to generate the process plan with less time and lower cost. However, there has been very little research on how to reuse the NC machining process of similar subparts. As a result, most reusable NC machining process still has to remain in the repository as tacit knowledge, which can easily get lost due to oblivion. This paper proposes a novel NC machining process reuse approach for similar subparts in which existing NC machining process cases are described in association with machining features. First, a feature-based parameter-driven model is established to formalize the links between information imbedded in the machining feature and the parameters of cutting tools, drive geometries, and machining strategies. Then, the NC process parameter-driven characteristic of similar feature is revealed from the perspective of machining geometry, machining precision of the feature, and cutter geometry. Moreover, an NC process reusability assessment approach of similar pocket/subpart is presented using the pocket's medial axis transform. Finally, the NC machining process inheritance mechanisms are explored to implement the NC machining process reuse automatically and efficiently. A prototype system based on CATIA has been developed to verify the effectiveness of the proposed approach.

© 2014 Elsevier Ltd. All rights reserved.

1. Introduction

With increasingly competitive environment for manufacturing enterprises, engineers are often challenged to design the NC machining process (called NC process for simplicity) of a part with less time and lower cost [1]. To deal with this challenge, a feasible strategy is to reuse the NC process of similar subparts in the repository as effectively as possible [2]. Here, a subpart of a 3D CAD model is composed of a set of machining features on a part model, which may appear in different 3D CAD models. In matured manufacturing enterprises, similar subparts are usually machined with similar NC processes, which indicate that there exists a large amount of NC processes that can be reused. In recent years, the content-based 3D CAD model retrieval has become an active research topic and a lot of work has been done [3,4], which provides a novel enabling tool to locate the similar subparts for reusing their NC processes in finer manner. However, most of the related works have focused on searching the similar subparts, not dealing with how to reuse the existing NC process of the retrieved similar subpart. Consequently, current NC process reuse approaches still rest on the level of similar subparts discovering, and the retrieved similar subparts are primarily taken as a reference for NC process reuse, which relies heavily on the experience and knowledge of engineers.

Today, computer-aided design (CAD), computer-aided manufacturing (CAM), and computerized numerical control (CNC) technologies have been widely used in machining complex parts, and a huge number of 3D CAD models with NC processes (also called

* Corresponding author. Tel.: +86 29 88460357; fax: +86 29 88491576.
E-mail address: huangrui053469@163.com (R. Huang).

http://dx.doi.org/10.1016/j.cad.2014.10.004
0010-4485/© 2014 Elsevier Ltd. All rights reserved.

CAM model) are generated in the repository. However, since the CAM models generated by CAM software (e.g. CATIA, UG) are always structured based on machining operations instead of machining features, they cannot be handled directly by computers for NC process reuse without transformation. Recently, we developed a feature-based machining process model (FMPM) for the CAM model to realize its feature-based structured representation [5], and then each machining feature of the CAM model case in the repository is associated with a machining operation sequence. The FMPM would be helpful to speed up the NC process planning by reusing the NC process of similar machining feature. However, some critical issues are still not addressed: (1) whether the machining operations associated with the similar feature can be reused by the query feature from a new part, (2) how to assess the reusability of multiple feasible NC process solutions from CAM model repository for the query feature, and (3) how to establish the inheritance mechanisms for the selected feasible NC process solution to implement the NC process reuse. Consequently, the NC process of the similar feature cannot be reused automatically and efficiently for the engineers. As a result, many successful NC processes containing machining know-how of skilled engineers, which often hide behind the geometrical models, still have to remain in the repository as tacit knowledge and can easily get lost due to oblivion [6], which lead to a huge waste for the enterprise, and hence the motivation of this research.

In this paper, a novel NC process reuse approach for similar subparts is presented to overcome the above-mentioned problems, in which NC process cases in the repository are described in association with machining features based on FMPM to generate the machining know-how database automatically. In particular, a feature-based parameter-driven model is proposed to formalize the links between information imbedded in the machining feature and the parameters of cutting tools, drive geometries, and machining strategies first. Then, the NC process parameter-driven characteristic of similar feature is revealed from the perspective of machining geometry, machining precision of the feature, and cutter geometry. Moreover, an NC process reusability assessment approach of similar pocket/subpart is presented based on the medial axis transform of the pocket. Finally, the NC process inheritance mechanisms are explored to implement the NC process reuse automatically and efficiently. The work presented in this paper is dedicated to NC process reuse for the parts machined with 2 1/2-axis CNC milling.

The rest of the paper is organized as follows. In Section 2, we review the related works. In Section 3, some basic concepts and an overview of our approach are provided. Section 4 gives the details of the NC process reusability assessment approach of similar subpart, and Section 5 describes various inheritance mechanisms for NC process reuse. Then in Sections 6 and 7, the experiments and discussion are provided. Finally, we conclude the paper and present the future work in Section 8.

2. Related works

Feature technology has been an active research topic since the feature concept was proposed in 1970s. Related works in the area of feature technology can be grouped into three main sub-aspects: feature recognition, feature-based process reuse and feature-based machining.

Feature recognition is used to generate machining features, and it plays a key role in achieving CAD/CAM integration [7]. The feature recognition approach examines the topology and geometry of a part and matches them with the appropriate definition of predefined features. Many research works have been published in the field of feature recognition and various approaches have been adopted [8,9]. However, the existing feature recognition technologies mainly focus on analyzing the geometric information of the mechanical part, ignoring the technological data (e.g. dimensional tolerance, geometrical tolerance, and roughness) to the impact of feature recognition [10], and the machining features with free-form surfaces or interacting machining features with multiple interpretations are still difficult to handle.

Benefiting from the development of feature technology, various feature-based process reuse technologies are presented and have been widely used in manufacturing industry, such as group technology, feature template technology, typical process and case-based process design technology. Zhang et al. [11] presented a method based on feature machining templates to realize the integration of CAD/CAPP/CAM for marine diesel engine parts, which can reduce repetition work in NC process planning. Zheng et al. [12] presented a systematic modeling and reusing approach for non-NC process knowledge to generate process plans efficiently and effectively by reusing typical non-NC process knowledge. Jiang et al. [13] introduced a methodology in tool selection for die and mold NC machining. They employed a similarity-based fuzzy rough set algorithm in feature weighting and reduction for case-based reasoning systems. Yan et al. [14] and Zhang et al. [15] presented a similar approach to recognize machining features from existing NC programs in order to interactively reuse the associated machining operation parameters. For simple features, their methods have been applied successfully. However, current feature-based process reuse technologies are still in their infancy, especially for NC process reuse. They usually need the support of experts to construct the NC machining know-how database in advance, and the detailed process knowledge is always reused by manual editing and evaluating, which cause a lot of repetitive work and lower reuse efficiency.

Since machining features could be used to associate machining process information effectively, feature-based NC machining technologies have gained much more attention [16]. Tapie et al. [17] presented a topological model for machining the parts with complex shapes, in which the topological relations between machining features are used to validate the parameters of cutting tool and machining strategies specified by the machining assistant. Mawussi et al. [18] presented a machining process model for complex forging die machining to decrease the time for machining preparation by formalizing the links among information imbedded in the machining feature and the parameters of cutting tools and machining strategies. In their approach, machining features are first recognized based on some machining criteria, and then the NC process is generated in terms of the machining criteria to select the cutting tools and machining strategies. Wang et al. [19] presented a feature-based and agent-driven NC tool path generation approach to response rapidly the design and machining process changes during the production course, in which machining features are activated by agents to make the proper responses for updating the tool path automatically. Hou et al. [20] discussed an automatic tool path generation approach in an integrated CAD/CAPP/CAM system based on machining features, which can effectively decrease the number of user interactions. In their work, machining features are utilized to carry machining geometry information from CAPP to CAM systems, and an integration layer between FBMach and UG is implemented for milling operations. However, these approaches are quite dependent on predefined feature library (associated with machining knowledge) or heuristic rules, which are usually established manually by experienced engineers. Thus, they lack flexibility and are difficult to be applied to the subpart level due to dynamically changed topologies and shapes of subparts.

From above analyses, it can be concluded that there still exists no flexible and effective NC process reuse implementing approach to automatically evaluate and reuse the associated NC process of similar feature/subpart. However, we will take advantage of the significant researches above to achieve our goals described in the previous section.

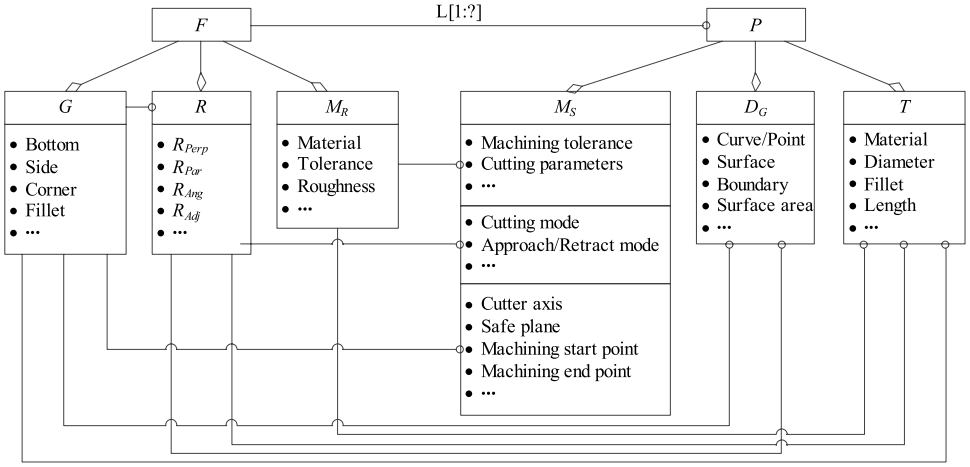

Fig. 1. Feature-based parameter-driven model.

3. Basic concepts and overview of the approach

In this section, we first define some basic concepts, and then briefly outline our approach.

3.1. Basic concepts

Definition 1. Feature-based parameter-driven model (FPDM). The parameter-driven model is a feature-based data model to formalize the links L between information imbedded in the machining feature F and the parameters of the generated machining operation P. It can be denoted as

$$\langle \text{FPDM} \rangle ::= \langle F \rangle \xrightarrow{L} (\langle P \rangle)$$
$$\langle F \rangle ::= [M_R](\langle G \rangle) \cup (\langle R \rangle)$$
$$\langle G \rangle ::= B \mid T_f \mid S \mid D$$
$$\langle R \rangle ::= R_{perp} \mid R_{par} \mid R_{Ang} \mid R_{Adj} \mid \cdots$$
$$\langle P \rangle ::= \langle T \rangle \cup \langle M_S \rangle \cup \langle D_G \rangle \cup \cdots$$

where M_R is the machining semantics associated with F, e.g. material, roughness, tolerance; G is the constraint geometry, including bottom face (B), top face (T_f), side faces (S), and datum face (D); R is the topological relation; R_{perp} is the perpendicular relationship, R_{par} is the parallelism relationship, R_{Ang} is the angle between two faces, and R_{Adj} is the adjacency relationship; T is the cutting tool, M_S is the machining strategy, and D_G is the drive geometry.

Definition 2. Reusability. The reusability of the NC process of similar feature in the repository is a quantitative indicator for evaluating its reusable degree to the query feature, which is codetermined by both roughing and finishing operations.

Definition 3. Inheritance. The inheritance, which normally means the process of transmission of characteristics from parents to offspring, is used here to refer to the process of reusing the process parameters of similar feature to generate the NC process of the query feature. Here, four different inheritances are listed, i.e. machining operation sequence inheritance, cutting tool inheritance, machining strategy inheritance, and drive geometry inheritance.

Fig. 1 shows the structure of FPDM, which can represent the association between a machining feature and a machining operation to be performed on that feature. As shown in Fig. 1, the constraint geometry, topological relation, and machining semantics codetermine the parameters of the machining strategy, drive geometry, and cutting tool. Conversely, whether the process parameters of similar feature can be reused, it depends on that whether the NC process of the query feature generated using the similar feature's process parameters can realize its machining and meet its manufacturing requirements.

3.2. Overview of the approach

Fig. 2 shows the general framework of our approach. This framework involves four parts: structured MBD (model-based definition) model construction, 3D CAD model retrieval, data mining for NC process case, and similar feature/subpart NC process reuse. Here we give a brief description of each part respectively:

(1) Structured MBD model construction. The MBD model of a part is structured in terms of machining features to capture manufacturing information [21]. The interacting machining features are recognized using the algorithm for the MBD model in Ref. [10].
(2) 3D CAD model retrieval. This step realizes feature/subpart similarity assessment merging with machining semantics and returns the retrieval results to the user, and the retrieval results have similar geometry, topology, and machining semantics with the query feature/subpart [22].
(3) Data mining for NC process cases. According to FMPM, data mining for NC process cases is carried out to construct the feature-based NC process case base. In this step, the machining operations associated with a given machining feature are clustered [5].
(4) Similar feature/subpart NC process reuse. It is in charge of reusing the process parameters of similar feature/subpart to generate the NC process segment of the query feature/subpart automatically, including three main steps, i.e. NC process parameter-driven characteristic evaluation, NC process reusability assessment of similar feature/subpart and NC process inheritance. In the work, this step is addressed at length to solve the critical problems mentioned in Section 1.

In general, our approach utilizes more machining know-how of skilled engineers in achieving better flexibility than existing feature-based NC process design approaches which usually need a predefined feature library or heuristic rules. Meanwhile, the NC process of various subparts can be generated through matched feature pairs with the support of 3D CAD model retrieval, which can get greater NC process reuse granularity and higher NC process generation efficiency. Moreover, NC process decision-making for the query feature/subpart can be achieved through assessing the NC process reusability of similar features/subparts. All the details about these characteristics and main steps of the approach will be given in the following sections.

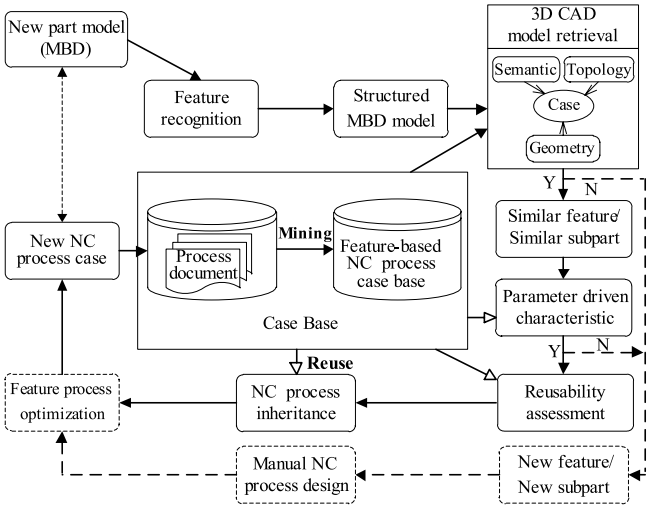

Fig. 2. General framework of our approach.

4. NC process reusability assessment of similar subpart

In this paper, NC process reusability assessment for similar subpart mainly focus on the pockets (without free-form surface) since they are frequently appeared in different parts with various topology and shape and take more than 80% of the total machining time of the part [19]. For pockets, it will be hardly feasible to construct a predefined feature library to cover all kinds of pockets associated with relative constant machining operations. However, by using the NC process reuse method, it will be capable of generating the NC process for similar pocket and their combination even though they are not stored in the predefined pocket feature library. To achieve this goal, one of crucial techniques is how to assess the NC process reusability of similar pocket/subpart.

4.1. NC process reusability assessment of similar feature

Generally, a pocket's NC process can be decomposed into three main steps: roughing, semi-finishing, and finishing. Suppose that the NC process of pocket F is OP(F), and its ith machining operation is op_i, then OP(F) can be denoted as

$$\mathrm{OP}(F) = \underbrace{\left[\bigcup_{i=1}^{k} op_i\right]}_{\text{Rough}} \cup \cdots \cup \underbrace{\left[\bigcup_{i=k+1}^{n} op_i\right]}_{\text{Finish}}. \tag{1}$$

In the above formula, note that there could exist multiple roughing operations (e.g. roughing, re-roughing) and finishing operations (e.g. bottom finish machining, side finish machining and corner/fillet finish machining) associated with a pocket.

The NC process reusability assessment of similar pocket involves the following two major issues: (1) NC process parameter-driven characteristic evaluation, and (2) NC process reusability calculation. Next, we discuss them in detail.

4.1.1. NC process parameter-driven characteristic evaluation

NC process parameter-driven characteristic evaluation is to determine whether the machining operations associated with the similar feature can be reused by the query feature on the new part. According to FPDM, to generate the NC process by using any CAM software, it is necessary to identify the machining geometry of the feature and to specify the process parameters. This task is performed starting from a geometrical data analysis with respect to the technological data. Therefore, in our case, the NC process parameter-driven characteristic should be revealed from three different aspects: machining geometry (M_G), machining precision (M_P), and cutter geometry (G_T).

1. Feature machining geometry

The prerequisite for NC process planning is to specify the machining region. By analyzing the machining geometries of the machining region, the required machining operation types for machining the feature can be defined. Machining geometry defines the area where the material should be removed. If the machining geometries of the two similar features are inconsistent, the required machining operation types are also inconsistent, and thus the NC process cannot be reused; otherwise, the required machining operation types are considered as the same.

For a pocket, the following machining geometries are usually involved: bottom f_B, fillet f_{BC}, side f_S, corner f_C, and sag f_{Sag}. The former two refer to as B, and the latter three refer to as S. Therefore, the machining region MR can be represented as

$$\mathrm{MR} = B \cup S$$
$$B = \{f_B, f_{BC}\}$$
$$S = \{f_S, f_C, f_{Sag}\}.$$

To represent MR, a 5 bit encoding P is established, where the ith of which is 1 if the number of f_k in the dimension denoted as Num(f_k) is greater than 0; otherwise, the ith of which is 0. Suppose that the encodings of the MRs of two pockets F_m and F_n are P^m and P^n, respectively; if the following condition is met:

$$\sum_{i=1}^{5}(p_i^m \wedge p_i^n) = \sum_{i=1}^{5} p_i^m = \sum_{i=1}^{5} p_i^n, \tag{2}$$

we call that the machining geometries of the two pockets are compatible.

2. Feature machining precision

In general, the NC process to be generated should satisfy the cutting conditions which depend on the technological data. Consequently, if the NC process of a feature case C can be reused by a query feature F, the technological data of F are usually required not higher than that of C. That is, the NC process of the feature case with higher machining precision can meet the technological requirements of the query feature with lower machining precision, while the NC process of the feature case with lower machining precision not always meets the technological requirements of the query feature with higher machining precision.

Suppose that for C and F, the matched technological data are T_i and $M(T_i)$ respectively; if the following condition is satisfied:

$$\forall T_i \in \boldsymbol{T_C}, \quad \exists M(T_i) \in \boldsymbol{T_F} \mid T_i \leq M(T_i),$$

we call that the machining precision between C and F is compatible. Here, $\boldsymbol{T}$ is a technological data set associated with a machining feature, and "$\leq$" denotes "not higher than". The technological data of a machining feature are extracted from Product Manufacturing Information (PMI) in the CAD model through using the APIs provided by CAD software.

Fig. 3 shows an example of the matched technological data. Since the technological data are associated with the faces of the feature, it is easy to get the matched technological data through the matched faces between two similar features. It can be seen from the figure that there exist three matched dimensional tolerance pairs, i.e. $(T_1, M(T_1))$, $(T_2, M(T_2))$, and $(T_3, M(T_3))$, and one matched surface finish pair, i.e. $(Ra_1, M(Ra_1))$. According to the value of the matched technological data of F_1 and F_2, we can conclude that the machining precision of F_2 is higher than that of F_1, and thus if F_2 is taken as a feature case, the machining precision between F_1 and F_2 is compatible, but not vice versa.

3. Cutter geometry

To select a cutting tool, it is necessary to check the accessibility of the feature machining geometries. The way to check the

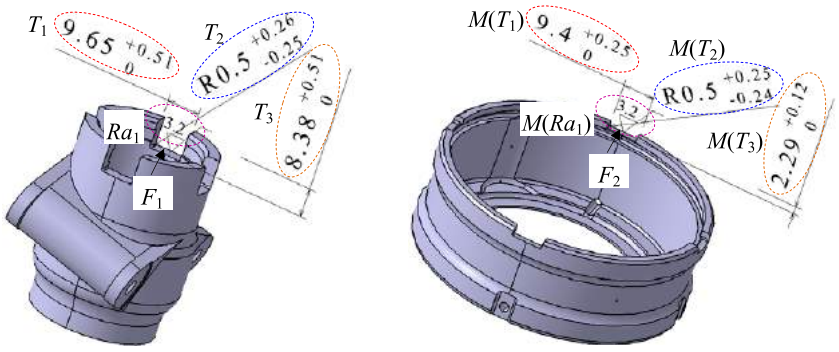

Fig. 3. Matched technological data.

accessibility without simulation is the analysis of machining region as a constraint on cutting tool movement [23]. As shown in Fig. 4, MR_{XY} related to feature's structure is defined as the restricting area in the XY plane, which is an important factor to check the accessibility of the cutting tool. Here, the transition position is introduced to represent MR_{XY}.

Definition 4. Transition position (T_p). Given a pocket F, its medial axis path (MAP) L_C is defined as a reference tool movement path between arbitrary vertices v_i and v_j in MR_{XY}. For an arbitrary MAP of F, denoted as $L_C = f(s),\ s \in [s^{\min}, s^{\max}]$, where s is the arc length of the tool movement path, and L_C is the radius of locally inscribed circle at s. If there exists a position $s_p \in (s^{\min}, s^{\max})$ that makes L_C be maximal or minimal, then s_p is called a transition position of F.

Taking the pocket in Fig. 4 as an example, Fig. 4(a) shows its medial axis (MA) [24], and Fig. 4(b) shows the MAP between v_i and v_j. As indicated in Fig. 4(b), there exist three extreme points, i.e. s_1, s_2, s_3, corresponding to three transition positions, where L_C acquires the maximum (7.22) at s_1 and s_2, and acquires the minimum (5.0) at s_3. At the minimal transition position, i.e. s_3, the tool movement region is the smallest of MAP. With the increase of cutting tool radius, the cutting tool will be overcut first at the minimum transition position. Therefore, the cutting tool radius (without regard to machining allowance) should be smaller than 5.0, and then the cutting tool will go through c_1c_2 without interference; otherwise, an overcut will happen.

To reuse a cutting tool existed in cutting tool library, the parameters of the cutter geometry should be compatible with the machining region of the query feature. Specifically, the following three factors should be considered:

(1) Cutting tool length

To avoid the interference between the cutting tool and the feature to be machined, the cutting tool length (i.e. T_L) is checked for the compatibility with the depth (i.e. h) of the pocket, if the following condition is met:

$$T_L > h,$$

the length of the cutting tool is compatible with the depth of the pocket.

(2) Cutting tool diameter for roughing

To avoid mass remaining materials left in roughing, every MAP needs to be go through by a feasible cutting tool without interference. Therefore, in roughing, the minimum of the cutting tool diameter should be less than the minimum width of all transition positions, and the maximum of the cutting tool diameter should be less than the maximum width of all transition positions, that is,

$$\begin{cases} \forall op_i \in \mathrm{OP}(F), \quad 1 \le i \le k \\ \min(D_i) \le \min(T_p) - 2 \times \delta \\ \max(D_i) \le \max(T_p) - 2 \times \delta \end{cases}$$

where δ is the machining allowance in roughing, and D_i is the diameter of the cutting tool applied on machining operation op_i.

In addition, if there exist machining allowance requirements for the corners of F in roughing, supposing that the machining allowance of the corner C_i in roughing is less than $\delta_i (\delta_i \ge \delta)$ and the radius of the corner is $R_c (R_c \ge 0)$, the cutting tool diameter $D(C_i)$ for C_i in roughing should be less than D_r, that is,

$$D(C_i) \le D_r = \frac{2\left(\delta_i \sin\frac{\varphi}{2} - \delta\right)}{1 - \sin\frac{\varphi}{2}} + 2R_c$$

where φ is the included angle of C_i.

Therefore, the minimum of the cutting tool diameter should be less than $\min(D_r)$ to satisfy the cutting conditions of the corners in roughing, which depend on the machining allowance, that is,

$$\forall\, op_i \in \mathrm{OP}(F), \quad \min(D_i) \le \min(D_r),\ 1 \le i \le k.$$

(3) Cutting tool diameter for finishing

Generally, in finishing, engineers select smaller cutting tools to cut the remaining materials left by the machining operations of roughing and semi-finishing. Therefore, the maximum of the cutting tool diameter should be less than the minimum width of all transition positions, i.e. $\forall op_i \in \mathrm{OP}(F), \max(D_i) \le \min(T_p),\ k+1 \le i \le n$, and this is the elementary constraint rule for cutting tool selection in finishing.

Moreover, when a corner needs an additional finishing operation, the diameter of the cutting tool for the corner finishing operation op_i should be less than the minimum of the corner radius at the same time, i.e. $D_i \le \min(2R_c),\ k+1 \le i \le n$, or when a fillet needs an additional finishing operation, the fillet radius of the cutting tool for the fillet finishing operation op_i should be less than the fillet radius of the pocket meanwhile, i.e. $r_i \le R_f,\ k+1 \le i \le n$.

In fact, corner finishing and fillet finishing can be realized through two independent machining operations respectively, or through some finishing operation (e.g. bottom finish machining, and side finish machining), which means that corner/fillet finish machining can be imbedded in other finishing operations. Therefore, the compatibility of the cutting tool diameter can be evaluated according to the functions of each machining operation (Table 1).

The flow chart of NC process parameter-driven characteristic evaluation approach is shown in Fig. 5. As illustrated in the figure, the NC process parameter-driven characteristic is revealed by checking the compatibility of M_G, M_P, and G_T between existing similar feature case C and query feature F. If M_G, M_P, and G_T are compatible respectively, the NC process parameters of C have the ability to drive F to generate its NC process, which indicates that the NC process of C can be associated with F. It can be represented as

$$f_{(C \mapsto F)} = M_G \cdot M_P \cdot G_T = 1$$

where $\cdot$ is the combination function.

Fig. 6 shows an NC process parameter-driven characteristic evaluation sample (M_G and M_P are compatible respectively). The width of the transition position and the radius of the corner of the

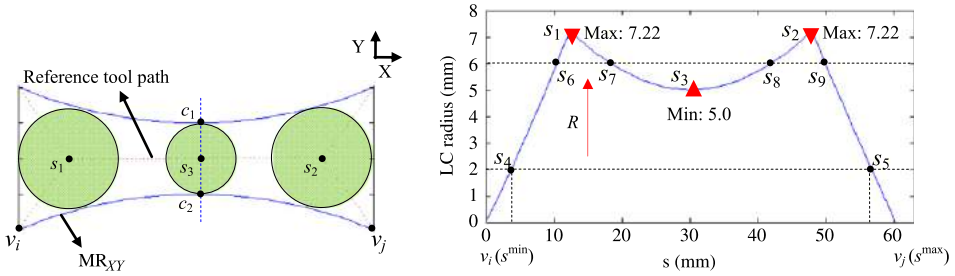

(a) Pocket F. (b) Medial axis path L_C.

Fig. 4. Transition position case.

Table 1
Function of machining operation.

Function	Compatibility condition
Multiple roughing (δ_i is not specified)	$\max(D_i) \le \max(T_p) - 2\delta$ $\min(D_i) \le \min(T_p) - 2\delta$
Multiple roughing (δ_i is specified)	$\max(D_i) \le \max(T_p) - 2\delta$ $\min(D_i) \le \min(\min(T_p) - 2\delta, \min(D_r))$
Roughing (δ_i is not specified) Roughing (δ_i is specified)	$D_i \le \min(T_p) - 2\delta$ $D_i \le \min(\min(T_p) - 2\delta, \min(D_r))$
① bottom/side finishing ① ∩ corner finishing	$D_i \le \min(T_p)$ $D_i \le \min(\min(T_p), \min(2R_c))$
① ∩ fillet finishing	$D_i \le \min(T_p)$ $r_i \le R_f$
① ∩ corner finishing ∩ fillet finishing	$D_i \le \min(\min(T_p), \min(2R_c))$ $r_i \le R_f$

two features F_1 and F_2 in Fig. 6(a) are equivalent respectively, only with the length of the feature changed slightly (from 38 to 28 mm). Thus, the NC processes of F_1 for F_2, or F_2 for F_1 have the parameter-driven ability. However, the parameters (i.e. width and radius) of the other two features F_3 and F_4 in Fig. 6(b) are all different. By using the formula in Table 1, the cutting tool diameter range of F_3 for roughing and finishing are [2, 40] and [2, 12], respectively, and that of F_4 are [2, 35] and [2, 8]. Therefore, the interactions of the cutting tool diameter ranges for roughing and finishing between F_3 and F_4 are [2, 35] and [2, 8], respectively. Suppose that a cutting tool D12 is selected for the finish machining of F_3, since D12 is not compatible with F_4 ($12 \notin [2, 8]$), the NC process of F_3 cannot be reused by F_4. In addition, the cutting tool diameter range of F_4 is a subset of F_3 (i.e. $[2, 35] \subset [2, 40]$, $[2, 8] \subset [2, 12]$), and thus no matter what the NC process of F_4 is, it can always be reused by F_3.

In fact, NC process parameter-driven characteristic evaluation is also a course of feasible NC process decision-making. Differing from existing feature-based NC process design approaches, our approach is not through forward reasoning based on the predefined feature library or heuristic rules, but through reversing verification based on the process parameters of similar feature. Therefore, it is especially suitable for pockets with various topology and shape even if they are not stored in the predefined library.

4.1.2. NC process reusability calculation of similar feature

According to FPDM, the NC process of F can be generated automatically and efficiently by inheriting the NC process of C. However, the generated NC process for F is only a feasible solution, rather than an optimal solution. Therefore, it is necessary to calculate the reusability of multiple feasible NC process solutions, which is an important criterion for optimal NC processes decision-making.

In general, for two features C and F, when the NC process of C has the parameter-driven ability for F, if the two features are

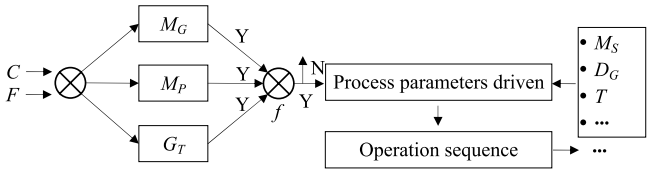

Fig. 5. NC process parameter-driven characteristic evaluation.

more similar from the point of view of cutting tool movement, the reusability of the NC process of C for F is higher. Since the MA of a feature is a compact representation of the feature's geometric and topological characteristics, it is introduced as the reference tool path for its unique characteristic to calculate the NC process reusability of similar feature in this work. Furthermore, L_C is accordingly generated for selected cutting tool location determination and movement.

According to the uniqueness of the reference tool paths, the principle of NC process reusability assessment is that the cutting tools cut along the reference tool paths. Since different cutting tools for a given feature have different accessible machining regions along MA, if the two features with the reference NC process are more similar, they have more similar accessible machining region pairs. Conversely, the similarity between the corresponding accessible machining region pairs can be used to calculate the reusability of the NC process. Here, the accessible machining region calculation includes the following two steps: (1) retrieve the reference tool paths and their L_C radius functions from the MA of the feature, and (2) calculate the intersection points between each L_C radius function curve and a horizontal line representing the selected cutting tool radius (Fig. 4(b)). The reference tool path points with larger values of the L_C radius function than the selected cutting tool radius define the accessible machining region for this cutter.

To illustrate the machining region calculation process, an example is shown in Fig. 4. Suppose that a cutting tool with radius R of 2 mm is used to cut the pocket. To calculate the machining region, a horizontal line of the cutting tool radius is drawn on the L_C radius function curve in Fig. 4(b), which intersects with the L_C radius function curve at two points, i.e. s_4 and s_5. Since the function values of the points between s_4 and s_5 are all greater than the cutting tool radius, their corresponding points on the reference tool path are the valid cutting tool locations. In addition, the horizontal line could intersect with the L_C radius function curve at more than two points. For example, if a cutting tool with radius R of 6 mm is adopted to cut the pocket, there are two machining sub-regions with four points, i.e. s_6 and s_7, s_8 and s_9.

Suppose that the MAs of C and F are MA_1 and MA_2, respectively, the NC process of C is denoted as OP(C), and its cutting tool sequence for roughing is $T = \{d_i\}$, $1 \le i \le k$, $d_i > d_{i+1}$, where d_i is the diameter of the ith cutting tool, and k is the number of the machining operations in roughing. For a cutting tool d_i ($d_i \in T$), corresponding to a machining operation op_i ($op_i \in$ OP), if its

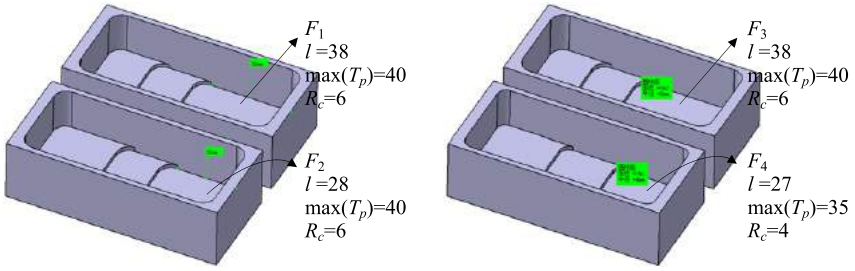

(a) Length difference. (b) Length and corner difference.

Fig. 6. NC process parameter-driven characteristic evaluation sample.

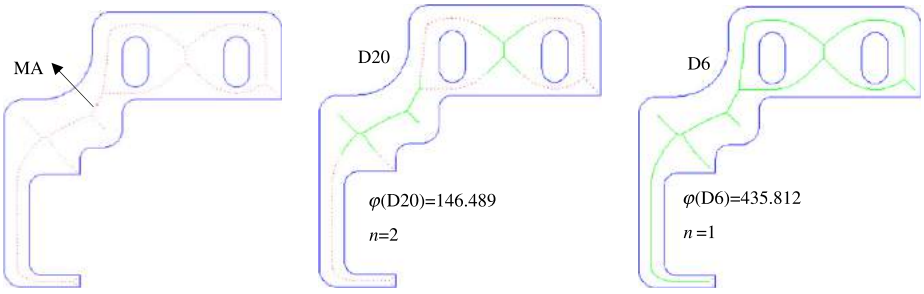

(a) MA of pocket F. (b) Machining region with D20. (c) Machining region with D6.

Fig. 7. Example of machining regions using D20 and D6. (For interpretation of the references to color in this figure legend, the reader is referred to the web version of this article.)

machining regions along MA_1 and MA_2 are represented by $\varphi_1(d_i)$ and $\varphi_2(d_i)$ respectively, the reusability of the machining operation denoted as σ_i is formulated as follows:

$$\sigma_i = \exp\left[-\frac{(n_1-n_2)^2}{2}\right] * \left(1 - \frac{|\varphi_1(d_i)-\varphi_2(d_i)|}{\max[\varphi_1(d_i),\varphi_2(d_i)]}\right) \tag{3}$$

where $\varphi(d_i)$ can be represented using area, volume, and arc length, etc.; n_1 and n_2 are the number of connected domains in the machining region, which are related to the number of tool retractions. In this work, the arc length is adopted to compute σ_i.

Fig. 7 shows an example of machining regions of F using two different cutting tools D20 and D6, and the MA (red dotted lines) of feature F is shown in Fig. 7(a). Fig. 7(b) and (c) show the accessible machining regions (green lines) covered by the two cutters respectively. As shown in the figure, there are two connected domains with D20, and the arc length is 146.489 mm, while only one connected domain with D6, and the arc length is 435.812 mm.

The NC process reusability between two similar features is then calculated as the weighted sum of the reusability of all machining operations in roughing, denoted as $\eta(F, C)$. A heuristic rule about the weight setting is that the weight of the large cutter is greater than the weight of the small cutter, i.e. $\omega_i > \omega_{i+1}$.

$$\eta(F,C) = \begin{cases} \sum_{i=1}^{k} \omega_i * \sigma_i & f_{C\mapsto F} = 1 \\ 0 & \text{others} \end{cases} \tag{4}$$

$$\sum_{i=1}^{k} \omega_i = 1.$$

4.2. NC process reusability of similar subpart

In order to calculate the NC process reusability of similar subpart, a successful match M between two subparts S_1 and S_2 needs to be found first. In the work, the machining feature coupled graph (MFCG) [21] G_1 and G_2 regarding the interactions between machining features are used to represent the subparts. A successful match M is a mapping from G_1 to G_2, and it can be found using the sub-graph isomorphism algorithm [25], in which each feature F in S_1 is mapped to a feature $M(F)$ in S_2 and each edge e in G_1 is mapped to an edge $M(e)$ in G_2. The mapping is injective since it is regarded as valid in the work that the query subpart is a part of the similar subpart in the repository but not vice versa [26].

After a successful match M between S_1 and S_2 is found, the NC process reusability between these two similar subparts is calculated based on the match M, denoted as $\eta(S_1, S_2)$, that is calculated as the weighted sum of the NC process reusability of the matched feature pairs $(F, M(F))$ with Eq. (4). Each feature pair has its own weight and the weights can be determined heuristically using the following rule: the feature pair in the high level has greater weight than the feature pair in the low level (here the word "level" refers to the depth of the feature pair in MFCG).

$$\eta(S_1,S_2) = \sum_{F\in S_1, M(F)\in S_2} \omega_F * \eta(F, M(F)) \quad \eta(F, M(F)) \neq 0$$
$$\sum_{F\in S_1} \omega_F = 1. \tag{5}$$

Fig. 8 shows the main steps for the NC process reusability calculation of similar subpart. In general, the properties of the nodes and edges in MFCG are used to find the match M first, and then the NC process reusability of F for $M(F)$ with the associated machining operation sequence is calculated. Since MFCG preserves abundant machining semantics embedded in the MBD model, it can represent the feature interactions, which are taken as a determining factor in NC process planning, especially in machining operation sequencing. Consequently, the result can reflect the NC process reusability between similar subparts.

In general, the goal of NC process reusability calculation of similar subpart is to select an optimal solution for the query subpart from multiple feasible NC process solutions. Since the NC process of the similar subpart has already possessed explicit machining sequencing characteristic, which is the direct representation of high-level NC process planning knowledge, we can avoid plenty

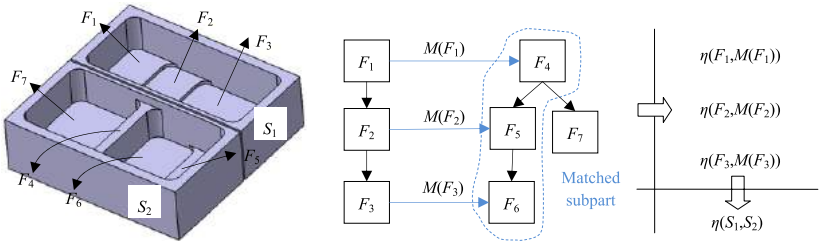

(a) Two similar subparts. (b) Calculation steps.

Fig. 8. NC process reusability calculation of similar subpart.

of complex work (e.g. machining operation sequencing and combination between features) done by existing feature-based NC process design approaches. In the work, the NC process segment of the similar subpart is reused as a whole by the query subpart. Thus, our approach possesses greater NC process reuse granularity.

5. NC process inheritance mechanism

In this section, we will discuss the NC process inheritance mechanism which allows us to implement the NC process reuse for the selected feasible NC process solution automatically and efficiently.

Intrinsically, inheritance could be regarded as the composition of specific "copy" and "adaption" operations (Fig. 9), in which "copy" means making a duplicate object from the original one and "adaption" means revising the duplicated object according to FPDM to make it appropriate for the query feature. Below we explain the details of the inheritance mechanisms for the multiple information inheritances described in Definition 3.

5.1. Cutting tool inheritance

Before appending a machining operation, the cutting tool applied on the machining operation should be considered first. Therefore, a cutting tool needs to be added in the machining resource according to its parameters before a machining operation is appended. In general, the cutting tool parameters to be inherited include: tool name, tool type, tool number, geometry attributes (e.g. diameter, corner radius, length, etc.). Since the cutting tool of the duplicated machining operation meets the compatibility condition, that is the geometry parameters of the cutting tool are compatible with the machining geometry of the query feature, it indicates that the cutting tool can realize the machining of the specified machining region of the feature. Thus, the parameters of the cutting tool are directly inherited without revision.

5.2. Machining operation sequence inheritance

With the machining operation sequence inheritance, the NC process of the query feature can be acquired quickly. First, each machining operation will be duplicated in terms of machining precedence, and then the machining operation will be revised through the adaption operation. Here, the duplication of the machining operation is actually the reuse of the process parameters, including machining operation type, drive geometry, machining strategy, cutting tool, etc. The inheritance mechanism of machining operation sequence is illustrated in Fig. 10.

Since partial order relations are existed among machining operations in a machining operation sequence, the constraints between the machining operations will make the duplicated machining operation sequence exist redundant machining operations. If they are not eliminated, the machining efficiency of the tool path generated

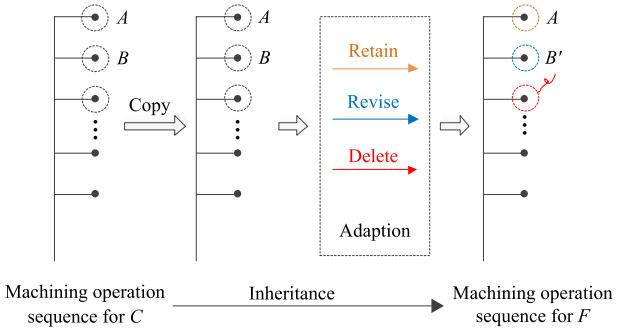

Fig. 9. NC process inheritance mechanism.

will decrease significantly because of much air machining. Therefore, a redundant machining operation evaluation rule is established to realize the adaption of the inherited machining operation sequence.

For two arbitrary machining operations op_i and op_j $(i < j)$ of the duplicated machining operation sequence, corresponding to two cutting tools d_i and d_j respectively, the redundant machining operations can be eliminated in terms of different machining stages. Specifically, it can be described as follows:

(1) **Roughing**. If op_i has the same drive geometries and machining regions along MA with op_j, that is,

$$\varphi(d_i) = \varphi(d_j) \wedge D_{Gi} = D_{Gj}, \quad 1 \le i < j \le k,$$

op_j is a redundant rough machining operation.

(2) **Finishing**. Suppose that op_j is a corner finishing operation, if the following condition is satisfied:

$$d_i \le \min(\min(T_p), \min(2R_c)) \wedge D_{Gj} \subseteq D_{Gi}, \quad k \le i < j \le n,$$

op_j is a redundant corner finishing operation.

Suppose that op_j is a fillet finishing operation, if the following condition is met:

$$d_i \le \min(T_p) \wedge r_i \le R_f \wedge D_{Gj} \subseteq D_{Gi}, \quad k \le i < j \le n,$$

op_j is a redundant fillet finishing operation.

5.3. Drive geometry inheritance

In general, tool path generation is driven by the process parameters and drive geometries. Here, the drive geometries are created by machining geometries of the feature itself. Therefore, for a machining operation, drive geometry inheritance is not to inherit the geometries of the feature case, but to inherit its driven method (e.g. curve, surface, and boundary) and construction logic (e.g. machining geometry, reference geometry). Hence, drive geometry inheritance is also called logic inheritance.

After a machining operation is duplicated, the parameters of driven method are directly inherited without revision, whereas the drive geometries should be revised in terms of feature interaction

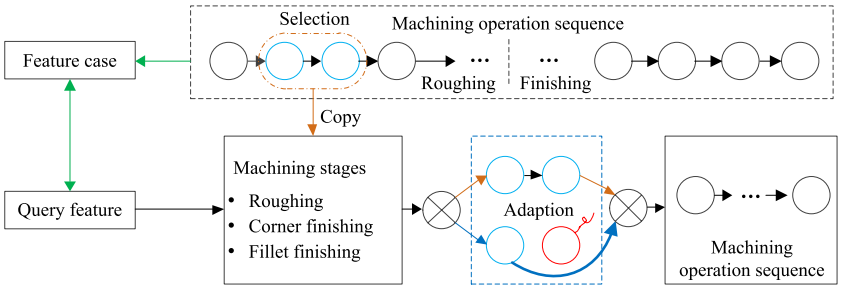

Fig. 10. Machining operation sequence inheritance mechanism.

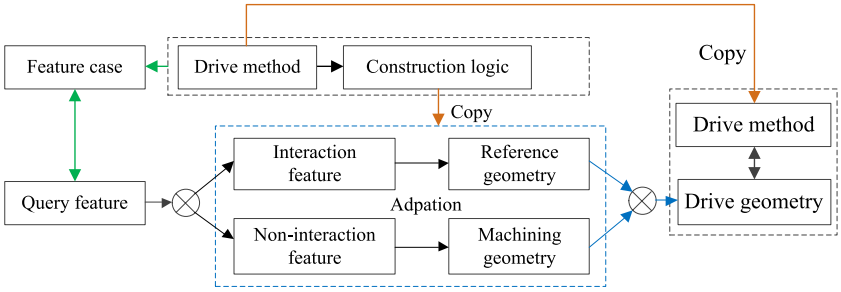

Fig. 11. Drive geometry inheritance mechanism.

and adjacent features. If the feature is a non-interaction feature, its machining geometry is referenced directly, while the feature is an interaction feature, the reference geometry is constructed as drive geometry according to its adjacent features in MFCG using the same construction logic of the feature case. Fig. 11 gives the drive geometry inheritance mechanism.

5.4. Machining strategy inheritance

In general, the machining strategy parameters to be inherited include: cutting mode (e.g. parallel, radiation, and spiral), approach/retract mode, cutting direction (e.g. downward and upward), machining tolerance, and cutting parameters (e.g. cutting speed v_c, feed rate f, axial depth of cut a_p, radial depth of cut a_e). As shown in Fig. 1, part of the parameters are related to the spatial position of machining geometry, i.e. safe plane, cutter axis; part of the parameters are related to the topological relations of machining geometries, i.e. cutting mode, approach/retract mode; and the other parameters are related to the technological data of the feature, i.e. machining tolerance, cutting parameters.

Since the topological relations are used in the feature similarity assessment as described in Refs. [5,22], it indicates that the query feature has similar topological relations with the feature case. Therefore, once the machining operation is duplicated, the parameters related to the topological relations are inherited without revision. In addition, since the query feature is compatible with the NC process of the feature case as described above, it indicates that the technological data are compatible respectively. Consequently, the parameters related to the technological data are also inherited. However, the parameters related to the spatial position should be revised according to the machining geometry of the feature. For instance, the cutter axis is specified as the normal of the feature. The machining strategy inheritance mechanism is illustrated in Fig. 12.

6. Experiments

In order to verify the feasibility and effectiveness of our approach presented in this paper, we have developed a prototype system for NC process reuse of similar subparts on the platforms of Microsoft Visual Studio 2003 and CATIA V5 R16 component application architecture (CAA).

6.1. NC process reusability assessment cases of similar subparts

Fig. 13 shows two parts Model_1 and Model_2 (in the repository) from an aviation manufacturing enterprise, of which the material is aluminum alloy LD5. Using the algorithm in Ref. [22], two matched features C_1 (Fig. 13(a)) and C_2 (Fig. 13(b)) are acquired. The MAs of the two features are shown in Fig. 13(a) and (b), respectively. As illustrated in the figure, there are two feasible NC process solutions for C_2 in the repository (Fig. 13(e)). Since the parameters of the cutter geometry of the two solutions are compatible with the machining region of C_1, both two NC process solutions have the parameter-driven ability. Here, the accessible machining regions (green lines) along MA of the rough machining operations of the two NC process solutions are computed respectively (Fig. 13(c) and (d)). With Eq. (4), the NC process reusability of the two solutions for C_1 is 7.26% and 98.72%, respectively.

It is noted that, although both two NC process solutions can realize the machining of feature C_1, since the number of tool retractions and accessible machining regions of solution 1 for C_1 and C_2 have great differences, the reusability of solution 1 is smaller. Whereas the number of tool retractions and accessible machining regions of solution 2 for C_1 and C_2 are all with little differences, and thus C_1 adopts solution 2 as its NC process preferentially.

Another sample with complex processes is used to illustrate the NC process reusability assessment of similar feature in Fig. 14. In this example, the topology and shape of the two matched features are quite different. The MAs of the two features are generated and plotted in Fig. 14(a), (b), and the critical parameters (e.g. roughness, h, T_p) for NC process parameter-driven characteristic evaluation are given in Fig. 14(c). According to the associated machining operations of C_4 in Fig. 14(d), the NC process of C_4 has the parameter-driven ability for C_3, and with Eq. (4), we get that the NC process reusability is 36.87%. Based on the proposed NC process inheritance mechanism, we find that the 5th machining operation is a redundant corner finishing operation, which has to be eliminated, and thus the NC process for C_3 is composed of five machining operations. By statistics analysis, each machining operation generated by CAM software requires user interactions by means of mouse and keyboard 20 times on average [19]. Therefore, more than 100 user interactions are required to accomplish the above-generated machining operations in the CAM software with traditional methods,

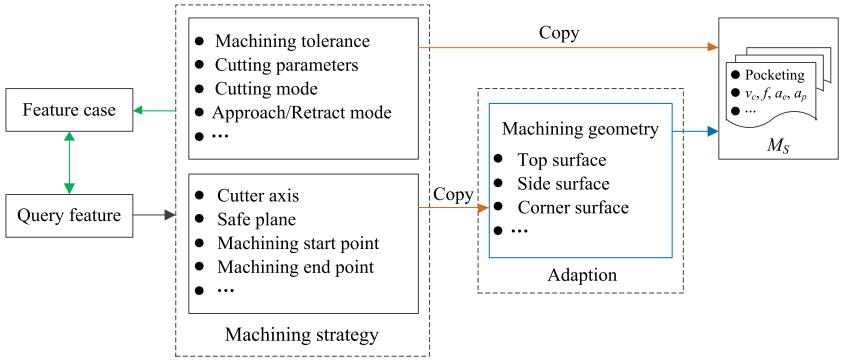

Fig. 12. Machining strategy inheritance mechanism.

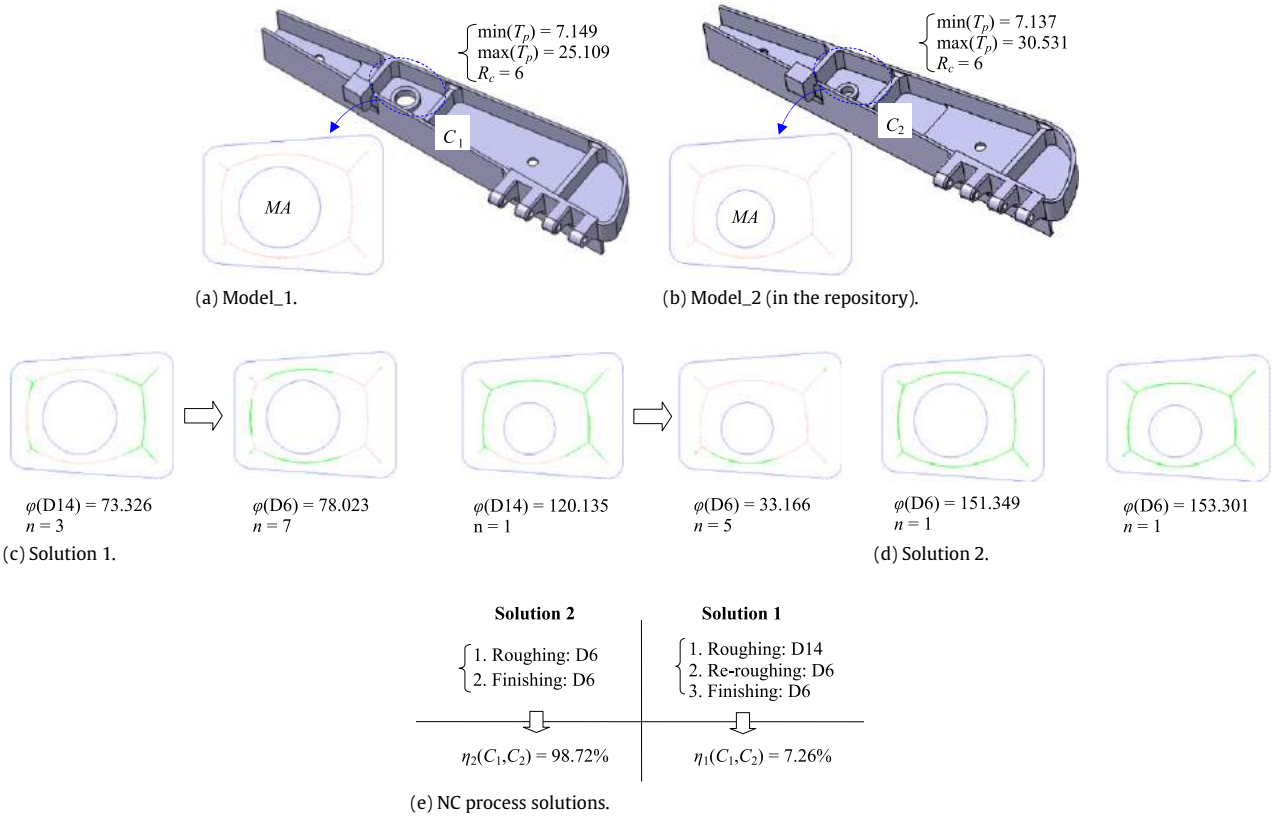

(a) Model_1.

(b) Model_2 (in the repository).

(c) Solution 1.

(d) Solution 2.

(e) NC process solutions.

Fig. 13. Example I of NC process reusability assessment of similar feature. (For interpretation of the references to color in this figure legend, the reader is referred to the web version of this article.)

which do not include the user interactions of reusable NC process searching and modifying. However, only about 6 user interactions are required to complete the above whole task with our approach.

Fig. 15 shows the example of NC process reusability assessment of similar subparts. Fig. 15(a) is the query subpart consisted of three features, i.e. F_1, F_2, and F_3, and Fig. 15(b)–(d) are the first three most similar subparts returned through 3D CAD model retrieval, i.e. S_2, S_3, and S_4. Their detailed machining operations are shown in the figure. Using the sub-graph isomorphism algorithm, three successful matches are found, i.e. M_1, M_2, and M_3, and the matched feature pairs in each subpart are acquired accordingly. With Eq. (5), the NC process reusability of each similar subpart is computed respectively. It can be seen from the computation results that the NC process of S_2 has the highest reusability (i.e. 95.03%) for S_1 than other two similar subparts. Therefore, reuse of the NC process of S_2 could more effectively speed up the design process.

6.2. NC process inheritance case

In Fig. 16, we take two pockets with islands C_1 and C_2 as an example to illustrate the NC process inheritance mechanism. By using the redundant rule for machining operations, we get that there does not exist redundant machining operations in solution 2. Therefore, the machining operation sequence is inherited directly, i.e. pocket rough machining and side finish machining. Fig. 16(a) shows the tool path of C_2 for side finish machining with cutting tool D6, and the cutter axis is (0, 1, 0). The tool path of C_1 for side finish machining will be generated automatically as shown in Fig. 16(b) by inheriting the parameters of M_S, T, and D_G. Here, the cutter axis, safe plane, and drive geometry should be revised in terms of the machining geometry of C_1. For instance, the cutter axis is specified as (0, −1, 0), and the drive geometry is changed to the outer loop of the bottom face of C_1. Moreover, the parameters are

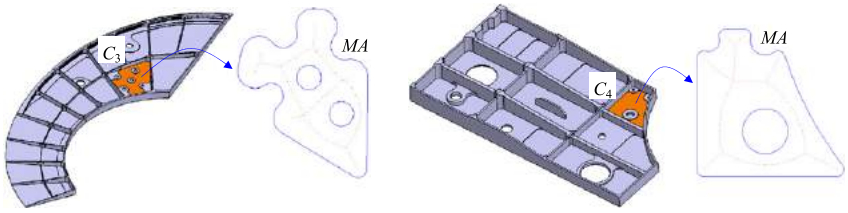

(a) Model_3. (b) Model_4 (in the repository).

Feature	Roughness	max(T_p)	min(T_p)	h	R_c
C_3	3.2	74.99	20.27	35.5	12.7
C_4	3.2	64.34	20	28	6

Feature	$\varphi(d_1)$ / n	$\varphi(d_2)$ / n	$\eta(C_3,C_4)$
C_3	553.22/ 1	92.96 / 7	–
C_4	198.53 / 2	156.17 / 7	–
σ	21.77%	59.53%	36.87%

(c) Reusability assessment.

No.	Operation	Cutting tool
1	Roughing	D32×R3×45
2	Re-roughing	D16×R3×45
3	Bottom finishing	D16×R3×45
4	Side finishing	D16×R3×45
5	Corner finishing	D12×R3×40
6	Boss finishing	D16×R3×45

(d) Associated machining operations of C_4.

Fig. 14. Example II of NC process reusability assessment of similar feature.

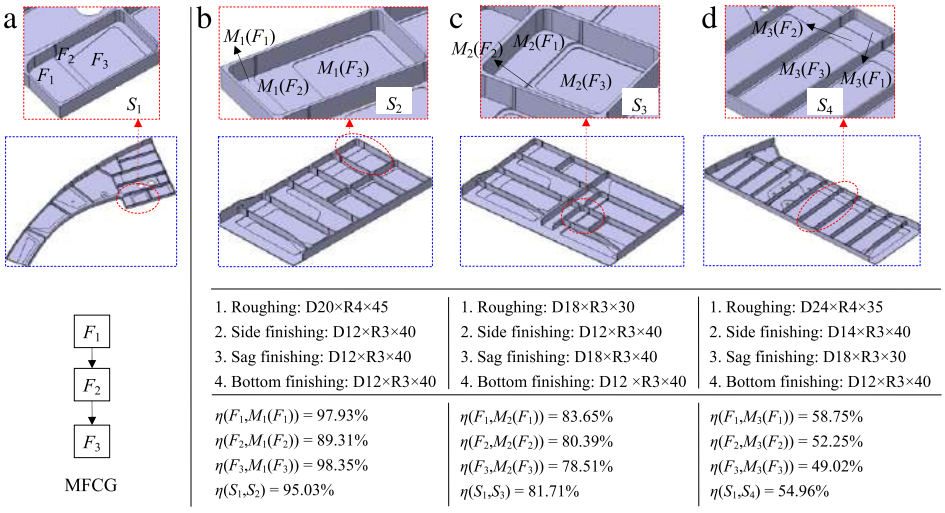

Fig. 15. Example of NC process reusability assessment of similar subparts.

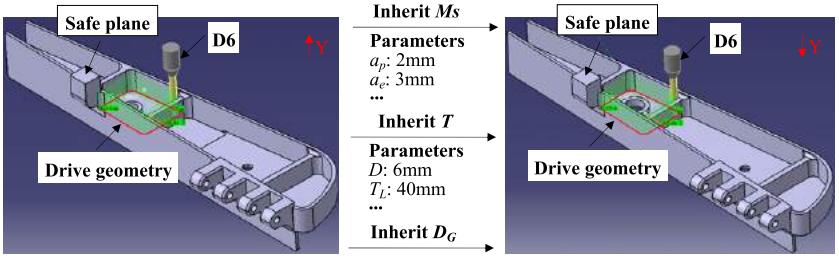

(a) Tool path of C_2. (b) Tool path of C_1.

Fig. 16. Example of NC process inheritance.

set automatically by using the APIs provided by CAM software to avoid plenty of repetitive work, which will improve the efficiency of NC process planning.

6.3. Prototype system

Fig. 17 shows the prototype system for NC process reuse, the using steps of the NC process segment generation for the query subpart are as follows: (1) select a similar subpart ID from the 3D CAD model retrieval result, and check its compatibility; (2) compute the NC process reusability of the similar subpart; (3) adapt the inherited NC process case. In Fig. 17(a), the ID of the query subpart is 7 (inherited from the structured MBD model), and the ID of the similar subpart in the retrieval result is 1. As illustrated in the figure, C_7 is compatible with the NC process of the similar subpart, and its reusability is 96.8%. The NC process of C_7, which is composed of 13 machining operations, will be generated automatically and efficiently through NC process inheritance shown in the bottom of the

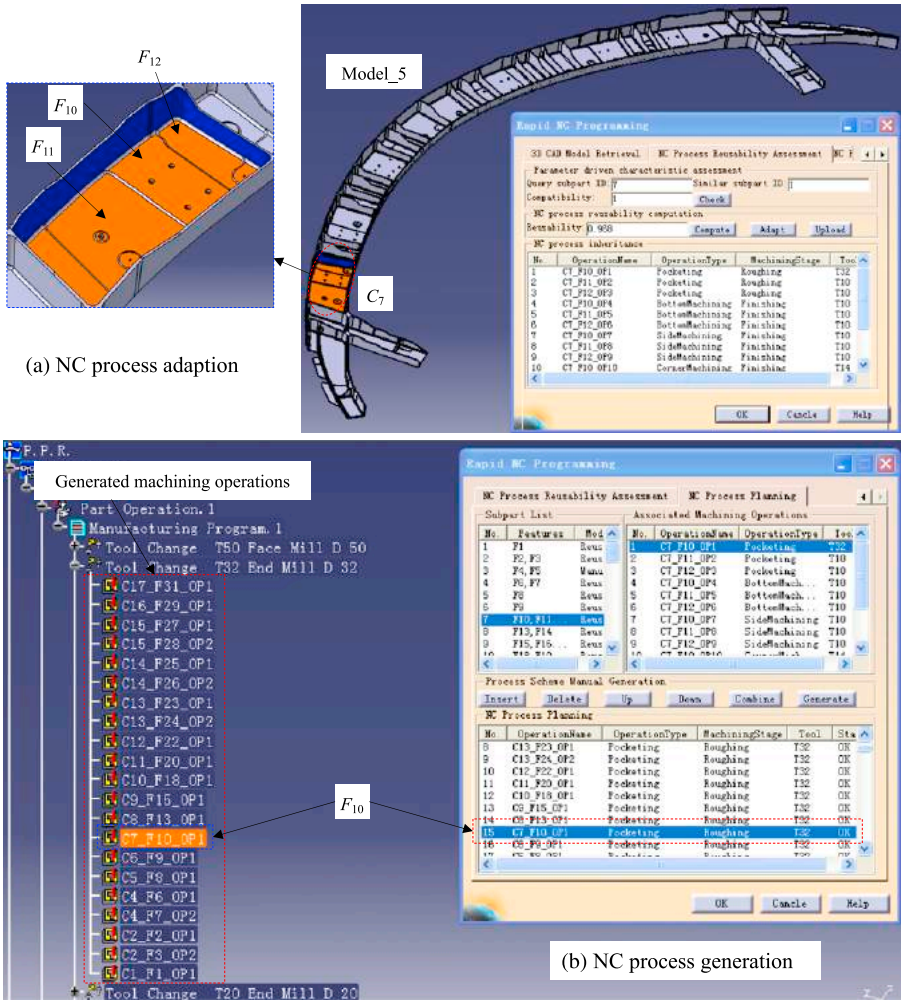

Fig. 17. Prototype system for NC process reuse.

figure, and then upload the automatically generated NC process solution to the NC process planning module for the part (Fig. 17(b)). According to the associated machining operations of the subparts, the NC process of the complex aircraft structural part Model_5 can be generated by manually sequencing these machining operations.

In order to demonstrate the significant improvement of our approach on efficiency, the comparisons with the interactive programming based on the CATIA system are listed in Table 2. It can be seen from the table that 317 machining operations are required to accomplish the NC programming for Model_5 which require more than 6340 user interactions and 1200 min through using the manual programming approach. However, with our approach, 289 machining operations, which are corresponding to 62 pockets with various topologies shapes and technological requirements, can be automatically generated which require only 418 user interactions, and the other 28 machining operations are manually completed which require less than 660 user interactions, and the programming time is about 226 min. The NC programming efficiency is improved by 5 times evidently since the reuse degree of the machining operations is 91.17%.

7. Discussion

In this section, we will further discuss the advantages, robustness and potential application domains of our approach.

As mentioned above, our approach establishes the FPDM to guide the entire NC process reuse course and reveal the NC process parameter-driven characteristic to associate the query feature with the NC process of similar feature. Essentially, NC process inheritance for query feature is to instantiate FPDM in terms of the process parameters of similar feature. Moreover, the reusability concept is introduced to quantize the reusable degree for the NC process of similar feature, which is an important criterion to determine the optimal NC process solution. Furthermore, our approach possesses the following flexibilities: (1) the feasible NC process solution for the query feature/subpart can be achieved even if it is not predefined, and (2) multiple feasible NC process solutions for the same query feature/subpart can be generated.

In order to illustrate the advantages of our approach, some comparisons between our approach and the typical existing methods are shown in Table 3. In our approach, the machining know-how is captured automatically from the existing successful CAM models, and the NC process reuse course is automatically realized with some user interactions. However, the existing methods still rely heavily on engineers' experience, and usually require a lot of user interactions to search and modify the reusable NC process case, or to construct the machining know-how database, e.g. predefined feature library and heuristic rules, and their flexibility is low since they cannot generate the machining operations of the features not stored in the machining know-how database. Moreover, their reuse granularity is only limited to the feature level, whereas our approach is extended to subpart level with greater NC process reuse granularity.

As for the robustness of our approach, the following two issues should be considered. One is the heterogeneity of 3D CAD models (e.g. a face is expressed with multiple sub-faces), and the other is

Table 2
Efficiency analysis.

Items for comparison	Manual programming based on CATIA	Programming with our approach	
		Automatic programming	Manual programming
Number of machining operations	317	289	28
Number of user interactions	More than 6340	418	Less than 660
Programming time (minute)	More than 1200	46	180
Efficiency improvement	81.17%		

Table 3
Comparisons between our approach and the typical existing methods.

Method	Feature recognition	Similar feature/subpart match	NC process reuse implementation			Flexibility
			Machining know-how capture	Reuse process	Reuse granularity	
Our method	Automatic	Automatic	Automatic	Automatic	Feature/subpart	High
Ref. [11]	Automatic	Manual	Manual	Manual	Feature	Low
Refs. [14,15]	Automatic	Manual	Automatic	Manual	Feature	Low
Ref. [18]	Manual	–	Manual	–	Feature	Low

the transition features (e.g. fillets and chamfers). Due to the topology influences from them, they may cause unexpected differences in feature recognition, MA generation and feature/subpart similarity assessment, and thus make the approach unstable. To overcome these influences, a preprocessing operation can be applied to provide a uniform representation for 3D CAD models. For instance, we can detect and merge the sub-faces, and detect the transition features and design some specified operations (e.g. suppressing and restoring) for them to improve the robustness of our approach.

Our approach has the potential to generate the query part's NC process by merging multiple NC process segments of similar subparts from different parts since 3D CAD model retrieval could help user effectively locate the similar subparts. That is, retrieve the similar subparts distributed on multiple 3D CAD models in the repository first, and then generate the process route of the query part through recombining and optimizing the NC process segments of multiple similar subparts. Moreover, although the pockets machined with 2 1/2-axis CNC milling are taken as examples to illustrate the NC process reuse principle in this paper, the principle of our approach is also suitable for pocket with free-form surfaces. Here, it needs to independently design corresponding algorithms in terms of the characteristics of free-form surface. In addition, the principle can be further extended to other domains, e.g. manufacturing cost estimation, feature-based fixture design, and assembly automation.

8. Conclusion and future work

In this paper, a novel NC machining process reuse approach for similar subparts is presented, which extends the feature-based NC process reuse to a greater granularity of subpart with better flexibility and higher NC process generation efficiency. A general framework for NC process reuse is proposed first, which combines 3D CAD model retrieval, data mining for NC process cases and NC process reuse technologies together. Moreover, a feature-based parameter-driven model is established to represent the association between a machining feature and a machining operation. The NC process parameter-driven characteristic of similar feature is revealed according to FPDM. In addition, an NC process reusability assessment approach of similar pocket/subpart based on medial axis transform is proposed, making NC process decision-making proceed from the qualitative to the quantitative. Finally, the NC process inheritance mechanisms are explored to implement the NC process reuse automatically and efficiently. The experiments with a prototype system indicate that our approach can effectively support NC process reuse of similar subpart.

In the near future, several issues are worth to be further explored to improve the practicability of our approach: (1) the NC process reuse for the pocket with free-form surface, and (2) the combination and optimization for the generated NC process segments of multiple different features/subparts from the query part.

Acknowledgment

The authors are grateful to the financial support from the National Natural Science Foundation of China (No. 51375397, 51175434).

References

[1] Chen Y, Huang J, Zhang Z, et al. A part affordance-based approach for capturing detailed design knowledge. Comput-Aided Des 2013;45(12):1617–29.
[2] Ruiz P, Kamsu-Foguem B, Noyes D. Knowledge reuse integrating the collaboration from experts in industrial maintenance management. Knowl-Based Syst 2013;50(9):171–86.
[3] Bai J, Gao S, Tang W, et al. Design reuse oriented partial retrieval of CAD models. Comput-Aided Des 2010;42(12):1069–84.
[4] Iyer N, Jayanti S, Lou K, et al. Three-dimensional shape searching: state-of-the-art review and future trends. Comput-Aided Des 2005;37(5):509–30.
[5] Huang R, Zhang S, Bai X, et al. 3D CAD model retrieval driven rapid NC programming method for NC process reuse. J Mech Eng 2014;50(3):191–8. [in Chinese].
[6] Demian P, Fruchter R. An ethnographic study of design knowledge reuse in the architecture, engineering, and construction industry. Res Eng Des 2006;16(4):184–95.
[7] Babic B, Nesic N, Miljkovic Z. A review of automated feature recognition with rule-based pattern recognition. Comput Ind 2008;59(4):321–37.
[8] Gao S, Shah JJ. Automatic recognition of interacting machining features based on minimal condition subgraph. Comput-Aided Des 1998;30(9):727–39.
[9] Rahmani K, Arezoo B. Boundary analysis and geometric completion for recognition of intersecting machining features. Comput-Aided Des 2006;38(8):845–56.
[10] Huang R, Zhang S, Bai X. Manufacturability driven interacting machining feature recognition algorithms for 3D CAD models. J Comput-Aid Des Comput Graph 2013;25(7):1089–98. [in Chinese].
[11] Zhang H, Zhang S, Zhao P. et al. (2012) Modularization of feature information for marine diesel engine parts. In: Proceedings of the 2nd international conference on electronic and mechanical engineering and information technology.
[12] Zheng LY, Dong HF, Vichare P, et al. Systematic modeling and reusing of process knowledge for rapid process configuration. Robot Comput-Integr Manuf 2008;24(6):763–72.
[13] Jiang Y, Chen J, Ruan X. Fuzzy similarity-based rough set method for case-based reasoning and its application in tool selection. Int J Mach Tools Manuf 2006;46(2):107–13.
[14] Yan X, Yamazaki K, Liu J. Recognition of machining features and feature topologies from NC Programs. Comput-Aided Des 2000;32(10):605–16.
[15] Zhang X, Nassehi A, Newman ST. Feature recognition from CNC part programs for milling operations. Int J Adv Manuf Technol 2014;70(1–4):397–412.
[16] Xu X, Wang L, Newman ST. Computer-aided process planning—a critical review of recent developments and future trends. Int J Comput Integr Manuf 2011;24(1):1–31.

[17] Tapie L, Mawussi B, Bernard A. Topological model for machining of parts with complex shapes. Comput Ind 2012;63(5):528–41.
[18] Mawussi KB, Tapie L. A knowledge base model for complex forging die machining. Comput Ind Eng 2011;61(1):84–97.
[19] Wang W, Li Y, Ma Y. Towards a feature-based agent-driven NC tool path generation to support design and process changes. Comput-Aided Des Appl 2013;10(4):603–18.
[20] Hou M, Faddis TN. Automatic tool path generation of a feature-based CAD/CAPP/CAM integrated system. Int J Comput Integr Manuf 2006;19(4):350–8.
[21] Huang R, Zhang S, Li L. et al. (2013) Multi-level structuralized MBD model for manufacturing reuse of mechanical parts. In: Proceedings of the 13th IEEE international conference on computer-aided design and computer graphics.
[22] Huang R, Zhang S, Bai X, et al. Manufacturing semantics based 3D CAD model retrieval method. Comput Integr Manuf Syst 2013;19(6):1177–85. [in Chinese].
[23] Li Y, Liu X, Gao JX, et al. A dynamic feature information model for integrated manufacturing planning and optimization. CIRP Ann—Manuf Technol 2012;61(1):167–70.
[24] Chen Z, Fu Q. An optimal approach to multiple tool selection and their numerical control path generation for aggressive rough machining of pockets with free-form boundaries. Comput-Aided Des 2011;43(6):651–63.
[25] Cordella LP, Foggia P, Sansone C, et al. A (sub) graph isomorphism algorithm for matching large graphs. IEEE Trans Pattern Anal Mach Intell 2004;26(10):1367–72.
[26] Chen X, Gao S, Guo S, et al. A flexible assembly retrieval approach for model reuse. Comput-Aided Des 2012;44(6):554–74.

Tiancheng Li, Miodrag Bolić, and Petar M. Djurić

Resampling Methods for Particle Filtering

Classification, implementation, and strategies

IMAGE LICENSED BY GRAPHIC STOCK

Two decades ago, with the publication of [1], we witnessed the rebirth of particle filtering (PF) as a methodology for sequential signal processing. Since then, PF has become very popular because of its ability to process observations represented by nonlinear state-space models where the noises of the model can be non-Gaussian. This methodology has been adopted in various fields, including finance, geophysical systems, wireless communications, control, navigation and tracking, and robotics [2]. The popularity of PF has also spurred the publication of several review articles [2]–[6].

Using the PF method, we aim to track various distributions that arise in dynamic state-space models. The tracking is carried out by exploring the space of the states with randomly generated samples (also called *particles*). The distributions of interest are approximated by the generated particles as well as weights assigned to the particles.

There are many PF methods, and almost all of them are based on three operations: 1) particle propagation, 2) weight computation, and 3) resampling. Particle propagation and weight computation amount to the generation of particles and assignment of weights, whereas resampling replaces one set of particles and their weights with another set.

Particle generation and weight computation are computationally the most intensive steps. However, they are application dependent and can be easily implemented in parallel if parallel hardware is available. The resampling step is universal and generally state-dimension-free but is not naturally suitable for parallel processing. The resampling is essential for PF; without this step, PF will quickly produce a degenerate set of particles, i.e., a set in which a few particles dominate the rest of the particles with their weights. This means that the obtained estimates will be

Digital Object Identifier 10.1109/MSP.2014.2330626
Date of publication: 6 April 2015

1053-5888/15©2015IEEE

inaccurate and will have unacceptably large variances. With resampling, such deteriorations are prevented, which is why it is highly important to PF. Consequently, resampling has been extensively researched, and, as a result, various resampling schemes have been proposed [7]–[10].

Surveys of resampling methods can be found in [11]–[14]. These papers, however, only cover a small number of basic resampling methods and have become somewhat outdated. Furthermore, no classification has been made in these papers. This has been a disadvantage to researchers in getting a better grasp of the overall picture of resampling and of being able to readily choose the scheme that would fit their needs. This article aims to correct these shortfalls. More specifically, the main goal of this article is to introduce a new classification of resampling algorithms and provide a qualitative comparison of them. An additional goal is to set the grounds for further developments in resampling.

We divide the resampling algorithms into sequential and distributed/parallel algorithms. The most common are the sequential algorithms, where resampling is carried out from the approximating distribution using the latest weights. We also refer to these algorithms as *traditional*. However, researchers have explored other solutions, such as resampling that takes into account the history of the weights, resampling from approximate distributions, and resampling from only a part of the sampling space. In addition, approaches based on different ways of grouping particles have been proposed where grouping can be implemented, e.g., by using thresholds or by combining adjacent particles. These approaches might be of use when it is important to reduce the number of operations or to reduce communication between processing elements (PEs) in parallel implementations. We also discuss the frequency of resampling.

With multicore processors, the existence of general-purpose graphical processing units (GP-GPUs) in almost every computer and the emergence of embedded multicore and GP-GPU hardware, parallel processing can be readily implemented. The implementations of parallel resampling, however, can vary, which, in turn, reflect on their accuracy and speed. Some of the efforts in this area are described in this article.

In our view, future research efforts will be directed to specific implementations and theoretical analysis of the methods. The former include simplifying the resampling algorithms, development of better schemes with the ultimate goal of improving filtering performance, parallelization, and real-time implementations. The latter addresses the effects of the resampling algorithms on convergence and accuracy of approximation. As this article focuses mainly on providing guidelines to the readers and on qualitative description of the solutions, we do not explore issues such as robustness and do not provide theoretical proofs of any sort.

BACKGROUND OF PF AND RESAMPLING

A BRIEF REVIEW OF PF

We start with a brief review of PF and introduce the notation. There is a state-space model described by

$$x_t = g(x_{t-1}, u_t), \tag{1}$$
$$y_t = h(x_t, v_t), \tag{2}$$

where t is a time index and $t = 1, 2, \ldots$; $x_t \in R^{d_x}$ is the state of the model that is hidden (not observed); $y_t \in R^{d_y}$ is the observation; $u_t \in R^{d_u}$ and $v_t \in R^{d_v}$ are white noises that are independent of each other; and g: $R^{d_x} \times R^{d_u} \to R^{d_x}$ and h: $R^{d_x} \times R^{d_v} \to R^{d_y}$ are known functions. An alternative representation of these equations is by the probability distributions of the state, $p(x_t \,|\, x_{t-1})$, and of the observation, $p(y_t \,|\, x_t)$, which can be obtained from (1) and (2) and the probability distributions of u_t and v_t, respectively. The interest is in nonlinear models and where the noises in (1) and (2) are not necessarily Gaussian.

The objective of PF is the sequential estimation of distributions of the state, including the filtering distribution $p(x_t \,|\, y_{1:t})$, the predictive distribution $p(x_t \,|\, y_{1:t-1})$, or the smoothing distribution $p(x_t \,|\, y_{1:T})$, where $t < T$. Here, we focus on the filtering distribution. This distribution can be expressed in terms of the filtering distribution at time instant $t-1$, $p(x_{t-1} \,|\, y_{1:t-1})$, i.e., in a recursive form by

$$p(x_t \,|\, y_{1:t}) \;\propto\; \int p(y_t \,|\, x_t)\, p(x_t \,|\, x_{t-1})\, p(x_{t-1} \,|\, y_{1:t-1}) dx_{t-1}, \tag{3}$$

where the symbol $\propto$ signifies "proportional to." This update cannot be implemented analytically except in a very few cases, and, therefore, one resorts to approximations.

We reiterate that with PF, the underlying approximation is to represent continuous distributions by discrete random measures composed of particles $x_t^{(m)}$, which are possible values of the unknown state x_t and weights $w_t^{(m)}$ assigned to the particles. The distribution $p(x_{t-1} \,|\, y_{1:t-1})$ is approximated by a random measure of the form $\chi_{t-1} = \{x_{t-1}^{(m)},\ w_{t-1}^{(m)}\}_{m=1}^{M}$, where M is the number of particles, i.e.,

$$p(x_{t-1} \,|\, y_{1:t-1}) \approx \textstyle\sum_{m=1}^{M} w_{t-1}^{(m)}\, \delta\big(x_{t-1} - x_{t-1}^{(m)}\big), \tag{4}$$

where $\delta(\cdot)$ is the Dirac delta impulse and all the weights sum up to one. With this approximation, the integral in (3) can readily be solved, and we can write

$$p(x_t \,|\, y_{1:t}) \;\dot{\propto}\; p(y_t \,|\, x_t) \sum_{m=1}^{M} w_{t-1}^{(m)}\, p\big(x_t \,|\, x_{t-1}^{(m)}\big), \tag{5}$$

where $\dot{\propto}$ means "approximate proportionality."

The last expression shows how we can obtain the approximation χ_t of the filtering distribution recursively in time. At time instant $t-1$, one starts the construction of χ_t by generating particles $x_t^{(m)}$, which are used for representing $p(x_t \,|\, y_{1:t})$. This step of PF is referred to as *particle propagation* because a particle $x_{t-1}^{(m)}$ is moved forward in time and is a parent of $x_t^{(m)}$. For particle propagation and weight computation, we employ the concept of importance sampling [15]. Ideally, the propagated particles should be drawn from $p(x_t \,|\, y_{1:t})$, and then they will all have equal weights. However, this is infeasible in most cases, and,

therefore, one uses an instrumental function $\pi(x_t)$. For example, in [1], this function is $p(x_t|x_{t-1})$.

The second basic step of PF is the computation of the particle weights. To have correct inference from the generated particles, the theory shows that the generated particles from $\pi(x_t)$, which is different from $p(x_t|y_{1:t})$, have to be weighted [15]. Under mild conditions, one can show that these weights can be recursively computed according to

$$w_t^{(m)} \propto w_{t-1}^{(m)} \frac{p(y_t|x_t^{(m)})\, p\left(x_t^{(m)}|x_{t-1}^{(m)}\right)}{\pi(x_t^{(m)})}. \tag{6}$$

Often, the computation of the expression to the right of the proportionality sign is followed by normalization of the weights (so that they sum up to one).

Ideally, the weights of the particles should all be equal. On the other extreme, it is most undesirable if all the particles have weights equal to zero or one or a few particles have most of the weight and the rest of the particle weights are negligible. This is commonly called *degeneracy* and is exactly what eventually happens when PF is realized by using only the aforementioned two steps. Then, as the processing of the observations proceeds, the variance of the weights increases and reaches a point at which the random measure is a very poor approximation of the filtering distribution. For this reason, PF needs a third step, referred to as *resampling*.

WHEN IMPLEMENTING RESAMPLING, SEVERAL DECISIONS MUST BE MADE. THEY INCLUDE CHOOSING THE DISTRIBUTION FOR RESAMPLING, SPECIFYING THE SAMPLING STRATEGY, DETERMINING THE RESAMPLED SIZE, AND SELECTING THE FREQUENCY OF RESAMPLING.

THE BASICS OF RESAMPLING

With resampling, one aims to prevent the degeneracy of the propagated particles by modifying the random measure χ_t to $\tilde{\chi}_t$ and improving the exploration of the state space at $t+1$. While alleviating degeneracy during resampling, it is important that the random measure approximates the original distribution as well as possible and prevents bias in the estimates [16]. Although the approximation by $\tilde{\chi}_t$ is very similar to that of χ_t, the set of particles of $\tilde{\chi}_t$ is significantly different from that of χ_t. Resampling means that the particles from χ_t with large weights are more likely to dominate $\tilde{\chi}_t$ than particles with small weights, and, consequently, in the next time step, more new particles will be generated in the region of large weights. This is the reason for the improvement in exploration after resampling. The focus of exploration is shifted to the parts of the space with large probability masses. Because of resampling, the propagated particles from $\tilde{\chi}_t$ will have weights that are less discriminate than if the propagation was from the particles of χ_t. This is an intuitive idea with important practical and theoretical implications.

Formally, resampling is a process in which one samples from the original random measure $\chi_t = \{x_t^{(m)}, w_t^{(m)}\}_{m=1}^{M}$ to create a new random measure $\tilde{\chi}_t = \{\tilde{x}_t^{(n)}, \tilde{w}_t^{(n)}\}_{n=1}^{N}$. Then, the random measure χ_t is replaced with $\tilde{\chi}_t$. In the process, some of the particles of χ_t are replicated, and, most likely, they are the particles with large weights. The particles of $\tilde{\chi}_t$ are used for propagation of new particles, and thus, they are the parents of $x_{t+1}^{(m)}$. We note that for the approximation of $p(x_t|y_{1:t})$, it is better to use χ_t than $\tilde{\chi}_t$. We also observe that the number of resampled particles N is not necessarily equal to the number of propagated particles. Traditional resampling methods keep them constant, and, usually, $M = N$. Finally, in most of the resampling methods, the weights of the particles after resampling are all equal.

Resampling, however, may introduce undesired effects. One of them is sample impoverishment. With resampling, low-weighted particles are most likely removed, and, thereby, the diversity of the particles is reduced [1], [9], [12]. For example, if a few particles of χ_t have most of the weight, many of the resampled particles will be the same, i.e., the number of different particles in $\tilde{\chi}_t$ will be small. The other effect is on the speedup of implementation of PF. We recall that PF is often used for signal processing when observations have to be processed in real time. A good solution for gaining in speed is to parallelize the PF. As will be shown, parallelizing the resampling is rather challenging.

The undesired effects of resampling have pushed researchers to investigate advanced methods for resampling. These methods have many features, including a variable number of particles, the removal of the restriction of equal weighting of the resampled particles, the avoidance of discarding low-weighted particles, and the introduction of parallel frameworks for resampling.

When implementing resampling, several decisions must be made. They include choosing the distribution for resampling, specifying the sampling strategy, determining the resampled size, and selecting the frequency of resampling.

CLASSIFICATION OF RESAMPLING SCHEMES

Our high-level classification of resampling methods with representative references is shown in Table 1. We first group the methods based on their implementation as sequential and parallel. We note that the parallel implementations represent two or more sequential implementations executed simultaneously. The sequential strategies are further classified based on whether the resampling is from a single distribution or from two or more distributions obtained from grouping of the particles (compound sampling). We also have a third category, referred to as *special strategies*. As the name suggests, the special strategies have features that separate them from single and compound sampling. Next, we make several remarks, of which the first four are also reflected in Table 1 (R1–R4).

[TABLE 1] THE HIGH-LEVEL CLASSIFICATION OF RESAMPLING METHODS.

CLASSIFICATIONS	R1 BASED ON THE DISTRIBUTION χ_t	R2 RESAMPLING OF ALL THE PARTICLES IN THE SAME WAY	R3 GROUPING	R4 USING INFORMATION FROM THE CURRENT TIME INSTANT
Sequential implementation	YES	YES/NO	YES/NO	YES/NO
■ SINGLE DISTRIBUTION SAMPLING [1], [7], [8], [10]	YES	YES	NO	YES
■ COMPOUND-SAMPLING		YES/NO FOR MANY: DIFFERENT OR NO RESAMPLING PER GROUP	BASED ON COMPOUND CRITERIA	
• THRESHOLDS/GROUPING-BASED RESAMPLING [11], [12], [24]				YES/NO FOR [11] AND [17]
• RESAMPLING THAT TAKES INTO ACCOUNT THE STATE [16]				YES
■ SPECIAL STRATEGIES		YES		
• MODIFIED RESAMPLING [11]	NO		NO	YES/NO FOR [18]
• VARIABLE-SIZE RESAMPLING [27]	YES			YES
• ROUGHENING [1]				
Parallel implementation			BASED ON ADJACENT PARTICLES	
■ MAPPING TO SPECIFIC HARDWARE PLATFORMS [31]–[33], [35]–[38] ■ DISTRIBUTED RESAMPLING [32], [40] ■ NORMALIZATION-FREE RESAMPLING [38], [39], [41]				

REMARK 1

One classification is based on the used distribution for resampling. Mainly, this is the distribution represented by χ_t. Other approaches include sampling from an approximate distribution. We will point out cases in which resampling is not performed from χ_t.

REMARK 2

Resampling can be performed in the same way on all of the particles, or it is possible to resample in different ways in different parts of the sampling space.

REMARK 3

There are methods that group the particles in some way before resampling is performed. In that respect, we distinguish among single-distribution sampling schemes (no grouping of particles), techniques that combine adjacent particles (which is the common approach in parallel implementations of resampling), and techniques that group particles for resampling based on some predefined criteria (referred to as *compound sampling*).

REMARK 4

Resampling can also be classified based on whether only particles from the current time step are involved in resampling, which is a common approach, the particles from previous time instants are considered [17], or some future particles are generated and taken into account for resampling [18]. Also, resampling can be classified based on whether only the weight is taken into account, which is the standard approach, or the state and the weight of particles are considered together [16].

REMARK 5

Resampling may be applied not in all but only in selected time steps. Compensations such as roughening [1] may be implemented with resampling for performance improvement.

REMARK 6

There are deterministic and stochastic resampling methods. The deterministic methods lead to a set of particles that are always the same for the same input set of particles.

IMPLEMENTATION OF RESAMPLING SCHEMES

In the following sections, we will explain various resampling methods and provide pseudocodes for selected algorithms. The pseudocodes are presented in a simple and unified way but not in forms that optimize the implementation of the algorithms. In practical implementations on a specific platform, programming techniques are required to maximally speed up the computation. For example, the cumulative sum calculation in code 1 can be implemented in MATLAB using vectors, which would be faster than the iterative calculation shown by code 1. Traditional sampling methods have already been described elsewhere; we present them here for completeness and because they are used in the compound, special, and parallel methods described later. We assume that the weights $w_t^{(m)}$ are normalized before resampling, i.e., $\sum_{m=1}^{M} w_t^{(m)} = 1$.

SINGLE-DISTRIBUTION SAMPLING METHODS

In this category, all the particles are resampled by using a single-distribution sampling procedure. The expected number of times $N_t^{(m)}$ that the mth particle is resampled is proportional to $w_t^{(m)}$, i.e.,

[TABLE 2] PSEUDOCODES OF MULTINOMIAL, STRATIFIED, SYSTEMATIC, RESIDUAL, BRANCH-KILL, AND ROUNDING-COPY RESAMPLING.

Code 1: Cumulative sum of normalized weights.

$[\{Q_t^{(m)}\}_{m=1}^{M}] = \text{CumulativeSum}[\{w_t^{(m)}\}_{m=1}^{M}]$

$Q_t^{(1)} = w_t^{(1)}$
FOR $m = 2{:}M$
  $Q_t^{(m)} = Q_t^{(m-1)} + w_t^{(m)}$
END

Code 2: Deterministic replication of particles.

$[\{\tilde{x}_t^{(n)}\}_{n=1}^{N}, N] = \text{Replication}[\{x_t^{(m)}, N_t^{(m)}\}_{m=1}^{M}]$

$n = 0$
FOR $m = 1{:}M$
  FOR $h = 1{:}N_t^{(m)}$
    $n = n + 1$
    $\tilde{x}_t^{(n)} = x_t^{(m)}$
  END
END
$N = n$

Code 3: Multinomial/stratified/systematic resampling.

$[\{\tilde{x}_t^{(n)}\}_{n=1}^{N}] = \text{Resample}[\{x_t^{(m)}, w_t^{(m)}\}_{m=1}^{M}, N]$

$[\{Q_t^{(m)}\}_{m=1}^{M}] = \text{CumulativeSum}[\{w_t^{(m)}\}_{m=1}^{M}]$
$n = 0$
/Systematic/stratified choice runs:
  $m = 1$
/Systematic choice runs
  $u_0 \sim U(0, 1/N]$
WHILE $(n \le N)$
/Stratified choice runs
  $u_0 \sim U(0, 1/N]$
/Systematic/stratified choice runs
  $u = u_0 + n/N$
/Multinomial choice runs
  $u \sim U(0, 1]; \ m = 1$
  WHILE $(Q_t^{(m)} < u)$
    $m = m + 1$
  END
  $n = n + 1$
  $\tilde{x}_t^{(n)} = x_t^{(m)}$
END

Code 4: Residual resampling/residual systematic resampling (RSR).

$[\{\tilde{x}_t^{(n)}\}_{n=1}^{N}] = \text{Resample}[\{x_t^{(m)}, w_t^{(m)}\}_{m=1}^{M}, N]$

/RSR choice runs
  $\Delta u \sim U(0, 1/N]$
FOR $m = 1{:}M$
/Residual choice runs the following two lines
  $N_t^{(m)} = \text{Floor}(N \times w_t^{(m)})$
  $\hat{w}_t^{(m)} = w_t^{(m)} - N_t^{(m)}/N$
/RSR choice runs the following two lines
  $N_t^{(m)} = \text{Floor}(N \times (w_t^{(m)} - \Delta u)) + 1$
  $\Delta u = \Delta u + N_t^{(m)}/N - w_t^{(m)}$
END
$[\{\tilde{x}_t^{(n)}\}_{n=1}^{N_t}, N_t] = \text{Replication}\ [\{x_t^{(m)}, N_t^{(m)}\}_{m=1}^{M}]$
/Residual choice runs the following four lines
  FOR $m = 1{:}M$
    $\hat{w}_t^{(m)} = \hat{w}_t^{(m)} \times N/(N - N_t)$
  END
  $[\{\tilde{x}_t^{(n)}\}_{n=N_t+1}^{N}] = \text{(Multinomial)Resample}[\{x_t^{(m)}, \hat{w}_t^{(m)}\}_{m=1}^{M}, N - N_t]$

Code 5: Branch-kill/rounding-copy resampling.

$[\{\tilde{x}_t^{(n)}\}_{n=1}^{N}] = \text{Resample}[\{x_t^{(m)}, w_t^{(m)}\}_{m=1}^{M}, N_{\text{ref}}]$

FOR $m = 1{:}\ M$
/Branch kill choice runs the following five lines
  $u \sim U(0, 1/N_{\text{ref}}]$
  $N_t^{(m)} = \text{Floor}(N_{\text{ref}} \times w_t^{(m)})$
  IF $(N_{\text{ref}} \times w_t^{(m)} - N_t^{(m)}) \ge u$
    $N_t^{(m)} = N_t^{(m)} + 1$
  END
/Rounding-copy choice runs
  $N_t^{(m)} = \text{Round}(N_{\text{ref}} \times w_t^{(m)})$
END
$[\{\tilde{x}_t^{(n)}\}_{n=1}^{N}, N] = \text{Replication}[\{x_t^{(m)}, N_t^{(m)}\}_{m=1}^{M}]$

Note: The different methods are described with different colors, and the black text is common for all of them in each group, except where otherwise stated. Code 3 presents resampling methods based on the cumulative sum of the normalized weights (obtained by code 1). Codes 4 and 5 are methods that use deterministic replication (implemented by code 2). All of these codes produce resampled particles with equal weights.

$$E(N_t^{(m)} | w_t^{(m)}) = Nw_t^{(m)}. \tag{7}$$

This constraint is known as the *unbiasedness* or *proper-weighting condition* [10].

TRADITIONAL METHODS

Multinomial Resampling

The core idea of multinomial resampling [1] is to generate independently N random numbers, $u_t^{(n)}$ from the uniform distribution on (0, 1] and use them to select particles from χ_t. In the nth selection, the particle $x_t^{(m)}$ is chosen when the following condition is satisfied:

$$Q_t^{(m-1)} < u_t^{(n)} \le Q_t^{(m)}, \tag{8}$$

where

$$Q_t^{(m)} = \sum_{k=1}^{m} w_t^{(k)}. \tag{9}$$

Thus, the probability of selecting $x_t^{(m)}$ is the same as that of $u_t^{(n)}$ being in the interval bounded by the cumulative sum of the normalized weights as shown in (8). This sampling scheme satisfies the unbiasedness condition. The pseudocode of the cumulative sum of normalized weights is shown by code 1 in Table 2.

Multinomial resampling (see code 3 in Table 2) is also referred to as *simple random resampling*. Since the sampling of each particle is random, the upper and lower limits of the number of times a given particle is resampled are zero (not sampled) and N_t (sampled N_t times), respectively. This yields the maximum variance of the resampled particles.

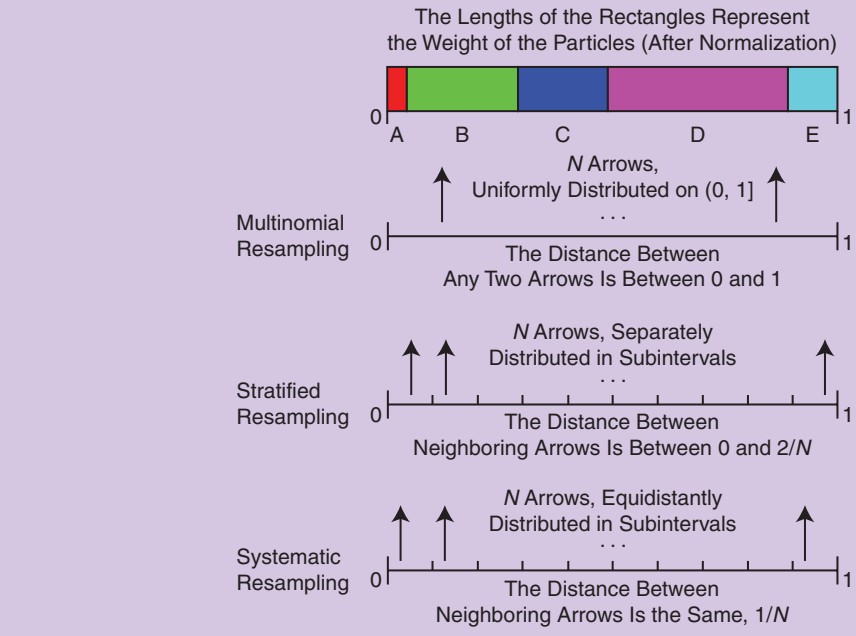

(a)

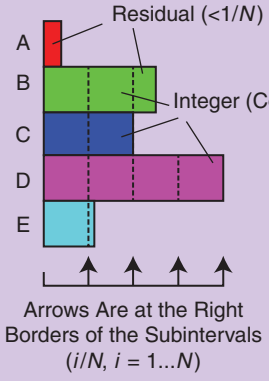

Residual resampling, RSR, branch-kill, and rounding-copy replicate the particle based on the integer parts of each weight in the same way but deal with the residual parts differently.

Residual Resampling: Sample from the normalized fractions by using multinomial resampling (proceeded in a separate loop different to the integer replication).

RSR: Cumulatively add up residuals and sample them by using the idea of systematic resampling (proceeded in the same loop with the integer replication).

Branch-kill: If the residual $\geq u\sim(0, 1/N]$, take it as an integer and replicate it one time. Otherwise, abandon it.

Rounding-Copy: If the residual $\geq 1/(2N)$, take it as an integer and replicate it once. Otherwise, abandon it.

} Parallel Processing of Each Particle

} Do Not Preserve Constant Sample Size

(b)

[FIG1] A description of the traditional resampling methods. (a) A multinomial, stratified, and systematic resampling based on the cumulative sum of the normalized particle weights. The arrows represent sampling locations, and a particle is sampled if it is targeted by an arrow. (b) Methods based on residual resampling. They include two parts. The particles from the first part are obtained by replicating $x_t^{(m)}\lfloor Nw_t^{(m)}\rfloor$ times if $\lfloor Nw_t^{(m)}\rfloor \geq 1$, and the particles from the second part are generated based on the residual weights.

The computational complexity of multinomial resampling is of order $O(NM)$, where the M factor arises from the search of the required m in (8). It is known that multinomial resampling is not efficient [8], and this has motivated a search for faster methods. The binary search is explored to execute the search of m in (8), which reduces the computational complexity from M to $\log(M)$ [8]. The variance of the number of times a particle is resampled can be reduced by, for example, stratification and deterministic sampling.

Stratified/Systematic Resampling

Stratified resampling [7] divides the whole population of particles into subpopulations called *strata*. It prepartitions the $(0, 1]$ interval into N disjoint subintervals $(0, 1/N] \cup \cdots \cup (1-1/N, 1]$. The random numbers $\{u_t^{(n)}\}_{n=1}^N$ are drawn independently in each of these subintervals, i.e.,

$$u_t^{(n)} \sim U\Big(\frac{n-1}{N}, \frac{n}{N}\Big], \quad n = 1, 2, \ldots, N, \tag{10}$$

and then the bounding method based on the cumulative sum of normalized weights as shown in (8) is used.

Systematic resampling [7], [8] also exploits the idea of strata but in a different way. Now, $u_t^{(1)}$ is drawn from the uniform distribution on $(0, 1/N]$, and the rest of the u numbers are obtained deterministically, i.e.,

$$\begin{aligned} u_t^{(1)} &\sim U\Big(0, \frac{1}{N}\Big], \\ u_t^{(n)} &= u_t^{(1)} + \frac{n-1}{N}, \quad n = 2, 3, \ldots, N. \end{aligned} \tag{11}$$

Both the stratified and the systematic procedures are presented in Table 2. Their complexity is of order $O(N)$. Note that the systematic method is computationally more efficient than the stratified method because of the smaller number of random numbers that are generated. A visual description of the multinomial, stratified, and systematic resampling methods is displayed in Figure 1(a).

The upper and lower limits of the times the mth particle is resampled in the systematic method are $\lfloor N w_t^{(m)} \rfloor$ and $\lfloor N w_t^{(m)} \rfloor + 1$, respectively, where $\lfloor x \rfloor$ denotes the floor operation (the largest integer not exceeding x). By contrast, for stratified resampling, they are $\max(\lfloor N w_t^{(m)} \rfloor - 1, 0)$ and $\lfloor N w_t^{(m)} \rfloor + 2$, respectively, because the variables $\{u_t^{(n)}\}_{n=1}^{N}$ are not equidistant, and instead $\Delta u = u_t^{(n)} - u_t^{(n-1)}$ for $n = 2, 3, \ldots, N$ varies between 0 and $2/N$. When Δu is close to 0, a particle with a very small weight (close to 0 but bigger than Δu) can be resampled twice and when Δu is bigger than $2/N$, a particle with weight between $1/N$ and Δu can be discarded. This indicates that the variance of the number of a resampled particle by the systematic method is smaller than that of the stratified method.

Residual Resampling (Remainder Resampling)

Residual resampling [9], [10] consists of two stages. The first is a deterministic replication of each particle whose weight is bigger than $1/N$, and the second is random sampling using the remaining of the weights (referred to as *residuals*). The code for deterministic replication is shown by code 2, where $N_t^{(m)}$ represents the number of times the particle $x_t^{(m)}$ is replicated in this way. With residual resampling, the mth particle is resampled $N_t^{(m)} + R_t^{(m)}$ times, where $N_t^{(m)}$ and $R_t^{(m)}$ are the numbers of replications from the first and second stage, respectively, and where $N_t^{(m)} = \lfloor N w_t^{(m)} \rfloor$. The total number of replicated particles in the first stage is $N_t = \sum_{m=1}^{M} N_t^{(m)}$, and in the second stage, $R_t = N - N_t$. The residual of the weight is obtained from

$$\hat{w}_t^{(m)} = w_t^{(m)} - \frac{N_t^{(m)}}{N}. \tag{12}$$

In the second stage, the particles are drawn according to the residual weights and by using multinomial resampling (or another random sampling method), where the probability for selecting $x_t^{(m)}$ is proportional to the residual weight of that particle. Residual resampling has two loops taking on the order of $O(M) + O(R_t)$ time for computing.

The first stage represents a deterministic replication, and so the variation of the number of times a particle is resampled is only attributed to the second stage. Thus, the upper and lower limits of the number of times that the mth particle is resampled are $\lfloor N w_t^{(m)} \rfloor$ and $\lfloor N w_t^{(m)} \rfloor + R_t$, respectively, if the second stage is implemented using multinomial resampling. The code of the residual resampling method is given by code 4.

VARIATIONS OF TRADITIONAL RESAMPLING

The aforementioned four traditional methods are probably the best known and most used. They have been modified in various ways. For example, one of them removes the computationally expensive multinomial resampling part in residual resampling and implements resampling in a single loop (see code 4 in Table 2). The method is called *residual systematic resampling (RSR)* [12], [19]. RSR accumulates the fractional contributions of each particle in the searching sequence until it is large enough to generate a sample (which is equivalent to the accumulation idea used in systematic resampling). Then, no additional procedure is required for the residuals. Thus, one can have one iteration loop, and the complexity is of order $O(N)$.

If it is not mandatory to keep the particle size M constant at every time step and instead, the size is allowed to vary, we have simple ways of dealing with the particles in parallel and in one loop. We describe here two approaches. In the first approach, the number of replicated particles of $x_t^{(m)}$ is equal to $N_t^{(m)} = \lfloor N w_t^{(m)} \rfloor$ with probability $1 - p$ or equal to $N_t^{(m)} = \lfloor N w_t^{(m)} \rfloor + 1$ with probability p, where $p = N w_t^{(m)} - \lfloor N w_t^{(m)} \rfloor$. This method is called the *branch-kill* procedure [20] or *branching* [21]. In the second approach, $N_t^{(m)}$ is the nearest integer of $N w_t^{(m)}$, i.e., the rounding result of $N w_t^{(m)}$. We refer to this method as *rounding-copy* resampling [22]. Both methods (see code 5 in Table 2) require no additional operation and satisfy the unbiasedness condition but generate a varying sample size. The upper and lower limits of the number of replications of the mth particle in the branch-kill, rounding-copy, and RSR methods are all $\lfloor N w_t^{(m)} \rfloor$ and $\lfloor N w_t^{(m)} \rfloor + 1$, respectively.

[TABLE 3] A COMPARISON OF TRADITIONAL RESAMPLING METHODS (ALL THE RESAMPLED PARTICLES HAVE EQUAL WEIGHTS).

RESAMPLING METHODS	COMPUTATIONAL COMPLEXITY	ABLE TO KEEP CONSTANT SAMPLE SIZE	NUMBER OF RANDOM NUMBERS USED	NUMBER OF TIMES A PARTICLE IS REPLICATED	
				LOWER LIMIT	UPPER LIMIT
MULTINOMIAL	$O(NM)$ (OR $O(N \log M)$)	YES	N	0	N
RESIDUAL	$O(M) + O(R_t)$	YES	R_t	$\lfloor N w_t^{(m)} \rfloor$	$\lfloor N w_t^{(m)} \rfloor + R_t$
STRATIFIED	$O(N)$	YES	N	$\max(\lfloor N w_t^{(m)} \rfloor - 1, 0)$	$\lfloor N w_t^{(m)} \rfloor + 2$
SYSTEMATIC	$O(N)$	YES	1	$\lfloor N w_t^{(m)} \rfloor$	$\lfloor N w_t^{(m)} \rfloor + 1$
RESIDUAL SYSTEMATIC	$O(N)$	YES	1	$\lfloor N w_t^{(m)} \rfloor$	$\lfloor N w_t^{(m)} \rfloor + 1$
BRANCH-KILL	$O(N)$	NO	M	$\lfloor N w_t^{(m)} \rfloor$	$\lfloor N w_t^{(m)} \rfloor + 1$
ROUNDING-COPY	$O(N)$	NO	0	$\lfloor N w_t^{(m)} \rfloor$	$\lfloor N w_t^{(m)} \rfloor + 1$

A succinct comparison of the properties of the aforementioned methods is given in Table 3. The computational speeds of the methods are presented in [14] and [22].

COMPOUND SAMPLING

The resampling methods addressed so far are based on an approach where all the particles are sampled in the same way. This entails obtaining relatively similar resampling results. In all of the methods, the condition of unbiasedness is satisfied, and the resampled particles are equally weighted. In the following, we describe methods where resampling is realized without attempting to satisfy the conditions of unbiasedness and equal-weighting. This may entail risks of which the practitioner must be aware.

The compound sampling methods are based on grouping the particles by using predefined criteria prior to applying resampling. The groups are nonoverlapping, and they represent a partition of the whole particle population. The criterion for grouping is usually based on weight thresholds so that particles with similar weights are put in the same group, and then resampling is performed of each group in different ways. The reasons for applying compound resampling include decreasing the execution time and preserving particle diversity.

Compound resampling has its roots in stratified sampling. We will classify the methods based on whether the grouping is performed using a predefined threshold, which is either a constant or a function of the weights, or it is based on the particle values. We note that particles are often grouped when we implement parallel resampling. However, in parallel resampling, the groups are most commonly formed just by clustering index-neighboring particles.

THRESHOLD-/GROUPING-BASED RESAMPLING

In this category, particles are placed into different groups based on weight thresholds, and one uses different sampling strategies for each group to provide more flexibility for resampling. The threshold can be dynamic/adaptive or fixed, and there can be one or more thresholds.

Dynamic Threshold

The optimal resampling from [24] automatically sets a threshold value c_t, where c_t is a unique solution of

$$N = \sum_{m=1}^{M} \min\left(\frac{w_t^{(m)}}{c_t}, 1\right), \tag{13}$$

where N is given, and $N < M$. All the particles whose weights are above this threshold are entirely preserved rather than replicated. Thus, there are no multiple copies of these particles in the final set of N particles. The other particles are resampled with a probability corresponding to their weights and assigned a weight c_t. We see that the resampled particles do not have equal weights (see code 6). The main advantage of the method is that, among the unbiased resampling methods, it is optimal in terms of minimizing the squared error-loss function

$$E\left(\sum_{m=1}^{M} (\tilde{w}_t^{(m)} - w_t^{(m)})^2\right), \tag{14}$$

where $\tilde{w}_t^{(m)}$ is the new weight of $x_t^{(m)}$ when it is resampled; otherwise, $\tilde{w}_t^{(m)}$ is equal to zero. The method is appropriate for PF that uses increased number of propagated particles, and optimal resampling reduces the number to $N < M$. A disadvantage of the method is the need for calculating the value of c_t at each iteration. Also, the resampled particles may still suffer from degeneracy as the variance of the weights remains high.

Code 6: Optimal resampling.

$[\{\tilde{x}_t^{(n)}, \tilde{w}_t^{(n)}\}_{n=1}^{N}] = $ (Optimal)Resample $[\{x_t^{(m)}, w_t^{(m)}\}_{m=1}^{M}, N]$
Compute c_t satisfying (13)
$n = 0$; $h = 0$
FOR $m = 1: M$
  IF $w_t^{(m)} \geq c_t$
    $n = n + 1$
    $\tilde{x}_t^{(n)} = x_t^{(m)}$; $\tilde{w}_t^{(n)} = w_t^{(m)}$
  ELSE
    $h = h + 1$
    $A^{(h)} = x_t^{(m)}$; $B^{(h)} = w_t^{(m)}$
  END
END
$N_1 = n$
$[\{\tilde{x}_t^{(n)}\}_{n=N_1+1}^{N}] =$ (Stratified)Resample $[\{A^{(r)}, B^{(r)}\}_{r=1}^{h}, N - N_1]$
FOR $n = N_1 + 1: N$
  $\tilde{w}_t^{(n)} = c_t$
END

There are similarities between optimal resampling, rejection control (RC) [17] and partial RC (PRC) [11]. In RC, a control threshold c_t is computed, which may be a quantity given in advance, e.g., the median or a quantile of the weights, and the mth particle is accepted with a probability

$$p = \min\left(1, \frac{w_t^{(m)}}{c_t}\right). \tag{15}$$

In PRC, the particles with weights that are greater than or equal to c_t are automatically accepted, whereas other particles are accepted with probability p. This can be viewed as a combination of the rejection method and importance sampling. An accepted particle $x_t^{(m)}$ is reweighted with a new weight $\max(c_t, w_t^{(m)})$, and the rejected particles are replaced by particles regenerated from particles from previous time instances. These two forms of RC differ primarily in how far one goes back to regenerate particles. The RC does it to the earliest time, $t = 0$, while the PRC only regenerates particles from time instant $t - 1$ so that one saves on computations. These methods cannot be considered as candidates for real-time implementation because they have nondeterministic execution time and large memory requirements.

Fixed Threshold

A partial deterministic reallocation approach is proposed in [11] based on a fixed threshold, say $1/N$, where N is the desired sample size. The mth particle with a weight larger than $1/N$, is replicated $\lfloor N w_t^{(m)} \rfloor$ (or $\lfloor N w_t^{(m)} \rfloor + 1$) times, and the weights

after resampling are $w_t^{(m)}/\lfloor Nw_t^{(m)}\rfloor$ (or $w_t^{(m)}/(\lfloor Nw_t^{(m)}\rfloor+1)$) (this is referred to as *particle splitting* in the article). The mth particle with weight smaller than $1/N$ is sampled with probability $Nw_t^{(m)}$ and is weighted as $1/N$ (see code 7). The resampled particles are not equally weighted, and, notably, their weight sum is not one (a normalization step is additionally required). The sampling method is biased.

Code 7: Reallocation resampling.

$\left[\{\tilde{x}_t^{(n)}, \tilde{w}_t^{(n)}\}_{n=1}^{N^*}\right]$ = (Reallocation)Resample $[\{x_t^{(m)}, w_t^{(m)}\}_{m=1}^{M}, N]$
$n = 0$
FOR $m = 1{:}\ M$
  IF $w_t^{(m)} \geq 1/N$
    $N_t^{(m)}$ = Floor $(N \times w_t^{(m)})$ (or $N_t^{(m)}$ = Floor $(N \times w_t^{(m)}) + 1$)
    FOR $h = 1{:}\ N_t^{(m)}$
      $n = n + 1$
      $\tilde{x}_t^{(n)} = x_t^{(m)};\ \tilde{w}_t^{(n)} = w_t^{(m)}/N_t^{(m)}$
    END
  ELSE
    $u \sim U(0,\ 1/N]$
    IF $w_t^{(m)} \geq u$
      $n = n + 1$
      $\tilde{x}_t^{(n)} = x_t^{(m)};\ \tilde{w}_t^{(n)} = 1/N$
    END
  END
END
$N^* = n$

To reduce the complexity of hardware realization and the required power consumption, resampling is performed on only some of the particles. This is the idea behind partial resampling (PR) [12]. PR consists of two steps: in the first, the particles are classified as moderate, negligible, or dominating; and in the second, different resampling strategies are applied to each group of particles. In [17], three different resampling functions are proposed for determining which particles are resampled/discarded and how to allocate the weights, and, to that end, two thresholds are used. To further increase the processing speed, the classification of the particles can be overlapped with the weight computation (overlapped PR).

Grouping strategies may also be applied to alleviate the impoverishment that is practically inevitable in all the resampling methods presented so far. For example, the double systematic resampling approach from [25] partitions the particles into two groups, in low- and high-weighted particles and where the number of particles to be resampled from each group is specified. In this way, the low-weighted particles are resampled independently from the group of high-weighted particles. Obviously, this may lead to biased sampling.

There are several other methods from the literature that are built on similar ideas. Before their adoption, however, their features need to be better understood and firm guidelines for use provided.

RESAMPLING THAT TAKES INTO ACCOUNT PARTICLE VALUES

All of the above resampling methods are based on the particle weights. A possible way to improve resampling is to exploit the particle values (the state information they contain) during resampling. The particle distribution in the state space exhibits their diversity and, therefore, is the key for monitoring impoverishment. In this category of resampling methods, the particles are grouped with respect to not only their weights but also their values.

Particles in close proximity in values may represent a similar state, and, thus, they can be merged to reduce the number of particles with different values. This is the basis of deterministic resampling [16], which replaces the second stage of residual resampling by merging particles using their residuals. This aims at preserving the diversity of the particles so that no particles are discarded at all, which is helpful when the number of particles is small. Contrary to particle merging, particle splitting replaces a particle with a large weight (larger than a threshold) with a set of particles with the same values and whose sum of weights is equal to the original weight (see Figure 2). Particle merging is implemented before the weight-updating step to reduce the sample size to save computation, while particle splitting is applied after weight updating as an alternative to resampling to reduce the weight variance and to recover the sample size [23]. A main disadvantage of these methods is that the dimensionality-free property of resampling is destroyed.

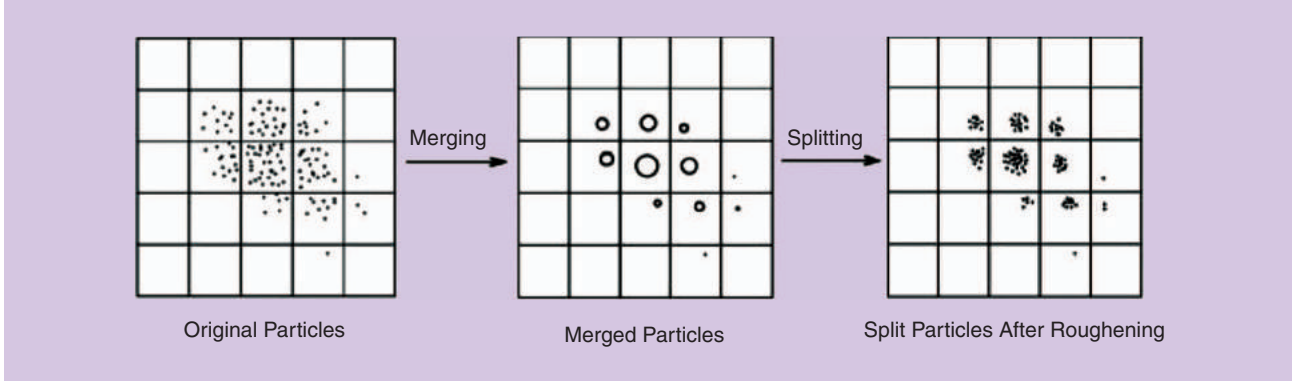

[FIG2] Particle merging and splitting in a two-dimensional state space. The size of the circles represents the weight of particles.

Resampling Methods	Grouping and Sampling Methods Adopted					Benefits Reported	Disadvantages
	Sampling Methods (Particles with Low Weights)	Thresholds (Defining Strata)		Sampling Methods (Particles with High Weights)			
Optimal Resampling [24]	Stratified Sampling	Dynamic, c_t Where c_t Is a Unique Solution of (13)		Preserved		Minimized Squared Error-Loss Function	Additional Computation of (13); The Sample Size Decreases
(Partial) RC [17]	Replaces Particles by Regenerating Them from Previous Particles	Dynamic, c_t Where c_t May Be a Quantity Given in Advance or the Median or a Quantile of the Weights		Preserved and Reweighted with a New Weight (Reject Sampling)		Advantageous in Dealing with Sudden Changes in the Dynamic System	Increased Computational Intensity
Reallocation [11]	Rejection Sampling	1/*N*		Split		Reduced Resampling Variance (As Compared with Traditional Resampling Methods)	Varying Sample Size
PR [12]	(Small Weight) Preserved or Discarded	Fixed Threshold 1	(Moderate Weight) Preserved and Reweighted with Equal Weights	Fixed Threshold 2	(Significant Weight) Preserved and Reweighted with Equal or Different Weights	Reduced Computational Complexity	Thresholds Need to Be Carefully Specified
Deterministic Resampling [16]	Merged	1/*N*		Integer Parts (1/*N*) Are Replicated and Residuals Are Merged		Preserved Diversity of Particles (Without Discarding Any Particle)	Sensitive to the Dimensionality of the State
Double Systematic Resampling [25]	Systematic Resampling	1/*N*		Systematic Resampling		Increased Resampling Flexibility (Higher Probability for Drawing Small-Weighted Particles)	Two Independent Weight Normalization and Resampling

[FIG3] A comparison of several compound sampling methods.

COMPARISON OF SEVERAL COMPOUND SAMPLING METHODS

We emphasize that the core idea of compound sampling is to deal with particles from different groups differently. In Figure 3, we provide a succinct overview of different compound sampling methods, where the following terms for particles are used:

- *Discarded*: Particles that are discarded and not resampled.
- *Preserved*: Particles that are preserved with their weights being kept unless otherwise stated.
- *Merged*: Particles (in a specified space) that are merged to one particle with a state value equal to the weighted mean of the states of merged particles and with a weight equal to the sum of the original weights of the merged particles.
- *Split*: A particle that is divided into several copies. The split copies have the same state and weight, and their sum of weights is equal to the weight of the original particle.
- *Replicated*: A particle that is replicated, and each copy has the same value as the original particle as well as the same weight, unless otherwise stated.

Furthermore, in Table 4, we provide features of some of the compound sampling methods. They include optimal resampling [24], (partial) RC [17], reallocation [11], partial resampling [12], deterministic resampling [16], and double systematic resampling [25].

SPECIAL STRATEGIES

As previously mentioned, the key to combating degeneracy while avoiding impoverishment by resampling is the introduction of a compromise between concentration (the replication of large-weighted particles) and diversification (the discarding of negligible particles). To that end, several strategies have been proposed, including modified resampling, variable-size resampling, and roughening.

[TABLE 4] THE SPECIAL PROPERTIES OF SEVERAL COMPOUND RESAMPLING METHODS.

BIASED SAMPLING	UNEQUAL WEIGHTED	VARYING NUMBER OF PARTICLES	STATE CONSIDERED	UNIQUE/OUTSTANDING HIGHLIGHTS
[11], [12], [17], [25]	[11], [12], [16], [17], [24],	[11], [16], [24]	[16]	[11]: PARTICLE SPLITTING IS APPLIED; THE WEIGHT SUM OF THE RESAMPLED PARTICLES IS NOT ONE [12]: TWO (OR MORE) THRESHOLDS ARE USED [16]: AVOIDS DISCARDING ANY PARTICLE [17]: PREVIOUS PARTICLES ARE CONSIDERED; REJECT METHOD IS USED [24]: MINIMIZE THE SQUARED ERROR LOSS FUNCTION [25]: LOW-WEIGHTED PARTICLES ARE PROTECTED

In brief, the idea behind modified resampling is to draw particles from a distribution derived from the weights of the particles. The variable-size resampling, as the name suggests, provides a different number of samples with time so that a predefined criterion is satisfied (e.g., to reduce computational requirements, one uses a smaller number rather than a large number of particles, or to improve accuracy of tracking, one draws a larger number of particles). Roughening entails perturbing the locations of the resampled particles so that we reduce impoverishment, and, thus, it is performed once the resampling is completed. Next, we describe each of the strategies in more detail.

MODIFIED RESAMPLING

In generalized resampling [11], particles are resampled according to the probabilities $p_t^{(m)}$. The latter are usually equal to the particle weights $w_t^{(m)}$, but more generally, one can draw particles with probabilities that are functions of the weights, i.e.,

$$p_t^{(m)} \propto \left(w_t^{(m)}\right)^{\alpha}, \tag{16}$$

where $\alpha > 0$. When $0 < \alpha < 1$, the low-weighted particles get boosted, and the large-weighted particles have suppressed probabilities, and, thereby, the particle diversity improves. By contrast, $\alpha > 1$ entails increased preference for higher-weighted particles.

Knowledge about the next observation before resampling can be implemented via auxiliary weights [18]. In that way, the particles that are likely to have higher likelihoods have a better chance of surviving. There, the step of generating the auxiliary variable, which represents the fitness of the particle, can be viewed as a resampling step that takes into account both the immediate future and present states when carrying out selection. It is an appealing idea to fuse the information from the newest observations with the current weights while making a decision on the selection of particles.

VARIABLE-SIZE RESAMPLING

The use of a constant number of particles is not always the best choice because the complexity of the distributions of interest can vary drastically over time. In obtaining the number of particles that is both efficient and sufficient for approximating the distribution of interest, the underlying idea is to choose a small number of particles if the distribution is focused on a small part of the state space and to adopt a large number of particles if the distribution is much more spread out. This is the core rationale of the Kullback–Leibler divergence (KLD)-sampling approach [26], which determines the needed number of particles based on the KLD between the sample-based maximum likelihood estimate and a distribution of interest.

The required number N of particles can be determined so that, with the probability $1-\rho$, the KLD between the sample-based maximum likelihood estimate of a desired distribution and that distribution is less than a prespecified error bound threshold ε. In [26], it is found that

$$N = \frac{1}{2\varepsilon} q, \tag{17}$$

where

$$q = F^{-1}(1-\rho), \tag{18}$$

with $F^{-1}(\cdot)$ being the inverse of the cumulative chi-squared distribution with $k-1$ degrees of freedom, and k the number of bins [nonoverlapping (multi)dimensional intervals] used for sorting the particles. The value of N in (17) could be approximately computed [26]. In practice, the number of particles for resampling may be hard-limited to be not less than a minimum threshold.

Ideally, one would want to use as a desired distribution the posterior of the state. In [26], the posterior is approximated by the predictive distribution. Theoretically, it is more rigorous and flexible to apply (17) during resampling than in sampling, which leads to KLD-resampling [27]. There, the particles are resampled one by one until the required amount given by (17) is reached. Obviously, the disadvantage of the KLD-based method is that the particles need to be sorted out in bins defined on the state space, which can be very computationally costly.

ROUGHENING STRATEGIES

In obtaining an optimal set of particles, instead of designing the optimal proposal distribution, one can employ compensation. If impoverishment has already occurred after resampling, one approach to reducing it is to spread the overcentralized particles by roughening or jittering their values. This simply means that we add random noise (roughening noise) to the resampled particles. The roughening noise is normally Gaussian with zero mean and constant covariance. In [1], it is suggested that the noise covariance is diagonal with a standard deviation for a particular state component given by $\sigma = KDN^{-1/d_x}$, where D is the difference between the maximum and minimum values of the state component, K is a positive tuning constant chosen by the user, N is the number of particles, and d_x is the dimension of the state. The roughening may be applied 1) only at selected steps, 2) only to selected particles that are resampled from the same particle, and

[TABLE 5] PARALLEL PLATFORMS FOR PF IMPLEMENTATION.

PLATFORM	ADVANTAGES	DISADVANTAGES	APPLICATION
VLSI [31]	■ CUSTOMIZED ARCHITECTURE FOR SPECIFIC APPLICATION ■ VERY HIGH PROCESSING SPEED CAN BE ACHIEVED	■ VERY COSTLY ■ VERY LONG DESIGN CYCLES	■ NOT USED YET—SUITABLE FOR EXTREMELY LARGE QUANTITIES
FPGA [32]	■ CUSTOMIZED ARCHITECTURE FOR SPECIFIC APPLICATION	■ LIMITED FLOATING-POINT CAPABILITIES ■ LONG DESIGN CYCLE AND NEED TO KNOW HARDWARE AND HARDWARE DESIGN LANGUAGES	■ PROTOTYPING PLATFORM FOR REAL-TIME SYSTEMS
MULTICORE CENTRAL PROCESSING UNIT [33], [34]	■ COURSE-GRAINED PARALLELISM ON TWO TO EIGHT CORES. RELATIVELY EASY TO ACCESS AND TO PROGRAM	■ LARGE AMOUNT OF SEQUENTIAL PROCESSING	■ ACCELERATING SIMULATIONS
GP-GPU [35]–[37]	■ FINE-GRAINED PARALLELISM CAN BE ACHIEVED ■ AVAILABLE ON ALMOST EVERY COMPUTER ■ EASY TO PROGRAM	■ KNOWLEDGE OF GPU PROGRAMMING LANGUAGES SUCH AS CUDA OR OPENCL	■ ACCELERATING SIMULATIONS AND SOME HIGH-PERFORMANCE REAL-TIME APPLICATIONS
EMBEDDED GPU	■ PROGRAM IN THE SAME WAYS AS GP-GPU ■ CANDIDATE FOR PF FOR EMBEDDED SYSTEMS	■ LESS PARALLELISM AVAILABLE THAN IN GP-GPU ■ KNOWLEDGE OF GPU PROGRAMMING LANGUAGES	■ NEW PLATFORMS FOR EMBEDDED SYSTEMS SUITABLE TO REAL-TIME PERFORMANCE
CLUSTER AND MULTICOMPUTERS [33], [39]	■ COMPLEX PARTICLE FILTERS CAN BE SIGNIFICANTLY ACCELERATED	■ KNOWLEDGE OF PARALLEL PROGRAMMING LANGUAGES SUCH AS OPENMP OR MESSAGE PASSING INFERENCE	■ ACCELERATING SIMULATIONS

3) only in a few dimensions of the state space. Similar ideas for diversification can be implemented by using Markov chain Monte Carlo (MCMC) sampling. The so-called resample-move algorithm from [28] has a move step after the resampling step based on MCMC sampling. The move step performs one or more iterations on each of the resampled particles, thereby rejuvenating the diversity of particles.

An important alternative to the roughening strategy is the use of Gaussian kernels. With the kernels, we smooth the posterior density by convolving each particle with a diffusion kernel. This is also known as *regularization*, and it amounts to replacing the discrete distribution defined by the particles and their weights with a continuous approximation [29]. The resampling step is then changed to simulations from the continuous distribution, which generates a new particle set. All of these approaches produce diversified copies of the same particles.

PF OFTEN SUFFERS FROM A HEAVY COMPUTATIONAL COST, ESPECIALLY WHEN THE DIMENSION OF THE STATE-SPACE MODEL IS HIGH AND THE NUMBER OF USED PARTICLES HAS TO BE LARGE.

PARALLEL PROCESSING

Despite its successful applications, PF often suffers from a heavy computational cost, especially when the dimension of the state-space model is high and the number of used particles has to be large. However, the execution of PF can be accelerated through parallelization for both offline and real-time processing. An important area where parallelized PF also takes place is in signal processing over networks, where PF operates in parallel at the nodes of the network [30]. There, the problems of PF are of a different nature than the ones we address here. In this article, we focus on describing the parallelization of sequential PF and the resampling algorithm.

PARALLEL PROCESSING ARCHITECTURES FOR PF

Parallel hardware devices where PF has been implemented and reported in the literature include custom very large-scale integration (VLSI) chips [31], field-programmable gate arrays (FPGAs) [32], multicore processors [33], [34], GP-GPUs [35]–[38], and computer clusters/multicomputers [33], [39]. The advantages, disadvantages, and potential applications of these platforms for PF implementation are shown in Table 5. Hardware implementations on VLSI and FPGA result in high-speed implementation since every mathematical function is customized and implemented in hardware. However, VLSI design is very expensive, and, to the best of our knowledge, there are no commercial chips with implemented PF yet. The number of floating point units that can be executed in parallel on an FPGA is smaller than on state-of-the-art GP-GPUs. Also, floating-to-fixed-point conversion is very complicated, and particle filters require a large number of bits in fixed-point representation. In addition, programming of GPUs is simpler than designing hardware for FPGAs. Multicore platforms and GP-GPUs are now available on almost every computer so that lately we have been witnessing more parallel PF implementations on GP-GPUs.

Recently, new chips with embedded multiple processors and GP-GPUs have appeared from various companies. They support the same programming models as GP-GPUs, including CUDA and Open Computing Language (OpenCL). They are intended for high-performance embedded applications and have much lower power consumption than GP systems. Furthermore, many-core chips that have more than 16 processors on a single chip have appeared and have started to be used for high-performance

embedded applications. As far as we know, PF has not yet been implemented on these embedded platforms.

CHALLENGES

The particle generation and weight updating are computationally the most intensive steps and can be implemented in parallel if parallel processing hardware is available. Resampling, normalization, and computing estimates are inherently sequential, and they limit the speedup that can be achieved with parallel processing. An additional step, called *particle allocation*, is usually needed for efficient parallel implementation. We describe this step with an example. Assume that parallel processing is performed using a generic architecture with three PEs. Let each PE perform sampling and weight computation of an equal number of particles equal to $M/3$, where $M/3$ is an integer. After resampling, some particles are replicated, and some are discarded. Now consider a situation where all the particles in PE1 and PE3 are discarded, and the majority of the particles in PE2 are replicated. When the next observation comes, there will be no particles in PE1 and PE3 for processing, and almost all the processing will occur sequentially in PE2, resulting in low PE utilization and load imbalance. To avoid this situation, particles from PE2 need to be redistributed (allocated) to the other PEs so that all the PEs have an equal amount of particles before the next step. The particle allocation can be done by sending particles and their weights in message-passing architectures or by reallocating particles (or their indexes) in the global memory in shared-memory architectures. Particle allocation requires additional time, and, consequently, it affects the speedup.

Major challenges for the parallel implementation of PF include:

- There might be computationally complex operations in the sampling and weight-computation steps, including random number generation. Some of these operations might not be supported by all processing architectures.
- Operations such as normalization, computation of output estimates, and computation of cumulative sums in some resampling algorithms are sequential and require particles from all PEs.
- Particle allocation requires frequent communication with the global shared memory in shared-memory systems, which is a bottleneck. Similarly, the communication between the PEs in message-passing systems consumes significant time.
- Platform-specific challenges are related to the fact that every platform requires modifications or implementations that are platform specific. For example, design of a hardware random number generator is required in FPGA platforms, while an efficient parallel software algorithm for random number generation is needed for GPUs.

PERFORMANCE METRICS AND TERMINOLOGY

The major objective of parallel implementation is to reduce the execution time, and the most commonly used metric is speedup [34], [35]. We define the execution time of particle filters as the time they need to process one observation [31], [32], [36]. The speedup is defined as the ratio of the execution time of the best possible serial algorithm (on a single processor) to the execution time of the chosen algorithm on a parallel system based on multiple processors. The efficiency is defined as the speedup divided by the number of processors [33]. System utilization indicates the percentage of resources that was kept busy during the execution of a parallel program. Communication overhead is defined as the percentage of time spent on interprocess communication and all noncomputing operations [33]. The degree of parallelism is a measure of the numbers of threads of computation that can be carried out simultaneously. Data dependencies are the result of precedence constraints between operations, and they prevent concurrent execution. For example, the degree of parallelism for the weight-computation step is equal to the number of particles. A number of papers have been devoted to increasing the degree of parallelism and system utilization during resampling to decrease execution time.

IF IMPOVERISHMENT HAS ALREADY OCCURRED AFTER RESAMPLING, ONE APPROACH TO REDUCING IT IS TO SPREAD THE OVERCENTRALIZED PARTICLES BY ROUGHENING OR JITTERING THEIR VALUES.

Other types of performance metrics are related to tracking the performance of the parallel particle filter. Researchers mainly rely on examples to monitor the change of the mean square error [32], [34] or the effective sample size [33], [40] of the parallel versus sequential implementation of PF. Theoretical work on the performance or loss of performance of PF due to parallel implementation is still missing. One attempt is made in [45], where the analysis of the sample variance of the weights, the distortion of the probability measure, and the variance of estimators of a distributed PF are given. In [33], the mean and standard deviation of the log likelihood are calculated to validate that the resampling procedure does not affect the performance of the particle filter.

DISTRIBUTED RESAMPLING

Much work has been focused on parallelization of traditional resampling, referred to as *distributed resampling*. Two main classes of approaches have been applied: 1) the algorithm is modified in a way that the result of resampling is not changed in comparison with the sequential algorithm, and 2) the algorithm is modified, and it has been shown that, mainly through simulations, its parallel implementation provides similar results to the original sequential resampling. The majority of the algorithmic modifications is performed to reduce the communication overhead mainly during the particle allocation step.

An example of an algorithm that does not change the result of standard resampling is distributed resampling with proportional allocation [32]. Here, the resampling step is divided into two steps. In the first step, each PE is considered as a particle whose weight is the cumulative weight of all the particles of this PE. The resampling is performed only on the cumulative weights to determine how many particles each PE needs to generate. Next, local resampling is performed in parallel in each PE. In this way, the degree of

parallelism for the resampling step is equal to the number of PEs. Subsequently, the particle allocation step is performed, in which the excess of particles after resampling from some PEs is communicated or made available to the PEs with the deficiency of particles. Central (sequential) processing is still needed for the first step of resampling, normalization, and computing the output estimate. A number of variations of this method have been devised where load unbalance and the amount of central processing are reduced. The load balancing solution for the GP-GPU platform has been proposed in [36] using CUDA. All the particles are stored in a global GP-GPU memory, which is a shared memory, and writing to it is slow. During the particle-allocation step, the same replicated particles are written many times to the memory. After the particle allocation, each set of particles from the global memory is apportioned to different parallel threads. The optimization performed here is architecture (GP-GPU) specific.

SERIAL COMPUTATION AND GLOBAL COMMUNICATION ARE INEVITABLE IN WEIGHT NORMALIZATION, AND, THEREFORE, ALTERNATIVES THAT ARE FREE OF NORMALIZATION BECOME ATTRACTIVE.

The aforementioned methods require some central (sequential) processing to perform resampling. To further improve the speed of resampling, it is desirable to perform local particle allocation without having a central unit. Localized particle allocation produces different results than traditional resampling algorithms, but it reduces communication overhead, making it concurrent. In localized resampling, only a subset of the particles is exchanged between neighboring PEs/threads, and the exchange is preferably performed in parallel. The resampling and all the other operations are also performed in parallel. Various solutions have been proposed that depend on different parameters, including the number of PEs, the number of particles to be exchanged, the types of particles to be exchanged, and the selection of PEs where the particles are sent. Resampling with nonproportional allocation (RNA) [32] allows for each PE to perform local resampling and to exchange some fixed number of particles with one neighboring PE. The platform where PF was implemented in [32] was an FPGA. RNA-based implementation of parallel resampling is carried out in one of the first implementations of PF on GP-GPU [37]. In other implementations, one or several of the largest particles are exchanged with neighboring PEs. As an example, [38] presents a GP-GPU implementation where local sorting is performed to order the particles that are being exchanged. In [40], a method is proposed for finding the optimal portion of particles for exchange between adjacent PEs and for achieving the mixing of the posterior distributions among the adjacent PEs, so as to preserve particle diversity.

NORMALIZATION-FREE RESAMPLING

Serial computation and global communication are inevitable in weight normalization, and, therefore, alternatives that are free of normalization become attractive. In this category, resampling is performed free of weight normalization, differing from all the resampling methods presented so far. In brief, the particles are (re-) sampled based on their relative magnitude of the (nonnormalized) weights, e.g., the ratios between the weights globally, or the absolute weight comparison between local neighboring (two or three) particles. The former is globally unbiased sampling, while the latter is local sampling that is almost surely biased.

Ratios Between Weights

Metropolis [38] and independent Metropolis–Hastings sampling [39] require only ratios between weights that do not need to be normalized and therefore threads can process in parallel, see code 8, for example. The solution presented in [38] addresses GP-GPU implementation where the amount of parallel computational resources is abundant, and it stresses that even though Metropolis sampling is more computationally intensive than traditional resampling algorithms, it is as fast on a GP-GPU because there are no dependent operations on the weights. There, sampling from $U(1,\ldots M)$ returns a value randomly selected from the set $\{1,\ldots,M\}$.

Code 8 is an iterative process of sampling based on constructing a Markov chain. More specifically, it uses a Metropolis–Hastings move step for searching in a particle set for a particle with a large weight to replace the current particle. The depth of the search (burn-in) is denoted by B. It is desirable that the number of times a particle is sampled is proportional to its weight. As in most MCMC algorithms, deeper searching will provide better results (closer to the desired distribution).

The selection of B is a tradeoff between speed and reliability. While runtime is reduced with fewer steps, the sample will be biased if B is too small to ensure convergence. Similarly, a number of additional particles for burn-in (the time during which the Markov chain is in a transient state) is needed. The particles that are generated in the burn-in period are discarded. A disadvantage of this method is that, in most cases, it is difficult to estimate the required burn-in period.

Code 8: Metropolis resampling.

$[\{\tilde{x}_t^{(m)}, \tilde{w}_t^{(m)}\}_{m=1}^{M}] =$ (Metropolis)Resample $[\{x_t^{(m)}, w_t^{(m)}\}_{m=1}^{M}, B]$
FOR $m = 1$: M (can be in parallel)
  $k = m$
  FOR $n = 1$: B
    $u \sim U(0,1]$; $l \sim U\{1,\ldots,M\}$
    IF $u \le w_t^{(l)}/w_t^{(k)}$
      $k = l$
    END
  END
  $\tilde{x}_t^{(m)} = x_t^{(k)}$; $\tilde{w}_t^{(m)} = 1/M$
END

Local Neighbor-Comparison Methods

Now, we consider more straightforward local methods that include local Monte Carlo [10] and Local Selection (LS) methods [41]. The

local methods consist of randomly sampling a particle from a small set of successive particles, where the sampling is based only on the weights of the particles in the set. The resampled particles preserve their weights. Assume, for simplicity, that the number of PEs K is equal to the number of particles M (if $K < M$, particles allocated to the same PE are processed serially), and the mth PE contains a particle $\{x_t^{(m)}, w_t^{(m)}\}$ in its memory, where $w_t^{(m)}$ is not normalized. Before the parallel resampling, a communication step is required, where the mth PE transmits its particle to its two neighboring PEs. Then, each PE contains three particles, and the LS resampling can be realized as by code 9.

For consistency of description, note that $w_t^{(0)}$ refers to $w_t^{(M)}$, while $w_t^{(M+1)}$ refers to $w_t^{(1)}$.

Obviously, the number of replications of each particle in LS is very limited in local groups and is maximally three. This can cause a biased result, especially if high-weighted particles are next to each other. Then, some of them will be discarded and the performance will be degraded.

THE RESAMPLING PROCESS REPRESENTS A BOTTLENECK IN PARALLEL IMPLEMENTATIONS.

Code 9: Local selection resampling.

$[\{\tilde{x}_t^{(m)}, \tilde{w}_t^{(m)}\}_{m=1}^{M}] = (\text{LS})\text{Resample}\ [\{x_t^{(m)}, w_t^{(m)}\}_{m=1}^{M}]$
FOR $m = 1{:}\ M$ (in parallel)
  $W = w_t^{(m-1)} + w_t^{(m)} + w_t^{(m+1)}$
  $T_1 = w_t^{(m-1)}/W$
  $T_2 = (w_t^{(m-1)} + w_t^{(m)})/W$
  $u \sim U(0, 1]$
  IF $u \le T_1$
    $\tilde{x}_t^{(m)} = x_t^{(m-1)};\ \tilde{w}_t^{(m)} = w_t^{(m-1)}$
  ELSE IF $T_1 < u \le T_2$
    $\tilde{x}_t^{(m)} = x_t^{(m)};\ \tilde{w}_t^{(m)} = w_t^{(m)}$
  ELSE
    $\tilde{x}_t^{(m)} = x_t^{(m+1)};\ \tilde{w}_t^{(m)} = w_t^{(m+1)}$
  END
END

We note that although weight normalization is avoided in these normalization-free resampling approaches, it is still necessary for computing the filtering estimates.

OTHER TYPES OF PARALLELIZATION OF PF

We reiterate that the resampling process represents a bottleneck in parallel implementations. For this reason, there have been efforts to develop PF methods that do not require resampling [see first item below] and overlap the operations of multiple PF or the steps of the same PF so that all the operations are sequential but are executed concurrently (second and fourth items below). More specifically, these efforts include the following:

1) Removing the resampling step from PF, such as in nonresampling PF detector [42] and Gaussian PF (GPF) [43], which are resampling-free.

2) Running several PFs independently on separate processors or a set of agents in a distributed network [30]. Some or all of the agents perform local PF and interact with other agents to calculate a global state estimate. These decentralized agent networks do not include a central unit.

3) Decomposing the state into two parts and considering the filtering problem as two nested subproblems. These two problems are then handled by separate PFs. This is also referred to as *decentralized PF* [44].

4) Pipelining the sampling and resampling: when a particle is resampled, it processes the sampling (particle propagation and weight updating) ahead that does not need to wait for other particles, i.e., the sampling in the next iteration will be produced before the resampling is finished.

Before concluding the subsection on parallel processing, we list some topics for further research on it. They include:

- Applying PF to real-world applications by implementing them on embedded multicore, embedded GPUs, and many-core chips and guaranteeing real-time performance (for example, current GPUs do not incorporate hard real-time features).
- Deriving optimization criteria that allow for evaluation of the quality of the localized distributed resampling algorithms versus sequential traditional resampling algorithms. Evaluating the practical benefit of parallel processing in terms of not only computing speed but also filtering accuracy. Some initial comparisons of parallel implementations of resampling that offer theoretical analysis and simulations are available. For example, analysis of resampling via RNA and LS in terms of reduction of the sample variance of the weights, the distortion of the probability measure, and the variance of estimators is given in [45].
- Devising new parallel algorithms for specific architectures—for example, communication is very expensive in GPGPUs, and therefore, one research direction is deriving algorithms with reduced communication between the PEs that can even be more computationally intensive.

FREQUENCY OF RESAMPLING

The benefits of resampling are accompanied with potential side effects such as sample impoverishment and prevention of parallel processing as explained above. Thus, resampling should only be applied when necessary and therefore it is important to have a method for determining how frequently or when to implement resampling. Two schedules for resampling have been proposed: deterministic and adaptive. In a deterministic schedule, one does resampling at fixed times $t_1, t_2, \ldots$, where t_i is often chosen to be $i \times t_1$. In an adaptive schedule, the times at which resampling occurs are selected by checking a criterion that assesses the quality of the current weights. In that case, whenever the criterion for quality is below a given threshold, the resampling step is triggered. This tends to produce better performance of PF than deterministic scheduling due to its flexibility.

As a key to adaptive schedules, the criterion for implementing resampling is usually based on the variation of the weights,

which reflects the degree of weight degeneracy. One such criterion is the effective sample size (ESS) N_{eff} defined by [46]

$$N_{\text{eff},t} = \frac{M}{1 + \text{Var}(w_t^*)}, \tag{19}$$

where w_t^* is a nonnormalized weight, and the variance is computed with respect to the sampling distribution. Typically, obtaining N_{eff} from (19) is impossible [46]. Instead, one may employ the rule of thumb estimate given by

$$N_{\text{eff},t} = \left(\sum_{m=1}^{M} \left(w_t^{(m)}\right)^2\right)^{-1}. \tag{20}$$

An application of the Cauchy–Schwarz inequality leads to the (intuitive) conclusion that $N_{\text{eff},t} \leq M$. It is also clear that $1 \leq N_{\text{eff},t} \leq M$. Resampling occurs when the ESS falls below a selected threshold, γ_r. If γ_r is set to $\gamma_r = 0$, resampling never takes place, and $\gamma_r = M$, meaning that resampling occurs at every time step. Several different criteria to calculate the ESS have also been proposed; see, e.g., [8], [47], and [48]. It is necessary to note that criteria based on (20) are primarily used in tracking low-dimensional states. In high-dimensional problems, other metrics may be more appropriate.

CONCLUSIONS

In this article, the state of the art of resampling methods was reviewed. The methods were classified and their properties were compared in the framework of the proposed classifications. The emphasis in the article was on the classification and qualitative descriptions of the algorithms. The intention was to provide guidelines to practitioners and researchers.

Some final comments:

- The resampling methods can hardly output much different results if they satisfy the unbiasedness condition, preserve a constant number of particles, and equally weight the resampled particles.
- If these restrictions are removed, some benefits may be obtained, e.g., adaptive adjustment of the number of particles, preservation of particle diversity, and alleviation of impoverishment.
- Compound sampling and special strategies, such as modified resampling and variable-size resampling, and compensations after resampling provide more flexibility. They balance the necessity for diversity and the need for concentration that lies in the center of sample degeneracy and impoverishment. They may offer better approximation and benefits in practice, but often at the price of higher computational costs.
- The normalization of weights and load imbalance of particles after resampling are main barriers for parallelization of resampling. Ways to carry out normalization, to output filter estimate, and to manage communication between PEs distinguish existing parallel PF algorithms.
- An issue that we have not discussed is the theoretical effects of resampling on the convergence of the PF estimates. The resampling step is crucial for uniform convergence results, and some recent theoretical results on this and related to deterministic and random resampling can be found in [49].
- The research on the resampling of particle filters is going in multiple directions:
  - implementation specific
    - simplifying resampling algorithms for real-time implementation
    - adjustment of the algorithms to specific hardware/processing architectures
    - parallelization of the resampling
    - application and acceleration of resampling to non–PF-based problems such as importance sampling and the forward-backward algorithm [50]
  - theoretical analysis
    - analysis of the features of resampling algorithms without considering them as a part of PF
    - analysis of the effects of different resampling algorithms on the PF convergence and accuracy of tracking.

ACKNOWLEDGMENTS

The work of Tiancheng Li has been supported by the Excellent Doctorate Foundation of Northwestern Polytechnical University and by the National Natural Science Foundation of China (under Award 51475383). The work of Petar M. Djurić has been supported by the NSF under Award CCF-1320626.

AUTHORS

Tiancheng Li (t.c.li@mail.nwpu.edu.cn) received his bachelor's degree in mechanical and electrical engineering, with a minor in business administration, from Harbin Engineering University, China, in 2008, and his Ph.D. degree in electrical and electronic engineering from London South Bank University, United Kingdom, in 2013. He is a currently a Ph.D. candidate in mechatronics engineering at Northwestern Polytechnical University, China, and a postdoctoral associate with the Bioinformatic, Intelligent Systems, and Educational Technology Group, University of Salamanca, Spain. His research interests are in the general area of statistical signal processing, information fusion, system modeling with a particular focus on particle filtering, finite set statistics, and multiple object tracking.

Miodrag Bolić (mbolic@eecs.uottawa.ca) received his B.Sc. and M.Sc. degrees in electrical engineering from the University of Belgrade, Serbia, in 1996 and 2001, respectively, and his Ph.D. degree in electrical engineering from Stony Brook University, New York, in 2004. Since 2004, he has been with the University of Ottawa, Canada, where he is an associate professor with the School of Electrical Engineering and Computer Science. His research interests include signal processing architectures, hardware/software accelerators, biomedical signal processing and instrumentation, and the Internet of Things. He is director of the Computer Architecture, Radio-Frequency Identification, and Medical Devices Research Groups at the University of Ottawa. He is a Senior Member of the IEEE.

Petar M. Djurić (petar.djuric@stonybrook.edu) received his B.S. and M.S. degrees in electrical engineering from the

University of Belgrade, Serbia, and his Ph.D. degree in electrical engineering from the University of Rhode Island. He is currently a professor in the Department of Electrical and Computer Engineering at Stony Brook University, New York. His research has been in signal and information processing, with an emphasis on Monte Carlo-based methods, signal processing over networks and applications in wireless sensor networks, and radio-frequency identification. He received the IEEE Signal Processing Magazine Best Paper Award in 2007 and the EURASIP Technical Achievement Award in 2012. He is a Fellow of the IEEE.

REFERENCES

[1] N. Gordon, D. Salmond, and A. Smith, "Novel approach to nonlinear/non-Gaussian Bayesian state estimation," *IEE Proc., F Radar Signal Process*., vol. 140, no. 2, pp. 107–113, 1993.

[2] A. Doucet and A. M. Johansen, "A tutorial on particle filtering and smoothing: Fifteen years later," in *Handbook of Nonlinear Filtering*, E. D. Crisan and B. Rozovsky, Eds. Oxford, London: Oxford Univ. Press, 2011, pp. 656–704.

[3] A. Doucet, S. J. Godsill, and C. Andrieu, "On sequential Monte Carlo sampling methods for Bayesian filtering," *Stat. Comput.*, vol. 10, no. 3, pp. 197–208, 2000.

[4] M. S. Arulampalam, S. Maskell, N. Gordon, and T. Clapp, "A tutorial on particle filters for online nonlinear/non-Gaussian Bayesian tracking," *IEEE Trans. Signal Processing*, vol. 50, no. 2, pp. 174–188, 2002.

[5] P. M. Djurić, J. H. Kotecha, J. Zhang, Y. Huang, T. Ghirmai, M. F. Bugallo, and J. Míguez, "Particle filtering," *IEEE Signal Processing Mag.*, vol. 20, no. 5, pp. 19–38, 2003.

[6] O. Cappé, S. J. Godsill, and E. Moulines, "An overview of existing methods and recent advances in sequential Monte Carlo," *IEEE Proc.*, vol. 95, no. 5, pp. 899–924, 2007.

[7] G. Kitagawa, "Monte Carlo filter and smoother and non-Gaussian nonlinear state space models," *J. Comput. Graph. Stat.*, vol. 5, no. 1, pp. 1–25, 1996.

[8] J. Carpenter, P. Clifford, and P. Fearnhead, "An improved particle filter for nonlinear problems," *IEE Proc., Radar Sonar Navigat.*, vol. 146, no. 1, pp. 2–7, 1999.

[9] E. R. Beadle and P. M. Djurić, "A fast-weighted Bayesian bootstrap filter for nonlinear model state estimation," *IEEE Trans. Aerosp. Electron. Syst.*, vol. 33, no. 1, pp. 338–343, 1997.

[10] J. Liu and R. Chen, "Sequential Monte-Carlo methods for dynamic systems," *J. Amer. Statist. Assoc.*, vol. 93, no. 443, pp. 1032–1044, 1998.

[11] J. S. Liu, R. Chen, and T. Logvinenko, "A theoretical framework for sequential importance sampling and resampling," in *Sequential Monte Carlo Methods in Practice*, A. Doucet, N. de Freitas, and N. Gordon, Eds. New York: Springer, 2001, pp. 225–246.

[12] M. Bolić, P. M. Djurić, and S. Hong, "Resampling algorithms for particle filters: A computational complexity perspective," *EURASIP J. Appl. Signal Process.*, vol. 2004, no. 15, pp. 2267–2277, 2004.

[13] R. Douc and O. Cappé, "Comparison of resampling schemes for particle filtering," in *Proc. 4th Int. Symp. Image and Signal Processing and Analysis*, 2005, pp. 64–69.

[14] J. D. Hol, T. B. Schön, and F. Gustafsson, "On resampling algorithms for particle filters," in *Proc. IEEE Nonlinear Statistical Signal Processing Workshop*, 2006, pp. 79–82.

[15] D. B. Rubin, "A noniterative sampling/importance resampling alternative to the data augmentation algorithm for creating a few imputations when fractions of missing information are modest: The SIR algorithm," *J. Amer. Statist. Assoc.*, vol. 82, no. 398, pp. 543–546, 1987.

[16] T. Li, T. P. Sattar, and S. Sun, "Deterministic resampling: Unbiased sampling to avoid sample impoverishment in particle filters," *Signal Process.*, vol. 92, no. 7, pp. 1637–1645, 2012.

[17] J. S. Liu, R. Chen, and W. H. Wong, "Rejection control and sequential importance sampling," *J. Amer. Statist. Assoc.*, vol. 93, no. 443, pp. 1022–1031, 1998.

[18] M. K. Pitt and N. Shephard, "Filtering via simulation: Auxiliary particle filters," *J. Amer. Statist. Assoc.*, vol. 94, no. 446, pp. 590–591, 1999.

[19] M. Bolić, P. M. Djurić, S. Hong, "New resampling algorithms for particle filters," in *Proc. IEEE Int. Conf. Acoustics, Speech and Signal Processing*, 2003, vol. 2, pp. 589–592.

[20] A. Budhiraja, L. Chen, and C. Lee, "A survey of numerical methods for nonlinear filtering problems," *Physica D*, vol. 230, no. 1–2, pp. 27–36, 2007.

[21] D. Crisan and T. Lyons, "A particle approximation of the solution of the Kushner-Stratonovitch equation," *Prob. Theory Relat. Fields*, vol. 115, no. 4, pp. 549–578, 1999.

[22] T. Li, T. P. Sattar, and D. Tang, "A fast resampling scheme for particle filters," in *Proc. Constantinides International Workshop on Signal Processing*, 2013, pp. 1–4.

[23] T. Li, S. Sun, and J. Duan, "Monte Carlo localization for mobile robot using adaptive particle merging and splitting technique," in *Proc. IEEE Int. Conf. Information and Automation*, 2010, pp. 1913–1918.

[24] P. Fearnhead and P. Clifford, "On-line inference for hidden Markov models via particle filters," *J. R. Statist. Soc.: Ser. B,* vol. 65, no. 4, pp. 887–899, 2003.

[25] J. Zheng, B. Bai, and X. Wang, "Increased-diversity systematic resampling in particle filtering for BLAST," *J. Syst. Eng. Electron.*, vol. 20, no. 3, pp. 493–498, 2009.

[26] D. Fox, "Adapting the sample size in particle filters through KLD-sampling," *Int. J. Robot. Res.*, vol. 22, no. 12, pp. 985–1003, 2003.

[27] T. Li, S. Sun, and T. Sattar, "Adapting sample size in particle filters through KLD-resampling," *Electron. Lett.*, vol. 46, no. 2, pp. 740–742, 2013.

[28] W. R. Gilks and C. Berzuini, "Following a moving target-Monte Carlo inference for dynamic Bayesian models," *J. R. Statist. Soc. B*, vol. 63, no. 1, pp. 127–146, 2001.

[29] C. Musso, N. Oudjane, and F. Legland, "Improving regularized particle filters," in *Sequential Monte Carlo Methods in Practice*, A. Doucet, N. de Freitas, and N. Gordon, Eds. New York: Springer, 2001, pp. 247–272.

[30] O. Hlinka, F. Hlawatsch, and P. M. Djurić, "Distributed particle filtering in agent networks: A survey, classification, and comparison," *IEEE Signal Process. Mag.*, vol. 30, no. 1, pp. 61–81, 2013.

[31] S. Hong, S. Chin, and P. M. Djurić, "Design and implementation of flexible resampling mechanism for high-speed parallel particle filters," *J. VLSI Signal Process.*, vol. 44, no. 1–2, pp. 47–62, 2006.

[32] M. Bolić, P. M. Djurić, and S. Hong, "Resampling algorithms and architectures for distributed particle filters," *IEEE Trans. Signal Processing*, vol. 53, no. 7, pp. 2442–2450, 2005.

[33] I. Strid, "Computational methods for Bayesian inference in macroeconomic models," Ph.D. dissertation, Stockholm School of Economics, 2010.

[34] O. Rosén, A. Medvedev, and M. Ekman, "Speedup and tracking accuracy evaluation of parallel particle filter algorithms implemented on a multicore architecture," in *Proc. IEEE Int. Conf. Control Applications*, 2010, pp. 440–445.

[35] G. Hendeby, R. Karlsson, and F. Gustafsson, "Particle filtering: The need for speed," *EURASIP J. Adv. Signal Process.*, vol. 2010, pp. 22:1–22:9, June 2010.

[36] K. Hwang and W. Sung, "Load balanced resampling for real-time particle filtering on graphics processing units," *IEEE Trans. Signal Processing*, vol. 61, no. 2, pp. 411–419, 2013.

[37] G. Hendeby, J. D. Hol, R. Karlsson, and F. Gustafsson, "A graphics processing unit implementation of the particle filter," in *Proc. European Signal Processing Conf.*, 2007, pp. 1639–1643.

[38] L. Murray, "GPU acceleration of the particle filter: The Metropolis resampler," arXiv preprint arXiv:1202.6163.

[39] A. C. Sankaranarayanan, A Srivastava, and R Chellappa, "Algorithmic and architectural optimizations for computationally efficient particle filtering," *IEEE Trans. Image Processing*, vol. 17, no. 5, pp. 737–748, 2008.

[40] B. Balasingam, M. Bolić, P. M. Djurić, and J. Míguez, "Efficient distributed resampling for particle filters," in *Proc. IEEE Int. Conf. Acoustics, Speech, Signal Processing*, 2011, pp. 3772–3775.

[41] J. Míguez, M. F. Bugallo, and P. M. Djuric´, "A new class of particle filters for random dynamical systems with unknown statistics," *EURASIP J. Appl. Signal Process.*, vol. 15, pp. 2278–2294, Jan. 2004.

[42] T. S. John, A. Nallanathan, and M. A. Armand, "A non-resampling sequential Monte Carlo detector for coded OFDM systems based on periodic termination of differential phase trellis," *IEEE Trans. Wireless Commun.*, vol. 5, no. 7, pp. 1846–1856, 2006.

[43] J. Kotecha, and P. M. Djurić, "Gaussian particle filtering," *IEEE Trans. Signal Processing*, vol. 51, no. 10, pp. 2592–2601, 2003.

[44] T. Chen, T. B. Schön, H. Ohlsson, and L. Ljung, "Decentralized particle filter with arbitrary state decomposition," *IEEE Trans. Signal Processing*, vol. 59, no. 2, pp. 465–478, 2011.

[45] J. Míguez, "Analysis of parallelizable resampling algorithms for particle filtering," *Signal Process.*, vol. 87, no. 12, pp. 3155–3174, 2007.

[46] A. Kong, J. S. Liu, and W. H. Wong, "Sequential imputations and Bayesian missing data problems," *J. Amer. Statist. Assoc.*, vol. 9, no. 425, pp. 278–288, 1994.

[47] N. Celik and Y.-J. Son, "State estimation of a shop floor using improved resampling rules for particle filtering," *Int. J. Prod. Econ.*, vol. 134, no. 1, pp. 224–237, 2011.

[48] A. A. Nasir, S. Durrani, and R. A. Kennedy, "Particle filters for joint timing and carrier estimation: Improved resampling guidelines and weighted Bayesian Cramér-Rao bounds," *IEEE Trans. Commun.*, vol. 60, no. 5, pp. 1407–1419, May 2012.

[49] R. Douc and E. Moulines, "Limit theorems for weighted samples with applications to sequential Monte Carlo," *Ann. Stat.*, vol. 36, no. 5, pp. 2344–2376, 2008.

[50] P. Fearnhead, "Computational methods for complex stochastic systems: A review of some alternatives to MCMC," *Stat. Comput.*, vol. 18, no. 2, pp. 151–171, 2008.

[SP]

International Journal of Machine Tools & Manufacture 88 (2015) 206–213

Contents lists available at ScienceDirect

International Journal of Machine Tools & Manufacture

journal homepage: www.elsevier.com/locate/ijmactool

Quantitative characterization and influence of parameters on surface topography in metal micro-droplet deposition manufacture

Le-hua Qi [a,b,*], Song-yi Zhong [a], Jun Luo [a], Dai-cong Zhang [a], Han-song Zuo [c]

[a] School of Mechanical Engineering, Northwestern Polytechnical University, Xi'an 710072, PR China
[b] The Key Laboratory of Contemporary Design and Integrated Manufacturing Technology, Ministry of Education, Xi'an 710072, PR China
[c] School of Material, Northwestern Polytechnical University, Xi'an 710072, PR China

ARTICLE INFO

Article history:
Received 24 June 2014
Received in revised form
22 September 2014
Accepted 25 September 2014
Available online 2 October 2014

Keywords:
Micro-droplet deposition manufacture
Characterization
Surface topography
Scan step
Offset distance

ABSTRACT

Metal micro-droplet deposition manufacture has potential applications and attracts increasing attention in wide areas. By quantitatively describing and predicting the surface topography, the influence of parameters on surface quality could be studied effectively. In present work, a new approach aimed to the characterization of part surface topography was proposed and the evaluation indexes such as arithmetic average height (R_a) and stratification angle (θ) were used to characterize the surface topography. Based on the surface geometrical profile, two prediction models were developed to calculate the evaluation indexes of part surface. Then experiments for fabricating thin wall parts were conducted and the evaluation indexes were measured experimentally. By comparing the experimental values with the predicted results, the mechanism of process parameters affecting surface topography was investigated. The results indicated that the top surface was mainly affected by scan step (W_d) which also could be represented by overlap ratio (μ). While overlap ratio was larger than 25.7%, excessive overlap resulting in poor surface topography occurred and the prediction model was invalid. In another hand, the side surface was mainly affected by offset distance (W_o) which also could be represented by offset ratio (τ). If offset ratio was too large, the ending side would collapse resulting in poor side surface topography and the prediction model would fail to calculate the side surface roughness. The experiment results indicated that collapse would occur while offset ratio was larger than 54.5%. In the last, the surface roughness of a cubic object was measured and the results demonstrated that the method proposed in present work was useful for evaluating surface quality of 3D object.

© 2014 Elsevier Ltd. All rights reserved.

1. Introduction

As a novel kind of 3D printing technology, metal micro-droplet deposition manufacture (MDDM) [1] is an effective method for fabricating 3D objects directly from CAD model [2]. In the process, molten metal droplets are firstly generated as building blocks. Then the droplets are deposited sequentially and fused together to fabricate 3D structures [3]. Because of its advantages of low cost, high material usage efficiency and wide range of material selection [4,5], the technique has great potential applications in automotive, electronics and other industry fields [6].

In present, the surface quality of the MDDM part is poor and it is affected by many factors. Chao et al. [1] fabricated vertical columns and 3D objects with rough surface. As reported in the paper, the surface topography was affected by the temperatures of droplet and substrate. Fang et al. [2,7,8] indicated that the substrate temperature, deposition frequency and substrate velocity had influence on the forming quality of deposited lines and vertical columns. Also, several researches were conducted to improve the surface quality. Qi et al. [9] developed two models based on mass conservation and proposed a novel method for selecting appropriate process parameters. Amirzadeh et al. [10] produced droplets whose diameters were smaller than the nozzle diameter and the small droplets were useful for improving parts quality. Pandey et al. [11] proposed a real time adaptive slicing procedure which could be used to improve surface quality than the other method while build time was same. The presented procedure was applicable to all RP system.

Though researches on improving surface quality were conducted, the descriptions on the surface quality in these researches were qualitative and subjective that was not conducive to study the influence of parameters on surface topography further. So it is necessary to propose a method to characterize and predict the surface quality. By quantitatively studying the relationship between surface topography and process parameters, the process

* Corresponding author at: School of Mechanical Engineering, Northwestern Polytechnical University, Xi'an 710072, PR China. Fax: +86 29 88491982.
E-mail address: qilehua@nwpu.edu.cn (L.-h. Qi).

http://dx.doi.org/10.1016/j.ijmachtools.2014.09.009
0890-6955/© 2014 Elsevier Ltd. All rights reserved.

parameters would be optimized and the post processing operation would be reduced. A few researches have been performed recently which focused on evaluating the surface roughness of RP parts and optimizing the technique parameters. Boschetto et al. [12,13] suggested a model to evaluate the roughness of parts fabricated by fused deposition manufacture (FDM) and the model was useful for optimizing the fabricating orientation. Luis et al. [14] presented a characterization of geometric roughness and the effectiveness of model was confirmed by using stereolithography (SLA) manufacturing technique. Based on the model, two possible strategies for rapid prototype manufacture were established. An elaborate prediction methodology was proposed by Ahn et al. [15] and the surface roughness values could be calculated at surface angles which were impossible to measure. However the procedure of metal micro-droplet deposition manufacture is quite different from the technologies referred above and the parts surfaces are not smooth due to the large surface tension of molten metal and fast solidification during droplet deposition. Research on characterizing micrgeometrical profiles of MDDM parts has seldom been reported. Thus it is imperative to quantitatively characterize the micro geometrical profiles and study the effect of process parameters on surface quality of MDDM part.

In this work, by analyzing the principle of metal micro-droplet deposition manufacture, a novel method for quantitatively characterizing parts surface topography was proposed and two mathematical models for predicting the evaluation indexes of surface quality were developed. By the well-formed formulations, arithmetic average height and stratification angle of parts could be calculated. A series of experiments for fabricating thin-wall parts were conducted and the roughness of parts surfaces were measured. Based on the comparison of experimental and predicted results, the influence of process parameters on surface quality were investigated and the effective ranges for the models were obtained. In the last, a cubic was fabricated and the surface quality was measured which agreed well with the previous experimental and predicted results.

2. Evaluation indexes of surface topography

Fig. 1 shows the schematic of the MDDM system which includes several subsystems e.g. pneumatic droplet generating system, 3D platform and low-oxygen environment. The droplet generating system and 3D platform are combined controlled by an industrial personal computer to deposit droplets in fix location. During the process, components are fabricated by depositing droplets sequentially.

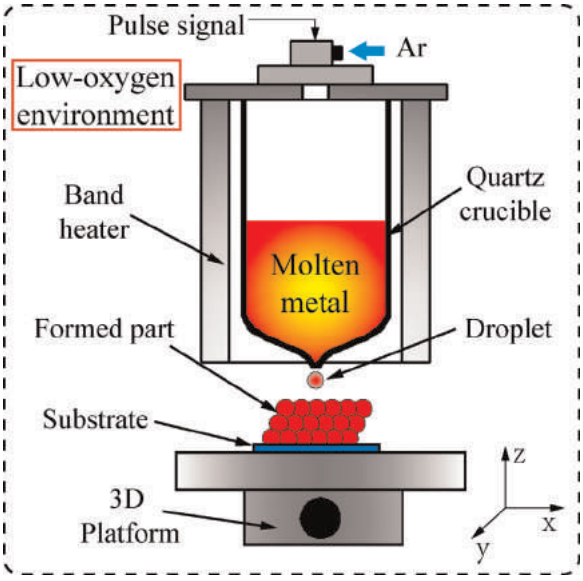

Fig. 1. Schematic of metal micro-droplet deposition manufacture system.

It is known that the shape of single droplet deposited on substrate is rotational symmetric and it could be considered as a spherical crown. Thus the component surface quality can be represented by the surface roughness of the maximum section as shown in Fig. 2. The maximum sections all include top surface and side surface which are affected by different process parameters. The top surface of part was parallel to the substrate and the side of part was defined as the surface which was perpendicular to the substrate or sloped.

In order to study the influence of parameters on surface quality, the microgeometrical profile of the section needs to be characterized quantitatively. In present work, arithmetic average height (R_a) as a roughness parameter was used to characterize the surface quality. R_a was defined as the average absolute deviation of the roughness irregularities from the reference line. The reference line was represented by the least squares line of the profile as shown in Fig. 2(b). The digital implementation of R_a [16] was:

$$R_a = \frac{1}{n}\sum_{i=1}^{n}|Z_i| \tag{1}$$

In addition, stratification angle (θ) was taken as another evaluation parameter to describe the side surface. It was defined as the angle between the least squares line and the substrate.

3. Prediction model of surface topography

In this section, two prediction models were proposed to calculate the evaluation indexes of the surface topography. Previous studies showed that the quality of top and side surface was mainly affected by scan step (W_d) and offset distance (W_o) respectively. So with a view to simplifying the prediction models, W_d and W_o were taken to be the main factor in each model.

3.1. Top surface model

In order to develop the top profile model, several assumptions were made:

(1) The shape of deposited droplet was considered as a spherical crown and the cross-section profile was symmetrical.
(2) While the process parameters were same, deposited droplets were uniform and the part profile was approximated by a periodic sequence of circumference's arcs (Fig. 3).
(3) The profile of previous droplet remained unchanged while the subsequent droplet deposited.

Calling r the radius of the arc and α the solidification angle, the profile was defined by Eq. (2)

$$f(x) = \sqrt{r^2 - x^2} + r\bullet\sin(\alpha - \frac{\pi}{2}) \tag{2}$$

By using Taylor series expansion limited to the second order term, Eq. (2) was computed as follow:

$$f(x) \cong r - \frac{x^2}{2r} + r\bullet\sin(\alpha - \frac{\pi}{2}) \tag{3}$$

As shown in Fig. 3, *L: (y=C)* was the least-squares line. *Q(C)* was defined as the quadratic sum of the distances from profile

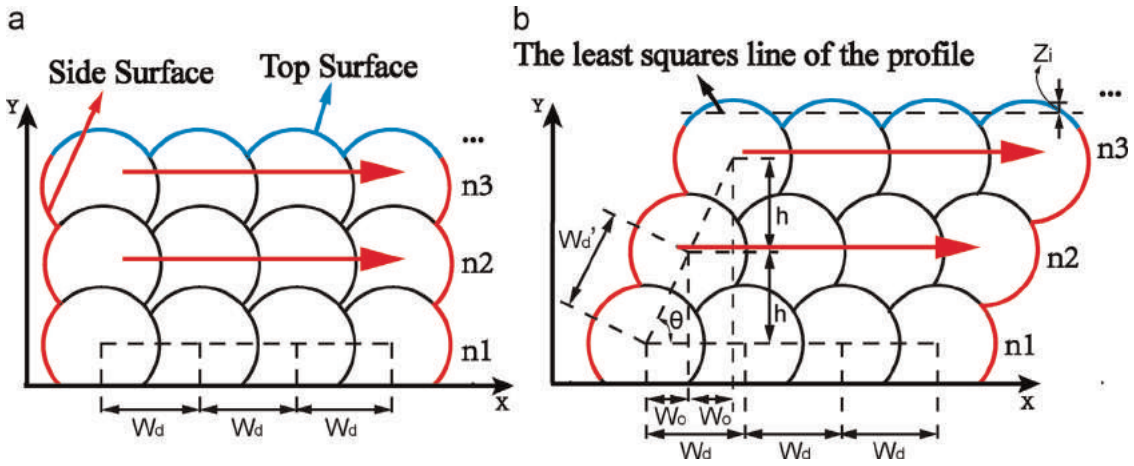

Fig. 2. Microgeometrical profiles of components maximum sections.

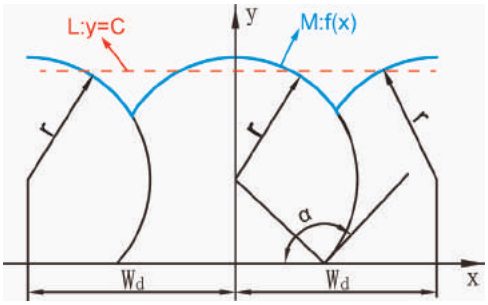

Fig. 3. Sketch of top surface model.

points to the line L.

$$Q(C) = \int_{-\frac{W_d}{2}}^{\frac{W_d}{2}} (f(x) - C)^2 dx \tag{4}$$

According to the definition of the least-squares line, while $\partial Q/\partial C = 0$, $Q(C)$ could be the minimum value. So C could be calculated by Eq. (5).

$$C = \frac{1}{W_d}\int_{-\frac{W_d}{2}}^{\frac{W_d}{2}} f(x)dx = r + r\bullet \sin(\theta - \frac{\pi}{2}) - \frac{W_d^2}{24r} \tag{5}$$

By substituting Eqs. (3) and (5) into Eq. (1), the arithmetical average height of the profile was:

$$R_a = \frac{1}{W_d}\int_{-\frac{W_d}{2}}^{\frac{W_d}{2}} |f(x) - C| dx = \frac{1}{W_d}\int_{-\frac{W_d}{2}}^{\frac{W_d}{2}} \left| -\frac{x^2}{2r} + \frac{W_d^2}{24r} \right| dx = \frac{W_d^2}{18\sqrt{3}r} \tag{6}$$

The shape of deposited droplet was considered as a spherical crown, so r could be calculated by following equation suggested by Qi [9]:

$$r = \frac{D\left[4/(1 - \cos\alpha)^2(2 + \cos\alpha)\right]^{1/3}}{2} \tag{7}$$

D was the droplet diameter.

By substituting Eq. (7) to Eq. (6), an equation described the top surface profile was obtained, and it was permitted to achieve R_a as a function of W_d, D and α:

$$R_a = \frac{W_d^2}{9\sqrt{3}D\left[\frac{4}{(1 - \cos\alpha)^2(2 + \cos\alpha)}\right]^{\frac{1}{3}}} \tag{8}$$

3.2. Side surface model

On the other hand, W_o was considered as the main factor in the side surface model. As shown in Fig. 2(b), the profile of side surface was similar with the top surface and it also could be approximated by a periodic sequence of circumference's arcs. So R_a of the side surface was calculated by replacing W_d in Eq. (8) with W_d'.

$$R_a = \frac{(W_d')^2}{9\sqrt{3}D\left[4/(1 - \cos\alpha)^2(2 + \cos\alpha)\right]^{1/3}} \tag{9}$$

W'_d was defined as the distance between the adjacent droplets on the side surface. According to the geometrical relationship shown in Fig. 2, W'_d was described as follow:

$$W_d'^2 = W_o^2 + h^2 \tag{10}$$

Table 1
Design of experiments for top surface roughness investigation.

Mean diameter of droplets (D)		270 μm						
Angle of solidification (α)		115°						
Spread diameter ($D_s = 2r$)		291 μm						
Scan step (W_d)		200 μm	210 μm	220 μm	230 μm	240 μm	250 μm	260 μm
Number of deposited layers (n)	1	√	√	√	√	√	√	√
	2	√	√	√	√	√	√	√
	3	√	√	√	√	√	√	√

h was defined as the vertical distance between two adjacent droplets on the side. It could be described as follow:

$$h = \gamma\left[r + r\sin\left(\alpha - \frac{\pi}{2}\right)\right] = \gamma D\left[\frac{4}{(1-\cos\alpha)^2(2+\cos\alpha)}\right]^{1/3}\frac{(1-\cos\alpha)}{2} \quad (11)$$

In Eq. (11), γ was a coefficient, and it was mainly affected by scan step and some other factors. By substituting Eq. (10) and Eq. (11) to Eq.(9), R_a of the side surface was calculated:

$$R_a = \frac{W_o^2 + \left[\gamma D\left[4/(1-\cos\alpha)^2(2+\cos\alpha)\right]^{1/3}(1-\cos\alpha)/2\right]^2}{9\sqrt{3}\,D\left[4/(1-\cos\alpha)^2(2+\cos\alpha)\right]^{1/3}} \quad (12)$$

In addition, the stratification angle was defined as follow:

$$\theta = \arctan\left(\frac{h}{W_o}\right) = \arctan\left\{\gamma D\left[\frac{4}{(1-\cos\alpha)^2(2+\cos\alpha)}\right]^{1/3}\frac{(1-\cos\alpha)}{2W_o}\right\} \quad (13)$$

Table 2
Design of experiments for side surface roughness investigation.

Mean diameter of droplets (D)	270 μm
Angle of solidification (α)	115°
Spread diameter ($D_s=2r$)	291 μm
Scan step (W_d)	220 μm
Offset distance (W_o)	40 μm, 80 μm, 120 μm, 160 μm, 180 μm, 200 μm, 240 μm, 280 μm, 320 μm, 360 μm, 400 μm, 440 μm

4. Influence of Parameters on Surface Topography

Based on the prediction models, the evaluation indexes of surface topography could be calculated in different conditions. In addition, a series of experiments were conducted and the evaluation indexes were measured. According to the comparison of predicted and experimental results, the influence of process

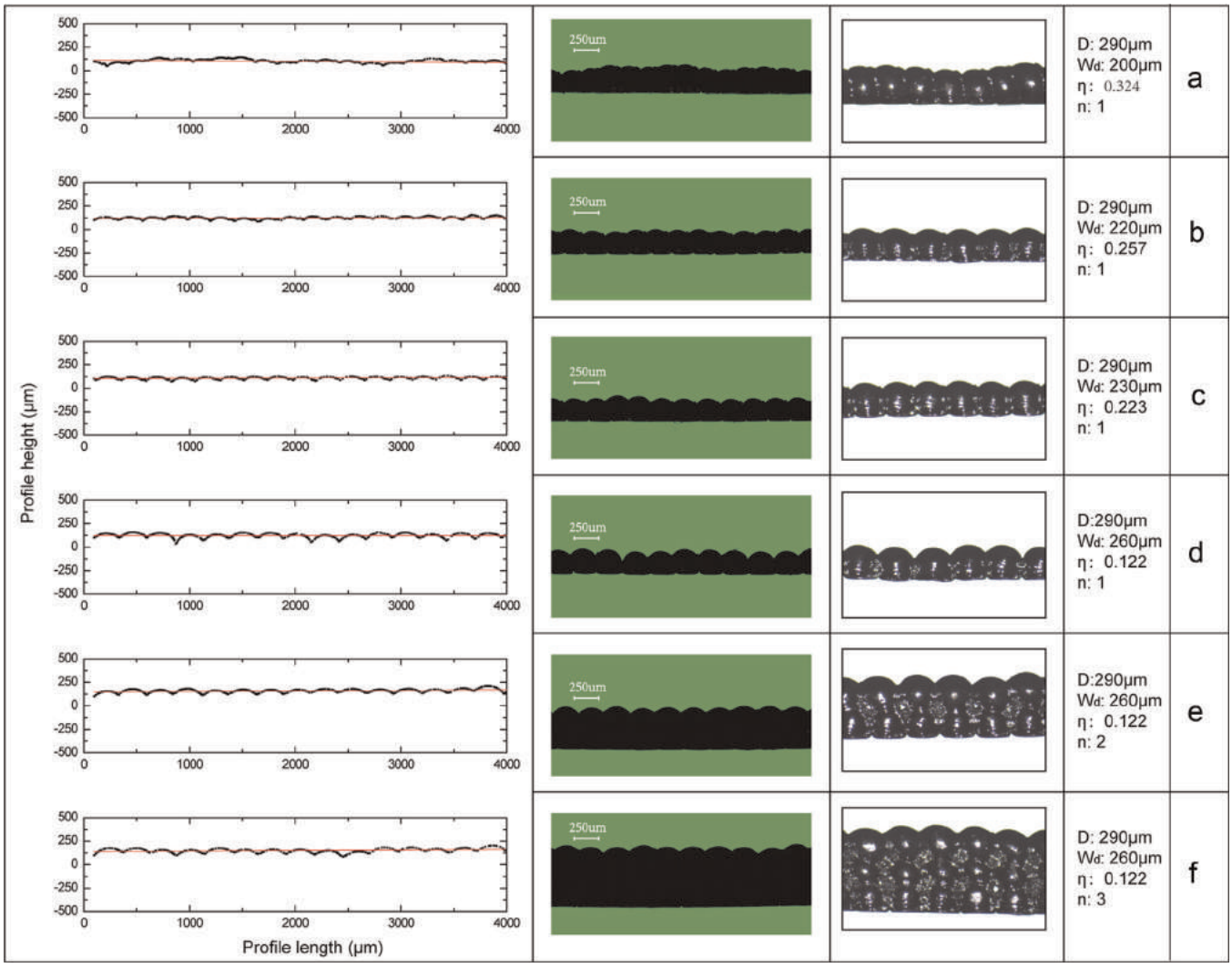

Fig. 4. Zoomed portion of top surface profiles for different manufacturing conditions.

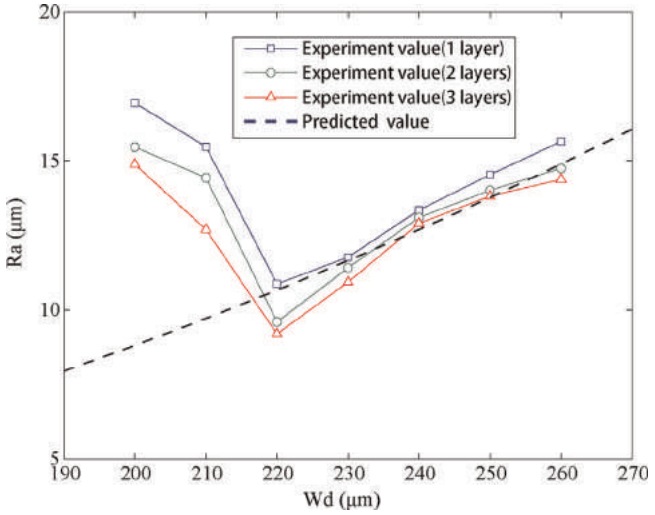

Fig. 5. Experimental and predicted values of arithmetic average height for different scan step.

parameters on surface topography was studied and the effective range for the model was obtained.

As shown in Tables 1 and 2 two sets of experiments were designed and single wall parts were fabricated by using Sn60–Pb40. In each condition, three samples were collected and the surface profiles data were measured by using a tool microscope (Nikon MM400).

4.1. Top surface

In Fig. 4, top surface profiles data for different levels of the investigated factors, together with the section images were reported. Different scan steps made different overlapping results and presented substantial difference in arithmetic average height of the profile and also in shape. While the scan step was too small, as shown in Fig. 4(a), the droplets excessively overlaped and the deposited droplet grew upward. After several droplets deposited, some latter droplets then collapsed due to thier own gravity. Hence, the formed line had large layer thickness and irregular surface. As the scan step increased, the line surface became regular (Fig. 4(b–d)). However, the droplets would not overlap if the scan step was larger than the spread diameter of droplets.

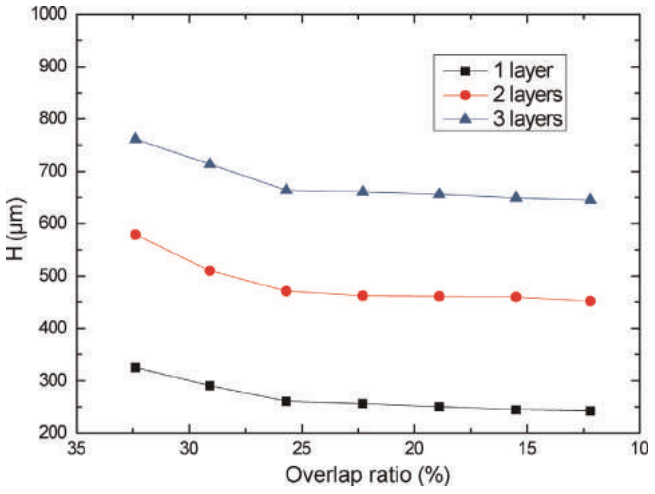

Fig. 6. Influence of overlap ratio and number of layers on the maximum layer thickness.

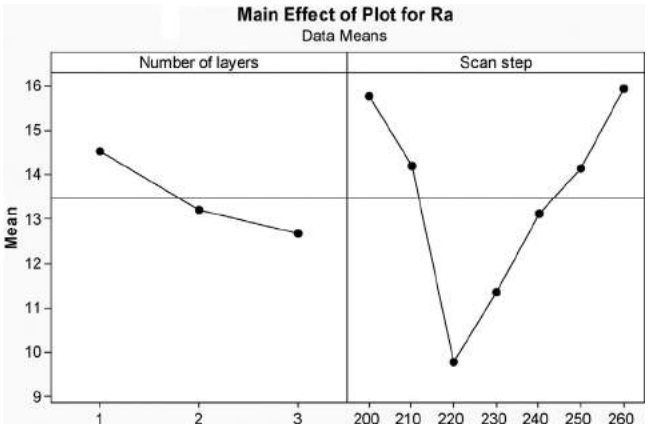

Fig. 7. Main effect plot for R_a.

Experimental values of R_a were measured and plotted versus scan step as shown in Fig. 5. As W_d increased, R_a firstly decreased and then increased. The predicted values of R_a were also marked on Fig. 5. The results indicated that the predicted values always increased with the increase of W_d which was quite different from the experimental results. As shown in Fig. 5, while scan step was greater than or equal to 220 μm, the predicted values agreed well with the experimental values and the mean relative deviation was 4.3%. While scan step was smaller than 220 μm, the predicted values and the experimental values were significantly different and the mean relative deviation was 37.5%. This phenomenon was mainly caused by the excessive overlap.

In order to study the excessive overlap further, the maximum height (H) of part was used to describe the surface topography. By using Eq. (14) [9,17], the scan step was converted into overlap ratio (μ), and the influence of overlap ratio on the maximum height of the profile was shown in Fig. 6.

$$\mu = 1 - \frac{W_d}{D_s} \tag{14}$$

While overlap ratio was equal to or smaller than 25.7%, the maximum heights of the parts with the same deposited layers were approximately same. While overlap ratio was greater than 25.7%, the maximum height varied much more obviously. Thus we considered that excessive overlap occurred and led to poor top surface quality while overlap ratio was greater than 25.7%. So scan step should not be too small for preventing excessive overlap in experiment. While the overlap ratio was less than 25.7%, there was no excessive overlap and the prediction model was effective. As the overlap ratio decreased further, the valley between the adjacent droplets could not be filled well that resulted in the increase of R_a.

In addition, Fig. 5 showed that R_a of the top surface decreased slightly as the number of deposited layers increased. This phenomenon was due to the increase of heat quantity in the deposited parts. As heat quantity increased, the droplet spread sufficiently and the valley was filled well. Analysis of main effect was conducted and the results shown in Fig. 7 indicated that the scan step had much greater influence on surface roughness than the number of deposited layers.

4.2. Side surface

A series of experiments (shown in Table 2) were conducted to fabricate single wall parts with slant side surfaces. Some zoomed portion images of the objects fabricated in different conditions

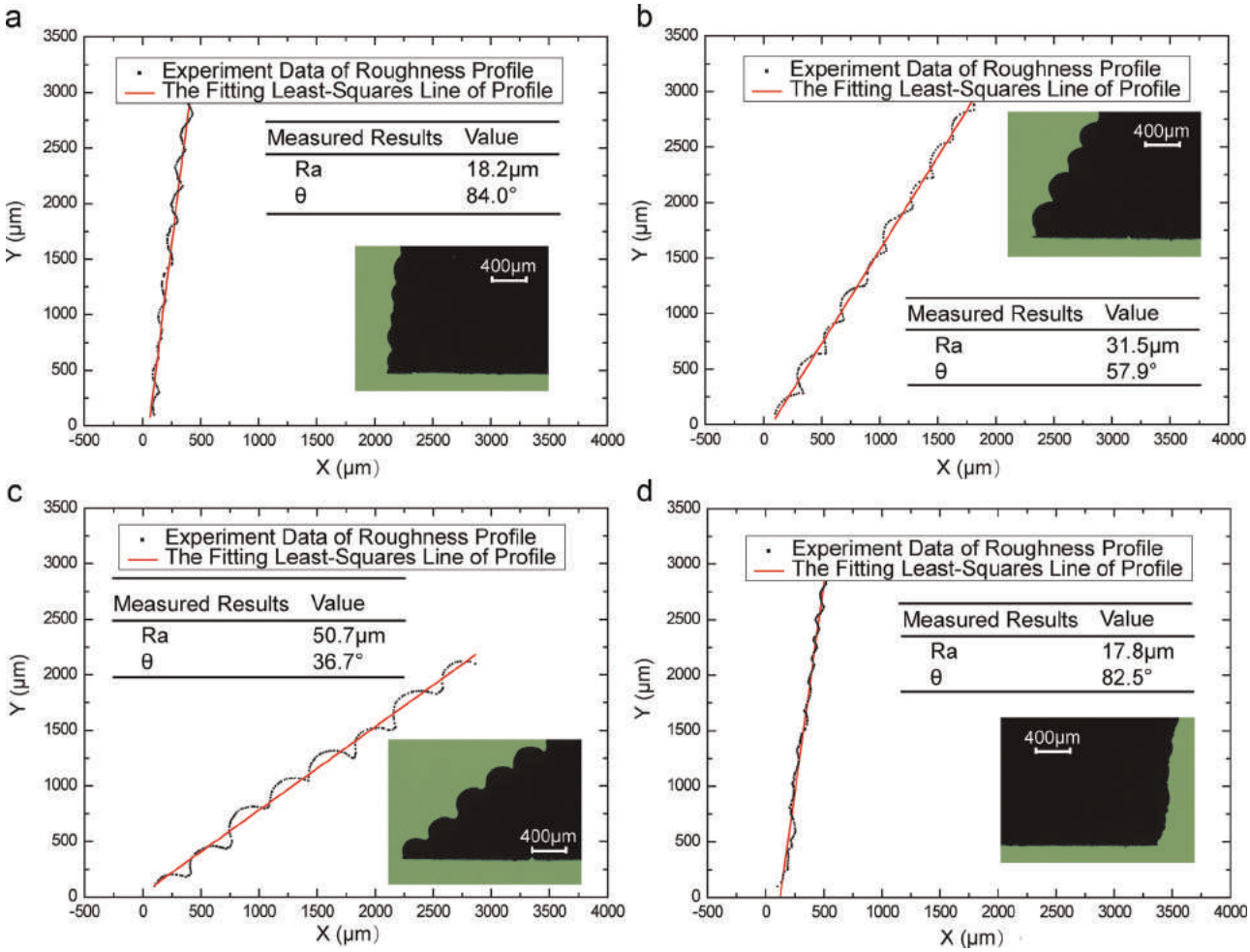

Fig. 8. Zoomed portion of side surface profiles for different offset distance: (a) W_o=40 μm, beginning side; (b) W_o=180 μm, beginning side; (c) W_o=360 μm, beginning side; and (e) W_o=40 μm, ending side.

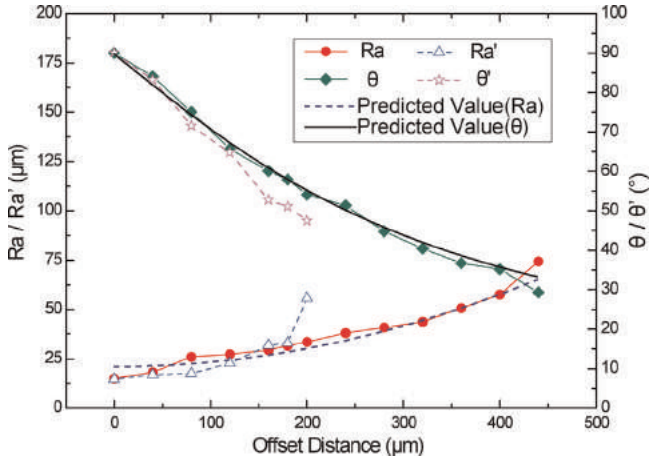

Fig. 9. Influence of offset distance on arithmetic average height and stratification angle.

were shown in Fig. 8. As W_o increased, the stratification angle decreased and the ripple of side surface became more and more obvious. According to the direction of the arrows (Fig. 2 (b)) which represented the depositing direction in the same layer, the two side surfaces of the section were named beginning side and ending side respectively. As shown in Fig. 8(a) and (d), the two sides of the same parts had different micro geometrical profiles.

The arithmetic average height and stratification angle were measured. As shown in Fig. 9, R_a and θ represented the arithmetic average height and stratification angle of the beginning side while R_a' and θ' represented the ones of the ending side. When W_o was 0 μm, the stratification angle was 90° and the arithmetic average heights of side surface had the minimum values. As the offset distance increased, the arithmetic average heights increased and stratification angle decreased. The predicted values also indicated the same tendency and agreed well with the experimental results of the beginning side. The mean relative deviations of R_a and θ were 8.6%, 7.3% respectively.

While W_o was equal to or smaller than 120 μm, R_a' and θ' were smaller than R_a and θ. This phenomenon was mainly caused by the different spread status of the first and the last droplets on each layer. By depositing droplets along with the direction shown in Fig. 2(b), the first deposited droplet of the second layer was supported totally and the center of the droplet was steady. On the contrary, the last deposited droplet of the second layer was supported partly and the surface spread along the surface of pre-deposited droplet resulting in that the center of last droplet was lower than the ones of previous droplets. While W_o was in the range of 160–200 μm, partly collapse occurred and it resulted in

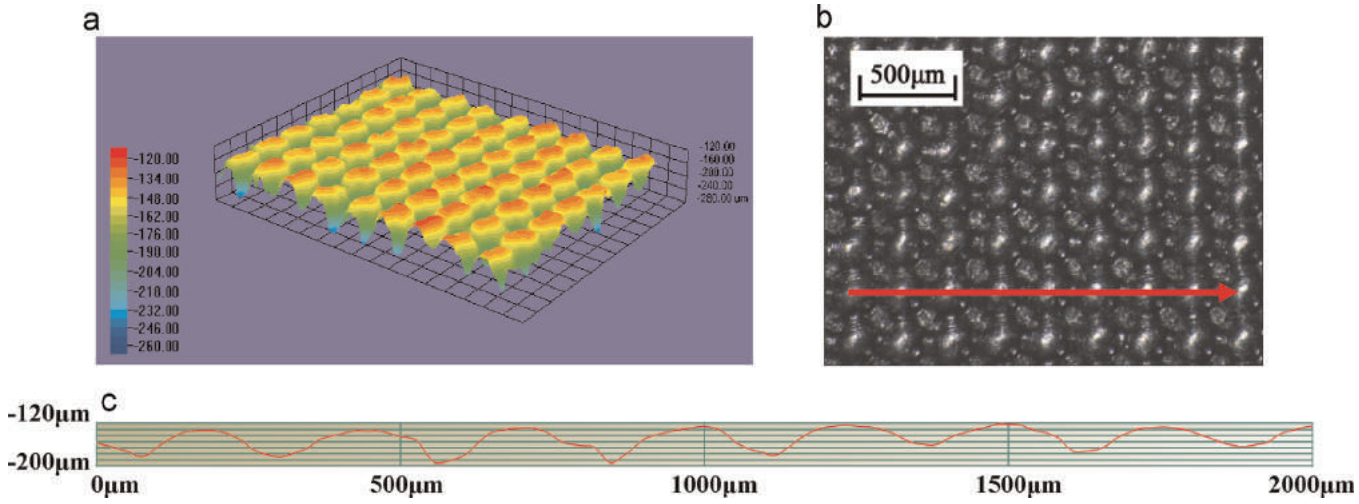

Fig. 10. Zoomed portion of the cube top surface (a) 3D topography; (b) image of top view; and (c) section profile according to the arrow shown in (b).

that R_a' and θ' varied rapidly. As shown in Fig. 9, there were big differences between the experimental and predicted values in these conditions. Even worse, while W_o was larger than 200 μm, the ending side totally collapsed and the profile data was not measured.

In order to describe the collapse quantitatively, decrease rate of stratification angle was defined as follow equation:

$$t = \frac{|\theta - \theta'|}{\theta} \tag{15}$$

By using Eq. (16), the offset distance was converted to offset ratio (τ).

$$\tau = \frac{W_o}{W_d} \tag{16}$$

While offset ratio were 0%, 18.2%, 36.4%, 54.5%, 72.7%, 81.8% and 90.9%, the decrease rate were 0%, 0.98%, 4.61%, 1.43%, 11.45%, 11.85% and 12.18% respectively. So it was considered that there was no collapse only while τ was equal to or smaller than 54.5%. In these conditions, two sides of the same section had similar topography and the prediction models were useful for calculating evaluation indexes. While τ was larger than 54.5%, the ending side of section would collapse and the prediction models were invalid.

In the last, a cubic object was fabricated with droplet diameter of 260 μm, scan step of 260 μm and solidification angle of 115°. As shown in Fig. 10, the 3D topography and the top view image of the top surface indicated that the top surface of the cubic had regular peaks and valleys. According to the arrow shown in Fig. 10(b), the maximum section of each row was obtained (shown in Fig. 10(c)) and R_{ai} was used to represent the arithmetic average height of the maximum section *i*. R_{as} represented the arithmetic average height of the top surface and it was calculated by using Eq. (16).

$$R_{as} = \frac{1}{n}\sum_{i=1}^{n} R_{ai} \tag{16}$$

$$\sigma = \sqrt{\frac{1}{n}\sum_{i=1}^{n}(R_{ai} - \bar{R}_a)^2} \tag{17}$$

In present work, five sections were used to calculate R_{as} and σ which were 15.1 μm and 0.91 μm respectively. The standard deviation was small indicating that the profiles of the different sections were similar, and R_{as} coincided well with the predicted and experimental results shown in Fig. 5 while the process parameters were same. So it was demonstrated that the component surface quality could be represented by the surface roughness of the maximum section.

5. Conclusions

In present paper, a novel method for characterizing micro geometrical profile of MDDM parts was proposed and several evaluation indexes included R_a and θ were used to quantify the surface quality. Based on the geometrical profile, prediction models were developed which were useful to calculate the evaluation indexes. By comparing the predicted values with the experimental results, the influence of process parameters on the surface quality was studied and the effective ranges for the prediction models were obtained. In the last, the experimental result also demonstrated that the surface quality of 3D object could be represented by the surface roughness of the maximum section. Several major conclusions were drawn as follows:

(1) The profile of top surface was mainly affected by scan step. As scan step increased, overlap ratio (μ) decreased, arithmetic average height (R_a) of top surface first decreased to the minimum value and then increased. The experiment results indicated that while overlap ratio was larger than 25.7%, excessive overlap occurred and resulted in poor surface quality.
(2) The side surface roughness was mainly affected by offset distance. As offset distance increased, offset ratio (τ) increased, arithmetic average height (R_a, R_a') increased and stratification angle (θ, θ') decreased. While offset ratio was larger than 54.5%, the ending side would collapse resulting in that R_a' and θ' varied dramatically. So we considered that slant side could be fabricated without support material only while offset ratio was equal to or smaller than 54.5%.
(3) The comparison between predicted and experimental results indicated that: (a) the top surface prediction model was available while excessive overlap didn't occur; and (b) the side surface prediction model was useful for calculating arithmetic average height and stratification angle while there was no collapse.

Acknowledgments

The authors gratefully acknowledge the support of this research by the National Defense Basic Scientific Research

(A1120133026), the National Natural Science Foundation of China (No.51105314) and the Doctoral Fund of Ministry of Education of China (NO.20126102110022).

References

[1] Y. Chao, L. Qi, H. Zuo, J. Luo, X. Hou, H. Li, Remelting and bonding of deposited aluminum alloy droplets under different droplet and substrate temperatures in metal droplet deposition manufacture, Int. J. Mach. Tools Manuf. 69 (2013) 38–47.
[2] M. Fang, S. Chandra, C.B. Park, Building three-dimensional objects by deposition of molten metal droplets, Rapid Prototyp. J. 14 (2008) 44–52.
[3] Y. Chao, L. Qi, Y. Xiao, J. Luo, J. Zhou, Manufacturing of micro thin-walled metal parts by micro-droplet deposition, J. Mater. Process. Technol. 212 (2012) 484–491.
[4] Y. Yingxue, G. Shengdong, C. Chengsong, Rapid prototyping based on uniform droplet spraying, J. Mater. Process. Technol. 146 (2004) 389–395.
[5] D.T. Pham, R.S. Gault, A comparison of rapid prototyping technologies, Int. J. Mach. Tools Manuf. 38 (1998) 1257–1287.
[6] J. Luo, L. Qi, S. Zhong, J. Zhou, H. Li, Printing solder droplets for micro devices packages using pneumatic drop-on-demand (DOD) technique, J. Mater. Process. Technol. 212 (2012) 2066–2073.
[7] M. Fang, S. Chandra, C.B. Park, Heat transfer during deposition of molten aluminum alloy droplets to build vertical columns, J. Heat Transf. 131 (2009) 112101–112107.
[8] M. Fang, S. Chandra, C.B. Park, Remelting and coalescence of molten metal droplets deposited on a plate, ASME Conf. Proc. 2004 (2004) 939–944.
[9] L. Qi, Y. CHAO, J. Luo, J. Zhou, X. Hou, H. Li, A novel selection method of scanning step for fabricating metal components based on micro-droplet deposition manufacture, Int. J. Mach. Tools Manuf. 56 (2011) 50–58.
[10] A. Amirzadeh Goghari, S. Chandra, Producing droplets smaller than the nozzle diameter by using a pneumatic drop-on-demand droplet generator, Exp. Fluids 44 (2008) 105–114.
[11] P.M. Pandey, N.V. Reddy, S.G. Dhande, Real time adaptive slicing for fused deposition modelling, Int. J. Mach. Tools Manuf. 43 (2003) 61–71.
[12] A. Boschetto, 3D roughness profile model in fused deposition modelling, Rapid Prototyp. J. 19 (2013) 240–252.
[13] A. Boschetto, V. Giordano, F. Veniali, Modelling micro geometrical profiles in fused deposition process, The, Int. J. Adv. Manuf. Technol. 61 (2011) 945–956.
[14] C.J. Luis Pérez, J. Vivancos Calvet, M.A. Sebastián Pérez, Geometric roughness analysis in solid free-form manufacturing processes, J. Mater. Process. Technol. 119 (2001) 52–57.
[15] D. Ahn, H. Kim, S. Lee, Surface roughness prediction using measured data and interpolation in layered manufacturing, J. Mater. Process. Technol. 209 (2009) 664–671.
[16] E.S. Gadelmawla, M.M. Koura, T.M.A. Maksoud, I.M. Elewa, H.H. Soliman, Roughness parameters, J. Mater. Process. Technol. 123 (2002) 133–145.
[17] W. Aiyiti, W. Zhao, B. Lu, Y. Tang, Investigation of the overlapping parameters of MPAW-based rapid prototyping, Rapid Prototyp. J. 12 (2006) 165–172.

Le-hua Qi is a professor from School of Mechanical Engineering at Northwestern Polytechnical University, and she also is the team member from Education Ministry Key Laboratory of Contemporary Design and Integrated Manufacturing Technology. Professor Qi received PhD degree in System Engineering from Northwestern Polytechnical University. Her research interests include micro-manufacturing based on metal droplet generation technology, manufacturing technology and forming mechanism of metal matrix composites and image recognition for the C/C composites.

Song-yi Zhong is a Ph.D. student at School of Mechanical Engineering, Northwestern Polytechnical University. His research interests include metal droplet ejection, metal droplet deposition and droplet based solid freeform fabrication.

Jun LUO is an associate professor from School of Mechanical Engineering at Northwestern Polytechnical University. His research is in package technology, metal droplet disposition, jet breakup simulation, droplet charging and deflection, droplet based solid freeform fabrication.

Dai-cong Zhang is a Ph.D. student at School of Mechanical Engineering, Northwestern Polytechnical University. His research interests include modeling of components, optimization of fabrication strategy and metal droplet deposition.

Han-song Zuo is a Ph.D student at School of Materials Science and Engineering, Northwestern Polytechnical University. His research is in performance and microstructure of parts formed by Solid Freeform Fabrication.

Composites Part B 78 (2015) 469–479

Contents lists available at ScienceDirect

Composites Part B

journal homepage: www.elsevier.com/locate/compositesb

Stress distribution modeling for interference-fit area of each individual layer around composite laminates joint

Danlong Song, Yuan Li, Kaifu Zhang*, Ping Liu, Hui Cheng, Tao Wu

The Ministry of Education Key Laboratory of Contemporary Design and Integrated Manufacturing Technology, Northwestern Polytechnical University, Xi'an 710072, Shaanxi, China

ARTICLE INFO

Article history:
Received 11 August 2014
Received in revised form
6 March 2015
Accepted 8 April 2015
Available online 17 April 2015

Keywords:
A. Laminates
B. Residual/internal stress
C. Analytical modeling
E. Joints/joining
Interference fit

ABSTRACT

The discussion about nonuniform stress distribution around interference-fit joint is particular significance in the design of composite laminates structures. In order to investigate the stress distribution of interference-fit area around composite laminates joint, an analytical model is developed for stress distribution based on the Lekhnitskii's complex potential theory. The normal and tangential stresses of contact are achieved by the relationship of deformation between pin and hole. The effects of ply orientation and interference percentage on stress components distributions of each individual layer around symmetrical laminates joint are discussed. In order to verify the validity of the analytical model, extensive 3D finite element models are established to simulate the stress components of laminates interference-fit joint. The results show that the analytical model is valid, and the laminate property and ply orientation have a significant effect on stress distribution trend while interference percentage mainly affects stress magnitude.

© 2015 Elsevier Ltd. All rights reserved.

1. Introduction

High performance fiber reinforced plastics (FRP) have plenty of advantages over conventional metal materials, and are widely used in aerospace technology, automobile and many other weight sensitive structures. In the structures assembly technology, composite laminates are usually fastened to other structural components by mechanical joints such as bolts and rivets. According to statistics, composite laminates joint is the weakest part of the structures where 60%–80% of structure failure occurs at the fastening joints [1]. The interference fit technology of joint was proved that it can improve the fatigue life of metal structures observably [2,3], but also was pointed out by the McDonnell Douglas Corporation that interference-fit joining improved the fatigue life of carbon epoxy composites [4–6]. Interference fit joints require drilling holes and pressing into the metal pin, which causes nonuniform residual stress and damage to the joints. The residual stress is related to interference percentage, fiber orientation and material property directly. The appropriate stress contributes to improving the fatigue performance of structures, but oversize stress will damage the structures. However, the stress distribution around interference-fit joint is quite complex. In order to optimally design and evaluate the damage of these interference-fit joints after being jointed, it is very necessary to determine the residual stress of interference-fit area around composite laminates joints.

Extensive researches about stress distribution around joints or holes have been discussed, especially in the case of pin-loaded joint, which is also a problem about contact between hole and pin and provides reference for the interference fit case.

The determination of stress and strain distribution in notched composite plates, which is the basis of research, has been in the focus of many researchers for a long time. In the literature, many studies can be found using experimental, FEM and analytical methods. For complicated stress problem of elastic theory, Muskhelishvili [7] firstly introduced complex potential theory, deduced stress function and boundary condition, and then obtained accurate solution of stress distribution successfully. Analytical solutions for the stress distribution around different shapes of holes in anisotropic plates have been given by Lekhnitskii [8] using complex series method. Savin [9] presented a much simpler approach by conformal mapping and Cauchy integrals. There are many literature focusing on the stress distribution around cutout of finite and infinite composite plate with external loading in recent years. Ukadgaonker et al. [10,11] developed a general solution for stresses

* Corresponding author. Tel.: +86 029 88493303.
E-mail address: zhangkf@nwpu.edu.cn (K. Zhang).

http://dx.doi.org/10.1016/j.compositesb.2015.04.013
1359-8368/© 2015 Elsevier Ltd. All rights reserved.

around triangular and arbitrary shape of holes in symmetrical laminates and unsymmetrical laminates under in-plane loading. Hufenbach et al. [12–15] published several analytical results of stress concentration for the case of elliptical, triangular, or square holes in single-layered composite plates and finite outer boundary. Wu and Mu [16] proposed an empirical calculation method for the stress concentrations for isotropic/orthotropic plates and cylinders with a circular hole, and the results agreed well with the FEM simulations which provided structure engineers a simple and efficient way to estimate the hole effect on plate structures or pressure vessels made of isotropic or orthotropic materials. Foust et al. [17] obtained the full-field individual stresses and strains throughout a finite pinned-wood joint with applying a thin birefringent coating by grey-field reflective photoelasticity test. Toubal et al. [18] experimentally investigated the tensile strain field of composite plates in the presence of stress concentration caused by geometrical cutout consisting of circular hole by Electronic Speckle Pattern Interferometer (ESPI).

Stress distribution for composite laminates with pin-load joint is investigated on the condition that the load of pin is given or supposed by experience, and they are clearance fit. De Jong [19] Zhang and Ueng [20] utilized the complex stress functions and obtained a compact analytical solution of stresses around a loaded hole with rigid pin in orthotropic plates including frictional effects. Grüber et al. [21] discussed the problem of stress concentrations in the area of pin-loaded holes. The load of pin was assumed to be a sinusoidal normal distribution of edge forces on a continuous part of the notch edge. Aluko O and Whitworth HA [22] developed an analytical method for stress components by displacement boundary method, with four trigonometry items, and friction effects were included in this research. The results showed that friction affected the stress distribution around the hole, and the maximum of stresses changed with values of frictional coefficient.

There are some research literature focusing on stress distribution for composite laminates with interference-fit joint utilizing numerical and experimental methods. Chakherlou [2] simulated cold expansion, a bigger pin squeezing through the smaller hole of plate by a 3-D FE model and calculated the residual stress distribution near the hole. Sundarraj et al. [23] achieved the 3-D stress distribution in a double-shear lap joint with interference-fit pin subjected to in-plane loads using FELJNT that is a finite element software developed for the special purpose, and the effects of clamping and flexure of the bolt are considered. Pradhan and Babu [6] created 3-D finite element models to simulate interference-fit pin-loaded joints in various composite laminates and study the effects of interference percentages for different material cases on circumferential edge stresses, stresses across the weakest section, and the out-of-plane stresses around the hole periphery. Lewis et al. [24] measured the contact stresses in a real shaft-sleeve interference-fit contact by an ultrasonic technique. The results from the experiment and FEA compared well both in the center of the fit and around the edges.

All the remarkable works contribute a lot to the analysis of the stress distribution of composite laminates. Compared with FE and experimental methods, the analytical solutions of stress distribution have many advantages in terms of reducing computation time, experimental cost and establishing theoretical basis for damage and failure. Most of the analytical solutions reported were mainly based on the fundamental works of Musskhelischwili and Lekhnitskii and integrated the mathematical methods of complex potential, conformal mapping and analytical continuation. However, these researches mainly focused on pin-loaded cases with clearance or snug fit where the pin was treated as rigid body and analytical solutions of stress distribution for composite laminates with interference-fit joint is not reported very often.

This paper is concerned with the stress distribution and magnitude of interference-fit area around composite laminates joint where the pin is made of elastic metal. An analytical method is developed for stress distribution based on Lekhnitskii's complex potential method. The normal and tangential stresses of contact are achieved by the relationship of deformations between the pin and hole. The effects of fiber orientation and interference percentage on stress distribution of individual layer around symmetrical laminates joint are discussed. In order to verify the validity of the analytical model, extensive 3-D finite element models have been established to simulate the stress components of interference-fit area around composite laminates joint. The stress components distributions of each individual layer and various interference percentages for two different composite laminates obtained from the analytical model are compared with the numerical results respectively.

2. Analytical modeling for stress distribution

2.1. Problem configuration of interference-fit joint

An infinite thin symmetrical anisotropic composite laminate with single-lap interference-fit joint, the initial diameter of pin is larger than that of hole, is considered. The geometry and configuration is shown in Fig. 1. Based on the elastic theory of anisotropic plate by Lekhnitskii [8], we can simplify the loaded laminates as a two-dimensional as a generalized plane stress problem. Multilayer CFRP (Carbon Fiber Reinforced Plastics) plate widely used in aviation is a kind of composite laminate layered by unidirectional carbon fiber reinforced lamina. The pin made of elastic metal, such as TC4, is pressed into the hole by the method of cold expansion. In the aerospace industry, relative interference percentages of diameter from 0.6% to 2% are usually used for composite laminates joints [2,25].

The relative interference percentages is defined in engineering application as

$$I = \frac{d_0 - D_0}{D_0} \times 100\% \tag{1}$$

where d_0 is the initial diameter of pin, and D_0 is the initial diameter of hole.

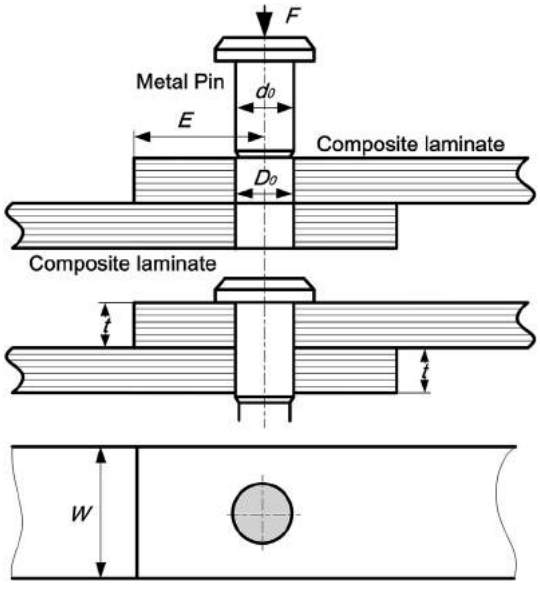

Fig. 1. Geometry and configuration for the interference-fit joint.

Since the interference percentage is very small and composite is usually considered to be non-plastic, only the linear elastic deformation of the pin and hole is considered. Fig. 2 shows the deformation and force analysis of pin and hole. The initial radiuses r_0,R_0 of pin and hole are squeezed into an intermediate dimension R_θ which varies with angle θ after being interference fitted. The contact load N between hole edge and pin can be decomposed into two parts: normal pressure P and tangential stress T, where P is the normal squeezing force per unit area and T is the tangential force per unit area. The contact stresses of pin and hole are equal in magnitude but opposite in direction.

2.2. Deformation displacement of the metallic pin

When the metal pin is pressed into the hole of composite laminates, the pin is squeezed thinner. Considering that the pin is homogenous and the strain is very small, the problem of loaded pin can be simplified to two-dimensional generalized plane strain problem which is dealt with in the same way by many references [7,8,19–22]. The composite laminate is anisotropic, and the stress distribution is not uniform along circumference, so axial symmetry method is not suitable. The complex stress functions for the pin can be deduced by load boundary condition, and stresses and displacements are represented by complex Airy's stress functions.

The cross section of the pin is circular which is expressed by a simply-connected region S_p before deforming, and the boundary of region S_p is expressed by L_p as shown in Fig. 2a. In addition, $z = x + iy$ is any point in the area S_p, t is any point and t_0 is a fixed point on the boundary L_p.

The stress function $U(x,y)$ can be represented by Ref. [7]:

$$\frac{\partial U}{\partial x} + i\frac{\partial U}{\partial y} = \varphi(z) + z\varphi'(z) + \overline{\psi(z)}, \quad z \in S_p \tag{2}$$

where the complex stress functions $\varphi(z)$ and $\psi(z)$ are arbitrary holomorphic functions in the area S_p according to complex analysis theory.

The complex stress functions should satisfy the boundary condition as follows [7]:

$$\varphi(t) + t\varphi'(t) + \overline{\psi(t)} = f(t), \quad t \in L_p \tag{3}$$

where $f(t)$ is a holomorphic function which represents the complex principal vector of external stress at arbitrary point t of the boundary L_p given by Eq. (9).

With regard to the circular area, Eq. (3) can be substituted by a Fredholm equation as follows:

$$\omega(t_0) + \frac{1}{2\pi i}\int_{L_p}\frac{\omega(t)}{t}dt + \frac{t_0}{2\pi r_0^2 i}\int_{L_p}\overline{\omega(t)}dt = f(t_0), \quad t, t_0 \in L_p \tag{4}$$

where $\omega(t)$ is given by:

$$\omega(t) = f(t) + A + Bt \tag{5}$$

$$A = -\frac{1}{2\pi i}\int_{L_p}\frac{\omega(t)}{t}dt, \quad B = -\frac{1}{2\pi r_0^2 i}\int_{L_p}\overline{\omega(t)}dt \tag{6}$$

and r_0 is the initial radius of the pin.

Introducing Eq. (5) into Eq. (6), and considering that the complex principal vector and principal moment of external stresses are equal to zero:

$$Re\int_{L_p} f(t)d\bar{t} = Re\int_{L_p}\overline{f(t)}dt = 0 \tag{7}$$

the expression of A and the real part of B can be acquired as follows:

$$A = -\frac{1}{4\pi i}\int_{L_p}\frac{f(t)}{t}dt$$
$$ReB = \frac{1}{4\pi}\mathrm{Im}\int_{L_p}\frac{f(t)}{t^2}dt \tag{8}$$

With the contact stresses P and T applied to the edge of pin, the complex principal vector of external stress on the boundary L_p from the fixed point t_0 to an arbitrary point t is integrated by

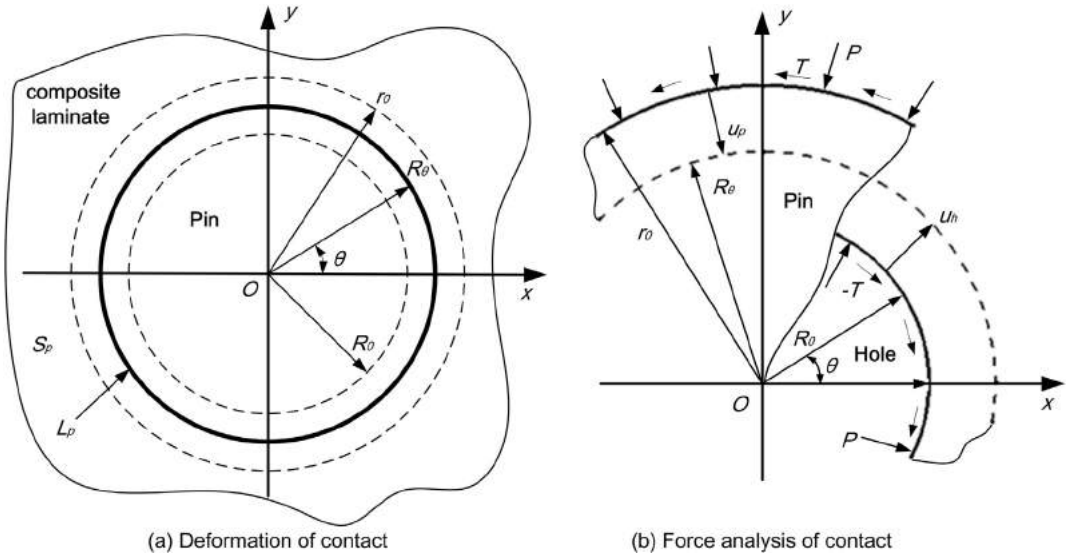

Fig. 2. Deformation and force analysis of pin and hole.

$$f(t) = i\int_{t_0}^{t}[X_n(t) + iY_n(t)]ds = -Pr_0e^{i\theta} + iTr_0e^{i\theta} \tag{9}$$

Introducing Eqs. (5), (8) and (9) into Eq. (4), and regardless of the imaginary part of B, the complex stress functions with the contact load P and T can be deduced as follows:

$$\begin{aligned}\varphi(z) &= \frac{1}{2\pi i}\int_L \frac{f(t)}{t-z}dt + ReB\cdot z = -\frac{Pz}{2}, \quad z\in S_p\\ \psi(z) &= \frac{1}{2\pi i}\int_L \frac{\overline{f(t)} - \bar{t}f'(t)}{t-z}dt = \frac{2Tr_0^2 i}{z}, \quad z\in S_p\end{aligned} \tag{10}$$

When the complex stress functions are prepared, the complex functions of displacement vector in Cartesian coordinate system are given by Ref. [7]:

$$2\mu(u_{xp} + iu_{yp}) = \kappa\varphi(z) - z\overline{\varphi'(z)} - \overline{\psi(z)}, \quad z\in S_p \tag{11}$$

Solving the Eq. (11), the results of displacement components are obtained the following Eq. (12):

$$\begin{cases} u_{xp} = Re\left[\dfrac{\kappa\varphi(z) - z\overline{\varphi'(z)} - \overline{\psi(z)}}{2\mu}\right] \\ u_{yp} = \mathrm{Im}\left[\dfrac{\kappa\varphi(z) - z\overline{\varphi'(z)} - \overline{\psi(z)}}{2\mu}\right] \end{cases}, \quad z\in S_p \tag{12}$$

where

$$\kappa = \frac{\lambda + 3\nu}{\lambda + \nu} \tag{13}$$

With regard to plane strain state, Lame Constants μ and λ are determined by:

$$\mu = \frac{E}{2(1+\nu)}, \quad \lambda = \frac{E\nu}{(1+\nu)(1-2\nu)} \tag{14}$$

where E and ν are the Young's modulus and the Poisson's ratio respectively.

2.3. Mean displacement and stress of the laminate

Considering a thin symmetrical anisotropic composite laminate under generalized plane stress of the external forces caused by the interference-fitted pin, the generalized Hooke's law is valid when the analysis is limited to the linear elastic range. The generalized Hooke's law in terms of mean stress components $\sigma_x,\sigma_y,\tau_{xy}$ and mean strain components $\varepsilon_x,\varepsilon_y,\gamma_{xy}$ through thickness is given by:

$$\begin{bmatrix}\varepsilon_x\\ \varepsilon_y\\ \gamma_{xy}\end{bmatrix} = \begin{bmatrix} a_{11} & a_{12} & a_{16}\\ & a_{22} & a_{26}\\ & & a_{66}\end{bmatrix}\begin{bmatrix}\sigma_x\\ \sigma_y\\ \tau_{xy}\end{bmatrix} \tag{15}$$

where $a_{mn}(m,n = 1,2,6)$ are the coefficients of the reduced compliance matrix of the symmetrical composite laminate which can be calculated using Appendix A of Ref. [10] by engineering constants of lamina and stacking sequences.

Without regard to body force, representing average stress components $\sigma_x,\sigma_y,\tau_{xy}$ in terms of an Airy's stress function $U(x,y)$,

$$\sigma_x = \frac{\partial^2 U}{\partial y^2}, \quad \sigma_y = \frac{\partial^2 U}{\partial x^2}, \quad \tau_{xy} = -\frac{\partial^2 U}{\partial x\partial y} \tag{16}$$

In order to ensure the integrity and continuity of strain, the average stress components must satisfy the equation of strain compatibility,

$$\frac{\partial^2\varepsilon_x}{\partial y^2} + \frac{\partial^2\varepsilon_y}{\partial x^2} = \frac{\partial^2\gamma_y}{\partial x\partial y} \tag{17}$$

and substituting Eq. (15) in terms of $U(x,y)$ into the equation of strain compatibility Eq. (17), a forth order biharmonic differential equation is obtained as follows:

$$\begin{aligned}&a_{22}\frac{\partial^4 U}{\partial x^4} - 2a_{26}\frac{\partial^4 U}{\partial x^3\partial y} + (2a_{12} + a_{66})\frac{\partial^4 U}{\partial x^2\partial y^2} - 2a_{16}\frac{\partial^4 U}{\partial x\partial y^3}\\ &+ a_{11}\frac{\partial^4 U}{\partial y^4}\\ &= 0\end{aligned} \tag{18}$$

The general solution of Eq. (18) depends on the roots of the following characteristic equation:

$$a_{11}s^4 - 2a_{16}s^3 + (2a_{12} + a_{66})s^2 - 2a_{26}s + a_{22} = 0 \tag{19}$$

and it can be proved that Eq. (19) has four distinct roots, which are always complex conjugates in pairs:

$$\begin{aligned}s_1 &= \alpha_1 + i\beta_1, \quad s_2 = \alpha_2 + i\beta_2\\ s_3 &= \alpha_1 - i\beta_1, \quad s_4 = \alpha_2 - i\beta_2\end{aligned} \tag{20}$$

These complex parameters given by Eq. (20) depend on the compliance coefficients $a_{mn}(m,n = 1,2,6)$ of the anisotropic composite laminate.

By the integral operation to Eq. (18), the complex Airy's stress function $U(x,y)$ of anisotropic composite laminate can be represented by:

$$U(x,y) = F_1(x + s_1y) + F_2(x + s_2y) + F_3(x + s_3y) + F_4(x + s_4y) \tag{21}$$

that is:

$$U(x,y) = F_1(z_1) + F_2(z_2) + \overline{F_1(z_1)} + \overline{F_2(z_2)}, \quad z_1, z_2\in S_h \tag{22}$$

where $z_k = x + s_ky$ are anisotropic complex coordinates, S_h represents outside region of the circular hole in the z-plane.

Two analytic functions $\varphi(z_1),\psi(z_2)$ are introduced:

$$\varphi(z_1) = \frac{dF_1}{dz_1}, \quad \psi(z_2) = \frac{dF_2}{dz_2}, \quad z_1, z_2\in S_h \tag{23}$$

With the external load applied by interference fitted pin, the contact loads of hole which are equal in magnitude but opposite in direction to those of pin can be expressed as P and $-T$. Then the load boundary conditions of hole at any point t of the boundary of hole L_h can be represented by:

$$\begin{cases} 2Re[\varphi(z_1) + \psi(z_2)] = R_0^2(P\cos\theta - T\sin\theta) \\ 2Re[s_1\varphi(z_1) + s_2\psi(z_2)] = R_0^2(T\cos\theta - P\sin\theta) \end{cases}, \quad z_1, z_2\in S_h \tag{24}$$

where R_0 is the initial radius of the hole.

The outside region S_h of the circular hole in the z-plane is mapped external to the unit circle S_h' in the ζ-plane by the conformal mapping method as follows:

$$\zeta_1 = \frac{z_1 + \sqrt{z_1^2 - R_0^2\left(1+s_1^2\right)}}{R_0(1-s_1 i)}, \quad \zeta_2 = \frac{z_2 + \sqrt{z_2^2 - R_0^2\left(1+s_2^2\right)}}{R_0(1-s_2 i)} \tag{25}$$

When the complex parameters are different $s_1 \neq s_2$, the complex stress functions with the contact load P and $-T$ will be deduced:

$$\begin{cases} \varphi(z_1) = \dfrac{R_0(T-Pi) + s_2 R_0(P-Ti)}{2(s_1-s_2)\zeta_1} \\ \psi(z_2) = -\dfrac{R_0(T-Pi) + s_1 R_0(P-Ti)}{2(s_1-s_2)\zeta_2} \end{cases}, \quad \zeta_1, \zeta_2 \in S_h' \tag{26}$$

When the complex stress functions are prepared, the stress components of Cartesian coordinate system in terms of $\varphi(z)$ and $\psi(z)$ are given by Ref. [7]:

$$\begin{cases} \sigma_x = 2Re\left[s_1^2\varphi'(z_1) + s_2^2\psi'(z_2)\right] \\ \sigma_y = 2[\varphi'(z_1) + \psi'(z_2)] \\ \tau_{xy} = -2Re[s_1\varphi'(z_1) + s_2\psi'(z_2)] \end{cases}, \quad z_1, z_2 \in S_h \tag{27}$$

And the displacement components of Cartesian coordinate system in terms of $\varphi(z)$ and $\psi(z)$ can be expressed by:

$$\begin{cases} u_{xh} = 2Re[p_1\varphi(z_1) + p_2\psi(z_2)] - \omega y + u_0 \\ u_{yh} = 2Re[q_1\varphi(z_1) + q_2\psi(z_2)] + \omega x + v_0 \end{cases}, \quad z_1, z_2 \in S_h \tag{28}$$

where

$$\begin{aligned} p_1 &= a_{11}s_1^2 + a_{12} - a_{16}s_1, \quad p_2 = a_{11}s_2^2 + a_{12} - a_{16}s_2 \\ q_1 &= a_{12}s_1 + \frac{a_{22}}{s_1} - a_{26}, \quad q_2 = a_{12}s_2 + \frac{a_{22}}{s_2} - a_{26} \end{aligned} \tag{29}$$

and ω,u_0,v_0 are arbitrary constants of integration, which are determined by rigid displacement of the composite laminate.

2.4. Contact relationship of displacements

The analysis of deformation and displacement is shown in Fig. 2. The displacement components of pin and hole are u_{xp},u_{yp},u_{xh},u_{yh} which have been obtained above, the contact relationship of displacements in x and y directions determined by the displacement continuity of interference-fit can be expressed as follows:

$$\begin{cases} (u_{xh} - u_{xp}) = (r_0 - R_0)\cos\theta \\ \left(u_{yh} - u_{yp}\right) = (r_0 - R_0)\sin\theta \end{cases} \tag{30}$$

The contact stresses P and T can be derived by solving the Eq. (30). However there are many complicated complex operations of conjugating and separating the real and imaginary parts, the explicit expressions of P and T solved by MATLAB are too long to be shown in the paper. The analytical procedure and computer implementation of the solution are listed in the Section 2.6.

When the contact stresses P and T between the pin and hole are prepared, by introducing them into Section 2.3, the complex stress functions for CFRP laminate are derived again. Combining the parameters of instance, the stress components distributions present themselves in our sight.

2.5. Stress distribution of individual layer

When the mean stress components of the laminate around the hole are prepared in the Section 2.3, the mean strain components can be obtained by Eq. (15). As to the symmetrical multilayered composite laminates, the mean strain is the same as that of middle-surface. According to the classical lamination theory [26], the strain is continuous through the thickness, so the strain of arbitrary point in individual layer k can be expressed in terms of the middle-surface strain $\varepsilon_{x,y}^0$ and curvature $K_{x,y}$ as follows:

$$\begin{bmatrix} \varepsilon_x \\ \varepsilon_y \\ \gamma_{xy} \end{bmatrix}_k = \begin{bmatrix} \varepsilon_x^0 \\ \varepsilon_y^0 \\ \gamma_{xy}^0 \end{bmatrix} + z\begin{bmatrix} K_x \\ K_y \\ K_{xy} \end{bmatrix} \tag{31}$$

or it can be written in contracted notation as:

$$\varepsilon_{x,y}^{(k)} = \varepsilon_{x,y}^0 + zK_{x,y} \tag{32}$$

In this paper, the interference fit of symmetrical composite laminates is studied, it can be proved that the coupling stiffness matrix is equal to zero, contact load of interference-fit will not cause the bending and torsion of composite laminates. Then the curvature of middle-surface is equal to zero $K_{x,y} = 0$. In this case, the strain at arbitrary point through the thickness is the same with the middle-surface and mean strain as follows:

$$\varepsilon_{x,y}^{(k)} = \varepsilon_{x,y}^0 = \varepsilon_{x,y} \tag{33}$$

Taking Eq. (33) into consideration, the stress components in the k^{th} ply in global coordinate is calculated by the following equation modified from Stress–Strain Equation:

$$\begin{bmatrix} \sigma_x \\ \sigma_y \\ \tau_{xy} \end{bmatrix}_k = \begin{bmatrix} \overline{Q}_{11} & \overline{Q}_{12} & \overline{Q}_{16} \\ \overline{Q}_{12} & \overline{Q}_{22} & \overline{Q}_{26} \\ \overline{Q}_{16} & \overline{Q}_{26} & \overline{Q}_{66} \end{bmatrix}_k \begin{bmatrix} \varepsilon_x \\ \varepsilon_y \\ \gamma_{xy} \end{bmatrix} \tag{34}$$

where $\overline{Q}_{ij}$ is the transformed reduced stiffness matrix for individual layers with oriented fibers in global coordinate determined by Eq. (2.85) given in Ref. [26].where

$$Q_{11} = \frac{E_1}{1-\nu_{12}\nu_{21}}, Q_{22} = \frac{E_2}{1-\nu_{12}\nu_{21}}, Q_{12} = \frac{\nu_{12}E_2}{1-\nu_{12}\nu_{21}}, Q_{66} = G_{12} \tag{35}$$

The stress components in Cartesian coordinate system given by Eq. (34) are transformed into cylindrical coordinate system, the radial stress σ_r, tangential stress $\sigma_{r\theta}$ and circumferential stress σ_θ in the k^{th} ply can be obtained by:

$$\begin{aligned} &\sigma_\theta^{(k)} + \sigma_r^{(k)} = \sigma_x^{(k)} + \sigma_y^{(k)} \\ &\sigma_\theta^{(k)} - \sigma_r^{(k)} + 2i\tau_{\theta r} = \left(\sigma_x^{(k)} - \sigma_y^{(k)} + 2i\tau_{xy}^{(k)}\right)e^{2i\alpha} \end{aligned} \tag{36}$$

2.6. Computer implementation and procedure of the solution

The analytical and computational procedure of stress components distributions for each layer is very complicated. Here are giving the computer implementation and procedure of the solution.

(a) Assuming the contact loads between the pin and hole to be normal pressure P and tangential stress T.

(b) Calculation of the deformation displacements of pin edge u_{xp} and u_{yp} in Eq. (13) based on complex potential method of elastic theory and contact loads in Section 2.2.
(c) Calculation of the deformation displacements of hole edge u_{xh} and u_{yh} in Eq. (29) based on the elasticity theory of anisotropic body and contact loads in Section 2.3.
(d) Calculation of the contact loads P and T depending on the contact relationship of deformation displacements between the pin and hole in Eq. (31).
(e) Introducing P and T into the expressions of stress components in Eq. (28), the mean stress components around the hole in Cartesian coordinate system are obtained.
(f) Calculation of the mean strain components by the stress components obtained in (e) and compliance matrix in Eq. (15).
(g) Calculation of the stress components of each layer in Cartesian coordinate system by Eq. (34).
(h) Transforming the stress components in Cartesian coordinate system into cylindrical coordinate system by Eq. (36), the radial stress, tangential stress and circumferential stress in the k^{th} ply can be obtained.

3. Numerical simulation by FE method

In order to assess the analytical model established in Section 2, extensive three-dimensional finite element models with various interference-fit conditions between the pin and hole are established to simulate the interference-fit process and nonlinear contact analysis is performed to study the stress components distributions of interference-fit area around composite laminates joint.

3.1. Finite element modeling

In this paper, FE models of the single-lap and single-pin composite laminates joints are developed and analyzed by the nonlinear FE code ABAQUS 6.11. An exemplary FE model is shown in Fig. 3. The interference-fit of pin and hole is simulated by simply modeling the pin, which is oversized with respect to the hole, and pressing the pin into the hole. The diameter of pin is constant 6.00 mm, and the diameter of hole varies from 5.90 mm to 5.98 mm in the extensive models which are simulated respectively. The pin and the laminates are assembled together with the holes of laminates aligned and the surface of pin just touching the edge of hole. The geometry dimensions of the FE models are shown in Table 1. The width of laminates is 60 mm where $W/D_0 \geq 10$, the end margin from the hole to the end of laminates is 30 mm where $E/D_0 \geq 5$ and the thickness is 4 mm.

Table 1
Geometry dimensions of the specimen (mm).

E	W	t	d_0	D_0
30	60	4	6.00	5.90, 5.94, 5.96, 5.98

Table 2
Material properties of the pin.

Material	E (GPa)	ν
TC4	110.00	0.31

Isotropic and elastic material properties given in Table 2 are used for the pin which is made of TC4, as titanium alloy Hi-Lock Bolt widely used in aviation. The composite laminates are made of carbon fiber reinforced epoxy resin matrix lamina (CFRP) T700/3234 and HTA/6376 with the same layup stacking sequences [0°/−45°/90°/45°]2s. The material properties of CFRP lamina are given in Table 3. In order to analyze the stress of individual layer, each layer of the laminates is assigned material properties of the lamina and ply orientations, and the domain of field output is set at Composite layup at the middle section points.

3.2. FE mesh and loading

The planar stress is analyzed only here. The finite element mesh consists of 3D eight-noded layered continuum shell elements for the laminates which is different from the conventional shell elements. As the calculation accuracy of quadratic elements is not very good in contact modeling, linear elements with reduced-integration (SC8R). The metallic pin is meshed with 3D eight-noded solid elements (C3D8R). The finite element mesh around the hole is much finer than that of other regions by partition as illustrated in Fig. 3.

The boundary conditions are also shown in Fig. 3. The laminates are clamped on the sides and the block is clamped on the bottom. In the first load step, a 0.001 mm pre-displacement is applied to the

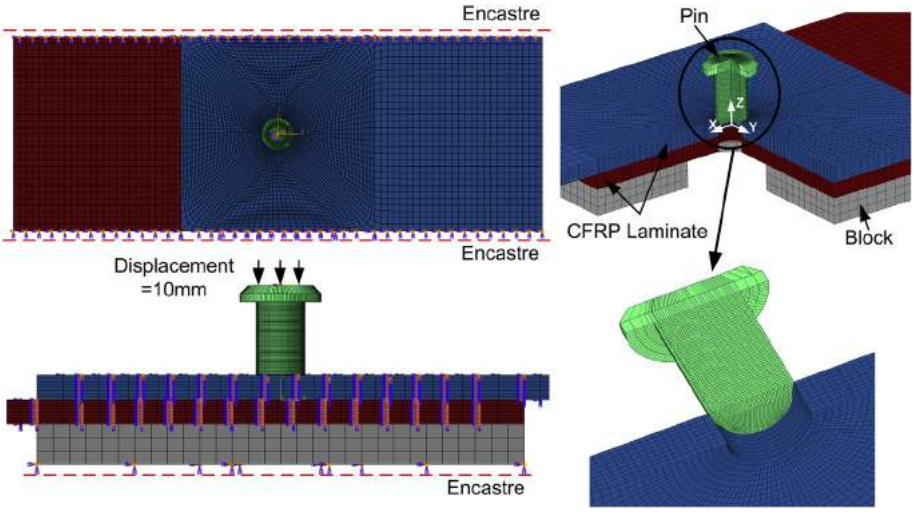

Fig. 3. Finite element model of the CFRP composite laminate with interference-fit joint.

Table 3
Material properties of the CFRP lamina.

CFRP lamina	E_1 (GPa)	$E_2 = E_3$ (GPa)	$\nu_{12} = \nu_{13}$	ν_{23}	$G_{12} = G_{13} = G_{23}$ (GPa)	Ply thickness (mm)
T700/3234	128.00	8.70	0.32	0.30	4.00	0.25
HTA/6376	140.00	10.00	0.30	0.50	5.20	0.25

pin to set up stable contact relationship between the pin and edge of hole. Then, the pin is pressed into the hole by applying a 10 mm driving full-displacement along the axis of hole in the second step which is shown in Fig. 3. Since the pin undergoes large displacement, geometric nonlinearity should be considered, and Nlgeom is set at ON here.

3.3. Contact interaction description

There are exiting some contact pairs in the process of interference fit. Contact interaction conditions are enforced by defining 3D surface-to-surface contact pairs between interacting surfaces. The master and slave surfaces are show in Fig. 4 in which slave surfaces are unable to penetrate their corresponding master surfaces. The 3D surface-to-surface discretization method is employed, which prevents surface penetration in an average sense and provides more accurate results than node-to-surface discretization method. The effect of pin movement on the near-hole stress distribution (due to changing contact areas) is essentially considered by the finite sliding contact model. Since the residual stress is modeled analytically regarding the interference-fit process, the FE models are simulated with frictionless sliding.

4. Results and discussion

The in-plane stress components distributions of composite laminates with interference-fit joint are investigated by the generalized analytical solution and FE method proposed above. The varying parameters such as ply orientation and interference percentage are considered, so extensive comparative analysis is performed for CFRP laminates made from T700/3234 and HTA/6376 the layup stacking sequences [0°/−45°/90°/45°]2s. It turns out that the material properties, ply orientation and interference percentage are significant influence factors to the stress distribution.

Representative results are presented here from the large number of performed verifying calculations. Because of the anisotropy of composite laminates and isotropy of pin, the boundary contour of pin and hole which is no longer circular is investigated. The stress components of various interference percentages and each individual layer are discussed respectively as follows. Overall, it turns out that in the case of all examined interference-fit joints, the numerical simulation and the results obtained by analytical methods show a high level of correlation.

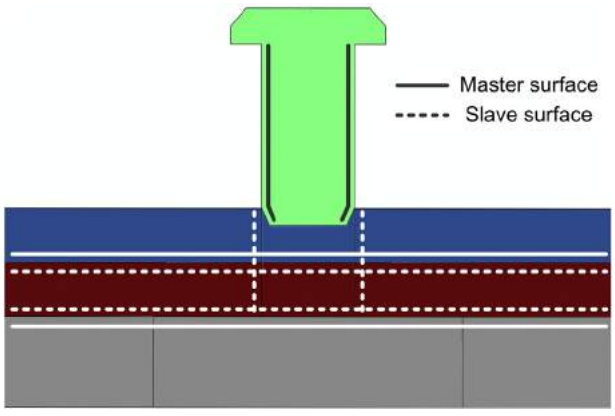

Fig. 4. Surface-to-surface contact law between the pin and hole.

4.1. Deformation displacement and contour of hole

Since the CFRP lamina is anisotropic, the stiffness varies with the deviation angle from fiber orientation. So the deformation displacement is different in each direction, where it is center symmetric. This behavior corresponds to expectations, due to the center symmetry of the lamina.

The contacted contour of pin and hole after deformation with interference percentage 1.69% (the diameters of pin and hole are 6.00 mm and 5.90 mm respectively) in 0°-layer which is made from T700/3234 lamina is approximate elliptic which is enlarged and shown in Fig. 5. The minimum of deformation displacement can be found at the fiber orientation and the maximum at perpendicular to the fiber orientation due to the variation of stiffness, it is the strongest at 0° and the weakest at 90°. The results of analytical model show good agreement with numerical simulation.

In addition, the deformation displacements u_x,u_y,u_r,u_θ in Cartesian and Cylindrical coordinate systems are shown respectively in Fig. 6 in detail. Since the CFRP lamina is anisotropic, there is a transverse shear force on the contact surface between pin and hole. The expressions of displacements are variant trigonometric functions. The radial displacement u_r is the same as that in Fig. 5. The results are obtained by analytical method and FE simulation, in which good agreement is observed and provides confidence in the accuracy of the present results.

4.2. Stress distribution of individual layer

The effect of ply orientation on the radial stress distribution is investigated by the proposed analytical model in this section. Fig. 7 shows the radial stresses distributions σ_r of 0°-layer, 45°-layer, 90°-layer, −45°-layer respectively in the composite laminates made from T700/3234 lamina. The trends of radial stress curves are coincident with different ply orientation, but the phase delay is different depending on the ply orientation. The reason of those is that the each individual layer of the laminate is the same and symmetrical. However, when the composite laminates are loaded by asymmetric force, the stress distribution will be complicated.

It is also observed in Fig. 7 that the maximum of radial stress σ_r can be found at the fiber orientation and the minimum of that appears at the perpendicular to the fiber orientation, which change with ply orientation. The corresponding deformation displacements are similar. In view of this, the pin deformed a very twisty cylinder actually in the axial direction. However, it is very difficult to be observed, since the deformation is tiny.

4.3. Effect of various interference percentages on stress distribution

The interference-fit joint is formed when the thicker pin is inserted into a smaller hole. The various interference percentages are generated by changing the diameters of hole, where the specification and diameter of pin is constant.

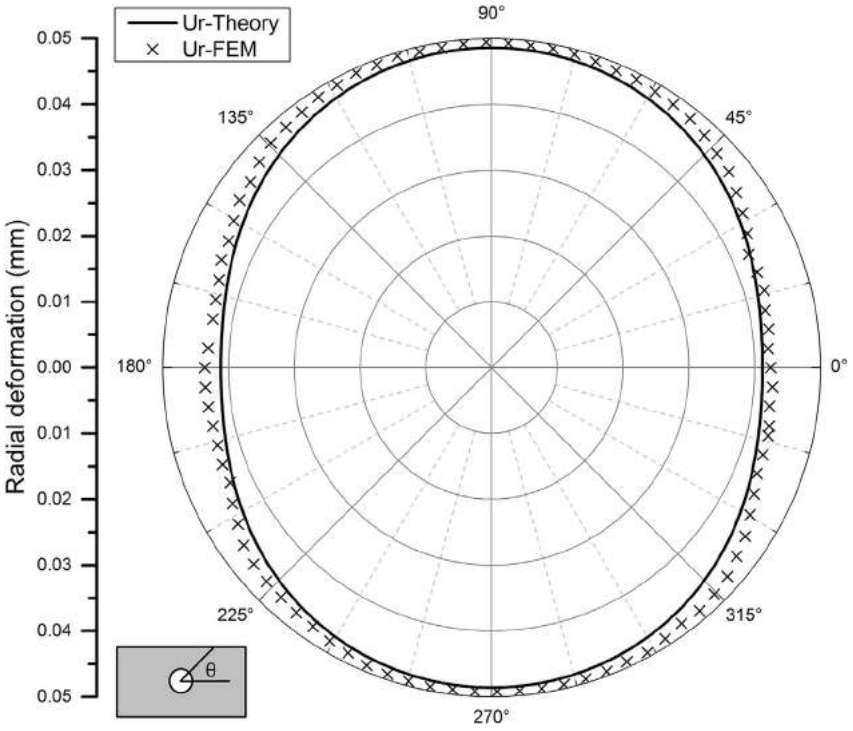

Fig. 5. Contour of the hole after deformation with interference 1.69% in 0°-layer.

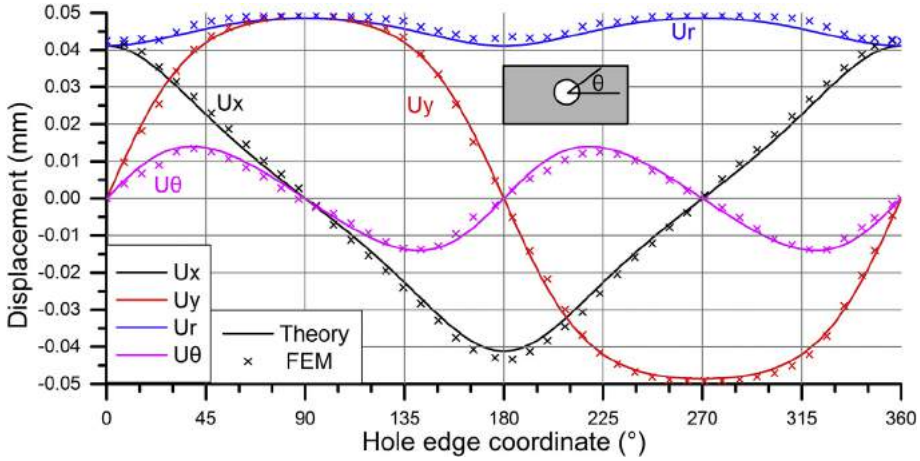

Fig. 6. Deformation displacement components u_x,u_y,u_r,u_θ with interference 1.69% in 0°-layer.

The effect of various interference percentages on stress components is shown in Fig. 8. The stress components distributions σ_r,σ_θ,$\sigma_{r\theta}$ in the Cylindrical coordinate system with interference percentages 0.33% and 1.01% (the diameters of hole are 5.98 mm and5.94 mm respectively) in 0°-layer which is made from T700/3234 and HTA/6376 lamina have been analyzed using proposed method. All the stress components are their absolute values in order to convenient diagram. It is observed in Figs. 8 and 9 which are represent stress distributions of different laminates that the trends of stress components curves are coincident in these cases, but the amplitudes increase with interference percentages and stiffness of material.

The maximum of radial stress σ_r is at 0°-direction and the minimum of that appears at 90°-direction, but the circumferential stress σ_θ at 90°-direction is the maximal value which is larger than the radial stress σ_r, and the tangential stress $\sigma_{r\theta}$ is much smaller than the other two. The circumferential stress σ_θ in the vicinity of 90°-direction and 270°-direction appears serious stress concentration. The nonuniform stress components distributions are caused by anisotropy of plate and isotropy of pin. Compared with the stress components simulated by FE method, the deviations at the peaks of stress range from 11% to 14% shown in Figs. 8 and 9. It proves that the analytical results are reasonable and valid in engineering. When the mesh is refined and optimized, the results of two methods will match each other better.

Fig. 10 depicts the radial stress σ_r around the edge of the hole with various diametrical interference percentages 0.33%, 0.67%, 1.01% and 1.69%. It is shown that the amplitudes of radial stress σ_r increases with the interference percentage linearly as expected. The values of stress components of I = 0.67% is twice as much as those of I = 0.33% at any angle, and similar situation is observed in other interference cases shown in Figs. 8 and 9. The behavior could

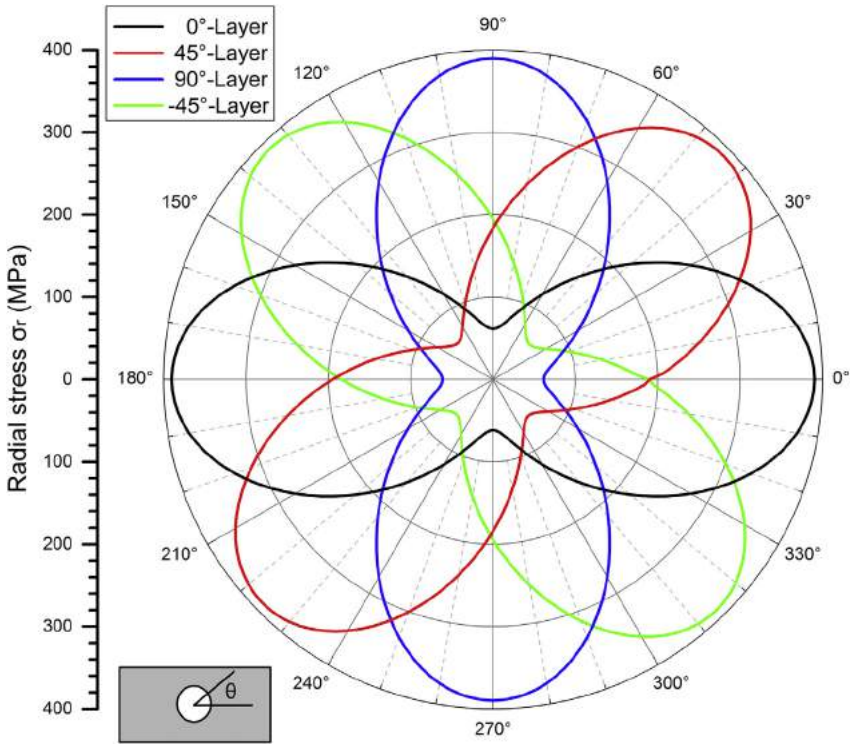

Fig. 7. Radial stress varies with ply orientation.

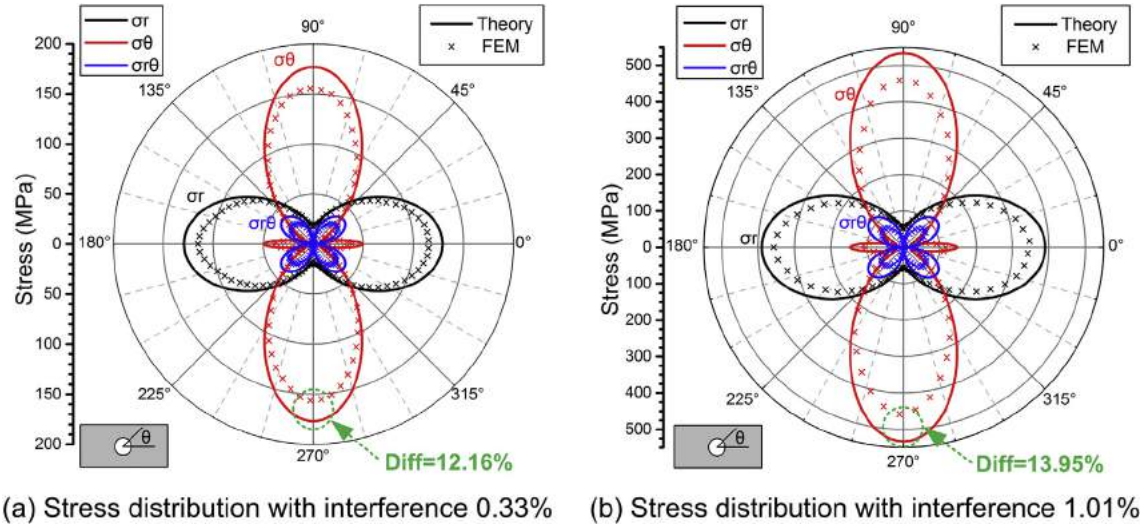

Fig. 8. Stress components distributions with various interferences in 0°-layer made from T700/3234.

be explained by linear elastic assumption of pin and laminate in analytical method.

It is proven that the right size interference percentage is beneficial for the fatigue life of structures [5,25]. But the oversized interference percentage will damage and weaken the composite laminates, so what is the right interference percentage will be investigated in the future based on the analytical model of stress distribution proposed in this paper. Here we just consider the calculation and analysis of stress components distributions.

In summary, a high level of correlation is determined between analytically calculated and numerically determined stress components curves for various interference percentages. Thus, the developed fundamentals for calculation of composite laminate with interference-fit joint represent a quick, dependable and easily manageable alternative to performing time-consuming FE analyses when dealing with stress distribution problems of interference-fit area. In particular, they allow to identify unusual phenomena in an early design phase and to take advantage of them deliberately in the optimization of composites joint.

5. Conclusions

In allusion to the interference-fit area of symmetrical composite laminates joint, an analytical model is developed for stress distribution using Lekhnitskii's complex variable approach in this paper. The deformation displacement and contour of the hole, stress

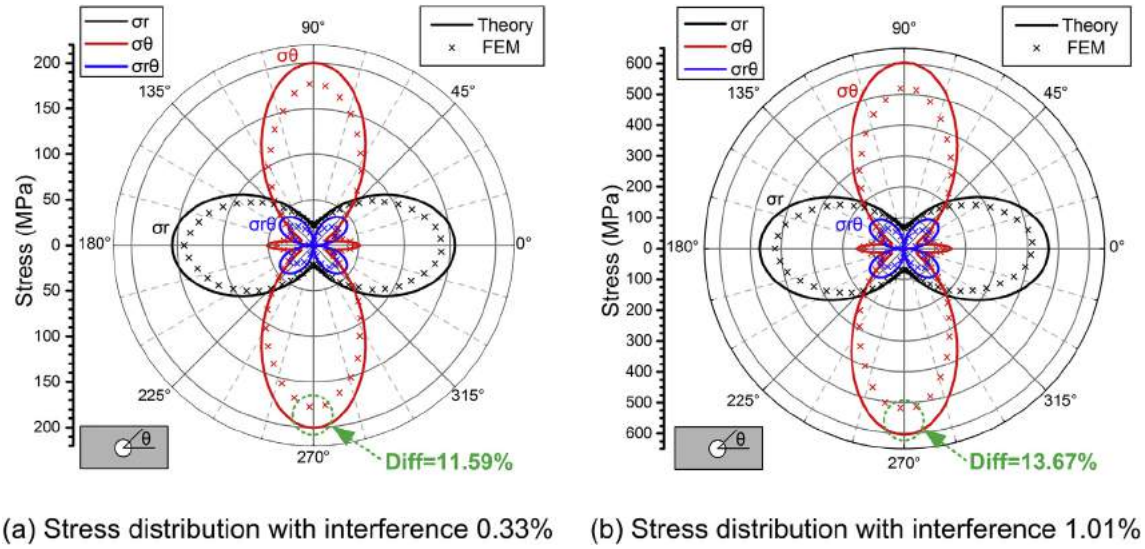

Fig. 9. Stress components distributions with various interferences in 0°-layer made from HTA/6376.

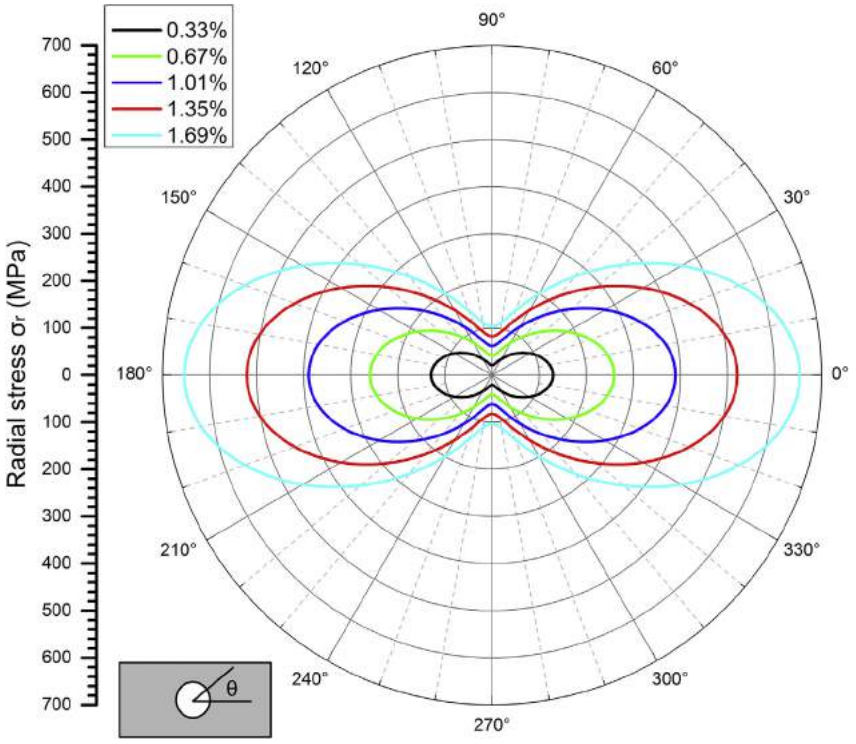

Fig. 10. Radial stress varies with interference percentages in 0°-layer.

distributions of individual layer and effect of various interference percentages on stress components distributions are discussed respectively by analytical and numerical methods. The general analytical solution presented above is extremely valid to obtain stress components of interference-fit area in individual layer of composite laminates with interference-fit joint, compared with results of a number of numerical simulations. Thus, the developed fundamentals for calculation of composite laminate with interference-fit joint represent a quick, dependable and easily manageable alternative to performing time-consuming FE analyses when dealing with stress distribution problems of interference-fit area. In particular, they allow to identify unusual phenomena in an early design phase and to take advantage of them deliberately in the optimization of composites joint. It should be emphasized that the presented methods calculate not only stresses, strains and displacements directly at the edge of the hole, but also their distributions throughout the entire area of the laminate.

(1) The stress components distributions are all nonuniform and periodic caused by the anisotropy of plate and isotropy of pin. The peak of circumferential stress σ_θ is larger than that of radial stress σ_r, but the tangential stress $\sigma_{r\theta}$ is much smaller.
(2) The elasticity of the pin is taken into consideration, the contours of pin and hole after deformation are ellipse-like shapes, and the stress distributions are more accurate in practical application compared with the case of rigid pin.

(3) The stress components magnitudes increase with the interference percentages linearly and stiffness of material before damage because of linear elasticity of pin and laminates, but the trends of those are similar.
(4) The trends of radial stress curves of each individual layer are consistent due to the same property of each lamina, but the phase delay is depended on the respective ply orientation.

Here we just consider the calculation and analysis of stress components distributions, ignoring the effect of interference percentage on the damage. It is proved that the right size interference percentage is beneficial for the fatigue life of structures [5,25]. But the oversized interference percentage will cause delamination or squeezed damage to the composite laminates, the undersized interference percentage will not show the benefit, so what is the right interference percentage and prediction of the micro damage location will be investigated next based on the stress distribution model proposed in this work.

Acknowledgments

The work reported herein is sponsored by National Natural Science Foundation of China (51175433 and 51305349) and Natural Science Basic Research Plan in Shaanxi Province (2014JQ7272). The authors would like to greatly acknowledge the editors and the anonymous referees for their insightful comments.

References

[1] Cao Z, Cardew-Hall M. Interference-fit riveting technique in fiber composite laminates. Aerosp Sci Technol 2006;10(4):327–30.
[2] Chakherlou TN, Vogwell J. The effect of cold expansion on improving the fatigue life of fastener holes. Eng Fail Anal 2003;10(1):13–24.
[3] Chakherlou TN, Mirzajanzadeh M, Abazadeh B, Saeedi K. An investigation about interference fit effect on improving fatigue life of a holed single plate in joints. Eur J Mech A Solid 2010;29(4):675–82.
[4] Bunin BL. Critical composite joint subcomponents analysis and test results. Washington: National Aeronautics and Space Administration, Scientific and Technical Information Branch; 1983.
[5] Kim S, He B, Shim C, Kim DD. An experimental and numerical study on the interference-fit pin installation process for cross-ply glass fiber reinforced plastics (GFRP). Compos Part B Eng 2013;54:153–62.
[6] Pradhan B, Babu PR. Assessment of beneficial effects of interference-fit in pin-loaded FRP composites. J Reinf Plast Comp 2007;26(8):771–88.
[7] Muskhelishvili NI. Some basic problems of the mathematical theory of elasticity. Berlin: Springer; 1977. Netherlands.
[8] Lekhnitskii SG. Theory of elasticity of an anisotropic body. Moscow: Mir Publishers; 1981.
[9] Savin G. Stress concentration around holes. New York: Pergamon Press; 1961.
[10] Ukadgaonker VG, Rao D. A general solution for stresses around holes in symmetric laminates under inplane loading. Compos Struct 2000;49(3):339–54.
[11] Ukadgaonker VG, Rao DKN. A general solution for stress resultants and moments around holes in unsymmetric laminates. Compos Struct 2000;49(1):27–39.
[12] Hufenbach W, Grüber B, Langkamp A, Lepper M, Kroll L. Advanced calculation method for notched textile-reinforced hybrid composites. J Plast Comp 2007;2:1–14.
[13] Hufenbach W, Gottwald R, Gruber B, Lepper M, Zhou B. Stress concentration analysis of thick-walled laminate composites with a loaded circular cut-out by using a first-order shear deformation theory. Compos Sci Technol 2008;68(10–11):2238–44.
[14] Hufenbach W, Grüber B, Lepper M, Gottwald R, Zhou B. An analytical method for the determination of stress and strain concentrations in textile-reinforced GF/PP composites with elliptical cutout and a finite outer boundary and its numerical verification. Arch Appl Mech 2013;83(1):125–35.
[15] Hufenbach W, Kroll L. Stress analysis of notched anisotropic finite plates under mechanical and hygrothermal loads. Arch Appl Mech 1999;69(3):145–59.
[16] Wu H, Mu B. On stress concentrations for isotropic/orthotropic plates and cylinders with a circular hole. Compos Part B Eng 2003;34(2):127–34.
[17] Foust BE, Lesniak JR, Rowlands RE. Stress analysis of a pinned wood joint by grey-field photoelasticity. Compos Part B Eng 2014;61:291–9.
[18] Toubal L, Karama M, Lorrain B. Stress concentration in a circular hole in composite plate. Compos Struct 2005;68(1):31–6.
[19] De Jong T. Stresses around pin-loaded holes in elastically orthotropic or isotropic plates. J Compos Mater 1977;11(3):313–31.
[20] Zhang K, Ueng CES. Stresses around a pin-loaded hole in orthotropic plates. J Compos Mater 1984;18(5):432–46.
[21] Grüber B, Hufenbach W, Kroll L, Lepper M, Zhou B. Stress concentration analysis of fibre-reinforced multilayered composites with pin-loaded holes. Compos Sci Technol 2007;67(7–8):1439–50.
[22] Aluko O, Whitworth HA. Analysis of stress distribution around pin loaded holes in orthotropic plates. Compos Struct 2008;86(4):308–13.
[23] Sundarraj N, Dattaguru B, Ramamurthy TS. Analysis of a double shear lap joint with interference fit pin. Comput Struct 1995;55(2):357–63.
[24] Lewis R, Yoxall A, Marshall MB. Comparison of numerical and ultrasonic techniques for quantifying interference fit pressures. P I Mech Eng C J Mec 2008;222(7):1125–30.
[25] Wei J, Jiao G, Jia P, Huang T. The effect of interference fit size on the fatigue life of bolted joints in composite laminates. Compos Part B Eng 2013;53:62–8.
[26] Jones RM. Mechanics of composite materials. 2nd ed. Boca Raton, FL: CRC Press; 1998.

Min Wan[1]
Professor
School of Mechanical Engineering,
Northwestern Polytechnical University,
Xi'an, Shaanxi 710072, China
e-mail: m.wan@nwpu.edu.cn

Zekai Murat Kilic
Department of Mechanical Engineering,
The University of British Columbia,
2054-6250 Applied Science Lane,
Vancouver, BC V6T 1Z4, Canada

Yusuf Altintas
Professor
Fellow ASME
Department of Mechanical Engineering,
The University of British Columbia,
2054-6250 Applied Science Lane,
Vancouver, BC V6T 1Z4, Canada
e-mail: altintas@mech.ubc.ca

Mechanics and Dynamics of Multifunctional Tools

The mechanics and dynamics of the combined processes are presented for multifunctional tools, which can drill, bore, and chamfer holes in one operation. The oblique cutting forces on each cutting edge with varying geometry are modeled first, followed by their transformations to tangential, radial, and axial directions of the cutter. The regenerative effect of lateral and torsional/axial vibrations is considered in predicting the dynamic chip thickness with multiple delays due to distribution of cutting edges on the cutter body. The lateral and torsional/axial chatter stability of the complete hole making operation is predicted in semidiscrete time domain. The proposed static cutting force and chatter stability prediction models are experimentally proven for two different multifunctional tools in drilling Aluminum Al7050 and Steel AISI1045. [DOI: 10.1115/1.4028749]

Keywords: chatter, multifunctional tools, multiple delays, cutting force

1 Introduction

Holes with large diameter, chamfers, and steps were traditionally machined by a sequence of operations with dedicated but different tools in the past. Consequently, the mechanics and dynamics of individual operations such as drilling, boring, and chamfering were presented in the literature [1]. However, such multistep operations have long machining cycle time with multiple tool changes hence it is not desirable in production. Recent trend is to complete the hole making operation with one tool with multiple cutting functions. For example, multifunctional tools shown in Fig. 1 can open a pilot hole, drill, enlarge, and chamfer a hole in one step, hence the operation becomes less time consuming with significantly reduced cost. However, the tool and process must be designed to keep the cutting forces under breakage, excessive static deflection within the tolerance and chatter under stability limits. This paper presents the combined mechanics and dynamics of making stepped holes with multifunctional tools.

The past literature has mainly been on the modeling of mechanics and dynamics of individual operations with dedicated tools. For example, the mechanics of drilling has been widely studied to predict cutting forces and torque. The models are based on empirical calibration of experimental measurements [2], analytical cutting mechanics supported by plasticity laws [3], and numerical with finite element techniques [4]. While Roukema and Altintas [3] used orthogonal to oblique cutting transformation of material's shear stress, shear angle, and friction coefficient, Sambhav et al. [5] used slip line theory to model the cutting forces in drilling. The application of analytical method is often limited by the mechanical parameters of the material such as stress, strain rate, and temperature, which are difficult to be calibrated accurately. The mechanistic methods identify the relationship between the chip area and cutting forces by empirically predicting the cutting force coefficients from a set of experimental measurements. Stephenson and Agapiou [6] statistically fitted the measured cutting forces as a polynomial function of inclination angle, rake angle, cutting speed, and uncut chip thickness.

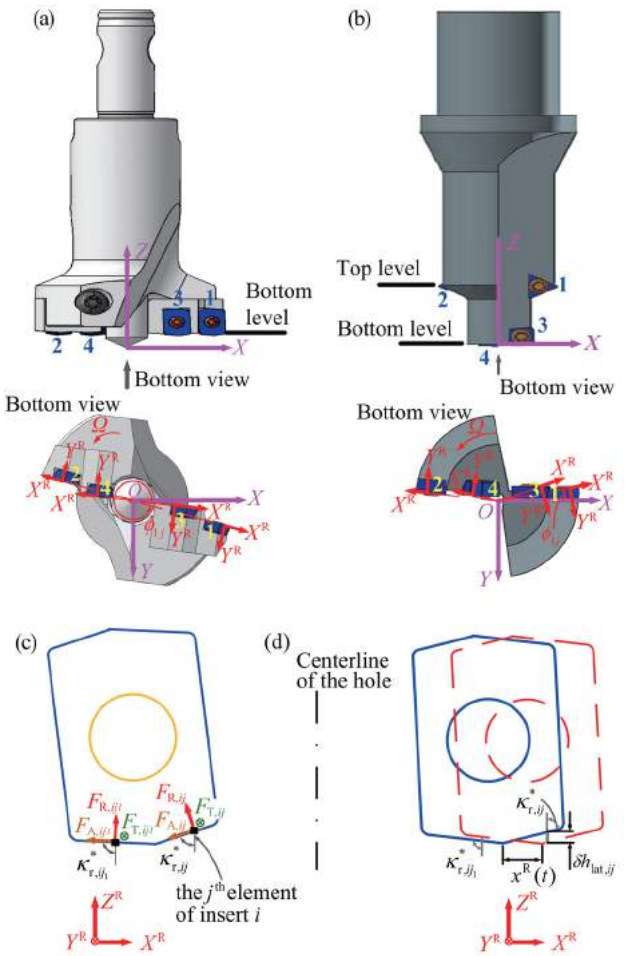

Fig. 1 Geometry, coordinates, and cutting forces of three multifunctional tools. (*a*) Tool 1—Kennametal drill with multiple inserts (*XYZ* is the Cartesian coordinate system); (*b*) tool 2—Sandvik TM880 drill with step and chamfer inserts; (*c*) cutting forces related to the cutting edge elements *j* and j_1 of insert *i*; and (*d*) chip thickness variation contributed by lateral deflections.

[1]The author was a Visiting Professor at the University of British Columbia supervised by Dr. Yusuf Altintas.

Contributed by the Manufacturing Engineering Division of ASME for publication in the Journal of Manufacturing Science and Engineering. Manuscript received January 11, 2014; final manuscript received October 1, 2014; published online December 4, 2014. Assoc. Editor: Y. B. Guo.

Copyright © 2015 by ASME

Downloaded From: http://manufacturingscience.asmedigitalcollection.asme.org/ on 04/29/2016 Terms of Use: http://www.asme.org/about-asme/terms-of-use

Chandrasekharan et al. [7] expressed the specific normal and tangential cutting force coefficients as a function of feed, cutting speed, and normal rake angle for conical drills for machining nonisotropic, fiber reinforced composite materials. Sambhav et al. [8] modeled the cutting forces for twist drills with generic point profiles, and used mechanistic method to achieve good correlations between the analytical and the experimental results. The numerical approach predicts the cutting forces and chip geometry from the finite element analyses through elastoplastic simulation of chip formation [4]. However, the prediction accuracy is highly dependent on the friction coefficient and thermomechanical model of the work material.

Considerable research has also been conducted on the modeling of forced and chatter vibrations of drilling. Pirtini and Lazoglu [9] predicted the effect of forced vibrations on the quality of holes by neglecting the regeneration of chip thickness, hence chatter. Flexible drills experience torsional, axial, and lateral vibrations which regenerate the chip thickness, and cause chatter [3]. Chatter stability of machining operations is studied numerically in time domain, or analytically in discrete time and frequency domains [10]. Ema et al. [11] modeled the lateral chatter stability of drilling to explain the mechanism behind whirling, which leads to noncircular holes. Bayly et al. [12] developed a frequency domain solution for torsional–axial chatter including edge rubbing, and showed that backward whirling modes of the drill occurs at the odd integer of spindle speeds. Gong et al. [13] used Hamilton's principle to model the drill's dynamic motion, and theoretically proved that the drilled hole is not an exactly cylindrical wall but has a distorted polygon-shape with an odd number of sides. Arvajeh and Ismail [14] simulated the combined lateral and torsional–axial chatter numerically by including gyroscopic effects [15]. They predicted the stability limits for both torsional and lateral vibrations, but with poor predictions when the drill was short. Filiz and Ozdoganlar [16] derived a unified dynamics model for both macro- and microdrills using spectral-Tchebychev technique. They pointed out that the model's efficiency can be increased by considering the tool's circular cross section (shank, extension, and tapered sections) as a one-dimensional beam while considering the fluted portion as a three-dimensional beam. Roukema and Altintas also presented both numerical [3] and frequency [17] domain prediction of hole shape, vibrations, and chatter stability of drilling by including lateral, torsional, and axial vibrations. However, the past chatter stability models showed poor agreement with experimental results due to unmodeled process damping mechanism. Ahmadi and Altintas [18] proposed a model to predict the drilling stability chart by including the lateral, torsional, and axial vibrations with process damping which led to improved accuracy in predicting chatter stability limits. Besides, with respect to the most up-to-date contributions in machining stability community, Karandikar et al. [19] used random walk strategy to predict stability for the milling case with uncertain factors considering both theory and experimental results, while Zheng et al. [20] predicted the critical depth of cut by a modified frequency response function (FRF), which is obtained by multiplying the original FRF of the structure with a complex scaling factor, corresponding to a scaling and a rotation of its original Nyquist plot.

In summary, the state of the art about the mechanics and dynamics on hole making process is as follows:

- Modeling of mechanics and dynamics was mainly conducted for standard twist drill, which has one chisel edge and two cutting lips.
- Because of the symmetrical distributions of cutting lips of twist drills, there was only one single delay item in the existing dynamic models. The multifunctional tools have combined drilling and boring processes conducted by varying tools on the cutter body, which leads to varying dynamics stiffness, complex chip geometries, and multiple time delays.

Hence, this paper presents a model that predicts the cutting forces and chatter stability of multifunctional tools which open stepped holes in one operation. Originality lies in modeling the complex process and how it is formulated to solve various mathematical theories such as semidiscretization method for the understanding of the underlying mechanics and dynamics. Contributions of this work are highlighted as follows:

(1) Comprehensive studies are carried out for the first time to develop static and dynamic models for multifunctional tools, which have step-located inserts with varying geometries.
(2) In-depth analyses are made to explain the complex process geometries related to every insert.
(3) Varying stiffness and multiple delay items induced by step-located inserts are analyzed in detail and included to establish the dynamic model.
(4) Cutting forces and stability predicted by the proposed models are validated by a series of experiments.

Finally, the paper is organized as follows. The geometric model of inserts that are distributed at the bottom, around the periphery of the tool, is presented in Sec. 2. The geometric model is used to identify the location of discretized cutting edges with the corresponding axial rake, radial rake, and cutting edge angles which are used in orthogonal to oblique cutting transformations. The predicted cutting coefficients vary along the cutting edge due to changing cutting edge geometry and speed. The differential forces along the cutting edge are summed and projected at the Cartesian coordinates of the tool to predict the static cutting forces. The dynamics of the multifunctional tool is presented in Sec. 3. The effect of torsional, axial, and lateral vibrations on the regenerative chip thickness is modeled. The effect of flank wear and cutting edge radius is included in the velocity dependent process damping forces. The dynamic cutting process is transformed into semidiscrete time domain which leads to the prediction of chatter stability. The prediction of cutting forces and chatter stability models are experimentally validated in Sec. 4 using two different multifunctional tools in machining AISI1045 steel and Al7050 Aluminum alloys.

2 Mechanics of Multifunctional Tools

Two different multifunctional tools, which are shown in Figs. 1 and 2, are used to demonstrate the modeling process. Tool 1 has a twist drill at the center to open a pilot hole, and four identical

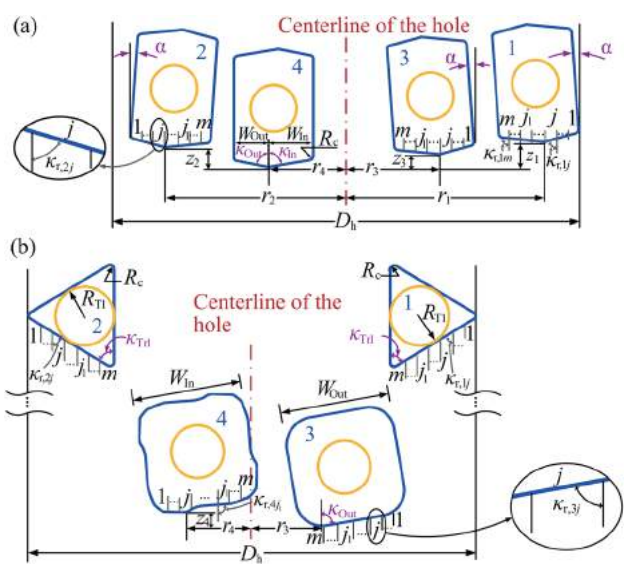

Fig. 2 Inserts' geometries and their locations on the shank bodies. (*a*) Tool 1—Kennametal drill and (*b*) tool 2—Sandvik TM880 drill.

Downloaded From: http://manufacturingscience.asmedigitalcollection.asme.org/ on 04/29/2016 Terms of Use: http://www.asme.org/about-asme/terms-of-use

inserts on its two flutes. Tool 2 has four inserts with different geometries. Each insert is divided into m number of differential cutting edge elements having three differential cutting forces in tangential ($F_{T,ij}$), radial ($F_{R,ij}$), and axial ($F_{A,ij}$) directions, as shown in Fig. 1(*c*), where i and j correspond to insert and differential cutting edge element indices, respectively. Since the geometry of each insert varies along its cutting edge, the cutting force coefficients are evaluated by applying oblique transformation of shear stress, shear angle, and friction coefficient [1]. The radial rake angle (γ_f), axial rake angle (γ_p), and insert cutting edge angle (κ_r), which are required in oblique transformation, are evaluated from the tool geometry as described in Ref. [21]. The number pattern of inserts is shown in Fig. 1, and cutting edge element j of each insert (i) is numbered in sequence that begins with 1 from the end close to the cutter's outer periphery.

The cutting edge angle $\kappa_{r,ij}$ for tool 1 is determined from Fig. 2 as

$$\kappa_{r,ij} = \begin{cases} \kappa_{Out} - \vartheta\alpha, & jb_{ij} < W_{Out} \\ \pi - \kappa_{In} - \vartheta\alpha, & \text{otherwise} \end{cases}$$
$$\leftarrow \vartheta = \begin{cases} 1, & i = 1,2,3 \\ 0, & 1 = 4 \end{cases}, \quad b_{ij} = \frac{W_{Out} + W_{In}}{m} \tag{1}$$

where W_{Out} and W_{In} are the segmented cutting edge lengths of insert as defined in Fig. 2(*a*).

The axial rake angle $\gamma_{p,ij}$ is defined as the angle between the tangential line and the radial line OQ1 between the rotation center and the cutting position of the element, as shown in Fig. 3. $\gamma_{p,ij}$ is positive if the angle is reached clockwise from OQ1 to the tangential line, and negative otherwise.

The cutting edge of insert on tool 1 is defined by the curve (C1C2) and two lines (C2C3 and C3C4), as shown in Fig. 3(*a*). The axial rake angle varies as the cutting edge element changes its geometry along the radial direction. The axial rake angles of other inserts for both tools can be evaluated in a similar way, as shown in Figs. 3(*a*) and 3(*b*).

The cutting forces contributed by the cutting edge element j of insert i is defined in cutting edge coordinate (RTA coordinate system) as follows [21]:

$$F_{R,ij} = K_{Rc,ij} b_{ij} h_{ij} + K_{Re,ij} c_{ij}$$
$$F_{T,ij} = K_{Tc,ij} b_{ij} h_{ij} + K_{Te,ij} c_{ij} \tag{2}$$
$$F_{A,ij} = K_{Ac,ij} b_{ij} h_{ij} + K_{Ae,ij} c_{ij}$$

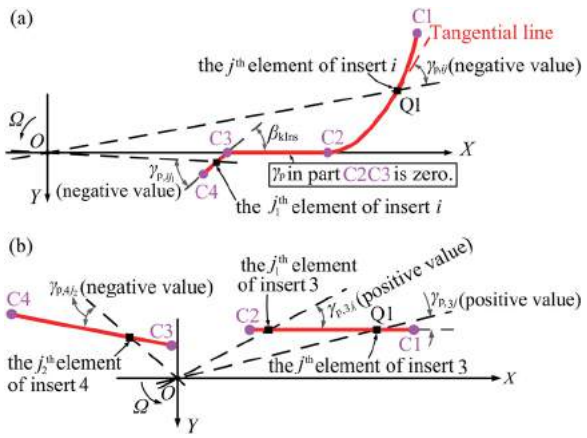

Fig. 3 Calculations of axial rake angles in bottom view. (*a*) Illustration for insert of Tool 1—Kennametal drill and (*b*) illustration for inserts of tool 2—Sandvik TM880 drill.

where h_{ij} and b_{ij} are the equivalent uncut chip thickness and width of the cutting edge element. h_{ij} is measured in spindle axis direction (Z) whereas b_{ij} is defined in the direction normal to Z axis. c_{ij} is the width of the cutting edge given as

$$c_{ij} = \frac{b_{ij}}{\sin \kappa^*_{r,ij}} \tag{3}$$

where $\kappa^*_{r,ij}$ is the true cutting edge angle measured in the $X^R Z^R$ plane of the insert reference frame $X^R Y^R Z^R$ [21], as shown in Fig. 1(*d*)

$$\kappa^*_{r,ij} = \arctan\left(\frac{\cos\gamma_{p,ij}\sin\kappa_{r,ij}}{\cos\gamma_f\cos\kappa_{r,ij} + \sin\gamma_f\sin\gamma_{p,ij}\sin\kappa_{r,ij}}\right) \tag{4}$$

The geometry of equivalent uncut chip thicknesses removed by the inserts is shown in Fig. 4. Without the loss of generality, insert 1 of tool 1 is taken as an example. The insert is separated into two segments as shown in Fig. 4(*a*). Segment L_{11} always removes the material left by itself during the previous revolution, whereas segment L_{12} removes the material left by segment L_{21} of insert 2 half a spindle rotation period ($T/2$) ago. Hence, segment L_{12} contains an overlapped cutting zone for both inserts 1 and 2. In summary

- The equivalent uncut chip thickness equals the feed per revolution f in segment L_{11}.
- For any cutting edge element along L_{12}, the equivalent uncut chip thickness is obtained by calculating the axial distance between the surface left previously and the surface to be generated at current time. For instance, f_1 illustrated in Fig. 4(*a*) schematically shows the evaluation of equivalent uncut chip thickness for one element along L_{12}.

The equivalent uncut chip thickness for other inserts and tools are evaluated in a similar fashion as illustrated in Fig. 4. $K_{Rc,ij}$,

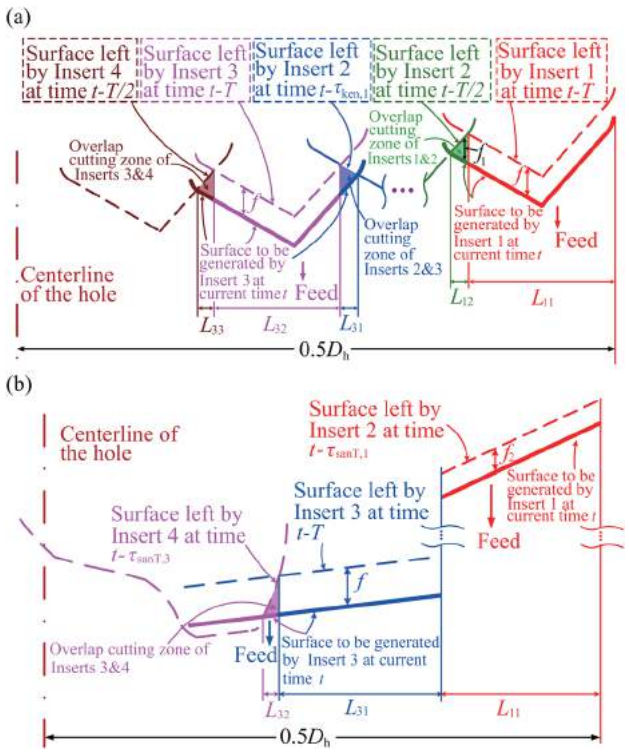

Fig. 4 Process geometries of the inserts during drilling process at a specified time *t*. (*a*) Schematics of inserts 1 and 3 being in cut for tool 1—Kennametal drill and (*b*) schematics of inserts 1 and 3 being in cut for tool 2—Sandvik TM880 drill.

Downloaded From: http://manufacturingscience.asmedigitalcollection.asme.org/ on 04/29/2016 Terms of Use: http://www.asme.org/about-asme/terms-of-use

$K_{Tc,ij}$, and $K_{Ac,ij}$ are cutting force coefficients contributed by the chip shearing, and $K_{Re,ij}$, $K_{Te,ij}$, and $K_{Ae,ij}$ are cutting force coefficients contributed by the edge ploughing [1]. The cutting force coefficients are evaluated from an orthogonal cutting database using the generalized transformations given in Ref. [21], and the coordinate transformations from the rake face to cutting edge are briefly summarized as follows:

$$\begin{aligned}\left[K_{Rc,ij}, K_{Tc,ij}, K_{Ac,ij}\right]^{T} &= \mathbf{T}_{1U}\left[K_{uc,ij}, K_{vc,ij}\right]^{T} \\ \left[K_{Re,ij}, K_{Te,ij}, K_{Ae,ij}\right]^{T} &= \mathbf{T}_{1U}\left[K_{ue,ij}, K_{ve,ij}\right]^{T}\end{aligned} \tag{5}$$

with

$$\mathbf{T}_{1U} = \begin{bmatrix} \cos\gamma_{n,ij}\cos\eta_{ij} & -\sin\gamma_{n,ij} \\ \sin\lambda_{s,ij}\sin\eta_{ij} + \cos\lambda_{s,ij}\sin\gamma_{n,ij}\cos\eta_{ij} & \cos\lambda_{s,ij}\cos\gamma_{n,ij} \\ -\cos\lambda_{s,ij}\sin\eta_{ij} + \sin\lambda_{s,ij}\sin\gamma_{n,ij}\cos\eta_{ij} & \sin\lambda_{s,ij}\cos\gamma_{n,ij} \end{bmatrix} \tag{6}$$

Where $\lambda_{s,ij}$, $\lambda_{n,ij}$, and η_{ij} are the oblique, normal rake, and chip flow angles associated with the cutting edge element j of insert i.

$$\begin{aligned}\lambda_{s,ij} &= \arctan\left(\frac{-\sin\gamma_f\cos\kappa_{r,ij} + \cos\gamma_f\sin\gamma_{p,ij}\sin\kappa_{r,ij}}{\cos\gamma_f\cos^2\kappa_{r,ij} + \sin\gamma_f\sin\gamma_{p,ij}\sin\kappa_{r,ij} + \cos\gamma_{p,ij}\sin^2\kappa_{r,ij}}\right) \\ \gamma_{n,ij} &= \arctan\left(\frac{\sin\gamma_f\sin\kappa_{r,ij} + \cos\gamma_f\sin\gamma_{p,ij}\cos\kappa_{r,ij}}{\cos\gamma_f\cos\gamma_{p,ij}}\right) \\ \eta_{ij} &= \lambda_{s,ij}\end{aligned} \tag{7}$$

$K_{uc,ij}$ and $K_{vc,ij}$ are the friction and normal cutting force coefficients, which are functions of shear stress τ, shear angle φ_n, and friction angle β_a [21]. $K_{ue,ij}$, and $K_{ve,ij}$ are the edge force coefficients that are dependent on the cutting edge geometry and determined from experiments or finite element models [22]. Detailed derivations of these equations from oblique transformation method are generalized in Ref. [21].

Based on the geometric relationship shown in Fig. 1 and Eq. (2), the cutting forces in X, Y, and Z directions and the torque in torsional direction can be evaluated as follows:

$$\left[F_{X,ij}, F_{Y,ij}, F_{Z,ij}, T_{c,ij}\right]^{T} = \mathbf{T}_{OR}\mathbf{T}_{R1}\left[F_{R,ij}, F_{T,ij}, F_{A,ij}, F_{T,ij}R_{ij}\right]^{T} \tag{8}$$

where R_{ij} is the local radius of the cutting edge element j of insert i. Transformation matrices $\mathbf{T}_{OR}$ and $\mathbf{T}_{R1}$ are functions of true cutting edge angle $\kappa^*_{r,ij}$ and position angle ϕ_{ij} as illustrated in Fig. 1

$$\mathbf{T}_{R1} = \begin{bmatrix} -\cos\kappa^*_{r,ij} & 0 & -\sin\kappa^*_{r,ij} & 0 \\ 0 & 1 & 0 & 0 \\ \sin\kappa^*_{r,ij} & 0 & -\cos\kappa^*_{r,ij} & 0 \\ 0 & 0 & 0 & 1 \end{bmatrix};$$

$$\mathbf{T}_{OR} = \begin{bmatrix} \cos\phi_{ij} & \sin\phi_{ij} & 0 & 0 \\ -\sin\phi_{ij} & \cos\phi_{ij} & 0 & 0 \\ 0 & 0 & 1 & 0 \\ 0 & 0 & 0 & 1 \end{bmatrix} \tag{9}$$

Total cutting forces (F_X, F_Y, and F_Z) and torque (T_c) acting on the whole tool are evaluated by summing the contribution of elemental cutting forces of all edges

$$\left[F_X, F_Y, F_Z, T_c\right]^{T} = \begin{cases} \left[F_{X,In}, F_{Y,In}, F_{Z,In}, T_{c,In}\right]^{T} + \left[F_{X,Ce}, F_{Y,Ce}, F_{Z,Ce}, T_{c,Ce}\right]^{T} & \text{for Tool 1} \\ \left[F_{X,In}, F_{Y,In}, F_{Z,In}, T_{c,In}\right]^{T}, & \text{for Tool 2} \end{cases} \tag{10}$$

where $\left[F_{X,In}, F_{Y,In}, F_{Z,In}, T_{c,In}\right]^{T} = \left[\sum_{i,j}F_{X,ij}, \sum_{i,j}F_{Y,ij}, \sum_{i,j}F_{Z,ij}, \sum_{i,j}T_{c,ij}\right]^{T}$ is the total cutting forces/torque vector contributed by inserts, and $\left[F_{X,Ce}, F_{Y,Ce}, F_{Z,Ce}, F_{c,Ce}\right]^{T}$ is the force/torque vector contributed by the chisel edge forces and the cutting lip forces from the central twist drill of tool 1. It is noted that since the chisel edge of the central twist drill does not cut but only spreads the material sideways, the mechanics of indentation is used to calculate the chisel edge forces [1]. Cutting lip forces are estimated by using the orthogonal-to-oblique transformation method as explained in Ref. [1].

3 Dynamics of Multifunctional Tools

The dynamics of the cutting process is presented by modeling the regenerative chip thickness, time delays caused by the distribution of inserts and semidiscrete time domain stability of the system with torsional/axial and lateral vibrations as follows.

Dynamic Chip Thickness. Since the static chip thickness does not contribute to the chatter stability of machining, only the regenerative chip generated by the lateral, axial, and torsional vibrations of the tool is considered. If the time delay is τ between the current and previously cut surface locations of the cutting edge element j of insert i, the equivalent dynamic chip thickness at time t is evaluated by considering the axial (Z), lateral (X, Y), and torsional (θ) vibrations as follows (Fig. 1(*d*)):

$$\Delta h_{ij} = \Delta h_{Z,ij} + \Delta h_{\theta,ij} + \Delta h_{lat,ij} \tag{11}$$

where the contributions of vibrations are derived as

$$\begin{aligned} &\text{Axial vibration} && : \Delta h_{Z,ij} = z(t-\tau) - z(t) \\ &\text{Torsional vibration} && : \Delta h_{\theta,ij} = \frac{f}{2\pi}\left[\theta(t-\tau) - \theta(t)\right] \\ &\text{Lateral vibration} && : \Delta h_{lat,ij} = \frac{x^R(t) - x^R(t-\tau)}{\tan\kappa^*_{r,ij}} \rightarrow x^R(t) \\ & && \quad = x(t)\cos\phi_{ij} - y(t)\sin\phi_{ij} \end{aligned} \tag{12}$$

Distributions of Time Delay Terms. Figure 5 shows the distribution of regenerative time delays for the two tools. Without the loss of generality, Fig. 5(*a*) is taken as an example to illustrate the modeling of regenerative delays.

Downloaded From: http://manufacturingscience.asmedigitalcollection.asme.org/ on 04/29/2016 Terms of Use: http://www.asme.org/about-asme/terms-of-use

- Insert 1: Segment L_{11} removes the material left by itself at time t–T, while segment L_{12} removes the material left by insert 2 at time t–$T/2$.
- Insert 2: Segment L_{21} removes the material left by insert 1 at time t–$T/2$. Segment L_{22} removes the material left by itself at time t–T, while segment L_{23} removes the material left by insert 3 at time t–$\tau_{\text{ken},2}$ with $\tau_{\text{ken},2} = ((\pi + \beta_1)/2\pi)T$.
- Insert 3: Segment L_{31} removes the material left by insert 2 at time t–$\tau_{\text{ken},1}$ with $\tau_{\text{ken},1} = ((\pi - \beta_1)/2\pi)T$. Segment L_{32} removes the material left by itself at time t–T, while segment L_{33} removes material left by insert 4 at time t–$T/2$.
- Insert 4: Segment L_{41} removes the material left by insert 3 at time t–$T/2$, while segment L_{42} removes the material left by itself at time t–T.
- Center twist drill: Cutting lip L_{51} or L_{61} removes the material left by the previous lip at time t–$T/2$.

In summary, the multifunctional tools have retarded dynamics with varying regenerative time delays. For example, tool 1 has four delay terms, i.e., $\tau_{\text{ken},1}$, $\tau_{\text{ken},2}$, $T/2$, and T. Similar analyses from Fig. 5(*b*) leads to five delay terms for tool 2.

Dynamics of Multifunctional Tools. The equation of motion for the cutter is modeled in physical domain as

$$\begin{aligned}\mathbf{M}\ddot{\mathbf{Q}}(t) + \mathbf{C}\dot{\mathbf{Q}}(t) + \mathbf{K}\mathbf{Q}(t) &= \mathbf{F}(t)\\ \mathbf{Q}(t) &= \left[x_1(t), y_1(t), z_1(t), \theta_1(t), \ldots, x_{N_s}(t),\right.\\ &\quad \left. y_{N_s}(t), z_{N_s}(t), \theta_{N_s}(t)\right]^{\mathrm{T}}\\ \mathbf{F}(t) &= \left[F_{X1}(t), F_{Y1}(t), F_{Z1}(t), T_{c1}(t), \ldots,\right.\\ &\quad \left. F_{XN_s}(t), F_{YN_s}(t), F_{ZN_s}(t), T_{cN_s}(t)\right]^{\mathrm{T}}\end{aligned} \tag{13}$$

for N_s number of lumped dynamic stations along the tool axis, i.e., $N_s = 1$ for tool 1 and $N_s = 2$ for tool 2, as shown in Figs. 1(*a*) and 1(*b*). $\mathbf{M}_{4N_s\times 4N_s}$, $\mathbf{C}_{4N_s\times 4N_s}$, and $\mathbf{K}_{4N_s\times 4N_s}$ are the lumped mass, damping, and stiffness matrices in physical domain. $\mathbf{F}(t)$ and $\mathbf{Q}(t)$ are the dynamic cutting force and vibration vectors, respectively. By substituting Eq. (11) into Eq. (2), dynamic cutting forces and torque related to the cutting edge element j of insert i can be expressed as a function of tool vibrations

$$\left[F_{\text{dR},ij}, F_{\text{dT},ij}, F_{\text{dA},ij}, T_{\text{dc},ij}\right]^{\mathrm{T}} = \mathbf{H}_{l,ij}\mathbf{Q}(t) - \mathbf{H}_{l,ij}\mathbf{Q}(t-\tau_l) + \mathbf{H}_{\text{d},l,ij}\dot{\mathbf{Q}}(t) \tag{14}$$

with

$$\mathbf{H}_{l,ij} = b_{ij}\begin{bmatrix} K_{\text{Rc},ij}\cos\phi_{ij}/\tan\kappa^*_{\text{r},ij} & -K_{\text{Rc},ij}\sin\phi_{ij}/\tan\kappa^*_{\text{r},ij} & -K_{\text{Rc},ij} & -fK_{\text{Rc},ij}/2\pi \\ K_{\text{Tc},ij}\cos\phi_{ij}/\tan\kappa^*_{\text{r},ij} & -K_{\text{Tc},ij}\sin\phi_{ij}/\tan\kappa^*_{\text{r},ij} & -K_{\text{Tc},ij} & -fK_{\text{Tc},ij}/2\pi \\ K_{\text{Ac},ij}\cos\phi_{ij}/\tan\kappa^*_{\text{r},ij} & -K_{\text{Rc},ij}\sin\phi_{ij}/\tan\kappa^*_{\text{r},ij} & -K_{\text{Rc},ij} & -fK_{\text{Ac},ij}/2\pi \\ R_{ij}K_{\text{Tc},ij}\cos\phi_{ij}/\tan\kappa^*_{\text{r},ij} & -R_{ij}K_{\text{Tc},ij}\sin\phi_{ij}/\tan\kappa^*_{\text{r},ij} & -R_{ij}K_{\text{Tc},ij} & -R_{ij}fK_{\text{Tc},ij}/2\pi \end{bmatrix}$$

$$\mathbf{H}_{\text{d},l,ij} = \frac{K_{\text{sp}}W_{\text{w}}^2 b_{ij}}{4V_{\text{c},ij}\tan\kappa^*_{\text{r},ij}}\begin{bmatrix} -\cos\phi_{ij}\cos^2\kappa^*_{\text{r},ij} & \sin\phi_{ij}\cos^2\kappa^*_{\text{r},ij} & \sin\phi_{ij}\cos\kappa^*_{\text{r},ij} & 0 \\ \mu\cos\phi_{ij}\cos\kappa^*_{\text{r},ij} & -\mu\sin\phi_{ij}\cos\kappa^*_{\text{r},ij} & -\mu\sin\kappa^*_{\text{r},ij} & 0 \\ \cos\phi_{ij}\sin\kappa^*_{\text{r},ij}\cos\kappa^*_{\text{r},ij} & -\sin\phi_{ij}\sin\kappa^*_{\text{r},ij}\cos\kappa^*_{\text{r},ij} & -\sin^2\kappa^*_{\text{r},ij} & 0 \\ \mu R_{ij}\cos\phi_{ij}\cos\kappa^*_{ij} & -\mu R_{ij}\sin\phi_{ij}\cos\kappa^*_{\text{r},ij} & -\mu R_{ij}\sin\phi_{ij} & 0 \end{bmatrix}$$

where K_{sp} is the material dependent indentation force coefficient to consider process damping, and μ is the friction constant between the tool and workpiece materials as presented in Ref. [23]. The process damping parameters (K_{sp}, μ) are identified from cutting tests [24]. $V_{\text{c},ij}$ (m/min) is the cutting speed associated with the differential cutting edge element, and W_{W} is the wear land of cutting edge. Note that $\mathbf{H}_{\text{d},l,ij}$ is the matrix related to the effect of process damping as presented in Ref. [18]. τ_l is the delay term related to the cutting edge element j of insert i. The elemental cutting forces and torque shown in Eq. (14) can be mapped along X, Y, Z, and θ directions of the machine coordinate system as

$$\begin{aligned}&\left[F_{\text{dX},ij}, F_{\text{dY},ij}, F_{\text{dZ},ij}, T_{\text{dc},ij}\right]^{\mathrm{T}}\\ &\quad = \mathbf{T}_{\text{OR}}\mathbf{T}_{\text{R1}}\mathbf{H}_{l,ij}\mathbf{Q}(t) - \mathbf{T}_{\text{OR}}\mathbf{T}_{\text{R1}}\mathbf{H}_{l,ij}\mathbf{Q}(t-\tau_l) + \mathbf{T}_{\text{OR}}\mathbf{H}_{\text{d},l,ij}\dot{\mathbf{Q}}(t)\end{aligned} \tag{15}$$

The total dynamic cutting force/torque vector ($\mathbf{F}(t)$) applied on the tool can be obtained from Eq. (15) as follows:

$$\mathbf{F}(t) = \sum_{l=1}^{N_{\text{d}}}\mathbf{H}_l\mathbf{Q}(t) - \sum_{l=1}^{N_{\text{d}}}\left[\mathbf{H}_l\mathbf{Q}(t-\tau_l)\right] + \mathbf{H}_{\text{d}}\dot{\mathbf{Q}}(t) \tag{16}$$

where N_{d} is the total number of delay items, and $N_{\text{d}} = 4$ for tool 1 and $N_{\text{d}} = 5$ for tool 2 $\mathbf{H}_l$ and $\mathbf{H}_{\text{d}}$ are directional coefficient matrices defined as follows:

$$\mathbf{H}_l = \begin{bmatrix} \mathbf{G}_{l,1} & & & \\ & \mathbf{G}_{l,2} & & \\ & & \ddots & \\ & & & \mathbf{G}_{l,N_s} \end{bmatrix}, \quad \mathbf{H}_{\text{d}} = \begin{bmatrix} \mathbf{E}_{\text{d},1} & & & \\ & \mathbf{E}_{\text{d},2} & & \\ & & \ddots & \\ & & & \mathbf{E}_{\text{d},N_s} \end{bmatrix} \tag{17}$$

with

$$\begin{aligned}\mathbf{G}_{l,v} &= \sum_{i,j}\mathbf{T}_{\text{OR}}\mathbf{T}_{\text{R1}}\mathbf{H}_{l,ij}\\ \mathbf{E}_{\text{d},v} &= \sum_{l,i,j}\mathbf{T}_{\text{OR}}\mathbf{H}_{\text{d},l,ij}, \quad v = 1, 2, \ldots, N_s\end{aligned} \tag{18}$$

where subscript v means that the edge element j of insert i associates with the lumped dynamic station v of the cutting system.

Substituting the dynamic force (Eq. (16)) into equation of motion (Eq. (13)) gives

Downloaded From: http://manufacturingscience.asmedigitalcollection.asme.org/ on 04/29/2016 Terms of Use: http://www.asme.org/about-asme/terms-of-use

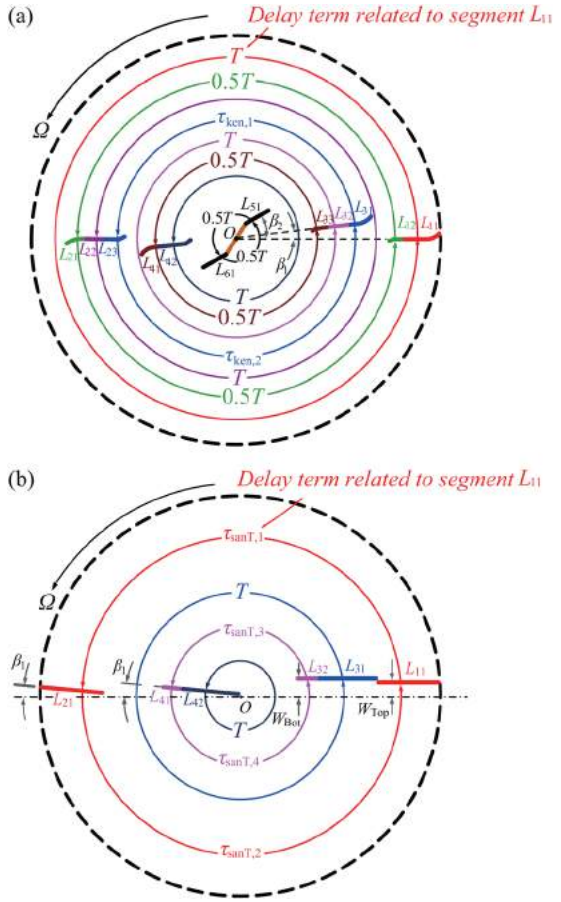

Fig. 5 Schematics of delay terms in cross-sectional views. (*a*) For tool 1—Kennametal drill and (*b*) for tool 2—Sandvik TM880 drill.

$$\mathbf{M}\ddot{\mathbf{Q}}(t)+\mathbf{C}\dot{\mathbf{Q}}(t)+\mathbf{K}\mathbf{Q}(t)=\sum_{l=1}^{N_d}\mathbf{H}_l\mathbf{Q}(t)-\sum_{l=1}^{N_d}[\mathbf{H}_l\mathbf{Q}(t-\tau_l)]+\mathbf{H}_d\dot{\mathbf{Q}}(t) \tag{19}$$

The vibration vector $\mathbf{Q}(t)$ can be expressed by the modal displacements $(\chi_l(t))$

$$\begin{aligned}\mathbf{Q}(t)&=\mathbf{U}\boldsymbol{\Gamma}(t)\\ \boldsymbol{\Gamma}(t)&=\left[\chi_1(t),\chi_2(t),\ldots,\chi_{N_m}\right]^T\end{aligned} \tag{20}$$

where $\mathbf{U}$ is the mass normalized mode shape and N_m is the number of dominant modes. Substituting Eq. (20) into Eq. (19) and then applying modal transformations yields

$$\begin{aligned}&\mathbf{U}^T\mathbf{M}\mathbf{U}\ddot{\boldsymbol{\Gamma}}(t)+\mathbf{U}^T\mathbf{C}\mathbf{U}\dot{\boldsymbol{\Gamma}}(t)+\mathbf{U}^T\mathbf{K}\mathbf{U}\boldsymbol{\Gamma}(t)\\ &=\mathbf{U}^T\sum_{l=1}^{N_d}\mathbf{H}_l\mathbf{U}\boldsymbol{\Gamma}(t)-\mathbf{U}^T\sum_{l=1}^{N_d}[\mathbf{H}_l\mathbf{U}\boldsymbol{\Gamma}(t-\tau_l)]+\mathbf{U}^T\mathbf{H}_d\mathbf{U}\dot{\boldsymbol{\Gamma}}(t)\\ &\Rightarrow\ddot{\boldsymbol{\Gamma}}(t)+2\boldsymbol{\xi}\boldsymbol{\omega}\dot{\boldsymbol{\Gamma}}(t)+\boldsymbol{\omega}^2\boldsymbol{\Gamma}(t)=\mathbf{U}^T\mathbf{H}\mathbf{U}\boldsymbol{\Gamma}(t)\\ &-\sum_{l=1}^{N_d}\left[\mathbf{U}^T\mathbf{H}_l\mathbf{U}\boldsymbol{\Gamma}(t-\tau_l)\right]+\mathbf{U}^T\mathbf{H}_d\mathbf{U}\dot{\boldsymbol{\Gamma}}(t),\quad\mathbf{H}=\sum_{l=1}^{N_d}\mathbf{H}_l\end{aligned} \tag{21}$$

where $\boldsymbol{\xi}$ and $\boldsymbol{\omega}$ are the diagonal damping ratio and natural frequency matrices with the size $N_m\times N_m$, respectively. Equation (21) is the general dynamic model of multifunctional tool in modal space.

As proven in Refs. [17] and [18], the chatter stability of hole making process can be analyzed separately for lateral and torsional/axial vibrations since they have uncoupled dynamics in regeneration mechanism.

Lateral Bending Stability. The torsional and axial deflections of the drill are neglected, and only the lateral forces and vibrations are considered. If there is a single delay ($N_d=1$), the stability of Eq. (21) has been well reported for standard twist drills in Refs. [1,14,15,17]. Here, the dynamics of multifunctional drill is represented by a set of differential equations with multiple delays, and analyzed with an extended semidiscretization method of Insperger and Stepan [25] as follows.

Equation (21) can be rewritten in the following compact format form:

$$\dot{\boldsymbol{\Upsilon}}(t)=\mathbf{A}\boldsymbol{\Upsilon}(t)+\sum_{l=1}^{N_d}\mathbf{B}_l\boldsymbol{\Upsilon}(t-\tau_l) \tag{22}$$

with

$$\begin{aligned}\boldsymbol{\Upsilon}(t)&=\left[\boldsymbol{\Gamma}(t)^T,\dot{\boldsymbol{\Gamma}}(t)^T\right]^T\\ \mathbf{A}&=\begin{bmatrix}\mathbf{O}_{N_m\times N_m}&\mathbf{I}_{N_m\times N_m}\\ -\boldsymbol{\omega}^2+\mathbf{U}^T\mathbf{H}\mathbf{U}&-2\boldsymbol{\xi}\boldsymbol{\omega}+\mathbf{U}^T\mathbf{H}_d\mathbf{U}\end{bmatrix}\\ \mathbf{B}_l&=\begin{bmatrix}\mathbf{O}_{N_m\times N_m}&\mathbf{O}_{N_m\times N_m}\\ -\mathbf{U}^T\mathbf{H}_l\mathbf{U}&\mathbf{O}_{N_m\times N_m}\end{bmatrix}\end{aligned} \tag{23}$$

where $\mathbf{O}_{*\times*}$ and $\mathbf{I}_{*\times*}$ are zero and identity matrices, respectively. If the spindle period (T) is divided into ς uniform discrete time intervals with length $\Delta t=T/\varsigma$, the solution of Eq. (22) at discrete time interval $(a+1)$ can be approximated as

$$\begin{aligned}\boldsymbol{\Upsilon}_{a+1}&=\mathbf{P}_a\boldsymbol{\Upsilon}_a+\sum_{l=1}^{N_d}\left(w_{l,1}\mathbf{V}_{l,a}\boldsymbol{\Upsilon}_{a-q_1+1}+w_{l,2}\mathbf{V}_{l,a}\boldsymbol{\Upsilon}_{a-q_l}\right)\\ \mathbf{P}_a&=e^{\mathbf{A}\Delta t},\quad\mathbf{V}_{l,a}=(\mathbf{P}_a-\mathbf{I})\mathbf{A}^{-1}\mathbf{B}_l\end{aligned} \tag{24}$$

where $\boldsymbol{\Upsilon}_a$ stands for the system's state $\boldsymbol{\Upsilon}(t_a)$ at discrete time $t_a=a\Delta t$. q_l is the number of intervals covering the delay period τ_l. The system's delayed state, $\boldsymbol{\Upsilon}(t_a-\tau_l)$, during the discrete interval a is calculated by $w_{l,1}\mathbf{V}_{l,a}\boldsymbol{\Upsilon}_{a-q_l+1}+w_{l,2}\mathbf{V}_{l,a}\boldsymbol{\Upsilon}_{a-q_l}$ with weighted factors $w_{l,1}=w_{l,2}=0.5$ which relate $\boldsymbol{\Upsilon}(t-\tau_l)$ with the state values at the two ends of the delayed interval $\left[t_{a-q_l},t_{a-q_l+1}\right]$ [26]. Equation (24) can be rewritten as the following the discrete map form:

$$\boldsymbol{\Theta}_{a+1}=\boldsymbol{\Phi}_a\boldsymbol{\Theta}_a \tag{25}$$

where $\boldsymbol{\Theta}_a$ is the state vector

$$\boldsymbol{\Theta}_a=\left[\boldsymbol{\Upsilon}_a^T,\boldsymbol{\Upsilon}_{a-1}^T,\ldots,\boldsymbol{\Upsilon}_{a-q_1}^T,\ldots\boldsymbol{\Upsilon}_{a-q_2}^T,\ldots\boldsymbol{\Upsilon}_{a-q_{N_d}}^T\right]^T \tag{26}$$

and the transition matrix $\boldsymbol{\Phi}_a$ is

Downloaded From: http://manufacturingscience.asmedigitalcollection.asme.org/ on 04/29/2016 Terms of Use: http://www.asme.org/about-asme/terms-of-use

Table 1 Geometric parameters of multifunctional tools (Figs. 2 and 5 for geometric definitions)

Items	Tool 1	Tool 2
r_1 (mm)	20.50	—
r_2 (mm)	16.20	—
r_3 (mm)	12.26	2.30
r_4 (mm)	7.92	2.54
z_1 (mm)	0.308	—
z_2 (mm)	0.15	—
z_3 (mm)	0.068	—
z_4 (mm)	—	0.141
W_{Out} (mm)	2.5	5.1
W_{In} (mm)	3.5	4.9
κ_{Out} (deg)	80	88
κ_{In} (deg)	82	—
κ_{Tr1} (deg)	—	60
R_{c} (mm)	0.4	0.4
R_{T1} (mm)	—	3.97
W_{Bot} (mm)	—	0.435
W_{Top} (mm)	—	0.104
α (deg)	2	—
β_1 (deg)	8	3
β_2 (deg)	30	—
D_{h} (mm)	46	20

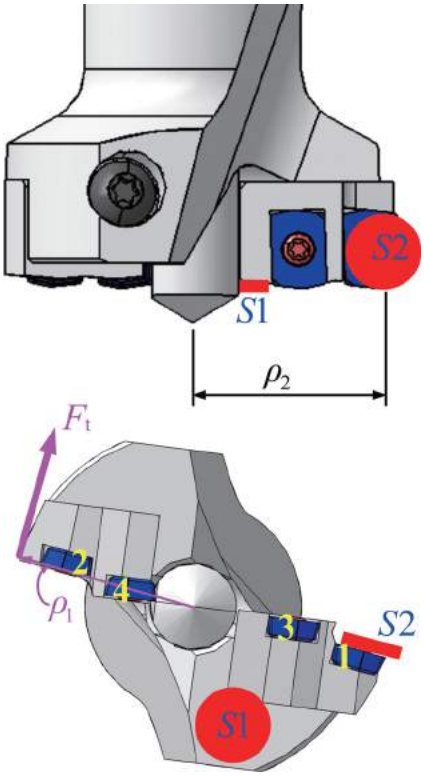

Fig. 6 Schematic setup for measuring torsional–axial transfer function

$$\mathbf{\Phi}_a = \begin{bmatrix} \mathbf{P}_a & 0 & 0 & \cdots & 0 & w_{1,1}\mathbf{V}_{1,a} & w_{1,2}\mathbf{V}_{1,a} & \cdots & 0 & w_{2,1}\mathbf{V}_{2,a} & w_{2,2}\mathbf{V}_{2,a} & \cdots & 0 & w_{N_d,1}\mathbf{V}_{N_d,a} & w_{N_d,2}\mathbf{V}_{N_d,a} \\ \mathbf{I} & 0 & 0 & \cdots & 0 & 0 & 0 & \cdots & 0 & 0 & 0 & \cdots & 0 & 0 & 0 \\ 0 & \mathbf{I} & 0 & \cdots & 0 & 0 & 0 & \cdots & 0 & 0 & 0 & \cdots & 0 & 0 & 0 \\ \vdots & \vdots & \vdots & \vdots & \vdots & \vdots & \vdots & \vdots & \vdots & \vdots & \vdots & \ddots & \vdots & \vdots & \vdots \\ 0 & 0 & 0 & \cdots & 0 & 0 & 0 & \cdots & 0 & 0 & 0 & \cdots & \mathbf{I} & 0 & 0 \\ 0 & 0 & 0 & \cdots & 0 & 0 & 0 & \cdots & 0 & 0 & 0 & \cdots & 0 & \mathbf{I} & 0 \end{bmatrix} \tag{27}$$

The discrete dynamics of the system (Eq. (25)) can be organized to cover the spindle period (T) as follows:

$$\mathbf{\Theta}_{\varsigma} = \mathbf{\Psi}\mathbf{\Theta}_0 \quad \leftarrow \quad \mathbf{\Psi} = \mathbf{\Phi}_{\varsigma-1}\mathbf{\Phi}_{\varsigma-2}\cdots\mathbf{\Phi}_1\mathbf{\Phi}_0 \tag{28}$$

Since the system is periodic at $T = \varsigma\Delta t$, e.g., $\mathbf{\Phi}_{\varsigma} = \mathbf{\Phi}_0$, the stability of the process can be assessed by applying Floquet theory [27,28]. If all the eigenvalues of $\mathbf{\Psi}$ at each spindle speed and radial depth of cut are less than unity, the system is asymptotically stable. Otherwise, if any one of the eigenvalues is outside the unit circle, the process is unstable. The critical stability occurs when the eigenvalues lie on the unit circle. By repeating the eigenvalue evaluation at the interested range of spindle speeds and radial depths of cut, the stability lobes can be constructed. Note that when the system is dominated by one mode ($N_{\text{m}} = 1$), the dimension of the transition matrix is reduced, so as the computation time.

Table 2 Modal parameters of the spindle-tool systems

Cutter type	Mode No.	Frequency (Hz)	Damping ratio (%)	Mass normalized mode shape vector
Tool 1	1	3677	0.51	$\mathbf{U} = \begin{bmatrix} u_{Z,1,1} \\ u_{\theta,1,1} \end{bmatrix} = \begin{bmatrix} 0.1761(1/\sqrt{\text{kg}}) \\ 188.4\left(1/\sqrt{\text{kgm}^2}\right) \end{bmatrix}$
Tool 2	1 2	936.66 928.57	2.51 3.93	$\mathbf{U} = \begin{bmatrix} u_{X,1,1} & u_{X,1,2} \\ u_{Y,1,1} & u_{Y,1,2} \\ u_{X,2,1} & u_{X,2,2} \\ u_{Y,2,1} & u_{Y,2,2} \end{bmatrix} = \begin{bmatrix} 0.838 & 0 \\ 0 & 0.881 \\ 0.801 & 0 \\ 0 & 0.814 \end{bmatrix} (1/\sqrt{\text{kg}})$

Note that the first two rows of $\mathbf{U}$ are measured at the bottom level, and the last two rows are measured at the top level

Downloaded From: http://manufacturingscience.asmedigitalcollection.asme.org/ on 04/29/2016 Terms of Use: http://www.asme.org/about-asme/terms-of-use

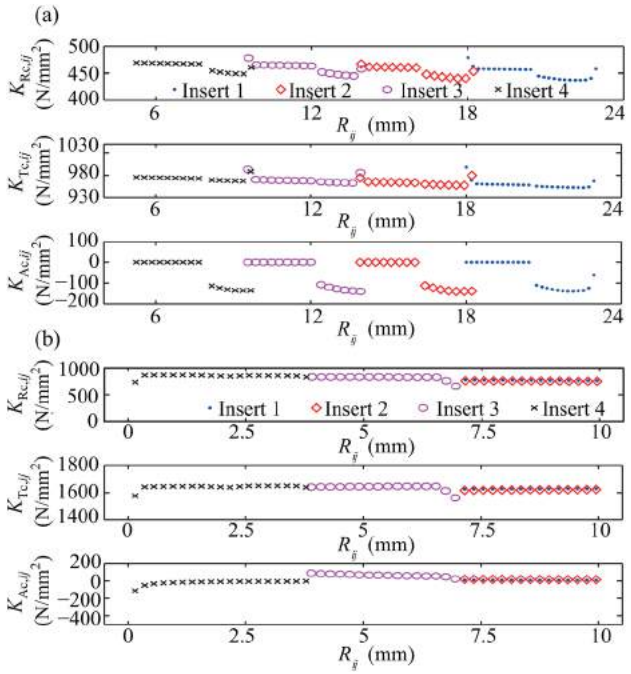

Fig. 7 Distribution of cutting force coefficients along the radius of the cutting tools. (*a*) Tool 1, Aluminum 7050-T7451, $K_{ue} = 21.4\,[\mathrm{N/mm}]$, $K_{ve} = 33.2\,[\mathrm{N/mm}]$ and (*b*) tool 2, AISI Steel 1045,. $K_{ue} = 44.0\,[\mathrm{N/mm}]$, $K_{ve} = 45.8\,[\mathrm{N/mm}]$.

Torsional–Axial Stability. Similar to the lateral stability, torsional–axial dynamics are modeled in modal space using the same equation form as given in Eq. (21) but with the following modifications:

- $\boldsymbol{\xi}$, $\boldsymbol{\omega}$, and $\mathbf{U}$ together with N_s and N_m are replaced by the parameters related to torsional–axial modes.
- The transition matrix $\boldsymbol{\Phi}_a$ obtained from Eq. (27) is time invariant and constant for a specified radial depth of cut, feed per tooth and speed in torsional–axial stability, hence the Floquet theory is applied directly to evaluate the eigenvalues of $\boldsymbol{\Phi}_a$ rather than $\boldsymbol{\Psi}$ obtained from Eq. (28).

4 Simulations and Experimental Results

A series of cutting tests have been conducted on a five-axis Mori Seiki NMV5000 machining center with two multifunctional tools. The geometric parameters of the two multifunctional drills are listed in Table 1. The workpiece materials were Aluminum 7050-T7451 and AISI Steel 1045. The cutting forces in *X*, *Y*, and *Z* directions have been measured with a Kistler table dynamometer 9255B.

Impact modal tests were conducted to measure FRF and modal parameters. Lateral parameters in two principal directions (*X* and *Y*) were measured by standard impact tests and modal analysis. For instance, as shown in Fig. 1, an impulse hammer instrumented with a force sensor was applied at the bottom level, and accelerometers were used to measure the accelerations of the cutter. Only bottom level is necessary to be measured for tool 1, whereas both bottom and top levels are needed for tool 2.

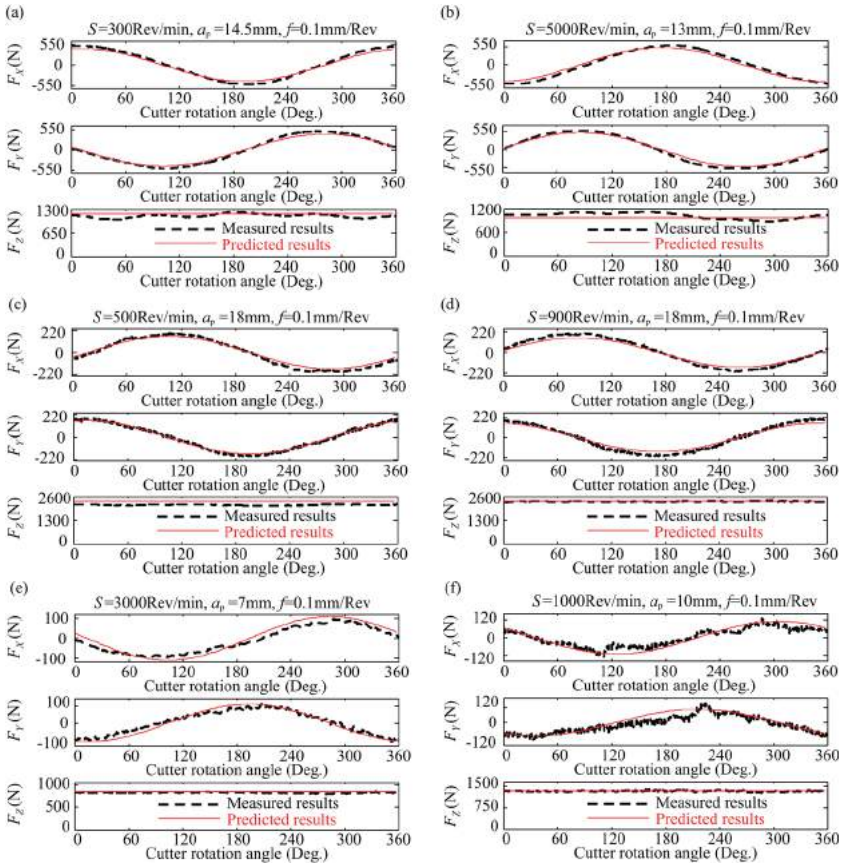

Fig. 8 Comparisons of predicted and measured cutting forces. (*a*) Tool 1, Aluminum 7050–T7451; (*b*) tool 1, Aluminum 7050–T7451; (*c*) tool 1, AISI Steel 1045; (*d*) tool 1, AISI Steel 1045; (*e*) tool 2 with bottom inserts only, AISI Steel 1045; and (*f*) tool 2 with all inserts, AISI Steel 1045. Note that in case (*e*) only the bottom inserts of tool 2 are in cut. In case (*f*), both bottom and top inserts of tool 2 are in cut.

Downloaded From: http://manufacturingscience.asmedigitalcollection.asme.org/ on 04/29/2016 Terms of Use: http://www.asme.org/about-asme/terms-of-use

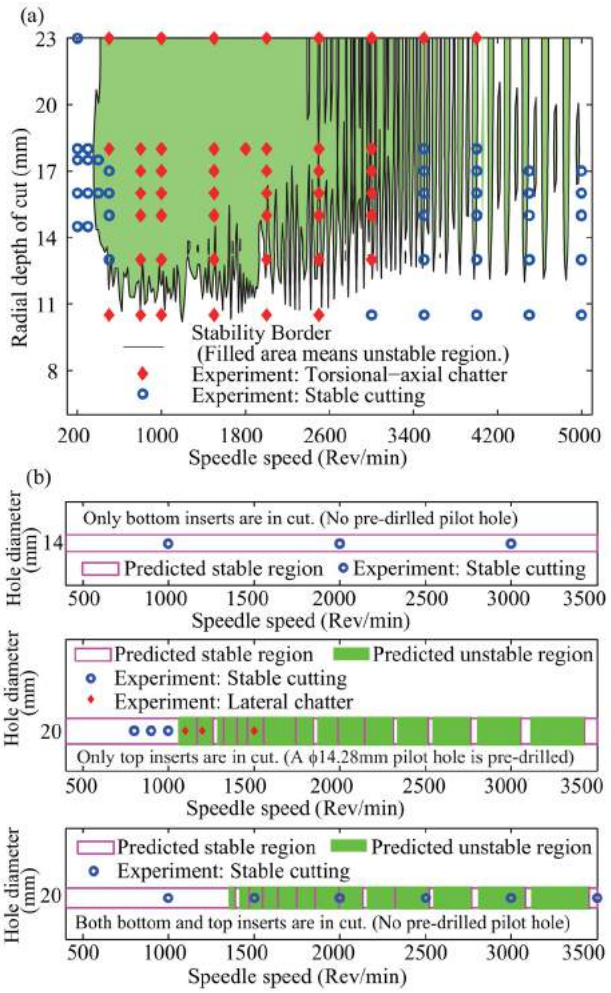

Fig. 9 Comparison of predicted and experimentally measured chatter stability limits for tool 1 and tool 2. Feedrate: 0.1 mm/rev. (*a*) Torsional–axial stability lobes for tool 1. Material: aluminum 7050–T7451 and (*b*) lateral stability limits for tool 2. Material: AISI Steel 1045.

The direct and cross FRF of the tools in axial and torsional directions (Z and θ) are measured as illustrated in Fig. 6. Accelerometer allocated at S1 is used to capture the axial (Z) vibrations. Accelerometer S2, which is placed on the front surface of the insert, is used to measure torsional vibrations. The impact force (F_Z) is applied in axial direction to find the direct and cross FRFs as follows:

$$\psi_{ZZ}(\omega) = \frac{F_Z}{S_1}; \quad \psi_{\theta Z}(\omega) = \frac{F_Z}{S_2/\rho_2} \tag{29}$$

where S_1 and S_2 represent the measured displacements, ρ_2 is the distance between S2 and the cutter axis. By applying a tangential impact force F_t on the periphery of the tool as shown in Fig. 6, the direct and cross FRFs of the torsional and axial responses due to cutting torque are evaluated as

$$\psi_{\theta\theta}(\omega) = \frac{F_t \times \rho_1}{S_2/\rho_2}; \quad \psi_{Z\theta}(\omega) = \frac{F_t \times \rho_1}{S_1} \tag{30}$$

where ρ_1 is the distance between torque arm. The modal parameters of the two tools are identified with CUTPRO^{TM} modal module and given in Table 2. Tool 1 exhibited only torsional, and tool 2 caused only lateral chatter due to their cutting edge orientations.

Verification of Static Cutting Force Model. The cutting force coefficients obtained through orthogonal to oblique cutting transformation are mapped along the cutting edges, as shown in Fig. 7. The orthogonal parameters of Aluminum 7050-T7451 and AISI Steel 1045 are given in Ref. [21]. The predicted and measured cutting forces are in agreement as shown in Fig. 8 for various cutting conditions for both tools. The radial depth of cut a_p is measured as the difference between the radius of the desired hole and that of the predrilled pilot hole.

Verification of Stability Model. The predicted stability limits with process damping effects have been experimentally verified as shown in Fig. 9 for tool 1 and tool 2 for cutting Aluminum 7050-T7451 and AISI steel 1045 materials. Since new tools were used in the experiments, flank wear land of 20 μm, which is close to the edge radius of tools, is assumed for all inserts. The indentation force coefficients of Aluminum 7050-T7451 and AISI Steel 1045 were previously identified as $K_{sp} = 1.5 \times 10^5$ N/mm^3 and 4×10^5 N/mm^3, respectively. Since there are no lateral bending chatter observations for tool 1, only the simulated stability results related to torsional–axial mode are plotted in Fig. 9(*a*). Opposite to tool 1, only bending chatters were experimentally experienced for tool 2 as shown in Fig. 9(*b*).

In Fig. 9(*a*), most experimental observations related to tool 1 agree with the predicted stability borders. A series of unstable islands can be observed at the spindle speed range of 3000–5000 rev/min. There is hardly any stability pocket at the 10.5 mm depth of cut, and torsional–axial mode chatters at the spindle speed range of 500–2500 rev/min, although some points close to the critical limit are predicted to be stable. The process is highly stable under 500 rev/min spindle speed due to process damping. The discrepancies are attributed to changes on the cutting edge geometry, inaccuracies in FRF measurements, and variations in the boundary conditions of the system when tool penetrates into the hole.

Figure 9(*b*) shows three sets of different conditions in drilling AISI1045 steel alloy. When only the bottom layer of inserts cuts without a predrilled pilot hole, the process is found to be stable at all cutting conditions which agrees with experiments. Only upper inserts cut when the 14.28 mm pilot hole is expanded to 20 mm diameter hole. The process is always predicted to be stable under 1000 rev/min due to process damping, and unstable beyond this speed. The experiments agree with the predictions. When the hole of 20 mm diameter hole is opened without any pilot hole, both lower and upper inserts cut. The process has been observed to be stable at all cutting tests, although the instability is predicted beyond 1400 rev/min. The source of stability in the experiments is attributed to stiffening effect when both lower and upper inserts are in contact (i.e., in the hole) with the material as proven in Ref. [18]. This phenomenon was not considered in the mathematical model of the multifunctional drill. The experiments conducted with a 14.28 mm pilot hole, where only upper inserts are in contact with the material, were to illustrate this phenomenon. On the other hand, it is noted that multifunctional tool 2 is designed to drill stepped holes directly without the requirement of machining pilot holes. This means that for tool 2, it is not necessary to design the radial depth of cut, which always equals half of the hole diameter. As a result, only one y-coordinate is labeled in Fig. 9(*b*), and this makes Fig. 9(*b*) different from a conventional stability diagram with varying depths of cut.

The chatter stability limits are identified from the force and sound measurements and their spectra. When the spectra of the measured signals are dominated by the spindle speed and/or tooth passing frequencies, the process is stable. The unstable processes are dominated by the tools' torsional–axial and lateral natural frequencies.

The measured cutting forces, sound, and their spectra for three sample tests are shown in Fig. 10. Figure 10(*a*) shows a torsional–axial chatter condition for Tool 1. It can be seen that the spectra of F_Y and F_Z are dominated by torsional/axial mode (~3545 Hz).

Downloaded From: http://manufacturingscience.asmedigitalcollection.asme.org/ on 04/29/2016 Terms of Use: http://www.asme.org/about-asme/terms-of-use

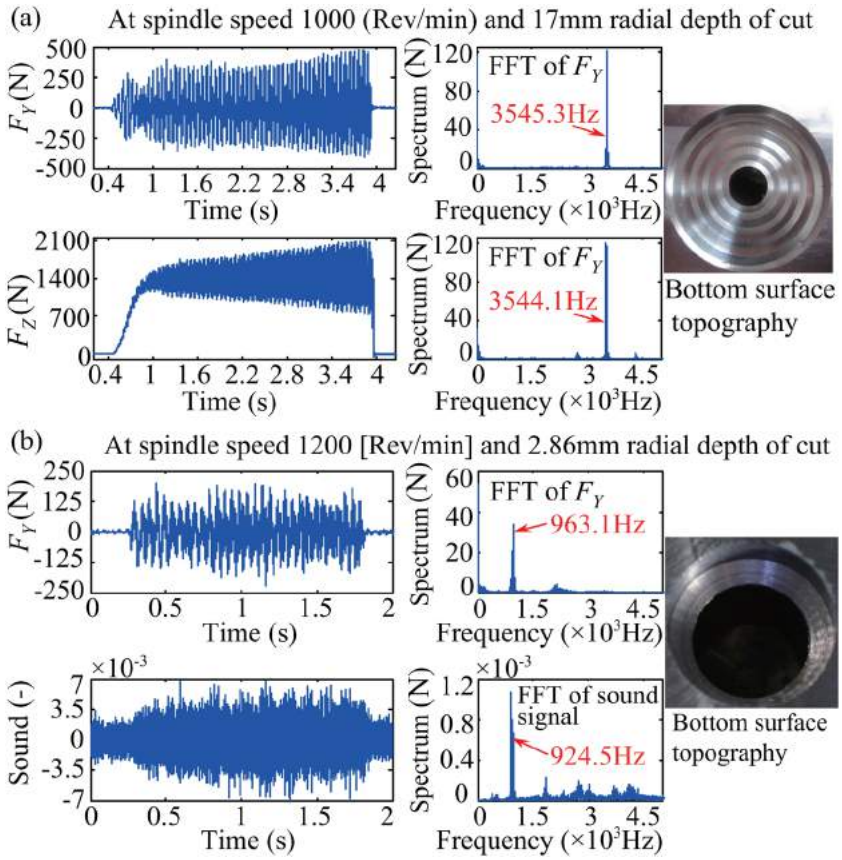

Fig. 10 Measured cutting forces and sound along with the photograph of hole shapes for sample experiments with chatter. (*a*) Tool 1 at spindle speed 1000 rev/min, radial depth of cut = 17 mm, federate = 0.1 mm/rev. Material: aluminum 7050–T7451 and (*b*) tool 2 at spindle speed 1200 rev/min, radial depth of cut = 2.86 mm, federate = 0.1 mm/rev. Only top inserts are in cut, Material: AISI Steel 1045.

The forces grow exponentially and the sun-rise pattern can be observed at the finished bottom of the hole which is typical for torsional–axial chatter phenomenon in drilling [17,18]. Lateral chatter occurs at the first bending mode of tool 2 (963.1 Hz and 924.5 Hz) which distorts the hole shape.

5 Conclusions

Mechanics and dynamics of multifunctional tools with multiple inserts are presented to predict cutting forces and chatter free cutting conditions to open stepped holes in one operation. Since the inserts have varying geometry with arbitrary placements on the tool body, the cutting force coefficients are best estimated from orthogonal to oblique cutting transformation. The chatter stability may also depend on the distribution of the dynamic forces; hence, the semidiscrete time domain stability solution that considers the varying directional factors, process damping and multiple time delays is advantageous over frequency domain solutions for multifunctional tools. The research is currently extended to cover the unified mechanics and dynamics of turning, drilling, boring and milling with a generalized solution.

Acknowledgment

This research has been supported by the National Natural Science Foundation of China under Grant No. 11272261, the Program for New Century Excellent Talents in University under Grant No. NCET-12-0467, and National Sciences and Engineering Research Council of Canada (NSERC) under CANRIMT and NSERC—Pratt & Whitney Canada Research Chair Grants. Sandvik Coromant and Kennametal provided the tools.

References

[1] Altintas, Y., 2012, *Manufacturing Automation: Principles of Metal Cutting Mechanics, Machine Tool Vibrations, and CNC Design*, Cambridge University, Cambridge, UK.
[2] Chandrasekharan, V., Kapoor, S. G., and DeVor, R. E., 1995, "A Mechanistic Approach to Predicting the Cutting Forces in Drilling: With Application to Fiber-Reinforced Composite Materials," ASME J. Eng. Ind., **117**(4), pp. 559–570.
[3] Roukema, J. C., and Altintas, Y., 2007, "Generalized Modeling of Drilling Vibrations, Part I: Time Domain Model of Drilling Kinematics, Dynamics and Hole Formation," Int. J. Mach. Tools Manuf., **47**(9), pp. 1455–1473.
[4] Strenkowski, J. S., Hsieh, C. C., and Shih, A. J., 2004, "An Analytical Finite Element Technique for Predicting Thrust Force and Torque in Drilling," Int. J. Mach. Tools Manuf., **44**(12–13), pp. 1413–1421.
[5] Sambhav, K., Tandon, P., Kapoor, S. G., and Dhande, S. G., 2013, "Mathematical Modeling of Cutting Forces in Microdrilling," ASME J. Manuf. Sci. Eng., **135**(1), p. 014501.
[6] Stephenson, D. A., and Agapiou, J. S., 1992, "Calculation of Main Cutting Edge Forces and Torque for Drills With Arbitrary Point Geometries," Int. J. Mach. Tools Manuf., **32**(4), pp. 521–538.
[7] Chandrasekharan, V., Kapoor, S. G., and DeVor, R. E., 1998, "A Mechanistic Model to Predict the Cutting Force System for Arbitrary Drill Point Geometry," ASME J. Manuf. Sci. Eng., **120**(3), pp. 563–570.
[8] Sambhav, K., Tandon, P., and Dhande, S. G., 2014, "Force Modeling for Generic Profile of Drills," ASME J. Manuf. Sci. Eng., **136**(4), p. 041019.
[9] Pirtini, M., and Lazoglu, I., 2005, "Forces and Hole Quality in Drilling," Int. J. Mach. Tools Manuf., **45**(11), pp. 1271–1281.
[10] Altintas, Y., and Weck, M., 2004, "Chatter Stability in Metal Cutting and Grinding," CIRP Ann. -Manuf. Technol., **53**(2), pp. 619–642.
[11] Ema, S., Fujii, H., and Marui, E., 1988, "Chatter Vibration in Drilling," ASME J. Eng. Ind., **110**(4), pp. 309–314.

Downloaded From: http://manufacturingscience.asmedigitalcollection.asme.org/ on 04/29/2016 Terms of Use: http://www.asme.org/about-asme/terms-of-use

[12] Bayly, P. V., Lamar, M. T., and Calvert, S. G., 2002, "Low-Frequency Regenerative Vibration and the Formation of Lobed Holes in Drilling," ASME J. Manuf. Sci. Eng., **124**(2), pp. 275–285.
[13] Gong, Y., Lin, C., and Ehmann, K. F., 2005, "Dynamics of Initial Penetration in Drilling: Part 2—Motion Models for Drill Skidding and Wandering With Experimental Verification," ASME J. Manuf. Sci. Eng., **127**(2), pp. 289–297.
[14] Arvajeh, T., and Ismail, F., 2006, "Machining Stability in High Speed Drilling—Part 2: Time Domain Simulation of a Bending–Torsional Model and Experimental Validations," Int. J. Mach. Tools Manuf., **46**(12–13), pp. 1573–1581.
[15] Arvajeh, T., and Ismail, F., 2006, "Machining Stability in High-Speed Drilling—Part 1: Modeling Vibration Stability in Bending," Int. J. Mach. Tools Manuf., **46**(12–13), pp. 1563–1572.
[16] Filiz, S., and Ozdoganlar, O. B., 2010, "A Model for Bending, Torsional, and Axial Vibrations of Micro- and Macro-Drills Including Actual Drill Geometry—Part I: Model Development and Numerical Solution," ASME J. Manuf. Sci. Eng., **132**(4), p. 041017.
[17] Roukema, J. C., and Altintas, Y., 2007, "Generalized Modeling of Drilling Vibrations. Part II: Chatter Stability in Frequency Domain," Int. J. Mach. Tools Manuf., **47**(9), pp. 1474–1485.
[18] Ahmadi, K., and Altintas, Y., 2013, "Stability of Lateral, Torsional and Axial Vibrations in Drilling," Int. J. Mach. Tools Manuf., **68**, pp. 63–74.
[19] Karandikar, J., Traverso, M., Abbas, A., and Schmitz, T., 2014, "Bayesian Inference for Milling Stability Using a Random Walk Approach," ASME J. Manuf. Sci. Eng., **136**(3), p. 031015.
[20] Zheng, C. M., Wang, J.-J. J., and Sung, C. F., 2013, "Analytical Prediction of the Critical Depth of Cut and Worst Spindle Speeds for Chatter in End Milling," ASME J. Manuf. Sci. Eng., **136**(1), p. 011003.
[21] Kaymakci, M., Kilic, Z. M., and Altintas, Y., 2012, "Unified Cutting Force Model for Turning, Boring, Drilling and Milling Operations," Int. J. Mach. Tools Manuf., **54–55**, pp. 34–45.
[22] Jin, X., and Altintas, Y., 2012, "Prediction of Micro-Milling Forces With Finite Element Method," J. Mater. Process. Technol., **212**(3), pp. 542–552.
[23] Eksioglu, C., Kilic, Z. M., and Altintas, Y., 2012, "Discrete-Time Prediction of Chatter Stability, Cutting Forces, and Surface Location Errors in Flexible Milling Systems," ASME J. Manuf. Sci. Eng., **134**(6), p. 061006.
[24] Budak, E., and Tunc, L. T., 2009, "A New Method for Identification and Modeling of Process Damping in Maching," ASME J. Manuf. Sci. Eng., **131**(5), p. 051019.
[25] Insperger, T., and Stépán, G., 2004, "Updated Semi-Discretization Method for Periodic Delay-Differential Equations With Discrete Delay," Int. J. Numer. Methods Eng., **61**(1), pp. 117–141.
[26] Wan, M., Zhang, W. H., Dang, J. W., and Yang, Y., 2010, "A Unified Stability Prediction Method for Milling Process With Multiple Delays," Int. J. Mach. Tools Manuf., **50**(1), pp. 29–41.
[27] Lakshmikanthan, V., and Trigiante, D., 1988, *Theroy of Difference Equations Numerical Methods and Applications*, Academic, London, UK.
[28] Kolmanovskiĭ, V. B., 1986, *Stability of Functional Differential Equations*, Academic, London, UK.

Downloaded From: http://manufacturingscience.asmedigitalcollection.asme.org/ on 04/29/2016 Terms of Use: http://www.asme.org/about-asme/terms-of-use

J Mater Sci (2015) 50:5014–5023
DOI 10.1007/s10853-015-9050-9

Binder droplet impact mechanism on a hydroxyapatite microsphere surface in 3D printing of bone scaffolds

Yan-en Wang[1] · Xin-pei Li[1] · Chuan-chuan Li[1] · Ming-ming Yang[1] · Qing-hua Wei[1]

Received: 22 October 2014 / Accepted: 22 April 2015 / Published online: 29 April 2015
© Springer Science+Business Media New York 2015

Abstract The combination of hydroxyapatite composite powder and three-dimensional (3D) printing rapid prototyping techniques has markedly improved skeletal interactions in orthopedic surgery applications. 3D printing methodology ensures effective bionic microstructure and shape interactions between an implant and the surrounding normal tissue. In effort to enhance the quality, precision, and mechanical properties of printed bone scaffolds, this study examines binder droplet spreading performance on the surface of hydroxyapatite (HA) microspheres. The piezoelectric nozzle diameter is about 10 μm, which sprays droplets 20 μm in diameter. The average size of HA powder particles is about 60 μm in diameter. Most laboratories, however, are limited to observation of a single droplet 20 μm or smaller in diameter impacting a spherical surface 60 μm in diameter. Based on non-dimensional scale similarity theory in axisymmetric Stokes flow dynamics, this study conducted experiments and simulation on the same collision conditions (droplet 200 μm in diameter, spherical surface 600 μm in diameter). Simulation results were consistent with experiment data, and form a basis for future research on modeling droplet impact on spherical surfaces.

✉ Yan-en Wang
wangyanen@nwpu.edu.cn

[1] Industry Engineering Department, School of Mechanical Engineering, Northwestern Polytechnical University, 127 West Youyi Road, Xi'an 710072, Shaanxi, People's Republic of China

Introduction

Researchers, developers, and medical professionals involved in bone tissue engineering have shown increased demand for artificial bone scaffolds; more specifically, for bone substitute, that is as sustainable as possible without sacrificing high quality mechanical, chemical, and biocompatibility properties. Three-dimensional printing (3DP) is a promising method that employs inkjet printing technology to bind bioceramic powder materials to fabricate human-specific, individual substitutes. Hydroxyapatite (HA) [1] is a typical bioactive material which occupies 75 wt% of human bone, regardless of water content. It is highly biocompatible, non-toxic, and able to promote bone growth and conjoin successfully with human bone. Both Mooney [2] and Felicity [3] proved hydroxyapatite [HA, $Ca_{10}(PO_4)_6(OH)_2$] to be a highly effective synthetic bone replacement material for artificial bone scaffolds, due to the material's favorable biocompatibility and osteoconductive properties. Previous studies [4, 5] have shown that the smaller the HA powder size, the more biocompatible the HA-implanted prosthesis. Suitable HA powder particle size is a key component of the biocompatibility and mechanical properties of an artificial bone scaffold. Lorna et al. [6] asserted that the porosity and mechanical properties of a bone scaffold are the most important factors in building bionic artificial bone. Bone scaffolds provide such functions as temporary mechanical support, osteoconductivity, and tissue regeneration.

In the bone scaffold fabrication experiments conducted in this study, average powder size was about 60 μm in diameter. Spraying biobinder volume on the surface of the HA powder bed is a crucial point in the fabrication process that controls the mechanical and porosity properties of the scaffold; for typical experimental assessment instruments,

however, it is practically impossible to capture an image of a microdroplet flying a distance of 1 mm with comparably high velocity (above 1.0 m s^{-1}). Based on similarity theory, this study built a droplet spray system to observe a single biobinder droplet of 200 μm or larger in diameter impacting a spherical surface of HA microsphere 600 μm in diameter. Comparison between simulation and experimental results presented here can improve inkjet spraying processes and bone scaffold fabrication processes in future by outlining methods for controlling biobinder droplet pattern.

The deposition of a liquid droplet impacting a solid surface is a topic of considerable importance in a variety of applications in aerospace, material science, manufacturing, and chemical industries, as it is related to inkjet printing, spray cooling and deposition, and pesticide spraying. To this effect, a substantial body of theoretical, experimental, and simulation studies on the topic have been conducted in recent years. Roux and Cooper-White et al. [7], for example, studied the spreading of a water droplet impacting a glass surface at different impact velocities, with particular attention to the dynamics of contact angle and its relationship to maximum expanding radius and capillary number. Their results clearly showed that conservation of energy alone is insufficient to describe the dynamics of impact events. Luo et al. [8] came to conclusion that droplet diameter decreased, but the ratio of droplet diameter to nozzle diameter increased rapidly, when nozzle diameter decreased to 100 μs. Pan et al. [9] investigated collisions between water droplets with dimensionless Weber number up to 12,000 and a solid plate with varied surface roughness. Fujimoto et al. [10] experimentally and numerically studied the collision of a liquid droplet with a hemispherical droplet on a horizontal solid surface using the volume of fluid (VOF) method, and the effects of the incoming droplet's impinging angle on the deformation process. Cao et al. [11] observed molten droplets generated through a graphite nozzle with a 0.3 mm diameter orifice by argon pulse pressure and found that droplets were typically generated at a rate of 1–5 droplets per second. Yarin et al. [12] provided a comprehensive review of previous theoretical and experimental studies on drop impact dynamics, and came to the conclusion that the collision of a liquid droplet on a solid surface is determined primarily by inertia, viscous forces, surface tension forces, and surface properties of the solid surface.

Most previous studies [13–15] focus on the impact of a droplet on a flat surface, and relatively few studies have investigated the impact on a spherical surface. Kim et al. [16, 17] investigated the mechanism of droplet formation from piezoelectric-type inkjet heads by simulating the two-phase flows of air and metal inks. They found that a buffer region helps to maintain stable meniscus features after ejection. Modifying the displacement waveform from the piezoelectric actuator makes it possible to control droplet size, ejection speed, and satellite droplets. Bakshi et al. [18] studied the effects of droplet Reynolds number and target-to-drop size ratio on the impact of a drop on a spherical surface. Li and Wang [19] developed a numerical model to simulate the deposition of a droplet with low-impact energy impinging onto a spherical surface, with special emphasis on the effects of impact velocity and impacted-sphere size. Bolster et al. [20] employed similarity theory to find empirical relationships between the non-dimensional parameters that characterize a physical system. Qing et al. [21] conducted a two-dimensional numerical simulation of dynamics of free-surface Stokes flow dynamics.

This study built a two-dimensional simulation of the spreading dynamics of a single droplet 200 μm in diameter impacting a spherical surface 600 μm in diameter, and explored the effects of impact velocity, viscosity, surface tension, and surface size on the deposition of the droplet.

Experimental

The piezoelectric nozzle used in this experiment is about 10 μm in diameter and sprays droplets 20 μm in diameter (Fig. 1). However, according to the actual experimental conditions of the vast majority of research facilities, droplet modeling is limited to a droplet of 200 μm or larger in diameter impacting a spherical surface 600 μm in diameter. This study used similarity theory to establish empirical relationships between non-dimensional parameters, and conducted experiments under the same collision conditions (droplet 200 μm in diameter, spherical surface 600 μm in diameter).

Droplet parameters in piezo injection experiments

As shown in Fig. 2, the droplet spray system consists of a pulse function generator and homemade piezoelectric nozzle. The piezoelectric droplet injection process is very complex. Impact events were observed with a high-speed video camera (Photron Fastcam SA4) with a typical frame rate of 5400 frames per second (fps) and corresponding pixel resolution of 1024 × 1024 pixels. No significant information loss was observed between 1000 and 2000 fps for drop impact velocities up to 1.5 m s^{-1}. Data for lower values of impact velocity (1.0 m s^{-1}) were recorded at 1000, and 2000 fps recording speed was used for high values of impact velocity (1.5 m s^{-1}). The camera, which was mounted on a boom stand, captured 1000 fps in full frame (2764 × 2048) and 2000 fps with a reduced matrix resolution (1382 × 1024). All video images were saved

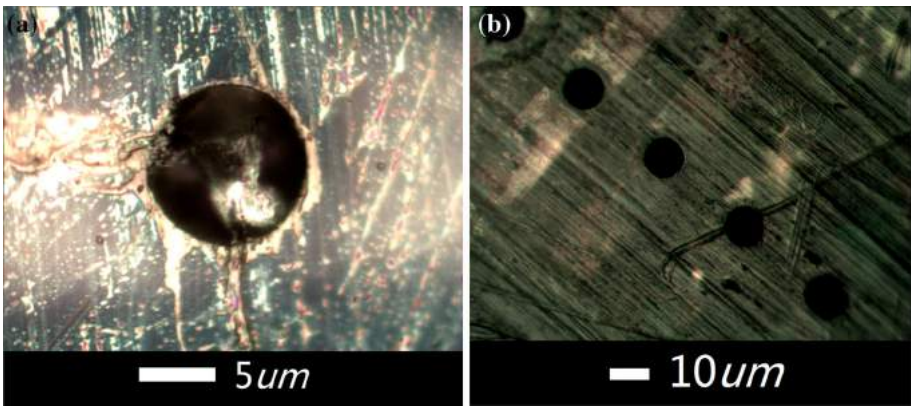

Fig. 1 Microscopic image of inkjet nozzle of 3D printing bone scaffold, **a** single nozzle microscopic image under ×500 amplification; **b** microscopic image of multi nozzle array under ×100 amplification

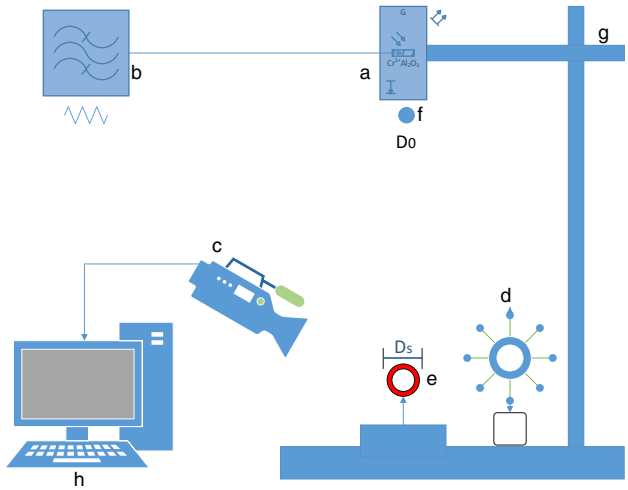

Fig. 2 Bioadhesive microdroplet piezoelectric injection experiment schematic diagram. **a** Piezoelectric nozzle, **b** power and pulse function generator, **c** CCD high-speed camera, **d** light source, **e** spherical substrate, **f** biobinder droplet, **g** movable bracket, **h** computer

directly to a computer for subsequent analysis. The microscope (Optem Zoom 65) used has a high-power (over 8 W) stroboscopic light source (Nova-Strobe DB Plus Digital), offering a maximum working distance of 110 mm and an extended zoom range for continuous coverage of 0.7–4.5 times. The microscope captured biobinder drop impact and the spreading process on the HA small ball surface.

Bioadhesive was used as the medium in the homemade piezoelectric nozzle to create spray droplets. The droplet diameter was about 200 μm. A square wave signal was generated by a 20 Hz frequency pulse function. The piezoelectric nozzle was stimulated to generate a 200 μm bioadhesive drop which impacted the microspherial surface of the 600 μm HA microsphere. A sustained high-brightness light source which guaranteed the background was clearly visible during experimentation.

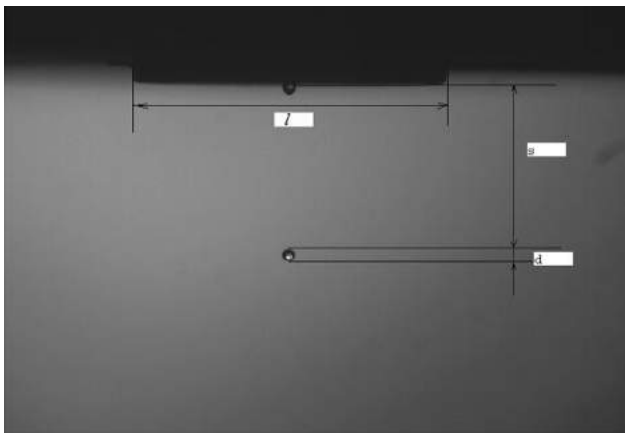

Fig. 3 Bioadhesive droplet generated by piezo injection according to experimental schematic (Fig. 2) in an ordinary room

The velocity and diameter of the binder droplet were calculated according to the following method. As shown in Fig. 3, nozzle diameter l is a known value, and bioadhesive drop flying distance is represented by $(s + d/2)$. d is the diameter of the biobinder droplet. Two variables were calculated by image processing software: the ratio of bioadhesive drop flying distance and nozzle diameter $[a=(s + d/2)/l]$, and the ratio of nozzle diameter and droplet diameter $(b = d/l)$. Thus, the velocity and diameter of the droplet can be calculated according to the following formulas:

$$v = (a_2 l - a_1 l)/(t_2 - t_1), \quad (1)$$

$$d = b_1 l \text{ or } d = b_2 l, \quad (2)$$

where v is the droplet's flying speed, d is droplet diameter, and t_1 and t_2 are different times. The ratio a_1 and a_2 corresponds to t_1 and t_2, the ratio b_1 and b_2 corresponds to t_1 and t_2, and l is the outer diameter of the nozzle.

In the experiments, a bioadhesive droplet (200 μm in diameter) collided with a spherical surface (diameter in 600 μm) at an initial velocity of 1.0 and 1.5 m s^{-1}. Both

the contact angles were 90°. The diameter of the bioadhesive droplet was similarly defined as 200 μm as it impacted the microspherial surface of HA particles during the numerical simulation process. Particle size was also set to 600 μm to investigate droplet impact phenomena, (which is difficult to capture axisymmetrically in practice, especially at higher Weber numbers.) Impact processes were captured by the above system as shown in Fig. 3.

Governing equation of fluid flow numerical simulation

The isothermal impact of a liquid droplet on a spherical surface is a non-steady process that involves the liquid droplet and air. It is assumed that there is no mass or heat transfer between the two phases. 2D models in Cartesian coordinates comprised of continuity, momentum, and energy equations were solved as follows:

$$\frac{\partial \rho}{\partial t} + \nabla \times (\rho \overrightarrow{v}) = 0, \tag{3}$$

$$\rho \frac{\mathrm{d}\overrightarrow{v}}{\mathrm{d}t} = -\nabla p + \mu \Delta \overrightarrow{v} + \frac{\mu}{3} \nabla \left(\nabla \times \overrightarrow{v}\right) + \overrightarrow{F}, \tag{4}$$

$$\frac{\partial (\rho E)}{\partial t} + \nabla \times \left(\overrightarrow{v}(\rho E + P)\right) = \nabla \times (\kappa \nabla T) + S_h, \tag{5}$$

where ρ is the density, t is the time, $\overrightarrow{v}$ is the velocity vector, p is pressure, μ is dynamic viscosity, T is temperature, $\overrightarrow{F}$ is the body force, κ is thermal conductivity, and S_h is the source of energy per unit volume per unit time.

In this study, the VOF method was used to obtain solutions. A single energy equation was solved for the mixture phase, the properties (ϕ) of which were proposed by Shen et al. [22]:

$$\phi = \frac{\sum \alpha_k \rho_k \phi_k}{\sum \alpha_k \rho_k}, \tag{6}$$

where α_k is the volume fraction of the kth fluid droplet, and ρ_k is the density of the kth fluid droplet.

The interface between phases was tracked for each computational cell by computing the volume fraction of the fluid k:

$$\frac{\partial \alpha_k}{\partial t} + V_k \times \nabla \alpha_k = 0. \tag{7}$$

Surface tension is a significant factor of fluids with non-zero contact angle on the surface. This effect can be incorporated into the momentum model by expressing it as an extra body force using the divergence theorem.

Initial/boundary conditions of numerical simulation

The effect of air is considered negligible due to its significantly smaller density and viscosity compared to the bioadhesive liquid, so the droplet surface is assumed to be a free surface. Fluent 6.3 was adopted to simulate biobinder droplet spraying behavior on the surface of the HA microsphere. As shown in Fig. 4, a droplet with an initial diameter D_0 impacts a spherical surface with a diameter of D_S at a velocity of v_0. The computational domain for 2D simulation is presented in Fig. 4. The domain dimensions of the mesh were determined based on the experimental observations of droplet maximum spread diameter. A domain size of 1.4 × 0.4 mm^2 was used for simulation, discretized by quadrilateral meshes of about 121,538 grids. Minimum grid spacing was 2 μm and maximum aspect ratio was 10 μm. Cells were dense near the spherical surface and grew gradually coarser toward the boundaries, effectively resolving the interface near the solid surface. The air–solid interface was considered to be a non-slip boundary. Contact angle varies in a narrow range during spreading and retraction according to Francois et al. [23], so here, it was set as a constant of $\alpha = 90°$. A total of 4438 cells were patched for the biobinder droplet during simulation. A residual of 10^{-4} was set for convergence of continuity, and momentum and volume fraction equations were performed using a time step of 10^{-6} with 20–30 iterations per time step. A first-order implicit time stepping approach was adopted.

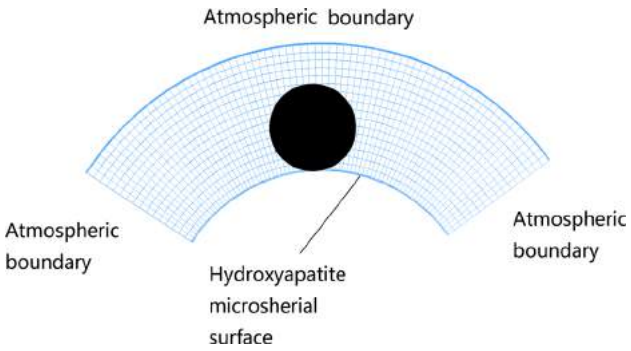

Fig. 4 Schematic of computational domain for microdroplet impacts on the hydroxyapatite particle

Results and discussion

In this study, spread diameter d is defined as the diameter of liquid lamella on the spherical surface, and spread thickness h as the thickness of liquid lamella at the central axis. Both parameters are critical in evaluating the droplet deposition on the hydroxyapatite spherical surface, and are non-dimensionalized with respect to the initial diameter D_0. The resulting spread factor ε and dimensionless spread thickness h^* are as follows:

$$\varepsilon = d/D_0, \quad (8)$$

$$h^* = h/D_0. \quad (9)$$

Numerically simulated spreading process of biobinder droplet

Figure 5 shows the CFD simulation of droplet deformation with static contact angle as the wall boundary. The simulations fully captured the dynamics of the system using dynamic contact angle, interpreting the real impact of droplets on spherical surfaces. The system can be decomposed into four distinct stages: kinetic, spreading, relaxation, and equilibrium. Each stage is governed by the interaction of inertia, viscous force, and surface tension. The computer simulation process allowed prototyping fabrication parameters to be deduced rapidly.

Kinetic phase

The droplet is assumed to be spherical in shape during the kinetic phase (first 10 μs in Fig. 5). A shock wave drives the oscillation that separates the compressed region at the lower part of the droplet from the non-compressed region at the upper part of the droplet. The upper part moves at a uniform velocity of v_0, and is not affected by spherical surface properties, while the compressed liquid begins spreading out over the surface. The spreading is completely dictated by inertia during this process, and the effects of surface tension and viscous forces are negligible. The inviscid theory is adopted in this case.

Spreading phase

The spreading phase extends from the deformation of radially expanding lamella ejected from the base of the droplet to the maximum spread diameter at about 200 μs. Inertia is the driving force of spreading, whereas surface tension and viscous force provide resisting force according to Bakshi et al. [16]. The inertial effect dominates the early spreading of the droplet, and spread thickness changes in a linear fashion (Table 1); inertia is then partially or even fully dissipated, especially when the contact line velocity is close to 0, and surface tension and viscous forces determine the spreading of the droplet.

Relaxation phase

The droplet will retract once it reaches maximum diameter according to the stored elastic energy provided by surface tension. Viscous forces oppose elastic forces.

Equilibrium phase

The droplet is finally brought to an equilibrium state once oscillations cease. After 500 μs, the spread diameter of the lamella remains largely unchanged, but the surface oscillates slightly. The kinetic energy of the droplet is then dissipated by viscous forces or converted into surface energy.

Simulation was conducted under the same collision conditions described above. The diameter of the solid sphere was set to 600 μm for all numerical calculations. Droplet shapes which varied (see images in Fig. 5) at various times were reproduced accurately through simulation consistently throughout the entire collision process. Agreement between the simulated model and experimental model further verify the accuracy of the method proposed in this study—simulation results can, in fact, be used to characterize droplet impacts on spherical surfaces.

Effect of impact velocity on droplet deposition

The spreading of a droplet ($D_0 = 200$ μm) impacting a spherical surface ($D_s = 600$ μm) was simulated at initial velocities of 0.5, 1.0, 1.25, and 1.5 m s^{-1}. In the liquid phase, density ρ_l was 990 kg m^{-3}, kinematic viscosity

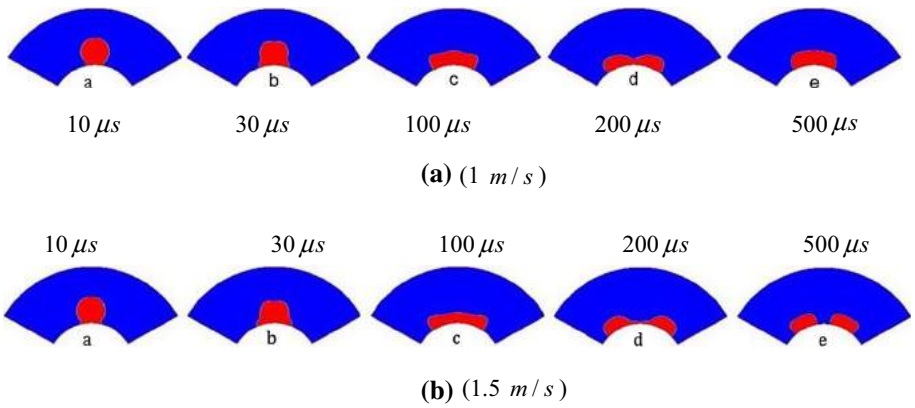

Fig. 5 CFD simulation using dynamic contact angle at two different spraying speeds, **a** bioadhesive droplet spraying velocity of 1 m s^{-1}; **b** droplet spray velocity of 1.5 m s^{-1}

Table 1 Droplet spread thickness for different impact velocities during the first 50 μs

Velocity (m s^{-1})	Time (μs)					
	0	10	20	30	40	50
0.5	200	195.2	188.2	180.5	172.8	166.2
1.0	200	190.6	178.5	166.7	155.2	144.9
1.25	200	188.4	174.2	160.5	147	135.1
1.5	200	185.2	169	154.3	139.1	126.5

coefficient μ_l was 0.0009 Pa s, and surface tension coefficient σ was 0.069 N m^{-1}. In the gas phase, density ρ_g was 1.215 kg m^{-3}, and dynamic viscosity coefficient μ_g was 1.6105 × 10 Pa s. Weber numbers ($W_e = \rho_l v_0^2 D_0/\sigma$), from smallest to largest, were 0.68, 2.73, 4.27, and 6.15, and Reynolds numbers ($R_e = \rho_l v_0 D_0/\mu_l$) were 99.82, 199.64, 249.55, and 449.19, respectively. Weber number and Reynolds number indicate the impact energy of the droplet; both were observed to be small, indicating that the impact energy was low.

Figure 6 shows the temporal evolution of the droplet spread factor for different impact velocities. Maximum spread factor was observed at about 200 μs, at which point droplets reached maximum diameter of 1.43–2.20 times their initial diameters. Maximum spread diameter also increased as impact velocity increased, because the kinetic energy of a droplet is partly dissipated by viscous forces and partly converted into surface energy during the spreading phase; thus, the greater the impact velocity, the larger the converted surface energy and the larger the surface area and diameter of the resultant lamella. As impact velocity increased from 0.5 to 1.5 m s^{-1}, the time needed for the droplet to reach maximum spreading decreased slightly, from 230 to 210 μs. The curves flattened, with small fluctuations after 500 μs, and the final spread factor decreased from 1.43 to 1.23 as impact velocity increased from 0.5 to 1.25 m s^{-1} before, surprisingly, increasing significantly (up to 2.02) with further increase in impact velocity (up to 1.5 m s^{-1}). This dramatic increase in spread factor can be attributed to the droplet breaking into smaller droplets at high impact velocity (1.5 m s^{-1}), as shown in Fig. 4a, b, which resulted in loss of surface tension energy. The lamella was thus unable to retract, creating large final spread diameter. (Spread diameter was defined as the external diameter of the lamella in this case.)

Figure 7 shows the temporal evolution of the dimensionless spread thickness of the droplet for different impact velocities. Dimensionless spread thickness first decreases in an approximately linear manner, where a higher decrease rate is to be expected at higher impact velocity. Minimum thickness was 150–250 μs. The higher the impact velocity, the thinner the minimum spread. Spread thickness neared 0 at velocity of 1.5 m s^{-1}, indicating where the droplet broke. Spread thickness remained largely unchanged after 500 μs, however.

Figure 8 shows spread thickness h in the first 50 μs plotted against time. Spread thickness decreased linearly, and the absolute value of the slope increased as impact velocity increased. The data in Table 1 were fitted with a linear function—let the slope of the linear function be k_{v_0}, where v_0 is the velocity of the droplet, then

$$h = 200 - k_{v_0} t. \quad (10)$$

According to Table 1, it is assumed that k_{v_0} equals v_0, thus

$$h = 200 - v_0 t. \quad (11)$$

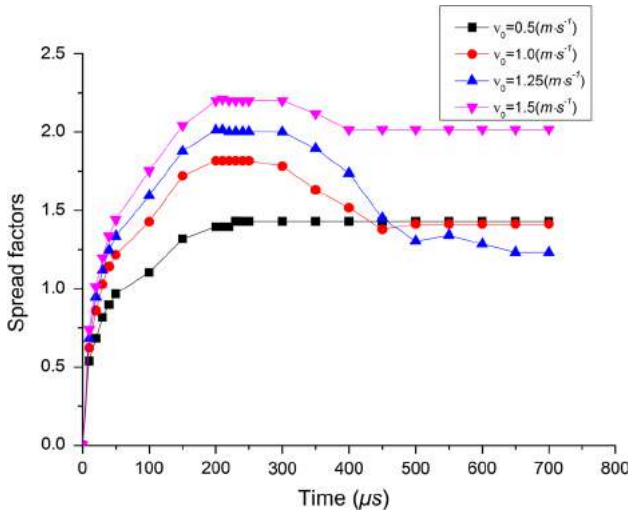

Fig. 6 Temporal evolution of spread factor for different impact velocities

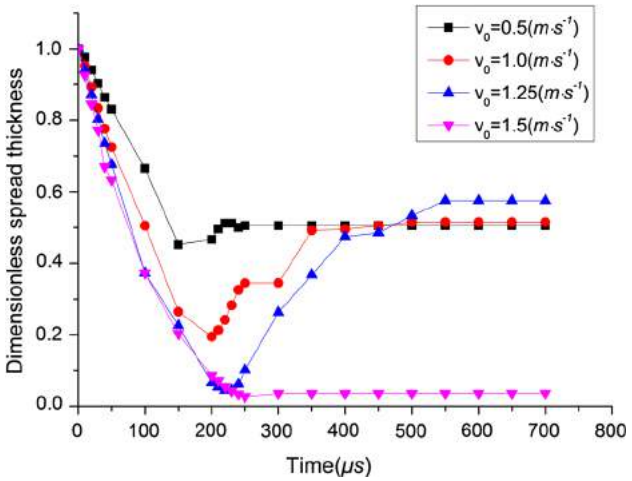

Fig. 7 Temporal evolution of dimensionless spread thickness for different impact velocities

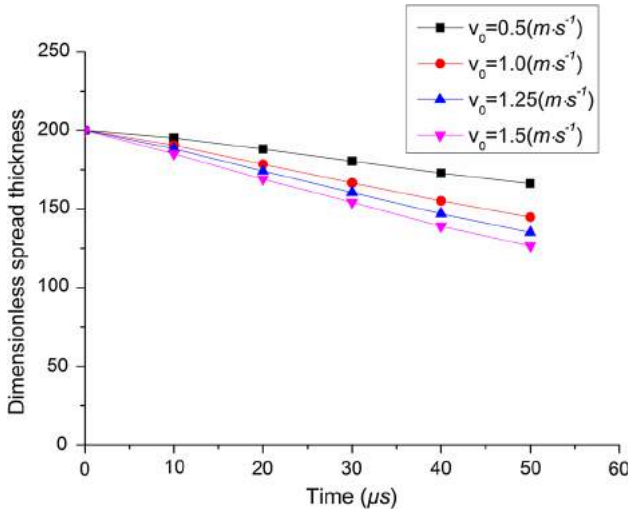

Fig. 8 Droplet spread thickness during the first 50 μs

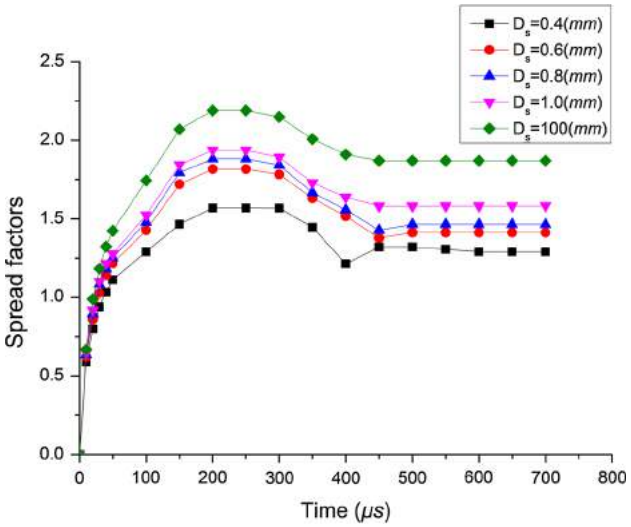

Fig. 9 Spread factors of a droplet impacting spherical surfaces with different diameters

Spread thickness is completely determined by impact velocity during the initial collision, and the effect of the spherical surface is negligible. The upper part of the droplet falls as a rigid body, whereas the lower part is compressed and spreads outward. Table 1 shows that better agreement between calculated and simulated results was obtained at high impact velocity, indicating that spread thickness is less likely affected by other factors in this case. The difference between calculated and simulated results grows with time, because impact velocity decreases gradually with the dissipation of inertial energy and the role of other factors, such as surface tension and viscous forces, becomes more prominent according to Bakshi et al. [16].

Effect of curvature on droplet deposition

A two-dimensional simulation of the spreading of a droplet ($D_0 = 200$ μm) impacting spherical surfaces with diameters of 400, 600, 800, 1000, and 10^5 μm at an initial velocity of 1.0 m s^{-1} was performed.

Figure 9 shows where during the initial collision no significant effect on spread factor the curvature had. Maximum spread factor at about 200 μs increased from 1.57 to 2.19 as the curvature increased from 400 to 10^5 μm. Curvature likewise had no effect on the time needed for the droplet to reach maximum diameter. Once the droplet stopped spreading and reached equilibrium, spread factor increased significantly alongside increasing curvature.

Figure 10 shows that during the initial collision, curvature had no significant effect on spread thickness. This further validates the conclusion drawn in the previous section that spread thickness decreases linearly with the v_0 slope, and is less affected by the properties of the spherical surface. The smaller the curvature, though, the thinner the minimum spread thickness; thus, when the curvature is small enough, the droplet breaks at the center. During the equilibrium phase, the spread thickness decreased slightly with increasing curvature.

When $D_s = 100$ μm, the collision can be considered to occur between the droplet and a flat surface, due to the significant difference in size between them. Pasandideh et al. [24] provided a simple analytical model to predict maximum droplet size after impact, and predications were well in accordance with experimental measurements reported in previous research (at error within 15 %).

Maximum spread factor can be expressed as follows:

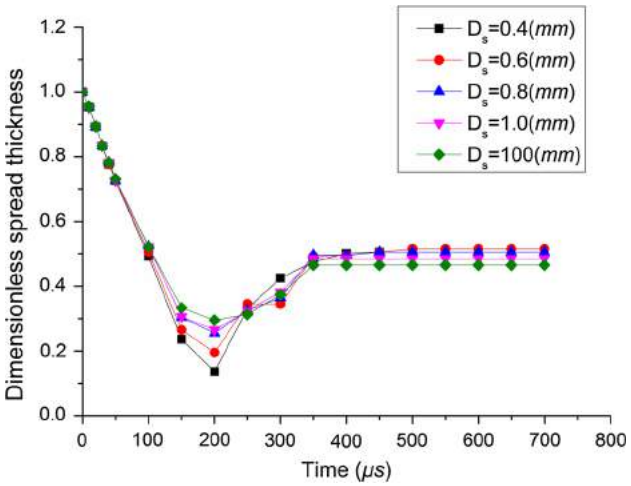

Fig. 10 Dimensionless spread thickness of droplet impacting spherical surfaces with different diameters

$$\varepsilon_{\max} = \sqrt{\frac{W_e + 12}{3(1 - \cos\theta_a) + 4(W_e/\sqrt{R_e})}}. \quad (12)$$

In this study, the theoretical value of maximum spread factor was 1.98, which had 9.59 % difference from the simulation value (2.19), confirming the reliability of the simulation results.

Effect of viscosity on droplet deposition

The spreading of a droplet ($D_0 = 200$ μm) impacting a spherical surface ($D_s = 600$ μm) at an initial velocity of 1.0 m s^{-1} under different viscosity coefficients ($\mu = 0.001$, 0.002, 0.003, 0.005, and 0.02 Pa s) was simulated.

Figure 11 shows the temporal evolution of the droplet spread factor for different viscosity coefficients. Maximum spread factor, as well as the time needed for the droplet to reach its maximum diameter, decreased with increasing viscosity. 200 μs was required to reach maximum diameter when $\mu = 0.003$ Pa s, 180 μs when $\mu = 0.005$ Pa s, and 150 μs was needed when $\mu = 0.02$ Pa s. This phenomenon can be attributed to the increase in viscous (resistance) force, while the droplet spread with increased viscosity coefficient.

Figure 11 also shows that when the viscosity coefficient was less than 0.003 Pa s, the spread factor increased alongside the increasing viscosity coefficient. This occurred because the increase in viscous force reduced the retraction of the lamella, thus resulting in larger spread diameter. When viscosity coefficient was larger than 0.003 Pa s, however, the final spread diameter decreased with increasing viscosity coefficient—the maximum spread diameter was small when $\mu = 0.02$ Pa s, thus the final diameter was also small. For instance, when $\mu = 0.02$ Pa s, the maximum spread factor was even smaller than the final spread diameter for other viscosity coefficients. The difference between maximum spread diameter and the spread diameter after the first retraction reflects the retraction ability of the droplet. The greater the viscosity coefficient, the greater the viscous force, and thus the smaller the difference and the poorer the retraction ability of the lamella.

Figure 12 shows that the curves of spread thickness against time for different viscosities coincide before 150 μs, indicating that viscosity had almost no effect on spread thickness during initial spreading. Minimum spread thickness increased as viscosity coefficient increased, however. At viscosity coefficients larger than 0.003 Pa s, the final spread thickness increased with viscosity.

Effect of surface tension on droplet deposition

The spreading of a droplet ($D_0 = 200$ μm) impacting a spherical surface ($D_s = 600$ μm) at an initial velocity of 1.0 m s^{-1} at different surface tensions ($\sigma = 0.03$, 0.05, and 0.073 N m^{-1}) was simulated.

Figure 13 shows the temporal evolution of the droplet spread factor under different surface tensions. Surface tension had almost no effect on the spread factor at first, and thus is negligible compared to the inertia; however, it is important to note that surface tension had a significant effect on the time needed for the droplet to reach its maximum spread factor. For instance, the time needed for the droplet to reach maximum spreading decreased from 350 to about 250 μs, and the maximum spread factor decreased from 2.23 to 1.82 as surface tension increased from 0.03 to 0.073 N m^{-1}. As surface tension increased, the resistance force during droplet spreading increased, and

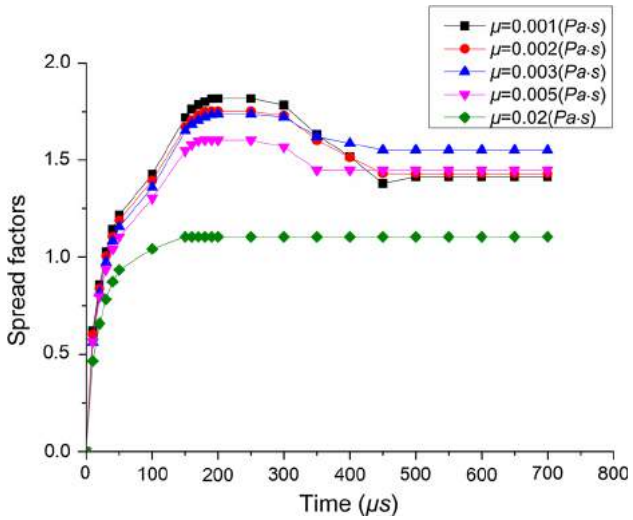

Fig. 11 Droplet spread factor for different viscosities

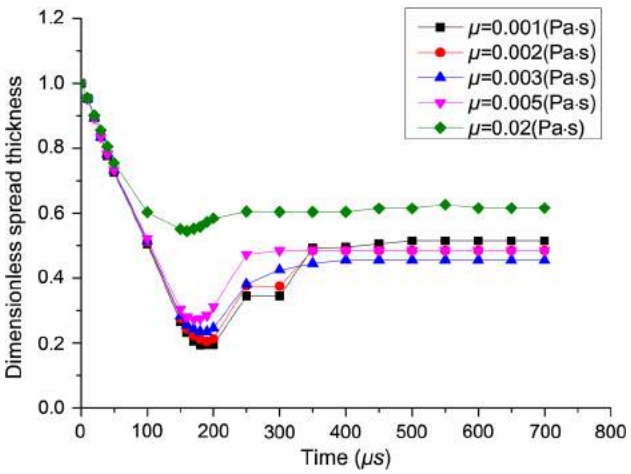

Fig. 12 Dimensionless spread thickness of droplet for different viscosities

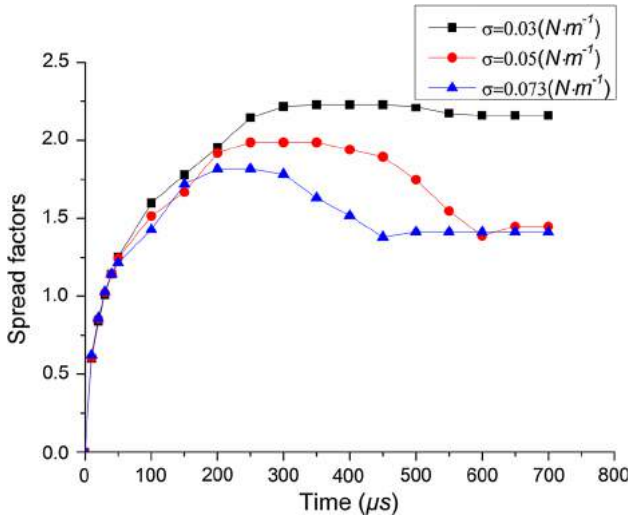

Fig. 13 Droplet spread factor for different surface tensions

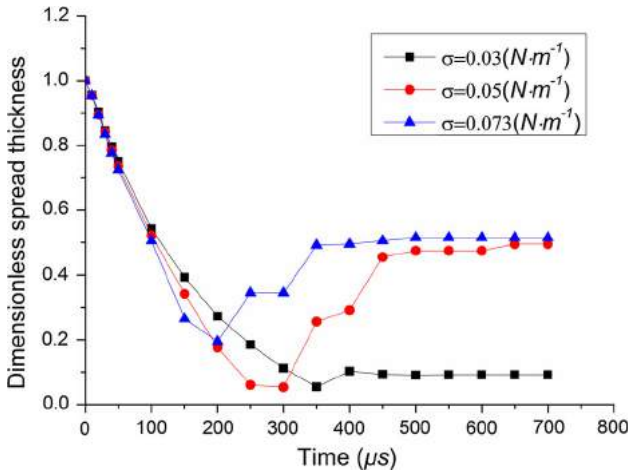

Fig. 14 Dimensionless spread thickness of droplet for different surface tensions

kinetic energy was rapidly converted into surface energy. Conversely, during the equilibrium phase, spread factor decreased significantly as the surface tension increased from 0.03 to 0.05 N m^{-1}, which can be attributed to the droplet breaking and resulting in lost surface tension energy. As surface tension increased, maximum spread diameter decreased and the retraction ability of the lamella increased. Thus, the diameter of the lamella decreased after retraction.

Figure 14 also shows that surface tension had almost no effect on dimensionless spread thickness at first. Minimum dimensionless spread thickness, as well as the dimensionless spread thickness during the equilibrium phase, increased with increasing surface tension, however. Surface tension thus shows a considerable effect on the spreading of a droplet impacting a spherical surface, especially as far as the time needed for the droplet to reach maximum spreading. As surface tension increases, maximum spread factor (as well as the time needed for the droplet to reach maximum diameter) decreases. Surface tension occurs in the direction opposite inertia, and thus inhibits the spreading of the droplet; however, it allows the retraction of the droplet once it reaches maximum diameter.

Conclusion

The most notable conclusions of this study can be summarized as follows:

(1) As impact velocity increases, the maximum spread diameter of the droplet increases, minimum spread thickness decreases, final spread diameter decreases, and final spread thickness increases. As curvature increases, maximum spread diameter increases, minimum spread thickness increases, final spread diameter increases, and final spread thickness decreases. As viscosity coefficient increases, maximum spread diameter decreases, minimum spread thickness increases, final spread diameter decreases, and final spread thickness increases. As surface tension coefficient increases, maximum spread diameter decreases, minimum spread thickness increases, final spread diameter decreases, and final spread thickness increases.

(2) Impact velocity, curvature, and viscosity coefficient have no significant effect on the time needed for the droplet to reach maximum spreading, but surface tension has a significant effect. Time needed decreases from 350 to about 250 μs as surface tension increases from 0.03 to 0.073 N m^{-1}.

(3) Dimensionless spread thickness first decreases in an approximately linear manner, and the rate of decrease is completely dictated by the impact velocity, whereas the effects of curvature, viscosity coefficient, and surface tension are negligible.

(4) When impact velocity is too high or the curvature of microspheres or biobinder surface tension is too small, the bioadhesive droplet breaks up into smaller droplets. Air at the liquid–solid interface is trapped at the moment of impact if the viscosity coefficient is too large.

Acknowledgements This project is sponsored by the National Natural Science Foundation of China, (Grant Nos. 51175432 and 50905147), the Doctor Special Science and Technological Funding of the China Ministry of Education (Grant No. 20116102110046), the Fundamental Research Funds for the Central Universities (3102014JCS05007), and the graduate starting seed fund of Northwestern Polytechnical University (Grant No. Z2015074).

References

1. Chen Biqiong (2005) Mechanical and dynamic viscoelastic properties of hydroxyapatite reinforced poly(3-caprolactone). Polym Testing 7(24):978–979
2. Mooney DJ, Baldwin DF, Suh NP (1996) Novel approach to fabricate porous sponges of ply(d, 1-lactic-co-glycolic acid) without the use of organic solvents. Biomaterials 17(14):1417–1422
3. Felicity PR, Lesley AC, David MG et al (2004) In vitro assessment of cell penetration into porous hydroxyapatite scaffolds with a central aligned channel. Biomaterials 25(1):507–514
4. Feng Z, Rho J, Han S, Ziv I (2000) Orientation and loading condition dependence of fracture toughness in cortical bone. Mater Sci Eng 11(1):41–46
5. Lin ASP, Barrows TH, Cartmell SH, Guldberg RE (2003) Microarchitectural and mechanical characteri-zation of oriented porous polymer scaffolds. Biomaterials 24(3):481–489
6. Gibson LJ (2005) Biomechanics of cellular solids. J Biomech 38:377–399
7. Roux DCD, Cooper-White JJ (2004) Dynamics of water spreading on a glass surface. Colloid Interface Sci 277:424–436
8. Luo J, Qi LH, Zhou JM, Hou XH, Li HJ (2012) Modeling and characterization of metal droplets generation by using a pneumatic drop-on-demand generator. J Mater Process Technol 212:718–726
9. Pan KL, Tseng KC, Wang CH (2010) Breakup of a droplet at high velocity impacting a solid surface. Exp Fluids 48:143–156
10. Fujimoto H, Ogino T, Takuda H et al (2001) Collision of a droplet with a hemispherical static droplet on a solid. Int J Multiph Flow 27:1227–1245
11. Cao W, Miyamoto Y (2006) Freeform fabrication of aluminum parts by direct deposition of molten aluminum. J Mater Process Technol 173:209–212
12. Yarin AL (2006) Drop impact dynamics: splashing, spreading, receding, bouncing. Annu Rev Fluid Mech 38:159–192
13. Ge Y, Fan LS (2005) Three-dimensional simulation of impingement of a Liquid droplet on a flat surface in the Leidenfrost regime. Phys Fluids 17:027104
14. Xu L (2007) Liquid drop splashing on smooth, rough, and textured surfaces. Phys Rev E 75:056316
15. Wang Y, Chen S (2015) Droplets impact on textured surfaces: mesoscopic simulation of spreading dynamics. Appl Surf Sci 327:159–167
16. Kim CS, Park S-J, Sim W, Kim Y-J, Yoo Y (2009) Modeling and characterization of an industrial inkjet head for micro-patterning on printed circuit boards. Comput Fluids 38:602–612
17. Szucs T, Brabazon D (2009) Effect of saturation and post processing on 3D printed calcium phosphate scaffolds. Key Eng Mater 396–398:663–666. doi:10.4028/0-87849-353-0.663
18. Bakshi S, Roisman IV, Tropea C (2007) Investigations on the impact of a drop onto a small spherical target. Phys Fluids 19(3):03210201–03210212
19. Li YP, Wang HR (2011) Three-dimension direct simulation of a droplet impacting onto a solid sphere with low-impact energy. Can J Chem Eng 89:83–91
20. Bolster D, Hershberger RE, Donnelly RJ (2011) Dynamic similarity, the dimensionless science. Phys Today 64:42–47
21. Qing N, Saleh T, Todd FD et al (2002) Singularity formation in free-surface Stokes flows. Contemp Math 306:147–165
22. Shen SQ, Li Y, Guo YL (2009) Numerical simulation of droplet impacting on isothermal flat solid surface. J Eng Thermophys 30:2116–2118
23. Francois M, Shyy W (2003) Computations of drop dynamics with the immersed boundary method, Part 2: drop impact and heat transfer. Numer Heat Transf 44:119–143
24. Pasandideh-fard M, Qiao YM, Chandra S et al (1996) Capillary effects during droplet impact on a solid surface. Phys Fluids 8(3):650–660

International Journal of Machine Tools & Manufacture 99 (2015) 48–67

Contents lists available at ScienceDirect

International Journal of Machine Tools & Manufacture

journal homepage: www.elsevier.com/locate/ijmactool

Generalized method for the analysis of bending, torsional and axial receptances of tool–holder–spindle assembly

Yun Yang, Wei-Hong Zhang**, Ying-Chao Ma, Min Wan*

School of Mechanical Engineering, Northwestern Polytechnical University, Xi'an, Shaanxi 710072, China

ARTICLE INFO

Article history:
Received 27 May 2015
Accepted 21 August 2015
Available online 29 August 2015

Keywords:
Frequency response functions (FRFs)
Bending
Torsional and axial receptances
Distributed tool–holder joint interface
Stability lobe diagram (SLD)
Rotating tools

ABSTRACT

Existing researches for the prediction of tool point receptances have focused on developing dedicated methods for cutting tools used in each single cutting operation such as milling and drilling processes. This paper presents a generalized method for the analysis of the tool point receptances of cutting tools suitable for being mounted on a rotating spindle. Translational and rotational dynamic responses related to all axes (*X*, *Y* and *Z*) are simultaneously modeled in a unified way to predict the tool point bending, torsional and axial receptances of all kinds of rotating tools, such as milling, drilling and boring cutters. To facilitate modeling, the tool–holder–spindle assembly is divided into four substructures, i.e., spindle–holder subassembly, shank of tool, fluted part of tool and tool–holder joint interface. The fluted part of tool is modeled as a three-dimensional Timoshenko beam with varying cross-section, while the tool–holder joint interface is regarded as a zero-thickness distributed layer and modeled as a joint substructure composed of a set of independent spring–damper elements. Assembling criterion is derived to couple the dynamic responses of all substructures to calculate the tool point receptances. Meanwhile, compared with past experimental means, a measurement procedure to eliminate the adapter's mass effect on torsional and axial receptances is designed. The proposed method is experimentally proven for two kinds of rotating tools, i.e., mills and drills.

© 2015 Elsevier Ltd. All rights reserved.

1. Introduction

Self-excited vibrations caused by regeneration of waviness [1], also known as regenerative chatter, result in unstable cutting process, poor surface finish, reduced productivity and damage on machine tools and cutters. In the past several decades, many efforts [2–8] were made by predicting stability lobe diagrams (SLDs) to select the chatter-free cutting process parameters. Reliable SLDs always require accurate frequency response function (FRF) of tool point. Usually, FRF of tool point is experimentally obtained by standard impact testing. This kind of means has two typical characteristics that may limit its wide applications in machining industries. First, it is strongly dependent on the combinations of tool, holder and spindle; hence, repeated and time-consuming measurements should be conducted once the sizes or materials of holder and tool change. Second, measurement of FRF is almost impractical for small-scale cutters widely used in micro- and nanomachining field. To this end, development of generalized computing methods becomes a vital alternative to predict the tool point receptance of the tool–holder–spindle assembly. The practical procedure to realize this can be described as follows:

(i) Divide the tool–holder–spindle system into some substructures.
(ii) Measure the receptance of the substructures that are difficult to be modeled theoretically, such as the spindle.
(iii) Model the dynamic response of the remaining substructures that are easy to be analyzed, such as tool and holder.
(iv) Establish criterion to couple the results obtained from Steps (ii) and (iii).

Regarding this technique, research kernel is how to divide the substructures (Step i) and how to establish the theoretical model of the substructures that could be analyzed (Step iii). Schmitz et al. [9] are the earlier researchers to study this topic and treated the tool–holder–

* The first corresponding author. Tel.: +86 29 88493914-1212; fax: +86 29 88495774.
** The second corresponding author. Tel./fax: +86 29 88495774.
E-mail addresses: zhangwh@nwpu.edu.cn (W.-H. Zhang), m.wan@nwpu.edu.cn (M. Wan).

http://dx.doi.org/10.1016/j.ijmachtools.2015.08.004
0890-6955/© 2015 Elsevier Ltd. All rights reserved.

Nomenclature

Matrix and vector

$\mathbf{H}_H(\omega)$ the frequency response function (FRF) matrix of the spindle–holder subassembly with ω being the angular frequency

$\mathbf{M}_c$ the mass matrix associated with the N_c nodes of the component c, where c=S or F

$\mathbf{C}_c$ the damping and stiffness matrices associated with the N_c nodes of the component c, where c=S, F or TH

$\mathbf{K}_c$ the stiffness matrices associated with the N_c nodes of the component c, where c=S, F or TH

$\mathbf{Q}_c = [\mathbf{q}_{c,1}^T, \mathbf{q}_{c,2}^T, \ldots, \mathbf{q}_{c,N_c}^T]^T$ denotes the displacements vector of the component c related to N_c nodes with c=H, S or F

$\mathbf{q}_{c,i} = [u_{c,i}, v_{c,i}, w_{c,i}, \theta_{c,i}, \phi_{c,i}, \psi_{c,i}]^T$ denotes the displacements vector of ith node of the component c, where $u_{c,i}$, $v_{c,i}$, $w_{c,i}$, $\theta_{c,i}$, $\phi_{c,i}$ and $\psi_{c,i}$ (c=H, S, or F) designate translational and angular displacements of ith node of the component c related to X, Y and Z axes, respectively

$\mathbf{F}_{c-\tilde{c}} = [\mathbf{f}_{c-\tilde{c},1}^T, \mathbf{f}_{c-\tilde{c},2}^T, \ldots, \mathbf{f}_{c-\tilde{c},N_c}^T]^T$ denotes the loads vector corresponding to the N_c nodes at the component c, and they are applied by the component $\tilde{c}$ (c=H, S or F; $\tilde{c}$ = H, S, F or TH and $\tilde{c} \neq c$)

$\mathbf{f}_{c-\tilde{c},i} = [f_{x,c-\tilde{c},i}, f_{y,c-\tilde{c},i}, f_{z,c-\tilde{c},i}, M_{x,c-\tilde{c},i}, M_{y,c-\tilde{c},i}, M_{z,c-\tilde{c},i}]^T$ denotes the loads vector corresponding to ith node at the component c, and they are applied by the component $\tilde{c}$, where $f_{x,c-\tilde{c},i}$, $f_{y,c-\tilde{c},i}$, $f_{z,c-\tilde{c},i}$, $M_{x,c-\tilde{c},i}$, $M_{y,c-\tilde{c},i}$ and $M_{z,c-\tilde{c},i}$ (c=H, S or F; $\tilde{c}$ = H, S, F or TH and $\tilde{c} \neq c$) designate the forces and moments applied on the ith node of the component c related to X, Y and Z) axes, respectively, and they are applied by the component $\tilde{c}$

Subscript

H the spindle–holder subassembly

S the shank of tool component

F the fluted part of tool component

TH the tool–holder joint interface component

spindle assembly as two substructures consisting of a spindle–holder subassembly, whose FRFs were experimentally measured, and an overhung part of tool, whose receptance was modeled by analytically considering its translational response. They proposed a receptance coupling substructure analysis (RCSA) procedure by which the analytical dynamic response of the overhung part of tool was coupled with the experimentally determined receptance of the spindle–holder subassembly to predict the tool point receptances.

Since RCSA was successfully applied to machining process, there are also some follow-up studies that divided tool–holder–spindle assembly into two substructures [10–14] or three substructures [15–21]. Actually, no matter how to divide, the key issue lies in reliably modeling the dynamic response of the substructures that could be analyzed. On the improvement of modeling accuracy, the past literature has mainly been on including the effect of rotational dynamic responses related to bending vibration [10,19,13], considering the shear deformation of tool and holder [14,16,17,21], and determining stiffness and damping properties of joint interfaces [11,12,18–20,22].

Park et al. [10] pointed out that besides the translational response used by Schmitz et al. [9], rotational degree of freedom also has important influence on the receptance of the tool point, and derived theoretical equations to analytically calculate tool point FRFs by considering translational and rotational dynamic responses related to X- and Y-axes. Albertelli et al. [13] used finite difference method to identify the translational and rotational receptances of the spindle–holder subassembly. Some other researchers [14,16,17,21] used Timoshenko beam theory to study the influences of shear deformation on the tool point FRFs, and found that the prediction accuracy at high frequency can be improved if shear deformations of tool and holder are well included. Specifically, Ozsahin and Altintas [21] studied the influence of tools' asymmetry on tool point receptances by considering the second moment of inertia of fluted tools. Mancisidor et al. [14] predicted the tool point dynamics using Timoshenko beam with fixed boundaries and pointed out that the cut-off frequency problem could be overcome by this approach in the receptance coupling procedure.

On the other hand, since the tool–holder–spindle system has been divided into many substructures, how to model the interfaces between different substructures is another important issue needed to be solved in FRFs prediction procedure. Schmitz et al. [18] developed multiple connection models for the tool–holder interface, and employed finite element method to determine the position-dependent stiffness and equivalent viscous damping values for thermal shrink fit holders. Ahmadi and Ahmadian [12] combined the measured FRFs of holder–spindle and analytical models of the tool via a distributed damped-elastic spindle–holder interface. Ahmadian and Nourmohammadi [20] separately analyzed tool, holder and spindle and synthesized dynamics of these three substructures. Park and Chae [22] utilized Euler–Bernoulli beam to calculate the tool point receptances of modular cutting tools including the dynamic effect of fastener joint, which was identified by using both analytical and experimental dynamic response.

It should be highlighted that the above work is mostly focused upon the prediction of the tool point bending receptances that are only associated with translational and rotational dynamic responses related to X- and Y-axes. This is generally sufficient for peripheral milling since its dynamic chatter problem is mainly bending instability. However, both the bending and axial receptances of tool–holder–spindle assemblies become important in ball end milling, bull-nose end milling and plunge milling applications [23,24]. What's more, the combined torsional–axial dynamics, as well as bending responses, are essential for drilling dynamics analysis [25,26]. That is, besides bending receptances, translational and rotational dynamic responses related to Z-axis has also aroused interests among researchers [27–31].

Schmitz [27] is the first scholar who took into account the translational and rotational dynamic responses related to all axes (X, Y and Z) in an extended RCSA method for the prediction of tool point FRFs in a tool–holder–spindle system. In this work [27], both the tool fluted geometry and the physical properties of joint interfaces, i.e., stiffness and damping, were not considered in the simulation model. Filiz and Ozdoganlar [28–30] investigated the effect of actual fluted geometry on free–free bending, torsional and axial vibrations of cutting tools, which were not amounted in the spindle. This theoretical model [28–30] was further extended by Bediz et al. [31] to predict the bending receptances of end milling tool in a tool–holder–spindle assembly. On the aspect of experimental study, only Schmitz [27] measured the tool point torsional and axial receptances to verify his theoretical model using a homemade additional adapter, which provided surfaces to

enable excitations of tools and measurements of the resulting vibrations, but the negative effect of the adapter's mass on measurements was not eliminated.

In summary, the state of the art about the obtaining methods of bending, torsional and axial receptances of tool–holder–spindle assembly is as follows:

- The only theoretical work [27] comprehensively revealing bending, torsional and axial receptances was mainly conducted for tools, whose actual fluted geometry was not modeled in the prediction procedure. Moreover, the interfaces between substructures were treated as rigid connection, and thus the stiffness and damping properties were not included in prediction.
- The modeling work [31] that considered the fluted geometry of tool was only carried out to predict the bending receptances of end milling cutters, while the torsional and axial receptances usually appearing in drilling system were not included.
- Since it is very difficult to directly measure the tool point torsional receptance of drills with small sizes, additional adapter was often used for assistance in practical measurement [27]. However, how to eliminate adapter's mass effect on measured results has not been reported in the literature.

Hence, these factors motivate the development of computing method as well as measurement method that can obtain the tool point bending, torsional and axial receptances of a tool–holder–spindle assembly in this paper. Originality lies in comprehensively modeling the actual physical properties of the complex assembly, such as fluted geometry of tools and joint interfaces, and how it is formulated to reveal the three-dimensional receptances including translational and rotational dynamic responses related to all axes (X, Y and Z) in a generalized manner so that it can be suitable for all kinds of cutting tools. Contributions of this work are highlighted in the following two aspects:

- Both the actual fluted geometry of tools and the physical properties of joint interfaces between substructures are included to establish generalized model that can predict the dynamic receptances for rotating tools.
- Experimental method including correction algorithm, which can well eliminate the additional adapter's mass effect, is developed to measure the tool point torsional and axial receptances.

The paper is organized as follows. The generalized geometry of rotating tools is summarized in Section 2. The generalized model that can both calculate the bending receptances often occurring in end milling process, and the torsional and axial receptances related to hole making process, is derived in Section 3. The tool–holder–spindle assembly is divided into four substructures, i.e., spindle–holder sub-assembly, shank of tool, fluted part of tool and tool–holder joint interface. The tool fluted geometry with varying cross-section is modeled by Timoshenko beam theory, while the tool–holder joint interface is considered as distributed damped-elastic layer. Detailed assembling criterion involving the receptances of all substructures is formulated to obtain the final tool point FRFs. Experimental method for the measurement of torsional and axial receptances is designed in Section 4. Correction algorithm for the elimination of the negative effect of adapter's mass on measurements is formulated. The accuracy and the generality of the established model are experimentally validated in Section 5 using both mills and drills.

2. Generalized geometry of rotating tools in spindle–holder system

Rotating tools refer to the cutters that can be mounted in rotating spindles. Fig. 1(a)–(e) shows some typical rotating tools, such as helix end mill, twist drill bit, taps and reamer. As can be seen from Fig. 1, each tool has dedicated and different sizes to ensure its machining function. For example, the fluted part of a drill is definitely different from that of a tap, as shown in Fig. 1(b) and (c). Thus, strictly speaking, these kinds of rotating tools cannot be theoretically defined in a general way to exactly reconstruct their shapes. However, the topic on tool dynamic response is mostly influenced by the structure's total configuration and not sensitive enough to the local geometry. In this sense, detailed local geometry such as small chamfer of reamer or thread form of tap does not significantly influence the tool point receptance. This means that in the analysis procedure of receptances, the local geometry of tool can be simplified to facilitate modeling.

Based on the understanding above, the geometry of rotating tools are modeled in a simplified and generalized way for the convenience of the analysis of tool dynamic response in this paper. The basic principle for simplification is that the complex fluted part is treated as a flat end mill-like envelope with equivalent nominal diameter, by ignoring its local geometrical details such as taper angle, point angle or threads, and other parts of the tool keep their designed shapes since they are relatively simple. According to this principle, tools mounted in rotating spindles can be generally described by the geometrical model shown in Fig. 1(f), in which nine parameters, i.e., L_S, D_S, L_{F1}, D_{F1}, L_{F2}, D_{F2}, β_H, L_{F3} and L_{F4}, are used to construct the cutter geometry. Here, L_S and D_S are the length and the diameter of the shank of tool, which is clamped in the holder. L_{F1} and D_{F1} are the length and the nominal diameter of fluted part with cutting edges. L_{F2} and D_{F2} are the length and the nominal diameter of fluted part without cutting edges. β_H is the helix angle of fluted part. L_{F3} and L_{F4} are the length of two transition parts between shank and fluted part. Distinct cutter geometries can be deduced from the general model when particular values are attributed to these parameters. For example, the parameters $\{D_S, D_{F1}, D_{F2}, \beta_H, L_{F1}, L_{F2}, L_{F3}, L_{F4}, L_S\}$ will be chosen as $\{D_S, D_{F1}, D_{F2}, \beta_H, L_{F1}, 0, 0, 0, L_S\}$ and $\{D_S, D_{F1}, D_{F2}, 0, L_{F1}, L_{F2}, 0, L_{F4}, L_S\}$ for the helical end mill and straight-flute tap, respectively.

The generalized geometric model is merged into the following section aiming at developing generalized dynamic method for receptance analysis.

3. Generalized modeling of 3D tool point dynamics

In this paper, the tool–holder–spindle assembly is divided into some substructures and the final tool point receptance is obtained by assembling the dynamic responses of the substructures. Fig. 2 schematically shows the typical structure of a tool–holder–spindle

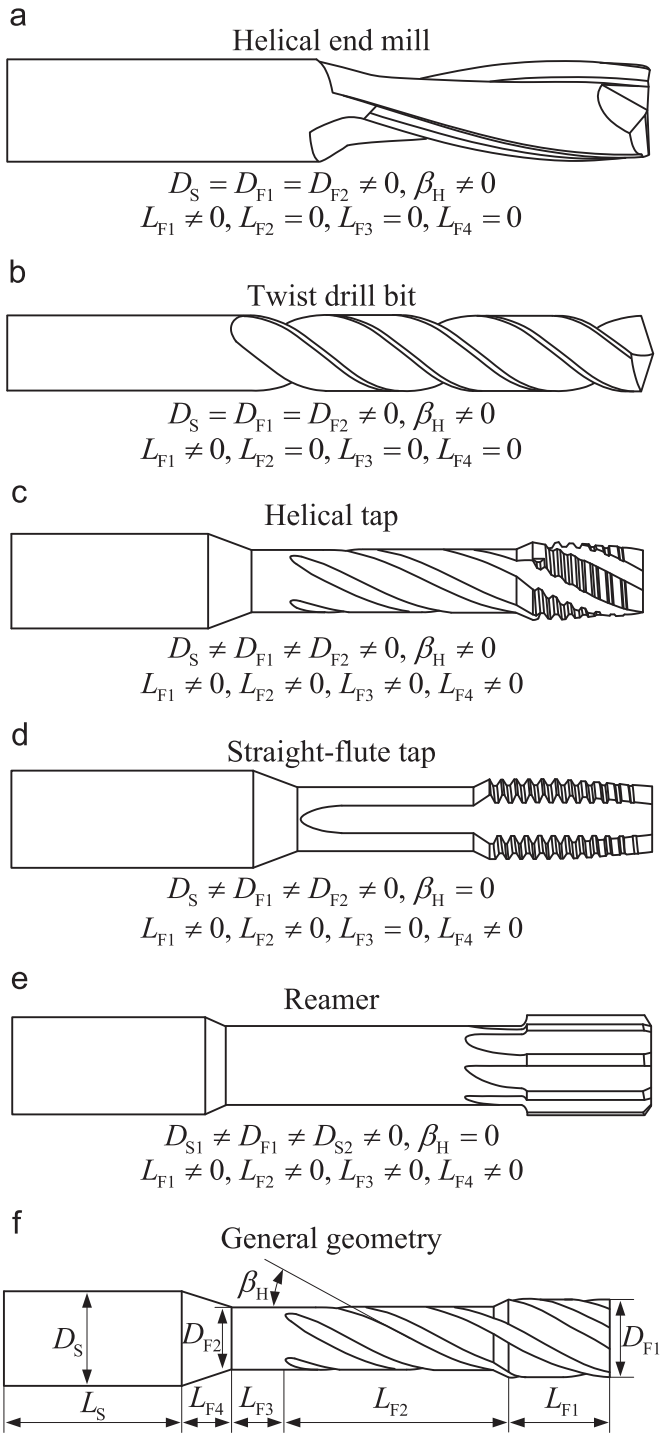

Fig. 1. Generalized geometry of rotating tools.

assembly, which is separated into four substructure, i.e., the spindle–holder subassembly (SHS), the shank of tool component (STC), the fluted part of tool component (FPTC) and the tool–holder joint interface component (THJIC). The relationship among substructures is detailed in Fig. 3. The tool rests on the holder via the tool–holder joint interface. The joint interface is regarded as a zero-thickness damped-elastic distributed layer.

In the following subsections, the dynamic equation of each component will be introduced first. They are then assembled based on substructure synthesis technique. Finally, the tool point bending, torsional and axial receptances are extracted from the receptance matrix of the assembly.

3.1. Dynamics of the spindle–holder subassembly

The spindle–holder subassembly is divided into $(N_H - 1)$ number of elements with equivalent axial length and contacts with tool–holder joint

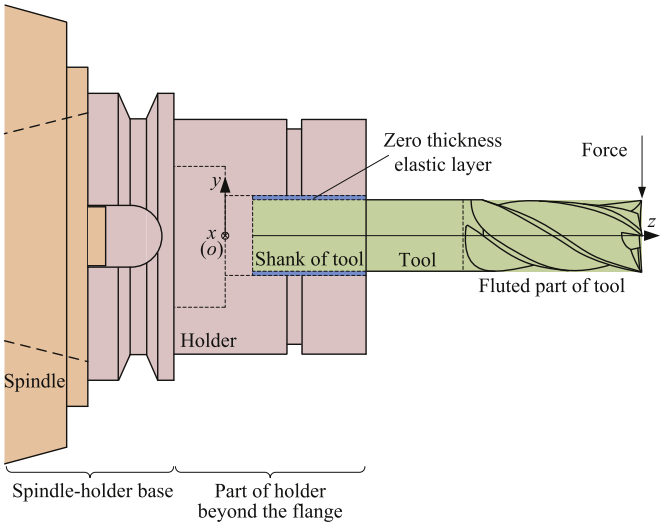

Fig. 2. Tool–holder–spindle assembly.

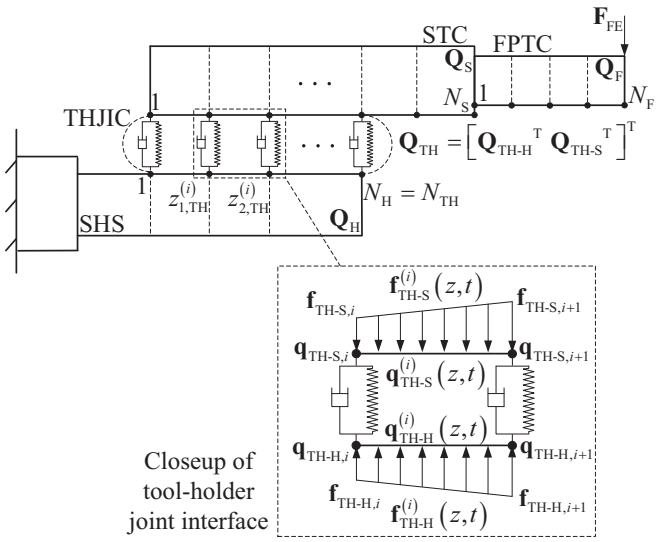

Fig. 3. Schematic view of tool–holder–spindle assembly.

interface component trough N_H number of nodes, as shown in Fig. 3. Dynamics of the spindle–holder subassembly yields the following equation:

$$\mathbf{Q}_H(\omega) = \mathbf{H}_H(\omega)\mathbf{F}_{H-TH}(\omega) \tag{1}$$

in which matrix $\mathbf{H}_H(\omega)$ is obtained by RCSA in this paper.

3.2. Dynamics of the fluted tool considering actual geometry

The shank of tool is divided into $(N_S - 1)$ number of elements with $N_S > N_H$, as shown in Fig. 3. Note that the 1st to $(N_H - 1)$ th shank elements have exact correspondence to those of the holder–spindle subassembly. The fluted part of tool is divided into $(N_F - 1)$ elements. The N_S th node of the shank geometrically corresponds to the 1st node of the fluted part, as shown in Fig. 3. Dynamics of the shank of tool component and the fluted part of tool component can be expressed as

$$\begin{aligned}\mathbf{M}_S\ddot{\mathbf{Q}}_S(t) + \mathbf{C}_S\dot{\mathbf{Q}}_S(t) + \mathbf{K}_S\mathbf{Q}_S(t) &= \mathbf{F}_{S-TH}(t) + \mathbf{F}_{S-F}(t)\\ \mathbf{M}_F\ddot{\mathbf{Q}}_F(t) + \mathbf{C}_F\dot{\mathbf{Q}}_F(t) + \mathbf{K}_F\mathbf{Q}_F(t) &= \mathbf{F}_{F-S}(t) + \mathbf{F}_{FE}(t)\end{aligned} \tag{2}$$

where $\mathbf{F}_{FE}(t) = [\mathbf{f}_{FE,1}(t)^T, \mathbf{f}_{FE,2}(t)^T, \ldots, \mathbf{f}_{FE,N_F}(t)^T]^T$ denote the external force vector on the nodes of the fluted part of tool component. $\mathbf{f}_{FE,i} = [f_{xFE,i}, f_{yFE,i}, f_{zFE,i}, M_{xFE,i}, M_{yFE,i}, M_{zFE,i}]^T$. $f_{xFE,i}$, $f_{yFE,i}$, $f_{zFE,i}$, $M_{xFE,i}$, $M_{yFE,i}$ and $M_{zFE,i}$ designate the external forces and moments applied on the ith node of the fluted part of tool component related to X, Y and Z axes, respectively.

In the following contents, details on how to calculate $\mathbf{M}_c$, $\mathbf{C}_c$ and $\mathbf{K}_c$ (c=S or F) will be given. The mass and stiffness matrices, i.e., $\mathbf{M}_c$ and

$\mathbf{K}_c$ (c=S or F), are generated as follows by assembling all elemental mass and stiffness matrices:

$$\mathbf{M}_c = \begin{bmatrix} \mathbf{M}_{c11}^{(1)} & \mathbf{M}_{c12}^{(1)} & & & & & & \\ \mathbf{M}_{c21}^{(1)} & \mathbf{M}_{c22}^{(1)} + \mathbf{M}_{c11}^{(2)} & \mathbf{M}_{c12}^{(2)} & & & & & \\ & \mathbf{M}_{c21}^{(2)} & \mathbf{M}_{c22}^{(2)} + \mathbf{M}_{c11}^{(3)} & \mathbf{M}_{c12}^{(3)} & & & & \\ & & \ddots & \ddots & \ddots & & & \\ & & & \mathbf{M}_{c21}^{(N_c-1)} & \mathbf{M}_{c22}^{(N_c-1)} + \mathbf{M}_{c11}^{(N_c)} & \mathbf{M}_{c12}^{(N_c)} & & \\ & & & & \mathbf{M}_{c21}^{(N_c)} & \mathbf{M}_{c22}^{(N_c)} & & \end{bmatrix} \tag{3}$$

$$\mathbf{K}_c = \begin{bmatrix} \mathbf{K}_{c11}^{(1)} & \mathbf{K}_{c12}^{(1)} & & & & & & \\ \mathbf{K}_{c21}^{(1)} & \mathbf{K}_{c22}^{(1)} + \mathbf{K}_{c11}^{(2)} & \mathbf{K}_{c12}^{(2)} & & & & & \\ & \mathbf{K}_{c21}^{(2)} & \mathbf{K}_{c22}^{(2)} + \mathbf{K}_{c11}^{(3)} & \mathbf{K}_{c12}^{(3)} & & & & \\ & & \ddots & \ddots & \ddots & & & \\ & & & \mathbf{K}_{c21}^{(N_c-1)} & \mathbf{K}_{c22}^{(N_c-1)} + \mathbf{K}_{c11}^{(N_c)} & \mathbf{K}_{c12}^{(N_c)} & & \\ & & & & \mathbf{K}_{c21}^{(N_c)} & \mathbf{K}_{c22}^{(N_c)} & & \end{bmatrix} \tag{4}$$

with

$$\begin{bmatrix} \mathbf{M}_{c11}^{(i)} & \mathbf{M}_{c12}^{(i)} \\ \mathbf{M}_{c21}^{(i)} & \mathbf{M}_{c22}^{(i)} \end{bmatrix} = \mathbf{M}_c^{(i)} = \rho A_c^{(i)} L_c^{(i)}$$

$$\left[\begin{array}{cccccc|cccccc} a_{1y,c}^{(i)} & 0 & 0 & 0 & a_{3y,c}^{(i)} & 0 & a_{2y,c}^{(i)} & 0 & 0 & 0 & -a_{4y,c}^{(i)} & 0 \\ & a_{1x,c}^{(i)} & 0 & -a_{3x,c}^{(i)} & 0 & 0 & 0 & a_{2x,c}^{(i)} & 0 & a_{4x,c}^{(i)} & 0 & 0 \\ & & \frac{1}{3} & 0 & 0 & 0 & & 0 & \frac{1}{6} & 0 & 0 & 0 \\ & & & a_{5x,c}^{(i)} & 0 & 0 & 0 & -a_{4x,c}^{(i)} & 0 & -a_{6x,c}^{(i)} & 0 & 0 \\ & & & & a_{5y,c}^{(i)} & 0 & a_{4y,c}^{(i)} & 0 & 0 & 0 & -a_{6y,c}^{(i)} & 0 \\ & & & & & \frac{I_{z,c}^{(i)}}{3A_c^{(i)}} & 0 & 0 & 0 & 0 & 0 & \frac{I_{z,c}^{(i)}}{6A_c^{(i)}} \\ \hline & & & & & & a_{1y,c}^{(i)} & 0 & 0 & 0 & -a_{3y,c}^{(i)} & 0 \\ & & & & & & & a_{1x,c}^{(i)} & 0 & a_{3x,c}^{(i)} & 0 & \\ & & & & & & & & \frac{1}{3} & 0 & & 0 \\ & & & & & & & & & a_{5x,c}^{(i)} & 0 & 0 \\ & & & & & & & & & & a_{5y,c}^{(i)} & 0 \\ & & & & & & & & & & & \frac{I_{z,c}^{(i)}}{3A_c^{(i)}} \end{array}\right]$$

Symmetric

$$\begin{bmatrix} \mathbf{K}_{c11}^{(i)} & \mathbf{K}_{c12}^{(i)} \\ \mathbf{K}_{c21}^{(i)} & \mathbf{K}_{c22}^{(i)} \end{bmatrix} = \mathbf{K}_c^{(i)} =$$

$$\left[\begin{array}{cccccc|cccccc}
b_{1y,c}^{(i)} & 0 & 0 & 0 & b_{3y,c}^{(i)} & 0 & -b_{1y,c}^{(i)} & 0 & 0 & 0 & b_{3y,c}^{(i)} & 0 \\
 & b_{1x,c}^{(i)} & 0 & -b_{3x,c}^{(i)} & 0 & 0 & 0 & -b_{1x,c}^{(i)} & 0 & -b_{3x,c}^{(i)} & 0 & 0 \\
 & & \dfrac{A_c^{(i)}E}{L_c^{(i)}} & 0 & 0 & 0 & 0 & 0 & \dfrac{-A_c^{(i)}E}{L_c^{(i)}} & 0 & & 0 \\
 & & & b_{2x,c}^{(i)} & 0 & 0 & 0 & b_{3x,c}^{(i)} & 0 & b_{4x,c}^{(i)} & 0 & 0 \\
 & & & & b_{2y,c}^{(i)} & 0 & -b_{3y,c}^{(i)} & 0 & 0 & 0 & b_{4y,c}^{(i)} & 0 \\
 & & & & & \dfrac{GI_{z,c}^{(i)}}{L_c^{(i)}} & 0 & 0 & 0 & 0 & 0 & \dfrac{-GI_{z,c}^{(i)}}{L_c^{(i)}} \\
\hline
 & & & & & & b_{1y,c}^{(i)} & 0 & 0 & 0 & -b_{3y,c}^{(i)} & 0 \\
 & \text{Symmetric} & & & & & & b_{1x,c}^{(i)} & 0 & b_{3x,c}^{(i)} & 0 & 0 \\
 & & & & & & & & \dfrac{A_c^{(i)}E}{L^{(i)}} & 0 & 0 & 0 \\
 & & & & & & & & & b_{2x,c}^{(i)} & 0 & 0 \\
 & & & & & & & & & & b_{2y,c}^{(i)} & 0 \\
 & & & & & & & & & & & \dfrac{GI_{z,c}^{(i)}}{L_c^{(i)}}
\end{array}\right]$$

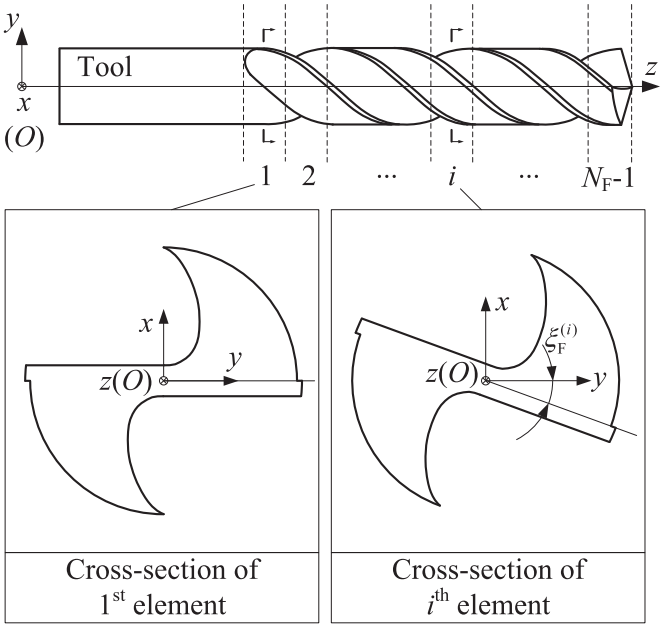

Fig. 4. Modeling of the fluted part.

where E, G and ρ are Young's modulus, shear modulus and density of the tool materials. $A_c^{(i)}$, $L_c^{(i)}$ and $J_c^{(i)}$ are the cross-section area, the element length and polar area moment of inertia related to the ith element of shank or fluted part. $a_{k,l,c}^{(i)}$ and $b_{k,l,c}^{(i)}$ (k=1, 2, 3, 4, 5 or 6;

$\tilde{k}$ = 1, 2, 3 or 4; l=x or y) are derived by using Timoshenko beam [32] as follows:

$$a_{1,l,c}^{(i)}(r_{l,c}^{(i)}, \varphi_{l,c}^{(i)}) = \frac{\frac{13}{35} + \frac{7}{10}\varphi_{l,c}^{(i)} + \frac{1}{3}\varphi_{l,c}^{(i)^2} + \frac{6}{5}\left(\frac{r_{l,c}^{(i)}}{L_c^{(i)}}\right)^2}{(1+\varphi_{l,c}^{(i)})^2} a_{2,l,c}^{(i)}(r_{l,c}^{(i)}, \varphi_{l,c}^{(i)}) = \frac{\frac{9}{70} + \frac{3}{10}\varphi_{l,c}^{(i)} + \frac{1}{6}\varphi_{l,c}^{(i)^2} - \frac{6}{5}\left(\frac{r_{l,c}^{(i)}}{L_c^{(i)}}\right)^2}{(1+\varphi_{l,c}^{(i)})^2}$$

$$a_{3,l,c}^{(i)}(r_{l,c}^{(i)}, \varphi_{l,c}^{(i)}) = \frac{\left(\frac{11}{210} + \frac{11}{120}\varphi_{l,c}^{(i)} + \frac{1}{24}\varphi_{l,c}^{(i)^2} + \left(\frac{1}{10} - \frac{1}{2}\varphi_{l,c}^{(i)}\right)\left(\frac{r_{l,c}^{(i)}}{L_c^{(i)}}\right)^2\right)L_c^{(i)}}{(1+\varphi_{l,c}^{(i)})^2}$$

$$a_{4,l,c}^{(i)}(r_{l,c}^{(i)}, \varphi_{l,c}^{(i)}) = \frac{\left(\frac{13}{420} + \frac{3}{40}\varphi_{l,c}^{(i)} + \frac{1}{24}\varphi_{l,c}^{(i)^2} - \left(\frac{1}{10} - \frac{1}{2}\varphi_{l,c}^{(i)}\right)\left(\frac{r_{l,c}^{(i)}}{L_c^{(i)}}\right)^2\right)L_c^{(i)}}{(1+\varphi_{l,c}^{(i)})^2}$$

$$a_{5,l,c}^{(i)}(r_{l,c}^{(i)}, \varphi_{l,c}^{(i)}) = \frac{\left(\frac{1}{105} + \frac{1}{60}\varphi_{l,c}^{(i)} + \frac{1}{120}\varphi_{l,c}^{(i)^2} + \left(\frac{2}{15} + \frac{1}{6}\varphi_{l,c}^{(i)} + \frac{1}{3}\varphi_{l,c}^{(i)^2}\right)\left(\frac{r_{l,c}^{(i)}}{L_c^{(i)}}\right)^2\right)L_c^{(i)^2}}{(1+\varphi_{l,c}^{(i)})^2}$$

$$a_{6,l,c}^{(i)}(r_{l,c}^{(i)}, \varphi_{l,c}^{(i)}) = \frac{\left(\frac{1}{140} + \frac{1}{60}\varphi_{l,c}^{(i)} + \frac{1}{120}\varphi_{l,c}^{(i)^2} + \left(\frac{1}{30} + \frac{1}{6}\varphi_{l,c}^{(i)} - \frac{1}{6}\varphi_{l,c}^{(i)^2}\right)\left(\frac{r_{l,c}^{(i)}}{L_c^{(i)}}\right)^2\right)L_c^{(i)^2}}{(1+\varphi_{l,c}^{(i)})^2}$$

$$b_{1,l,c}^{(i)}(I_{l,c}^{(i)}, \varphi_{l,c}^{(i)}) = \frac{48EI_{l,c}^{(i)} + 4k'GA_c^{(i)}\varphi_{l,c}^{(i)^2}L_c^{(i)^2}}{4L_c^{(i)^3}(1+\varphi_{l,c}^{(i)})^2}$$

$$b_{2,l,c}^{(i)}(I_{l,c}^{(i)}, \varphi_{l,c}^{(i)}) = \frac{(16 + 8\varphi_{l,c}^{(i)} + 4\varphi_{l,c}^{(i)^2})EI_{l,c}^{(i)}L_c^{(i)^2} + k'GA^{(i)}\varphi_{l,c}^{(i)^2}L_c^{(i)^4}}{4L_c^{(i)^3}(1+\varphi_{l,c}^{(i)})^2}$$

$$b_{3,l,c}^{(i)}(I_{l,c}^{(i)}, \varphi_{l,c}^{(i)}) = \frac{24EI_{l,c}^{(i)}L_c^{(i)} + 2k'GA_c^{(i)}\varphi_{l,c}^{(i)^2}L_c^{(i)^3}}{4L_c^{(i)^3}(1+\varphi_{l,c}^{(i)})^2}$$

$$b_{4,l,c}^{(i)}(I_{l,c}^{(i)}, \varphi_{l,c}^{(i)}) = \frac{(8 - 8\varphi_{l,c}^{(i)} - 4\varphi_{l,c}^{(i)^2})EI_{l,c}^{(i)}L_c^{(i)^2} + k'GA_c^{(i)}\varphi_{l,c}^{(i)^2}L_c^{(i)^4}}{4L_c^{(i)^3}(1+\varphi_{l,c}^{(i)})^2}$$

with

$$\varphi_{l,c}^{(i)} = \frac{12EI_{l,c}^{(i)}}{k'GA_c^{(i)}L_c^{(i)^2}},$$

$$r_{l,c}^{(i)} = \sqrt{\frac{I_{l,c}^{(i)}}{A_c^{(i)}}},$$

where $I_{l,c}^{(i)}$ is the moment inertia of cross-section area normal to direction l (l=x or y) of the ith element of shank or fluted part and k' is the shear coefficient which depends on the cross-section shape and Poisson's ratio ν and is calculated by the method proposed in [33].

In above equations, the critical variables are the moment inertia of cross-section area $I_{l,c}^{(i)}$ and area of cross-section $A_c^{(i)}$, which are calculated by the following procedures.

(i) For arbitrary element of shank of tool or transition parts $I_{l,S}^{(i)}$ and $A_S^{(i)}$ can be calculated as

$$I_{l,S}^{(i)} = \frac{\pi D_S^{(i)^4}}{64}$$

$$A_S^{(i)} = \frac{\pi D_S^{(i)^2}}{4} \tag{5}$$

with $D_S^{(i)}$ being the diameter of ith element of shank of tool or transition parts.

(ii) *For fluted part of tool*

Since the cross-section of the fluted part of tool is relatively complex, the moment inertia of cross-section area and area of cross-section, i.e., $I_{l,F}^{(i)}$ and $A_F^{(i)}$, cannot be analytically calculated. In this section, a CAD software-based method will be described in detail.

Due to the existence of helix angle, $I_{l,F}^{(i)}$ may change as the ith element varies along the axis of cuter. Thus, for each element, $I_{l,F}^{(i)}$ can be calculated either by directly using CAD software or by utilizing the following approximate means.

The basic principle is that based on several elemental moments of inertia of cross-section directly calculated from CAD software,

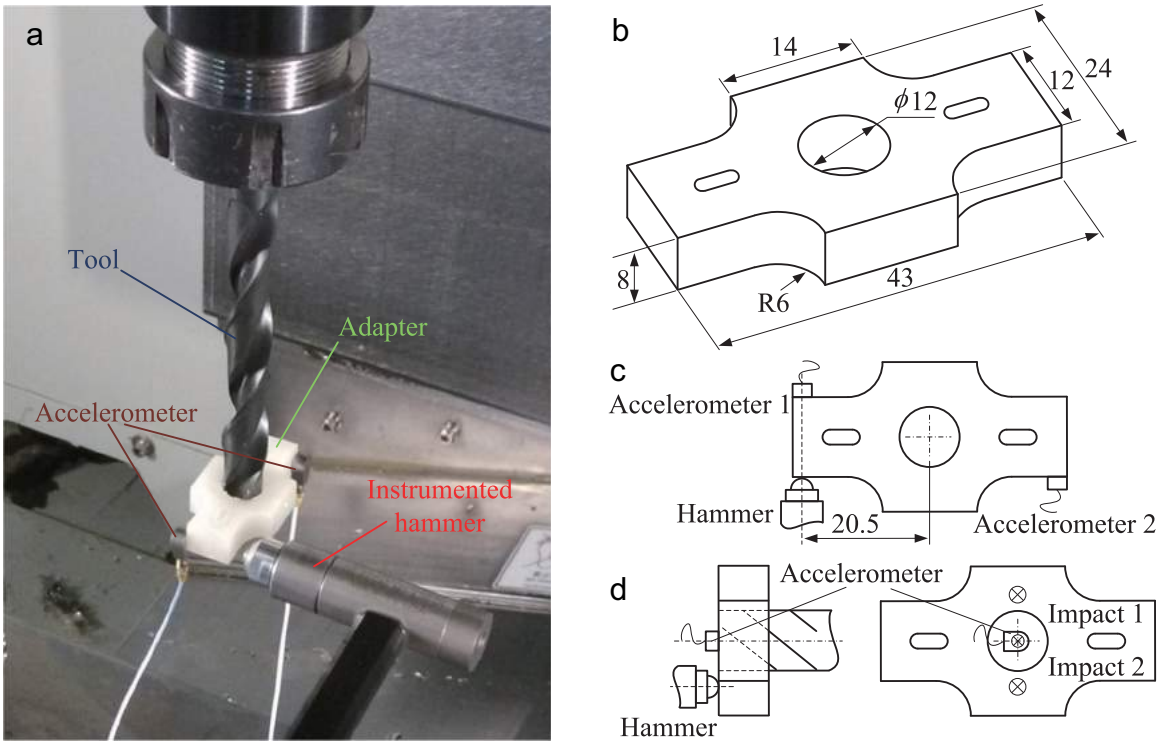

Fig. 5. Measurements for tool point torsional and axial receptances: (a) the setup to measure tool point receptances; (b) geometries of the measurement adapter; (c) torsional receptance measurements and (d) axial receptance measurements.

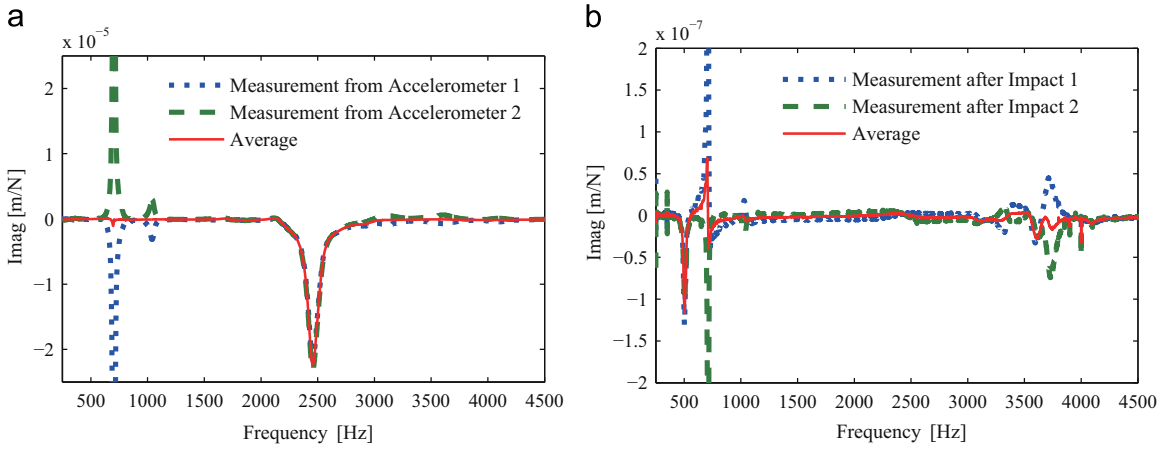

Fig. 6. Examples of canceling bending modes in measurement of torsional and axial receptances: (a) torsional receptances and (b) axial receptances.

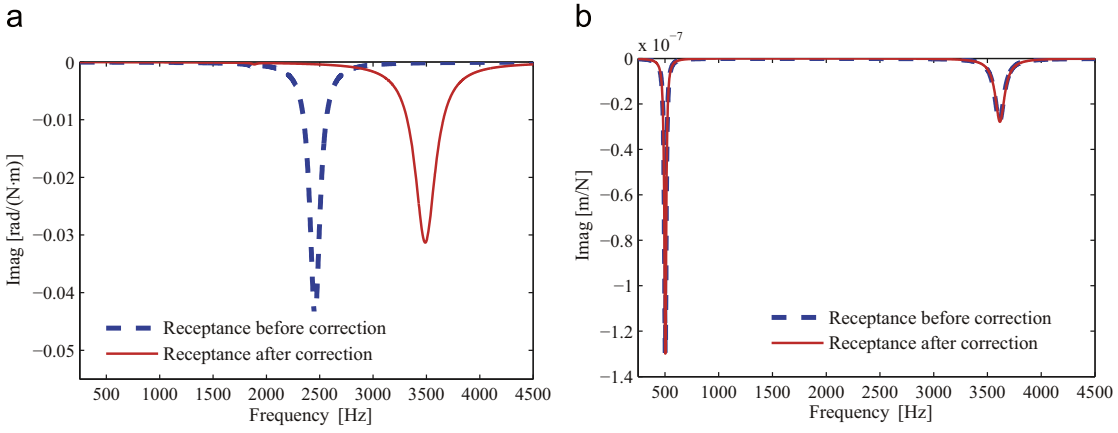

Fig. 7. Examples of eliminating adapter's mass effect on torsional and axial receptances: (a) torsional receptances and (b) axial receptances.

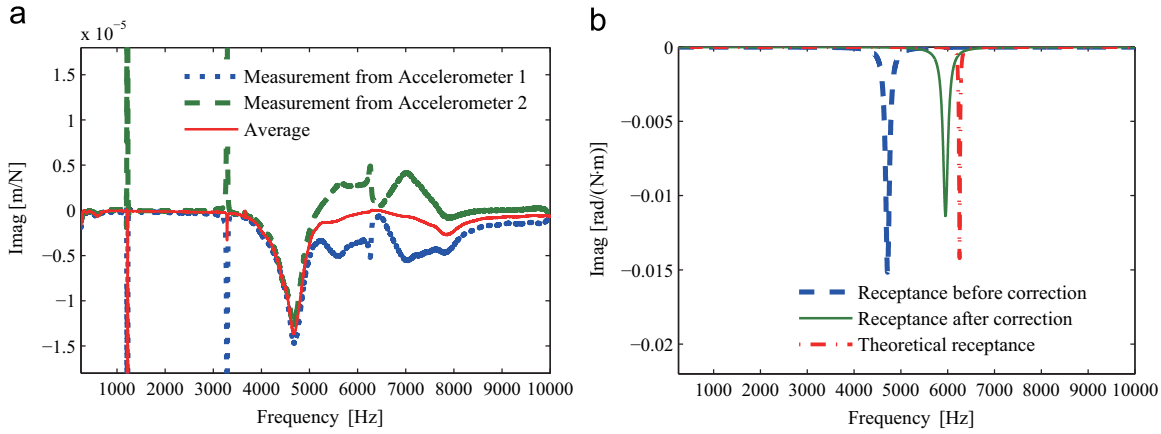

Fig. 8. Validation of the proposed measurement procedure: (a) canceling bending modes and (b) eliminating adapter's mass effect.

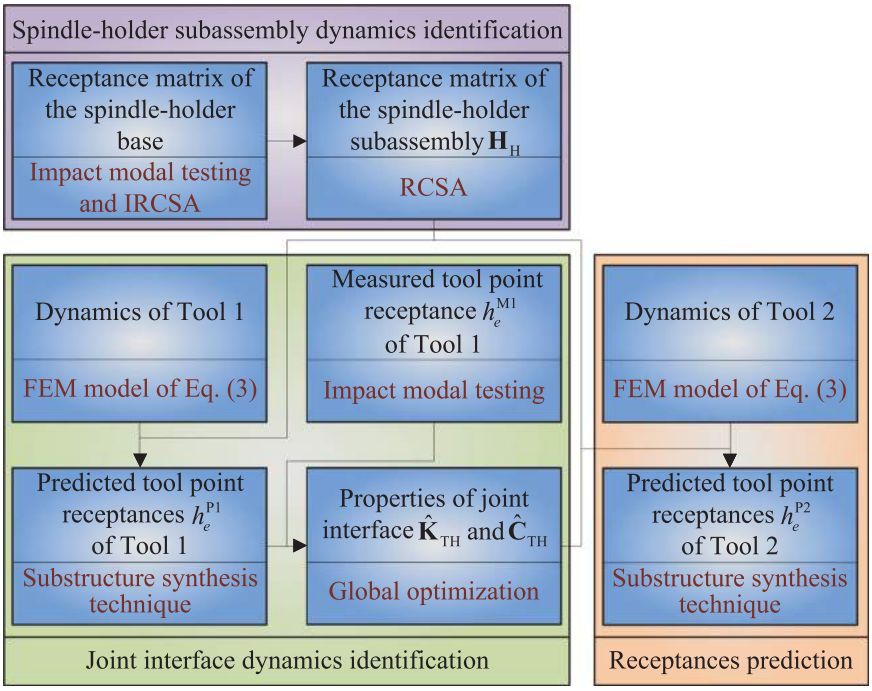

Fig. 9. Prediction procedure of tool point receptances.

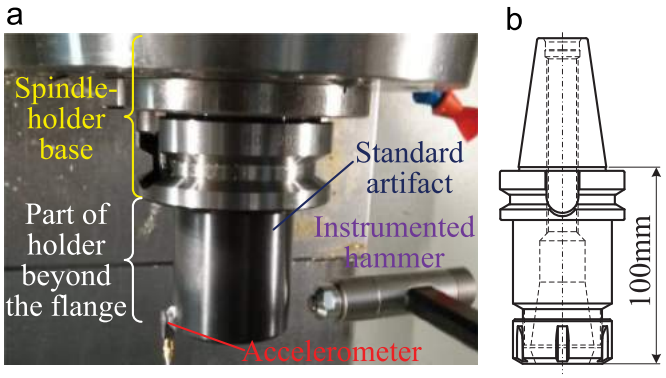

Fig. 10. The employed holders: (a) the standard artifact used to identified the receptance matrix of the spindle-holder base and (b) long holder BT40-ER32-100.

equation for calculating $I_{i,F}^{(i)}$ is formulated by adopting axis rotation formulae related to the moment inertia of cross-section area. It is detailed as follows. As shown in Fig. 4, the location of cross-section related to the cutting edge of the ith element of fluted part will be different from that of the 1st element when considering helix angle β_H. The lead angle $\xi_F^{(i)}$ corresponding to the ith element is calculated as

Table 1
Experimental conditions and percent differences between measured and predicted dominant natural frequencies in all tests.

Test no.	Receptance type	Tool type	Diameter (mm)	Total length (mm)	Tooth length (mm)	Number of flutes	Material	Percent difference (%)
1	Bending	Mill	12	110	42	4	HSS	0.23
2	Bending	Mill	16	123	50	3	Carbide	1.34
3	Torsional	Mill	12	141	60	4	HSS	0.11
4	Axial	Mill	12	141	60	4	HSS	1.79
5	Bending	Mill	12	83	26	3	HSS	0.99
6	Bending	Mill	12	110	42	2	HSS	0.44
7	Bending	Mill	12	110	42	3	HSS	0.46
8	Bending	Mill	12	141	60	2	HSS	0.94
9	Bending	Mill	12	141	60	3	HSS	2.02
10	Bending	Mill	12	141	60	4	HSS	0.12
11	Bending	Mill	16	92	50	3	Carbide	0.83
12	Bending	Mill	16	166	65	3	Carbide	4.67
13	Torsional	Mill	12	110	42	3	HSS	2.88
14	Torsional	Mill	12	110	42	4	HSS	2.13
15	Torsional	Mill	12	141	60	2	HSS	2.40
16	Torsional	Mill	12	141	60	3	HSS	2.34
17	Torsional	Drill	12	150	100	2	HSS	1.68
18	Axial	Mill	12	110	42	4	HSS	1.60
19	Axial	Mill	12	141	60	2	HSS	2.38
20	Axial	Mill	12	141	60	3	HSS	1.59
21	Axial	Drill	12	150	100	2	HSS	1.58

Table 2
Tool material properties.

Material	Young's modulus (GPa)	Density (kg/m^3)	Poisson ratio	Solid damping factor
Carbide	610	14,500	0.29	0.0015
HSS	220	8080	0.22	0.0015

Table 3
The identified properties of joint interfaces.

Test no.	Receptance type	Stiffness	Structural damping
1	Bending	$\kappa_{TH,v0} = 3.43 \times 10^{10}$ N/m	$\eta_{TH,v} = 3.16 \times 10^{-2}$
		$\kappa_{TH,\psi 0} = 6.33 \times 10^{6}$ N m/rad	$\eta_{TH,\psi} = 1.53 \times 10^{-2}$
2	Bending	$\kappa_{TH,v0} = 4.28 \times 10^{10}$ N/m	$\eta_{TH,v} = 7.10 \times 10^{-2}$
		$\kappa_{TH,\psi 0} = 7.95 \times 10^{5}$ N m/rad	$\eta_{TH,\psi} = 7.97 \times 10^{-2}$
3	Torsional	$\kappa_{TH,\theta 0} = 2.52 \times 10^{6}$ N m/rad	$\eta_{TH,\theta} = 6.25 \times 10^{-2}$
4	Axial	$\kappa_{TH,u0} = 1.00 \times 10^{14}$ N/m	$\eta_{TH,u} = 1.00 \times 10^{-2}$

$$\xi_F^{(i)} = \frac{2(z_F^{(i)} - z_F^{(1)})\tan\beta_H}{D_F^{(i)}}$$

where $z_F^{(i)}$ and $z_F^{(1)}$ are the coordinates corresponding to the 1st and ith elements respectively. $D_F^{(i)}$ is the nominal diameter corresponding to the ith element. If the 1st element is taken as the reference element with the moment inertia of cross-section area in the X- and the Y-direction and product inertia of area being symbolized as $I_{l,F}^{(1)}$ (l=x or y) and $I_{xyF}^{(1)}$, $I_{l,F}^{(i)}$ related to the ith element can be calculated as

$$\begin{aligned} I_{xF}^{(i)} &= I_{yF}^{(1)} \sin^2 \xi_F^{(i)} - I_{xyF}^{(1)} \sin 2\xi_F^{(i)} + I_{xF}^{(1)} \cos^2 \xi_F^{(i)} \\ I_{yF}^{(i)} &= I_{xF}^{(1)} \sin^2 \xi_F^{(i)} + I_{xyF}^{(1)} \sin 2\xi_F^{(i)} + I_{yF}^{(1)} \cos^2 \xi_F^{(i)} \end{aligned} \quad (6)$$

It should be noted that for symmetric tools such as 3- or 4-fluted helical tools, the moment inertia of cross-section area of each element of the fluted part is equal. However, for asymmetric tools such as 2-flute tools, due to the pretwisted shape of the flutes, the moment inertia of cross-section area is not constant and can be calculated by using Eq. (6).

Besides, it should be mentioned that the CAD model of the fluted part is established by using the generalized geometric model described in Section 2. $A_F^{(i)}$ corresponding to the fluted part is directly extracted from the CAD model.

The damping matrices can be calculated as follows by using structural damping mechanism [34]:

$$\mathbf{C}_S = \frac{\eta_S}{\omega}\mathbf{K}_S,\ \mathbf{C}_F = \frac{\eta_F}{\omega}\mathbf{K}_F \quad (7)$$

where η_S and η_F are the structural damping factors of shank and the fluted part of the tool, respectively.

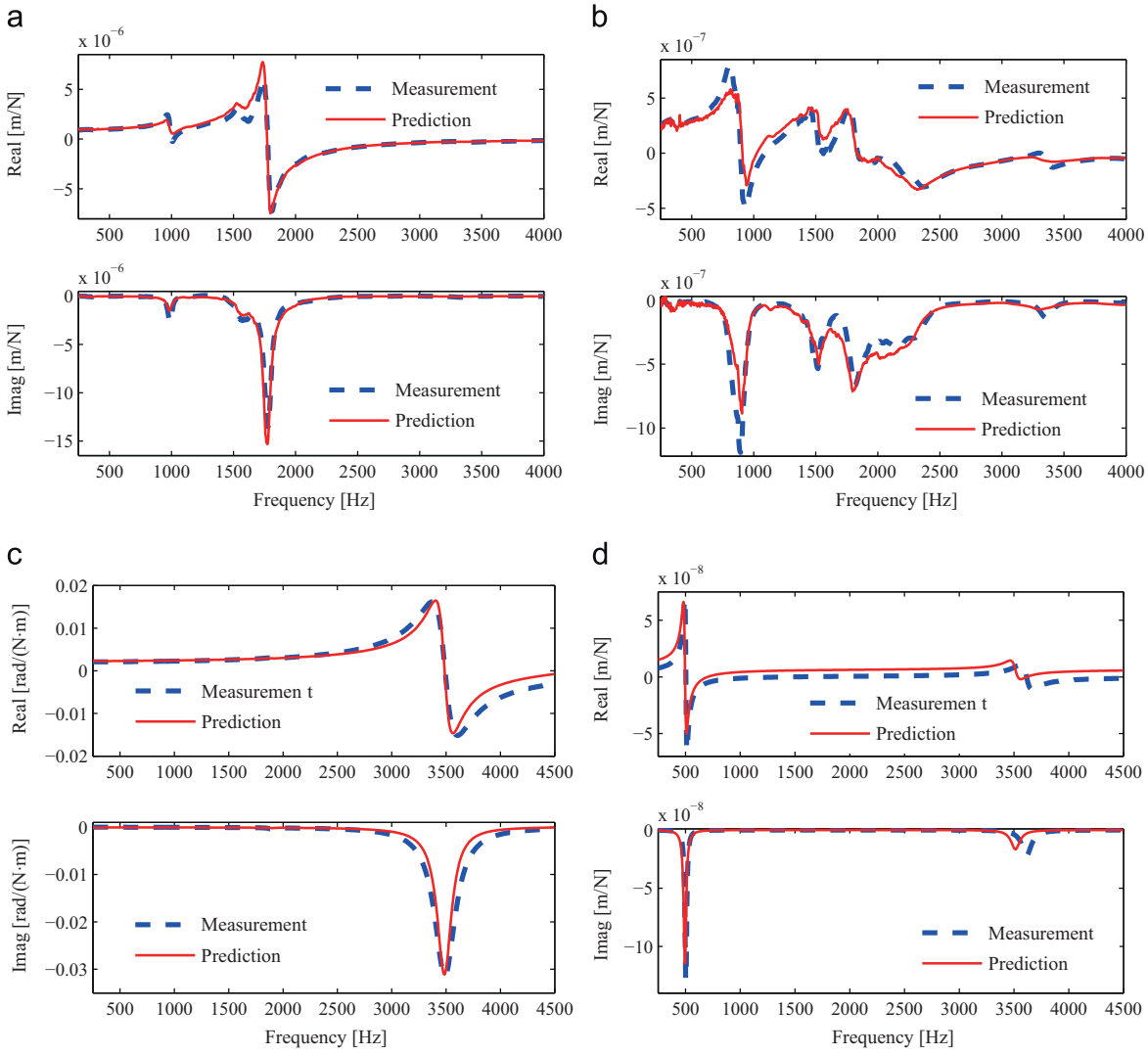

Fig. 11. Comparisons of predicted and measured tool point receptances for tests 1–4 in identification procedure: (a) Test 1, (b) Test 2, (c) Test 3 and (d) Test 4.

3.3. *Modeling of tool–holder joint interface*

The tool–holder joint interface is regarded as a zero-thickness distributed layer and modeled as a substructure which is a connection of tool and holder. As shown in Fig. 3, the tool–holder joint interface is discretized into $(N_{TH} - 1)$ independent spring–damper elements with 4 nodes. It contacts with the spindle–holder subassembly and shank of tool through the lower boundary and upper boundary, respectively. The distributed loads on the ith joint element consist of the force applied by the spindle–holder subassembly, i.e. $\mathbf{f}^{(i)}_{TH-H}(z, t)$, and the force applied by the tool component, i.e. $\mathbf{f}^{(i)}_{TH-S}(z, t)$. They are calculated as

$$\begin{aligned}\mathbf{f}^{(i)}_{TH-H}(z, t) &= \hat{\mathbf{K}}_{TH}(z)(\mathbf{q}^{(i)}_{TH-H}(z, t) - \mathbf{q}^{(i)}_{TH-S}(z, t))\\ \mathbf{f}^{(i)}_{TH-S}(z, t) &= -\hat{\mathbf{K}}_{TH}(z)(\mathbf{q}^{(i)}_{TH-H}(z, t) - \mathbf{q}^{(i)}_{TH-S}(z, t))\end{aligned} \tag{8}$$

where $\mathbf{q}^{(i)}_{TH-H}(z, t)$ and $\mathbf{q}^{(i)}_{TH-S}(z, t)$ are the displacement functions of the boundary of the ith joint element corresponding to the contact surface of holder and that of the shank, respectively. z and t stand for axial coordinate and time. $\hat{\mathbf{K}}_{TH}(z)$ is the stiffness function defined as

$$\hat{\mathbf{K}}_{TH}(z) = \mathrm{diag}\left[K_{TH,u}(z)\ K_{TH,v}(z)\ K_{TH,w}(z)\ K_{TH,\theta}(z)\ K_{TH,\phi}(z)\ K_{TH,\psi}(z)\right] \tag{9}$$

where $K_{TH,x}(z)$, $K_{TH,y}(z)$ and $K_{TH,z}(z)$ are the stiffnesses that correspond to translational displacement and lateral force in X-, Y - and Z-directions, respectively. $K_{TH,\theta}(z)$, $K_{TH,\phi}(z)$ and $K_{TH,\psi}(z)$ are the stiffnesses that correspond to the angular displacement and moment related to A-, B- and C-axes, respectively. These six parameters can be approximated as polynomials [12]

$$K_{TH,s}(z) = \kappa_{TH,s0} + \kappa_{TH,s1}z + \kappa_{TH,s2}z^2 (s = \mathrm{u, v, w, \theta, \phi\ or\ \psi}) \tag{10}$$

where $\kappa_{TH,s0}$, $\kappa_{TH,s1}$ and $\kappa_{TH,s2}$ are polynomial coefficients corresponding to $K_{TH,s}(z)$, respectively.

Discretization of the distributed loads $\mathbf{f}^{(i)}_{TH-H}(z, t)$ and $\mathbf{f}^{(i)}_{TH-S}(z, t)$ in Eq. (8) to the nodes of ith element gives

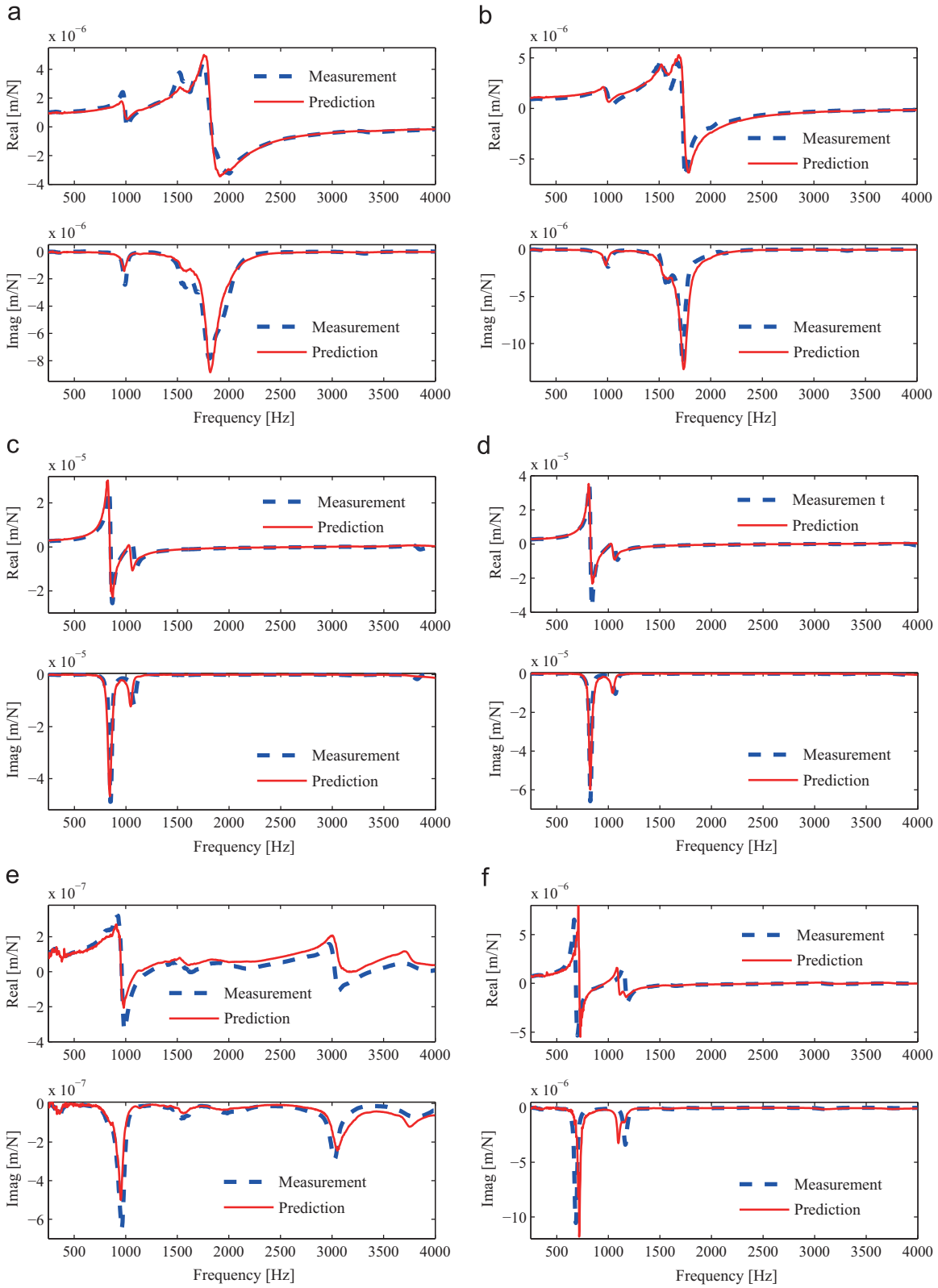

Fig. 12. Sample curves of predicted and measured tool point bending receptance using the identified stiffness coefficients of joint interface: (a) Test 6, (b) Test 7, (c) Test 8, (d) Test 10, (e) Test 11 and (f) Test 12.

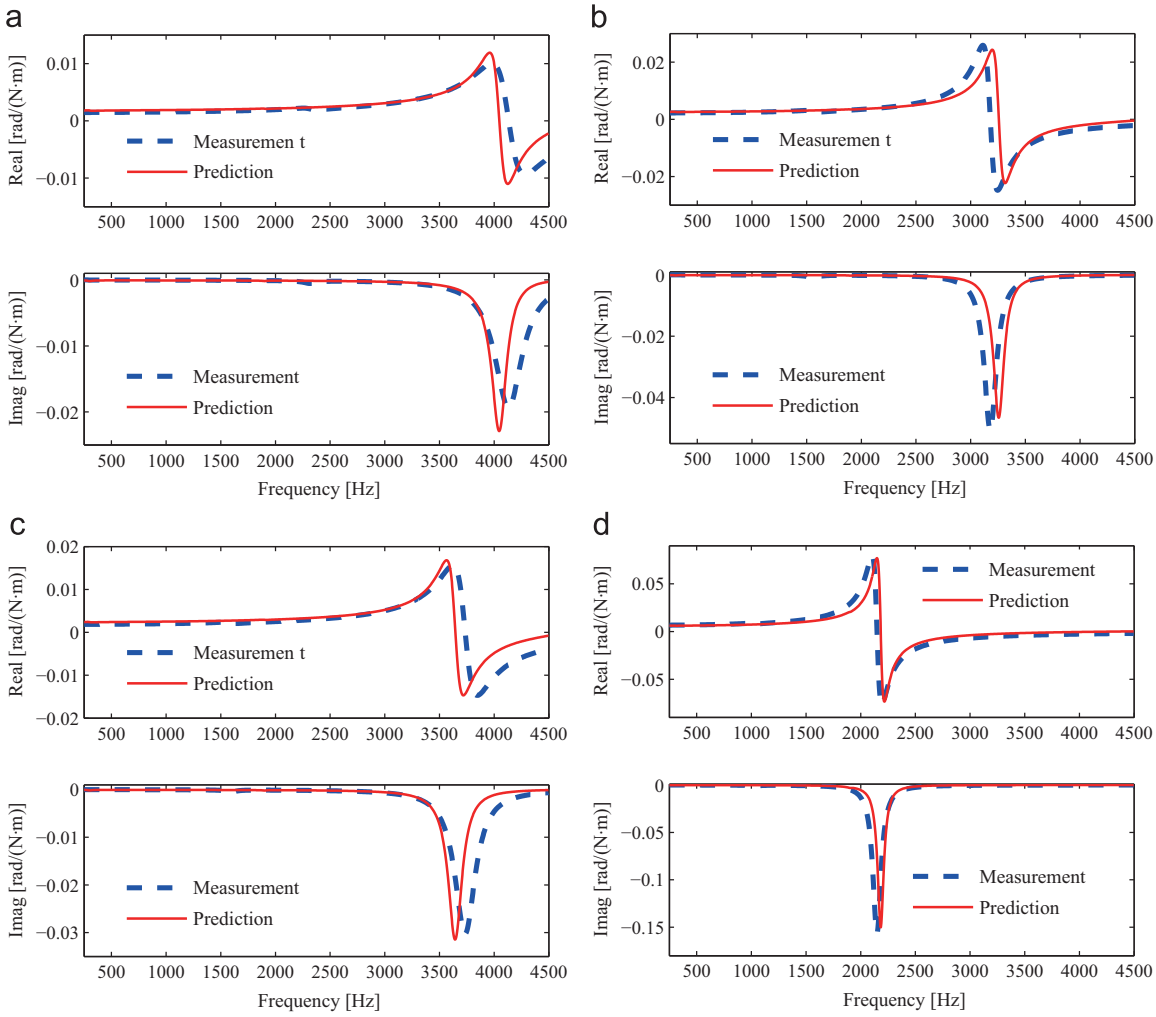

Fig. 13. Sample curves of predicted and measured tool point torsional receptance using the identified stiffness coefficients of joint interface: (a) Test 13, (b) Test 14, (c) Test 15 and (d) Test 16.

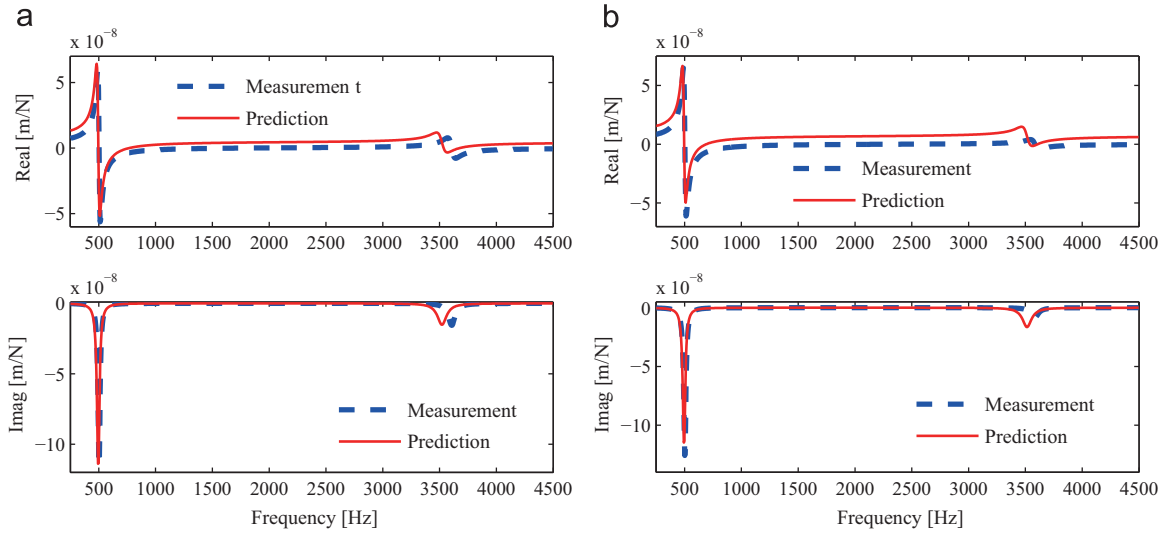

Fig. 14. Sample curves of predicted and measured tool point axial receptance using the identified stiffness coefficients of joint interface: (a) Test 18 and (b) Test 20.

$$\mathbf{f}_{TH}^{(i)}(t) = \mathbf{K}_{TH}^{(i)}\mathbf{q}_{TH}^{(i)}(t) \tag{11}$$

with

$$\mathbf{K}_{TH}^{(i)} = \int_{z_{1,TH}^{(i)}}^{z_{2,TH}^{(i)}} \mathbf{N}_{TH}^{(i)}(z)^{T}\hat{\mathbf{K}}_{TH}(z)\mathbf{N}_{TH}^{(i)}(z)\,dz$$

$$\mathbf{f}_{TH}^{(i)}(t) = \left[\mathbf{f}_{TH-H,i}(t)^{T}\ \ \mathbf{f}_{TH-H,i+1}(t)^{T}\ \ \mathbf{f}_{TH-S,i}(t)^{T}\ \ \mathbf{f}_{TH-S,i+1}(t)^{T}\right]^{T}$$

$$\begin{aligned}\mathbf{q}_{TH}^{(i)}(t) &= \left[\mathbf{q}_{TH-H,i}(t)^{T}\ \ \mathbf{q}_{TH-H,i+1}(t)^{T}\ \ \mathbf{q}_{TH-S,i}(t)^{T}\ \ \mathbf{q}_{TH-S,i+1}(t)^{T}\right]^{T}\\ &= \left[\mathbf{q}_{TH-H,i}(t)^{T}\ \ \mathbf{q}_{TH-H,i+1}(t)^{T}\ \ -\mathbf{q}_{TH-H,i}(t)^{T}\ \ -\mathbf{q}_{TH-H,i+1}(t)^{T}\right]^{T}\end{aligned}$$

where $z_{1,TH}^{(i)}$ and $z_{2,TH}^{(i)}$ are the coordinates of the left and right nodes of ith element, respectively. $\mathbf{f}_{TH-H,i}$ and $\mathbf{f}_{TH-H,i+1}$ are the loads on the left and right nodes at the boundary related to the contact surface of the holder, respectively. $\mathbf{f}_{TH-S,i}$ and $\mathbf{f}_{TH-S,i+1}$ are the loads on the left and right nodes at the boundary associated with the contact surface of the shank, respectively. $\mathbf{q}_{TH-H,i}$ and $\mathbf{q}_{TH-H,i+1}$ are the displacements of the left and right nodes at the boundary related to the contact surface of the holder, respectively. $\mathbf{q}_{TH-S,i}$ and $\mathbf{q}_{TH-S,i+1}$ are the displacements of the left and right nodes at the boundary associated with the contact surface of the shank, respectively. Schematic illustration is shown in Fig. 3. $\mathbf{N}_{TH}^{(i)}(z)$ is defined as

$$\mathbf{N}_{TH}^{(i)}(z) = \left[N_{1,TH}^{(i)}(z)\mathbf{I}\ \ N_{2,TH}^{(i)}(z)\mathbf{I}\ \ -N_{1,TH}^{(i)}(z)\mathbf{I}\ \ -N_{2,TH}^{(i)}(z)\mathbf{I}\right] \tag{12}$$

with

$$N_{1,TH}^{(i)}(z) = \frac{1}{2}\left(1 - \frac{2z - z_{1,TH}^{(i)} - z_{2,TH}^{(i)}}{z_{2,TH}^{(i)} - z_{1,TH}^{(i)}}\right)\quad\text{and}\quad N_{2,TH}^{(i)}(z) = \frac{1}{2}\left(1 + \frac{2z - z_{1,TH}^{(i)} - z_{2,TH}^{(i)}}{z_{2,TH}^{(i)} - z_{1,TH}^{(i)}}\right).$$

where $\mathbf{I}$ is a 6×6 identity matrix. Assembling the stiffness matrix of each element into global stiffness matrix of the tool–holder joint interface component $\mathbf{K}_{TH}$ by using the means similar to Eq. (4) leads to

$$\mathbf{K}_{TH}\mathbf{Q}_{TH}(t) = \mathbf{F}_{TH}(t) \tag{13}$$

where $\mathbf{F}_{TH}(t) = [\mathbf{f}_{TH-H,1}(t)^{T}, \mathbf{f}_{TH-H,2}(t)^{T}, \ldots, \mathbf{f}_{TH-H,N_{TH}}(t)^{T}, \mathbf{f}_{TH-S,1}(t)^{T}, \mathbf{f}_{TH-S,2}(t)^{T}, \ldots, \mathbf{f}_{TH-S,N_{TH}}(t)^{T}]$ and $\mathbf{Q}_{TH} = [\mathbf{q}_{TH-H,1}(t)^{T}, \mathbf{q}_{TH-H,2}(t)^{T}, \ldots, \mathbf{q}_{TH-H,N_{TH}}(t)^{T}, \mathbf{q}_{TH-S,1}(t)^{T}, \mathbf{q}_{TH-S,2}(t)^{T}, \ldots, \mathbf{q}_{TH-S,N_{TH}}(t)^{T}]$ are the global load and global displacement vectors of the joint interface, respectively.

The damping effect related to the joint interface can be modeled by using structural damping mechanism

$$\hat{\mathbf{C}}_{TH} = \mathrm{diag}\left[\frac{\eta_{TH,u}}{\omega}\ \frac{\eta_{TH,v}}{\omega}\ \frac{\eta_{TH,w}}{\omega}\ \frac{\eta_{TH,\theta}}{\omega}\ \frac{\eta_{TH,\phi}}{\omega}\ \frac{\eta_{TH,\psi}}{\omega}\right]\hat{\mathbf{K}}_{TH} \tag{14}$$

where $\eta_{TH,s}$ (s = u, v, w, θ, ϕ or ψ) is the structural damping factor of the tool–holder joint interface component corresponding to $K_{TH,u}(z)$, $K_{TH,v}(z)$, $K_{TH,w}(z)$, $K_{TH,\theta}(z)$, $K_{TH,\phi}(z)$, $K_{TH,\psi}(z)$. The global damping matrix of the tool–holder joint interface component $\mathbf{C}_{TH}$ is calculated by the similar derivation of $\mathbf{K}_{TH}$ shown in Eq. (13), and can be expressed as

$$\mathbf{C}_{TH} = \mathbf{B}_{TH}\mathbf{K}_{TH}/\omega \tag{15}$$

where $\mathbf{B}_{TH}$ is the damping factor matrix of the tool–holder joint interface component.

With the stiffness, i.e., $\mathbf{K}_{TH}$, and the damping, i.e., $\mathbf{C}_{TH}$, matrices obtained above, the dynamics of the tool–holder joint interface component can be modeled as

$$\mathbf{C}_{TH}\dot{\mathbf{Q}}_{TH}(t) + \mathbf{K}_{TH}\mathbf{Q}_{TH}(t) = \mathbf{F}_{TH}(t) \tag{16}$$

3.4. Assembling criterion of the dynamic responses of all substructures

After obtaining the dynamic equation of each component, assembling criterion will be established in this section. By implementing Fourier transform to Eqs. (2) and (16), one can have

$$\left\{-\omega^{2}\begin{bmatrix}0&0&0\\0&\mathbf{M}_S&0\\0&0&\mathbf{M}_F\end{bmatrix} + \omega\mathrm{j}\begin{bmatrix}\mathbf{C}_{TH}&0&0\\0&\mathbf{C}_S&0\\0&0&\mathbf{C}_F\end{bmatrix} + \begin{bmatrix}\mathbf{K}_{TH}&0&0\\0&\mathbf{K}_S&0\\0&0&\mathbf{K}_F\end{bmatrix}\right\}\begin{Bmatrix}\mathbf{Q}_{TH}(\omega)\\\mathbf{Q}_S(\omega)\\\mathbf{Q}_F(\omega)\end{Bmatrix} = \begin{Bmatrix}\mathbf{F}_{TH}(\omega)\\\mathbf{F}_{S-TH}(\omega) + \mathbf{F}_{S-F}(\omega)\\\mathbf{F}_{F-S}(\omega) + \mathbf{F}_{FE}(\omega)\end{Bmatrix} \tag{17}$$

where j is the imaginary unit.

Substituting damping matrices in Eq. (17) with Eqs. (7) and (15) and combining Eqs. (1) and (17) lead to

$$\left\{\begin{bmatrix}\mathbf{Z}_H(\omega) & 0 & 0 & 0\\ 0 & 0 & 0 & 0\\ 0 & 0 & 0 & 0\\ 0 & 0 & 0 & 0\end{bmatrix} - \omega^2\begin{bmatrix}0 & 0 & 0 & 0\\ 0 & 0 & 0 & 0\\ 0 & 0 & \mathbf{M}_S & 0\\ 0 & 0 & 0 & \mathbf{M}_F\end{bmatrix} + \mathrm{j}\begin{bmatrix}0 & 0 & 0 & 0\\ 0 & \mathbf{B}_{TH}\mathbf{K}_{TH} & 0 & 0\\ 0 & 0 & \eta_S\mathbf{K}_S & 0\\ 0 & 0 & 0 & \eta_F\mathbf{K}_F\end{bmatrix} + \begin{bmatrix}0 & 0 & 0 & 0\\ 0 & \mathbf{K}_{TH} & 0 & 0\\ 0 & 0 & \mathbf{K}_S & 0\\ 0 & 0 & 0 & \mathbf{K}_F\end{bmatrix}\right\}\begin{Bmatrix}\mathbf{Q}_H(\omega)\\ \mathbf{Q}_{TH}(\omega)\\ \mathbf{Q}_S(\omega)\\ \mathbf{Q}_F(\omega)\end{Bmatrix} = \begin{Bmatrix}\mathbf{F}_{H-TH}(\omega)\\ \mathbf{F}_{TH}(\omega)\\ \mathbf{F}_{S-TH}(\omega)+\mathbf{F}_{S-F}(\omega)\\ \mathbf{F}_{F-S}(\omega)+\mathbf{F}_{FE}(\omega)\end{Bmatrix} \tag{18}$$

with $\mathbf{Z}_H(\omega) = \mathbf{H}_H(\omega)^{-1}$. In Eq. (18),

$$\mathbf{Q}_S = \left[\mathbf{Q}_{S-TH}^T\ \mathbf{Q}_{S-O}^T\ \mathbf{Q}_{S-F}^T\right]^T$$

$$\mathbf{Q}_F = \left[\mathbf{Q}_{F-S}^T\ \mathbf{Q}_{F-O}^T\right]^T$$

$$\mathbf{Q}_{TH} = \left[\mathbf{Q}_{TH-H}^T\ \mathbf{Q}_{TH-S}^T\right]^T$$

$$\mathbf{F}_{TH} = \left[\mathbf{F}_{TH-H}^T\ \mathbf{F}_{TH-S}^T\right]^T$$

where $\mathbf{Q}_{S-TH}$ denotes the displacement vector of the nodes at the segment of the shank of tool component which connects to the tool–holder joint interface component. $\mathbf{Q}_{S-O}$ denotes the displacement vector of the nodes at segment of the shank of tool component which does not contact the holder. $\mathbf{Q}_{S-F}$ denotes the displacement vector of the node of shank that connects with the fluted part. $\mathbf{Q}_{F-S}$ denotes the displacement vector of the node of the fluted part that connects with the shank. $\mathbf{Q}_{F-O}$ denotes the displacement vector of the nodes at segment of the fluted part of tool component which is not in contact with other component. $\mathbf{Q}_{TH-H}$ and $\mathbf{Q}_{TH-S}$ denote the displacement vectors of the nodes at the tool–holder joint interface component which connect to the tool and the holder, respectively. $\mathbf{F}_{TH-H}$ and $\mathbf{F}_{TH-S}$ denote the load vectors on the nodes at the tool–holder joint interface component applied by the tool and the holder, respectively.

Compatibility conditions of displacements and loads on the boundaries between different substructures involve

Compatibility conditions of displacement

$\mathbf{Q}_H = \mathbf{Q}_{TH-H}$ the boundary between SHS and THJIC

$\mathbf{Q}_{TH-S} = \mathbf{Q}_{S-TH}$ the boundary between THJIC and STC

$\mathbf{Q}_{S-F} = \mathbf{Q}_{F-S}$ the boundary between STC and FPTC

Compatibility conditions of load

$\mathbf{F}_{H-TH} = -\mathbf{F}_{TH-H}$ the boundary between SHS and THJIC

$\mathbf{F}_{TH-S} = -\mathbf{F}_{S-TH}$ the boundary between THJIC and STC

$\mathbf{F}_{S-F} = -\mathbf{F}_{F-S}$ the boundary between STC and FPTC

The independent coordinates in Eq. (18) are

$$\tilde{\mathbf{Q}} = \left[\mathbf{Q}_H^T\ \mathbf{Q}_S^T\ \mathbf{Q}_{F-O}^T\right]^T$$

$$= \left[\mathbf{Q}_H^T\ \mathbf{Q}_{S-TH}^T\ \mathbf{Q}_{S-O}^T\ \mathbf{Q}_{S-F}^T\ \mathbf{Q}_{F-O}^T\right]^T$$

The displacement vector in Eq. (18) can be further expressed as

$$\begin{Bmatrix}\mathbf{Q}_H\\ \mathbf{Q}_{TH}\\ \mathbf{Q}_S\\ \mathbf{Q}_F\end{Bmatrix} = \begin{Bmatrix}\mathbf{Q}_H\\ \mathbf{Q}_{TH-H}\\ \mathbf{Q}_{TH-S}\\ \mathbf{Q}_S\\ \mathbf{Q}_F\end{Bmatrix} = \begin{Bmatrix}\mathbf{Q}_H\\ \mathbf{Q}_H\\ \mathbf{Q}_{S-TH}\\ \mathbf{Q}_{S-TH}\\ \mathbf{Q}_{S-O}\\ \mathbf{Q}_{S-F}\\ \mathbf{Q}_{S-F}\\ \mathbf{Q}_{F-O}\end{Bmatrix} = \begin{bmatrix}\mathbf{I} & 0 & 0 & 0 & 0\\ \mathbf{I} & 0 & 0 & 0 & 0\\ 0 & \mathbf{I} & 0 & 0 & 0\\ 0 & \mathbf{I} & 0 & 0 & 0\\ 0 & 0 & \mathbf{I} & 0 & 0\\ 0 & 0 & 0 & \mathbf{I} & 0\\ 0 & 0 & 0 & \mathbf{I} & 0\\ 0 & 0 & 0 & 0 & \mathbf{I}\end{bmatrix}\begin{Bmatrix}\mathbf{Q}_H\\ \mathbf{Q}_{S-TH}\\ \mathbf{Q}_{S-O}\\ \mathbf{Q}_{S-F}\\ \mathbf{Q}_{F-O}\end{Bmatrix} = \mathbf{U}\tilde{\mathbf{Q}} \tag{19}$$

with

$$\mathbf{U} = \begin{bmatrix}\mathbf{I} & 0 & 0 & 0 & 0\\ \mathbf{I} & 0 & 0 & 0 & 0\\ 0 & \mathbf{I} & 0 & 0 & 0\\ 0 & \mathbf{I} & 0 & 0 & 0\\ 0 & 0 & \mathbf{I} & 0 & 0\\ 0 & 0 & 0 & \mathbf{I} & 0\\ 0 & 0 & 0 & \mathbf{I} & 0\\ 0 & 0 & 0 & 0 & \mathbf{I}\end{bmatrix}$$

Substituting Eq. (19) into Eq. (18) and multiplying both sides of these equations with $\mathbf{U}^T$ gives the dynamic equations of the tool–holder–spindle assembly

$$\mathbf{Z}_A(\omega)\tilde{\mathbf{Q}}(\omega) = \tilde{\mathbf{F}}_A(\omega) + \tilde{\mathbf{F}}_{AE}(\omega) = \tilde{\mathbf{F}}_{AE}(\omega) \tag{20}$$

where $\tilde{\mathbf{F}}_A = \mathbf{U}^T\mathbf{F}_A = \mathbf{O}$ and $\tilde{\mathbf{F}}_{AE} = \mathbf{U}^T\mathbf{F}_{AE}$. $\mathbf{Z}_A$ denotes dynamic stiffness matrix and is calculated as

$$\mathbf{Z}_A = \mathbf{U}^T\left\{\begin{bmatrix}\mathbf{Z}_H(\omega) & 0 & 0 & 0\\ 0 & 0 & 0 & 0\\ 0 & 0 & 0 & 0\\ 0 & 0 & 0 & 0\end{bmatrix} - \omega^2\begin{bmatrix}0 & 0 & 0 & 0\\ 0 & 0 & 0 & 0\\ 0 & 0 & \mathbf{M}_S & 0\\ 0 & 0 & 0 & \mathbf{M}_F\end{bmatrix} + \begin{bmatrix}0 & 0 & 0 & 0\\ 0 & (\mathrm{j}\mathbf{B}_{TH} + \mathbf{I})\mathbf{K}_{TH} & 0 & 0\\ 0 & 0 & (\mathrm{j}\eta_S + 1)\mathbf{K}_S & 0\\ 0 & 0 & 0 & (\mathrm{j}\eta_F + 1)\mathbf{K}_F\end{bmatrix}\right\}\mathbf{U}$$

where $\mathbf{O}$ is zero vector.

3.5. Extraction of tool point receptances

Based on the dynamic equation of the tool–holder–spindle assembly obtained above, receptance matrix of system can be expressed as:

$$\mathbf{H}_A(\omega) = \mathbf{Z}_A^{-1}(\omega) = [h_{A,ij}]_{N_A \times N_A} \tag{21}$$

where $N_A = (N_H + N_S + N_F - 1) \times 6$. $h_{A,ij}$ is the entry of receptance matrix $\mathbf{H}_A$.

Tool point bending, torsional and axial receptances , i.e. h_{BEY}, h_{BEY}, h_{TOR} and h_{AX} can be extracted from Eq. (21)

$$\begin{aligned} h_{BEX} &= h_{A,(N_A-5)(N_A-5)}\\ h_{BEY} &= h_{A,(N_A-4)(N_A-4)}\\ h_{TOR} &= h_{A,N_AN_A}\\ h_{AX} &= h_{A,(N_A-3)(N_A-3)} \end{aligned} \tag{22}$$

Note that h_{BEX} and h_{BEY} designate the bending receptances corresponding to the *X*- and the *Y*-direction, while h_{TOR} and h_{AX} denote the torsional and axial receptances, respectively.

4. Improved measurement procedure for torsional and axial receptances

Tool point bending receptances are convenient to be measured by attaching an accelerometer to the tool tip, whereas the measurements of tool point torsional and axial receptances are not straightforward to conduct. In this section, an experimental procedure for the measurement of tool point torsional and axial receptances is described in detail. In order to enable torsional and axial testing for the tool–holder–spindle assembly, surfaces must be provided for both excitation of the tool and measurement of its resulting vibration. A lightweight additional adapter with a mass of 5.7 g is attached to the tool tip, as illustrated in Fig. 5(a). The dimensions of the adapter are designed as shown in Fig. 5(b). The adapter made of resin is cemented to the tool tip using cyanoacrylate. The procedure of measurements will be detailed below.

4.1. Measurement of torsional receptances

To obtain torsional receptances, a pair of complementary measurements should be carried out as shown in Fig. 5(c), in which two accelerometers, i.e., Accelerometer 1 and 2, were attached at corners on the diagonal. The impact point was at the corner on the opposite of Accelerometer 1.

This excited the torsional vibration modes of the assembly. However, the lateral force also effectively excited the bending modes and corrupted the torsional receptance. Thus, the average of the measurements from both accelerometers was used to cancel the bending modes and isolate the torsional modes, since the sign of torsional receptances captured by the two accelerometers was nominally the same but bending receptances are in oppositive directions. Fig. 6(a) shows the average from both measurements. It is seen that the bending modes were successfully canceled by averaging the two measurements. Torsional response was obtained by dividing the average receptance by the square of the distance from the axis of the accelerometer to the axis of the tool, according to Refs. [27,35]. The distance is 20.5 mm in the case of Fig. 5(c).

4.2. Measurement of axial receptances

In measurement of tool point axial receptances, impacts have to be applied at locations with lateral offset from the axis of accelerometer. Cutting tools are compliant in bending relative to the holder and spindle; hence, the bending modes were easily excited since there was always a lateral offset between the accelerometer and hammer impact locations in axial direction. In this sense, it is impossible to excite tools and measure vibrations exactly along the tool axis. To cancel the bending modes, two measurements were also performed

and averaged. As shown in Fig. 5(d), the accelerometer was attached using wax to the tool tip. Two impacts on the adapter, i.e., Impacts 1 and 2 in Fig. 5(d), were applied to switch the couple direction. An example of canceling bending modes in measurement of axial receptances is plotted in Fig. 6(b). As expected, the bending modes around 700 Hz, 1100 Hz, 3400 Hz and 3700 Hz are eliminated, while the axial modes around 500 Hz and 3600 Hz are maintained.

4.3. Correction algorithm of adapter's mass effect on measurements

Since a relatively large adapter is used to assist testing, its mass may have non-ignorable effect on measurements. In order to study this effect, structural modification techniques proposed by Ozguven [36] are adopted to correct the measured tool point receptances. Main steps are as follows.

(i) *Pretreating the measured receptances*
It is expected that the accompanying bending modes during the measuring procedure could be completely removed by using the averaging method described above. However, in practical executing procedure, some uncontrollable factors, such as the tiny difference in precision of accelerometers and incomplete symmetry of the positions of accelerometers or impact, will still cause more or less residual error even averaging is performed. For example, as shown in Fig. 6(a), relatively obvious residual content can be observed near 700 Hz after averaging. This kind of residual content will greatly influence the reliability of the following correcting algorithm. To this end, before conducting the following correction, the averaged measurements are first pretreated by ignoring this item of residual error and then fitting the remaining concerned modes.

(ii) *Correcting the measured receptances*
The receptances after correction can be calculated by the following equations:

$$h_{\mathrm{TOR}}^{\mathrm{C}} = \frac{h_{\mathrm{TOR}}^{\mathrm{UC}}}{1 + h_{\mathrm{TOR}}^{\mathrm{UC}} \times \omega^2 J_{\mathrm{A}}}, \quad \text{for torsional receptances}$$
$$h_{\mathrm{AX}}^{\mathrm{C}} = \frac{h_{\mathrm{AX}}^{\mathrm{UC}}}{1 + h_{\mathrm{AX}}^{\mathrm{UC}} \times \omega^2 M_{\mathrm{A}}}, \quad \text{for axial receptances} \tag{23}$$

where $h_{\mathrm{TOR}}^{\mathrm{C}}$ and $h_{\mathrm{AX}}^{\mathrm{C}}$ are torsional and axial receptances after correction, respectively. $h_{\mathrm{TOR}}^{\mathrm{UC}}$ and $h_{\mathrm{AX}}^{\mathrm{UC}}$ are torsional and axial receptances before correction, respectively. J_{A} and M_{A} are moment of inertia and mass of the measurement adapter, respectively. Receptances before and after correction are shown in Fig. 7. It can be seen that the effect of adapter mass on torsional receptances is obvious, and the natural frequency of torsional mode shifts from about 2500 Hz to about 3500 Hz after modification (see Fig. 7(a)). However, as seen from Fig. 7(b), the adapter mass has ignorable influence on axial receptances.

(iii) *Verifying the correction algorithm*
A steel bar with diameter and length being 18 mm and 250 mm was selected to verify the correction algorithm. The bar's Young's modulus, density, Poisson ratio and solid damping factor are 200 GPa, 7870 kg/m^3, 0.3 and 0.004, respectively. The adapter with mass and moment of inertia being 10.08 g and 1.0226×10^{-6} kg m^2 was attached on one end of the bar by cyanoacrylate. The bar and adapter assembly was tested under free-free boundary condition, and the same measuring plan as shown in Fig. 5(c) was adopted for testing.
Measured receptances together with their the average are plotted in Fig. 8(a). It is observed that the averaged results can well cancel the bending modes around 1200 Hz, 3300 Hz, 5600 Hz, 6200 Hz and 7000 Hz while maintaining torsional mode. Based on the correction algorithm, the average is modified and plotted in Fig. 8(b). Theoretical prediction obtained from beam theory is also plotted in Fig. 8(b) to validate the correctness of the corrected results. It can be seen that after correction, the percent difference between the experimental and theoretical natural frequency of torsional mode decreases from 24.60% to 4.78%, and overall, the natural frequency and the amplitude of the corrected torsional mode match with the theoretical result.
Besides, it should be mentioned that the aim of this section is to study the correctness of the proposed correction algorithm by comparing with theoretical results. Since the practical status of the tool being installed in machine spindle is not a strict clamped-free boundary condition, it is difficult to give accurate theoretical torsional mode. However, the free–free boundary used in this section can be easily carried out in actual operation and its theoretical mode can also be precisely solved.

5. Experimental validation

A series of experiments and simulations were conducted to verify the mathematical model of tool point receptances for two kinds of rotating tools, i.e., mills and drills. Fig. 9 presents a prediction procedure for the calculation of tool point receptance as well as the identification of the properties of tool–holder joint interfaces. Key steps are as follows:

Step 1: Obtain the receptance matrix of the spindle–holder base using method proposed by Schmitz [15];
Step 2: Calculate the receptance matrix of spindle–holder subassembly using RCSA method [37] and results of Step 1;
Step 3: Measure tool point receptance h_e^{M1} of Tool 1 using experimental method proposed in Section 4;
Step 4: Calculate dynamics of shank of tool and fluted part of tool component of Tool 1 using Eq. (2);
Step 5: Predict tool point receptances h_e^{P1} of Tool 1 using Eqs. (20)–(22);
Step 6: Identify properties of tool–holder joint interface $\hat{\mathbf{K}}_{\mathrm{TH}}$ and $\hat{\mathbf{C}}_{\mathrm{TH}}$ by comparing measured tool point receptances in Step 3 and predicted tool point receptances of Tool 1 in Step 5;
Step 7: Calculate dynamics of shank of tool and fluted part of tool component of Tool 2 using Eq. (3);
Step 8 Predict tool point receptances h_e^{P2} of Tool 2 using the properties of tool–holder joint interface identified from Step 6 and the

receptance matrix of spindle–holder subassembly obtained from Step 2.

Note that Tool 1 is a sample tool used for identifying properties of tool–holder joint interface, while Tool 2 is the tool to be predicted. Some steps related to experiments will be detailed in the following subsections.

5.1. Obtaining of spindle–holder subassembly receptance

The spindle–holder subassembly receptance matrix is determined by the method reported in Ref. [37]. First, the receptance matrix of the spindle–holder base, including bending, torsional and axial receptances, is obtained experimentally on a vertical machine center by the inverse RCSA procedure [15,27]. In actual experiment, a standard artifact (see Fig. 10(a)) with the required spindle interface (i.e., BT-40) is inserted in the spindle and measurements are performed at the free end of the assembly.

Second, the spindle–holder subassembly receptance matrix is calculated by rigidly coupling the receptance of other holder part beyond the flange with the receptance matrix of the spindle-holder base obtained above. The holder used in this paper is shown in Fig. 10(b), and is made of 20CrMnTi steel alloy with Young's modulus, density, Poisson ratio and damping factor being 2.07×10^{11} N/m^2, 7800 kg/m^3, 0.29 and 0.0015.

5.2. Identification of joint interface properties

The stiffness and damping properties of the tool–holder joint interface are identified by minimizing the discrepancy between the predicted and measured FRFs of a sample tool

$$\min_{\hat{\mathbf{K}}_{TH},\hat{\mathbf{C}}_{TH}} \| \log|h_e^M - h_e^P|\|(e = \text{BEX, BEY, TOR, AX}) \tag{24}$$

where h_e^M is the measured tool point receptances. h_e^P is the predicted tool point receptances by using the calculation procedure described in Section 3. Zero-order polynomial forms of Eq. (10) are used to characterize the stiffness and damping coefficients of the tool–holder joint interface. MultiStart in Matlab is employed as a gradient-based global optimization solver to determine the properties of the tool–holder joint interface. Four samples of milling tools with different combinations of diameters and materials, as listed in the first four rows of Table 1, are used for identifying the corresponding property parameters of joint interface. Tools were inserted in the collet holder (in Fig. 10(b)) mounted in the spindle of a vertical machine center. Impact tests required in Eq. (24) were conducted with the collet holder, in which samples of milling tools were inserted with the identical length of 40 mm. Geometrical and material parameters of all tools used for verifications are listed in Tables 1 and 2. The identified properties of joint interfaces are tabulated in Table 3.

5.3. Comparisons of predictions and measurements

The receptance matrix of spindle–holder subassembly obtained in Section 5.1 and the parameters listed in Table 3 are now adopted to predict tool point receptances using the proposed method. Fig. 11 gives predicted and measured tool point receptances for the four samples of milling tools, which are in good agreement. Verifications are also made for the milling and drilling tools with the length or flutes different from those of the four samples. The parameters of these tools are listed in Table 1. Figs. 12–14 show the predicted and measured tool point bending, torsional and axial receptances, respectively. Percent differences between measured and predicted dominant natural frequencies are also listed in Table 1. It should be noted that to ensure the consistency of contact status, all tools are mounted into the holder with the same inserted length under the same clamping torques. It can be seen that both frequency and amplitude of simulation results match well with experimental results.

6. Conclusions

Besides bending receptances, torsional and axial receptances usually occurring in drilling or tapping process also have significant effects on process chatter dynamics, however, past prediction methods on FRFs were mainly established for dedicated tools and mostly contributed to bending receptance appearing in end milling process. Since rotating tools (drills, mills or taps, etc.) have similar geometrical and assembly features, their dynamic responses are modeled in a generalized way to be suitable for predicting the FRFs of all kinds of rotating tools used in milling, drilling or tapping process. Detailed derivation of formulae includes the following important theoretical tools: (1) Timoshenko beam theory, which is adopted to comprehensively model the translational and rotational dynamic responses related to all axes (X, Y and Z), as well as the influences of shear deformation on the receptances of tool fluted part at high frequency, (2) distributed damped-elastic interface hypothesis, which is used to model the tool–holder contact condition that was previously treated as rigid contact, (3) substructure synthesis technique, which is used to develop assembling criterion involving the receptances of all substructures and (4) structural modification technique, which is used to develop correction algorithm for the elimination of the adapter's mass effect on torsional and axial measurements.

Experimental verifications show the following conclusions:

- The proposed measurement procedure is valid for measuring tool point torsional and axial receptances since the adapter's mass effect can be well eliminated by the inlaid correction algorithm.
- The proposed FRFs prediction method can either predict the bending receptance related to milling or calculate both bending and torsional–axial receptances associated with drilling. All percentage differences between the measured and predicted dominant natural frequencies are less than 5%.

Acknowledgments

This research has been supported by the National Natural Science Foundation of China under Grant nos. 11272261 and 11432011, the Program for New Century Excellent Talents in University under Grant no. NCET-12-0467 and the Doctorate Foundation of Northwestern Polytechnical University under Grant no. CX201502.

References

[1] J. Tlusty, Machine Dynamics, Chapman and Hall, New York (1985), p. 49–153.
[2] J. Tlusty, F. Ismail, Basic nonlinearity in machining chatter, CIRP Ann.—Manuf. Technol. 30 (1981) 299–304.
[3] I. Minis, T. Yanushevsky, R. Tembo, R. Hocken, Analysis of linear and nonlinear chatter in milling, CIRP Ann.—Manuf. Technol. 39 (1990) 459–462.
[4] Y. Altintas, E. Budak, Analytical prediction of stability lobes in milling, CIRP Ann.—Manuf. Technol. 44 (1995) 357–362.
[5] E. Budak, Y. Altintas, Analytical prediction of chatter stability in milling, Part I: general formulation, Trans. ASME—J. Dyna. Syst. Meas. Control 120 (1998) 22–30.
[6] P. Bayly, J. Halley, B. Mann, M. Davies, Stability of interrupted cutting by temporal finite element analysis, Trans. ASME—J. Manuf. Sci. Eng. 125 (2003) 220–225.
[7] B. Mann, P. Bayly, M. Davies, J. Halley, Limit cycles, bifurcations, and accuracy of the milling process, J. Sound Vib. 277 (2004) 31–48.
[8] T. Insperger, G. Stepan, Updated semi-discretization method for periodic delay-differential equations with discrete delay, Int. J. Numer. Methods Eng. 61 (2004) 117–141.
[9] T. Schmitz, R. Donaldson, Predicting high-speed machining dynamics by substructure analysis, CIRP Ann.—Manuf. Technol. 49 (2000) 303–308.
[10] S.S. Park, Y. Altintas, M. Movahhedy, Receptance coupling for end mills, Int. J. Mach. Tools Manuf. 43 (2003) 889–896.
[11] M. Movahhedy, J. Gerami, Prediction of spindle dynamics in milling by sub-structure coupling, Int. J. Mach. Tools Manuf. 46 (2006) 243–251.
[12] K. Ahmadi, H. Ahmadian, Modelling machine tool dynamics using a distributed parameter tool–holder joint interface, Int. J. Mach. Tools Manuf. 47 (2007) 1916–1928.
[13] P. Albertelli, M. Goletti, M. Monno, A new receptance coupling substructure analysis methodology to improve chatter free cutting conditions prediction, Int. J. Mach. Tools Manuf. 72 (2013) 16–24.
[14] I. Mancisidor, A. Urkiola, R. Barcena, J. Munoa, Z. Dombovari, M. Zatarain, Receptance coupling for tool point dynamic prediction by fixed boundaries approach, Int. J. Mach. Tools Manuf. 78 (2014) 18–29.
[15] T.L. Schmitz, G.S. Duncan, Three-component receptance coupling substructure analysis for tool point dynamics prediction, Trans. ASME—J. Manuf. Sci. Eng. 127 (2005) 781–790.
[16] A. Erturk, H. Ozguven, E. Budak, Analytical modeling of spindle–tool dynamics on machine tools using Timoshenko beam model and receptance coupling for the prediction of tool point FRF, Int. J. Mach. Tools Manuf. 46 (2006) 1901–1912.
[17] A. Erturk, H. Ozguven, E. Budak, Effect analysis of bearing and interface dynamics on tool point frf for chatter stability in machine tools by using a new analytical model for spindle-tool assemblies, Int. J. Mach. Tools Manuf. 47 (2007) 23–32.
[18] T.L. Schmitz, K. Powell, D. Won, G.S. Duncan, W.G. Sawyer, J.C. Ziegert, Shrink fit tool holder connection stiffness/damping modeling for frequency response prediction in milling, Int. J. Mach. Tools Manuf. 47 (2007) 1368–1380.
[19] M. Namazi, Y. Altintas, T. Abe, N. Rajapakse, Modeling and identification of tool holder–spindle interface dynamics, Int. J. Mach. Tools Manuf. 47 (2007) 1333–1341.
[20] H. Ahmadian, M. Nourmohammadi, Tool point dynamics prediction by a three-component model utilizing distributed joint interfaces, Int. J. Mach. Tools Manuf. 50 (2010) 998–1005.
[21] O. Ozsahin, Y. Altintas, Prediction of frequency response function (FRF) of asymmetric tools from the analytical coupling of spindle and beam models of holder and tool, Int. J. Mach. Tools Manuf. 92 (2015) 31–40.
[22] S. Park, J. Chae, Joint identification of modular tools using a novel receptance coupling method, Int. J. Adv. Manuf. Technol. 35 (2008) 1251–1262.
[23] Y. Altintas, Analytical prediction of three dimensional chatter stability in milling, JSME Int. J. Ser. C 44 (3) (2001) 717–723.
[24] Y. Altintas, J. Ko, Chatter stability of plunge milling, CIRP Ann.—Manuf. Technol. 55 (2006) 361–364.
[25] J. Roukema, Y. Altintas, Generalized modeling of drilling vibrations, Part I: time domain model of drilling kinematics, dynamics and hole formation, Int. J. Mach. Tools Manuf. 47 (2007) 1455–1473.
[26] J. Roukema, Y. Altintas, Generalized modeling of drilling vibrations, Part II: chatter stability in frequency domain, Int. J. Mach. Tools Manuf. 47 (2007) 1474–1485.
[27] T. Schmitz, Torsional and axial frequency response prediction by RCSA, Precis. Eng. 34 (2010) 345–356.
[28] S. Filiz, O. Ozdoganlar, A model for bending, torsional, and axial vibrations of micro and macro-drills including actual drill geometry—Part I: model development and numerical solution, J. Manuf. Sci. Eng.—Trans. ASME 132 (2010) 041017–1–8.
[29] S. Filiz, O. Ozdoganlar, A model for bending, torsional, and axial vibrations of micro and macro-drills including actual drill geometry—Part II: validation and application, J. Manuf. Sci. Eng.—Trans. ASME 132 (2010) 041018–1–10.
[30] S. Filiz, O. Ozdoganlar, A three-dimensional model for the dynamics of micro-endmills including bending, torsional and axial vibrations, Precis. Eng. 35 (2011) 24–37.
[31] B. Bediz, U. Kumar, T.L. Schmitz, O. Ozdoganlar, Modeling and experimentation for three-dimensional dynamics of end mills, Int. J. Mach. Tools Manuf. 53 (2012) 39–50.
[32] T. Yokoyama, Vibrations of a hanging Timoshenko beam under gravity, J. Sound Vib. 142 (2) (1990) 245–258.
[33] G. Cowper, The shear coefficient in Timoshenko's beam theory, Trans. ASME—J. Appl. Mech. 33 (1966) 335–340.
[34] S.S. Rao, Mechanical Vibrations, 5th ed., Prentice-Hall, Upper Saddle River, NJ, 2011.
[35] J. Roukema, Mechanics and dynamics of drilling (Ph.D. thesis), 2006.
[36] H. Ozguven, Structural modifications using frequency response functions, Mech. Syst. Signal Process. 4 (1990) 53–63.
[37] T.L. Schmitz, K.S. Smith, Machining Dynamics: Frequency Response for Improved Productivity, Springer, New York, 2009.

Int. J. Production Economics 165 (2015) 282–292

Contents lists available at ScienceDirect

Int. J. Production Economics

journal homepage: www.elsevier.com/locate/ijpe

An optimization method for shopfloor material handling based on real-time and multi-source manufacturing data

Yingfeng Zhang *, Geng Zhang, Wei Du, Junqiang Wang, Ebad Ali, Shudong Sun

Key Laboratory of Contemporary Design and Integrated Manufacturing Technology, Ministry of Education, Northwestern Polytechnical University, Xi'an 710072, China

ARTICLE INFO

Article history:
Received 31 December 2013
Accepted 27 December 2014
Available online 7 January 2015

Keywords:
Real-time and multi-source data
Material handling
Dynamical optimization
Intelligent trolley

ABSTRACT

With the wide use of auto-ID devices in manufacturing shop floors, it creates a huge number of real-time and multi-source manufacturing data. To make a better decision based on the real-time and multi-source manufacturing data, in this paper, a dynamical optimization model for shopfloor material handling (DOM-SMH) is designed. Contrast to a traditional material handling method, each trolley is an active entity which will request the transport tasks. Then, the optimal transport tasks will be assigned to the optimal trolleys according to their real-time status. The key technologies such as intelligent trolley, real-time information exchange and optimization for material handling tasks are designed and developed to implement the dynamical optimization model. The presented method is demonstrated by a case study, and its effectiveness is also analyzed and discussed through the empty-loading ratio and total distance.
© 2015 Elsevier B.V. All rights reserved.

1. Introduction

With the rapid development of industrial wireless network and auto-ID technologies (e.g., radio frequency identification, RFID, Bluetooth and Wi-Fi), many enterprises adopt these advanced technologies to implement real-time traceability, visibility and interoperability in improving the performance of shopfloor planning, execution and control (Huang et al., 2009), and a huge number of manufacturing data has been produced during manufacturing execution stage. According to a report from McKinsey & Company, in 2010, the manufacturing and service sectors stored about two exabytes of new data, which is more than any other sectors (http://www.ge-ip.com/library/detail/13170).

Material handling in the shopfloor has gained extensively attention in order to improve the production efficiency. Herrmann et al. (1995) design the material flow networks to improve the transport efficiency and reduce the transport time. Anwar and Nagi (1998) put forward a heuristic method to the simultaneous scheduling problem of material handling transporters in the production of complex assembled product. Lee and Maneesavet (1999) provide dispatching strategies for the rail-guided vehicle scheduling problem in a flexible manufacturing system. Khayat et al. (2006) propose an integrated formulation to solve the combined production and material handling scheduling problems. Asef-Vaziri et al. (2007) develop the heuristic procedures to minimize the total loaded and empty vehicle trip distances. Boonprasurt and Nanthavanij (2012) present an optimal model for the vehicle routing problem with manual material handling.

Recently, by extending the IoT (Internet of Things) technologies such as RFID and Barcode to manufacturing environment (Zhang et al., 2014b), real-time and multi-source data has become more accessible and ubiquitous, contributing to the big data environment. The real time data streams coming from this sensor network will challenge the traditional approaches to a material handling system. Recent advances and trends of a future manufacturing system in big data environment are described by Lee et al. (2013). They point out that material handling will be more efficient based on the huge real-time data.

Despite significant progress achieved by the researchers in the field of material handling, major challenges still exist in applying real-time and multi-source manufacturing data driven decision to material handling in a manufacturing big data environment. They are summarized as follows:

1) How to design a new allocation strategy of material handling tasks to implement real-time move tasks assignment. Generally, move tasks are centrally assigned according to a given objective, for example, the minimum total transport time. However, during the execution, the deviation between the plan and execution is often produced because of the unpredictable exceptions. The more the move tasks, the greater the deviations. These deviations will further lead to serious production exceptions. Therefore, a new material handling strategy should be considered to avoid or reduce the deviation based on the real-time data.

* Correspondence to: RM 509, Hangkong Building, Northwestern Polytechnical University, No. 127, Youyi West Road, Xi'an, Shaanxi, China. Tel.: +86 13991135396.
E-mail address: zhangyf@nwpu.edu.cn (Y. Zhang).

http://dx.doi.org/10.1016/j.ijpe.2014.12.029
0925-5273/© 2015 Elsevier B.V. All rights reserved.

2) How to apply auto-ID devices and information technologies to enable the trolleys have the capability of active sensing and intelligence so that the real-time material handling can be achieved. By introducing the intelligence and auto-ID devices to the trolleys, they can sense the different manufacturing resources (e.g., operator, material, pallet, location etc.) and actively request the move tasks, and the real-time status of each trolley could be timely tracked and traced. Based on these multi-source data, real-time data driven intelligent navigation can be implemented to enhance the delivery efficiency.
3) How to combine the different move tasks according to the priority of tasks, maximum load and volume of the trolleys to implement green transport and optimal transport route. In the traditional material handling method, the combination optimization method of move tasks is rarely taken into account. In fact, for the low carbon purpose, it is necessary to design a combination method of move tasks to improve the efficiency and reduce the transport cost.

To address the above challenges, in this research, a dynamical optimization method for shopfloor material handling (DOM-SMH) based on real-time and multi-source manufacturing data is proposed. It integrates three important features. The first is a new allocation strategy for move tasks. The second is the intelligent trolleys with the capability of active sensing and self-decision. The third is the combination optimization method of move tasks to reduce the transport cost and energy. The designed DOM-SMH will provide a new paradigm for manufacturing enterprises to implement real-time data driven optimization of material handling.

The rest of the paper is organized as follows. Section 2 reviews the related literature. Section 3 outlines the new active material handling strategy and an overall architecture of DOM-SMH. Section 4 describes the overall solution for implanting the intelligent trolley with the capability of active sensing, interaction and self-decision. A dynamic optimization model supported by real-time information is described in Section 5. In Section 6, a case study is used to illustrate the implementation of the proposed DOM-SMH. Conclusions and future works are given in Section 7.

2. A literature review

Two streams of the literature are relevant to this research. They are material handling and real-time data capturing in manufacturing field.

2.1. Material handling

Specialists have proposed many optimization models to improve the material distribution. Solomon (1987) summarizes some heuristic algorithms for vehicle routing and scheduling problem with time-window constraints and finds that several heuristics performed well in different problem environments. Basu et al. (1996) present the formalism for modelling intelligent control of material handling equipment in a distribution center. Then Veeravalli et al. (2002) present a framework for an efficient schedule of material delivery. In this framework, an optimal scheduling of Automated Guided Vehicle (AGV) is designed to increase the efficiency of the manufacturing process by minimizing the idle time of Machine Centers (MC) waiting for the raw materials. Zografos and Androutsopoulos (2004) design a new heuristic algorithm for solving hazardous materials distribution problems. Meng et al. (2005) describe a novel vehicle routing and scheduling problem with time-window constraints in hazardous material distribution. Ala-Risku and Kärkkäinen (2006) provide a potential solution for managing the material distribution of construct projects. Considering 300 mm semiconductor manufacturing, Im et al. (2009) propose an efficient vehicle dispatching rule to minimize the vehicle blocking and delivery times in automatic material handling systems. In order to improve the material distribution operations, Chakravorty (2009) emphasizes that the implementation of the material distribution system involves both human factors and technical factors.

2.2. Real-time data capturing in manufacturing field

In recent years, many approaches, models and methodologies have been proposed in the IoT application domains, especially for the RFID-based applications. Lee and Özer (2007) have addressed RFID technology to be a promising technology to track movements of goods in supply chain. Chow et al. (2006) design a RFID case-based resource management system for warehouse operations. Kim et al. (2010) present a market-based approach for dynamic vehicle deployment planning using RFID information. In order to explore the potential business cases for RFID, Delen et al. (2007) conduct a case study using actual RFID data collected by a major retailer for the cases shipped by one of its major suppliers. Zhang et al. (2011a) present a novel research on implementing the RFID technology in the application of assembly guidance in an augmented reality environment. Kim et al. (2008) analyze the positive value of location-enabled RFID information on delivery chain performance. Several relevant models incorporating with RFID technology have been applied to real-time manufacturing cases. Zhang et al. (2011b, 2014a) propose an agent-based smart gateway for RFID-enabled real-time wireless manufacturing. In addition, they have been respectively illustrated in RFID-enabled fixed-position assembly (Huang et al., 2007), wireless shop-floor inventory management (Huang et al., 2008a) and wireless production line (Huang et al., 2008b). A distributed work flow management model from shop-floor level (Zhang et al., 2010) is established to define, configure and execute the real-time RFID enabled manufacturing processes. Ferrer et al. (2011) evaluate the use of RFID technology for improving the remanufacturing efficiency in a large job shop. Qu et al. (2012) have implemented RFID technologies for constructing real-time shop-floor material management.

Above studies focus mainly on the material handling problems in a traditional manufacturing environment. The IoT and big data will bring the new decision strategies to the manufacturing system in many perspectives. For example, the significant amount of data generated will promote the real-time decision models. Therefore, some research questions should be further studied in the manufacturing big data environment. The first is the new allocation strategy of material handling tasks based on the real-time and multi-source data. The second is how to make the trolleys intelligent. The third is how to rapidly combine the different move tasks and optimal transport routes for the distributed trolleys. To address these research problems, a DOM-SMH is presented and designed to implement real-time data driven optimization of material handling in the manufacturing big data environment.

3. Overview of DOM-SMH based on real-time and multi-source manufacturing data

This research focuses mainly on the discrete manufacturing and the fixed position assembly environment. The objective of the DOM-SMH proposed in this paper is to implement the interactive ability of distribution resources by extending auto-ID technologies to the process of material handling, and thus achieve dynamical optimization of move tasks based on the real-time status of the trolleys.

For better understanding, two kinds of material handling strategies are shown in Fig. 1. Fig. 1(a) and (b) describes the traditional material handling strategy and active material handling strategy based on real-time data respectively.

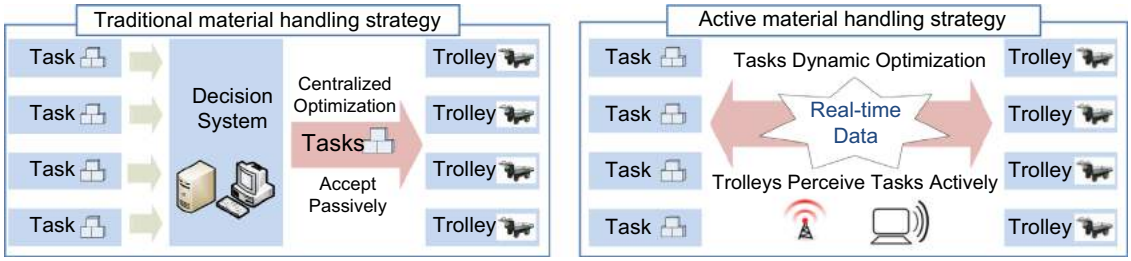

Fig. 1. Comparison between two kinds of material handling strategies. (a) Traditional material handling strategy (b) active material handling strategy.

In the traditional material handling strategy, all the tasks are centrally assigned to the corresponding trolleys by a distribution system. The decision model is centralized and the trolleys do not interact with the other distribution resources. As a result, the real-time information of distribution resource has not been considered in the traditional method. And the deviation between the plan and execution is often produced because of the unpredictable exceptions. Moreover, the computational complexity is higher with the increasing of move tasks and trolleys.

In the active material handling strategy based on real-time and multi-source data, all the move tasks will form a tasks pool at first, then each trolley will automatically send its real-time status and request of the move tasks when it is idle. The move tasks server continually interacts with the trolleys. The optimal move tasks will be assigned to the optimal trolleys and operators according to their real-time status. The active material handling strategy follows this rule: at each time, only one optimal move task will be assigned to the requested trolley. When the trolley finishes the assigned task, it will automatically send its current status and request the move tasks again until all the tasks are finished.

The proposed active material handling strategy has the following advantages. At any time, each trolley can obtain the optimal move task. The complexity of this problem is stable with the increasing of move tasks and trolleys because only one optimal task is selected for one trolley at each time. Since the task allocation is real-time data driven and the allocation strategy is only started for the idle trolleys, the deviation between plan and execution in traditional strategy can be largely eliminated through the active material handling strategy.

Based on the proposed active material handling strategy, a conceptual architecture for DOM-SMH is designed as seen in Fig. 2. It includes three main modules, namely (1) intelligent trolleys, (2) real-time information exchange, and (3) optimization for material handling tasks.

Intelligent trolleys module is used to make the trolleys have the capability of active perception and dynamic interaction by adopting auto-ID and web services technologies. This module is a core technology of active shopfloor material handling. Real-time information exchange module is responsible for building up a bridge to exchange the real-time and multi-source data between the distributed trolleys and the move tasks pool. Then, the optimal tasks can be dynamically assigned to the suitable trolleys. Optimization for material handling tasks module is used to combine the move tasks according to the priority of tasks, maximum load and volume of the trolleys to implement green transportation and optimal transport routes.

4. Overall solution of intelligent trolleys

In the active material handling strategy, the capturing and usage of real-time and multi-source data of trolleys play an important role. This section will describe how to make the trolleys be intelligent by using the advanced technologies such as auto-ID, web services and workflow.

Fig. 3 shows the overall solution of intelligent trolleys. It aims to make the trolleys have the capability of active sensing, interaction and self-decision. It consists of three components, namely real-time and multi-source data sensing and encapsulation, real-time information exchange and workflow based real-time navigation. The functions of each component are described as follows.

(1) Real-time and multi-source data sensing and encapsulation
It is responsible for providing the active sensing capability for the trolleys. As seen in the middle of Fig. 3, some hardware devices are used to timely capture the real-time data. Here, the main hardware includes industrial control computer, RFID reader and antennas. The details of hardware are listed in Table 1. Some software and temp real-time data are designed and stored in the industrial control computer. RFID reader and antennas are used to sense the status of manufacturing resources attached to RFID tags, for example, operators, key WIP (work-in-progress) items, locations, pallets and so on.
For better managing and exchanging, an information model of trolleys is built up to encapsulate the real-time and multi-source data shown in the lower-left of Fig. 3. The information model contains four nodes, namely code of trolleys, maximum volume, current location and used volume. It is stored in the matrix *V*. The instance of the information model at time '*t*' is the real-time status to the related trolley at the same time '*t*'.

$$V = \begin{bmatrix} VID_1 & V^1_{max} & CL_1 & V^1_u \\ VID_2 & V^2_{max} & CL_2 & V^2_u \\ VID_3 & V^3_{max} & CL_3 & V^3_u \\ \dots & \dots & \dots & \dots \\ VID_i & V^i_{max} & CL_i & V^i_u \end{bmatrix}$$

Here VID_i is defined as the code of trolley i, V^i_{max} is defined as the maximum volume of trolley i, CL_i is defined as the real-time location of trolley i, V^i_u is defined as the used volume of trolley i. By this way, each event and detailed data of each operation related to move task execution could be tracked and traced.

(2) Real-time information exchange
It is used to implement the real-time information exchange between the trolleys and the move tasks server. The lower-right of Fig. 3 shows the work logic of information transfer mechanism. SOA (Service-oriented Architecture) is used in this component to implement real-time and multi-source data sending and receiving. The process can be described as follows: for any idle intelligent trolleys, the real-time status of the trolley will be first formed an XML-based schema including trolley ID, maximum volume, current location and current operator. Then, the sendCurrentStatus() method will be invoked to send the real-time information (an XML instance) to the move task server. Then, the web service of move tasks server side can receive the real-time status information of the requested trolley, and the taskOptimizationMethod() is started to calculate the optimal move task according to the real-time information of trolleys and move tasks. Finally, the sendMoveTask() method is invoked to

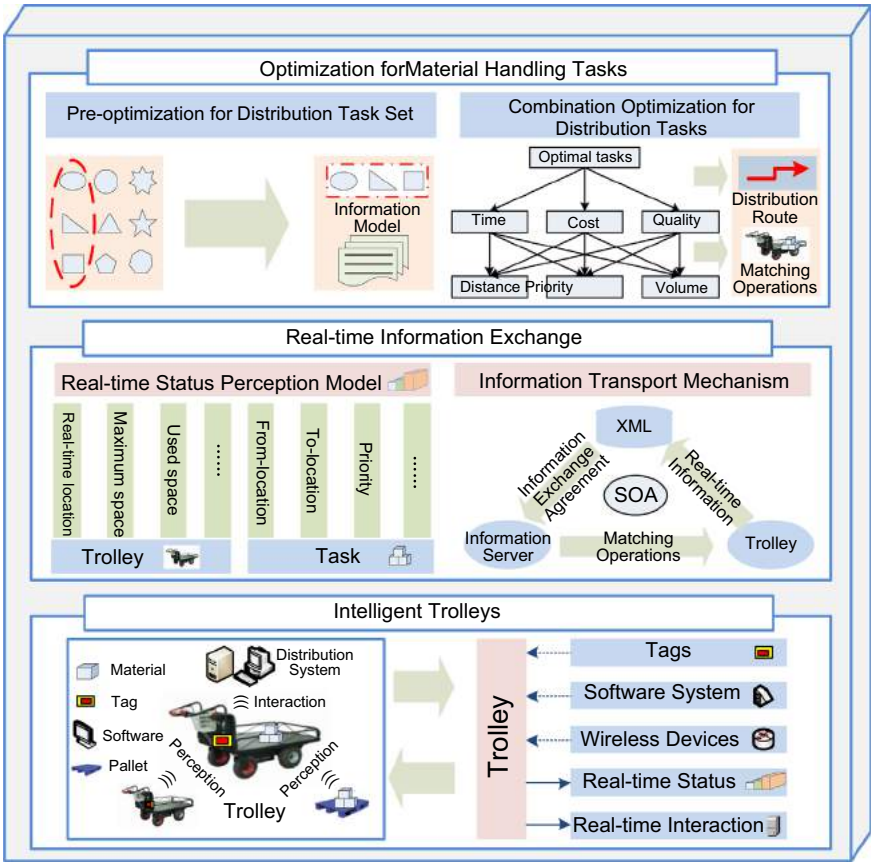

Fig. 2. Overall architecture of DOM-SMH.

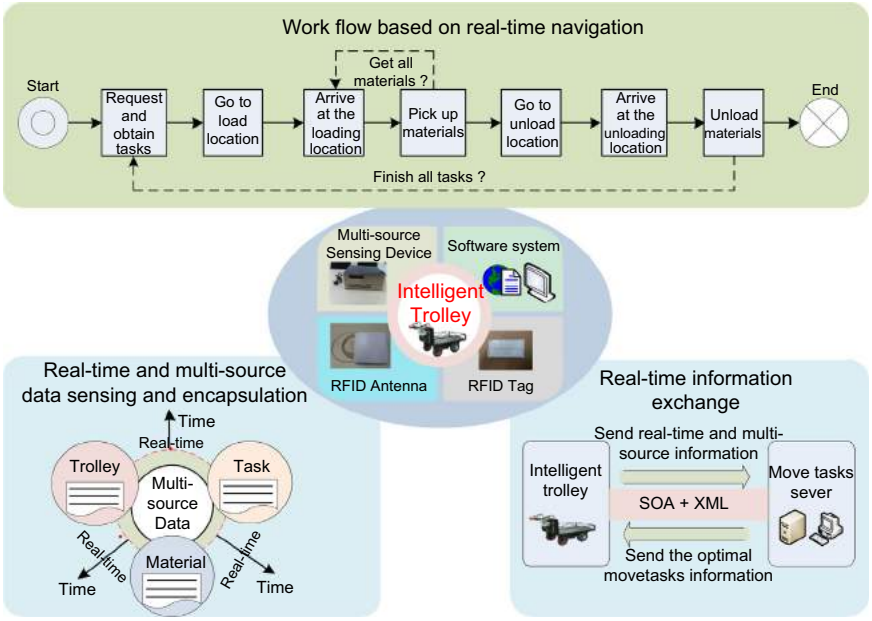

Fig. 3. Overall solution of the proposed intelligent trolleys.

transfer the result of the taskOptimizationMethod(). The optimization method will be described in Section 5.

(3) Workflow based real-time navigation

It is used to provide the self-decision capability and real-time data driven navigation for trolleys and operators. To fulfil this purpose, workflow is introduced to this component. As seen in the top of Fig. 3, the topology of key processes involved in move tasks execution is pre-defined. It includes seven activities, namely (1) request and obtain task, (2) go to load location, (3) arrive at the loading location, (4) pick up materials, (5) go to unload

Table 1
The details of the hardware devices of the intelligent trolley.

Hardware name	Main parameters	Function
Industrial control computer	• Model: PCA-6007LV • Memory: 1 G • Hard disk: 160 G	• Connect the RFID reader and capture the real-time data • Send the real-time status of the trolley to handling task server and get the assigned handling tasks from the task server • Real-time navigate the operator
RFID reader	• Model: XAFD6132C • Working frequency: 902–928 MHz • RF power: 0–30 dB m, adjustable • Interface: support RS232, RS485, TCPIP • Antenna interfaces: 4 • Reading distance: 0–2 m, adjustable	• Connect the three antennas for sensing the operator, material items, and position data • Transmit the captured real-time data to industrial control computer through RS232
Antenna	• Type: UHF • Gain: 16 dBi • VSWR: d1.5 • F/B ratio: >25 dB • Impedance: 50 Ω	• Three antennas are deployed at the trolley to sense the real-time data of the tags attached to different manufacturing resources such as operator, material items, and position data

location, (6) arrive at the unloading location, and (7) unload materials. The flow (2) to (4) or flow (5) to (7) is repeated if the move task includes multi load locations or multi unload locations.

During the move task execution, the real-time navigation will be graphically shown in the screen to help the operators finish the tasks with high efficiency and correctness. The details will be described and illustrated in Section 6.

5. Two-stage material handling tasks optimization method

Based on the intelligent trolleys designed in Section 4, a dynamic optimization model for move tasks will be designed in this section. It acquires the optimal combination of better tasks for current trolley by dealing with multi-source information and integrating real-time distribution requirements. Because of the huge move tasks in the manufacturing enterprises, a two-stage optimization method is designed to reduce the complexity of the tasks combination and improve the solving efficiency for the real-time decision. In this two-stage optimization method, the first stage is used to obtain a candidate task set from the whole move tasks. The second stage is used to combine the optimal tasks from the candidate task set. The objective of this optimization method is to combine and optimize a series of material handling tasks based on the real-time and multi-source manufacturing data.

5.1. Real-time information models of move tasks

Before describing the optimization method, it is necessary to introduce the information model of the tasks. There are N tasks in the move task pool. Information of each task includes following aspects: code of task, from and to locations of task, due time, priority of task, and index number of task and material information such as material code, material number and material volume matched with its index. The information models of N tasks are stored in the matrix N. Here TID_j represents the code of task j, FL_j represents from-location of task j, TL_j represents the to-location of task j, D_j represents the due time of task j, P_j represents priority of task j, IID_j represents material index number of task j.

$$N=\begin{bmatrix} TID_1 & FL_1 & TL_1 & D_1 & P_1 & IID_1 \\ TID_2 & FL_2 & TL_2 & D_2 & P_2 & IID_2 \\ \cdots & \cdots & \cdots & \cdots & \cdots & \cdots \\ TID_j & FL_j & TL_j & D_j & P_j & IID_j \\ \cdots & \cdots & \cdots & \cdots & \cdots & \cdots \\ TID_N & FL_N & TL_N & D_N & P_N & IID_N \end{bmatrix}$$

The information models of materials contain following nodes, code of material, names of materials, quantity of material and unit volume of each material. Material information model of task j is stored in matrix W_j. Here $ICode_{jk}$ is defined as the code of material k, $Name_{jk}$ is defined as the name of material k, Q_{jk} is defined as the quantity of material k, V_{jk} is defined as the unit volume of material k.

$$W_j=\begin{bmatrix} ICode_{j1} & Name_{j1} & Q_{j1} & V_{j1} \\ ICode_{j2} & Name_{j2} & Q_{j2} & V_{j2} \\ ICode_{j3} & Name_{j3} & Q_{j3} & V_{j3} \\ \cdots & \cdots & \cdots & \cdots \\ \cdots & \cdots & \cdots & \cdots \\ ICode_{jk} & Name_{jk} & Q_{jk} & V_{jk} \end{bmatrix}$$

5.2. Pre-optimization for candidate tasks set

Pre-optimization for candidate tasks set is used to select better tasks for further combining and optimization. It could avoid data redundancy because there are too many handling tasks in the task pool. All the handling tasks are pre-optimized according to their priority. The priority of each task is defined based on its due time. Generally, the earlier the due time, the higher the priority.

Candidate task set could be formed as following manner: select q tasks according to priorities values from high to low; if tasks have the same priorities values, select the task having earlier due

time. Information of candidate task set is stored in the matrix q.

$$q=\begin{bmatrix} TID_{q.1} & FL_{q.1} & TL_{q.1} & D_{q.1} & P_{q.1} & IID_{q.1} \\ TID_{q.2} & FL_{q.2} & TL_{q.2} & D_{q.2} & P_{q.2} & IID_{q.2} \\ TID_{q.3} & FL_{q.3} & TL_{q.3} & D_{q.3} & P_{q.3} & IID_{q.3} \\ \cdots & \cdots & \cdots & \cdots & \cdots & \cdots \\ \cdots & \cdots & \cdots & \cdots & \cdots & \cdots \\ TID_{q.q} & FL_{q.q} & TL_{q.q} & D_{q.q} & P_{q.q} & IID_{q.q} \end{bmatrix}$$

The feasible tasks combinations are formed based on the above candidate task set. Any one task or more tasks are selected form the candidate task set, and form one feasible tasks combination. It is a rule that the volume of any feasible tasks combination must not exceed the maximum volume of current trolley.

5.3. AHP-based combination optimization

AHP is known as a multiple criteria decision-making tool that has been used in almost all the applications related with decision-making (Vaidya and Kumar (2006)). Therefore, an AHP-based combination optimization is designed to create the optimal move tasks combination from the tasks set selected in Section 5.2. It combines the different move tasks according to the priority of tasks, maximum load and volume of the trolleys to implement green transport. In this research, the transport distance of trolley, the priorities of move tasks and the used volume of trolley are considered as important factors to combine the task set.

In this section, the AHP is introduced to identify the weight coefficients of the handing distance, priority and the used volume of the trolley in the optimal combination for the real-time handling tasks. Fig. 4 describes the AHP model of the optimal combination for the real-time handling tasks. Where the distribution cost, distribution time and distribution quality are taken as the criterion layer, and distance, priority and used volume are taken as the project layer.

To obtain the reasonable weight coefficient, the paired comparison method is firstly used to obtain the judgment matrix (A), which is represented by:

$$A=(a_{ij})_{n\times n}=\begin{bmatrix} a_{11} & a_{12} & \cdots & a_{1n} \\ a_{21} & a_{22} & \cdots & a_{2n} \\ \vdots & \vdots & \vdots & \vdots \\ a_{n1} & a_{n2} & \cdots & a_{nn} \end{bmatrix}$$

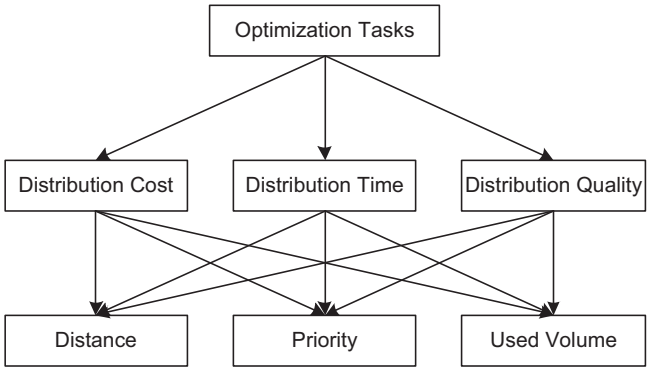

Fig. 4. The AHP model of the optimal combination for the real-time handling tasks.

Table 2
The defined notations.

c	One task combination
z	Number of material kind in one task
m	Number of tasks in one tasks combination,
L_c	Distribution distance of task combination c,
P_c	Priority of task combination c
U_c	Used volume of task combination c
w_L	Weights of L in function $f(L_c, P_c, U_c)$
w_P	Weights of P in function $f(L_c, P_c, U_c)$
w_U	Weights of U in function $f(L_c, P_c, U_c)$
P_0, L_0, U_0	Used to unify the dimensions of P, L, U
P_{cj}	Priority of task j in task combination c

Based on the judgment matrix A, the weight coefficient can be calculated by

$$w_i=\frac{\sqrt[n]{\prod_j a_{ij}}}{\sum \sqrt[n]{\prod_j a_{ij}}} \text{ and } \sum_i^n w_i=1, \quad W=(w_1,w_2,...,w_n)^T \tag{1}$$

Then, the consistency test is introduced to verify the effectiveness of the obtained weight coefficient. It includes the following steps.

First, establish the feature equation of the matrix A according to Eq. (2) and getting the maximum eigenvalue λ_{max} according to Eq. (3). Second, calculate the coincident indicator I_{CI} according to Eq. (4) and attain the average random coincident indicator $I_{RI}(n)$ corresponding to the variable$n$. Finally, make the consistency test according to Eq. (5). If the variable I_{CR} meets the following constraints: $I_{CR}<0.1$, then the judgment matrix is acceptable, namely the weight coefficients of the handing distance, priority and the used volume of the trolley in the optimal combination for the real-time handling tasks are identified as the vector: $(w_L,w_P,w_U)^T$.

$$A\lambda_{max}=\lambda_{max}W \tag{2}$$

$$\lambda_{max}=\frac{1}{n}\sum_i\left(\frac{(AW)_i}{w_i}\right) \tag{3}$$

$$I_{CI}=\frac{\lambda_{max}-n}{n-1} \tag{4}$$

$$I_{CR}=\frac{I_{CI}}{I_{RI}} \tag{5}$$

For better describing, the notations are defined as seen in Table 2.

The weights of distance, priority and used volume can be calculated according to steps of AHP. Then, the AHP-based combination optimization method can be implemented through the following steps described in Fig. 5.

(1). Construct the objective function of the tasks combination. Here, P_c represents priority of the tasks combination c, L_c represents distribution distance of c, U_c represents the used volume of c, w_L, w_P, w_U respectively represents the weights of P, L, U in function $f(L_c, P_c, U_c)$, P_0, L_0, U_0 are used to unify the dimensions of P, L, U, so the objective function could be:

$$\max \quad f(L_c,P_c,U_c)=w_L L_0/L_c+w_P P_c/P_0+w_U U_c/U_0 \tag{6}$$

(2). Calculate the run distance L_c of the tasks combination c. Here, L_C is the shortest distance of the tasks combination completed by current trolley. It is calculated based on the distances of all the positions that the trolley passed. A matrix

//The flow of AHP-based combination optimization

Input: The feasible tasks combinations related with current trolley.

Start

(1). **For** each incoming tasks combination c // c represents the incoming tasks combination

(2). **For** (c=1; c<=s; c++) // s represents the number of the tasks combinations

(3). Construct the objective function of task combination c

$$\max\ f(L_c,P_c,U_c)=w_L L_0/L_c+w_P P_c/P_0+w_U U_c/U_0$$

(4). Calculate the run distance of the tasks combination c // The shortest distance of current trolley will be gotten

(5). Calculate the priority of the tasks combination c $P_c=\sum_{j=1}^{m}P_{cj}$

(6). Calculate used volume of the tasks combination c $U_c=\sum_{j=1}^{m}\sum_{k=1}^{z}Q_{jk}V_{jk}$

(7). Calculate P_0, L_0, U_0 , $L_0=\frac{1}{S}\sum_{c=1}^{S}L_c$, $P_0=\frac{1}{S}\sum_{c=1}^{S}P_c$, $U_0=\frac{1}{S}\sum_{c=1}^{S}U_c$

(8). Calculate weights w_L , w_P , w_U according to the AHP

(9). Calculate the value of $f(L_c,P_c,U_c)$ according to the equation

(10). Find the task combination with biggest $f(L_c,P_c,U_c)$

End

Output: Detailed information of the tasks combination with biggest $f(L_c,P_c,U_c)$

Fig. 5. The flows of AHP-based combination optimization.

D is used to store the values of the distances between any two positions in the shopfloor.

$$D=\begin{bmatrix} DP_{11} & DP_{12} & \cdots & DP_{1i} & \cdots & DP_{1j} & \cdots & DP_{1n} \\ DP_{21} & DP_{22} & \cdots & DP_{2i} & \cdots & DP_{2j} & \cdots & DP_{2n} \\ \vdots & \vdots & \ddots & \vdots & \vdots & \vdots & \vdots & \vdots \\ DP_{i1} & DP_{i2} & \cdots & DP_{ii} & \cdots & DP_{ij} & \cdots & DP_{in} \\ \vdots & \vdots & \vdots & \vdots & \ddots & \vdots & \vdots & \vdots \\ DP_{j1} & DP_{j2} & \cdots & DP_{ji} & \cdots & DP_{jj} & \cdots & DP_{jn} \\ \vdots & \vdots & \vdots & \vdots & \vdots & \vdots & \ddots & \vdots \\ DP_{n1} & DP_{n2} & \cdots & DP_{ni} & \cdots & DP_{nj} & \cdots & DP_{nn} \end{bmatrix}$$

where DP_{ij} represents the distance between the position ID_i and the position ID_j, obviously, $DP_{ii}=0$, $DP_{jj}=0$,$DP_{ij}=DP_{ji}$.

(3). Calculate the priority P_c of the tasks combination c according to Eq. (8). Here, m is the number of tasks in one tasks combination and P_c is the priority of task combination c.

$$P_c=\sum_{j=1}^{m}P_{cj} \tag{7}$$

(4). Calculate the used volume U_c of task combination c according to Eq. (8). Here, z is the number of material kind in one task.

$$U_c=\sum_{j=1}^{m}\sum_{k=1}^{z}Q_{jk}V_{jk} \tag{8}$$

(5). Calculate P_0, L_0, U_0 according to Eqs. (9)–(11) respectively. Here, S is the number of the feasible tasks combination.

$$L_0=\frac{1}{S}\sum_{c=1}^{S}L_c \tag{9}$$

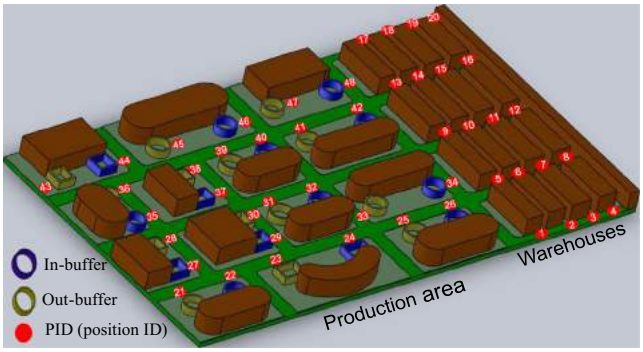

Fig. 6. Layout of a sensing manufacturing environment.

Table 3
Information of trolleys.

Code	PID (Current location)	Maximum use of volume	Used volume
VID_1	10	15	12
VID_2	38	15	8
VID_3	33	15	0
VID_4	26	15	8

Table 4
Information of distribution tasks.

Code	PID (from-location)	PID (to-location)	Due time	Priority	Index no.	Volume
TID_1	5	32	150	1	IID_1	11
TID_2	45	27	140	1	IID_2	3
TID_3	23	35	130	1	IID_3	5
TID_4	11	44	120	1	IID_4	12
TID_5	21	37	110	1	$IID5$	8
TID_6	16	34	100	1	IID_6	4
TID_7	43	29	90	2	IID_7	10
TID_8	13	24	80	2	IID_8	6
TID_9	25	9	70	2	$IID9$	9
TID_{10}	39	22	60	2	IID_{10}	7
TID_{11}	28	40	50	3	IID_{11}	5
TID_{12}	31	46	40	3	IID_{12}	7
TID_{13}	7	42	30	3	IID_{13}	10
TID_{14}	30	48	20	4	IID_{14}	4
TID_{15}	41	19	10	4	IID_{15}	6

$$P_0 = \frac{1}{S}\sum_{c=1}^{S} P_c \tag{10}$$

$$U_0 = \frac{1}{S}\sum_{c=1}^{S} U_c \tag{11}$$

(6). Obtain the reasonable weights w_L, w_P, w_U according to Eqs. (1)–(5).
(7). Calculate the value of $f(L_c, P_c, U_c)$ according to Eq. (6).

The value of $f(L_c, P_c, U_c)$ is used to evaluate the quality of the tasks combinations. The bigger the value of $f(L_c, P_c, U_c)$, the better the tasks combinations. Current trolley will perform the tasks combination with the biggest$f(L_c, P_c, U_c)$. Tasks sever will transfer the information of the task combination to the trolley, and the trolley will execute the task according to the given information.

6. Case study

A material handling case is described and analyzed in this section to illustrate the strategy and methods designed in this research.

Table 5
Information of candidate task set.

Code	PID (from-location)	PID (to-location)	Due time	Priority	Index no.	Volume
TID_{11}	28	40	50	3	IID_{11}	5
TID_{12}	31	46	40	3	IID_{12}	7
TID_{13}	7	42	30	3	IID_{13}	10
TID_{14}	30	48	20	4	IID_{14}	4
TID_{15}	41	19	10	4	IID_{15}	6

Table 6
Values of parameters.

Parameter	P_0	L_0	U_0	w_p	w_L	w_u
Value	4.833	214	9.75	0.333	0.333	0.333

6.1. Configuration of a sensing manufacturing environment

For simplicity of understanding but without losing generality of principle, some basic manufacturing resources are selected for configuring a sensing manufacturing environment. As shown in Fig. 6, this demo manufacturing environment consists of the following main components, namely a production area with fourteen workstations, each workstation has an in-buffer and an out-buffer; a stock area and 3D shelves for storing materials, WIP and finished products; four trolleys with the capability of active sensing, interaction and self-decision by installing auto-ID devices, industrial control computer and web services.

In order to implement the active sensing of real-time and multi-source manufacturing data during material handling execution, some types of manufacturing resources are attached tags. The first is the locations. Each crossing, in-buffer, out-buffer and shelf is tagged for providing the real-time location data. Then, each pallet and key WIP item should be tagged for providing the material data. Each logistic operator also has a staff card (RFID tag) to provide operator information.

6.2. Implementation of the active material handling strategy and methods

In this case, four intelligent trolleys and 15 move tasks are used to illustrate the proposed active material handling strategy and methods. The information of trolleys and move tasks are listed in Tables 3 and 4, where the position IDs (PID) represent the location of 'Current location', 'From-location' and 'To-location'. Fig. 6 shows the PIDs of the designed shopfloor. Then, the distance of each handling task can be easily calculated based on the matrix D defined in Section 5.3. In the priority column of, 1 represents 'common' task, 2 represents 'important' task, 3 represents 'urgent' task, 4 represents 'more urgent' task.

Construct real-time information model (V) of trolleys according to the information listed in Table 3;

$$V = \begin{bmatrix} VID_1 & 10 & 15 & 12 \\ VID_2 & 38 & 15 & 8 \\ VID_3 & 33 & 15 & 0 \\ VID_4 & 26 & 15 & 8 \end{bmatrix}$$

(2) Construct real-time information model (N) of distribution tasks according to information listed in Table 4; select 5 tasks as candidate tasks set and construct information model (q) of candidate task set. Table 5 lists the information of candidate

task set.

$$N=\begin{bmatrix} TID_1 & 5 & 32 & 150 & 1 & IID_1 \\ TID_2 & 45 & 27 & 140 & 1 & IID_2 \\ TID_3 & 23 & 35 & 130 & 1 & IID_3 \\ TID_4 & 11 & 44 & 120 & 1 & IID_4 \\ TID_5 & 21 & 37 & 110 & 1 & IID_5 \\ TID_6 & 16 & 34 & 100 & 1 & IID_6 \\ TID_7 & 43 & 29 & 90 & 2 & IID_7 \\ TID_8 & 13 & 24 & 80 & 2 & IID_8 \\ TID_9 & 25 & 9 & 70 & 2 & IID_9 \\ TID_{10} & 39 & 22 & 60 & 2 & IID_{10} \\ TID_{11} & 28 & 40 & 50 & 3 & IID_{11} \\ TID_{12} & 31 & 46 & 40 & 3 & IID_{12} \\ TID_{13} & 7 & 42 & 30 & 3 & IID_{13} \\ TID_{14} & 30 & 48 & 20 & 4 & IID_{14} \\ TID_{15} & 41 & 19 & 10 & 4 & IID_{15} \end{bmatrix}$$

$$q=\begin{bmatrix} TID_{11} & 28 & 40 & 50 & 3 & IID_{11} \\ TID_{12} & 31 & 46 & 40 & 3 & IID_{12} \\ TID_{13} & 7 & 42 & 30 & 3 & IID_{13} \\ TID_{14} & 30 & 48 & 20 & 4 & IID_{14} \\ TID_{15} & 41 & 19 & 10 & 4 & IID_{15} \end{bmatrix}$$

Table 7
Parameters of distribution tasks combinations.

Trolley	Task combination	Priority (*P*)	Distance (*L*)	Volume (*U*)	Value of *f* (*P*, *L*, *U*)
3	TID_{11}	3	141	5	0.801
3	TID_{12}	3	129	7	0.910
3	TID_{13}	3	163	10	0.902
3	TID_{14}	4	153	4	0.787
3	TID_{15}	4	143	6	0.883
3	TID_{11}, TID_{12}	6	225	12	1.024
3	TID_{11}, TID_{13}	6	255	15	1.088
3	TID_{11}, TID_{14}	7	245	9	0.958
3	TID_{11}, TID_{15}	7	207	11	1.073
3	TID_{12}, TID_{14}	7	173	11	1.136
3	TID_{12}, TID_{15}	7	235	13	1.101
3	TID_{13}, TID_{14}	7	183	14	1.213
3	TID_{14}, TID_{15}	8	229	10	1.066
3	TID_{11}, TID_{14}, TID_{15}	11	293	15	*1.335*

(3) It can be seen from the information model *V* that trolley 3 is in idle state. Then form the distribution task combinations related to trolley 3 according to the rule and method referred in Section 5.2.
(4) Construct objective function and select the best distribution tasks combinations according to the method referred in Section 5.3. The values of parameters are listed in Table 6 and all parameters of distribution tasks combinations are listed in Table 7.

According to Table 7, we can conclude that the task combination of TID_{11}, TID_{14} and TID_{15} has the biggest value. So trolley 3 will execute the three tasks at once. Fig. 7 shows the distribution routing of TID_{11}, TID_{14} and TID_{15} for trolley 3.

Fig. 8 demonstrates the flows of active material transport strategy based on real-time data of one intelligent trolley. The flow goes from the request-obtain a new move task of an idle intelligent trolley. As seen in Fig. 8(a), at beginning, when an operator come to and take one trolley, the staff information will be sensed and displayed by the intelligent trolley. And the idle intelligent trolley automatically sends its current status and requests task from the move tasks server. Then, the trolley will obtain the optimal move tasks according to the designed optimization method. Then, the real-time navigation of the intelligent trolley will navigate the operator to go the location to pick up materials as seen in Fig. 8(b) through an optimal route. When the operator and the trolley arrive at the loading location, a web page with the detailed materials location of the 3D shelf is popped up as seen in Fig. 8(c). During the materials loading, the event of each item loading into the trolley will be sensed by the intelligent trolley, and the loaded items will be marked in green as seen in Fig. 8(d). If the desired materials have been loaded, the navigation system will guide the operator and trolley to the next location for uploading as seen in Fig. 8(e). When the trolley arrives at the unloading location, the corresponding operations are started according to the navigation as seen in Fig. 8(f). Once the item leaves the trolley, the leaving event will be sensed by the intelligent trolley, and this item will be also marked in green. If the desired materials have been unloaded, this move task is finished, and the intelligent trolley will automatically send its current status and request task from the move tasks server again. Flows (a) to (f) are repeated by each intelligent trolley until all the tasks are assigned.

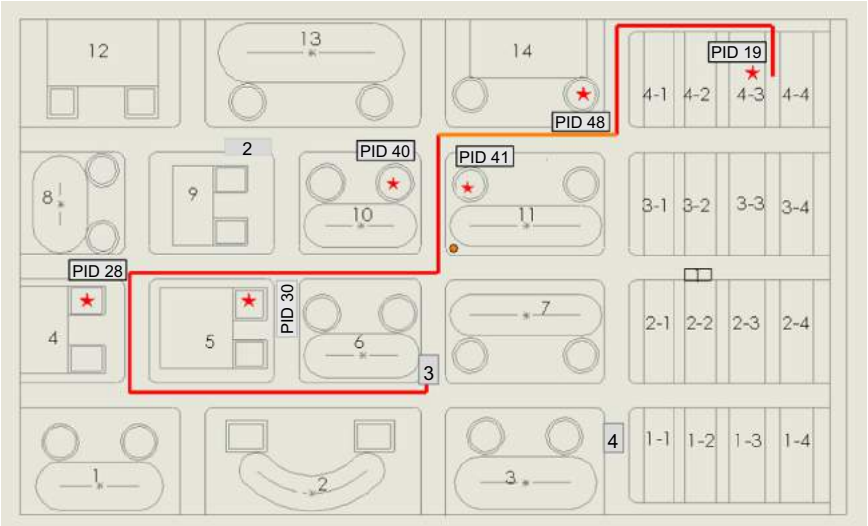

Fig. 7. Distribution routing of TID_{11}, TID_{14} and TID_{15}.

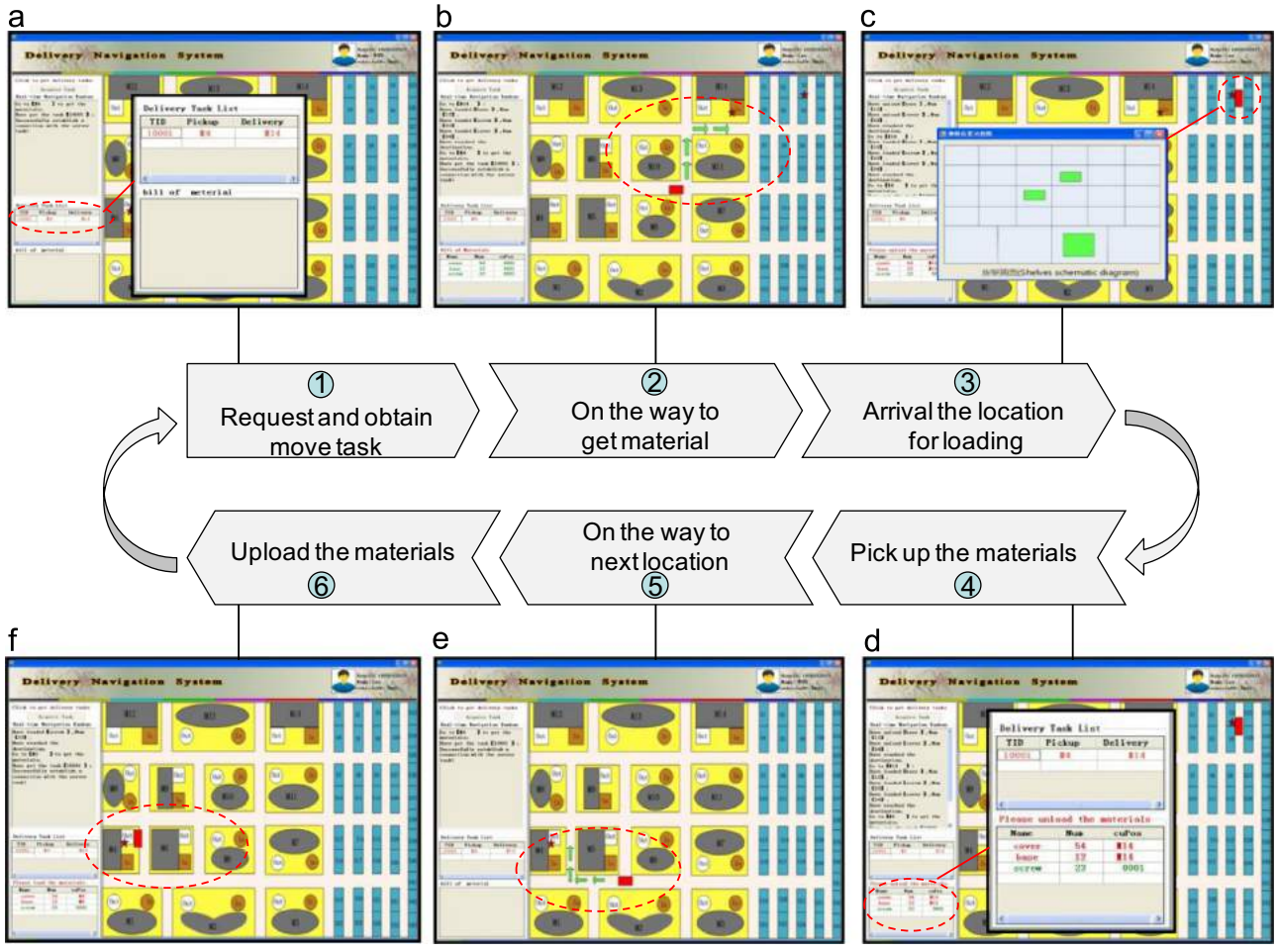

Fig. 8. Real-time data driven navigation of the intelligent trolley.

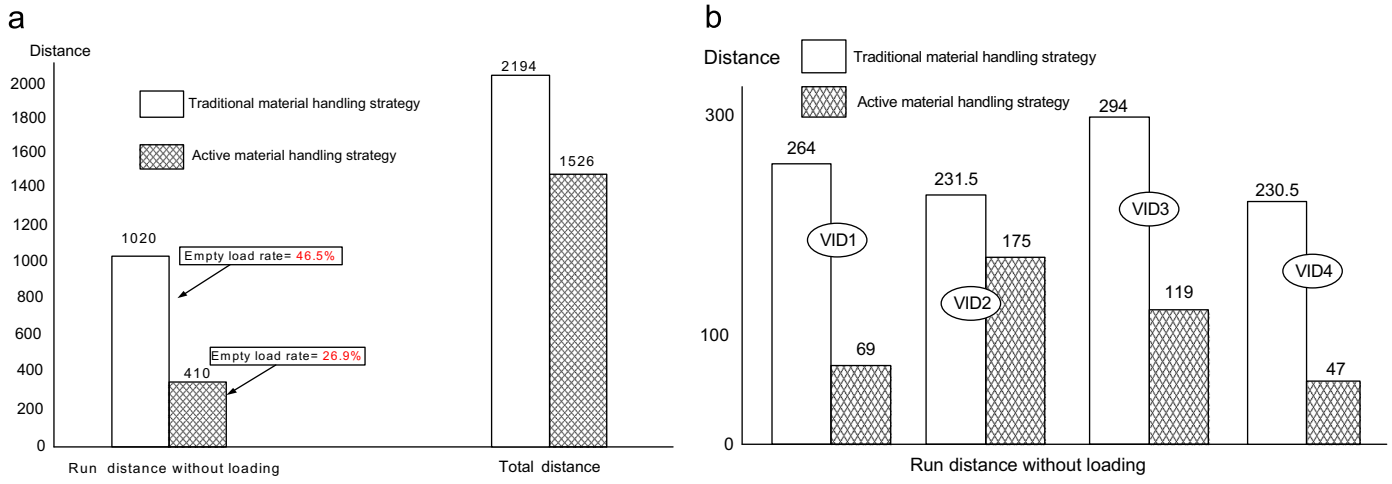

Fig. 9. Results analysis and discussion. (a) Load/no-load comparison of all trolleys (b) load/no-load comparison of each trolley.

6.3. *Analysis and discussion of the active material handling strategy and methods*

Fig. 9 shows the results comparison for the traditional distribution method and active material transport strategy based on real-time data. Fig. 9(a) shows the load/no load ratio comparison of 4 trolleys from run distance with/without load. Fig. 9(b) shows the load/no load comparison of each trolley from run distance with/without load.

From the results comparison, the presented active material transport strategy and method has the following advantages.

(1) The no-load ratio of all the trolleys is 19.6% lower as seen in the left of Fig. 9(a).

(2) The total run distance of all trolleys for finishing all the tasks is 668 units shorter as seen in the right of Fig. 9(a).
(3) The run distance of each trolley without loading is 195 (VID_1), 56.5 (VID_2), 175 (VID_3), 183.5 (VID_4) units shorter as seen in Fig. 9(b).

7. Conclusion

Recently, auto-ID technology (e.g., RFID, barcode) has been widely used in manufacturing shopfloors. Such an automatic data collection approach brings new challenges, for example, how to use the real-time and multi-source manufacturing data to design and develop dynamical decision support systems for improving the performance of shopfloor planning, execution and control. In this research, a new allocation strategy and dynamical optimization method of shopfloor material handling are proposed to provide a new paradigm for manufacturing enterprises to enhance the efficiency of material handling and reduce the delivery cost and energy.

Three contributions are important in this research. The first contribution is the active allocation strategy and overall architecture of the proposed DOM-SMH dynamical optimization method. Contrast to the traditional centrally allocation strategy, a new active allocation strategy is proposed. The distributed trolleys are active entities, they can active request the move tasks when they are idle and the task management center will timely assign the optimal tasks to the requesting trolley according to their real-time status. The second contribution is the intelligent trolleys with the capability of active sensing and self-decision. By applying auto-ID and web service techniques, each trolley has the capability of capturing the dynamical data from different manufacturing resources, sending the real-time and multi-source data, requesting and obtaining the move tasks, navigating the process of material handling etc. The third contribution is the combination optimization model for move tasks. Considering the low carbon in the optimal objective, a combination model of move tasks is designed using a two-stage optimization method for further improving the efficiency and reducing the transport cost.

The proposed active material handling strategy and relevant method of DOM-SMH just provide a new kind of mechanism to improve shopfloor transport efficiency by using the real-time and multi-source manufacturing data. Future research works will focus mainly on the integration of the DOM-SMH with the real-time production scheduling system. In addition, how to easily deploy and apply the key technologies of DOM-SMH to manufacturing industry is also to be taken into account.

Acknowledgment

Authors would like to acknowledge financial supports of National Natural Science Foundation of China (51175435), the Program for New Century Excellent Talents in University (NCET-12-0463), the research fund for the Doctoral Program of Higher Education (20136102110022), the Fundamental Research Funds for the Central Universities (3102014JCS05005), and the 111 project of NPU (B13044).

References

Ala-Risku, T., Kärkkäinen, M., 2006. Material delivery problems in construction projects: a possible solution. Int. J. Prod. Econ. 104 (1), 19–29.
Anwar, M.F., Nagi, R., 1998. Integrated scheduling of material handling and manufacturing activitiesfor just-in-time production of complex assemblies. Int. J. Prod. Res. 36 (3), 653–681.
Asef-Vaziri, A., Laporte, G., Ortiz, R., 2007. Exact and heuristic procedures for the material handling circular flow path design problem. Eur. J. Oper. Res. 176 (2), 707–726.
Basu, S., Huynh, V.M., Dutta, S.P., 1996. A formalism for modelling intelligent control of material handling equipment in a distribution centre. Int. J. Prod. Res. 34 (5), 1381–1398.
Boonprasurt, P., Nanthavanij, S., 2012. Optimal fleet size, delivery routes, and workforce assignments for the vehiclerouting problem with manual materials handling. Int. J. Ind. Eng. 19 (6), 252–263.
Chakravorty, S.S., 2009. Improving distribution operations: implementation of material handling systems. Int. J. Prod. Econ. 122 (1), 89–106.
Chow, H.K.H., Choy, K.L., Lee, W.B., Lau, K.C., 2006. Design of a RFID case-based resource management system for warehouse operations. Expert Syst. Appl. 30 (4), 561–576.
Delen, D., Hardgrave, B.C., Sharda, R., 2007. RFID for better supply-chain management through enhanced information visibility. Prod. Oper. Manag. 16 (5), 613–624.
Ferrer, G., Heath, S.K., Dew, N., 2011. An RFID application in large job shop remanufacturing operations. Int. J. Prod. Econ. 113 (2), 612–621.
Herrmann, J.W., Ioannou, G., Minis, I., 1995. Design of material flow networks in manufacturing facilities. J. Manuf. Syst. 14 (4), 277–289.
Huang, G.Q., Wright, P.K., Newman, S.T., 2009. Wireless manufacturing: a literature review, recent developments, and case studies. Int. J. Comput. Integr. Manuf. 22 (7), 579–594.
Huang, G.Q., Zhang, Y.F., Jiang, P.Y., 2007. RFID-based wireless manufacturing for walking-worker assembly islands with fixed-position layouts. Robot. Comput.-Integr. Manuf. 23, 469–477.
Huang, G.Q., Zhang, Y.F., Jiang, P.Y., 2008a. RFID-based wireless manufacturing for real-time management of job shop WIP inventories. Int. J. Adv. Manuf. Technol. 36 (7–8), 752–764.
Huang, G.Q., Zhang, Y.F., Newman, S., 2008b. RFID-enabled real-time wireless manufacturing for adaptive assembly planning and control. J. Intell. Manuf. 19 (6), 701–713.
Im, K., Kim, K., Park, T., Lee, S., 2009. Effective vehicle dispatching method minimising the blocking and delivery times in automatic material handling systems of 300 mm semiconductor fabrication. Int. J. Prod. Res. 47 (14), 3997–4011.
Khayat, G.E., Langevin, A., Riopel, D., 2006. Integrated production and material handling scheduling using mathematical programming and constraint programming. Eur. J. Oper. Res. 175 (3), 1818–1832.
Kim, J., Ok, C., Kumara, S., Yee, S., 2010. A market-based approach for dynamic vehicle deployment planning using radio frequency identification (RFID) information. Int. J. Prod. Econ. 128 (1), 235–247.
Kim, J., Tang, K., Kumara, S., Yee, S., Tew, J., 2008. Value analysis of location-enabled radio-frequency identification information on delivery chain performance. Int. J. Prod. Econ. 112 (1), 403–415.
Lee, H., Özer, Ö., 2007. Unlocking the value of RFID. Prod. Oper. Manag. 16 (1), 40–64.
Lee, J., Lapira, E., Bagheri, B., Kao, H.A., 2013. Recent advances and trends in predictive manufacturing systems in big data environment. Manufacturing Letters 1 (1), 38–41.
Lee, J., Maneesavet, R., 1999. Dispatching rail-guided vehicles and scheduling jobs in a flexible manufacturing system. Int. J. Prod. Res. 37 (1), 111–123.
Meng, Q., Lee, D., Cheu, R.L., 2005. Multi objective vehicle routing and scheduling problem with time window constraints in hazardous material transportation. J. Transp. Eng.-ASCE 131 (9), 699–707.
Qu, T., Yang, H.D., Huang, G.Q., Zhang, Y.F., Luo, H., Qin, W., 2012. A case of implementing RFID-based real-time shop-floor material management for household electrical appliance manufactures. J. Intell. Manuf. 23 (6), 2343–2356.
Solomon, M.M., 1987. Algorithms for the vehicle routing and scheduling problems with time window constraints. Oper. Res. 35 (2), 254–265.
Vaidya, O.S., Kumar, S., 2006. Analytic hierarchy process: an overview of applications. Eur. J. Oper. Res. 169 (1), 1–29.
Veeravalli, B., Rajesh, G., Viswanadham, N., 2002. Design and analysis of optimal material distribution policies in flexible manufacturing systems using a single AGV. Int. J. Prod. Res. 40 (12), 2937–2954.
Zhang, J., Ong, S.K., Nee, A.Y.C., 2011a. RFID-assisted assembly guidance system in an augmented reality environment. Int. J. Prod. Res. 49 (13), 3919–3938.
Zhang, Y.F., Huang, G.Q., Qu, T., Ho, K., 2010. Agent-based workflow management for RFID-enabled real-time reconfigurable manufacturing. Int. J. Comput. Integr. Manuf. 23 (2), 101–112.
Zhang, Y.F., Qu, T., Ho, O.K., Huang, G.Q., 2011b. Agent-based Smart Gateway for RFID-enabled real-time wireless manufacturing. Int. J. Prod. Res. 49 (5), 1337–1352.
Zhang, Y.F., Huang, G.Q., Sun, S.D., Yang, T., 2014a. Multi-agent based real-time production scheduling method for radio frequency identification enabled ubiquitous shopfloor environment. Int. J. of Comput. Ind. Eng. 76, 89–97.
Zhang, Y.F., Zhang, G., Wang, J.Q., Sun, S.D., Si, S.B., Yang, T., 2014b. Real-time information capturing and integration framework of the internet of manufacturing things. Int. J. Comput. Integr. Manuf. http://dx.doi.org/10.1080/0951192X.2014.900874.
Zografos, K.G., Androutsopoulos, K.N., 2004. A heuristic algorithm for solving hazardous materials distribution problems. Eur. J. Oper. Res. 152 (2), 507–519.